# FUNCTIONAL MATERIALS FOR BIO-APPLICATIONS

EDITED BY: Laura Maria Vergani, Mario Guagliano and Admir Masic
PUBLISHED IN: Frontiers in Materials and
Frontiers in Bioengineering and Biotechnology

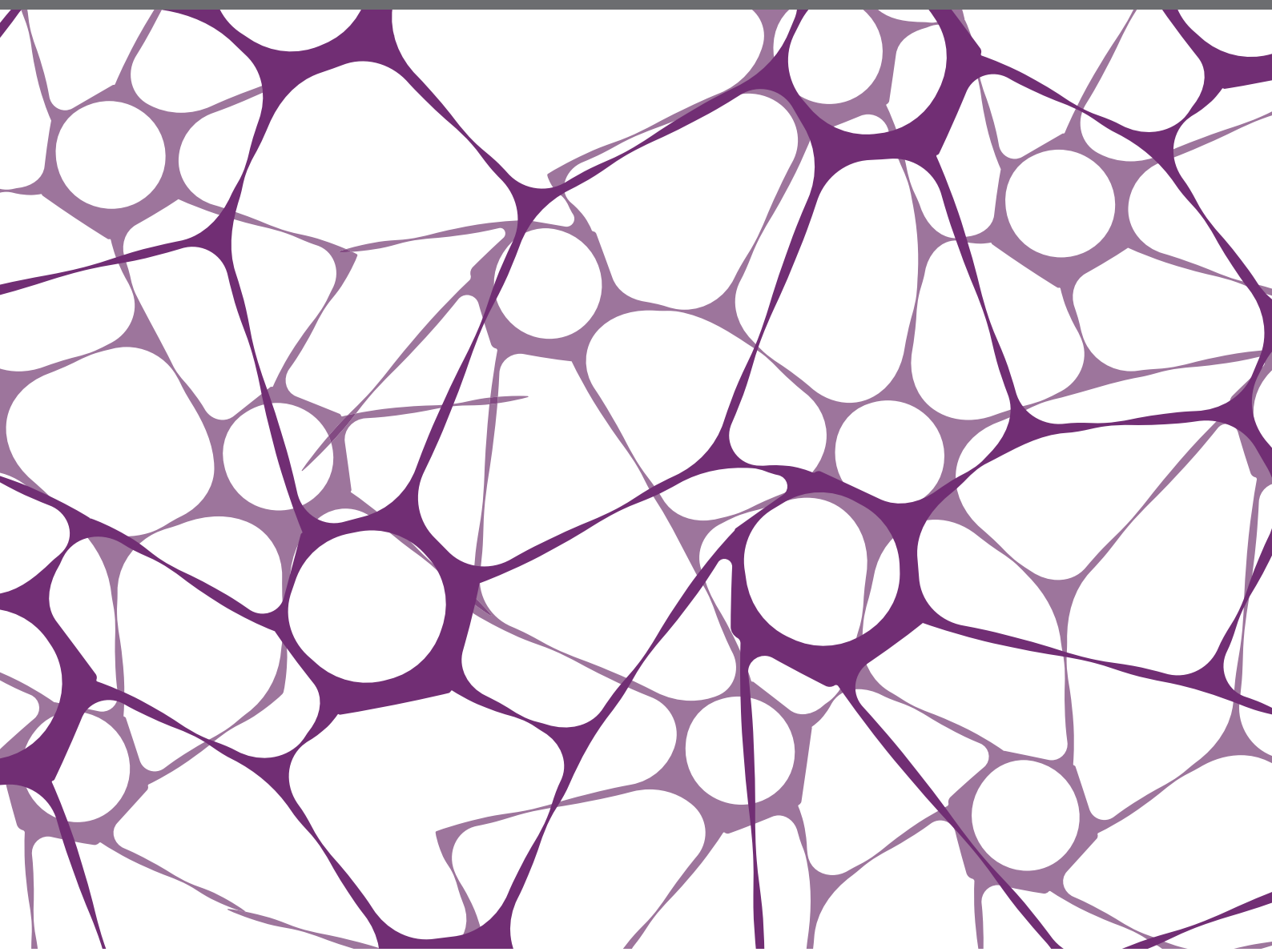

frontiers Research Topics

# frontiers



ISSN 1664-8714
ISBN 978-2-88966-230-2
DOI 10.3389/978-2-88966-230-2

## About Frontiers

Frontiers is more than just an open-access publisher of scholarly articles: it is a pioneering approach to the world of academia, radically improving the way scholarly research is managed. The grand vision of Frontiers is a world where all people have an equal opportunity to seek, share and generate knowledge. Frontiers provides immediate and permanent online open access to all its publications, but this alone is not enough to realize our grand goals.

## Frontiers Journal Series

The Frontiers Journal Series is a multi-tier and interdisciplinary set of open-access, online journals, promising a paradigm shift from the current review, selection and dissemination processes in academic publishing. All Frontiers journals are driven by researchers for researchers; therefore, they constitute a service to the scholarly community. At the same time, the Frontiers Journal Series operates on a revolutionary invention, the tiered publishing system, initially addressing specific communities of scholars, and gradually climbing up to broader public understanding, thus serving the interests of the lay society, too.

## Dedication to Quality

Each Frontiers article is a landmark of the highest quality, thanks to genuinely collaborative interactions between authors and review editors, who include some of the world's best academicians. Research must be certified by peers before entering a stream of knowledge that may eventually reach the public - and shape society; therefore, Frontiers only applies the most rigorous and unbiased reviews.
Frontiers revolutionizes research publishing by freely delivering the most outstanding research, evaluated with no bias from both the academic and social point of view. By applying the most advanced information technologies, Frontiers is catapulting scholarly publishing into a new generation.

## What are Frontiers Research Topics?

Frontiers Research Topics are very popular trademarks of the Frontiers Journals Series: they are collections of at least ten articles, all centered on a particular subject. With their unique mix of varied contributions from Original Research to Review Articles, Frontiers Research Topics unify the most influential researchers, the latest key findings and historical advances in a hot research area! Find out more on how to host your own Frontiers Research Topic or contribute to one as an author by contacting the Frontiers Editorial Office: researchtopics@frontiersin.org

# FUNCTIONAL MATERIALS FOR BIO-APPLICATIONS

Topic Editors:
**Laura Maria Vergani,** Politecnico di Milano, Italy
**Mario Guagliano,** Politecnico di Milano, Italy
**Admir Masic,** Massachusetts Institute of Technology, United States

**Citation:** Vergani, L. M., Guagliano, M., Masic, A., eds. (2020). Functional Materials for Bio-Applications. Lausanne: Frontiers Media SA.
doi: 10.3389/978-2-88966-230-2

# Table of Contents

frontiers in Materials

ORIGINAL RESEARCH
published: 22 May 2019
doi: 10.3389/fmats.2019.00107

# To Improve Total Knee Prostheses Performance Using Three-Phase Ceramic-Based Functionally Graded Biomaterials

*Majid Reza Ayatollahi*[1]*, *Mohammad Hossein Davari*[1], *Hadi Asgharzadeh Shirazi*[1] and *Alireza Asnafi*[2]

[1] Fatigue and Fracture Research Laboratory, Center of Excellence in Experimental Solid Mechanics and Dynamics, School of Mechanical Engineering, Iran University of Science and Technology, Tehran, Iran, [2] Hydro-Aeronautical Research Center, Shiraz University, Shiraz, Iran

One of the common issues that occur after total knee replacement surgery is the aseptic loosening. The problem usually occurs after about 15 years from the surgery. The destructive effects of residual particles due to wear, the stress shielding effect, and micro-movements are the causative factors for this type of loosening. In this research, using the advantages of functionally graded biomaterials (FGBM), it is tried to design a prosthetic system that can reduce the above-mentioned effects. For this purpose, the materials used in the most important part of the prosthesis system, i.e., the femoral part are redesigned so that the bioactivity between the prosthesis and bone, and the stress applied to the adjacent tissues increase simultaneously. In addition, to reduce the effect of wear at contact areas, wear-resistant biocompatible ceramics such as alumina and zirconia are used. The value of stress at the bone-prosthesis interface and adjacent tissues is the most important parameters. Two types of three-phase ceramic-based FGBMs are recommended. The prosthesis with three-phase hydroxyapatite-titanium-zirconia has increased the average stress in the bone tissues around high-risk areas up to 71.8% with respect to a commonly used Cr-Co prosthesis. The result for the prosthesis with three-phase hydroxyapatite-titanium-alumina is up to 65%, respectively. At bone-prosthesis interfaces, an increase of 92% in the stress for both zirconia-based and alumina-based is seen. Briefly, the recommended FGBMs can improve the bone-prosthesis performance in all desired indices.

**Keywords: ceramic-based FGBM, finite element method, stress shielding effect, bone-prosthesis system, orthopedic prosthesis, femoral diseases**

OPEN ACCESS

***Edited by:***
*Laura Maria Vergani, Politecnico di Milano, Italy*

***Reviewed by:***
*Sergey V. Dorozhkin, Independent Researcher, Moscow, Russia*
*Steve Meikle, Independent Researcher, Eastbourne, United Kingdom*

***Correspondence:**
*Majid Reza Ayatollahi*
*m.ayat@iust.ac.ir*

***Specialty section:***
*This article was submitted to Biomaterials, a section of the journal Frontiers in Materials*

***Received:*** *24 February 2019*
***Accepted:*** *24 April 2019*
***Published:*** *22 May 2019*

***Citation:***
*Ayatollahi MR, Davari MH, Shirazi HA and Asnafi A (2019) To Improve Total Knee Prostheses Performance Using Three-Phase Ceramic-Based Functionally Graded Biomaterials. Front. Mater. 6:107. doi: 10.3389/fmats.2019.00107*

## INTRODUCTION

The knee, as one of the complex joints in the body, connects the femur bone to the tibia and fibula. The kneecap patella is another component of this important joint. It is also surrounded by a joint capsule, synovial membrane (containing synovial fluid) and ligaments. Synovial fluid reduces joint friction and also plays a role in feeding the cartilages. In a knee replacement surgery, damaged cartilages, and bones are removed from the joint and replaced by a prosthesis system. Depending on the type of damage, the prosthesis system may include from one to three layers. In a total

replacement of the knee, the lower part of the femur and the upper part of the tibia are connected with the prosthesis.

Due to any reason, the weakening of the connection between the prosthesis and the bone is a factor that in many cases results in a re-surgical procedure. In this case, there is a need to replace the prosthesis system with a newer one that has its own limitations with significantly lower success and more costs. In 2011, Bahraminasab and Jahan (2011) considered the challenge of aseptic loosening as the most important factor after the knee replacement operation. They showed that three factors of excessive wear, stress shielding effect, and development of soft tissue between the prosthesis and the bone are the most important reasons in the occurrence of this phenomenon.

The knee prosthesis has attracted the attention of many researchers, in terms of geometry and material. Saari et al. (2006) studied the geometry of the tibia-prosthesis component and showed how the posterior stabilization leads to bone loss. Wang et al. (2011) investigated the basic geometry of femoral knee prosthesis and considered eight different geometries to obtain the distribution of stress and type of bone destructions in the models. Zietz et al. (2012) focused their studies on the effects of different femoral bone segments on the behavior of bone-prosthesis systems to recommend the best model in terms of reduction in stress shielding effect.

As far as geometry is concerned for prostheses, there are numerous articles on the types and properties of the prostheses materials. Long and Rack (1998) focused on the comparison of Titanium alloy to stainless steel with a concentration on fatigue and wear and examined the advantages of Titanium alloys in this respect. Peterson et al. (1988) compared the behaviors of Titanium and Cobalt-Chromium-Molybdenum alloys in terms of wear for the femoral part of the knee prosthesis. McEwen et al. studied the effect of material, local movement and prosthesis geometry on the wear of an ultra-high molecular weight polyethylene (UHMWPE) prosthesis system. They showed that the backside motion contributes to an overall rate of UHMWPE wear in the system.

Due to the fact that several materials with different and sometimes contradictory properties can be used in the structure of functionally graded materials, these materials are recommended as suitable alternatives for the design of new generation of the knee prostheses. Also, in these materials, the properties between the components vary continuously; so, there is no need to worry about the disadvantages of composite laminated materials. For example, the prosthesis can be designed to reduce the effects of loosening, including wear, micro-motion and the effect of shielding stress simultaneously. At contact bearing surfaces, wear-resistant materials should be used while in areas close to bone tissues, materials with less elastic modulus are recommended to reduce the effect of shielding stress. Finally, at direct contact areas of the prosthesis and bone, a bioactive material to reduce the micro-motions is suggested. The use of functionally graded biomaterials in medical prosthetics has been considered in recent researches (Sadollah and Bahreininejad, 2011; Gong et al., 2012; Enab and Bondok, 2013). Some works on the use of these materials in knee prostheses have also been reported in the literature (Bahraminasab et al., 2013a,b); however, the bioactivity that prevents micro-motions, the reduction in the effects of shielding stress, and establishing strength have not been sufficiently taken into consideration.

In this research, two types of ceramic-based prosthesis systems using three-phase functionally graded biomaterials are proposed by considering the effects of stress shielding, wear resistance, and bioactivity simultaneously. Also, the required strength and toughness are also investigated. The behavior and performance of the proposed prosthesis systems and the ones commonly used in previous works are compared to each other.

# MATERIALS AND METHODS

## Mechanical Requirements of FGBM Prostheses

The mechanical strength of an artificial knee can effect both the performance and failure of the prosthesis system. If the osseointegration between the prosthesis and bone does not form well, soft fibrous tissues are formed in the connection, results in more relative movement between the implants and the bone. Initially, this causes increased pain in the patient and after a certain period, the implant loses its effectiveness and the need for implant replacement is inevitable (Geetha et al., 2009). It should be noted that the high strength of the prosthesis with the low elastic modulus is of great importance (Wang, 1996; Long and Rack, 1998). A high difference between the modulus of the implant's elasticity and the surrounding bone can contribute to the effect of shielding stress. This phenomenon may lead to a weakening of the bone and its connections to the implant and, consequently, the loosening of the prosthesis system. Additionally, the low elastic modulus means higher flexibility and damping capacity which directly increases the absorption energy of the impact and reduces the stress between the bones and the knee prosthesis. Therefore, the modulus of implant material elasticity is a major factor for the selection of materials for knee replacement prosthesis.

Low resistance to wear or high friction coefficient can also cause loosening in the implants (Ramsden et al., 2007). In addition, the remaining particles of wear are biologically active and may produce a severe inflammatory reaction. This may damage the immune supporting bone. Friction also increases the possibility of corrosion.

Another important requirement for orthopedic biomaterials is biocompatibility. Biocompatibility refers to the ability of prosthesis to communicate with the living tissue of the surrounding bones. Biocompatibility is not just about the implications of the implant and the surrounding tissues, and it is important to check its effects on the rest of the organic system (Navarro et al., 2008; Williams, 2008).

The osseointegration process is another major orthopedic necessity related to the bone improvement process. In some cases, for example, due to relative micro-movements, the implant cannot properly bind to the surrounding bone and tissues. This leads to the formation of fibrous tissues around the implant, and ultimately accelerates the loosening process (Viceconti et al., 2000).

In addition to the above, the corrosion which is an important factor in the field of biomaterials, and the issues related to the manufacturing process of biomaterials such as ductility, toughness, etc. should also be taken into account.

## A Discussion on Prosthesis Biomaterials

Titanium alloys are among the most popular orthopedic materials. Titanium alloys have excellent properties such as high strength, low density, good corrosion resistance, complete non-toxicity to the body, and moderate elastic modulus suitable for planting in the body (Nag et al., 2009). Titanium and its alloys can provide a relatively strong bond to the bone, which greatly improves the fixity of the implant and significantly prevents micro-movement. The elastic modulus of titanium alloys is about 110 GPa, less than steel and cobalt-chromium alloys. Therefore, a titanium implant is expected to reduce the shielding stress effect compared to a more elastic modulus material; however, the occurrence of this phenomenon is still possible due to the large difference between the modulus of elasticity of titanium alloys and human bones. Unfortunately, these alloys have a low wear resistance (one of the first factors in aseptic loosening) due to relative movements at bearing surfaces between themselves and other metals. Due to oxidation of titanium and the low adhesion of the oxidized layer, some particles are removed from the material and remain on the bearing surfaces. Based on experimental results, it has been shown that for the relative motion between UHMWPE and Ti-6Al-4V, the wear rate of both metal and polymer is much higher than that of stainless steel or cobalt-chromium-molybdenum alloy. In addition, the residual particles of wear from titanium alloys cause side effects like tissue discoloration indicative of metallosis (Nasser et al., 1990). Therefore, the use of titanium in areas with the high potential of wear i.e., knee and hip joints is limited (Nag et al., 2009). Also, there is concern about the release of aluminum and vanadium ions in titanium alloys that may lead to health problems (Okazaki and Gotoh, 2005; Navarro et al., 2008; Geetha et al., 2009).

Alumina ($Al_2O_3$) ceramics belongs to the group of oxide ceramics and polycrystalline materials with properties including high stiffness, good stability, high oxidation ability, very low friction coefficient (high wear resistance) and good biocompatibility (Hannouche et al., 2005). The earliest clinical use of pure ceramics was seen in 1970 for the hip prostheses (Boutin, 1971). It has been expected that the use of these materials for knee replacement can essentially improve in two aspects to minimize bone osteolysis: greater stability in biocompatibility and reduction of residual particles due to wear. Therefore, based on the results of the knee simulator, it was attempted to use a combination of alumina ceramics and UHMWPE as an alternative for knee prostheses (Heimke et al., 2002; Oonishi et al., 2006). The serious problem if the alumina ceramics is used alone is its high modulus of elasticity (350 GPa) which resulted in the effect of shielding stress and the aseptic loosening in the bone-prosthesis system (Boutin, 1971).

Unfortunately, alumina is not bioactive and cannot directly create a level of bone and implant interface, which results in micro-movements and thus aseptic loosening. It also has a low failure toughness than metal materials used in orthopedic applications. It shows brittle behavior i.e., no significant deformation is seen to fracture (Hannouche et al., 2003). To overcome the limitations of the mechanical properties of alumina, zirconia ($ZrO_2$) was introduced. High strength, high toughness (about twice the alumina) and higher flexural strength (500-1,000 MPa) can be attributed to this ceramic. However, in contrast to alumina, zirconia has an unstable and multifaceted crystalline structure including monoclinic, tetragonal, and cubic. Therefore, phase transfer can occur from a crystalline structure to another, especially from the tetragonal phase to monoclinic. Phase transformation with shape and volume changes makes the material susceptible to cracking (Bal et al., 2006).

## The Need of Functionally Graded Change of Properties

For optimal use of material properties, every advantage and every interest should be used in the right position and situation. To satisfy all conditions, a three-phase functionally graded biomaterial is proposed. At the site of bone bonding, hydroxyapatite (HA) is recommended for maximum biocompatibility. At bearing surfaces, alumina or zirconia ceramics is suggested to have maximum wear resistance. Titanium alloys are also offered in the middle of the material to provide both required strength and toughness. **Figure 1** shows a schematic distribution of properties in a cross section of the material. The properties of materials used in this study to propose new FGBMs can be seen in **Table 1**. It should be noted that due to the almost same Poisson coefficient of materials used in the design of the FGBM, this coefficient is considered 0.3 in all simulations.

The functions of how to change the properties including the modulus of elasticity and the Poisson coefficient are:

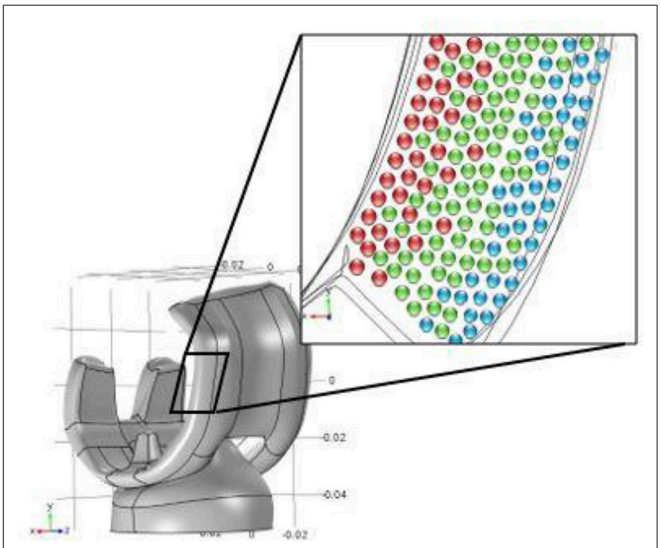


**FIGURE 1 |** The schematic of material properties distribution in a cross section of the functionally graded biomaterial; red spheres: HA, green spheres: Ti, blue spheres: Al2O3 or ZrO2.

**TABLE 1 |** The properties of materials used in this study.

| Material | | Young's modulus (GPa) | Poisson's ratio |
|---|---|---|---|
| HA (Bahraminasab et al., 2013b) | | 48 | 0.30 |
| Ti (Hedia, 2005) | | 116 | 0.32 |
| Zirconia (Bahraminasab et al., 2013a) | | 175 | 0.30 |
| Bone (Hedia, 2005) | Cancellous | 0.4 | 0.30 |
| | Cortical | 16 | |
| Alumina (Bahraminasab et al., 2013a) | | 365 | 0.30 |
| UHMPE (Hedia, 2005) | | 0.9 | 0.30 |

$$\begin{cases} E = E_0\left\{1 + n(r/b)^{\beta}\right\} \\ v = v_0\left\{1 + n(r/b)^{\beta}\right\} \end{cases} \quad (1)$$

$$\begin{cases} E|r_{in} = E_1 \\ E|r_{middle} = E_2 \\ E|r_{out} = E3 \end{cases} \quad \begin{cases} v|v_{in} = v_{HA} \\ v|r_{middle} = V_{Ti} \\ v|r_{out} = v_{zirconia} \end{cases}$$

Where

$$\begin{cases} n = \frac{E_{zirconia}}{E_{HA}} - 1 \\ \beta = \frac{\ln((E_{Ti} - E_{HA})/(E_{zirconia} - E_{HA}))}{\ln(r_{middle}/r_{in})} \\ v = 0.3 \end{cases} \quad (2)$$

## Finite Element Modeling

In a finite element modeling, considering the desired function and selecting the material for each phase, a 3D model of the knee prosthesis and surrounding bone tissue was prepared and analyzed to obtain the distribution of stress and deformation in the system (see **Figure 2**).

The element type in the 3-D model is tetrahedron. The number of elements after the sensitivity analysis was 82,387 elements. It should be noted that the method of function assignment to a model is possible in two ways:

1- Partitioning the model into a number of layers (30 to 40 layers) proportional to the direction of changing the properties in the model and assigning the properties of the material with the approximation of its value from the desired function, or
2- Applying the function in the matrix of the properties of the material.

In this research, we try to use the function directly to assign material properties using the COMSOL Multiphysics5.2 software. The results of each route were only reported after a mesh study was done so that we ensured about the correctness of the outcomes and the convergence phenomenon.

## Load and Boundary Conditions

The basis of knee and knee prosthesis modeling is based on dynamic analysis and a variety of created conditions caused by daily activities. In these activities, such as walking, running, climbing, etc. modeling the force applied to different points of the knee and prosthesis has a lot of complexity. This article focuses on the effect of changing the properties of the prosthesis on the surrounding bones, which can be generally examined for different loading conditions. In this research, the maximum value of the force at most dominant gait i.e., the walking is selected as a static load and then applied to the model. The amount of static load was considered to be 3110N (Bergmann et al., 2014) along the axial direction of the femur. This amount of load is reported in the literature for walking gait (Bergmann et al., 2014). The displacement of the lower surface of the tibia from the knee prosthesis is fixed in direction of the force applied, and in other directions are bounded by a point. Two contact constraints were defined; the first contact is associated with the area of the bone and prosthetic contact area, and the second contact is related to the prosthetic contact area and the tibia component. The contact between the prosthesis and the bone should be a constraint without any displacement; otherwise, the prosthesis is removed from the bone, which is not the basis of this research. Therefore, this constraint is considered as an all-inclusive fully fixed constraint between bone and prosthesis elements. The contact between the prosthesis and the tibia component is considered non-frictional. In fact, because of the absence of a specific friction coefficient in that environment between the prosthesis and the tibia component, which is subject to a variety of factors, the exact modeling has a particular complexity.

# RESULTS

The values of Von Mises stress are evaluated along 12 directions in the prosthesis-bone system regarding a 3D model (see **Figures 3A,B** for more details). The center point is the midpoint of the prosthetic along-side its arms, with paths of 15, 20, 30 mm radius and at angles of 45, 135, 225, and 315 relative to the horizon line, and are numbered according to the **Figure 3**.

According to reports in the literature (Van Loon et al., 2001), the most damaged areas due to stress shielding effect are along directions 9 and 10; after that 5 and 6 and finally 1 and 2 (see **Figures 3B,C**). Here, the results are obtained in these directions for the commonly used cobalt-chromium prosthesis, also; alumina and zirconia-based three-phase FG biomaterials. **Tables 2**, **3** demonstrate the average and bone-prosthesis interface stresses along assumed paths at Cr-Co and alumina/zirconia-based proposed FG biomaterials. In **Figure 4**, one can follow the Von Mises stress vs. proximal distance from the interface in response to all paths for both Cr-Co and alumina-based proposed FG biomaterial. **Figure 5** present the same results reported previously in **Figure 4** except that the zirconia-based FGBM is used. Qualitatively, the same similarities are seen but there are some quantitative differences. It is again to be noted that the results presented in **Figures 4**, **5** and **Tables 2–4** are based on the paths considered in **Figures 3A,B**.

# DISCUSSION

The Von Mises stress is considered as an indicator to be obtained in both the prosthesis and surrounding bones in our simulations. This measure is related to other factors such as wear, strength,

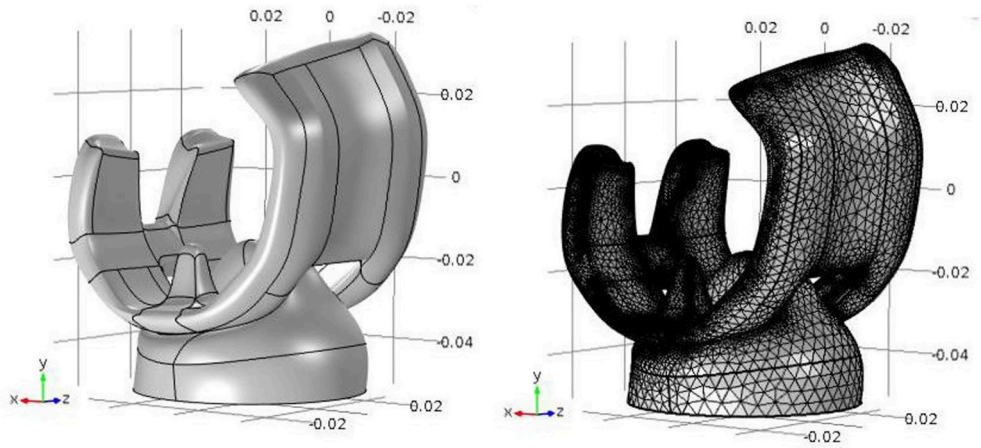


**FIGURE 2 |** The geometry **(left)** and the generated mesh **(right)** for finite element analysis.

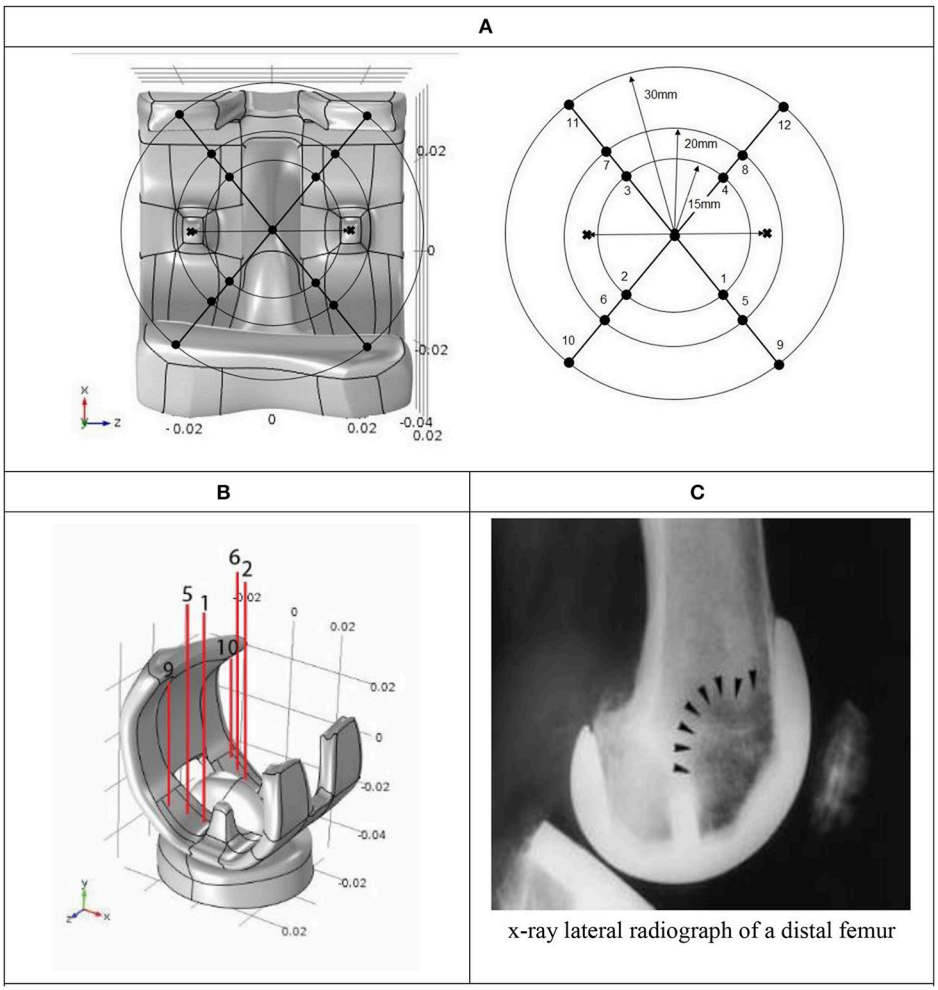


**FIGURE 3 | (A)** Twelve assumed directions in the prosthesis-bone system; **(B)** The most important directions in 3-D model; **(C)** The most damaged areas due to stress shielding effect based on lateral radiograph of a distal femur showing distal anterior femoral osteopenia behind the femoral component (arrowheads) (Van Loon et al., 2001).

and shielding stress effect; so, one can use it to have an almost precise look at the global and local behavior and performance of the prosthesis system. To show the performance of the recommended FGBM prosthesis, three comparisons were made; the first two are between the commonly used cobalt-chromium prosthesis with the three-phase FG biomaterials proposed in

**TABLE 2 |** Average and bone-prosthesis interface stresses along assumed paths at Cr-Co and alumina-based proposed FG biomaterial [PoI: Percent of increase (%)].

| | Average stress | | | Stress at the bone-prosthesis interface | | |
|---|---|---|---|---|---|---|
| **Paths** | **FGBM ($Al_2O_3$-Ti-HA) (MPa)** | **Cr-Co (MPa)** | **PoI** | **FGBM ($Al_2O_3$-Ti-HA) (MPa)** | **Cr-Co (MPa)** | **PoI** |
| 1 | 0.760 | 0.677 | 12.33 | 0.897 | 0.481 | 86.5 |
| 2 | 0.767 | 0.692 | 10.82 | 0.859 | 0.466 | 84.4 |
| 3 | 0.899 | 0.808 | 11.32 | 0.485 | 0.254 | 90.9 |
| 4 | 0.899 | 0.805 | 10.39 | 0.399 | 0.223 | 79 |
| 5 | 0.739 | 0.673 | 9.76 | 0.651 | 0.330 | 97.3 |
| 6 | 0.760 | 0.709 | 7.32 | 0.611 | 0.315 | 94 |
| 7 | 0.902 | 0.825 | 9.38 | 0.518 | 0.308 | 68.2 |
| 8 | 0.895 | 0.823 | 8.70 | 0.466 | 0.287 | 62.5 |
| 9 | 0.365 | 0.269 | 35.76 | 0.470 | 0.244 | 92.8 |
| 10 | 0.361 | 0.218 | 65.55 | 0.428 | 0.224 | 91.1 |
| 11 | 1.023 | 1.023 | 0.02 | 0.475 | 0.323 | 47 |
| 12 | 1.019 | 1.017 | 0.20 | 0.457 | 0.308 | 48.4 |

**TABLE 3 |** Average and bone-prosthesis interface stresses along assumed paths at Cr-Co and zirconia-based proposed FG biomaterial [PoI: Percent of increase (%)].

| | Average stress | | | Stress at the bone-prosthesis interface | | |
|---|---|---|---|---|---|---|
| **Paths** | **FGBM ($ZrO_2$-Ti-HA) (MPa)** | **Cr-Co (MPa)** | **PoI** | **FGBM ($ZrO_2$-Ti-HA) (MPa)** | **Cr-Co (MPa)** | **PoI** |
| 1 | 0.774 | 0.677 | 14.3 | 0.911 | 0.481 | 89.5 |
| 2 | 0.779 | 0.692 | 12.4 | 0.869 | 0.466 | 86.5 |
| 3 | 0.943 | 0.808 | 15.6 | 0.59 | 0.254 | 132.4 |
| 4 | 0.918 | 0.805 | 14 | 0.488 | 0.223 | 118.8 |
| 5 | 0.748 | 0.673 | 11 | 0.651 | 0.33 | 97.3 |
| 6 | 0.767 | 0.709 | 8.3 | 0.608 | 0.315 | 93 |
| 7 | 0.935 | 0.825 | 13.4 | 0.661 | 0.308 | 114.7 |
| 8 | 0.924 | 0.823 | 12.2 | 0.592 | 0.287 | 106.4 |
| 9 | 0.379 | 0.269 | 41 | 0.469 | 0.244 | 92.2 |
| 10 | 0.374 | 0.218 | 71.8 | 0.429 | 0.224 | 91.6 |
| 11 | 1.025 | 1.023 | 0.2 | 0.552 | 0.323 | 71 |
| 12 | 1.019 | 1.017 | 0.24 | 0.524 | 0.308 | 70.3 |

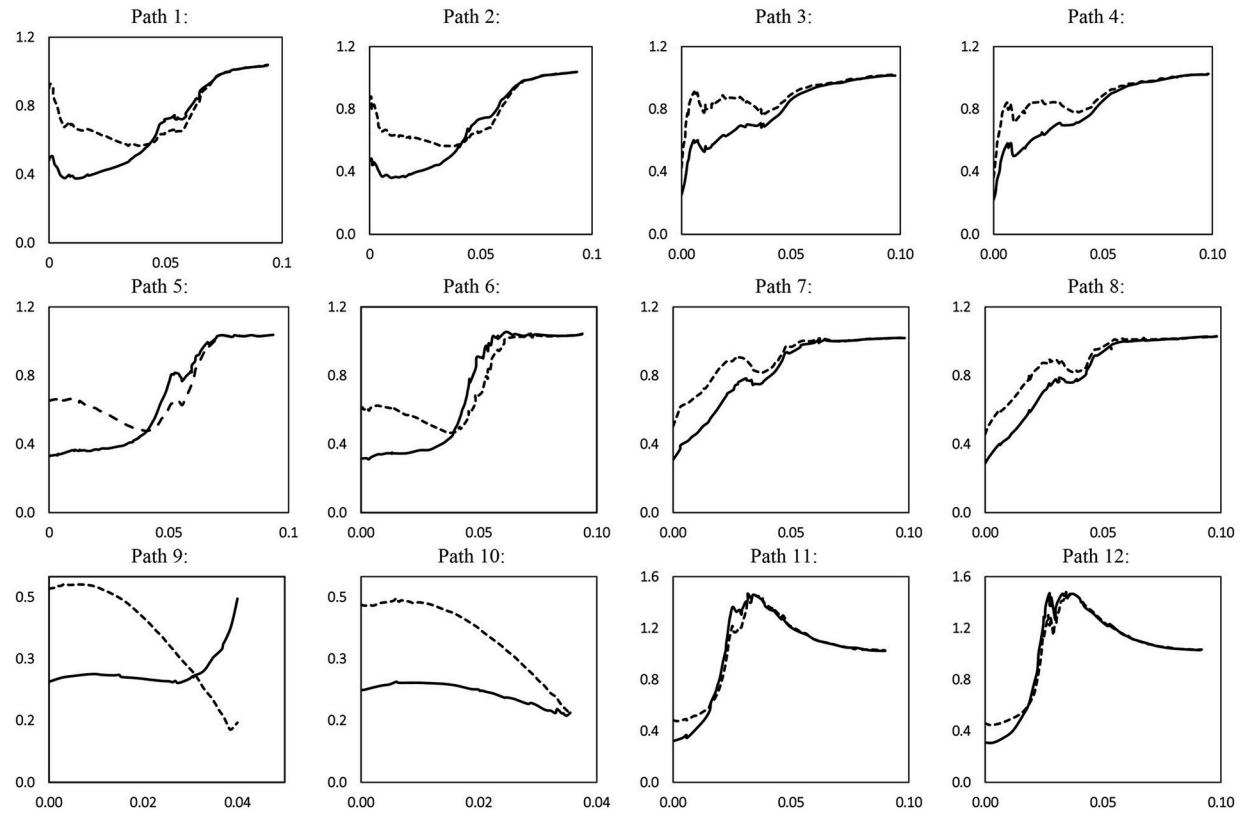


**FIGURE 4 |** Von Mises stress (MPa) vs. proximal distance from the interface (m) in response to the all paths for both Cr-Co (solid line) and alumina-based proposed FG biomaterial (dashed line).

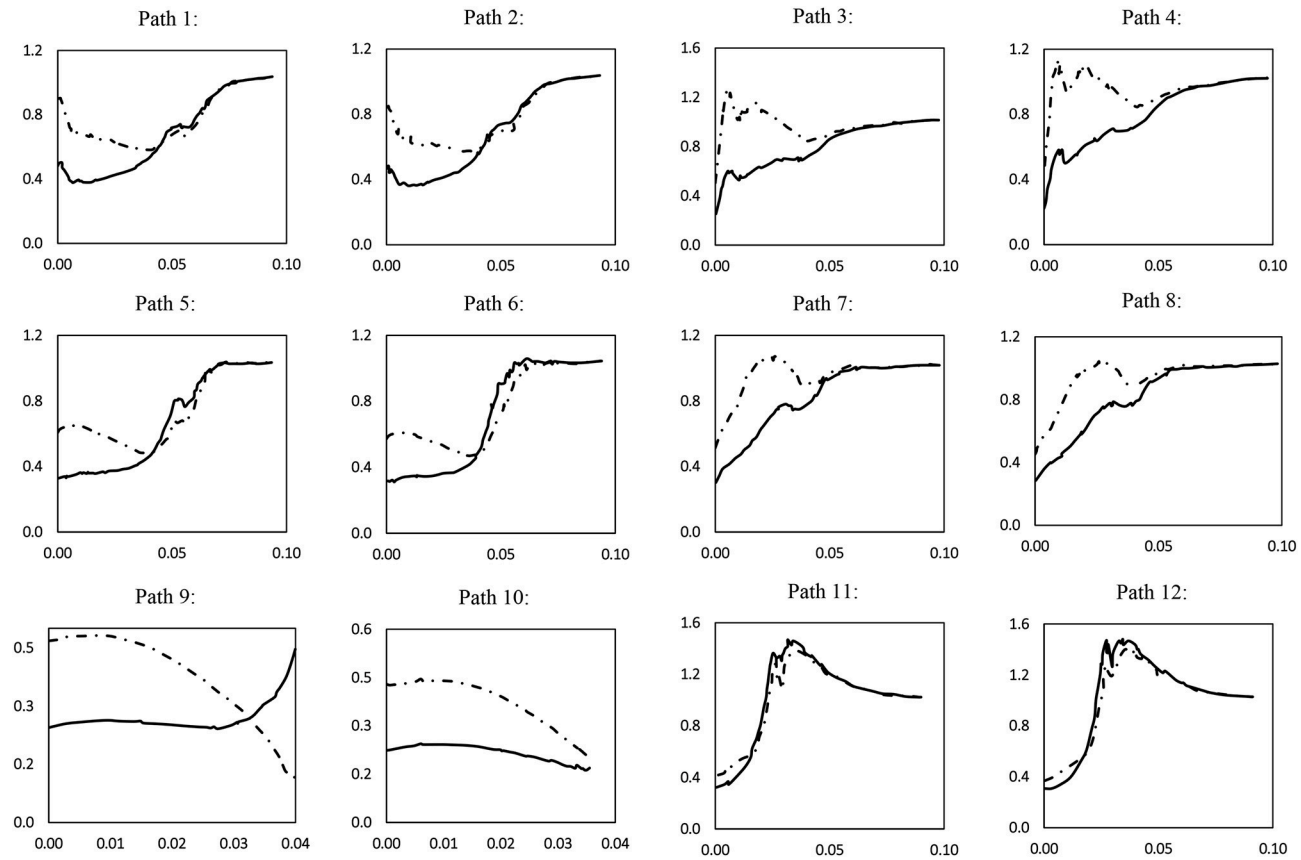


**FIGURE 5 |** Von Mises stress (MPa) vs. proximal distance from the interface (m) in response to the all paths for both Cr-Co (solid line) and zirconia-based proposed FG biomaterial (dashed line).

**TABLE 4 |** Average and bone-prosthesis interface stresses along assumed paths at alumina-based and zirconia-based proposed FG biomaterials [PoI: Percent of increase (%)].

| | Average stress | | | Stress at the bone-prosthesis interface | | |
|---|---|---|---|---|---|---|
| **Paths** | **$ZrO_2$-based FGBM (MPa)** | **$Al_2O_3$-based FGBM (MPa)** | **PoI** | **$ZrO_2$-based FGBM (MPa)** | **$Al_2O_3$-based FGBM (MPa)** | **PoI** |
| 1 | 14.3 | 12.33 | 16.0 | 89.5 | 86.5 | 3.5 |
| 2 | 12.4 | 10.82 | 14.6 | 86.5 | 84.4 | 2.5 |
| 3 | 15.6 | 11.32 | 37.8 | 132.4 | 90.9 | 45.7 |
| 4 | 14.0 | 10.39 | 34.7 | 118.8 | 79.0 | 50.4 |
| 5 | 11.0 | 9.76 | 12.7 | 97.3 | 97.3 | 0.0 |
| 6 | 8.30 | 7.32 | 13.4 | 93.0 | 94.0 | −1.1 |
| 7 | 13.4 | 9.38 | 42.9 | 114.7 | 68.2 | 68.2 |
| 8 | 12.2 | 8.70 | 40.2 | 106.4 | 62.5 | 70.2 |
| 9 | 41.0 | 35.76 | 14.7 | 92.2 | 92.8 | −0.6 |
| 10 | 71.8 | 65.55 | 9.5 | 91.6 | 91.1 | 0.5 |
| 11 | 0.20 | 0.18 | 10.0 | 71.0 | 47.0 | 51.1 |
| 12 | 0.24 | 0.20 | 20.0 | 70.3 | 48.4 | 45.2 |

this study, one is based on alumina and the other on zirconia. The third comparison was also made between the two proposed FG biomaterials.

## Three-Phase Alumina-Based FG Biomaterial vs. Cr-Co One

According to the results presented in **Table 2**, for the three-phase FG biomaterial (alumina-titanium-hydroxyapatite), all routes in the design of FGM have shown moderate stress in bone tissue, which means a reduction in stress shielding effect. The paths on which the stress values were calculated are the same as those shown in **Figures 3A,B**. Reference (Van Loon et al., 2001) indicated that paths 9 and 10 played a more important role in the shielding stress phenomenon; thus, the study of these two paths is more important. According to **Table 2**, the proposed material has been able to increase the average stress by 65.55% and 35.76% in these pathways, which reduces the effect of shielding stress and, consequently, aseptic loosening. In major paths such as 1, 2, 5 and 6, and most of the paths, stress in the bone has increased. Only on the 11th and 12th routes, little changes are observed. In fact, the change in properties of the prosthesis has not had a significant change in the stress of these two paths, which can be concluded

that stress in these two paths is independent of the properties of the prosthetic material.

In **Figure 4**, it can be noted that the stress in the bone-prosthesis interfaces has increased significantly. The percent values of increase at interfaces along each path are listed in **Table 2**. As previously indicated, moderate values of stress at bone- prosthesis interfaces are important to reduce the shielding stress effect and consequently the aseptic loosening. The maximum increase occurred on route 9, with the lowest increase in path 11. Using this FG biomaterial, the maximum change in the stresses is seen at the bone-prosthesis interfaces which are quite desirable and valuable.

### Three-Phase Zirconia-Based FG Biomaterial vs. Cr-Co One

In the same way previously indicated in section Three-Phase Alumina-Based FG Biomaterial vs. Cr-Co One, the average stresses along the assumed paths together with the bone-prosthesis interface stresses are obtained for a zirconia-based FG biomaterial and compared to the ones of the commonly used cobalt-chromium prosthesis. Same qualitative similarities are seen while the quantitative values are different. There is again a significant increase in stresses in all directions except the average stresses along paths 11 and 12. More important paths 9 and 10 show an average increase of 41 and 71.8%, respectively. The values of stress are greater in comparison with the amount in the same path for the alumina-based FGBM. One can follow the values of average and interface stresses for this case in **Table 3**.

### Alumina-Based vs. Zirconia-Based FG Biomaterial

In this section, a comparison is done between two proposed FG biomaterials. Based on the results listed in **Table 4**, Zirconia-based FG biomaterial has a better performance in terms of stress shielding effect reduction in the bone tissues. It is due to the fact that the Young modulus of zirconia which is equal to 175 GPa is much less than the modulus of alumina which is equal to 365 GPa. The greatest increase in terms of both average stress and interface one occurred in routes 7 and 8. Along important paths 9 and 10, zirconia-based FG biomaterial shows better performance in terms of average stress whereas no significant change in terms of stress in the interface is seen for these two paths. As shown in **Table 4**, the stress values in bone tissues for all paths are higher when the zirconia-based FG biomaterial is employed. The largest differences are seen for paths 7 and 8.

## CONCLUSION

To improve the performance of the bone-prosthesis system and prevent the aseptic loosening in a total knee replacement surgery, two types of ceramic-based functionally graded biomaterials were proposed in this article. To have a right investigation, 12 directions in a 3D finite element model of the prosthesis system were considered. The Von Mises stress values along the paths, as an important indicator, were obtained for proposed materials and then compared to commonly-used Cr-Co prosthesis. Specifically, the average values and the stress at the bone-prosthesis interfaces along the paths were compared to each other. Along all the paths, both the alumina-based and zirconia-based FG biomaterials showed significantly better performance. The average stress when the zirconia-based FGBM was used was higher than that of alumina-based one. Generally, both recommended FGBMs can reduce the effect of shielding stress, while the zirconia-based one shows better performance in this respect.

## DATA AVAILABILITY

The datasets for this manuscript are not publicly available because There is no public link related to this data but the raw data supporting the conclusions of this manuscript will be made available by the authors, without undue reservation, to any qualified researcher. Requests to access the datasets should be directed to Pr. MA (m.ayat@iust.ac.ir).

## AUTHOR CONTRIBUTIONS

MRA gave the idea, interpreted the results, and checked the final version of the article. MHD surveyed the literature in this respect and prepared the history of the research and the first version of the article and also helped derive and solve the equations. HAS derived and solved the equations and drew the figures in corresponding software. AA wrote the main text of the article together with the abstract and conclusion and investigated the correctness of the equations and text of the article.

## REFERENCES


Bahraminasab, M., and Jahan, A. (2011). Material selection for femoral component of total knee replacement using comprehensive VIKOR. *Mater. Design* 32, 4471–4477. doi: 10.1016/j.matdes.2011.03.046

Bahraminasab, M., Sahari, B., Edwards, K. L., Farahmand, F., and Arumugam, M. (2013a). Aseptic loosening of femoral components–materials engineering and design considerations. *Mater. Design.* 44, 155–163. doi: 10.1016/j.matdes.2012.07.066

Bahraminasab, M., Sahari, B., Edwards, K. L., Farahmand, F., and Hong, T. (2013b). Material tailoring of the femoral component in a total knee replacement to reduce the problem of aseptic loosening. *Mater. Design.* 52, 441–451. doi: 10.1016/j.matdes.2013.05.066

Bal, B. S., Garino, J., Ries, M., and Rahaman, M. N. (2006). Ceramic materials in total joint arthroplasty. *Semi. Arthroplasty 17*, 94–101. doi: 10.1053/j.sart.2006.09.002

Bergmann, G., Bender, A., Graichen, F., Dymke, J., Rohlmann, A., Trepczynski, A., et al. (2014). Standardized loads acting in knee implants. *PLoS ONE.* 9:e86035. doi: 10.1371/journal.pone.0086035

Boutin, P. (1971). Alumina and its use in surgery of the hip.(Experimental study). *La Presse. Med.* 79, 639.

Enab, T. A., and Bondok, N. E. (2013). Material selection in the design of the tibia tray component of cemented artificial knee using finite element method. *Mater. Design.* 44, 454–460. doi: 10.1016/j.matdes.2012.08.017

Geetha, M., Singh, A., Asokamani, R., and Gogia, A. (2009). Ti based biomaterials, the ultimate choice for orthopaedic implants–a review. *Prog. Mater. Sci.* 54, 397–425. doi: 10.1016/j.pmatsci.2008.06.004

Gong, H., Wu, W., Fang, J., Dong, X., Zhao, M., and Guo, T. (2012). Effects of materials of cementless femoral stem on the functional adaptation of bone. *J. Bionic. Eng.* 9, 66–74. doi: 10.1016/S1672-6529(11)60098-X

Hannouche, D., Hamadouche, M., Nizard, R., Bizot, P., Meunier, A., and Sedel, L. (2005). Ceramics in total hip replacement. *Clin. Orthop. Relat. Res.* 430, 62–71. doi: 10.1097/01.blo.0000149996.91974.83

Hannouche, D., Nich, C., Bizot, P., Meunier, A., Nizard, R., and Sedel, L. (2003). Fractures of ceramic bearings: history and present status. *Clin. Orthop. Relat. Res.* 417, 19–26. doi: 10.1097/01.blo.0000096806.78689.50

Hedia, H. (2005). Comparison of one-dimensional and two-dimensional functionally graded materials for the backing shell of the cemented acetabular cup. *J. Biomed. Mater. Res. Part B: Appl. Biomater.* 74, 732–739. doi: 10.1002/jbm.b.30258

Heimke, G., Leyen, S., and Willmann, G. (2002). Knee arthoplasty: recently developed ceramics offer new solutions. *Biomaterials* 23, 1539–1551. doi: 10.1016/S0142-9612(01)00262-9

Long, M., and Rack, H. J. (1998). Titanium alloys in total joint replacement—a materials science perspective. *Biomaterials* 19, 1621–1639. doi: 10.1016/S0142-9612(97)00146-4

Nag, S., Samuel, S., Puthucode, A., and Banerjee, R. (2009). Characterization of novel borides in Ti–Nb–Zr–Ta+ 2B metal-matrix composites. *Mater. Charac.* 60, 106–113. doi: 10.1016/j.matchar.2008.07.011

Nasser, S., Campbell, P. A., Kilgus, D., Kossovsky, N., and Amstutz, H. C. (1990). Cementless total joint arthroplasty prostheses with titanium-alloy articular surfaces: a human retrieval analysis. *Clin. Orthop. Relat. Res.* 261, 171–185. doi: 10.1097/00003086-199012000-00020

Navarro, M., Michiardi, A., Castano, O., and Planell, J. (2008). Biomaterials in orthopaedics. *J. R. Soc. Interf.* 5, 1137–1158. doi: 10.1098/rsif.2008.0151

Okazaki, Y., and Gotoh, E. (2005). Comparison of metal release from various metallic biomaterials *in vitro*. *Biomaterials* 26, 11–21. doi: 10.1016/j.biomaterials.2004.02.005

Oonishi, H., Kim, S. C., Kyomoto, M., Iwamoto, M., and Ueno, M. (2006). "PE wear in ceramic/PE bearing surface in total knee arthroplasty: clinical experiences of more than 24 years," in *Bioceramics and Alternative Bearings in Joint Arthroplasty* (Steinkopff), 101–110.

Peterson, C., Hillberry, B., and Heck, D. (1988). Component wear of total knee prostheses using Ti-6Al-4V, titanium nitride coated Ti-6Al-4V, and cobalt-chromium-molybdenum femoral components. *J. Biomed. Mater. Res. Part A.* 22, 887–903. doi: 10.1002/jbm.820221005

Ramsden, J., J., Allen, D., M., Stephenson, D., J., et al. (2007). The design and manufacture of biomedical surfaces. *CIRP Ann. Manuf. Technol.* 56, 687–711,. doi: 10.1016/j.cirp.2007.10.001

Saari, T., Uvehammer, J., Carlsson, L. V., Regnér, L., and Kärrholm, J. (2006). Posterior stabilized component increased femoral bone loss after total knee replacement. 5-year follow-up of 47 knees using dual energy X-ray absorptiometry. *The Knee* 13, 435–439. doi: 10.1016/j.knee.2006.08.002

Sadollah, A., and Bahreininejad, A. (2011). Optimum gradient material for a functionally graded dental implant using metaheuristic algorithms. *J. Mech. Behav. Biomed. Mater.* 4, 1384–1395. doi: 10.1016/j.jmbbm.2011.05.009

Van Loon, C., Oyen, W., de Waal Malefijt, M., and Verdonschot, N. (2001). Distal femoral bone mineral density after total knee arthroplasty: a comparison with general bone mineral density. *Arch. Orthop. Trauma Surg.* 121, 282–285. doi: 10.1007/s004020000232

Viceconti, M., Muccini, R., Bernakiewicz, M., Baleani, M., and Cristofolini, L. (2000). Large-sliding contact elements accurately predict levels of bone–implant micromotion relevant to osseointegration. *J. Biomech.* 33, 1611–1618. doi: 10.1016/S0021-9290(00)00140-8

Wang, C. J., Shi, J., F., Morgan, C., and Mynors, D. J. (2011). Design and simulation of a femoral component peg in total knee replacement. *Key Eng. Mater.* 450, 111–114. doi: 10.4028/www.scientific.net/KEM.450.111

Wang, K. (1996). The use of titanium for medical applications in the USA. *Mater. Sci. Eng. A.* 213, 134–137. doi: 10.1016/0921-5093(96)10243-4

Williams, D. F. (2008). On the mechanisms of biocompatibility. *Biomaterials* 29, 2941–2953. doi: 10.1016/j.biomaterials.2008.04.023

Zietz, C., Bergschmidt, P., Fritsche, A., Kluess, D., Mittelmeier, W., and Bader, R. (2012). Comparison of cross-sections of different femoral components for revision total knee replacement. *J. Orthop. Surg.* 20, 32–36. doi: 10.1177/230949901202000107

**Conflict of Interest Statement:** The authors declare that the research was conducted in the absence of any commercial or financial relationships that could be construed as a potential conflict of interest.

frontiers in Materials

REVIEW
published: 31 July 2019
doi: 10.3389/fmats.2019.00179

# A Comprehensive Review of Magnetic Nanomaterials Modern Day Theranostics

*Saima Gul*[1], *Sher Bahadar Khan*[2], *Inayat Ur Rehman*[3], *Murad Ali Khan*[1] *and M. I. Khan*[1]*

[1] Department of Chemistry, Kohat University of Science & Technology, Kohat, Pakistan, [2] Center of Excellence for Advanced Materials Research (CEAMR), King Abdulaziz University, Jeddah, Saudi Arabia, [3] Gandhara College of Pharmacy, Gandhara University Peshawar, Peshawar, Pakistan

Substances at nanoscale, commonly known as "nanomaterials," have always grabbed the attention of researchers for hundreds of years. Among these different types of nanomaterials, magnetic nanomaterials have been the focus of considerable attention during the last two decades as evidenced by an unprecedented increase in the number of research papers focusing these materials. Iron oxide magnetic nanoparticles have occupied a vital position in imaging phenomena; as drug vehicles, controlled/sustained release phenomena and hyperthermia; atherosclerosis diagnosis; prostate cancer. In fact, these are wonderful "theranostic" agents with some under clinical trials for human use. In this review, we have attempted to highlight the advances taking place in the field of magnetic nanoparticles as theranostic agents. Extensive progress has been made in the two most important parameters, namely, control over the size and shape which decide the importance of iron oxide magnetic nanoparticles by developing suitable procedures like precipitation, co-precipitation, thermal decomposition, hydrothermal synthesis, microemulsion synthesis and plant mediated synthesis. After using a suitable synthetic route, workers encounter the most daunting task linked with the materials at nanoscale i.e., the protection against corrosion. Only properly protected iron oxide magnetic nanoparticles can be further connected to different functional systems to make building blocks for application in catalysis, biology and medicines. Finally, "theranostics" which is a combined application of imaging and drug delivery has been discussed. With all the potential uses, toxicity of the of iron oxide magnetic nanoparticles has been discussed.

**Keywords: iron oxide magnetic nanoparticles, synthetic routes, drug delivery, imaging, theranostic, atherosclerosis**

OPEN ACCESS

***Edited by:***
*Mario Guagliano,*
*Politecnico di Milano, Italy*

***Reviewed by:***
*Walter Caseri,*
*ETH Zürich, Switzerland*
*Jian Yang,*
*Wuyi University, China*

***Correspondence:**
*M. I. Khan*
*gorikhan@kust.edu.pk*

***Specialty section:***
*This article was submitted to Polymeric and Composite Materials, a section of the journal Frontiers in Materials*

***Received:*** *12 February 2019*
***Accepted:*** *09 July 2019*
***Published:*** *31 July 2019*

***Citation:***
*Gul S, Khan SB, Rehman IU, Khan MA and Khan MI (2019) A Comprehensive Review of Magnetic Nanomaterials Modern Day Theranostics. Front. Mater. 6:179. doi: 10.3389/fmats.2019.00179*

## INTRODUCTION

Scientists, and materials scientists particularly, have shown remarkable interest in the properties of magnetic materials on the nanometer scale, while life scientists are also benefiting from nanomagnets (Buzug, 2010). Iron oxide magnetic nanoparticles are quite different from other nanomaterials as the fundamental properties of magnets are defined at the nanoscale and measurements can be made in the range of a micrometer to a few nanometers in size (Riaz et al., 2015; Monsalve et al., 2017). Iron oxide magnetic nanoparticles are one of the most promising

substances in clinical diagnostic and therapeutic applications (theranostics) (Ho et al., 2011; Ahmed et al., 2012). Superparamagnetism displayed by iron oxide magnetic nanoparticles makes ferromagnets useful for application in biomedical sciences; briefly, when compared with other nanomaterials, these are usually coated with inorganic materials like silica, organic fatty acids phospholipids, and so on, and these can be directed to active site by controlling with external AC magnetic field making these attractive for biomedical applications (**Figure 1**) (Li et al., 2013).

Recently, substantial efforts have been made in the field of iron oxide magnetic nanoparticles to develop and understand their behavior and for improving their applicability (Bansal et al., 2017). Control over the synthetic procedures including surface functionalization is imperative as it leads to their unique properties, such as physicochemical, stability and biological fate. For application in pharmaceutical and biomedical purposes, iron oxide magnetic nanoparticles should possess smaller size (50–160 nm) and high magnetization values (Mohammed et al., 2017). Surface coatings are meant to ensure stability and biocompatibility for specific localization at the target site (**Figure 2**) (Kandasamy, 2017).

Nevertheless, the intrinsic instability is an inevitable problem related with these particles when stored over certain periods of time; as these small particles tend to agglomerate and reduce the energy associated with high surface to volume ratio of the nanoparticles (Kovár et al., 2017). Uncapped magnetic iron oxide nanoparticles are highly reactive and prone to easy oxidation under ambient conditions damaging in magnet behavior and dispersion (Yu et al., 2014). For these reasons, it is critical to devise strategies to achieve stability of the naked magnetic iron oxide nanoparticles and degradation in the course and after the synthetic procedures. One approach is to coat the magnetic nanoparticles with layers of organic or inorganic stabilizing agents; the major advantage of this strategy is that the coating not only gives stability, but these can further be used for functionalization depending on the anticipated application (Tombácz et al., 2015). After surface functionalization, iron oxide magnetic nanoparticles are capable of use as catalysts and biomarkers etc. (Pang et al., 2016). The objective this review is to bring into focus the syntheses and wide-ranging applications of iron oxide magnetic nanoparticles.

## SYNTHESIS OF IRON OXIDE MAGNETIC NANOPARTICLES

A huge number of research papers have appeared during the last several decades describing the synthesis of magnetic iron oxide nanoparticles with versatile compositions and phases.

Synthetic routes are selected to control shape, stability and dispersion trends of iron oxide magnetic nanoparticles (**Figure 3**). Excellent quality iron oxide magnetic nanoparticle can be synthesized by adopting versatile synthetic approaches include thermal decomposition, co-precipitation, micelle formation, hydrothermal and laser pyrolysis techniques. It was difficult for us to compile all this literature and we have attempted to present each synthetic approach by giving a few examples along with the corresponding formation mechanism (Ali et al., 2016; Martínez-Cabanas et al., 2016; Elrouby et al., 2017; Kandasamy, 2017; Lin et al., 2017; Liu et al., 2017; Rajiv et al., 2017; Sathya et al., 2017).

### Solution Precipitation

To date, precipitation from homogeneous solutions is a classical in use for decades for the lab-scale preparation of iron oxide magnetic nanoparticles (Pang et al., 2016). Routinely, during a precipitation reaction, a precipitating agent is added to the aqueous solution of metal precursor generating an insoluble solid product and the major benefit is the higher yields of the products. Another advantage of homogeneous precipitation reaction is the uniformity of the particles, a process that depends largely on the separation, the nucleation and growth of the particles (Yang et al., 2014).

Overall, precipitation methods are simple and allow the preparation of magnetic iron oxide nanoparticles with rigorous size and shape control and these reactions are employed to obtain uniform size of the product. Nucleation must be avoided during the growth process for achieving the monodispersity of the iron oxide magnetic nanoparticles (Mahmed et al., 2011).

### Co-precipitation Methods

Co-precipitation is perhaps a more suitable method to prepare magnetic iron oxide nanoparticles from aqueous solution containing Fe(II) and Fe(III) by adding a base under anaerobic condition at ambient or high temperatures (Lodhia et al., 2010). However, there are certain factors like the type of iron salts, Fe(II):Fe(III) ratio, temperature of the reaction, pH of the medium, volume and ionic strength of the solution that markedly affect size, shape and composition of the magnetic iron oxide nanoparticles (Surowiec et al., 2017). In the co-precipitation approach, once the synthetic conditions are met, the quality of the magnetic iron oxide nanoparticles is successfully reproducible. At laboratory conditions, nanoscale magnetite tend to decompose easily to maghemite when dissolved in an acidic solution which is a ferrimagnetic material; therefore, magnetite can be deliberately oxidized to maghemite. This can be achieved by dispersing magnetite in acidic medium followed by the addition of Fe(III) nitrate; thus, the product obtained furnished excellent chemical stability to basic as well as acidic conditions. Therefore, altering conditions of the aforesaid process is the key in controlling the dispersion behavior of magnetic iron oxide nanoparticles; the size and shape of the SPIONs can be successfully tailored by adjustment of pH, ionic strength, temperature, nature of the salts used and concentration ratio of $Fe^{II}/Fe^{III}$. While addition of organic chelating agents or polymers surface complexing agents during the formation of magnetite can help to control the size of the nanoparticles (Mascolo et al., 2013).

Recently, monodispersed magnetic iron oxide nanoparticles of variable sizes have been reported by the use of the stabilizing agent polyvinylalcohols in chainlike clusters signifying the importance of appropriate surfactant for stability (Freitas et al., 2015). Organic stabilizing agents containing carboxylate and hydroxide anions have been the priority choices as they

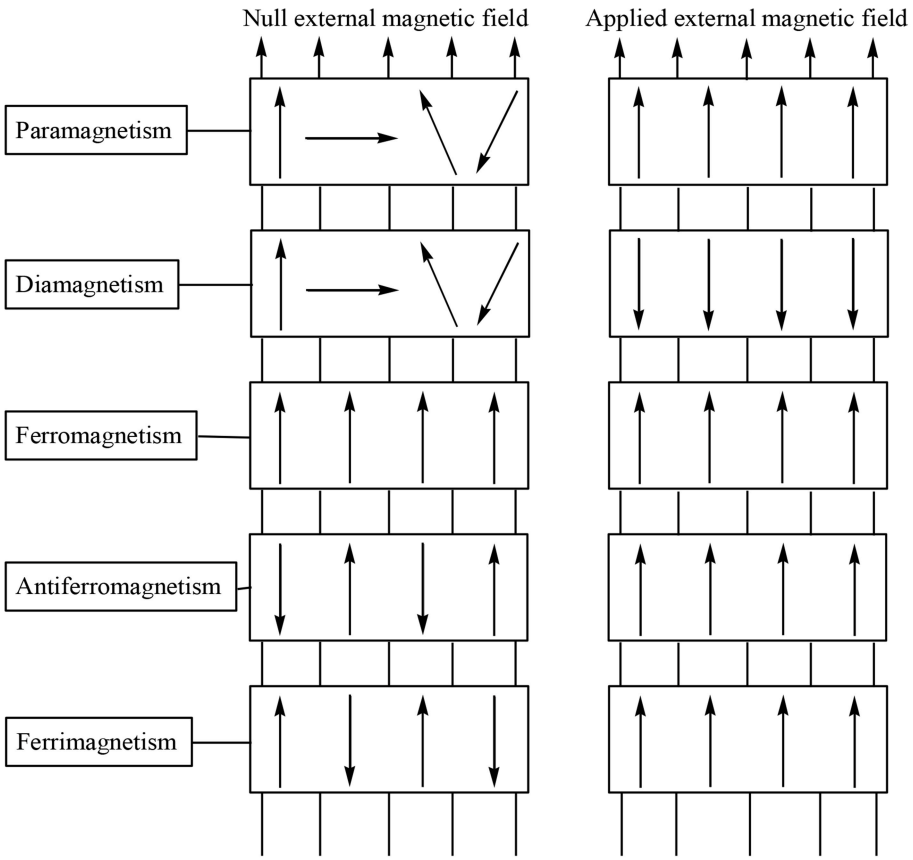


**FIGURE 1 |** Magnetism in the presence and absence of an external applied magnetic field.

form surface complexes by competing mechanisms (Lu et al., 2007). First is the complex formation of metal ions which prevents nucleation; second is the adsorption of additives on nuclei thereby inhibiting particles' growth (Boyer et al., 2010). All these facts make co-precipitation as the most widely used excellent synthetic route to obtain magnetic iron oxide nanoparticles.

## Thermal Decomposition Approach

In this approach, generally organometallics compounds are decomposed; organometallic precursors are decomposed in organic solvents using surfactants as capping agents under anaerobic conditions and it is a very diverse approach for the synthesis of magnetic iron oxide nanoparticles (Laurent et al., 2008). Thermal decomposition helps achieve control of the size and shape and dispersion behaviors of the nanomaterials; however, safety issues are associated at higher temperatures and pressure of organic liquids and vapor phases used during the reactions conducted in the absence of air (**Figure 4**) (Dong et al., 2015). But one question has always arisen that, If the reaction is carried out in the absence of oxygen, how can metal oxide nanoparticles be formed successfully and reproducibly? The answer to this is example of iron oxide as in the first step ferrous hydroxide is formed, which is then oxidized to iron oxide by the protons of water to different types of iron oxides.

Reaction conditions, for instance temperature, duration of the reaction and the aging may also be vital for controlling size and morphology (Patsula et al., 2016). Annealing temperature is another factor which allows for the control of size and size distribution, namely the dispersion of the synthesized iron oxide magnetic nanoparticles, their structural motifs and magnetic properties. Monodispersed iron oxide magnetic nanoparticles in the size range of 6–20 nm were reported prepared by the polymer-catalyzed decomposition of reaction of $Fe(CO)_5$ (Smith and Wychick, 1980; Huber, 2005). Literature also reports very precise control of the size of iron oxide magnetic nanoparticles; this was successfully achieved by thermally decomposing larger concentrations of expensive and toxic precursors as well as surfactants in organic medium. Precursors containing zero-valent metal like $Fe(CO)_5$, initially lead to metallic nanoparticles followed by oxidation yielded high quality monodisperse iron oxide magnetic nanoparticles (Effenberger et al., 2017). In contrast, iron(III) acetylacetonate when treated under identical conditions decomposed to cationic metal centers (Hufschmid et al., 2015). Another drawback associated with this method is the solubility of magnetic nanoparticles in organic solvents; this restricts their usage in biology and medicine. Even surface

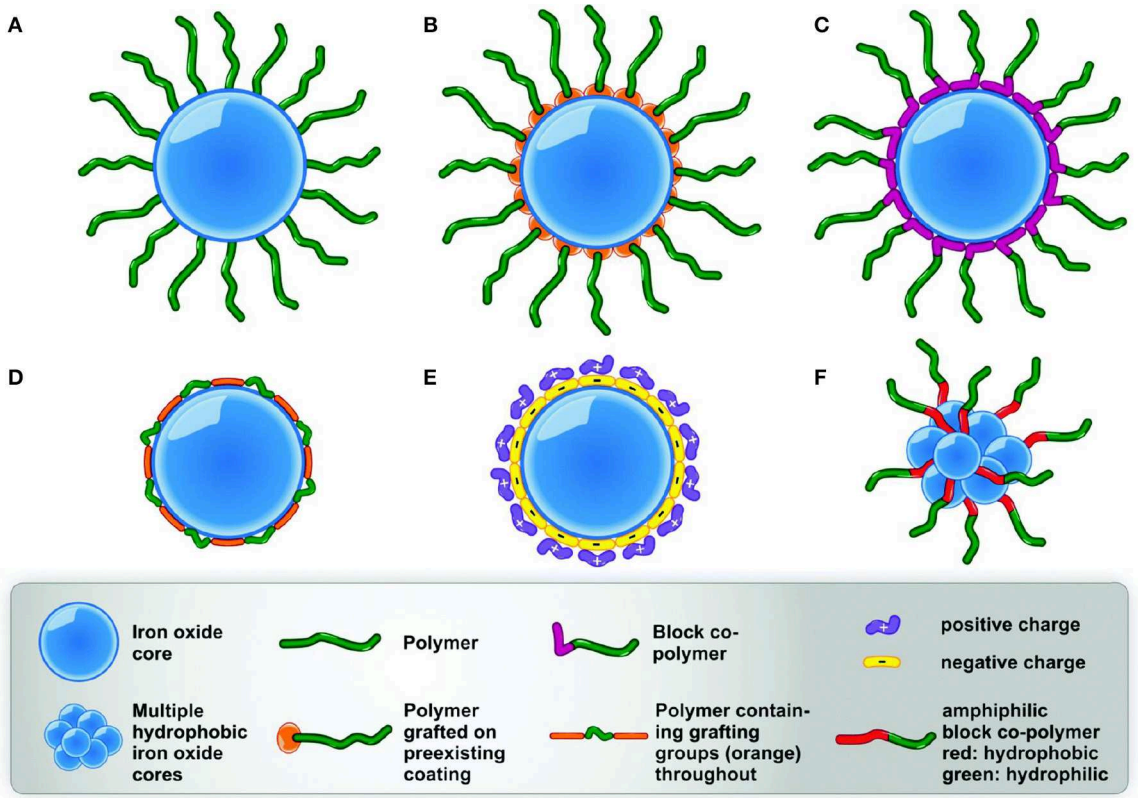


**FIGURE 2 |** Stabilization of iron oxide nanoparticles; **(A)** polymer end bearing functional group **(B)** polymer-grafted **(C)** di-block copolymer with grafting groups **(D)** wrapping conformation of the polymer **(E)** coatings with opposite charges **(F)** amphiphilic polymers [adapted and modified from Barrow et al. (2015) and Habibi et al. (2017)].

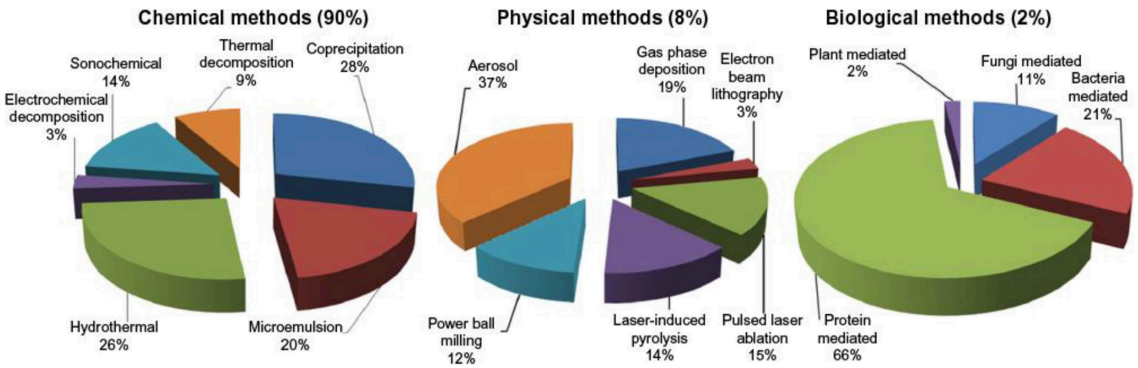


**FIGURE 3 |** Comparative presentation of the synthesis of iron oxide magnetic nanoparticles by three different routes [adapted and modified from Ali et al. (2016)].

modification has no significant impact on the solubility of nanoparticles which are generally only dissolved in non-polar solvents (Dong et al., 2015).

## Polyol Method

Polyol method is a liquid-phase synthetic approach for magnetic iron oxide nanoparticles in multivalent alcohols under higher boiling conditions (Hufschmid et al., 2015). Ethylene glycol is the simplest representative of the polyol family and, based on this, polyols comprise of a series of glycols diethylene glycol, triethylene glycol, tetraethylene glycol up to polyethylene glycol (**Figure 5**) (Deshmukh and Niederberger, 2017). Polyethylene glycol is available in a wide range of molecular weights and the respective product may contain up to 100,000 ethylene groups; other examples of this family are propanediol, butanediol, pentanediol, glycerol, and pentaerythritol and certain

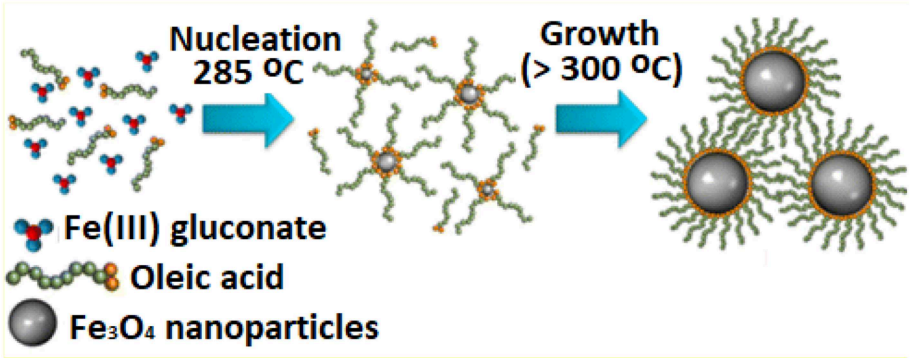


**FIGURE 4 |** Thermal decomposition of iron(III) glucuronate to synthesize superparamagnetic $Fe_3O_4$ nanoparticles [adapted and modified from Patsula et al. (2016)].

carbohydrates. Polyol is a very promising approach to synthesize uniform magnetic iron oxide nanoparticles, having the potential use in magnetic resonance imaging. The reason for the success of the polyol method is that all these polyols are water-comparable and chelation; polyols instantaneously coordinate to the nuclei formed and this allow excellent control of particle size, dispersity and particle distribution. Post synthesis treatment for the removal of polyols can be achieved easily by repeated washing with simple water, coordination exchangers like carboxylates, amines etc. and thermal annealing (Watt et al., 2017). Particle size increases with the increasing precursor's concentration and water; particle size can be limited to minimum depending on the solubility of the product in the polyol. A bigger advantage of the polyol method is the production of highly crystalline oxide nanoparticles based on elevation of the temperature of reaction medium; this rules out any post-sintering treatment of the product (Yang et al., 2014). Apart from conventional heating, other sources like microwaves and ultrasonic waves have been successfully applied (Hemery et al., 2017). The synthesis of metal oxides can be restricted by the reducing action of polyols yielding elemental metals, and it is also possible by adjusting the reaction temperature (Wee et al., 2017).

## Microemulsion Synthesis

When two immiscible solvents are mixed together, a thermodynamically stable isotropic dispersion is formed which is defined as microemulsion with the presence of an interfacial layer of surfactant's molecules (de Toledo et al., 2018). Surfactants molecules generally bearing hydrophilic heads soluble in water and hydrophobic tails soluble in oil phase form a monolayer at the interface of the two immiscible liquids (water-oil) (Williams et al., 2016). Surfactant is an amphiphilic molecule playing a role to lower the water-oil interfacial tension to give a transparent solution. Microemulsion technique has several advantages when compared with other synthetic strategies. For example, with the use of simple equipment, a great variety of nanomaterials can be synthesized with excellent control over size, shape and composition, desired crystalline structure and high specific surface area, simple synthetic conditions at ambient/near ambient temperatures and pressures (Zhao et al., 2016). Microemulsions of water-in-oil are formed when microdroplets (up to 50 nm) of water surrounded by a monolayer of surfactant molecules are dispersed in continuous hydrocarbon phase (Drozdov et al., 2016). If two identical water-in-oil microemulsions containing the desired reagents are mixed, the microdroplets formed will experience continuous collisions, coalesce and break again and again leading to the appearance of precipitate inside the micelles. After completion of the reaction, acetone or ethylalcohol are added for extracting the precipitate via filtration or by centrifugation.

Microemulsions are termed as "nanoreactors" to produce nanoparticles, mixed metal-iron oxide magnetic ($MFe_2O_4$, M: first row transition metals) nanoparticles are one of the most interesting materials used for electronic applications (Gutiérrez et al., 2015). $MnFe_2O_4$ nanoparticles in the range 4–15 nm are successfully synthesized through water-toluene inverse micelles with sodium dodecylbenzenesulfonate surfactant, aqueous solutions of $Mn(NO_3)_2$ and $Fe(NO_3)_3$ as starting precursors. The microemulsion method used for the magnetic nanoparticles yielded spheroids with a rectangular cross section or as tube (Hasany et al., 2013). A wide range of magnetic nanomaterials have been synthesized using the microemulsion method with good control and the sizes, as well as shapes, usually varied over a wider range. In the microemulsion technique, large quantities of solvents are used to produce considerable amounts of nanomaterial; based on this, it's categorized as a very efficient procedure and relatively difficult to be applied at large scale (**Figure 6**) (Kumar et al., 2013; Williams et al., 2016).

## Hydrothermal Route

Hydrothermal or solvothermal route is one of the most successful methods to prepare magnetic nanoparticles and ultrafine powders (Malo de Molina et al., 2016). By using this technique, crystals of different materials have been grown satisfactorily. Generally, hydrothermal synthesis accompanies higher temperatures (125–250°C) at very high pressures (0.3–4 MPa) (Cai et al., 2013; Madadlou et al., 2014; Yelenich et al., 2015). Powdery iron oxide magnetic nanoparticles with 40 nm diameter have been reported using hydrothermal route (140°C)

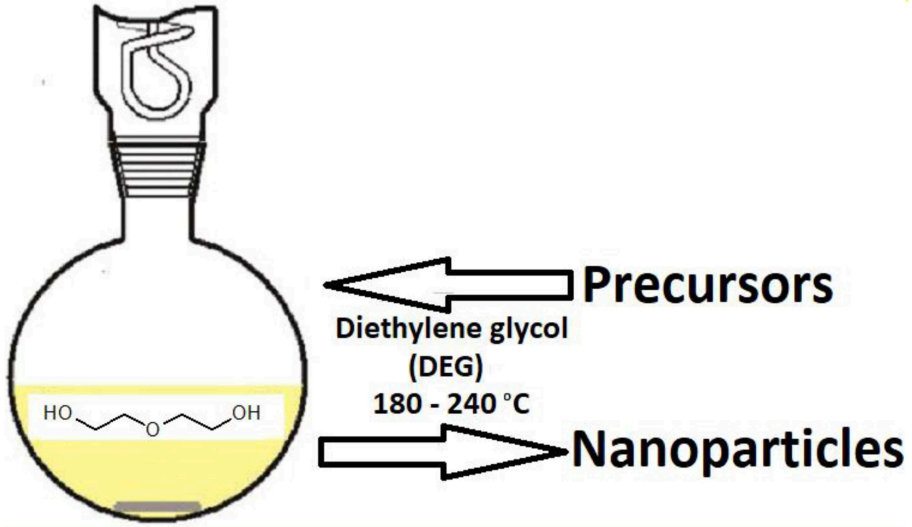


**FIGURE 5 |** Polyol route for the synthesis of nanoparticles [adapted and modified from Dong et al. (2015)].

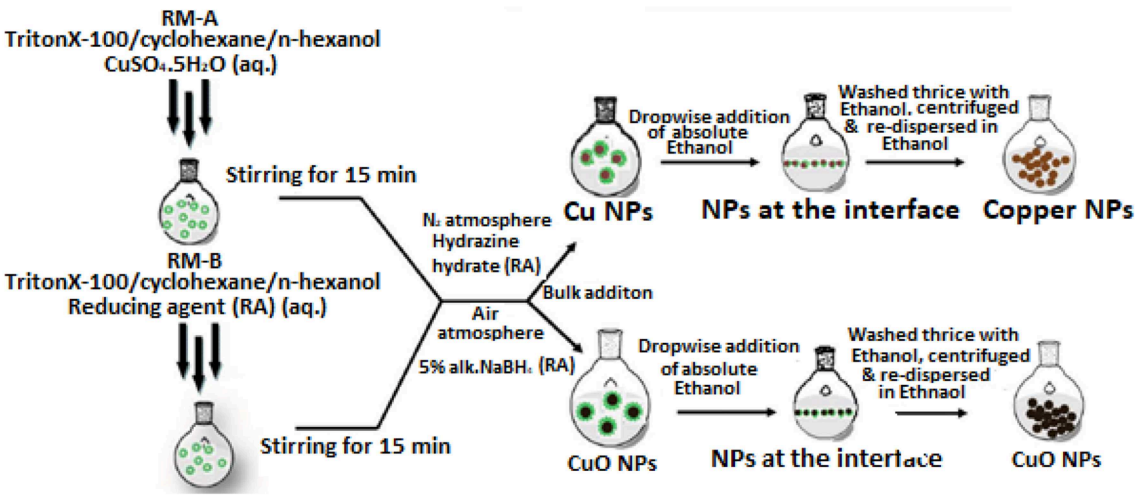


**FIGURE 6 |** Reverse phase microemulsion route for size-controlled synthesis of Cu and CuO nanoparticles [adapted and modified from Kumar et al. (2013) and Williams et al. (2016)].

and a saturation magnetization of 85.8 emu. $g^{-1}$, which is far lower than that of the bulk iron oxide.

Precursors' concentration controls the size and size distribution; however, the duration of the reaction had affected the average particle size more significantly; monodisperse particles were obtained at shorter reaction times (Guo et al., 2013). An increase in the precursors' concentration with the rest of the variables kept constant lead to spherical particles (15.6–4 nm) (Naghibi et al., 2014). A major drawback of the hydrothermal route is the slowness of kinetics at any given temperature; but this problem can be addressed using microwaves which can increase the kinetics of crystallization. A reaction mixture containing ethylene glycol, iron(III) chloride, sodium acetate and polyethylene glycol sealed inside a stainless-steel autoclave (Teflon-lined) was and heated at 200°C for 8–72 h, yielded monodisperse spheres in the range of 200–800 nm. The mechanism is not yet clear, and the multicomponent approach seemed to be powerful in directing the formation of the desired materials.

## Biological Synthesis

The introduction of Green Chemistry in nanotechnology has grabbed a great deal of attention from workers around the globe (Maryanti et al., 2014). The green chemistry approach includes chemical manipulations with the aim to either decrease or eliminate toxic materials dumped into the environment (Tadic et al., 2014; Nassar et al., 2016). Biological synthesis of metallic nanomaterials by plants resources is

currently under development and one of the most researched areas under investigation. Plant-mediated syntheses of metallic nanomaterials is the most modern option for researchers, carried out by using various parts of plants including tissue, extracts, exudates and other parts of the living plants. Green methods that are environmentally-friendly, safe and non-toxic for the development of reliable and eco-friendly methods to produce nanomaterials are of great importance in biomedical applications.

Biological resources including microbes, enzymes, fungi and plant extracts have been utilized as eco-friendly alternates for the synthesis of nanoparticles (Shah et al., 2015; Dhal et al., 2017). In some papers, plants and/or their parts proved to be beneficial over the other biological processes like microbial or enzymatic resources by elaborating work to maintain microbial culture. Plants are green resources for the biological synthesis of nanoparticles containing reducing agents for instance citric acid, ascorbic acid, flavones, crude enzymes like dehydrogenases, reductases and extracellular electron shuttles, which plays a key role in the biological synthesis of nanoparticles (**Figure 7**) (Bai et al., 2009; Makarov et al., 2014; Baranwal et al., 2016).

Carob leaf extract has been successfully employed as a rapid, non-toxic, facile and green resource for preparation of iron oxide magnetic nanoparticles in a single step reaction using Fe(III): Fe(II) and sodium hydroxide solutions (Baxter-Plant et al., 2003). The reaction occurred at a relatively low temperature range in a single-vessel reaction with an average diameter of the monodispersed nanoparticles (4–8 nm) coated with carboxylic groups of respective amide-I and II chain of the proteins present in the extract (Rai et al., 2015).

As the biological synthesis of nanoparticles is a comparatively newer approach and is developing, these are certain disadvantages associated with it, for example, plants produce low quantities of secreted proteins which lead to a decreased rate of synthesis, creating the following implications: culturing microorganisms which takes more time; the prime objective of the synthesis of nanoparticles regarding control over size, shape and crystallinity is only achieved with difficultly; and most importantly is the dispersity of the nanoparticles, which are preferably monodispersed. Another disadvantage is that all the plants are not capable of being put to use for the synthesis of nanoparticles. The researchers are still working on the mechanisms of metal ion uptake and biological reduction by green approach.

## DRUG DELIVERY

About 40 years ago, the concept of "magnetic drug delivery" was introduced as a very promising application of magnetic nanomaterials (Iravani, 2011). The concept of magnetic targeting starts with attaching drug molecules to magnetic nanomaterials followed by the injection and guidance of these particles to a site of action under the influence of localized magnetic field-gradients and holding there at site till the completion of therapy and final removal (Awwad et al., 2013). Literature reveals six types of magnetic materials, i.e., diamagnetic, paramagnetic, ferromagnetic, superparamagnetic, ferromagnetic and antiferromagnetic (Njagi et al., 2010). When the external field is removed, paramagnetic substances lose magnetic momentum and superparamagnetic materials become non-magnetic, but if an external field is placed, these develop a mean magnetic momentum. Magnetic nanoparticles can carry large doses of drugs to achieve high local concentration, avoiding toxic and other adverse side effects arising due to high drug doses in other parts of the organism (Langer, 1990). *In vivo* studies proved that actual clinical trials are a challenging task due to size control, stability, biocompatibility and coating-layer for drug binding and other physiological parameters.

The objective of developing and/or improving drug delivery systems is to position medications to target parts of the subject's body through a medium that can control the therapy's administration by means of a physiological or chemical trigger (Mody et al., 2014). Polymeric microspheres, micelles and hydrogels proved to be effective in enhancing drug target specificity, systemic drug toxicity lowering, improved treatment absorption rate and protection of pharmaceuticals against biochemical degradation (Bucak et al., 2012; Kharissova et al., 2013; Kharisov et al., 2014; Hola et al., 2015; Jiles, 2015; Anselmo and Mitragotri, 2017; Seeli and Prabaharan, 2017). In addition to these, biodegradable polymer and dendrimers based experimental drug delivery systems displayed exciting signs of promise (**Figure 8**).

Dendrimers, due to their size and structure, are suitable carriers and these can be easily processed to good biocompatibility and biodegradation, but these are poor coating materials magnetic nanoparticles (Yu et al., 2017). Suitable materials may be nanoparticles, emulsions, micelles and dendrimers etc.; a typical drug delivery process includes the loading of drugs in biocompatible carrier materials, transferred to bodies for cancer treatment. Biocompatibility, subcellular size and targeting action make nanoparticles excellent carrier materials and several nanosized materials have shown interesting potential for drug delivery; this potential stems from their intrinsic magnetic properties, such as room temperature superparamagnetism, magnetization and high magnetic susceptibility (**Figure 9**).

Surface functionalization by chemical as well as biological means improve stability and biocompatibility of the magnetic nanoparticles. The most interesting aspect of magnetic nanoparticles in drug delivery is the controlled delivery of drugs to target site under external magnetic fields. Magnetic driving of drugs to the target area is based on the binding of drugs to ferrofluid and desorption from the ferrofluid after reaching the target site by external magnetic field. Still, a lot of work is needed to be done, as successful drug delivery is affected by different factors, for example pH, temperature, osmolality, and so on (Veiseh et al., 2010). The strength of the external applied magnetic field may hamper the magnetic drug delivery process as living cells withstand to a certain extent. The responsive nature of the magnetic nanoparticles carriers to external magnetic fields is due to the presence of incorporated magnetic materials, for example magnetite and some other transition metals and mix-metals (**Figure 10**).

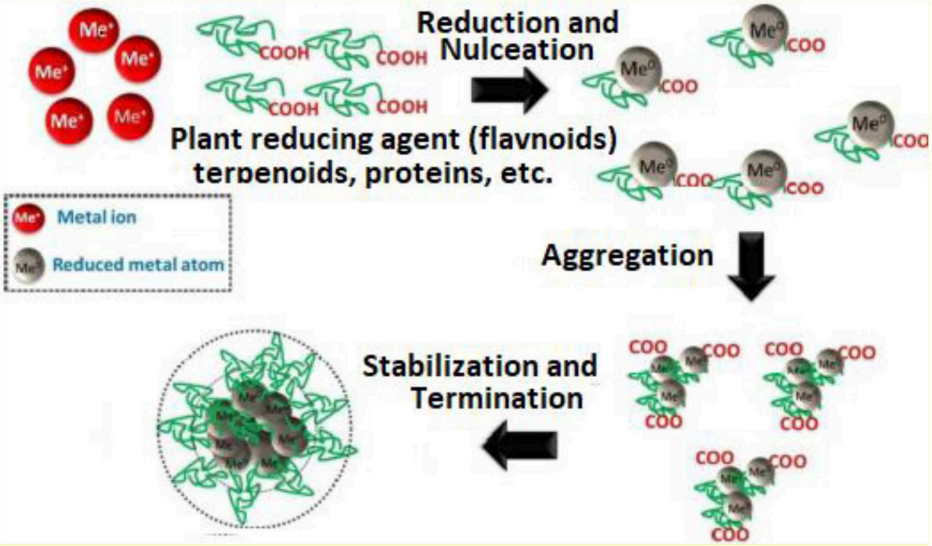


**FIGURE 7 |** Plant-mediated synthesis of metallic nanomaterials showing reduction as well as stabilization by secondary metabolites present in plant extracts for numerous applications in clinical research [adapted and modified from Makarov et al. (2014) and Baranwal et al. (2016)].

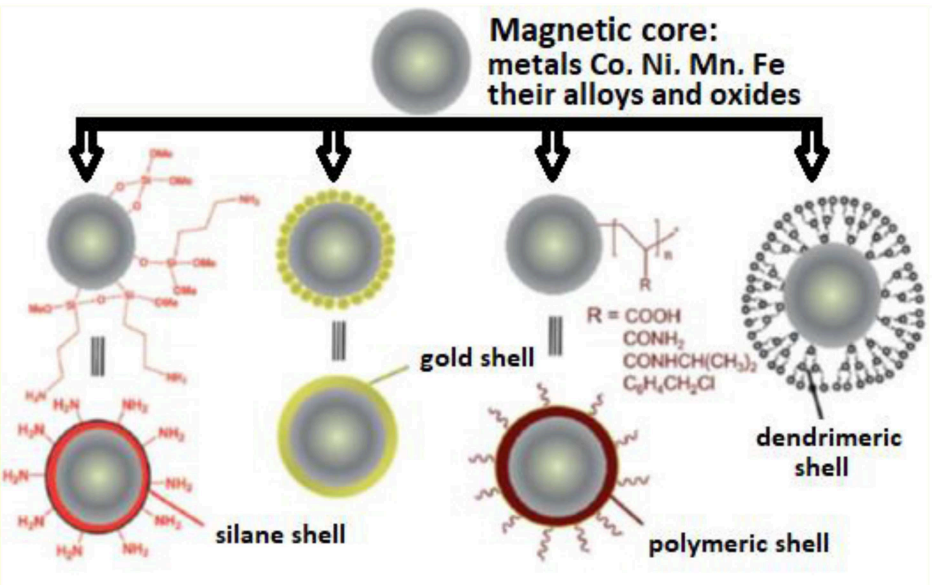


**FIGURE 8 |** Transition metal/metal oxides magnetic core-shell nanoparticles [adapted and modified from Kharissova et al. (2013)].

While designing a magnetic targeted drug delivery system, certain factors must be borne in mind like strength of the applied magnetic field and geometry. There are some other factors like magnetic properties and particles size, magnetic field strength, drug loading capacity, remoteness of the target site and blood flow rate. The aim of the magnetically targeted drug delivery system is to carry the drug to the site of action at a rate needed by the body during the treatment time (Funke and Szeri, 2017).

## IMAGING

The most advanced application of nanoscale materials toward human health is the application of iron oxide magnetic nanoparticles-based formulations as a contrasting agent in magnetic resonance imaging (Fish et al., 2017). The past 50 years have seen remarkable improvements in diagnostic imaging procedures; for example in tumor diagnoses, damaged tissues and neurological disorders. Among various diagnostic imaging

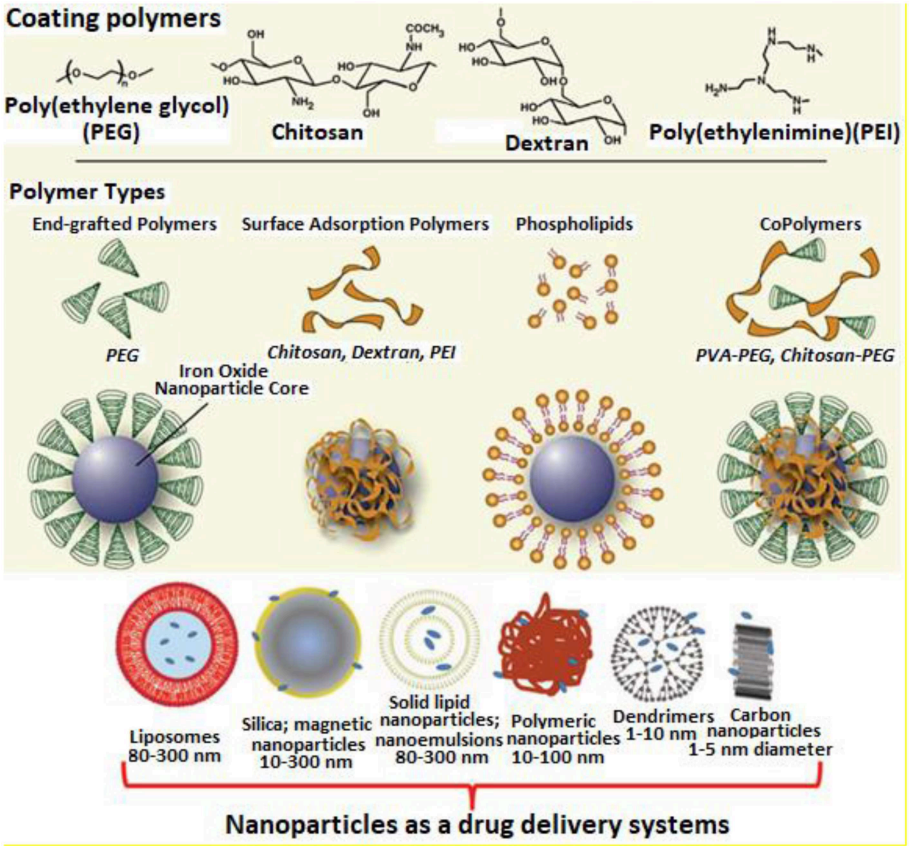


**FIGURE 9 |** Novel drug-carrier systems depicting different types of coating polymers and copolymers [adapted and modified from Veiseh et al. (2010)].

techniques, Magnetic Resonance Imaging abbreviated as MRI is an established tool in biomedical applications; exhibit stronger contrast of tissues makes it a favorable diagnostic test in medicine. In other diagnostic techniques like X-ray, the contrast quality is hindered leading to the misdiagnosis of several medical conditions. Looking at the superior contrast properties of MRIs, developments are needed and are made possible using a special medium called contrast agent (Hyeon et al., 2016). Contrast agent consists of a metal-based core with an external coating of a biocompatible material; the contrast agent intensifies the contrast of images obtained from MRI for accurate diagnoses. MRI equipment exerts a strong magnetic field within the CAs as well as other magnetic particles of biological significance respond (Hachani et al., 2016). MRI contrasting agents are classified into five categories as: $T_1$, $T_2/T_2^*$, CEST, $^{19}$F-based and hyperpolarized agents ($T_1$ and $T_2$ are relaxation rates) (Sood et al., 2017).

T1 agents include paramagnetic $Gd^{III}$ or $Mn^{II}$ complexes capable of enhancing the magnetic resonance water signal known as "signal brightening." The benefits of using $T_1$ contrasting agents relies on the high versatility of the interesting contrast mechanism that is dependent on their structures and biological aspects; for example, the use of paramagnetic complexes to see the delivery as well as the drug release from liposomes (Xiao et al., 2016). However, these systems have got limited sensitivity based on the local concentration. To tackle this problem, scientists proposed the use of nanoscale materials which will aggravate numerous contrasting unit's necessary to detect a $T_1$ contrast. $T_1/T_2^*$ contrasting agents are mostly superparamagnetic iron oxide nanoparticles capable of shortening $T_1/T_2^*$ of water protons than $T_1$ signal; in fact, they darken the MRI due to signal loss. $T_1/T_2^*$ show higher intrinsic sensitivity than $T_1$ contrasting agents which make them highly helpful in cellular imaging; this signal loss is undesirable as in the case of intrinsically low signal locations such as the lungs, while $r_2$ is the relaxivity of the CA as a function of effect of concentration of the solution on the relaxation rates reflects the (**Figure 11**). This can be explained by classical outer-sphere relaxation theory that, with the increase in particle size, the relaxavity ratio ($r_1/r_2$) increases while decrease in particle's size lead to better T1-shortening (Taboada et al., 2007; Xiao et al., 2016).

CEST (Chemical Exchange Saturation Transfer) is the future of MRI contrasting agents; the principal governing CEST imaging is that these agents generate MRI contrast signals through chemical exchange of saturated protons from donor (CEST) to acceptor (water) (Taboada et al., 2007; Xiao et al., 2016). The uniqueness of using CEST agents is that the contrasting signal can be detected by irradiating with the characteristic NMR resonance of the donor. The $^{19}$F nucleus is the most sensitive

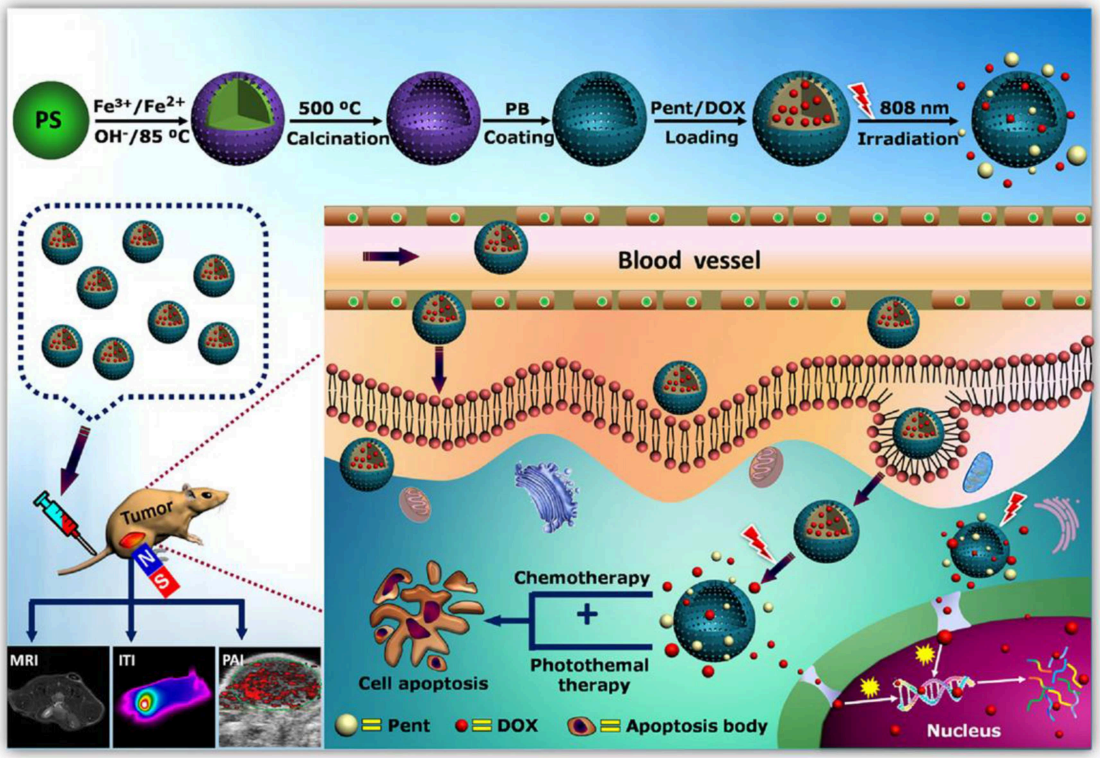


**FIGURE 10 |** Controlled delivery of anti-tumor drug with a new design incorporating a phase-change material in magnetic nanoparticles allowing chemo-photothermal combined tumor therapy with multimodal tumor imaging [adapted and modified from: http://www.advancedsciencenews.com/pent-drug-delivery-tumor-therapy-trimodal-imaging (accessed on July 07, 2018, 2200 PST)].

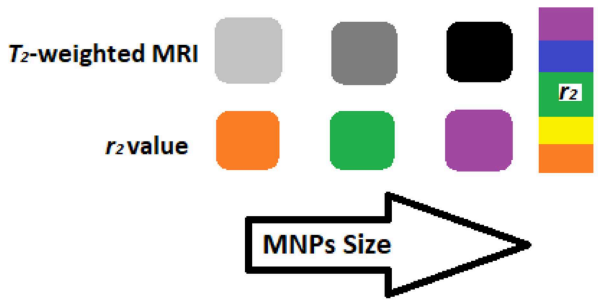


**FIGURE 11 |** $T_2$-weighted contrasts and $r_2$ color maps for iron oxide nanoparticles of different sizes (Nanoparticles in magnetic resonance imaging: from simple to dual contrast agents) [adapted and modified from Estelrich et al. (2015) and Xu et al. (2016)].

spin after proton so needs no enrichment, bearing similar detection sensitivity to CEST. Fluorinated agents are preferred over other media agents, due to possible correlation of signal to agent concentration (Bünzli, 2016). Hyper polarized agents are the most sensitive media contrasting agents using polarization techniques which dramatically increase the population difference between the spin energy levels. These have got limited use because of the signal loss over time.

Before extending our discussion about nanoscale magnetic materials as contrasting media, some *in vivo* considerations must be discussed like toxicity, size and shape, and charge. Iron oxide magnetic nanoparticles are regarded as harmless for *in vivo* applications; based on iron's concentration inside the human body. Iron becomes toxic at a concentration level of 60 mg/kg; iron oxide magnetic nanoparticles have been used as contrasting agents for more than two decades in clinics are below 1 mg/kg. However, iron oxide magnetic nanoparticles have been reported to have adverse effects on cell cultures based on the proposal that the internalization of nanoparticles alters the fate of the cells. Iron oxide magnetic nanoparticles consist of two components, namely magnetic core and organic coatings, and the role of the contribution of either of these is difficult to assess. Moreover, the toxicity of iron oxide magnetic nanoparticles is not dependent only on organic coating but cell type as well. Iron oxide magnetic nanoparticles can induce oxidative stress by disturbing oxidant/antioxidant balance.

Based on the size, charge and shape, the potential toxicity of iron oxide magnetic nanoparticles has been closely related to two factors, their size and charge, while less is reported about the relation to shape. Sizes between 10 and 100 nm have longer half-lifes in the blood and are small enough to go through capillaries; these considerations are to be kept in mind while cancer imaging is under discussion relevant to size (Estelrich et al., 2015; Xu et al.,

2016). Organic polymers of molecular weights above 50 kDa has been found to have an effective blood half-life of 6 h. The *in vivo* effect of shape on the toxic behavior of iron oxide magnetic nanoparticles is difficult to assess because of the difficulty in the preparation of comparable samples of nanoparticles with different shapes (McMahon and Bulte, 2018).

## THERANOSTICS

Theranostic is the seamless integration of therapy and diagnosis into one step; it is perhaps one of the trend setters in modern day research. The pivotal idea behind theranostic is that nanoparticles are unique in nature, i.e., these are capable of imaging and treating a lesion simultaneously (Khandhar et al., 2017). A careful survey of the literature revealed it was 2006 when this term was coined for the first time in scientific literature; theranostics was described as "Future nanotechnology developments will most likely include the capability of designing and fabricating multifunctional nanoparticles to combine imaging and therapeutic capabilities ("theranostics")" (Sun et al., 2016). In this regard, iron oxide magnetic nanoparticles have attracted interest due to their unique magnetic properties which make these excellent MRI contrasting agents and effective cytotoxic agents against tumors.

The use of nanoparticles allows imaging and treatment to be achieved simultaneously, in addition it also assists multiple treatment modalities in combination. This multi-modal approach was observed during the use of cisplatin-bonded gold nanospheres to administer chemo-radiotherapy in GBM cell models, leading to apoptic cell death after the intracellular uptake (Li et al., 2017). During the experiment, it was observed that due exposure to radiation in either of the metals started functioning as high atomic number radiosensitising agents and initiated the release of photoelectrons and Auger electrons. Radiosensitisation of the nanoparticle's formulations enhanced the *in vitro* cytotoxic effects of chemo- and radiotherapy and contributed to the photoablation of tumor cells (Bissonnette and Bergeron, 2006). These results upstretched the prospect of concomitant administration of diagnostics and multiple forms of therapy.

Photoablation therapy is used for cancer treatment and is divided into two types, photothermal therapy (PTT) and photodynamic therapy (PDT) (Zheng et al., 2008). Among these, PTT is an excellent contender for cancer treatment and focuses on the use of photo-induced heat to kill cancer cells (Her et al., 2017). While in PDT treatment, a poorly soluble drug and visible light irradiations are used at certain wavelengths for generating reactive oxygen species such as singlet oxygen to kill cancer cells (McNamara and Tofail, 2017). PTT is an attractive method owing to advantages such as the safety of non-target regions, its minimally invasive nature, fast recovery, and so on. Magnetic nanoparticles generate heat when placed in a varying magnetic field due to magnetic hysteresis loss (Neel-relaxation and Brown-relaxation). This led scientists to apply these magnetic in hyperthermia treatment which is considered as a supplementary treatment to radiation, chemotherapy and surgery in cancer therapy (Marangon et al., 2017). Magnetic induction hyperthermia is based on the fact that when alternating magnetic field is applied to magnetic nanoparticles, induced currents are generated and consequently heat is produced in magnetic nanoparticles. Based on this principal, when magnetic fluids are exposed to alternating magnetic field, the fluids turn into powerful heat sources, destroying tumor cells, since these cells are more sensitive to temperatures more than 41°C than their normal counterparts (Gomer et al., 2016). PTT has certain disadvantages as well, like the need for high-power lasers and the thermal destruction of cancer selective cell lines. Recently, PDT has attracted considerable attention in cancer treatment, as it is a non-invasive method, low energy light, site-specific tumor targeting and negligible side effects. Due to the poor solubility of drugs in water, these tend to accumulate in physiological media, hence indicating the need to work on developing improved drug delivery systems.

Photoacoustic imaging is a new method which is a combination of optical and acoustic imaging of burns, studying blood vessels, melanoma sites etc. This technique gives in-depth analysis of various tissues, e.g., breast cancer cells, brain cancer cells and tumor monitoring (Sakellari et al., 2016). In photoacoustic tomography, the laser system used for photoacoustic imaging (532 nm) has great promise for non-invasive early diagnosis and the imaging of tumor cells and tissues. Gold nanoparticles have proven to be excellent non-invasive contrasting agents for early diagnosis of tumor by photoacoustic imaging. Computed tomography is one of the most common hospital's diagnostic tools; it is another excellent imaging method for grabbing anatomical information. It is a choice made for clinical applications because of cost, efficiency, availability, deep tissue penetration and high spatial resolution. In this method, gold nanoparticles can be used as contrasting agents because of the high X-ray absorption, lower toxicity and slow clearance in the body. it was also suggested that gold nanoparticles may replace conventional iodine based contrasting agents as these reagents display renal toxicity and fast excretion. Gold nanoparticles displayed excellent biocompatibility, enhanced stability and increased accumulation in computed tomography tumor imaging (Kobayashi et al., 2016). Ultrasound imaging is a clinical diagnostic tool extensively used due to interesting features such as being non-invasive, cost-effective and portable. Like all the other diagnostic imaging methods, contrasting agents can be adopted to enhance imaging precision in ultrasound imaging. In this method, microscale fluorocarbon bubbles are typically used as contrasting agents: in literature, ultrasound imaging contrasting agents should feature four characteristics, easy fabrication, easy administration, high biosafety and excellent echogenicity.

## ATHEROSCLEROSIS

Atherosclerosis, a complex disease and one of the leading causes of death in the developed world (Chen et al., 2016). It is a chronic inflammation and remodeling processes which leads to the stenosis of the aorta; generally, it's a gradual process spanning

over decades, but under certain conditions, it grows rapidly leading to an ischaemia.

In recent years, an extraordinary number of research projects have been funded to make advances in the diagnosis, prognosis and treatment of this fatal disease (Yildirim et al., 2016). Pathological detection of atherosclerosis has improved significantly with the use of magnetic resonance imaging due to contrasting agents and their excellent spatial resolution and average sensitivity; modern-day research in this area is probing new contrasting agents for improved imaging (Fernández-Ruiz, 2016). Other techniques used to detect early-stage atherosclerosis include computed tomography, photoacoustic tomography, positron emission tomography, single-photon emission computed tomography and fluorescence molecular tomography and every technique has pluses as well as minuses. For example, some methods give outstanding sensitivity but low resolution while others have excellent resolution but lower sensitivity. Magnetic nanomaterials have shown the promise to implement magnetic nanomaterials binding to specific surfaces to reduce the detection time (Brown et al., 2016).

As discussed earlier, iron oxide magnetic nanoparticles' magnetic moments rotate rapidly when exposed to external magnetic field and the magnetic flux gets enhanced; and upon the removal of the magnetic field, Brownian motion causes randomization of the magnetic field; this condition is superparamagentism which is observable only at nanoscale. Commonly used as good contrasting agents are gadolinium-based substances; with adverse characteristics including cytotoxicity and the persistent accumulation of gadolinium. Iron oxide magnetic nanoparticles have better results as magnetic resonance imaging contrasting agents when compared with gadolinium and manganese oxide nanoparticles (Li et al., 2016). Gadolinium-based formulations are still dominating contrasting agents; however, after a careful survey of literature and recent clinical trials evidences, the future of iron oxide magnetic nanoparticles is highly promissory for diagnostic imaging guided therapy with the suitable incorporation of specific ligands to well-defined pathologies. So far, we have learnt that atherosclerosis may occur anywhere in the vascular system and the lack of sensitivity in the use of commercially available contrasting agents is a major challenge for the early diagnosis of the plaque which usually possesses a thickness and length. Positron emission tomography has low resolution for the detection of atherosclerotic plaque while the magnetic resonance imaging technique has excellent resolution but lacks sensitivity for pertinent screening. Superparamagnetic iron oxide nanoparticles synthesized by polyol method were successfully applied to mice as an MRI contrasting agent with promising results 5 h after post-injection treatment (Wang et al., 2016). More recently, the *in vivo* application of magnetic nanoparticles in the range of 90 nm allowed for excellent visuals of atherosclerotic plaque in mice; similarly, the NIR-fluorescence based method approach have also been applied with interesting results (Cuadrado et al., 2016; Yoo et al., 2016; Schneider and Lassalle, 2017). In all three techniques, it was observed that the magnetic nanoparticles got accumulated in the atherosclerotic area.

## CONCLUDING REMARKS

Magnetic nanoparticles possess a great promise in drug-delivery systems due to their unique properties to overcome some of the problems to efficiently target diverse cell types. The future is encouraging as well as challenging and novel research ideas are needed to be worked out to prevent its limitations for the therapy of more diseases. Iron oxide magnetic nanoparticles possess a strong candidature for aqueous/non-aqueous phase solubility with great potential in medical applications. To achieve this, several factors play a key-role including suitable precursors, pH of the medium, coating agents and solvents for the synthesis of magnetic nanoparticles. Aqueous phase solubility can be significantly improved by using water-soluble surface functionalization agents via thermal decomposition, co-precipitation, microwave and high-temperature methods.

MRI is a non-invasive imaging technique used to study anatomical site and biologically compatible nanomaterials aid in detailed images for more accurate diagnosis. Magnetic nanoparticles act as contrasting agents which are advantageous to improve the contrast in these images. Magnetic iron oxide nanoparticles have been the key focus in this review article; which are stabilized by increasing the hydrophilicity through coatings onto the metal surface followed by the attachment of additional ligands like antibodies etc. Next is the specific linking to signal-secreting cells which permits specific agglomeration of nanoparticles to the inflamed/tumor bearing site. Contrast is still a challenge in MRI and new improvements are being sought through labeled magnetic nanoparticles with a fluorescent protein, such as green fluorescent protein or red fluorescent protein; giving rise to a distinct color of the target area under investigation. This research requires more intense *in vivo* studies which will lead to improve the biological compatibilities and any possible negative side effects associated with the injection of magnetic nanoparticles. Magnetic iron oxide nanoparticles comparatively proved to be a highly reliable and better theranostic option as gadolinium complexes gives excellent contrast, but these are nephrotoxic.

Finally, the scientific information collected here while compiling this review opens novel insights into the role of magnetic nanoparticles to develop nanocarriers enabled to increase the efficiency of the modern-day theranostics.

## AUTHOR CONTRIBUTIONS

SG compiled this review article with collective scholarly contribution of all the co-authors.

## REFERENCES


Ahmed, N., Fessi, H., and Elaissari, A. (2012). Theranostic applications of nanoparticles in cancer. *Drug Discovery Today* 17, 928–934. doi: 10.1016/j.drudis.2012.03.010

Ali, A., Hira Zafar, M. Z., ul Haq, I., Phull, A. R., Ali, J. S., and Hussain, A. (2016). Synthesis, characterization, applications, and challenges of iron oxide nanoparticles. *Nanotechnol. Sci. Appl.* 9:49. doi: 10.2147/NSA.S99986

Anselmo, A. C., and Mitragotri, S. (2017). Impact of particle elasticity on particle-based drug delivery systems. *Adv. Drug Delivery Rev.* 108, 51–67. doi: 10.1016/j.addr.2016.01.007

Awwad, A. M., Salem, N. M., and Abdeen, A. O. (2013). Green synthesis of silver nanoparticles using carob leaf extract and its antibacterial activity. *Int. J. Ind. Chem.* 4:29. doi: 10.1186/2228-5547-4-29

Bai, H. J., Zhang, Z. M., Guo, Y., and Yang, G. E. (2009). Biosynthesis of cadmium sulfide nanoparticles by photosynthetic bacteria Rhodopseudomonas palustris. *Colloids Surfaces B Biointerfaces* 70, 142–146. doi: 10.1016/j.colsurfb.2008.12.025

Bansal, R., Nagórniewicz, B., Storm, G., and Prakash, J. (2017). Relaxin-coated superparamagnetic iron-oxide nanoparticles as a novel theranostic approach for the diagnosis and treatment of liver fibrosis. *J. Hepatol.* 66:S43. doi: 10.1016/S0168-8278(17)30348-3

Baranwal, A., Mahato, K., Srivastava, A., Maurya, P. K., and Chandra, P. (2016). Phytofabricated metallic nanoparticles and their clinical applications. *RSC Adv.* 6, 105996–106010. doi: 10.1039/c6ra23411a

Barrow, M., Taylor, A., Murray, P., Rosseinsky, M. J., and Adams, D. J. (2015). Design considerations for the synthesis of polymer coated iron oxide nanoparticles for stem cell labelling and tracking using MRI. *Chem. Soc. Rev.* 44, 6733–6748. doi: 10.1039/c5cs00331h

Baxter-Plant, V. S., Mikheenko, I. P., and Macaskie, L. E. (2003). Sulphate-reducing bacteria, palladium and the reductive dehalogenation of chlorinated aromatic compounds. *Biodegradation* 14, 83–90. doi: 10.1023/A:1024084611555

Bissonnette, L., and Bergeron, M. G. (2006). Next revolution in the molecular theranostics of infectious diseases: microfabricated systems for personalized medicine. *Expert Rev. Mol. Diagnost.* 6, 433–450. doi: 10.1586/14737159.6.3.433

Boyer, C., Whittaker, M. R., Bulmus, V., Liu, J., and Davis, T. P. (2010). The design and utility of polymer-stabilized iron-oxide nanoparticles for nanomedicine applications. *NPG Asia Mater.* 2:23. doi: 10.1038/asiamat.2010.6

Brown, A. J., Teng, Z., Evans, P. C., Gillard, J. H., Samady, H., and Bennett, M. R. (2016). Role of biomechanical forces in the natural history of coronary atherosclerosis. *Nat. Rev. Cardiol.* 13:210. doi: 10.1038/nrcardio.2015.203

Bucak, S., Yavuztürk, B., and Sezer, A. D. (2012). "Magnetic nanoparticles: synthesis, surface modifications and application in drug delivery," in *Recent Advances in Novel Drug Carrier Systems* (IntechOpen). Available online at: https://www.cd-bioparticles.com/t/Drug-Delivery_51.html (accessed October 22, 2017).

Bünzli, J. C. G. (2016). Lanthanide light for biology and medical diagnosis. *J. Luminescence* 170, 866–878. doi: 10.1016/j.jlumin.2015.07.033

Buzug, T. M. (2010). "Magnetic nanoparticles: particle science, imaging technology, and clinical applications," in *Proceedings of the First International Workshop on Magnetic Particle Imaging*. Singapore: World Scientific.

Cai, H., An, X., Cui, J., Li, J., Wen, S., Li, K., et al. (2013). Facile hydrothermal synthesis and surface functionalization of polyethyleneimine-coated iron oxide nanoparticles for biomedical applications. *ACS Appl. Mater. Interfaces* 5, 1722–1731. doi: 10.1021/am302883m

Chen, Y., Ma, M., Chen, H., and Shi, J. (2016). "Multifunctional hollow mesoporous silica nanoparticles for MR/US imaging-guided tumor therapy," in *Advances in Nanotheranostics II*, ed Z. Dai (Singapore: Springer), 189–222. doi: 10.1007/978-981-10-0063-8_6

Cuadrado, I., Saura, M., Castejón, B., Martin, A. M., Herruzo, I., Balatsos, N., et al. (2016). Preclinical models of atherosclerosis. The future of Hybrid PET/MR technology for the early detection of vulnerable plaque. *Expert Rev. Mol. Med.* 18:e6. doi: 10.1017/erm.2016.5

de Toledo, L. D. A. S., Rosseto, H. C., and Bruschi, M. L. (2018). Iron oxide magnetic nanoparticles as antimicrobials for therapeutics. *Pharmaceut. Dev. Technol.* 23, 316–323. doi: 10.1080/10837450.2017.1337793

Deshmukh, R., and Niederberger, M. (2017). Mechanistic aspects in the formation, growth and surface functionalization of metal oxide nanoparticles in organic solvents. *Chem. Eur. J.* 23, 8542–8570. doi: 10.1002/chem.201605957

Dhal, S., Mohanty, A., Yadav, I., Uvanesh, K., Kulanthaivel, S., Banerjee, I., et al. (2017). Magnetic nanoparticle incorporated oleogel as iontophoretic drug delivery system. *Colloids Surfaces B Biointerfaces* 157, 118–129. doi: 10.1016/j.colsurfb.2017.05.061

Dong, H., Chen, Y. C., and Feldmann, C. (2015). Polyol synthesis of nanoparticles: status and options regarding metals, oxides, chalcogenides, and non-metal elements. *Green Chem.* 17, 4107–4132. doi: 10.1039/C5GC00943J

Drozdov, A. S., Ivanovski, V., Avnir, D., and Vinogradov, V. V. (2016). A universal magnetic ferrofluid: nanomagnetite stable hydrosol with no added dispersants and at neutral pH. *J. Colloid Interface Sci.* 468, 307–312. doi: 10.1016/j.jcis.2016.01.061

Effenberger, F. B., Couto, R. A., Kiyohara, P. K., Machado, G., Masunaga, S. H., Jardim, R. F., et al. (2017). Economically attractive route for the preparation of high quality magnetic nanoparticles by the thermal decomposition of iron (III) acetylacetonate. *Nanotechnology* 28:115603. doi: 10.1088/1361-6528/aa5ab0

Elrouby, M., Abdel-Mawgoud, A. M., and El-Rahman, R. A. (2017). Synthesis of iron oxides nanoparticles with very high saturation magnetization form TEA-Fe (III) complex via electrochemical deposition for supercapacitor applications. *J. Mol. Struct.* 1147, 84–95. doi: 10.1016/j.molstruc.2017.06.092

Estelrich, J., Sánchez-Martín, M. J., and Busquets, M. A. (2015). Nanoparticles in magnetic resonance imaging: from simple to dual contrast agents. *Int. J. Nanomed.* 10:1727. doi: 10.2147/ijn.s76501

Fernández-Ruiz, I. (2016). Immune system and cardiovascular disease. *Nat. Rev. Cardiol.* 13:503. doi: 10.1038/nrcardio.2016.127

Fish, M. B., Fromen, C. A., Lopez-Cazares, G., Golinski, A. W., Scott, T. F., Adili, R., et al. (2017). Exploring deformable particles in vascular-targeted drug delivery: softer is only sometimes better. *Biomaterials* 124, 169–179. doi: 10.1016/j.biomaterials.2017.02.002

Freitas, J. C. D., Branco, R. M., Lisboa, I. G. O., Costa, T. P. D., Campos, M. G. N., Jafelicci Júnior, M., et al. (2015). Magnetic nanoparticles obtained by homogeneous coprecipitation sonochemically assisted. *Mater. Res.* 18, 220–224. doi: 10.1590/1516-1439.366114

Funke, C., and Szeri, A. J. (eds.). (2017). "Osmolarity as a contributing factor in topical drug delivery," in *APS Division of Fluid Dynamics Meeting Abstracts* (Vancouver, BC).

Gomer, C. J., Luna, M., Ferrario, A., Rucker, N., and Wong, S. (2016). "The tumor microenvironment modulates responsiveness to photodynamic therapy," in *Photodynamic Medicine: From Bench to Clinic*, eds H. Kostron and T. Hasan (The Royal Society of Chemistry), 87–99. doi: 10.1039/9781782626824-00087

Guo, Y., Wang, Z., Shao, H., and Jiang, X. (2013). Hydrothermal synthesis of highly fluorescent carbon nanoparticles from sodium citrate and their use for the detection of mercury ions. *Carbon* 52, 583–589. doi: 10.1016/j.carbon.2012.10.028

Gutiérrez, L., Costo, R., Grüttner, C., Westphal, F., Gehrke, N., Heinke, D., et al. (2015). Synthesis methods to prepare single-and multi-core iron oxide nanoparticles for biomedical applications. *Dalton Transac.* 44, 2943–2952. doi: 10.1039/C.4D.T.03013C

Habibi, N., Pastorino, L., Babolmorad, G., Ruggiero, C., Guda, T., and Ong, J. L. (2017). Polyelectrolyte multilayers and capsules: S-layer functionalization for improving stability and biocompatibility. *J. Drug Delivery Sci. Technol.* 38, 1–8. doi: 10.1039/C5CS00331H

Hachani, R., Lowdell, M., Birchall, M., Hervault, A., Mertz, D., Begin-Colin, S., et al. (2016). Polyol synthesis, functionalisation, and biocompatibility studies of superparamagnetic iron oxide nanoparticles as potential MRI contrast agents. *Nanoscale* 8, 3278–3287. doi: 10.1039/C5NR03867G

Hasany, S., Abdurahman, N., Sunarti, A., and Jose, R. (2013). Magnetic iron oxide nanoparticles: chemical synthesis and applications review. *Curr. Nanosci.* 9, 561–575. doi: 10.2174/15734137113099990085

Hemery, G., Keyes A. C. Jr., Garaio, E., Rodrigo, I., Garcia, J. A., Plazaola, F., et al. (2017). Tuning sizes, morphologies, and magnetic properties of monocore versus multicore iron oxide nanoparticles through the controlled addition of water in the polyol synthesis. *Inorg. Chem.* 56, 8232–8243. doi: 10.1021/acs.inorgchem.7b00956

Her, S., Jaffray, D. A., and Allen, C. (2017). Gold nanoparticles for applications in cancer radiotherapy: mechanisms and recent advancements. *Adv. Drug Delivery Rev.* 109, 84–101. doi: 10.1016/j.addr.2015.12.012

Ho, D., Sun, X., and Sun, S. (2011). Monodisperse magnetic nanoparticles for theranostic applications. *Accounts Chem. Res.* 44, 875–882. doi: 10.1021/ar200090c

Hola, K., Markova, Z., Zoppellaro, G., Tucek, J., and Zboril, R. (2015). Tailored functionalization of iron oxide nanoparticles for MRI, drug delivery, magnetic separation and immobilization of biosubstances. *Biotechnol. Adv.* 33, 1162–1176. doi: 10.1016/j.biotechadv.2015.02.003

Huber, D. L. (2005). Synthesis, properties, and applications of iron nanoparticles. *Small* 1, 482–501. doi: 10.1002/smll.200500006

Hufschmid, R., Arami, H., Ferguson, R. M., Gonzales, M., Teeman, E., Brush, L. N., et al. (2015). Synthesis of phase-pure and monodisperse iron oxide nanoparticles by thermal decomposition. *Nanoscale* 7, 11142–11154. doi: 10.1039/C5NR01651G

Hyeon, T., Piao, Y., and Park, Y. I. (2016). *U.S. Patent No. 9,352,058*. Washington, DC: U.S. Patent and Trademark Office.

Iravani, S. (2011). Green synthesis of metal nanoparticles using plants. *Green Chem.* 13, 2638–2650. doi: 10.1039/c1gc15386b

Jiles, D. (2015). *Introduction to Magnetism and Magnetic Materials*. Boca Raton, FL: CRC Press.

Kandasamy, R. (2017). A novel single step synthesis and surface functionalization of iron oxide magnetic nanoparticles and thereof for the copper removal from pigment industry effluent. *Separation Purification Technol.* 188, 458–467. doi: 10.1016/j.seppur.2017.07.059

Khandhar, A. P., Keselman, P., Kemp, S. J., Ferguson, R. M., Goodwill, P. W., Conolly, S. M., et al. (2017). Evaluation of PEG-coated iron oxide nanoparticles as blood pool tracers for preclinical magnetic particle imaging. *Nanoscale* 9, 1299–1306. doi: 10.1039/C6NR08468K

Kharisov, B. I., Dias, H. R., Kharissova, O. V., Vázquez, A., Pena, Y., and Gomez, I. (2014). Solubilization, dispersion and stabilization of magnetic nanoparticles in water and non-aqueous solvents: recent trends. *RSC Adv.* 4, 45354–45381. doi: 10.1039/c4ra06902a

Kharissova, O. V., Dias, H. R., Kharisov, B. I., Pérez, B. O., and Pérez, V. M. J. (2013). The greener synthesis of nanoparticles. *Trends Biotechnol.* 31, 240–248. doi: 10.1016/j.tibtech.2013.01.003

Kobayashi, T., Ito, A., and Honda, H. (2016). "Magnetic nanoparticle-mediated hyperthermia and induction of anti-tumor immune responses," in *Hyperthermic Oncology from Bench to Bedside*, eds S. Kokura, T. Yoshikawa, and T. Ohnishi (Singapore: Springer), 137–150. doi: 10.1007/978-981-10-0719-4_13

Kovár, D., Malá, A., Mlčochová, J., Kalina, M., Fohlerová, Z., Hlaváček, A., et al. (2017). Preparation and characterisation of highly stable iron oxide nanoparticles for magnetic resonance imaging. *J. Nanomater.* 2017:7859289. doi: 10.1155/2017/7859289

Kumar, A., Saxena, A., De, A., Shankar, R., and Mozumdar, S. (2013). Facile synthesis of size-tunable copper and copper oxide nanoparticles using reverse microemulsions. *Rsc Adv.* 3, 5015–5021. doi: 10.1039/c3ra23455j

Langer, R. (1990). New methods of drug delivery. *Science* 249, 1527–1533. doi: 10.1126/science.2218494

Laurent, S., Forge, D., Port, M., Roch, A., Robic, C., Vander Elst, L., et al. (2008). Magnetic iron oxide nanoparticles: synthesis, stabilization, vectorization, physicochemical characterizations, and biological applications. *Chem. Rev.* 108, 2064–2110. doi: 10.1021/cr068445e

Li, J., Wang, S., Shi, X., and Shen, M. (2017). Aqueous-phase synthesis of iron oxide nanoparticles and composites for cancer diagnosis and therapy. *Adv. Colloid Interface Sci.* 249, 374–385. doi: 10.1016/j.cis.2017.02.009

Li, L., Jiang, W., Luo, K., Song, H., Lan, F., Wu, Y., et al. (2013). Superparamagnetic iron oxide nanoparticles as MRI contrast agents for non-invasive stem cell labeling and tracking. *Theranostics* 3:595. doi: 10.7150/thno.5366

Li, X., Wang, C., Tan, H., Cheng, L., Liu, G., Yang, Y., et al. (2016). Gold nanoparticles-based SPECT/CT imaging probe targeting for vulnerable atherosclerosis plaques. *Biomaterials* 108, 71–80. doi: 10.1016/j.biomaterials.2016.08.048

Lin, L., Starostin, S. A., Hessel, V., and Wang, Q. (2017). Synthesis of iron oxide nanoparticles in microplasma under atmospheric pressure. *Chem. Eng. Sci.* 168, 360–371. doi: 10.1016/j.ces.2017.05.008

Liu, Y., Yang, J., Xie, M., Xu, J., Li, Y., Shen, H., et al. (2017). Synthesis of polyethyleneimine-modified magnetic iron oxide nanoparticles without adding base and other additives. *Mater. Lett.* 193, 122–125. doi: 10.1016/j.matlet.2017.01.056

Lodhia, J., Mandarano, G., Ferris, N. J., Eu, P., and Cowell, S. F. (2010). Development and use of iron oxide nanoparticles (Part 1): synthesis of iron oxide nanoparticles for MRI. *Biomed. Imag. Intervent. J.* 6:e12. doi: 10.2349/biij.6.2.e12

Lu, A. H., Salabas, E. L., and Schüth, F. (2007). Magnetic nanoparticles: synthesis, protection, functionalization, and application. *Angew. Chem. Int. Ed.* 46, 1222–1244. doi: 10.1002/anie.200602866

Madadlou, A., Jaberipour, S., and Eskandari, M. H. (2014). Nanoparticulation of enzymatically cross-linked whey proteins to encapsulate caffeine via microemulsification/heat gelation procedure. *LWT-Food Sci. Technol.* 57, 725–730. doi: 10.1016/j.lwt.2014.02.041

Mahmed, N., Heczko, O., Söderberg, O., and Hannula, S. P. (2011). "Room temperature synthesis of magnetite ($Fe_3O_4$) nanoparticles by a simple reverse co-precipitation method," in *IOP Conference Series: Materials Science and Engineering* (Bristol: IOP Publishing). doi: 10.1088/1757-899X/18/3/032020

Makarov, V. V., Makarova, S. S., Love, A. J., Sinitsyna, O. V., Dudnik, A. O., Yaminsky, I. V., et al. (2014). Biosynthesis of stable iron oxide nanoparticles in aqueous extracts of *Hordeum vulgare* and *Rumex acetosa* plants. *Langmuir* 30, 5982–5988. doi: 10.1021/la5011924

Malo de Molina, P., Zhang, M., Bayles, A. V., and Helgeson, M. E. (2016). Oil-in-water-in-oil multinanoemulsions for templating complex nanoparticles. *Nano Lett.* 16, 7325–7332. doi: 10.1021/acs.nanolett.6b02073

Marangon, I., Silva, A. A., Guilbert, T., Kolosnjaj-Tabi, J., Marchiol, C., and Natkhunarajah, S. (2017). Tumor stiffening, a key determinant of tumor progression, is reversed by nanomaterial-induced photothermal therapy. *Theranostics* 7:329. doi: 10.7150/thno.17574

Martínez-Cabanas, M., López-García, M., Barriada, J. L., Herrero, R., and de Vicente, M. E. S. (2016). Green synthesis of iron oxide nanoparticles. Development of magnetic hybrid materials for efficient As(V) removal. *Chem. Eng. J.* 301, 83–91. doi: 10.1016/j.cej.2016.04.149

Maryanti, E., Damayanti, D., and Gustian, I. (2014). Synthesis of ZnO nanoparticles by hydrothermal method in aqueous rinds extracts of Sapindus rarak DC. *Mater. Lett.* 118, 96–98. doi: 10.1016/j.matlet.2013.12.044

Mascolo, M., Pei, Y., and Ring, T. (2013). Room temperature co-precipitation synthesis of magnetite nanoparticles in a large pH window with different bases. *Materials* 6, 5549–5567. doi: 10.3390/ma6125549

McMahon, M. T., and Bulte, J. W. (2018). Two decades of dendrimers as versatile MRI agents: a tale with and without metals. *Wiley Interdisciplinary Rev. Nanomed. Nanobiotechnol.* 10:e1496. doi: 10.1002/wnan.1496

McNamara, K., and Tofail, S. A. (2017). Nanoparticles in biomedical applications. *Adv. Phys.* 2, 54–88. doi: 10.1080/23746149.2016.1254570

Mody, V. V., Cox, A., Shah, S., Singh, A., Bevins, W., and Parihar, H. (2014). Magnetic nanoparticle drug delivery systems for targeting tumor. *Appl. Nanosci.* 4, 385–392. doi: 10.1007/s13204-013-0216-y

Mohammed, L., Gomaa, H. G., Ragab, D., and Zhu, J. (2017). Magnetic nanoparticles for environmental and biomedical applications: a review. *Particuology* 30, 1–14. doi: 10.1016/j.partic.2016.06.001

Monsalve, A., Vicente, J., Grippin, A., and Dobson, J. (2017). Poly (lactic acid) magnetic microparticle synthesis and surface functionalization. *IEEE Magn. Lett.* 8, 1–5. doi: 10.1109/LMAG.2017.2726505

Naghibi, S., Sani, M. A. F., and Hosseini, H. R. M. (2014). Application of the statistical Taguchi method to optimize $TiO_2$ nanoparticles synthesis by the hydrothermal assisted sol–gel technique. *Ceramics Int.* 40, 4193–4201. doi: 10.1016/j.ceramint.2013.08.077

Nassar, M. Y., Ahmed, I. S., Mohamed, T. Y., and Khatab, M. (2016). A controlled, template-free, and hydrothermal synthesis route to sphere-like α-Fe 2 O 3 nanostructures for textile dye removal. *RSC Adv.* 6, 20001–20013. doi: 10.1039/C5RA26112K

Njagi, E. C., Huang, H., Stafford, L., Genuino, H., Galindo, H. M., Collins, J. B., et al. (2010). Biosynthesis of iron and silver nanoparticles at room temperature using aqueous sorghum bran extracts. *Langmuir* 27, 264–271. doi: 10.1021/la103190n

Pang, Y. L., Lim, S., Ong, H. C., and Chong, W. T. (2016). Research progress on iron oxide-based magnetic materials: synthesis techniques and photocatalytic applications. *Ceramics Int.* 42, 9–34. doi: 10.1016/j.ceramint.2015.08.144

Patsula, V., Kosinová, L., Lovri,c, M., Ferhatovic Hamzic, L., Rabyk, M., Konefal, R., et al. (2016). Superparamagnetic $Fe_3O_4$ nanoparticles: synthesis by thermal decomposition of iron (III) glucuronate and application in magnetic resonance imaging. *ACS Appl. Mater. Interfaces* 8, 7238–7247. doi: 10.1021/acsami.5b12720

Rai, M., Maliszewska, I., Ingle, A., Gupta, I., and Yadav, A. (2015). "Diversity of microbes in synthesis of metal nanoparticles: progress and limitations," in *Bio-Nanoparticles: Biosynthesis and Sustainable Biotechnological Implications*, ed O. V. Singh (Chichester: Wiley), 1–30. doi: 10.1002/9781118677629.ch1

Rajiv, P., Bavadharani, B., Kumar, M. N., and Vanathi, P. (2017). Synthesis and characterization of biogenic iron oxide nanoparticles using green chemistry approach and evaluating their biological activities. *Biocatalysis Agricult. Biotechnol.* 12, 45–49. doi: 10.1016/j.bcab.2017.08.015

Riaz, S., Naseem, S., and Han, X. (2015). "Citric acid coated iron oxide nanoparticles—Structural and magnetic properties," in *2015 IEEE International Magnetics Conference (INTERMAG)* (IEEE). doi: 10.1109/INTMAG.2015.7157349

Sakellari, D., Brintakis, K., Kostopoulou, A., Myrovali, E., Simeonidis, K., Lappas, A., et al. (2016). Ferrimagnetic nanocrystal assemblies as versatile magnetic particle hyperthermia mediators. *Mater. Sci. Eng. C* 58, 187–193. doi: 10.1016/j.msec.2015.08.023

Sathya, K., Saravanathamizhan, R., and Baskar, G. (2017). Ultrasound assisted phytosynthesis of iron oxide nanoparticle. *Ultrasonics Sonochem.* 39, 446–451. doi: 10.1016/j.ultsonch.2017.05.017

Schneider, M. G. M., and Lassalle, V. L. (2017). Magnetic iron oxide nanoparticles as novel and efficient tools for atherosclerosis diagnosis. *Biomed. Pharmacother.* 93, 1098–1115. doi: 10.1016/j.biopha.2017.07.012

Seeli, D. S., and Prabaharan, M. (2017). Guar gum oleate-graft-poly (methacrylic acid) hydrogel as a colon-specific controlled drug delivery carrier. *Carbohydrate Polymers* 158, 51–57. doi: 10.1016/j.carbpol.2016.11.092

Shah, M., Fawcett, D., Sharma, S., Tripathy, S., and Poinern, G. (2015). Green synthesis of metallic nanoparticles via biological entities. *Materials* 8, 7278–7308. doi: 10.3390/ma8115377

Smith, T. W., and Wychick, D. (1980). Colloidal iron dispersions prepared via the polymer-catalyzed decomposition of iron pentacarbonyl. *J. Phys. Chem.* 84, 1621–1629. doi: 10.1021/j100449a037

Sood, A., Arora, V., Shah, J., Kotnala, R. K., and Jain, T. K. (2017). Multifunctional gold coated iron oxide core-shell nanoparticles stabilized using thiolated sodium alginate for biomedical applications. *Mater. Sci. Eng. C* 80, 274–281. doi: 10.1016/j.msec.2017.05.079

Sun, Z., Worden, M., Thliveris, J. A., Hombach-Klonisch, S., Klonisch, T., van Lierop, J., et al. (2016). Biodistribution of negatively charged iron oxide nanoparticles (IONPs) in mice and enhanced brain delivery using lysophosphatidic acid (LPA). *Nanomed. Nanotechnol. Biol. Med.* 12, 1775–1784. doi: 10.1016/j.nano.2016.04.008

Surowiec, Z., Budzynski, M., Durak, K., and Czernel, G. (2017). Synthesis and characterization of iron oxide magnetic nanoparticles. *Nukleonika* 62, 73–77. doi: 10.1515/nuka-2017-0009

Taboada, E., Rodríguez, E., Roig, A., Oró, J., Roch, A., and Muller, R. N. (2007). Relaxometric and magnetic characterization of ultrasmall iron oxide nanoparticles with high magnetization. Evaluation as potential T 1 magnetic resonance imaging contrast agents for molecular imaging. *Langmuir* 23, 4583-4588. doi: 10.1021/la063415s

Tadic, M., Panjan, M., Damnjanovic, V., and Milosevic, I. (2014). Magnetic properties of hematite ($\alpha$-$Fe_2O_3$) nanoparticles prepared by hydrothermal synthesis method. *Appl. Surface Sci.* 320, 183–187. doi: 10.1016/j.apsusc.2014.08.193

Tombácz, E., Turcu, R., Socoliuc, V., and Vékás, L. (2015). Magnetic iron oxide nanoparticles: recent trends in design and synthesis of magnetoresponsive nanosystems. *Biochem. Biophys. Res. Commun.* 468, 442–453. doi: 10.1016/j.bbrc.2015.08.030

Veiseh, O., Gunn, J. W., and Zhang, M. (2010). Design and fabrication of magnetic nanoparticles for targeted drug delivery and imaging. *Adv. Drug Delivery Rev.* 62, 284–304. doi: 10.1016/j.addr.2009.11.002

Wang, Y., Chen, J., Yang, B., Qiao, H., Gao, L., Su, T., et al. (2016). *In vivo* MR and fluorescence dual-modality imaging of atherosclerosis characteristics in mice using profilin-1 targeted magnetic nanoparticles. *Theranostics* 6, 272. doi: 10.7150/thno.13350

Watt, J., Bleier, G. C., Austin, M. J., Ivanov, S. A., and Huber, D. L. (2017). Non-volatile iron carbonyls as versatile precursors for the synthesis of iron-containing nanoparticles. *Nanoscale* 9, 6632–6637. doi: 10.1039/C7NR01028A

Wee, S.-B., Oh, H.-C., Kim, T.-G., An, G.-S., and Choi, S.-C. (2017). Role of N-methyl-2-pyrrolidone for preparation of $Fe_3O_4$@ $SiO_2$ controlled the shell thickness. *J. Nanoparticle Res.* 19:143. doi: 10.1007/s11051-017-3813-y

Williams, M. J., Sánchez, E., Aluri, E. R., Douglas, F. J., MacLaren, D. A., Collins, O. M., et al. (2016). Microwave-assisted synthesis of highly crystalline, multifunctional iron oxide nanocomposites for imaging applications. *RSC Adv.* 6, 83520–83528. doi: 10.1039/C6RA11819D

Xiao, Y.-D., Paudel, R., Liu, J., Ma, C., Zhang, Z.-S., and Zhou, S.-K. (2016). MRI contrast agents: classification and application. *Int. J. Mol. Med.* 38, 1319–1326. doi: 10.3892/ijmm.2016.2744

Xu, X., Yadav, N. N., Song, X., McMahon, M. T., Jerschow, A., Van Zijl, P. C., et al. (2016). Screening CEST contrast agents using ultrafast CEST imaging. *J. Magn. Resonance* 265, 224–229. doi: 10.1016/j.jmr.2016.02.015

Yang, K. M., Cho, H. I., Choi, H. J., and Piao, Y. (2014). Synthesis of water well-dispersed PEGylated iron oxide nanoparticles for MR/optical lymph node imaging. *J. Mater. Chem. B* 2, 3355–3364. doi: 10.1039/C4TB00084F

Yang, X. C., Shang, Y. L., Li, Y. H., Zhai, J., Foster, N. R., Li, Y. X., et al. (2014). Synthesis of monodisperse Iron oxide nanoparticles without surfactants. *J. Nanomater.* 2014:231. doi: 10.1155/2014/740856

Yelenich, O. V., Solopan, S. O., Kolodiazhnyi, T. V., Greneche, J. M., and Belous, A. G. (2015). "Synthesis of iron oxide nanoparticles by different methods and study of their properties," in *Solid State Phenomena, Vol. 230* (Zurich: Trans Tech Publications), 108–113. doi: 10.4028/www.scientific.net/SSP.230.108

Yildirim, A., Chattaraj, R., Blum, N. T., and Goodwin, A. P. (2016). Understanding acoustic cavitation initiation by porous nanoparticles: toward nanoscale agents for ultrasound imaging and therapy. *Chem. Mater.* 28, 5962–5972. doi: 10.1021/acs.chemmater.6b02634

Yoo, S. P., Pineda, F., Barrett, J. C., Poon, C., Tirrell, M., and Chung, E. J. (2016). Gadolinium-functionalized peptide amphiphile micelles for multimodal imaging of atherosclerotic lesions. *ACS Omega* 1, 996–1003. doi: 10.1021/acsomega.6b00210

Yu, S. M., Laromaine, A., and Roig, A. (2014). Enhanced stability of superparamagnetic iron oxide nanoparticles in biological media using a pH adjusted-BSA adsorption protocol. *J. Nanopart. Res.* 16:2484. doi: 10.1007/s11051-014-2484-1

Yu, W., Sun, T. W., Ding, Z., Qi, C., Zhao, H., Chen, F., et al. (2017). Copper-doped mesoporous hydroxyapatite microspheres synthesized by a microwave-hydrothermal method using creatine phosphate as an organic phosphorus source: application in drug delivery and enhanced bone regeneration. *J. Mater. Chem. B* 5, 1039–1052. doi: 10.1039/C6TB02747D

Zhao, H., Liu, R., Zhang, Q., and Wang, Q. (2016). Effect of surfactant amount on the morphology and magnetic properties of monodisperse $ZnFe_2O_4$ nanoparticles. *Mater. Res. Bull.* 75, 172–177. doi: 10.1016/j.materresbull.2015.11.052

Zheng, Y., Hunting, D. J., Ayotte, P., and Sanche, L. (2008). Radiosensitization of DNA by gold nanoparticles irradiated with high-energy electrons. *Radiat. Res.* 169, 19–27. doi: 10.1667/RR1080.1

**Conflict of Interest Statement:** The authors declare that the research was conducted in the absence of any commercial or financial relationships that could be construed as a potential conflict of interest.

frontiers in Bioengineering and Biotechnology

ORIGINAL RESEARCH
published: 27 September 2019
doi: 10.3389/fbioe.2019.00247

# Customizable Implant-specific and Tissue-Specific Extracellular Matrix Protein Coatings Fabricated Using Atmospheric Plasma

*Fei Tan* [1,2,3]* *and Mohamed Al-Rubeai* [4]

[1] Department of Otolaryngology - Head & Neck Surgery, Shanghai East Hospital, Tongji University School of Medicine, Shanghai, China, [2] School of Chemical and Bioprocess Engineering, and Conway Institute of Biomolecular and Biomedical Research, University College Dublin—National University of Ireland, Dublin, Ireland, [3] The Royal College of Surgeons of England, London, United Kingdom, [4] Department of Biology, Cihan University-Erbil, Erbil, Iraq

Progression in implant science has benefited from ample amount of technological contributions from various disciplines, including surface biotechnology. In this work, we successfully used atmospheric plasma to enhance the biological functions of surgical implants by coating them with extracellular matrix proteins. The developed collagen and laminin coatings demonstrate advantageous material properties. Chemical analysis by XPS and morphological investigation by SEM both suggested a robust coating. Contact angle goniometry and dissolution study in simulated body fluid (SBF) elicited increased hydrophilicity and physiological durability. Furthermore, these coatings exhibited improved biological interactions with human mesenchymal and neural stem cells (NSCs). Cell adhesion, proliferation, and differentiation proved markedly refined as shown by enzymatic detachment, flow cytometry, and ELISA data, respectively. Most importantly, using the pathway-specific PCR array, our study discovered dozens of deregulated genes during osteogenesis and neurogenesis on our newly fabricated ECM coatings. The coating-induced change in molecular profile serves as a promising clue for designing future implant-based therapy. Collectively, we present atmospheric plasma as a versatile tool for enhancing surgical implants, through customizable implant-specific and tissue-specific coatings.

**Keywords: atmospheric plasma, implant, coating, collagen, laminin, bone, nerve**

OPEN ACCESS

***Edited by:***
*Mario Guagliano, Politecnico di Milano, Italy*

***Reviewed by:***
*Jangho Kim, Chonnam National University, South Korea*
*David K. Mills, Louisiana Tech University, United States*

***Correspondence:**
*Fei Tan*
*iatrologist@163.com*

***Specialty section:***
*This article was submitted to Biomaterials, a section of the journal Frontiers in Bioengineering and Biotechnology*

***Received:*** *21 July 2019*
***Accepted:*** *16 September 2019*
***Published:*** *27 September 2019*

***Citation:***
*Tan F and Al-Rubeai M (2019) Customizable Implant-specific and Tissue-Specific Extracellular Matrix Protein Coatings Fabricated Using Atmospheric Plasma. Front. Bioeng. Biotechnol. 7:247. doi: 10.3389/fbioe.2019.00247*

## INTRODUCTION

Surgical implants are the quintessence of modern medicine. They represent a unique therapeutic modality owing to their interdisciplinarity. They are designed to replace missing body parts, to support damaged organs and tissues, or to enhance deficient biological functions (van Eck et al., 2009). Depending on the type of target tissue, implants can be roughly categorized into those repairing hard tissue and those restoring soft tissue. In head and neck surgery, the two best examples are bone anchored hearing aid (BAHA) and cochlear implant (CI), which influence bone and nerve tissue, respectively (Gaylor et al., 2013; Ghossaini and Roehm, 2019). Metals and polymers are the dominant classes of biomaterial used in these implants. Metals possess exceptional mechanical

properties and corrosion resistance (Spriano et al., 2018), whereas polymers feature extraordinary flexibility and long-term stability (Teo et al., 2016). However, none of these materials is functionally perfect, as each has its advantageous and disadvantageous properties. Thus, there is constant need and drive to enhance the current surgical implants.

The surface of a surgical implant is the key area where implant-tissue reaction occurs. Biotechnology targeting the implant surface can promote the performance profiles of surgical implants. Recent innovations in surface biotechnology have demonstrated at least four intriguing strategies: substitute biomaterial, surface modification, drug delivery, and coating (Tan et al., 2013). Coating normally uses an entirely different material from the underlying surgical implant, attempting to combine the advantages of both layers. For example, from an osteogenic perspective, coating the intracortical screw of BAHA with ceramic can significantly improve its osteoconductivity while maintaining the implant's high mechanical strength (Sanden et al., 2002; Tan et al., 2012a). From a neurogenic perspective, coating the electrode of CI with conducting polymer can greatly enhance its neural biocompatibility without affecting the implant's electrical conductivity (Quigley et al., 2009; Green et al., 2012). Therefore, a coating should be implant-specific to enhance its established therapeutic function.

Furthermore, an ideal coating should also be tissue-specific. The native extracellular matrix (ECM) happens to consist of a tissue-specific, highly complex network of proteins and polysaccharides which provide structural scaffolding and biochemical cues for surrounding cells, including stem cells (Theocharis et al., 2016). In addition, the main protein components of ECM: collagen, laminin, and fibronectin have substantial impact on tissue-specific stem cell morphogenesis, differentiation, and homeostasis (Frantz et al., 2010; Ahmed and Ffrench-Constant, 2016). For example, collagen promotes mesenchymal stem cell (MSC) proliferation and encourages osteogenic differentiation from MSCs (Somaiah et al., 2015). On the other hand, laminin enhances neural stem cell (NSC) migration, expansion, differentiation into neurons, and their derived neurite outgrowth (Flanagan et al., 2006). Many coating techniques have been explored to deposit proteins onto surgical implants. These include simple immersion (Rammelt et al., 2004), covalent immobilization (Ao et al., 2016), and chemical bonding (Hum and Boccaccini, 2018). These methods all share a common characteristic, i.e., non-thermality, due to the heat-sensitive nature of proteins.

Atmospheric plasma is an emerging non-thermal biotechnology. In simple term, non-thermal plasma is a technical, adjustable, and ambient version of thermal plasma (e.g., solar corona) (Tendero et al., 2006). Atmospheric plasma has been recently applied in medicine and the life sciences. Depending on the approach, application can involve direct, or indirect treatment (Fridman et al., 2008). Direct plasma treatments can assist in wound healing and skin rejuvenation in dermatology (Heinlin et al., 2011), and perform effective dissection and precise tissue removal in head and neck surgery (Metcalfe et al., 2017). Meanwhile, indirect plasma treatments exert the therapeutic effect mainly through processing the surface of biomedical devices (e.g., surgical implants). Recent examples cover most of the strategies in surface biotechnology: surface modification (Prasad et al., 2010; Tan et al., 2012b), drug delivery (Yoshida et al., 2013; Dowling et al., 2016), and implant coatings (Dowling et al., 2009; Tynan et al., 2009). We have successfully used atmospheric plasma as a surface modification method to activate ceramic implants, thereby achieving better osteogenesis (Tan et al., 2012b). However, coating surgical implants by atmospheric plasma remains an underexploited area, especially with ECM proteins.

The primary objective of this study was to establish implant-specific (metal and polymer) and tissue-specific (osteogenic and neurogenic) ECM coatings (collagen and laminin) facilitated by atmospheric plasma. The secondary objective was to compare coatings deposited using different techniques (atmospheric plasma vs. traditional adsorption). Particular emphasis was placed on material properties (physical and chemical), cellular interactions (MSC and NSC), and transcriptomic activities (osteogenesis and neurogenesis pathways). The final objective was to elucidate the molecular basis through which these novel coatings enhance tissue-specific differentiation from stem cells.

# MATERIALS AND METHODS

## Atmospheric Plasma Set-Up

In order to simulate the metal and polymer surgical implants, grade V Titanium (Ti) alloy coupon (Lisnabrin Engineering Ltd., Cork, Ireland) and tissue culture grade polystyrene (PS) disk (Thermo Scientific, Surrey, UK) sized 20 × 20 × 1 mm were used, respectively. Surface roughness plays an important role in cell attachment and differentiation (Ponsonnet et al., 2003; Li et al., 2016). Since polystyrene surfaces tend to be relatively smooth, for comparison purposes, we created a rough surface via grit-polishing and grit-blasting Ti samples. The Ti alloy substrates were polished to a 1,200 grit size using silicon carbide paper. The polished samples were ultrasonically cleaned for 5 min to remove residual particulates, consecutively in acetone, methanol, and isopropyl alcohol (Sigma-Aldrich, Dorset, UK). They were then blasted by $Al_2O_3$ (Comco Incorporated, Burbank, USA) with a mean particle size of 100 μm using a microblasting platform (ENBIO, Dublin, Ireland) (Tan et al., 2012a). Finally, the roughened metal disks and as-received polymer specimens were immersed in deionized water (dI $H_2O$) and ultrasonically cleaned for 5 min. They were dried at room temperature, stored in a desiccator, and prepared for the coating process.

The PlasmaPlus® technology (Plasmatreat GmbH, Steinhagen, Germany) was used to facilitate coating formation (Bringmann et al., 2009; Dowling et al., 2009; Scopece et al., 2009). It is essentially an atmospheric pressure plasma jet (APPJ) based on air or nitrogen plasma (**Figure 1**). The Plasmatreater AS 400 laboratory system was modified for this study. The plasma was driven by a DC power supply operating at 23 kHz (280 V, 15 A). Clean dry industrial air with a flow rate of 35 l/min was used as ionization gas in the plasma torch. The plasma cycle time (PCT), an indicator of plasma intensity, was set at 100%. The APPJ was mounted on an X-Y-Z motion system, which traveled in a raster pattern at a line speed of 180 mm/s and a scanning

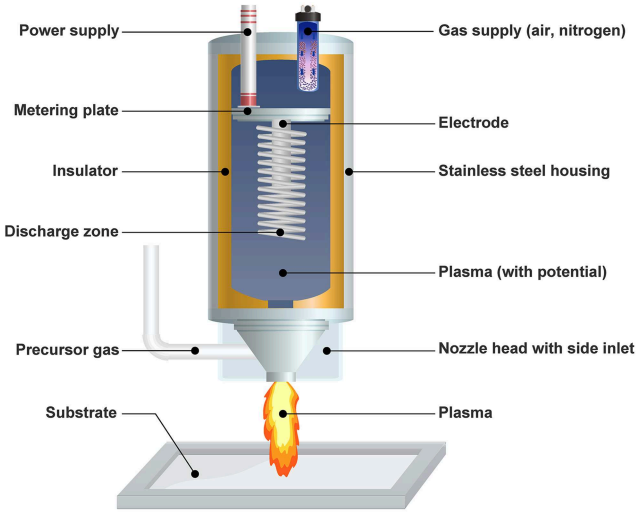


**FIGURE 1 |** Cross-section diagram of the PlasmaPlus APPJ coating nozzle.

interval of 1 mm. The plasma jet orifice was placed above the test substrates at a standoff distance of 15 mm.

## Deposition of ECM Coatings

In order to obtain ECM coatings on the aforementioned implants, type I collagen from human fibroblasts, and laminin from human fibroblasts and epithelial cells co-culture were used, respectively (Sigma-Aldrich). A 10 μg/ml working solution of collagen or laminin was prepared. The former was diluted from stock using phosphate-buffered saline (PBS) and pH-adjusted to 7.2–7.6 using 0.1 M NaOH or 0.01 M HCl (Heino, 2007), whereas the latter was simply diluted using Hank's balanced salt solution (HBSS) (Kleinman, 2001). The above reagents all came from Fisher Scientific, Dublin, Ireland. All samples were divided into three groups: negative control (substrate only), positive control (coating by adsorption), and test group (coating by atmospheric plasma) (**Figure 2**).

In the test group, the Ti or PS substrates were each surface-activated by atmospheric plasma with ten passes. The collagen or laminin working solution was then sprayed immediately after plasma activation in order to maximize its efficacy. The ECM protein was applied in a nebulized form to the substrate using a piezoelectric sonication system (Breathnach et al., 2018). The nebulized collagen or laminin was sprayed for 3 s using nitrogen at a relatively low flow rate of 3 l/min. The amount of ECM protein solution delivered was ∼3 ml per substrate.

In the positive control group, where the coating was created using an adsorption method, the stored metallic and polymeric specimens were placed in 6-well tissue culture plates (Sarstedt, Wexford, Ireland). Each well was immersed with 3 ml of collagen and laminin working solution, respectively. They were then incubated at 37°C for 20 min and rinsed 3 times with PBS or HBSS. Irrespective of the coating method, the coated samples were air dried under a laminar flow hood.

## Material Characterization of Coatings

The chemical composition of coatings was disclosed by X-ray photoelectron spectroscopy (XPS) analysis using VersaProbe XPS microprobe (ULVAC-PHI Inc., Kanagawa, Japan). This instrument provided dual beam charge neutralization. Measurement was conducted on three areas of each sample, and data were recorded as relative atomic percentage concentration.

The hydrophilicity of coatings was quantified using the static sessile drop technique at room temperature by a computer automated goniometer (OCA 20, Dataphysics, Filderstadt, Germany). In detail, the static contact angle of simulated body fluid (SBF) was measured for eight separate locations on each sample (Tan et al., 2012b). In order to obtain SBF with an ion concentration close to that of human blood plasma, reagent grade powders were dissolved in dI $H_2O$ at 37°C, and pH-adjusted to 7.4 using 50 mM Tris aminomethane and 45 mM HCl (Kokubo, 1991). All reagents were supplied by Fisher Scientific, Dublin, Ireland. Due to the limit of the equipment, surfaces with a contact angle <5° were all considered super-hydrophilic.

The topography of ECM protein coatings was documented using a white light optical profilometer (Wyko NT1100, Veeco, Cambridge, UK). The arithmetical mean roughness Ra was calculated using corresponding formula.

The collagen coatings acquired in this study were used as examples for morphological analysis, which included both scanning electron microscopy (SEM) and stereomicroscopy. On one hand, coating samples were coated with gold by a turbo pumped high-resolution sputter coater (K575X, EmiTech, Kent, UK) prior to examination under a scanning electron microscope (Quanta 3D FEG, FEI Ltd., Cambridge, UK) which operated at 5 kV and 6.66 pA with an observation angle at 90°. On the other hand, the robustness of collagen coatings was analyzed using the Sircol collagen assay (Biocolor, Carrickfergus, UK). This assay is based on the binding of a dye, Sirius Red, to the intact triple helix organization of native collagens. In brief, the Sircol dye reagent was mixed with dI $H_2O$ (1:1 v/v). The stained samples were then visualized under a SZX12 stereomicroscope (Olympus, Southend-on-Sea, UK).

The kinetic dissolution of collagen and laminin coatings was quantified using an enzyme-linked immunosorbent assay (ELISA). The coated implants were incubated at 37°C in SBF with a constant agitation at 6 rpm. At each time point, protein-containing aliquots were replaced by fresh SBF. The type I collagen level was measured using a MicroVue sandwich ELISA kit (Quidel California, USA), which detects the carboxy-terminal propeptide of type I collagen (CICP). Whereas, the laminin concentration was determined using a QuantiMatrix ELISA kit (Millipore, Cork, Ireland), which employs the principal of competitive antibody inhibition and chromogenic detection. The light absorbance of the colored end solution from above coatings was measured at 405 and 450 nm, respectively. A standard colorimetric curve was used to calculate the ECM proteins concentration. The results present an average of three analyses. The replacement of aliquots with fresh SBF was taken into account for calculation.

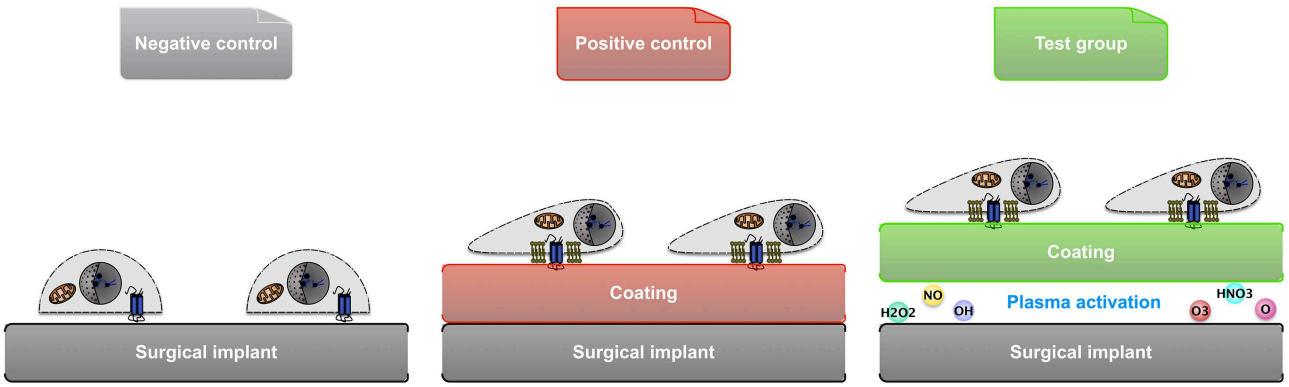


**FIGURE 2 |** Illustration of the 3 groups of samples used in material comparison and cellular study: negative control (substrate only), positive control (coating by adsorption), and test group (coating facilitated by atmospheric plasma).

## Stem Cell Cultures

This study used the StemPro® human bone marrow-derived MSCs and StemPro® human fetal brain-derived NSCs (Thermo Scientific, Surrey, UK) as cellular models. Unique to these cells is the low-oxygen manufacturing process in which they are isolated and expanded, resulting in higher yields of potent stem cells (Vertelov et al., 2013). They were cultured at 37°C in a humidified 5% $CO_2$ atmosphere in a commercial complete cell culture medium. For the MSCs culture, the MesenPRO RS™ complete medium with a Dulbecco's modified Eagle's medium (DMEM)-based and reduced-serum formulation was used. In order to avoid reduced multipotency of MSCs, cells were passaged when they reach 70% confluency, cell viability was at least 90%, and the growth rate was in mid-logarithmic phase. Cells were harvested according to the company's protocol. The MSCs were differentiated into osteogenic lineage in the StemPro® osteogenesis differentiation kit containing ascorbic acid and dexamethasone.

In contrast, the NSCs were maintained in suspension culture for proliferation because plating NSCs on a matrix as an adherent culture would trigger differentiation. The complete NSC culture medium contained 97% DMEM, 2% StemPro® neural supplement, 20 ng/ml basic fibroblast growth factor (bFGF) and 20 ng/ml epidermal growth factor (EGF), 2 mM L-alanyl-L-glutamine, 6 units/ml heparin, and 200 μM ascorbic acid (Sigma-Aldrich). The NSCs were harvested using Accutase® (Sigma-Aldrich) cell dissociation reagent to separate the neurospheres in the suspension culture system. Spontaneous neural differentiation of NSCs was allowed using the differentiation medium which consisted of complete NSC culture medium without bFGF and EGF. Passages 3–8 of stem cells were used to minimize change in growth pattern by *in vitro* expansion. Cellular experiments on coated and non-coated implants were performed in 6-well tissue culture plates (Sarstedt) with each well-immersed in 3 ml of medium.

## Cell Attachment and Adhesion

Cell attachment was analyzed quantitatively and qualitatively using flow cytometry and confocal laser scanning microscopy (CLSM), respectively. The number of attached cells was quantified using the Cell Lab Quanta SC flow cytometry system (Beckman Coulter Inc., Florida, US), employing propidium iodide (PI) as a fluorescent DNA dye. Stem cells were inoculated onto the implants at a concentration of $8 \times 10^5$ cells/ml. This relatively high concentration was used to saturate the bonding capacity of each surface to prevent falsely low results. After 12 h incubation at 37°C, unattached cells were gently rinsed away with Dulbecco's phosphate buffered saline (DPBS). Following enzymatic detachment, cells were carefully collected and counted by flow cytometer.

After 12 h of culture, MSCs were fixed *in situ* with 4% (w/v) paraformaldehyde DPBS solution, gently washed twice with wash buffer containing 0.05% (v/v) Tween-20, permeabilized with 0.1% (v/v) Triton X-100 solution, and blocked with 1% (w/v) bovine serum albumin (BSA). The immunofluorescent staining was completed using the actin cytoskeleton and focal adhesion staining kit (Millipore, Watford, UK). In brief, 1% (v/v) primary anti-Vinculin antibody, 1% (v/v) fluorescein isothiocyanate (FITC)-conjugated secondary antibody, and 1% tetramethylrhodamine isothiocyanate (TRITC)-conjugated phalloidin were used successively. The stained MSCs were observed using an LSM 510 Meta confocal laser scanning microscope (Carl Zeiss Ltd., Cambridge, UK).

Cell adhesion on the implants was measured via cell detachment by Accutase. Prior to detachment, the stem cells were inoculated at a concentration of $1 \times 10^6$ cells/ml to saturate the bonding capacity of the substrate. Over-seeded cells were gently rinsed away with warm DPBS. Following 24 h of incubation, the adherent cell number was determined using alamarBlue assay (Invitrogen, Paisley, UK), which is an *in situ*, non-toxic metabolism-based cell counting method. Then 3 ml of Accutase was added to each well and incubated for 2 min at 37°C. After enzymatic detachment, floating cells were discarded, and residual cells were collected and counted. The cell viability was always over 90% after cell adhesion assay. Fraction of adherent cells is defined as the post-detachment cell number divided by the pre-detachment cell number.

## Cell Cycle and Proliferation

Human MSCs and NSCs were inoculated onto the non-coated and coated implants at a density of $2 \times 10^5$ cells/ml. This relatively low concentration was to prevent the cells from reaching confluency too soon. As previously mentioned, MSCs and NSCs used in this study were maintained in different culture types: adherent culture vs. adherent/suspension culture, respectively. Therefore, different approaches were taken during medium change and cell quantification in each implant-containing well of the tissue culture plate. For the MSCs groups, only the adherent cells on the implants were collected. Whereas, for the NSCs groups, both the adherent cells and those suspending in the medium were harvested. The spent cell culture medium was replaced every 2 days. At each time point, cells were enzymatically detached from the implants, carefully collected, and counted using flow cytometry.

In order to simplify the comparison of cell cycle distribution, only the negative control and test group were used. After the initial cell seeding, a sufficient volume of medium was added on day 1 so that nutrient deprivation would not occur even after 5 days of continuous culture (Tan et al., 2012b). In short, the collected stem cell pellet was mixed with hypotonic DNA staining buffer (0.1% sodium citrate, 0.3% v/v Triton-x100, 0.01% PI, and 0.002% ribonuclease A in dI $H_2O$; all from Sigma-Aldrich), and analyzed using a C6 flow cytometer (Accuri, Cambridge, UK) which was equipped with FlowJo 9 software (TreeStar Inc., Oregon, USA).

## Stem Cell Differentiation

The osteogenic differentiation from MSCs and neurogenic differentiation from NSCs were measured after culturing in corresponding differentiation media for 14 days and 10 days, respectively. The osteogenic capacity was reflected by calcium deposition in the secreted mineral matrix. On day 14, the MSCs were decalcified with 0.6 M HCl for 24 h. The calcium content of the HCl supernatant was quantified colorimetrically, using the *o*-cresolphthalein complexone method (Sigma-Aldrich) (Mori et al., 1998). Following decalcification, the MSCs were washed three times with PBS and solubilized with 0.1 M NaOH/0.1% sodium dodecyl sulfate (SDS). The intracellular protein content was estimated using a bicinchoninic acid (BCA) protein assay kit (Sigma-Aldrich), and the amount of calcium was normalized to the total protein content.

On the other hand, the neurogenic competence was demonstrated by neurite formation. Since the PS substrate used was naturally transparent, the NSCs-grown implants were examined with a DM 500 light inverted phase contrast microscope (Leica, Milton Keynes, UK). On day 10, eight random locations (x100 magnification ratio) were chosen from each sample. The number of differentiated neurons and the total cell number in each visual field were counted. The cells with one or more neurites were considered differentiated neurons (Xiong et al., 2014). The differentiation ratio was quantified as the percentage of neurons.

## Pathway Expression Analysis

On day 12 of osteogenic and neurogenic differentiation, the target mRNA strands were reverse transcribed into their DNA complements (cDNA) and amplified using a reverse transcription polymerase chain reaction (RT-PCR). The RNA was extracted and purified using the RNeasy Plus Mini kit (QIAGEN, West Sussex, UK), which was followed by a quality check of total RNA using an ND-1000 NanoDrop spectrophotometer (Thermo Scientific) and an Agilent 2100 Bioanalyzer (Agilent Technologies, Cork, Ireland). Then cDNA was synthesized by using the $RT^2$ PCR array First Strand Kit (SABiosciences, Frederick, USA) to ensure compatibility with the subsequent PCR array analysis.

The human osteogenesis and neurogenesis $RT^2$ Profiler PCR Array (SABiosciences) were used to profile the expression of a focused panel of genes related to the pathways of osteogenesis/MSC differentiation and neurogenesis/NSC differentiation, respectively. This system used a 7900HT Fast Real-Time PCR (Q-PCR) machine (Applied Biosystems, Cheshire, UK) with 96-well plates. Each plate contained primers for 84 target genes and 5 housekeeping genes, 1 control to rule out human genomic DNA contamination, triplicates of the reverse transcription control to confirm RNA quality, and triplicates of positive PCR control to quality-control the general PCR performance (Tan et al., 2012b). The $RT^2$ Q-PCR master mix containing SYBR Green/ROX was mixed with cDNA and aliquoted into 96 wells. PCR cycling was performed with the following thermal profile: 1 cycle of 10 min at 95°C for enzyme activation, 40 cycles of 15 s at 95°C for denaturation, and 1 min at 60°C for annealing and extension. The $RT^2$ PCR Array Data analysis Web Portal (SABiosciences) was used to import cycle threshold ($C_T$) values to enable data calculation. The fold change and fold up/down regulation (test group vs. negative control) was calculated using the $2^{-\Delta\Delta CT}$ method (Livak and Schmittgen, 2001). Statistical comparison of the mean $C_T$ values originated from the triplicates of each implant specimen, expressed as *P*-value, was calculated using the Student's *t*-test. In this study, gene expression was considered significantly altered only when two conditions were simultaneously met: the fold regulation $>2$ or $<-2$, and the *P*-value $<0.05$ (Tan et al., 2012b).

**TABLE 1 |** Quantitative XPS analysis of Ti substrate with and without collagen coating, and PS substrate with and without laminin coating (Data is shown as atomic % elemental composition).

| Atomic % | Ti implants | | PS implants | |
|---|---|---|---|---|
| | Non-coated | Coated | Non-coated | Coated |
| O | 43.9 | 21.7 | 1.0 | 12.9 |
| C | 33.5 | 60.4 | 98.7 | 80.4 |
| N | 1.2 | 15.9 | 0.3 | 6.7 |
| Ti | 18.1 | 1.9 | | |
| Al | 3.3 | 0.1 | | |

*Hydrogen atoms are neglected.*

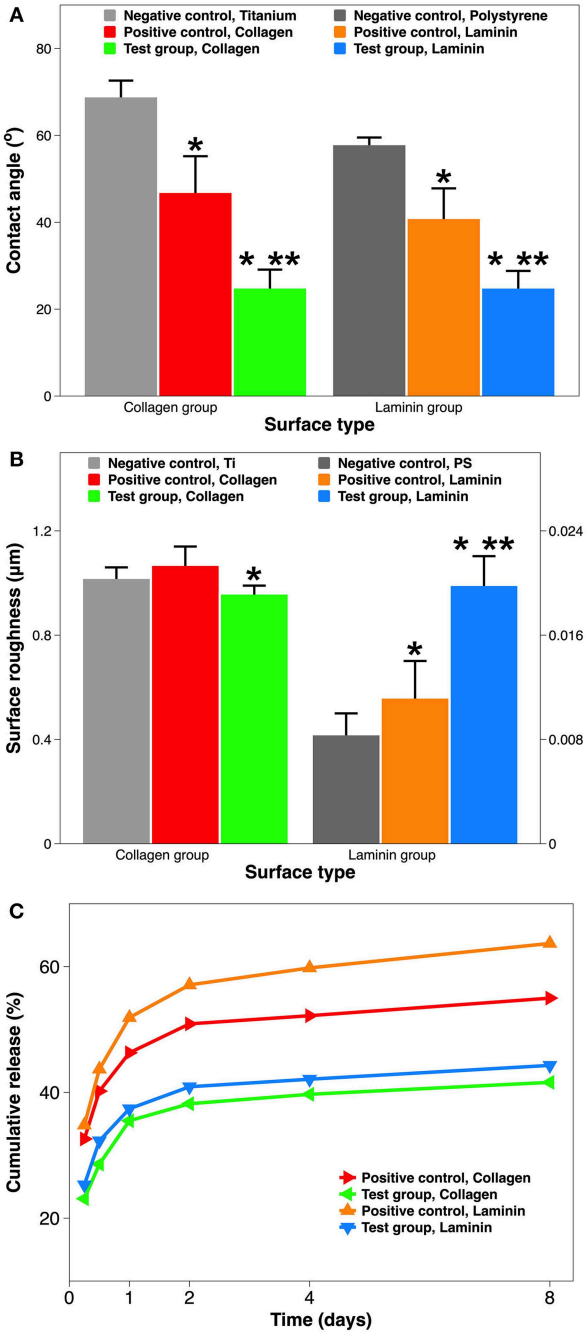


**FIGURE 3 |** Material characterization of implant surface with and without ECM protein coatings. **(A)** Surface hydrophilicity measured by goniometry (expressed as water contact angle in SBF). **(B)** Surface roughness measured by profilometry (expressed as *Ra* in μm). **(C)** Dissolution of ECM coatings over 8 days, quantified using ELISA (expressed as % cumulative release). A single asterisk denotes statistical significance when comparing a test group or positive control with a negative control, and a double asterisk when comparing a test group with a positive control.

The data of our pathway-focused gene analysis was verified at the protein level. A total of 8 genes from the above PCR array results were picked to represent up- and down-regulated genes during the osteogenesis and neurogenesis differentiation. The Quantikine® colorimetric sandwich ELISA kits (R&D Systems, Abingdon, UK) quantified the translated proteins from these genes. The analytes and standards were immobilized and sandwiched by capture antibodies and detection antibodies, respectively. Streptavidin-HRP was then used to bond the detection antibodies, and substrate solution was added to develop colors. The reaction was terminated using the acidic stop solution, and the optical density of each well was determined immediately at 450 nm (Ketelaar et al., 2016).

## Statistical Analysis

Student's *t*-test was conducted for one-to-one comparison unless stated otherwise. A statistical difference was claimed when the *P* value was $<0.05$. In order to signify the statistical differences in tables and figures, a single asterisk was used when comparing a test group or positive control with a negative control, and a double asterisk, when comparing a test group with a positive control). All statistical calculations were performed using SPSS Statistics 25 (IBM®, Chicago, IL).

# RESULTS AND DISCUSSION

## Material Characterization of the Coated and Non-coated Implants

This study assessed the material characteristics of surgical implants before and after coating as to four aspects: chemical properties, physical properties, morphological appearance, and biological stability. XPS revealed distinct shifting in the surface chemical composition when comparing Ti and PS implants (**Table 1**). The native Ti-6Al-4V substrate exhibited an abundant $TiO_2$ layer along with possibly either a hydrocarbon layer on top or carbon contamination from the passivation process (Sittig et al., 1999). The minor presence of aluminum on the surface was most likely due to residuals from the micro-blasting process, which used $Al_2O_3$ to roughen the surface (Milošev et al., 2000). Vanadium is not usually detected in spontaneously formed surface oxides (Ask et al., 1990). After coating the Ti implant with collagen, a substantial increase in carbon (from 33.5 to 60.4%) and nitrogen (from 1.2 to 15.9%) was noticed, indicating a robust layer of amino acid-based protein molecules. The dramatic reduction of titanium (from 18.1 to 1.9%) suggests a reasonable coverage of the collagen coating over the implant surface. These elemental changes are very similar to collagen coatings realized by other methods (Morra et al., 2006; Scarano et al., 2019). By comparison, even though polystyrene's chemical formula is $(C_8H_8)n$, the native PS surface is seemingly composed of carbon only (**Table 1**). This is because hydrogen cannot be directly detected using the XPS technique. After coating the PS implant with laminin, the strong appearance of nitrogen (6.7%) was accompanied by a considerable drop in carbon (from 98.7 to 80.4%). Laminin is a macromolecule with the skeleton of the molecular chain mainly consisting of C and N; and previous work has shown that the C/N ratio of laminin layer is around 12 (He et al., 2013). This ratio is identical to our finding, denoting the successful deposition of the laminin layer.

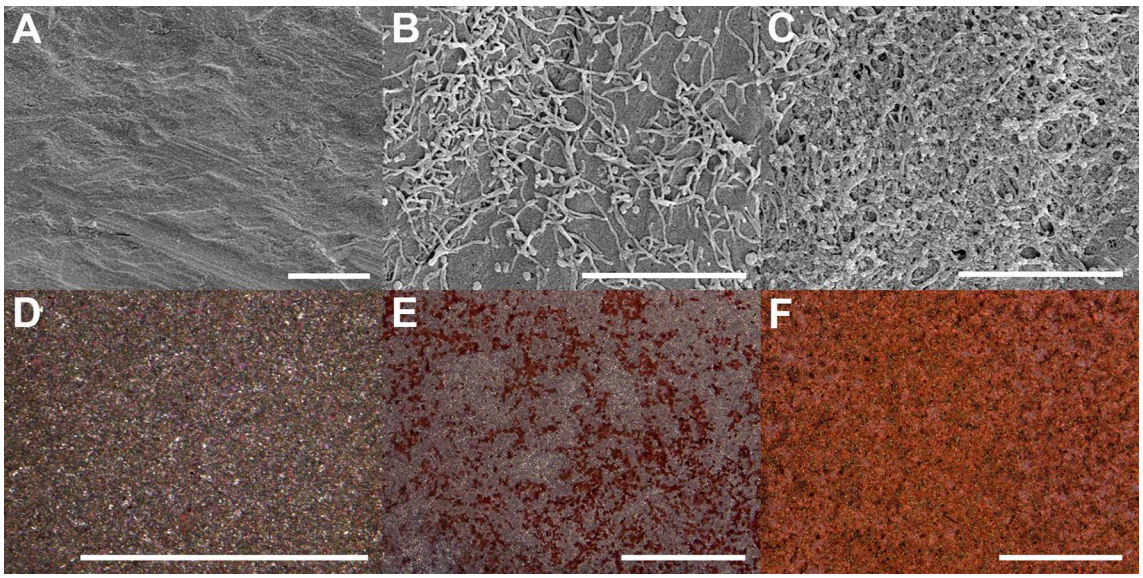


**FIGURE 4 |** Surface morphology of Ti implants with and without collagen coatings visualized using SEM **(A–C)** and Sircol staining **(D–F)**. **(A,D)** Ti substrate only. **(B,E)** Coating by adsorption. **(C,F)** Coating by atmospheric plasma. Scale bar = 5 μm **(A–C)** & 1 mm **(D–F)**, respectively.

Surface wettability is another important chemical property of implant material. In order to predict the implant wettability under physiological conditions, SBF was used instead of DI $H_2O$ during contact angle goniometry (Tan et al., 2012b). Both Ti and PS surfaces are considered hydrophilic, as they have water contact angles are <90° (Zeiger et al., 2013; Strnad et al., 2016). Coating these implants with ECM proteins seems to enhance their hydrophilicity, with a greater effect seen in the plasma-facilitated coatings (from 65° to 25°) (**Figure 3A**). Although coatings by adsorption reduce the contact angle to ∼45°, this results in a much larger standard deviation, indicating a less homogenous surface. It is well-known that hydrophilic surfaces tend to provide superior stem cell behavior than hydrophobic surfaces (Ahn et al., 2014; Hao et al., 2014; Yang et al., 2017). In addition, among surfaces with various degrees of hydrophilicity, moderately hydrophilic ones (20°−40° water contact angle) might render optimum cell attachment, spreading, and cytoskeletal organization (Webb et al., 1998). Thus, using atmospheric plasma to apply collagen and laminin coatings have the potential to create more favorable surfaces for MSCs and NSCs.

Surface roughness is a key physical property of implant material. Moreover, roughness and hydrophilicity are two independent but synergistic material properties for implant-related biocompatibility (Ponsonnet et al., 2003). Using optical profilometry, surface roughness is reflected by *Ra* which is the average distance from an arithmetic center line. The Ti and PS implants are considered relatively rough and smooth, respectively, as their surface roughness are at the micro-scale and nano-scale (1.21 μm vs. 8.5 nm). However, the effect of collagen or laminin coating on surface roughness is curiously opposite (**Figure 3B**). For the Ti implant group, adding a collagen coating by atmospheric plasma marginally reduces the surface roughness (from 1.02 to 0.96 μm). On the contrary, for the PS group, coating using the plasma with laminin significantly increases the surface roughness (from 8.4 to 19.9 nm). This unexpected change is best explained by the nanometer dimension of ECM proteins (Sharma et al., 2019). Depending on the roughness scale, nm proteins could "shallow" rougher surface and "deepen" smoother surface, respectively. Exciting recent studies demonstrate that, either an average roughness of 0.93 μm alone (Faia-Torres et al., 2015), or collagen itself (Lan and Wang, 2003), can serve as compelling alternatives to osteogenic supplements in stimulating osteogenic differentiation of MSCs.

The surface morphology of non-coated and coated implants was observed using SEM and functional staining (**Figure 4**). The Ti substrate exhibited a typical topography after grit-polishing and micro-blasting (**Figure 4A**). Its surface was carved with unidirectional linear grooves which are from polishing with sand paper, and decorated with random troughs and peaks which are from $Al_2O_3$ blasting. In addition, little residual micro-grit could be found on the surface. Collagen coatings by adsorption and plasma shows completely different morpholoies. The plasma-facilitated collagen coating is dense, compact, multilayered, and homogenous (**Figure 4C**). On the contrary, the adsorbed collagen coating is thin, loose, disorganized, and heterogenous (**Figure 4B**). Zooming out from the μm-scale SEM analysis to the mm-scale Sircol collagen staining, again they exhibit obvious differences. The non-coated Ti substrate does not seem to be stained, and displays a typical grainy and randomly reflective morphology (**Figure 4D**). The adsorbed collagen coating has rather a patchy and incomplete collagen clusters, and is only partially stained (**Figure 4E**). The plasma-facilitated collagen coating, on the other hand, demonstrates the typical tint of Sirius red, and is completely colored (**Figure 4F**). In addition, atmospheric plasma deposited 5.3 times more collagen than

the adsorption method. These results support coating by atmospheric plasma as the more robust method, and agree with the findings on collagen coatings created using other advanced techniques (Truong et al., 2012; Kim and Kim, 2016).

Coating dissolution in SBF is a reliable predictor for its durability in physiological conditions. **Figure 3C** demonstrates the cumulative amount of collagen and laminin released in SBF over an 8-day period. All samples shared a similar release kinetics: a burst release in the first day, followed by a slower release over the next week. The comparison among coatings is 2-fold: collagen coating vs. laminin coating, and coating by adsorption vs. coating by atmospheric plasma. Firstly, a collagen coating has a slower release than laminin coating, especially when they are deposited by simple immersion (55.0 vs. 63.7% at day 8). This most likely occurs due to the coating coverage on the substrate. Coatings applied by simple adsorption are incomplete, resulting in much greater exposure of the underlying Ti or PS substrate (**Figure 4**). Meanwhile, commercial Ti has a better protein adsorption than tissue culture PS (Derhami et al., 2001). Thus, the difference in substrate implants translated into the difference in coating dissolution. Secondly, coating by atmospheric plasma has a slower dissolution than coating by adsorption (41.6 vs. 55.0% at day 8). We suspect the key to this advantage comes from the plasma activation step during the coating process. Atmospheric plasma is a partially ionized low-pressure gas comprising of ions, electrons, ultraviolet photons, and reactive neutral species including radicals and excited atoms and molecules (Breathnach et al., 2018). Plasma activation bombards the implant surface with these ions and radicals inserting reactive functionality. The advantage of this surface biotechnology includes increased surface wettability without any structural damage (Tan et al., 2012b) and improved protein adsorption on the implant surface (Stallard et al., 2012). Thus, the resultant surface is suitable for crosslinking or subsequent deposition of organic and bioactive agents (Hauser et al., 2010). A recent study of collagen coating showed that introducing more reactive -OH groups on the surface can increase the amount of covalently bonded collagen (Hum and Boccaccini, 2018). It should be noticed that the initial burst release of the ECM coatings is still significant (35.5% of collagen and 37.4% of laminin). This is because the plasma activation only alters ECM proteins close to the surface; those not covalently bonded to the surface still diffuse relatively fast.

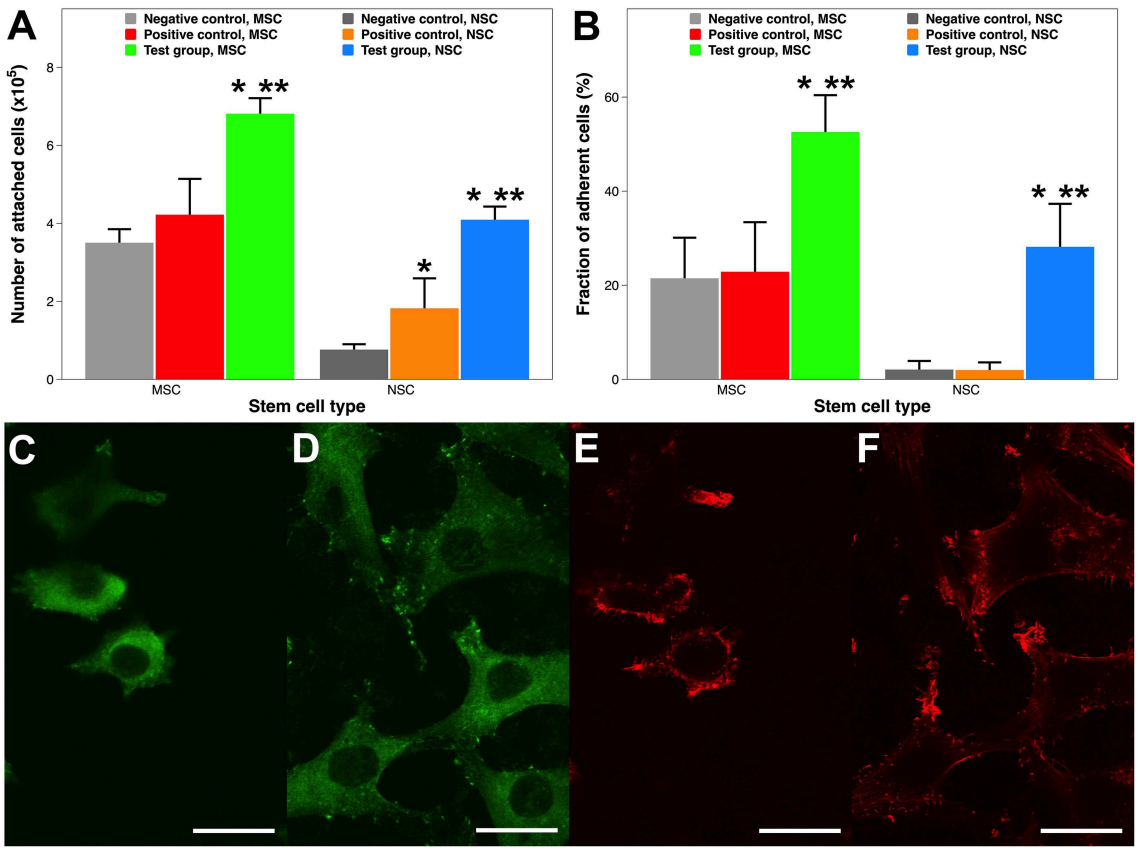


**FIGURE 5 |** Stem cell attachment and adhesion on surgical implants with and without ECM protein coatings. **(A)** Quantitative evaluation of MSC and NSC attachment 12 h after inoculation. **(B)** Adherence fraction of stem cells after enzymatic detachment. **(C–F)** CLSM images of MSCs morphology. **(C)** Vinculin focal adhesion on Ti substrate. **(D)** Vinculin focal adhesion on collagen coating by atmospheric plasma. **(E)** Actin cytoskeleton on Ti substrate. **(F)** Actin cytoskeleton on coating by atmospheric plasma. Scale bar = 15 μm. A single asterisk denotes statistical significance when comparing a test group or positive control with a negative control, and a double asterisk when comparing a test group with a positive control.

Collectively, ECM protein coatings facilitated by atmospheric plasma are more chemically hydrophilic, biologically rough, morphologically robust, and physiologically durable, than their counterparts deposited by simple adsorption. The interaction between these coatings and stem cells will be probed at cellular, protein, and genetic levels in the subsequent experiments.

## Stem Cell Attachment and Adhesion

Human stem cells were seeded onto the Ti and PS implants, incubated for 12 h, and counted using flow cytometry. Unlike MSCs, an adherent cell line, NSCs can be grown either as floating 3D neurospheres or attached 2D monolayers on specially coated plates (Conti et al., 2005). Therefore, enhancing cell attachment by ECM protein coatings has a greater importance for MSCs than for NSCs. Compared to non-coated Ti samples, collagen coating by atmospheric plasma nearly doubles the MSC attachment (6.84 vs. 3.53 $\times$ $10^5$ cells) (**Figure 5A**). However, there is no statistical difference between cell attachment on Ti only and coating by adsorption. Collagen is well-known for better promoting attachment and the subsequent proliferation of MSCs (Somaiah et al., 2015). But it only recently became clear that surface matrix has a much more profound effect than induction medium on MSC cellular events (He et al., 2017). In other words, an *in-situ* collagen coating is more potent than diffused collagen during MSC attachment. Similarly, coating a PS surface with laminin by either technique also dramatically enhances NSC attachment, as NSC attachment on non-coated tissue culture PS is minimal (0.79 $\times$ $10^5$ cells). In addition, laminin coating by atmospheric plasma attached more than twice as many cells than that by adsorption (4.12 vs. 1.85 $\times$ $10^5$ cells). It is a common practice to coat tissue culture containers with attachment proteins such as laminin and poly-L-lysine in laboratory and industrial settings to improve stem cell attachment and proliferation (Lam and Longaker, 2012). Thus, our findings on plasma-facilitated ECM coatings possess huge potential for regenerative medicine and related disciplines.

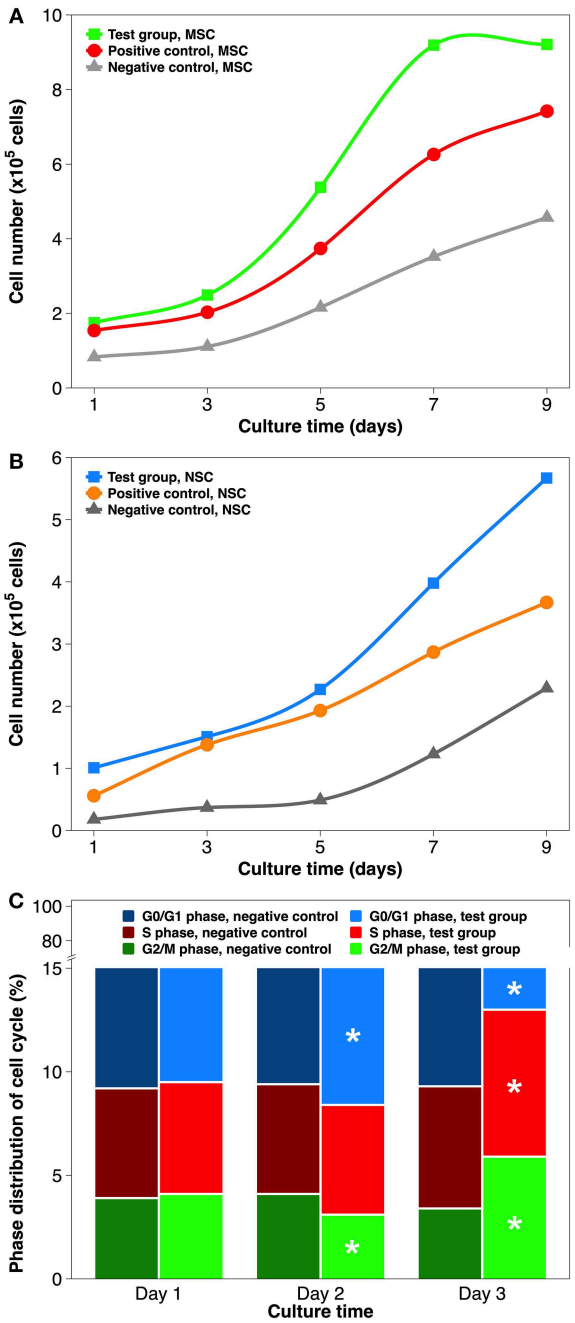


**FIGURE 6 |** Stem cell proliferation and cell cycle distribution on non-coated and coated surgical implants in non-differentiating culture. **(A)** MSCs growth curve over 9 days of culture. **(B)** NSCs growth curve over 9 days of culture. **(C)** Cell cycle distribution of MSCs grown on the Ti implant and collagen coating by atmospheric plasma, respectively. Statistical annotation is per section Statistical analysis.

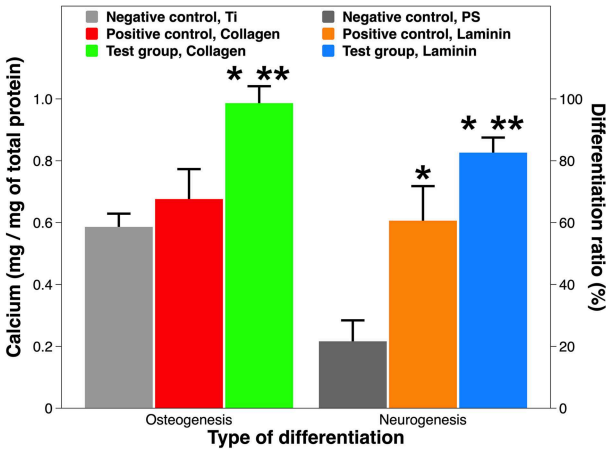


**FIGURE 7 |** Osteogenic and neurogenic differentiation from stem cells. Osteogenesis is expressed as calcium production by MSCs on Ti implants with and without collagen coatings; neurogenesis is expressed as neuron ratio among NSCs on PS implants with and without laminin coatings. A single asterisk denotes statistical significance when comparing a test group or positive control with a negative control, and a double asterisk when comparing a test group with a positive control.

Stem cell attachment was also qualitatively examined using CLSM 12 h after the initial inoculation, when cells on all surfaces were similarly settled (Tan et al., 2011). Cell attachment is reflected by the distribution of intracellular actin filaments and extracellular vinculin focal adhesion. MSCs attached onto the Ti substrate and collagen coating by atmospheric plasma exhibited substantially different morphologies (**Figures 5C–F**). Firstly, fewer cells are attached on the Ti surface, which is consistent with the findings in **Figure 5A**. Secondly, cells attached on the collagen coating had more well-defined, robust, and dotted vinculin-containing focal adhesion plaques (Humphries et al., 2007), which are patterned along the entire edge of the cells helping them to anchor to the implant surface (**Figure 5D**). Thirdly, cells attached onto the collagen coating are more relaxed and are dispersed with a sturdy actin network consisting of cortical and radial fibers (**Figure 5F**). Thus, cell attachment is morphologically better on collagen coatings.

Cell adhesion is a relatively static state compared to cell attachment, which is a dynamic process. Various methods have been established to test cell adhesion on surgical implants (Tan et al., 2012a,b; Fong et al., 2017); this study uses an enzymatic one. Around half of the MSCs still remained attached on the collagen coating facilitated by plasma, whereas nearly 80% of cells were dissociated on the Ti and collagen coating by adsorption (**Figure 5B**). Comparably, almost all the NSCs are detached from the PS surface and the laminin coating by adsorption, while roughly a third of cells remain adhered to the laminin coating by atmospheric plasma. Therefore, cells adhered much more firmly on ECM protein coatings created by atmospheric plasma.

Collectively, ECM protein coatings facilitated by atmospheric plasma supported superior cell attachment and adhesion. This

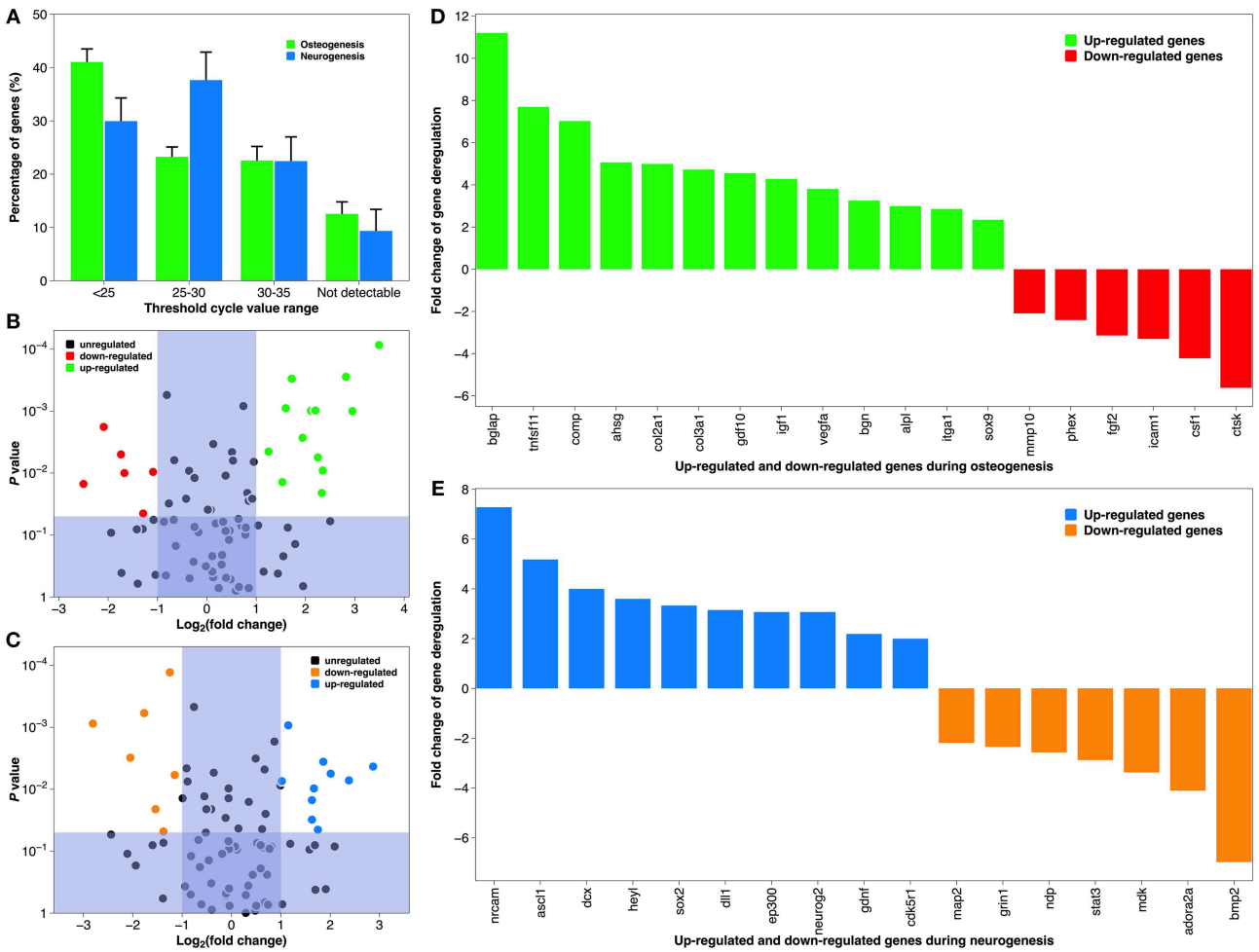


**FIGURE 8 |** Gene expression during osteogenic differentiation of MSCs and neurogenic differentiation of NSCs. **(A)** The average $C_T$ distribution of 84 genes studied in the atmospheric plasma-facilitated ECM coating samples. $C_T$ <25 indicates genes are expressing with high transcript copy number, and $C_T$ >35 suggests gene expression falls below the detection threshold of the equipment. **(B)** "Volcano plot" of the fold change and statistical significance of the expressed genes during osteogenesis. **(C)** "Volcano plot" of the fold change and statistical significance of the expressed genes during neurogenesis. **(D)** Histogram demonstrating significantly deregulated genes during osteogenesis. **(E)** Histogram demonstrating significantly deregulated genes during neurogenesis. Tick labels in X-axis are composed of gene symbols.

enhancement might be multifactorial: such a coating not only features better chemico-physical material properties, such as hydrophilicity (Paital and Dahotre, 2009) and roughness (Ponsonnet et al., 2003), but also furnishes biologically adhesive functionality (Hagbard et al., 2018). It should be noticed that attachment or adhesion not only anchors cells in place but also plays a critical role in stem cell survival and phenotypic maintenance (Flanagan et al., 2006).

## Stem Cell Proliferation and Cell Cycle Distribution

Cell growth curves of both stem cell types (**Figures 6A,B**) exhibit three distinct kinetic patterns. At almost every time point within a 9-day culture, the quantity of grown cells on each surface type was as follows: test group (ECM coating by atmospheric plasma) > positive control (coating by simple adsorption) > negative control (substrate only). In detail, after the initial lag phase, cells on plasma-facilitated ECM coatings entered the exponential growth phase sooner. In addition, cell growth appeared to decelerate on plasma-facilitated collagen coating from day 7, which helpfully signals the start of the stationary phase. It is worth mentioning that the MSCs tended to propagate more quickly than NSCs, which is consistent with the data from the stem cell provider. Based on the values in the exponential phase, cells in the test group coatings had a higher specific growth rate and a lower generation time/doubling time when compared to those on positive control coatings and negative control substrates. In other words, coatings with same ingredient but created by different methods (e.g., atmospheric plasma vs. traditional adsorption) can influence cellular activity to a different extent (Hauser et al., 2010). In any case, reaching cell confluency faster is vital for engineering stem cell-grown implants *in vitro* because MSCs could age sooner than expected, and it is much better to consider them for cell and gene therapy early on (Bonab et al., 2006; Paccola Mesquita et al., 2019).

In order to establish whether the higher cell numbers during cell proliferation followed indirectly from improved cell attachment or was caused directly by elevated growth rate, cell cycle distribution was analyzed by flow cytometry (**Figure 6C**). The cell cycle comprises of five phases: $G_0$ phase (quiescence), $G_1$ phase (cell growth), S phase (DNA synthesis), $G_2$ phase (continued cell growth), and M phase (mitosis & cytokinesis). The cell cycles are tightly controlled: activation of each phase depends on the progression and completion of the previous one (Sclafani and Holzen, 2007). Therefore, the results of cell cycle phase distribution are best analyzed chronologically. To simplify the comparison, collagen coating by atmospheric plasma and substrate only were chosen. On day 1, the percentages of $G_0/G_1$, S, and $G_2$/M phases did not differ significantly. On day 2, slightly more cells were found in the $G_0/G_1$ phase and fewer

**TABLE 2 |** Functional grouping of up- and down-regulated genes in the osteogenic pathway of human MSCs grown on collagen coatings (coating by atmospheric plasma vs. coating by adsorption).

| Function group | Subdivision of function | Gene |
|---|---|---|
| Skeletal development | Cartilage condensation | *col2a1, sox9* |
| | Ossification | *alpl, bglap, col2a1, csf1, fgf2, sox9, tnfsf11* |
| | Osteoclast differentiation | *bglap, csf1, tnfsf11* |
| | Osteoblast differentiation | *bglap, fgf2* |
| | Other | *alpl* |
| Bone mineral metabolism | Bone mineralization | *ahsg, bglap, sox9* |
| | Calcium ion binding & homeostasis | *bglap, comp, fgf2* |
| Extracellular matrix (ECM) molecules | Collagens | *col2a1, col3a1* |
| | ECM protease inhibitors | *ahsg* |
| | ECM Proteases | *ctsk, mmp10, phex* |
| | Other | *alpl, bgn* |
| Cell adhesion molecules | Cell-cell adhesion | *col2a1, icam1, sox9, tnfsf11* |
| | Cell-ECM adhesion | *csf1, itga1* |
| | Other | *bglap,* |
| Growth factors | | *fgf2, gdf10, igf1, vegfa* |
| Transcription factors | | *sox9* |

*Full list of genes in the human osteogenesis RT² profiler PCR array can be found on https://www.qiagen.com/gb/shop/pcr/primer-sets/rt2-profiler-pcr-arrays/?catno=PAHS-026Z#geneglobe.*

**TABLE 3 |** Functional grouping of up- and down-regulated genes in the neurogenic pathway of human NSCs grown on laminin coatings (coating by atmospheric plasma vs. coating by adsorption).

| Function group | Subdivision of function | Gene |
|---|---|---|
| Neuronal migration | | *ascl1, dcx, cdk5r1, neurog2, nrcam* |
| Cell differentiation | Neuronal differentiation | *ascl1, bmp2, cdk5r1, heyl, nrcam, sox2, neurog2* |
| | Neuronal cell fate determination | *ascl1, sox2* |
| | Other | *mdk* |
| Synaptic functions | Regulation of synaptic plasticity | *grin1* |
| | Synaptic transmission | *grin1* |
| | Synaptogenesis | *nrcam* |
| | Axonogenesis | *dcx, map2, nrcam* |
| Growth factors & cytokines | Growth factors | *gdnf, mdk, ndp* |
| | Cytokines | *bmp2, mdk* |
| Apoptosis | | *ep300, gdnf* |
| Cell adhesion molecules | | *dll1, nrcam* |
| Cell cycle | | *ep300, mdk* |
| Signal transduction | Notch signaling | *ascl1, dll1, heyl* |
| | WNT signaling | *ndp* |
| | TGFβ signaling | *bmp2* |
| | G-protein coupled receptor signaling | *adora2a* |
| Transcription factors & cofactors | | *ascl1, ep300, heyl, neurog2, sox2, stat3* |

*Full list of genes in the human neurogenesis RT² profiler PCR array can be found on https://www.qiagen.com/gb/shop/pcr/primer-sets/rt2-profiler-pcr-arrays/?catno=PAHS-404Z#geneglobe.*

in the $G_2$/M phase, while proving virtually same in the S phase, when comparing test group and negative control. On day 3, all 3 cell cycle phases had statistically different distributions: S phase (7.1 vs. 5.9%), $G_2$/M phase (5.9 vs. 3.4%), and $G_0/G_1$ phase (87.0 vs. 90.7%). Overall, using atmospheric plasma to deposit collagen coating on the Ti substrate stimulated MSCs to transit more rapidly from $G_1$ to S phase. Cell cycle machinery plays a profound role in the establishment or maintenance of the stem cell state (Morgan, 2007), and is possibly mediated by the timely phosphorylation of focal adhesion kinase (Tan et al., 2012b) and the precocious activity of cyclin-dependent protein kinase (White and Dalton, 2005). The results of NSC cell cycle distribution induced by laminin coating were similar to aforementioned MSCs/collagen group, except that their phase change was slightly delayed due to the slower proliferation rate.

## Osteogenic and Neurogenic Differentiation From Stem Cells

One defining feature of stem cells is their unique ability to develop into specialized cell types in the body. MSCs are multipotent stromal cells that can differentiate into osteoblasts, chondrocytes, myocytes, and adipocytes (Ullah et al., 2015), whereas NSCs primarily differentiate into neurons, astrocytes, and oligodendrocytes (Bergström and Forsberg-Nilsson, 2012). The target differentiation pathways studied in this work were osteogenesis and neurogenesis (**Figure 7**). The osteogenic differentiation from MSCs on the Ti substrate and on collagen coatings was reflected by calcium mineralization normalized to the total protein content. No statistical difference was found between the Ti substrate and the collagen coating by adsorption. But the calcium deposition on plasma-facilitated collagen coating nearly doubled that on the metallic substrate (99.7 vs. 58.8%).

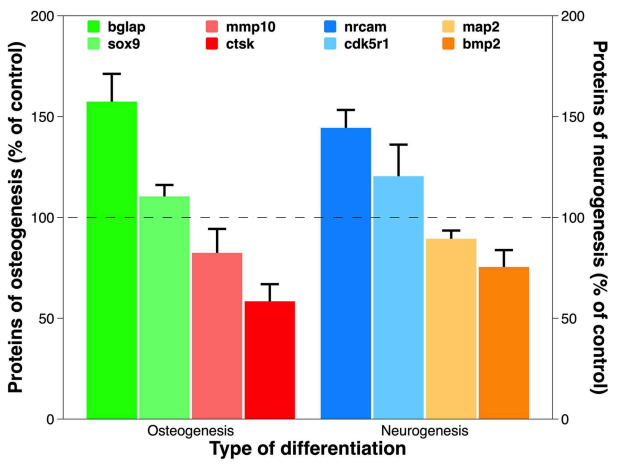


**FIGURE 9 |** Expression of proteins translated from representative deregulated genes discovered in PCR array analysis for osteogenesis and neurogenesis. Using the optical absorbance at 450 nm during ELISA, the data are presented as percentage of control. Statistical annotation is omitted because the difference between test group and control is statistically significant for each protein tested.

Comparable results were found on laminin coatings. The non-coated PS surface is a poor candidate to support neurogenic differentiation as just over 20% of NSCs have developed into neurons. Laminin coatings by either deposition technique overcame this disadvantage, increasing the neurogenic ratio up to 83.1%, even though laminin coating by atmospheric plasma still proved superior to its counterpart, simple adsorption.

Our results on tissue-specific differentiation induced by ECM proteins are consistent with peer work. Firstly, MSCs adhere to ECM proteins with varying affinity, resulting in different degrees of osteogenic differentiation: collagen I > vitronectin > laminin (Salasznyk et al., 2004). Interestingly, ECM contact alone may suffice to induce differentiation without osteogenic drugs. Secondly, combining laminin coatings with various surface geometry, topography, and micropatterns might further increase neuronal differentiation (Liu et al., 2006; Christopherson et al., 2009; Xie et al., 2014). Last but not least, mixing various ECM proteins (e.g., Matrigel® and Cultrex®) and co-culturing of MSCs/NSCs might provide synergistic solutions for implant-based therapies (Gattazzo et al., 2014; Yang et al., 2018).

## Pathway-Specific Gene and Protein Analysis

Although the depiction of tissue-specific differentiation here is straightforward, the underlying molecular mechanism can be very complicated (Tan et al., 2012b). Therefore, we conducted pathway-specific gene analysis using a PCR array, which combines the multi-gene profiling capabilities of a microarray with the performance of Q-PCR. Both MSCs on a collagen coating and NSCs on a laminin coating showed constitutive expression of majority of the 84 genes associated with human osteogenesis and neurogenesis, respectively (**Figure 8A**). But PCR efficiency differed between the two groups, as their predominant $C_T$ value was distributed differently (<25 vs. 25–30). This was most likely due to differences in the cell lines (Brendel et al., 2005). Comparing the $C_T$ value of the test group and the positive control, 19 genes during osteogenesis and 17 genes during neurogenesis were deregulated, respectively. The organization of these statistically significantly deregulated genes (fold change >2 or <-2, and $P$-value <0.05), along with the organization of biologically significantly deregulated genes (fold change between −2 and 2 & $P$-value <0.05, and fold change >2 or <-2 & $P$-value >0.05) are best appreciated in the "volcano" charts (**Figures 8B,C**). A distinct gene expression pattern can be discovered, where the "volcano" axis is shifted to the right during osteogenesis (more genes up-regulated than down-regulated) and centralized during neurogenesis (a balanced number of up- and down-regulated genes). A breakdown of these deregulated genes is illustrated in **Figures 8D,E**. The fold changes of gene deregulation range from 11.24 (*bglap*) to −5.66 (*ctsk*) during osteogenesis and from 7.31 (*nrcam*) to −7.01 (*bmp2*) during neurogenesis. These deregulated genes are categorized into various functional groups covering all major aspects of osteogenic and neurogenic pathways (**Tables 2**, **3**). We believe that the cause of gene deregulation induced by atmospheric plasma-facilitated ECM coatings is multifactorial, since implant

parameters such as surface wettability (Tan et al., 2012b), surface roughness (Brett et al., 2004), collagen (Shekaran et al., 2015), and laminin (Liu et al., 2016) surface modification all can influence the gene expression of interfacial cells. Thus, it would be very intriguing to use atmospheric plasma as a surface biotechnology to combine the above parameters, hoping to achieve a novel implant-based therapy with gene-altering capabilities.

The above transcriptomic data were verified at the translational level. All eight of the representative genes chosen from the above gene assay of osteogenesis and neurogenesis were appropriately translated (**Figure 9**). Osteocalcin (aka bone gamma-carboxyglutamate protein), encoded by the up-regulated gene *bglap*, is among the most abundant proteins in bone and is produced exclusively by osteoblasts (Zoch et al., 2016). It is a well-known biochemical marker for bone formation, and its level *in vivo* can be affected by the design of surgical implant and post-implantation osteolysis (Qureshi et al., 2002). Cathepsin K, the protein product of the down-regulated gene *ctsk*, is an ECM protease involved in bone remodeling and resorption through osteoclast activation (Costa et al., 2011). Its expression is diminished during bone formation on biomaterials cultured with human MSCs and induced pluripotent stem cells (Jeon et al., 2016). On the other hand, deregulated genes during neurogenesis also reveal transcriptomic authenticity. The neuronal cell adhesion molecule, translated from the up-regulated gene *nrcam*, can induce neurite outgrowth and mediate adhesion among neurons (Weledji and Assob, 2014). Tethering neuronal cell adhesion molecule on biomaterial has become a promising strategy to promote neural adhesion and ultimately, neural tissue regeneration (Rao and Winter, 2009). Bone morphogenetic protein 2, translated from the down-regulated gene *bmp2*, is a potent osteoinductive agent that enhances bone therapy (Poon et al., 2016). Interestingly, it is also heavily involved in the central nervous system where it irreversibly alters NSCs from neurogenesis to undesirable gliogenesis, leading to a failure of neuronal regeneration (Nakashima et al., 2001).

To recapitulate, collagen and laminin coatings created by atmospheric plasma can significantly alter the gene expression of MSCs and NSCs during osteogenesis and neurogenesis, respectively. This improvement over coatings using the traditional technique is reflected within multiple functional pathways among tissue-specific differentiation. The 36 deregulated genes discovered in this study can be used as potential targets to design treatments delivered by surgical implants. One option with great promise for clinical therapies would be biomaterials capable of localized gene delivery that synergistically target multiple cell processes, leading to the regeneration of many tissues (Gower and Shea, 2013).

## CONCLUSIONS

Extracellular proteins were coated onto surgical implants using the atmospheric plasma. Coatings formed by this novel technique were compared with those created by the conventional adsorption method. The study compared how both methods affected material characteristics and biological interactions with stem cells. XPS, SEM, and functional staining collectively revealed that atmospheric plasma created complete and homogeneous coatings. The resultant collagen and laminin coatings proved more hydrophilic *in vitro* and potentially more durable *in vivo*. Quantitative and qualitative assessment confirmed the superior mesenchymal and NSC attachment and adhesion on plasma-facilitated coatings. In addition, cell proliferation was independently faster, as verified by the cell cycle distribution analysis. Finally, tissue-specific differentiation from mesenchymal and NSCs was also significantly boosted by our newly designed ECM coatings. The underlying molecular mechanism was probed using pathway-specific PCR array. A total of 36 genes were discovered to be deregulated during osteogenesis and neurogenesis. The overall transcriptomic advantage of these promising coatings was evidenced throughout diverse functional pathways. Altogether, we have demonstrated the versatility of atmospheric plasma as a surface biotechnology, since it produces an implant-specific coating which offers tissue-specific enhancement. Future work could include using atmospheric plasma for implant-based drug delivery in regenerative medicine.

## DATA AVAILABILITY STATEMENT

All datasets generated for this study are included in the manuscript/Supplementary Files.

## AUTHOR CONTRIBUTIONS

FT designed, performed the experiements, analyzed the data, and wrote the manuscript. MA-R corrected the manuscript.

## FUNDING

This work was sponsored by Shanghai Pujiang Program (project no. 19PJ1408800). It was initiated by Science Foundation Ireland.

## ACKNOWLEDGMENTS

The authors wish to thank Professor Denis Dowling in UCD Centre for Biomedical Engineering and experts in the National Centre for Plasma Science & Technology.

## REFERENCES

Ahmed, M., and Ffrench-Constant, C. (2016). Extracellular matrix regulation of stem cell behavior. *Curr. Stem Cell Rep.* 2, 197–206. doi: 10.1007/s40778-016-0056-2

Ahn, H. H., Lee, I. W., Lee, H. B., and Kim, M. S. (2014). Cellular behavior of human adipose-derived stem cells on wettable gradient polyethylene surfaces. *Int. J. Mol. Sci.* 15, 2075–2086. doi: 10.3390/ijms15022075

Ao, H. Y., Xie, Y. T., Yang, S. B., Wu, X., D., Li, K., and Tang, T. T. (2016). Covalently immobilised type I collagen facilitates osteoconduction and

osseointegration of titanium coated implants. *J. Orthop. Translat*. 5, 16–25. doi: 10.1016/j.jot.2015.08.005

Ask, M., Rolander, U., Lausmaa, J., and Kasemo, B. (1990). Microstructure and morphology of surface oxide films on Ti−6A1–4V. *J. Mater. Res.* 5, 1662–1667. doi: 10.1557/JMR.1990.1662

Bergström, T., and Forsberg-Nilsson, K. (2012). Neural stem cells: brain building blocks and beyond. *Ups. J. Med. Sci*. 117, 132–142. doi: 10.3109/03009734.2012.665096

Bonab, M., Alimoghaddam, K., Talebian, F., Ghaffari, S., Ghavamzadeh, A., and Nikbin, B. (2006). Aging of mesenchymal stem cell *in vitro*. *BMC Cell Biol.* 7:14. doi: 10.1186/1471-2121-7-14

Breathnach, R., McDonnell, K. A., Chebbi, A., Callanan, J. J., and Dowling, D. P. (2018). Evaluation of the effectiveness of kINPen Med plasma jet and bioactive agent therapy in a rat model of wound healing. *Biointerphases* 13:051002. doi: 10.1116/1.5046489

Brendel, C., Kuklick, L., Hartmann, O., Kim, T. D., Boudriot, U., and Neubauer, A. (2005). Distinct gene expression profile of human mesenchymal stem cells in comparison to skin fibroblasts employing cDNA microarray analysis of 9600 genes. *Gene Exp.* 12, 245–257. doi: 10.3727/000000005783992043

Brett, P. M., Harle, J., Salih, V., Mihoc, R., Olsen, I., and Tonetti, M. (2004). Roughness response genes in osteoblasts. *Bone* 35, 124–133. doi: 10.1016/j.bone.2004.03.009

Bringmann, P., Rohr, O., Gammel, F. J., and Jansen, I. (2009). Atmospheric pressure plasma deposition of adhesion promotion layers on aluminium. *Plasma Proce. Polym.* 6, S496–S502. doi: 10.1002/ppap.200931105

Christopherson, G. T., Song, H., and Mao, H. Q. (2009). The influence of fiber diameter of electrospun substrates on neural stem cell differentiation and proliferation. *Biomaterials* 30, 556–564. doi: 10.1016/j.biomaterials.2008.10.004

Conti, L., Pollard, S. M., Gorba, T., Reitano, E., Toselli, M., and Smith, A. (2005). Niche-independent symmetrical self-renewal of a mammalian tissue stem cell. *PLoS Biol.* 3:e283. doi: 10.1371/journal.pbio.0030283

Costa, A. G., Cusano, N. E., Silva, B. C., Cremers, S., and Bilezikian, J. P. (2011). Cathepsin K: its skeletal actions and role as a therapeutic target in osteoporosis. *Nat. Rev. Rheumatol.* 7, 447–456. doi: 10.1038/nrrheum.2011.77

Derhami, K., Zheng, J., Li, L., Wolfaardt, J. F., and Scott, P. G. (2001). Proteomic analysis of human skin fibroblasts grown on titanium: novel approach to study molecular biocompatibility. *J. Biomed. Mater. Res.* 56, 234–244. doi: 10.1002/1097-4636(200108)56:2<234::AID-JBM1090>3.0.CO;2-#

Dowling, D. P., Maher, S., Law, V. J., Ardhaoui, M., Stallard, C., and Keenan, A. (2016). Modified drug release using atmospheric pressure plasma deposited siloxane coatings. *J. Phys.* 49:364005. doi: 10.1088/0022-3727/49/36/364005

Dowling, D. P., Ramamoorthy, A., Rahman, M., Mooney, D. A., and MacElroy, J. M., D. (2009). Influence of atmospheric plasma source and gas composition on the properties of deposited siloxane coatings. *Plasma Proc. Polym.* 6, S483–S489. doi: 10.1002/ppap.200931110

Faia-Torres, A. B., Charnley, M., Goren, T., Guimond-Lischer, S., Rottmar, M., and Neves, N. M. (2015). Osteogenic differentiation of human mesenchymal stem cells in the absence of osteogenic supplements: a surface-roughness gradient study. *Acta Biomater.* 28, 64–75. doi: 10.1016/j.actbio.2015.09.028

Flanagan, L. A., Rebaza, L. M., Derzic, S., Schwartz, P. H., and Monuki, E. S. (2006). Regulation of human neural precursor cells by laminin and integrins. *J. Neurosci. Res.* 83, 845–856. doi: 10.1002/jnr.20778

Fong, D., Duceppe, N., and Hoemann, C. D. (2017). Mesenchymal stem cell detachment with trace trypsin is superior to EDTA for *in vitro* chemotaxis and adhesion assays. *Biochem. Biophys. Res. Commun.* 484, 656–661. doi: 10.1016/j.bbrc.2017.01.171

Frantz, C., Stewart, K., M., and Weaver, V., M. (2010). The extracellular matrix at a glance. *J. Cell Sci.* 123, 4195–4200. doi: 10.1242/jcs.023820

Fridman, G., Friedman, G., Gutsol, A., Shekhter, A. B., Vasilets, V. N., and Fridman, A. (2008). Applied plasma medicine. *Plasma Proc. Polym.* 5, 503–533. doi: 10.1002/ppap.200700154

Gattazzo, F., Urciuolo, A., and Bonaldo, P. (2014). Extracellular matrix: a dynamic microenvironment for stem cell niche. *Biochim Biophys Acta* 1840, 2506–2519. doi: 10.1016/j.bbagen.2014.01.010

Gaylor, J. M., Raman, G., Chung, M., Lee, J., Rao, M., and Poe, D. S. (2013). Cochlear implantation in adults: a systematic review and meta-analysiscochlear implantation in adults. *JAMA Otolaryngol. Head Neck Surg.* 139, 265–272. doi: 10.1001/jamaoto.2013.1744

Ghossaini, S. N., and Roehm, P. C. (2019). Osseointegrated auditory devices: bone-anchored hearing aid and PONTO. *Otolaryngol. Clin. North Am.* 52, 243–251. doi: 10.1016/j.otc.2018.11.005

Gower, R. M., and Shea, L. D. (2013). Biomaterial scaffolds for controlled, localized gene delivery of regenerative factors. *Adv Wound Care* 2, 100–106. doi: 10.1089/wound.2011.0325

Green, R. A., Hassarati, R. T., Bouchinet, L., Lee, C. S., Cheong, G. L., and Lovell, N. H. (2012). Substrate dependent stability of conducting polymer coatings on medical electrodes. *Biomaterials* 33, 5875–5886. doi: 10.1016/j.biomaterials.2012.05.017

Hagbard, L., Cameron, K., August, P., Penton, C., Parmar, M., Hay, D., and Kallur, T. (2018). Developing defined substrates for stem cell culture and differentiation. *Philos. Trans. R. Soc. Lond. B Biol. Sci.* 373. doi: 10.1098/rstb.2017.0230

Hao, L., Yang, H., Du, C., Fu, X., Zhao, N., Xu, S., et al. (2014). Directing the fate of human and mouse mesenchymal stem cells by hydroxyl-methyl mixed self-assembled monolayers with varying wettability. *J. Mater. Chem. B* 2, 4794–4801. doi: 10.1039/C4TB00597J

Hauser, J., Koeller, M., Bensch, S., Halfmann, H., Awakowicz, P., Steinau, H., et al. (2010). Plasma mediated collagen-I-coating of metal implant materials to improve biocompatibility. *J. Biomed. Mater. Res.* 94, 19–26. doi: 10.1002/jbm.a.32672

He, J., Guo, J., Jiang, B., Yao, R., Wu, Y., and Wu, F. (2017). Directing the osteoblastic and chondrocytic differentiations of mesenchymal stem cells: matrix vs. induction media. *Regen Biomater.* 4, 269–279. doi: 10.1093/rb/rbx008

He, L., Tang, S., Prabhakaran, M. P., Liao, S., Tian, L., and Ramakrishna, S. (2013). Surface modification of PLLA nano-scaffolds with Laminin multilayer by LbL assembly for enhancing neurite outgrowth. *Macromol. Biosci.* 13, 1601–1609. doi: 10.1002/mabi.201300177

Heinlin, J., Isbary, G., Stolz, W., Morfill, G., Landthaler, M., Shimizu, T., et al. (2011). Plasma applications in medicine with a special focus on dermatology. *J. Eur. Acad. Dermatol. Venereol.* 25, 1–11. doi: 10.1111/j.1468-3083.2010.03702.x

Heino, J. (2007). The collagen family members as cell adhesion proteins. *Bioessays* 29, 1001–1010. doi: 10.1002/bies.20636

Hum, J., and Boccaccini, A. R. (2018). Collagen as coating material for 45S5 bioactive glass-based scaffolds for bone tissue engineering. *Int. J. Mol. Sci.* 19:1807. doi: 10.3390/ijms19061807

Humphries, J. D., Wang, P., Streuli, C., Geiger, B., Humphries, M. J., and Ballestrem, C. (2007). Vinculin controls focal adhesion formation by direct interactions with talin and actin. *J. Cell Biol.* 179, 1043–1057. doi: 10.1083/jcb.200703036

Jeon, O. H., Panicker, L. M., Lu, Q., Chae, J. J., Feldman, R. A., and Elisseeff, J. H. (2016). Human iPSC-derived osteoblasts and osteoclasts together promote bone regeneration in 3D biomaterials. *Sci. Rep.* 6:26761. doi: 10.1038/srep26761

Ketelaar, M. E., Nawijn, M. C., Shaw, D. E., Koppelman, G. H., and Sayers, I. (2016). The challenge of measuring IL-33 in serum using commercial ELISA: lessons from asthma. *Clin. Exp. Allergy* 46, 884–887. doi: 10.1111/cea.12718

Kim, C. L., and Kim, D. E. (2016). Self-healing characteristics of collagen coatings with respect to surface Abrasion. *Sci. Rep.* 6:20563. doi: 10.1038/srep20563

Kleinman, H. K. (2001). Preparation of basement membrane components from EHS tumors. *Curr. Protoc. Cell Biol.* Chapter 10, Unit 10.2. doi: 10.1002/0471143030.cb1002s00

Kokubo, T. (1991). Bioactive glass ceramics: properties and applications. *Biomaterials* 12, 155–163. doi: 10.1016/0142-9612(91)90194-F

Lam, M. T., and Longaker, M. T. (2012). Comparison of several attachment methods for human iPS, embryonic and adipose-derived stem cells for tissue engineering. *J. Tissue Eng. Regen. Med.* 6 (Suppl 3), s80–s86. doi: 10.1002/term.1499

Lan, C. W., and Wang, Y. J. (2003). Collagen as an immobilization vehicle for bone marrow stromal cells enriched with osteogenic potential. *Artif. Cells Blood Substit Immobil. Biotechnol.* 31, 59–68. doi: 10.1081/BIO-120018003

Li, Z., Wang, W., Kratz, K., Küchler, J., Xu, X., Zou, J., et al. (2016). Influence of surface roughness on neural differentiation of human induced pluripotent stem cells. *Clin. Hemorheol. Microcirc.* 64, 355–366. doi: 10.3233/CH-168121

Liu, B. F., Ma, J., Xu, Q. Y., and Cui, F. Z. (2006). Regulation of charged groups and laminin patterns for selective neuronal adhesion. *Colloids Surf. B Biointerfaces* 53, 175–178. doi: 10.1016/j.colsurfb.2006.08.018

Liu, Y. Q., Zhan, L. B., Bi, T. T., Liang, L, and Sui, H. (2016). Neural stem cell neural differentiation in 3D extracellular matrix and endoplasmic reticulum stress microenvironment. *RSC Adv.* 6, 34959–34969. doi: 10.1039/C6RA04370D

Livak, K. J., and Schmittgen, T. D. (2001). Analysis of relative gene expression data using real-time quantitative PCR and the 2[-Delta Delta C(T)] method. *Methods* 25, 402–408. doi: 10.1006/meth.2001.1262

Metcalfe, C., Muzaffar, J., Daultrey, C., and Coulson, C. (2017). Coblation tonsillectomy: a systematic review and descriptive analysis. *Eur. Arch. Otorhinolaryngol.* 274, 2637–2647. doi: 10.1007/s00405-017-4529-4

Milošev, I., Metikoš-Huković, M., and Strehblow, H. H. (2000). Passive film on orthopaedic TiAlV alloy formed in physiological solution investigated by X-ray photoelectron spectroscopy. *Biomaterials* 21, 2103–2113. doi: 10.1016/S0142-9612(00)00145-9

Morgan, D. O. (2007). *The Cell Cycle: Principles of Control*. Corby: Oxford University Press. Northants, UK, Northants.

Mori, K., Shioi, A., Jono, S., Nishizawa, Y., and Morii, H. (1998). Expression of matrix Gla protein (MGP) in an *in vitro* model of vascular calcification. *FEBS Lett.* 433, 19–22. doi: 10.1016/S0014-5793(98)00870-9

Morra, M., Cassinelli, C., Cascardo, G., Mazzucco, L., Borzini, P., Fini, M., et al. (2006). Collagen I-coated titanium surfaces: mesenchymal cell adhesion and *in vivo* evaluation in trabecular bone implants. *J. Biomed. Mater. Res.* 78, 449–458. doi: 10.1002/jbm.a.30783

Nakashima, K., Takizawa, T., Ochiai, W., Yanagisawa, M., Hisatsune, T., Nakafuku, M., et al. (2001). BMP2-mediated alteration in the developmental pathway of fetal mouse brain cells from neurogenesis to astrocytogenesis. *Proc. Natl. Acad. Sci. U.S.A.* 98, 5868–5873. doi: 10.1073/pnas.101109698

Paccola Mesquita, F. C., Hochman-Mendez, C., Morrissey, J., Sampaio, L. C., and Taylor, D. A. (2019). Laminin as a potent substrate for large-scale expansion of human induced pluripotent stem cells in a closed cell expansion system. *Stem Cells Int.* 9:ePub 3. doi: 10.1155/2019/9704945

Paital, S. R., and Dahotre, N. B. (2009). Calcium phosphate coatings for bio-implant applications: materials, performance factors, and methodologies. *Mater. Sci. Eng.* 66, 1–70. doi: 10.1016/j.mser.2009.05.001

Ponsonnet, L., Reybier, K., Jaffrezic, N., Comte, V., Lagneau, C., Lissac, M., et al. (2003). Relationship between surface properties (roughness, wettability) of titanium and titanium alloys and cell behaviour. *Mater. Sci. Eng.* 23, 551–560. doi: 10.1016/S0928-4931(03)00033-X

Poon, B., Kha, T., Tran, S., and Dass, C. R. (2016). Bone morphogenetic protein-2 and bone therapy: successes and pitfalls. *J. Pharm. Pharmacol.* 68, 139–147. doi: 10.1111/jphp.12506

Prasad, B. R., Brook, M. A., Smith, T., Zhao, S., Chen, Y., and Rochev, Y. (2010). Controlling cellular activity by manipulating silicone surface roughness. *Colloids Surfaces B* 78, 237–242. doi: 10.1016/j.colsurfb.2010.03.006

Quigley, A. F., Razal, J. M., Thompson, B. C., Moulton, S. E., Kita, M., and Kapsa, R. M. (2009). A conducting-polymer platform with biodegradable fibers for stimulation and guidance of axonal growth. *Adv. Mater.* 21, 4393–4397. doi: 10.1002/adma.200901165

Qureshi, A. A., Virdi, A. S., Didonna, M. L., Jacobs, J. J., Masuda, K., and Sumner, D. R. (2002). Implant design affects markers of bone resorption and formation in total hip replacement. *J. Bone Miner Res.* 17, 800–807. doi: 10.1359/jbmr.2002.17.5.800

Rammelt, S., Schulze, E., Bernhardt, R., Hanisch, U., Scharnweber, D., Worch, H., et al. (2004). Coating of titanium implants with type-I collagen. *J. Orthop. Res.* 22, 1025–1034. doi: 10.1016/j.orthres.2004.02.011

Rao, S. S., and Winter, J. O. (2009). Adhesion molecule-modified biomaterials for neural tissue engineering. *Front Neuroeng.* 2:6. doi: 10.3389/neuro.16.006.2009

Salasznyk, R. M., Williams, W. A., Boskey, A., Batorsky, A., and Plopper, G. E. (2004). Adhesion to vitronectin and collagen i promotes osteogenic differentiation of human mesenchymal stem cells. *J. Biomed. Biotechnol.* 2004, 24–34. doi: 10.1155/S1110724304306017

Sanden, B., Olerud, C., Petren-Mallmin, M., and Larsson, S. (2002). Hydroxyapatite coating improves fixation of pedicle screws. A clinical study. *J. Bone Joint Surg. Br.* 84, 387–391. doi: 10.1302/0301-620X.84B3.0840387

Scarano, A., Lorusso, F., Orsini, T., Morra, M., Iviglia, G., and Valbonetti, L. (2019). Biomimetic surfaces coated with covalently immobilized collagen type i: an X-ray photoelectron spectroscopy, atomic force microscopy, micro-CT and histomorphometrical study in rabbits. *Int. J. Mol. Sci.* 20:E724. doi: 10.3390/ijms20030724

Sclafani, R. A., and Holzen, T. M. (2007). Cell cycle regulation of DNA replication. *Annual Rev. Genet.* 41, 237–280. doi: 10.1146/annurev.genet.41.110306.130308

Scopece, P., Viaro, A., Sulcis, R., Kulyk, I., Patelli, A., and Guglielmi, M. (2009). SiOx-based gas barrier coatings for polymer substrates by atmospheric pressure plasma jet deposition. *Plasma Proc. Polym.* 6, S705–S710. doi: 10.1002/ppap.200931707

Sharma, D., Jia, W., Long, F., Pati, S., Chen, Q., Qyang, Y., et al. (2019). Polydopamine and collagen coated micro-grated polydimethylsiloxane for human mesenchymal stem cell culture. *Bioactive Mater.* 4, 142–150. doi: 10.1016/j.bioactmat.2019.02.002

Shekaran, A., Sim, E., Tan, K. Y., Chan, J. K., Choolani, M., and Oh, S. (2015). Enhanced *in vitro* osteogenic differentiation of human fetal MSCs attached to 3D microcarriers versus harvested from 2D monolayers. *BMC Biotechnol.* 15, 102. doi: 10.1186/s12896-015-0219-8

Sittig, C., Textor, M., Spencer, N. D., Wieland, M., and Vallotton, P. H. (1999). Surface characterization of implant materials c.p. Ti, Ti-6Al-7Nb and Ti-6Al-4V with different pretreatments. *J. Mater. Sci. Mater. Med.* 10, 35–46. doi: 10.1023/A:1008840026907

Somaiah, C., Kumar, A., Mawrie, D., Sharma, A., Patil, S. D., and Jaganathan, B. G. (2015). Collagen promotes higher adhesion, survival and proliferation of mesenchymal stem cells. *PLoS ONE* 10:e0145068. doi: 10.1371/journal.pone.0145068

Spriano, S., Yamaguchi, S., Baino, F., and Ferraris, S. (2018). A critical review of multifunctional titanium surfaces: new frontiers for improving osseointegration and host response, avoiding bacteria contamination. *Acta Biomater.* 79, 1–22. doi: 10.1016/j.actbio.2018.08.013

Stallard, C. P., McDonnell, K. A., Onayemi, O. D., O'Gara, J. P., and Dowling, D. P. (2012). Evaluation of protein adsorption on atmospheric plasma deposited coatings exhibiting superhydrophilic to superhydrophobic properties. *Biointerphases* 7:31. doi: 10.1007/s13758-012-0031-0

Strnad, G., Chirila, N., Petrovan, C., and Russu, O. (2016). Contact angle measurement on medical implant titanium based biomaterials. *Proc. Tech.* 22, 946–953. doi: 10.1016/j.protcy.2016.01.094

Tan, F., Naciri, M., and Al-Rubeai, M. (2011). Osteoconductivity and growth factor production by MG63 osteoblastic cells on bioglass-coated orthopedic implants. *Biotechnol. Bioeng.* 108, 454–464. doi: 10.1002/bit.22955

Tan, F., Naciri, M., Dowling, D., and Al-Rubeai, M. (2012a). *In vitro* and *in vivo* bioactivity of CoBlast hydroxyapatite coating and the effect of impaction on its osteoconductivity. *Biotechnol. Adv.* 30, 352–362. doi: 10.1016/j.biotechadv.2011.07.008

Tan, F., O'Neill, F., Naciri, M., Dowling, D., and Al-Rubeai, M. (2012b). Cellular and transcriptomic analysis of human mesenchymal stem cell response to plasma-activated hydroxyapatite coating. *Acta Biomater.* 8, 1627–1638. doi: 10.1016/j.actbio.2011.12.014

Tan, F., Walshe, P., Viani, L., and Al-Rubeai, M. (2013). Surface biotechnology for refining cochlear implants. *Trends Biotechnol.* 31, 678–687. doi: 10.1016/j.tibtech.2013.09.001

Tendero, C., Tixier, C., Tristant, P., Desmaison, J., and Leprince, P. (2006). Atmospheric pressure plasmas: a review. *Spectrochim. Acta Part Atomic Spectrosc.* 61, 2–30. doi: 10.1016/j.sab.2005.10.003

Teo, A. J. T., Mishra, A., Park, Y. I., Kim, W. J., Park, T., and Yoon, Y. J. (2016). Polymeric biomaterials for medical implants and devices. *ACS Biomater. Sci. Eng.* 2, 454–472. doi: 10.1021/acsbiomaterials.5b00429

Theocharis, A. D., Skandalis, S. S., Gialeli, C., and Karamanos, N. K. (2016). Extracellular matrix structure. *Adv. Drug. Deliv. Rev.* 97, 4–27. doi: 10.1016/j.addr.2015.11.001

Truong, Y. B., Glattauer, V., Briggs, K. L., Zappe, S., and Ramshaw, J. A. (2012). Collagen-based layer-by-layer coating on electrospun polymer scaffolds. *Biomaterials* 33, 9198–9204. doi: 10.1016/j.biomaterials.2012.09.012

Tynan, J., Ward, P., Byrne, G., and Dowling, D. P. (2009). Deposition of biodegradable polycaprolactone coatings using an in-line atmospheric pressure plasma system. *Plasma Proc. Polym.* 6, S51–S56. doi: 10.1002/ppap.200930310

Ullah, I., Subbarao, R. B., and Rho, G. J. (2015). Human mesenchymal stem cells - current trends and future prospective. *Biosci Rep.* 35:e00191. doi: 10.1042/BSR20150025

van Eck, C. F., Chen, A. F., Klatt, B. A., D'Antonio, J., and Fu, F. (2009). The classification of implants: class I, II, III. *J. Long Term Eff. Med. Implants* 19, 185–193. doi: 10.1615/JLongTermEffMedImplants.v19.i3.30

Vertelov, G., Kharazi, L., Muralidhar, M. G., Sanati, G., Tankovich, T., and Kharazi, A. (2013). High targeted migration of human mesenchymal stem cells grown in hypoxia is associated with enhanced activation of RhoA. *Stem Cell Res Ther*. 4:5. doi: 10.1186/scrt153

Webb, K., Hlady, V., and Tresco, P., A. (1998). Relative importance of surface wettability and charged functional groups on NIH 3T3 fibroblast attachment, spreading, and cytoskeletal organization. *J. Biomed. Mater. Res*. 41, 422–30. doi: 10.1002/(SICI)1097-4636(19980905)41:3<422::AID-JBM12>3.0.CO;2-K

Weledji, E. P., and Assob, J. C. (2014). The ubiquitous neural cell adhesion molecule (N-CAM). *Ann. Med. Surg.* 3, 77–81. doi: 10.1016/j.amsu.2014.06.014

White, J., and Dalton, S. (2005). Cell cycle control of embryonic stem cells. *Stem Cell Rev*. 1, 131–138. doi: 10.1385/SCR:1:2:131

Xie, J., Liu, W., MacEwan, M. R., Bridgman, P. C., and Xia, Y. (2014). Neurite outgrowth on electrospun nanofibers with uniaxial alignment: the effects of fiber density, surface coating, and supporting substrate. *ACS Nano* 8, 1878–1885. doi: 10.1021/nn406363j

Xiong, Z., Zhao, S., Mao, X., Lu, X., He, G., Yang, G., et al. (2014). Selective neuronal differentiation of neural stem cells induced by nanosecond microplasma agitation. *Stem Cell Res.* 12, 387–399. doi: 10.1016/j.scr.2013.11.003

Yang, L., Jiang, Z., Zhou, L., Zhao, K., Ma, X., and Cheng, G. (2017). Hydrophilic cell-derived extracellular matrix as a niche to promote adhesion and differentiation of neural progenitor cells. *RSC Adv*. 7, 45587–45594. doi: 10.1039/C7RA08273H

Yang, Y., Zhang, Y., Chai, R., and Gu, Z. (2018). Designs of biomaterials and microenvironments for neuroengineering. *Neural Plast* 2018:1021969. doi: 10.1155/2018/1021969

Yoshida, S., Hagiwara, K., Hasebe, T., and Hotta, A. (2013). Surface modification of polymers by plasma treatments for the enhancement of biocompatibility and controlled drug release. *Surface Coat. Tech.* 233, 99–107. doi: 10.1016/j.surfcoat.2013.02.042

Zeiger, A. S., Hinton, B., and Van Vliet, K. J. (2013). Why the dish makes a difference: quantitative comparison of polystyrene culture surfaces. *Acta Biomater*. 9, 7354–7361. doi: 10.1016/j.actbio.2013.02.035

Zoch, M. L., Clemens, T. L., and Riddle, R. C. (2016). New insights into the biology of osteocalcin. *Bone* 82, 42–49. doi: 10.1016/j.bone.2015.05.046

**Conflict of Interest:** The authors declare that the research was conducted in the absence of any commercial or financial relationships that could be construed as a potential conflict of interest.

frontiers in Materials

ORIGINAL RESEARCH
published: 25 October 2019
doi: 10.3389/fmats.2019.00263

# An Alternative Approach to the Surface Methacrylation of Non-stoichiometric Hydroxyapatite Nanoparticles for Use in Bone-Inspired Composites

*Patricia A. Comeau and Thomas Willett**

*Composite Biomaterial Systems Laboratory, Department of Systems Design Engineering, University of Waterloo, Waterloo, ON, Canada*

Modification of the inorganic particle surface is one approach toward enhancing the mechanical and swelling properties of a bone-inspired composite. In this study we sought to manipulate the surface of non-stoichiometric nHA particles by utilizing a gentler methacrylation approach with two different methacrylates—methacrylic anhydride (MAh) and glycidyl methacrylate (GMA). While silanization of nHA (Si-nHA) is a recognized functionalization approach, one notable disadvantage is the need for relatively harsh reaction conditions. Here, ATR-FTIR and liquid state $^{13}$C-NMR provided evidence for a stronger affinity of the nHA surface for methacrylic anhydride compared to glycidyl methacrylate under the same reaction conditions; fewer GMA molecules reacted with the nHA surface. However, the affinity of MAh is more electrostatic in nature, whereas GMA attachment involves some covalent bond formation. In addition, while in water, there was no detectable dependence of particle settling on methacrylate choice, in ethanol, native nHA and nHA methacrylated with GMA each had detectably greater stability in suspension than the other sample groups. Lastly, the addition of GMA-nHA detectably increased the dynamic stiffness and did not impact the swelling in 37°C water of a GelMA-based composite compared to that observed upon adding native nHA. Overall, the GMA-based methacrylation approach was found to be a viable alternative to silanization and offers possibilities for future fabrication of bone-inspired composites.

**Keywords: nano-hydroxyapatite, methacrylation, methacrylic anhydride, glycidyl methacrylate, surface functionalization, nanocomposite, dynamic stiffness, swelling**

OPEN ACCESS

***Edited by:***
*Laura Maria Vergani, Politecnico di Milano, Italy*

***Reviewed by:***
*Walter Caseri, ETH Zürich, Switzerland*
*Abu Zayed M. Saliqur Rahman, The Ohio State University, United States*

****Correspondence:***
*Thomas Willett*
*thomas.willett@uwaterloo.ca*

***Specialty section:***
*This article was submitted to Polymeric and Composite Materials, a section of the journal Frontiers in Materials*

***Received:*** *29 June 2019*
***Accepted:*** *10 October 2019*
***Published:*** *25 October 2019*

***Citation:***
*Comeau PA and Willett T (2019) An Alternative Approach to the Surface Methacrylation of Non-stoichiometric Hydroxyapatite Nanoparticles for Use in Bone-Inspired Composites. Front. Mater. 6:263. doi: 10.3389/fmats.2019.00263*

## INTRODUCTION

As an osteoconductive ceramic which resembles the inorganic component of bone, hydroxyapatite (HA; $Ca_{10}(PO_4)_6(OH)_2$) is interesting to biologists and biomaterial scientists alike. To date, HA has found use in applications such as a bone filler (Frame et al., 1981), orthopedic implant coating (Liu et al., 2009), composite filler (Liu et al., 2013), and cell culture substrate (Cheng et al., 2013). In many of these cases, the ability to control or manipulate the surface properties of HA is very important and informs how successful the application will be. For example, the incorporation of HA in bone cement formulations has previously been found to reduce the strength of these

materials (Leite Ferreira et al., 2014); this is likely due to a poor interfacial bonding between the polymeric matrix and HA, as well as agglomeration of the HA leading to stress concentrations (Leite Ferreira et al., 2014). It is well-recognized that interfacial adhesion between organic matrix and inorganic fillers is one attribute which contributes to the successful development of a composite with good mechanical properties (Ji et al., 2003; Xie et al., 2004). To address this challenge, coupling agents may be used to modify the HA surface and tune conditions at the composite interface (Vaz et al., 2002; Roether and Deb, 2004), including the ability to disperse the HA within the chosen organic matrix. Fortunately, several groups have found that HA may strongly interact with both polar and polarizable molecules, including various proteins and cells (Redey et al., 1999; El-Ghannam, 2005; Pieters et al., 2010; Gamelas and Martins, 2015). As one class of coupling agents, methacrylates covalently attached to a particle surface provide an opportunity for selective radical reactions within a composite. Methacrylated groups can aid in the covalent cross-linking between inorganic and organic phases within a composite; this can be very beneficial in the processing and application of nanocomposites in various industries, including for the biomedical materials and devices industries. Grafting of HA micro-particles with methacrylates has been previously achieved using a redox initiating system with some success (Murugan and Panduranga Rao, 2003; Murugan and Ramakrishna, 2004). However, the gentler approach offered in this study should generate fewer potentially cytotoxic by-products (or unreacted residual chemicals) (Temenoff et al., 2003). In addition, our proposed approach is expected to be more controlled than a redox initiation system owing to the lack of radicals (or growing macroradicals) which may terminate reactive sites (Murugan and Panduranga Rao, 2003). In this paper, we first present the results of direct functionalization of non-stoichiometric HA nanoparticle (nHA) surfaces using two different methacrylates under mild conditions—methacrylic anhydride (MAh), and glycidyl methacrylate (GMA)—and subsequently report changes to nHA particle dispersion in different media, before adding the nHA to methacrylated gelatin (GelMA) and assessing the composite stiffness and swelling in a proof-of-concept investigation. A surface functionalization control for this study is the well-studied silanated-nHA (Si-nHA), achieved using methacryloxypropyltrimethoxysilane (MPTS) (Cisneros-Pineda et al., 2014; Lung et al., 2016). Unfortunately, typical silanization reactions involve harsh reaction conditions (e.g., acidic pH), and a high risk of forming unstable multilayers (Liu et al., 2001; Halvorson et al., 2003; Amdjadi et al., 2017), neither of which is ideal toward the development of an nHA-based bone-mimetic composite.

Crystalline HA consists of $Ca^{2+}$, $PO_4^{3-}$, and $OH^-$ groups packed closely together in a hexagonal structure (Valle et al., 2014; Poralan et al., 2015). While $OH^-$ serves as the backbone, the 6 phosphate ions helically arranged around the c-axis are responsible for stabilizing the skeletal frame of HA (Poralan et al., 2015). With a Ca/P ratio lower than the stoichiometric value for HA (i.e., 1.67), there are calcium vacancies on the surface of non-stoichiometric HA. As a result, the surface calcium atoms are likely covered by excess phosphate ions (El Shafei and Moussa, 2001; Sarig, 2004; Jahromi et al., 2013) which, when protonated in the aqueous solutions, will produce predominantly P-OH groups at the surface. We hypothesized that these surface hydroxyl groups would play a key role in the methacrylation of non-stoichiometric HA nanoparticles (nHA) and aid in the formation of covalent bonds between the nHA surface and the methacrylate agents. Furthermore, the amount of nHA surface methacrylation would also be highly dependent on the type of methacrylate reagent, with glycidyl methacrylate less successful at neutral pH conditions than methacrylic anhydride. Methacrylic anhydride surface functionalization will be more enhanced owing to a notable side reaction which forms methacrylic acid, reduces the pH, and displaces calcium from the nHA surface; this increases the availability of surface hydroxyl groups available for methacrylation. Meanwhile, the GMA reaction at neutral pH involves both transesterification (which divides GMA in to methacrylate and glycidyl groups) and epoxide ring opening; together these processes encourage both covalent bonding and electrostatic interactions at the nHA surface.

The formation of agglomerates and particle settling are detrimental to the formation and performance of nanocomposites. Finding a surface functionalization approach which addresses nanoparticle agglomeration and dispersion is key to the development of uniformly mixed and dispersed nanocomposites and their bulk properties for subsequent successful application (Lee et al., 2006). Particles suspended in liquids inherently form aggregates and eventually settle as a result of gravity (Liyanage et al., 2016). A single particle in a static fluid will show a settling rate that is dependent on the density and viscosity of the fluid, as well as the nature of the particle (density, size, shape, surface texture) (Witharana et al., 2012). At higher particle concentrations, some inter-particle interaction must also be considered. In the case of nanoparticles, when dispersed in liquids, the intermolecular forces along with the thermal vibrations and diffusivity play a greater role than Newtonian forces (and gravity). As a result, nanoparticles have a more random (and less vertically downward) motion during settling than particles that are 1 μm or larger in size. We hypothesized that the dispersion of the methacrylated particles in different media will be largely dependent on methacrylate reagent type, with each reagent resulting in a different surface charge owing to differences in the nature of surface coverage with the methacrylate agent.

Lastly, a proof-of-concept investigation was pursued to study the impact of nHA surface methacrylation on the dynamic stiffness and swelling of a nHA-added GelMA composite. We hypothesized that successful surface methacrylation of nHA would result in greater composite dynamic stiffness and reduced swelling in water.

## MATERIALS AND METHODS

Non-stoichiometric nHA was purchased from MKNano (division of M K Impex Corp, Canada). All other reagents were purchased from Sigma-Aldrich Canada. We have previously reported on the characteristics of this nHA (Comeau and Willett, 2018). The

nHA powder has been found to have a crystallinity of 66%, a Ca/P of 1.52 and is rod shaped with a ∼120 nm length and 20–30 nm width on average (Comeau and Willett, 2018). In addition, ATR-FTIR spectroscopy of the raw native nHA has confirmed its carbonated nature (Comeau and Willett, 2018).

## Methacrylation of the Non-stoichiometric nHA Surface

0.425 M solutions of methacrylic anhydride and glycidyl methacrylate were first prepared using MilliQ distilled water (MQ $dH_2O$), and brought to a pH of 7.4 using 4.0 M sodium hydroxide (NaOH), before 300 mL of this mixture was added to 12 g of nHA within a 1 L capped flask. The pH of the nHA-based mixture was then maintained at a pH of 7.4 using 4.0 M NaOH, while placed on a horizontal shaking plate at 200 rpm for 2 h. After 2 h, the mixture was centrifuged at 2,000 rpm for 10 min, before the liquid was decanted, the powder re-suspended in MQ $dH_2O$, and the mixture centrifuged for a second time. Once the liquid was decanted for a second time, the nHA powder pellet was manually crushed and placed in a 60°C oven for 5 days in order to dry. **Figure 1** provides a schematic of the proposed surface reaction between nHA and either MAh or GMA.

## Silanization of the Non-stoichiometric nHA Surface

First, following a modification of a published protocol (Lung et al., 2016), 30 % by-volume of methacryloxypropyltrimethoxysilane (MPTS) was added to a 90% ethanol solution, the pH was adjusted to 4 with 3.4 M acetic acid, and the mixture was placed under aluminum foil on a magnetic stir plate at 200 rpm for 1 h. Next, the mixture was added to 12 g of nHA powder in a 1 L glass capped flask, and the suspension sonicated for 15 min at 50°C in a water bath. The ratio of reactant moles per gram of nHA powder is the same under silanization conditions as under methacrylation conditions (e.g., 0.1275 mol reactant /12 g nHA). After 15 min, the suspension was returned to the magnetic stir plate at 200 rpm for 24 h. Finally, the Si-nHA suspension was dialyzed for 2 h against MQ $dH_2O$, before being collected and dried at room temperature for several days. Owing to the high concentration of MPTS, this powder also required additional rinsing with 100% ethanol and drying in a furnace for 1 week at 60°C.

## Functionalized nHA Powder Characterization

The nHA powder was analyzed by Attenuated Total Reflectance - Fourier Transform Infrared (ATR-FTIR) spectroscopy (Tensor 27, Bruker) to confirm the presence of methacrylate groups ($n = 3$). From the ATR-FTIR spectra, vibrations corresponding to $PO_4^{3-}$ were identified at 1,028, 605, and 565 $cm^{-1}$, while bands indicating C=O and C=C (from the methacrylates) could be found at 1,680–1,740 and 1,600–1,680 $cm^{-1}$, respectively (Arcís et al., 2002; Gonzalez-McQuire et al., 2004). The peak area for the C=C functional group was calculated using DMFit 2010 Software, following normalization to that of the phosphate vibration at 605 $cm^{-1}$ and subtraction of the similarly normalized native nHA peaks. The C=C functionalization is of greatest interest for our research group with regards to future use of a methacrylated nHA in UV-curable nanocomposites. However, the identification of C=O in the ATR-FTIR spectra is very relevant for the recognition of how the different reactant species interact with the nHA surface. Additional analysis of the chemical structure of the methacrylated nHA was obtained using liquid-state nuclear magnetic resonance imaging (NMR; Bruker 500 MHz Ultrashield™) with a $^{13}C$ probe. Prior to NMR, the nHA powder was first dissolved in 400 mM ethylenediaminetetraacetic acid (EDTA) and the solution filtered with cheese cloth (to ensure complete dissolution) before adding deutrium oxide ($D_2O$) and placing the sample in liquid NMR tubes. Samples were run at a frequency of 125.77 MHz using a 90-degree pulse of 15 μs. Spectra were reported in ppm using the reference of methanol in $D_2O$. Peaks in the $^{13}C$ NMR spectra were identified using Topspin (Bruker) software. It is important to recognize an important source of error resulting from the hydrolysis of nHA during liquid NMR sample preparation. However, native (i.e., unmodified) nHA was used as a control in both ATR-FTIR and NMR characterization; this helps to mitigate this concern.

Following drying, the surface charge and relative suspension stability of the methacrylated nHA was assessed by characterizing the zeta potential of nHA-$dH_2O$ solutions with a zeta potential analyzer (Wallis™, Cordouan Technologies) and ZetaQ V1.7.0 software ($n = 5$). Sample suspensions of 0.5 mg/mL nHA were prepared in unbuffered solutions of MQ $dH_2O$ or 100% ethanol (EtOH). MQ $dH_2O$ and EtOH were the two media chosen owing to their suitability in future biomimetic composite fabrication. Zeta potential is a common method to measure the electrostatic interaction between suspended particles and the overall colloidal stability of the solution (Salopek et al., 1992; White et al., 2007). Typically, a zeta potential magnitude of >15 mV indicates that the particles will have some beginning stability from electrostatic considerations; however, a magnitude >30 mV is associated with more apparent (and "medium") suspension stability (Salopek et al., 1992; White et al., 2007).

## nHA Particle Gravity Settling Experiments in Polar Liquid

To further assess the ease of dispersion and likelihood of particle settling in different liquids, 0.1 g of each nHA powder was added to a 20 mL glass scintillation vial and 20 mL of liquid (either MQ $dH_2O$ or 100% ethanol) was added to match zeta potential measurement conditions. This concentration is chosen as it is close to the upper limit for inter-particle interference in light scattering and imagining techniques (Witharana et al., 2012). Next, an ultrasonicator with a micro-horn (Symphony™, VWR) was used to initially disperse the powder for 30 s (30% power setting). Immediately following the completion of sonication (i.e., time of 0 s), a digital image of the powder suspension was recorded using a Canon (Powershot Digital ELPH) camera. The suspension was then left undisturbed overnight with images taken at 1, 2, 5, 10, 20, and 30 min, as well as at 24 h.

After 30 min of gravity settling, 5 μL of particle-suspended solution (0.1 g in 20 mL MQ $dH_2O$ or EtOH) was removed

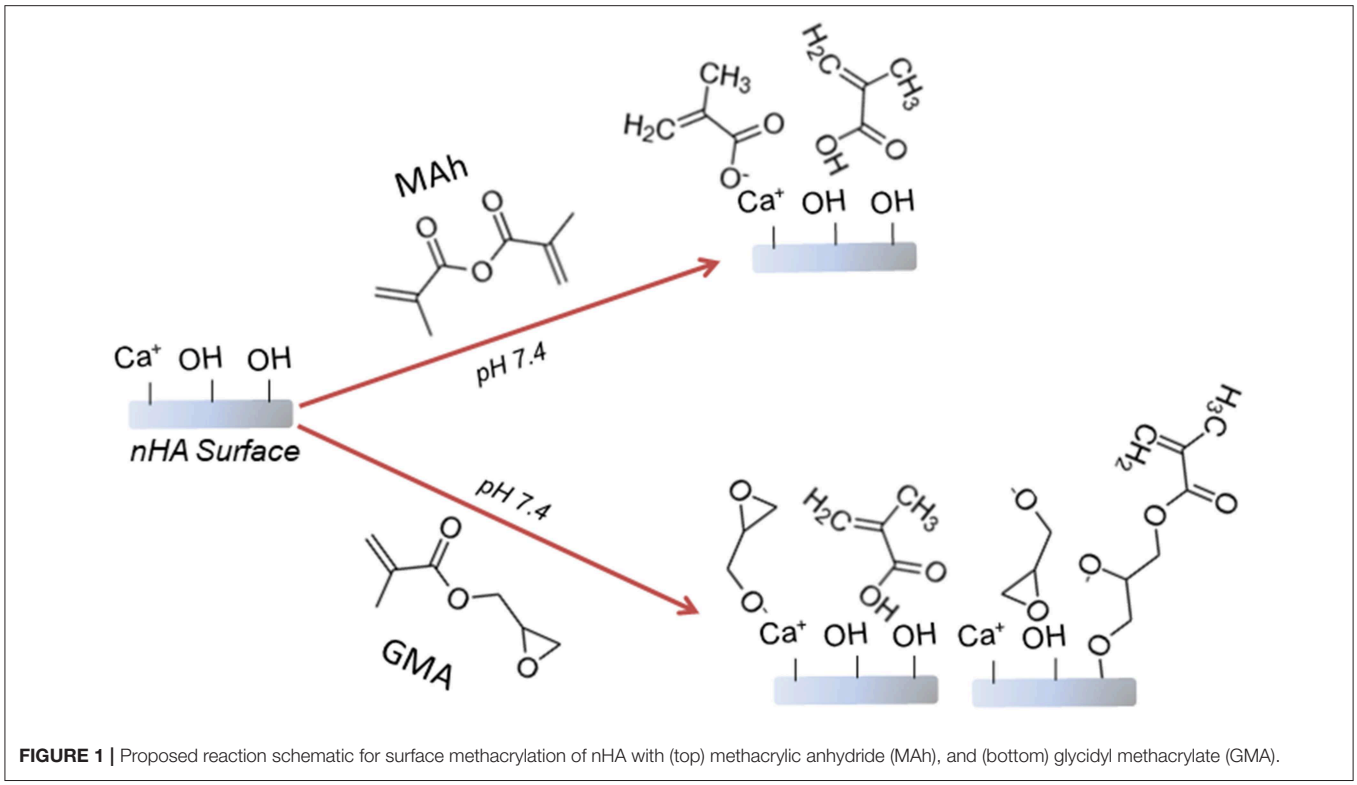


**FIGURE 1 |** Proposed reaction schematic for surface methacrylation of nHA with (top) methacrylic anhydride (MAh), and (bottom) glycidyl methacrylate (GMA).

from the vials at the middle of the volume, and added to SEM stubs using carbon tape. The stubs were then left in a desiccator with Drierite® for 24 h in order to dry prior to SEM imaging (Zeiss Merlin FESEM 1530). Operating conditions for SEM consisted of a working distance of 10.5 mm, an accelerating voltage of 10.00 kV, and a vacuum of 1.21 $e^{-006}$ mbar.

## Fabrication of nHA-Added GelMA Composite

Type B, 225 bloom gelatin was methacrylated according to an existing protocol. Gelatin (25 g) was slowly added to 40°C MilliQ distilled water (MQ $dH_2O$; 100 mL) and the pH then adjusted to 7.40 using sodium hydroxide (NaOH; 4 M) solution. Next, methacrylic anhydride was added while maintaining the pH at 7–7.4 with NaOH (4 M). Sufficient methacrylic anhydride was added to obtain a methacrylic anhydride–to–amine group ratio of 10:1 during reaction. Over the next 2 h the reaction was continued while maintaining the pH at 7–7.4 with NaOH (4 M). After 2 h, the pH of the gelatin solution was adjusted to 8 with NaOH (4 M), before dialyzing the methacrylated gelatin (GelMA) solution with 13 kDA cut-off tubing against MQ $dH_2O$ for seven days. The GelMA solution was then frozen overnight and subsequently freeze dried (Labconco Freezone 1L Benchtop) for 2–3 days to obtain dried GelMA. Finally, GelMA-based inks containing 8% /vol nHA were prepared by adding nHA (MKNano, MK Impex Corp.) to an aqueous 62% w/v GelMA solution using a mechanical mixer (Caframo®) at 60 rpm.

## Dynamic Mechanical Analysis of nHA-Added GelMA Composite

To obtain viscoelastic properties of the 30 s UV-cured nHA-GelMA samples (of ∼4.8 mm diameter and ∼∼4.5 mm height), the fresh samples were preloaded in compression to 0.1 N before subjecting them to cyclic sinusoidal loading between 0 and 10% compressive strain at a frequency of 0.1 Hz using a 50 N loading cell (UniVert, CellScale, Waterloo, Ontario, Canada). Data was acquired at 100 Hz and analyzed using Matlab code. From this analysis, the dynamic modulus ($E^*$), storage modulus ($E'$), and loss modulus ($E''$) were determined ($n = 6$).

## Swelling of nHA-Added GelMA Composite in Water

To assess the swelling of freshly prepared nHA-GelMA composite samples, the mass of each sample (again, cured for 30 s) was first recorded ("$m_1$") and then added directly to 37°C MQ $dH_2O$. After 3 days, the mass of the samples was recorded ("$m_2$"). The swelling percentage of the UV-cured samples in water was calculated according to Equation (1) ($n = 6$).

$$\frac{(m_2 - m_1)}{m_1} \times 100\% \quad (1)$$

## Statistical Analysis

Differences in the means of study outcomes were analyzed using IBM® SPSS® Statistics software and a one-way or two-way general linear model with a significance value of $p = 0.05$ (and a *post-hoc* Tukey analysis). Specific $p$-values for given data sets are

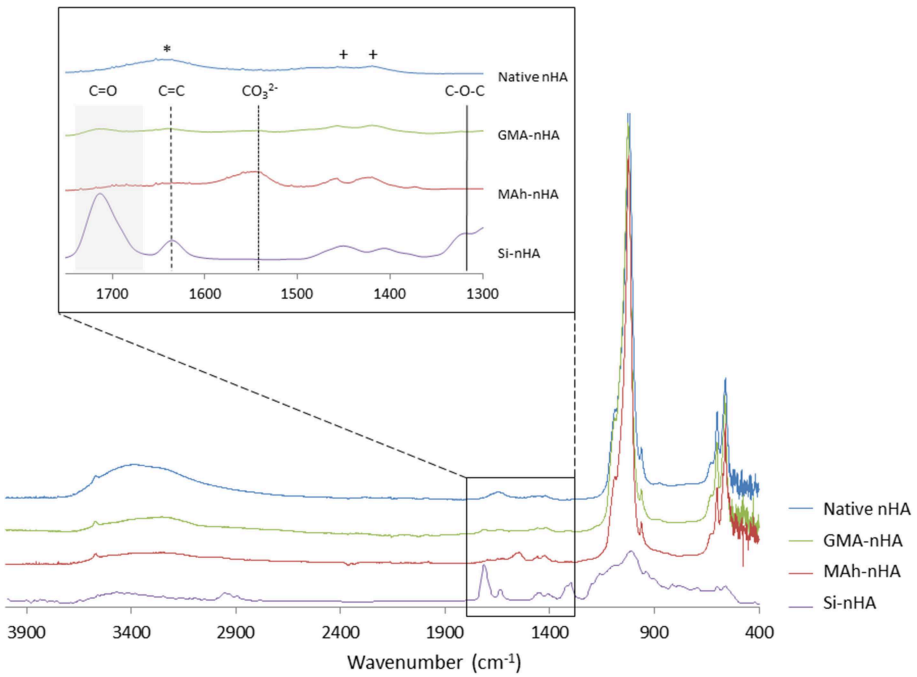


**FIGURE 2 |** ATR-FTIR spectroscopy of native and methacrylated nHA particles. In this study, nHA was methacrylated using methacrylic anhydride (MAh) or glycidyl methacrylate (GMA). Phosphate peaks in the fingerprint region of the spectra (500–1,200 $cm^{-1}$) are evident, with spectra of methacrylated nHA also presenting additional peaks. Peaks owing to C=C stretch are identified by dashed vertical lines and C=O broad stretch peak by a gray region for the functionalized nHA samples. The peaks identifying carbonate groups that have replaced tetrahedral phosphate sites are indicated by $^+$, while a free residual water (H-O-H) peak is indicated by * in the native nHA spectra.

provided (noting that $p$-values $< 0.05$ are significant). All data are presented in this paper as mean $\pm$ one standard deviation.

## RESULTS AND DISCUSSION

### Characterization of Functionalized nHA Powders

nHA particles were functionalized using the two methacrylates—methacrylic anhydride (MAh) and glycidyl methacrylate (GMA). A 0.425 M concentration of methacrylate reagents was chosen to encourage full saturation of the nHA surface with excess remaining in solution following reaction. This methacrylate reagent concentration also closely matches the previously reported study of GMA-functionalization of HA micrometer-sized particles using a redox-initiating system (Murugan and Panduranga Rao, 2003; Murugan and Ramakrishna, 2004). Meanwhile, these two methacrylates were chosen for their different chemical structure and potential differences in bonding to the nHA surface upon reaction (e.g., electrostatic or covalent in nature). ATR-FTIR spectroscopy (**Figure 2**) of the two methacrylated powders shows evidence of additional peaks (compared to native nHA) that correspond to the presence of methacrylate groups.

ATR-FTIR spectroscopy confirmed the carbonate-substitution of the native, non-stoichiometric nHA with peaks at 1,423 and 1,457 $cm^{-1}$ attributed to asymmetric stretching modes of carbonate groups which replaced the tetrahedral phosphate sites (Figueiredo et al., 2012; Tkalčec et al., 2014). The broad peak at 1,642 $cm^{-1}$ for native nHA is attributed to free residual water (H-O-H) (Zou et al., 2012), which following methacrylation is less evident in the MAh-nHA and GMA-nHA samples. Several additional peaks also appear in the spectra following methacrylation of the nHA. For example, the band at 1,566 $cm^{-1}$ for MAh-nHA is representative of the carboxylate group formed during the ionic side reaction between methacrylic acid and calcium ions at the nHA surface (Cisneros-Pineda et al., 2014); this suggests a large amount of electrostatic interactions at the nHA surface. In addition, C=O and C=C bond stretches are apparent for each methacrylate reagent; these are indicative of at least the presence of these reagents at the nHA surface (Arcís et al., 2002; Cisneros-Pineda et al., 2014). For MAh-nHA, the C=O peak occurs at 1,696 $cm^{-1}$, while the C=C peak occurs at 1,634 $cm^{-1}$. For GMA-nHA, these same peaks occur at 1,715 and 1,640 $cm^{-1}$, respectively. In addition, for MAh-nHA and GMA-nHA, the C=C and C=O peak areas are similar (data for C=O peak fitting not shown)—this is likely indicative that the $COO^-$ functional group is not the sole form of attachment for the respective reagents at the nHA surface. Finally, GMA-nHA spectra show a band at $\sim$1,300 $cm^{-1}$ which is attributable to the C-O-C bond present in the respective reagent; notably MAh-nHA spectra does not show such a peak (Cisneros-Pineda et al., 2014). Meanwhile, the reduced peak area under C=C peaks for GMA-nHA compared to MAh-nHA suggests that

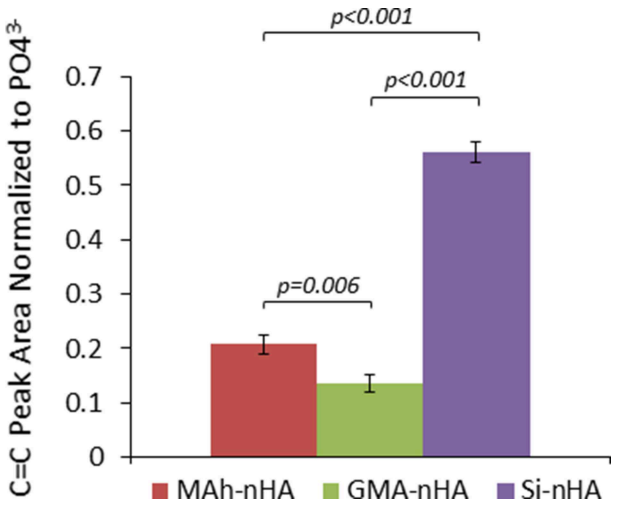


**FIGURE 3 |** ATR-FTIR analysis of the methacrylated nHA C=C peak area normalized to $PO_4^{3-}$ peak area. Horizontal bars indicate statistically detectable difference ($p$-values indicated) ($n = 3$).

fewer methacrylate groups are present at the nHA surface for the GMA-nHA group (**Figure 3**).

The difference in means between sample groups was statistically detectable for normalized C=C peak area ($p < 0.001$). For example, GMA-nHA was found to have detectably less C=C signal than MAh-nHA ($p = 0.006$). Meanwhile, upon normalization of the C=C peak area to that of the 605 $cm^{-1}$ phosphate peak, it is evident that the silanization protocol (Lung et al., 2016) resulted in detectably more C=C bonds at the surface of Si-nHA than nHA functionalized with either methacrylate reagent ($p < 0.001$). Such C=C bonds are integral to the radical photopolymerization reaction; introducing these groups on the nHA surface should encourage radical photopolymerization with similar groups within the GelMA matrix (once nHA and GelMA are blended together in a bone-inspired composite).

Liquid-state $^{13}$C-NMR spectra further support this difference between the different functionalization approaches and gives insight in to the nature of bonding and/or surface interaction with the different reagents (**Figure 4**).

The $^{13}$C-NMR spectra confirm silanization or methacrylation of the nHA following the respective protocols. The highlighted peaks [at (i)–(iv)] are detected in the spectra of MAh-nHA and GMA-nHA, but not in that of native nHA. For example, at 120–145 ppm (peak "ii"), there are two strong peaks for MAh-nHA and GMA-nHA that indicate the presence of vinyl carbon atoms (i.e., $=CR_2$ and $=CH_2$) (Reis et al., 2009; Mertz et al., 2014). For MAh-nHA the $=CR_2$ peak has been shifted downfield (i.e., more positive ppm) to 142 ppm, while for GMA-nHA this same peak is at 127 ppm. This difference in peak position is likely due to greater van der Waals attractive interactions between MAh and nHA (Li and Chesnut, 1986; Chesnut et al., 1988). The $=CH_2$ peak is at the same position (i.e., 120 ppm) for MAh-nHA and GMA-nHA. Meanwhile, peaks between 160 and 180 ppm (peak "i") in all spectra are associated with carbonyl carbon atoms (Mertz et al., 2014), and the presence of a peak at 70 ppm (peak "iii") in GMA-nHA supports the presence of a C-O-P covalent bond (Avci and Mathias, 2005). Interestingly, there is no apparent C-O-P peak in $^{13}$C NMR spectra for MAh-nHA; this suggests that while functionalization results in a covalent bond between GMA and nHA, this is not the case for MAh. Therefore, MAh interaction with the surface of nHA may be more electrostatic in nature. Lastly, methylene carbon atoms are likely represented by the peak at 20 ppm (peak "iv"). Based on a larger vinyl carbon signal, as well as the additional peaks in $^{13}$C-NMR spectra of MAh-nHA compared to that of GMA-nHA, the methacrylation with methacrylic anhydride results in more methacrylate groups being present at the nHA surface following functionalization; however, these are not covalently bonded to nHA. This is corroborated with a stronger C=C peak in ATR-FTIR spectra for MAh-nHA compared to GMA-nHA (**Figures 1**, **2**). Altogether, the ATR-FTIR and $^{13}$C NMR results support the initial hypothesis that methacrylic anhydride surface functionalization will be more successful with a greater abundance of vinyl groups, owing to the formation of methacrylic acid and the increased presence of hydroxyl groups at the nHA surface. Meanwhile, GMA functionalization involves notable covalent bonding (as a result of epoxide ring opening) and non-covalent interactions (resulting from hydrogen bonding and interactions with $Ca^{2+}$ at the nHA surface). A notable limitation of liquid $^{13}$C-NMR analysis is the use of ethylenediaminetetraacetic acid (EDTA) to dissolve the nHA, as this creates additional carbon peaks in the spectra. However, identification of peaks due to EDTA and native non-stoichiometric nHA aided in distinguishing those peaks due to the surface functionalization process alone. This was found to be an acceptable approach for processing the liquid NMR spectra and assessing surface functionalization success; particularly when compared with ATR-FTIR spectroscopy results.

Prior to performing settling experiments, the powder was assessed with a Zeta Potential Analyzer in unbuffered MQ $dH_2O$ and EtOH. There was a noticeable dependence of the zeta potential of the particles on the choice of methacrylating agent in either of the two unbuffered media (**Figure 5**).

The impact of sample type and solution type on zeta potential was statistically detectable ($p = 0.015$ and $p < 0.001$, respectively). In fact, the interaction between sample type and solution type was also found to be significant ($p < 0.001$). Both MAh-nHA and Si-nHA were found to have a detectably less negative zeta potential in MQ $dH_2O$ than GMA-nHA ($p = 0.035$ and $p < 0.001$, respectively). Meanwhile, in EtOH, MAh-nHA and Si-nHA were found to have a detectably less positive zeta potential than either native nHA or GMA-nHA ($p < 0.001$ for each respective pair).

To explain the zeta potential dependence on methacrylating reagent, the reactions which are uniquely specific to each reagent at the nHA surface must be considered. For example, upon methacrylating nHA with methacrylic anhydride, a side reaction between methacrylic anhydride and water produces methacrylic acid. These methacrylic acid molecules are able to stick to the nHA surface and, subsequently, release additional protons into the solution. Meanwhile, methacrylating nHA with glycidyl methacrylate itself involves additional interactions between the glycidyl groups (formed during the transesterification of glycidyl

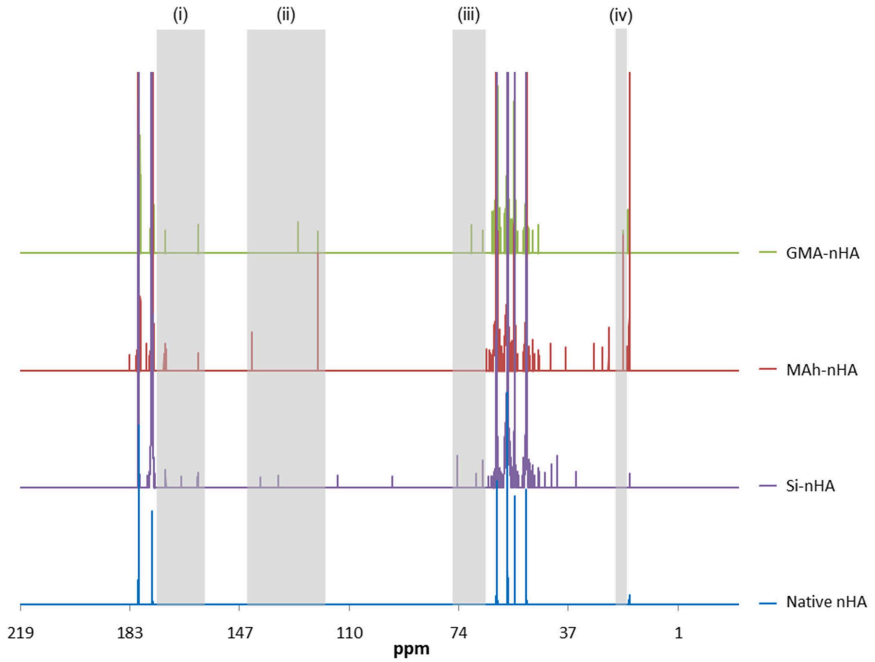


**FIGURE 4 |** Liquid state $^{13}C$ NMR spectra of native, silanated and methacrylated nHA. In this study, nHA is methacrylated using methacrylic anhydride (MAh) or glycidyl methacrylate (GMA). There are several peaks labeled (i)–(iv) in the Si-nHA, MAh-nHA and GMA-nHA spectra which do not appear in the native nHA spectrum.

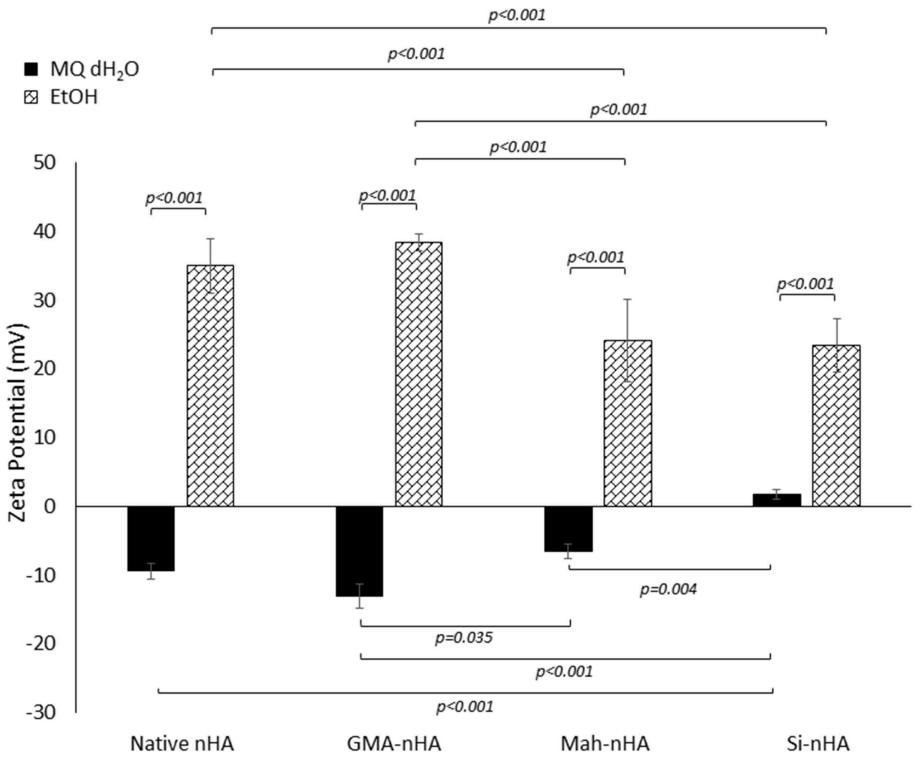


**FIGURE 5 |** Zeta potential analysis of methacrylated and silanated nHA particles in unbuffered MQ $dH_2O$ and EtOH. In this study nHA was methacrylated using methacrylic anhydride (MAh) or glycidyl methacrylate (GMA); silanated nHA is represented by Si-nHA. Horizontal bars indicate statistically detectable difference ($p$-values indicated) ($n = 5$).

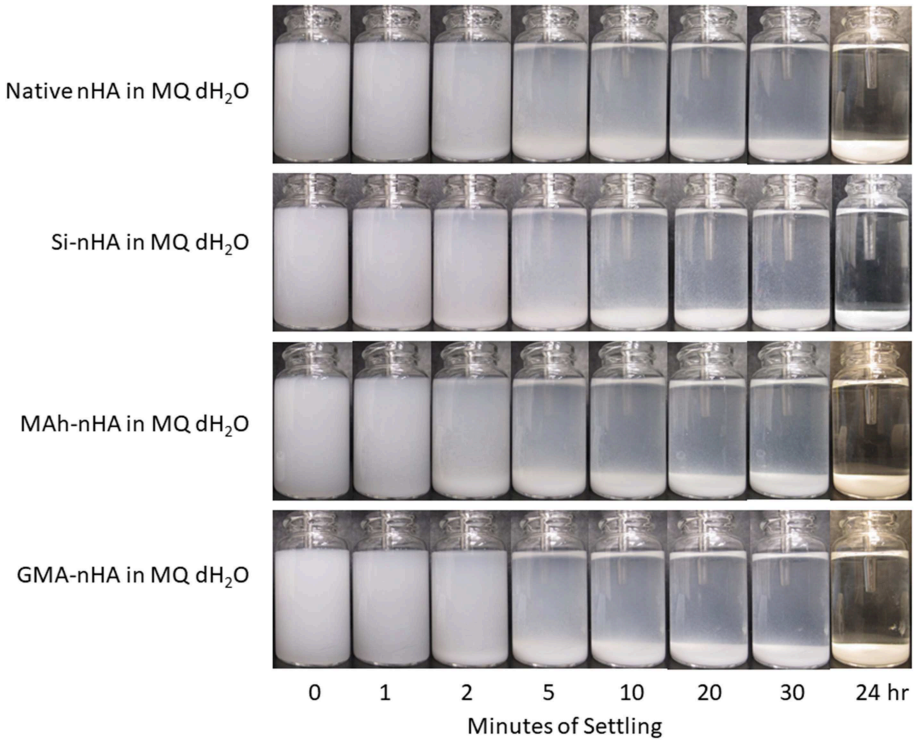


**FIGURE 6 |** Gravity settling of native, methacrylated, and silanated nHA in MQ $dH_2O$ at room temperature. In this study, nHA is methacrylated using methacrylic anhydride (MAh) or glycidyl methacrylate (GMA); silanated nHA is represented by Si-nHA.

methacrylate) and the hydroxyl groups and/or positive charge (e.g., $Ca^{2+}$) at the nHA surface. Altogether, the zeta potential of the two methacrylated nHA supports a theory of less glycidyl methacrylate bonding to the hydroxyl groups at the nHA surface (and less coverage of the negative surface charge reported for unmodified nHA). In fact, there is no statistically detectable difference in zeta potential between native nHA and GMA-nHA in either media measured. From the zeta potential measurements alone, it would then be anticipated that none of the sample groups will exhibit appreciable particle stability (i.e., suspension) in MQ $dH_2O$. Meanwhile, in EtOH native nHA and GMA-nHA particles show more particle stability than either Si-nHA or MAh-nHA particles.

There are a number of mechanisms responsible for developing charge—the three of notable relevance here are (1) ionization of surface groups, (2) differential ion adsorption from electrolyte solution, and (3) differential ion dissolution from a crystal lattice. For example, water is dissociated to a larger extent than alcohols (e.g., ethanol) (Logtenberg and Stein, 1986). As a result, a greater concentration of $H^+$ and $OH^-$ are available to be adsorbed by the nHA surface when in water; this coincides with some dissolution of the positive divalent calcium ion from the nHA lattice and an altogether more negative zeta potential in water. In ethanol (EtOH), there are fewer ions available to adsorb on to nHA, and the calcium ions are less mobile in leaving nHA; this results in a more positive zeta potential. Owing to the silane groups on the Si-nHA, the surface is more hydrophobic (Roether and Deb, 2004), with much lower adsorption of $H^+$ and $OH^-$, and the zeta potential is the most positive of the four nHA sample groups upon dispersion in water. This also explains why the difference of Si-nHA zeta potential in water compared to that in ethanol is the smallest (of the four groups studied).

## nHA Particle Settling Experiments

Results from gravity settling experiments of the sample groups in MQ $dH_2O$ and EtOH are shown in **Figures 6**, **7**, respectively.

Consistent with the zeta-potential results, the unstable suspension of the sample groups in MQ $dH_2O$ demonstrates quick settling, particularly during the first 2–5 min of the experiment. The liquid above the particle bed becomes more transparent after 2 min for the native nHA and nHA methacrylated with either agent; this suggests more of the particles have settled out. For each sample group, the liquid phase is not completely clear within the first 30 min in $dH_2O$—this is indicative that some small particles remain suspended at each time point. However, 24 h later, most of the particles have settled to the bottom of the vial. Zeta potential results in MQ $dH_2O$ correlate well with the observed particle settling in $dH_2O$; the magnitude of zeta potential is $<15$ mV for each sample (which itself suggests poor nanoparticle suspension in the given media). Meanwhile, the suspensions of all but the Si-nHA sample group particles in ethanol may be considered stable for at least the first 30 min recorded, as few particles appear to settle. Following 24 h of settling in ethanol, the MAh-nHA particles have largely settled to the bottom of the vial, while Si-nHA have a few particles still suspended, and

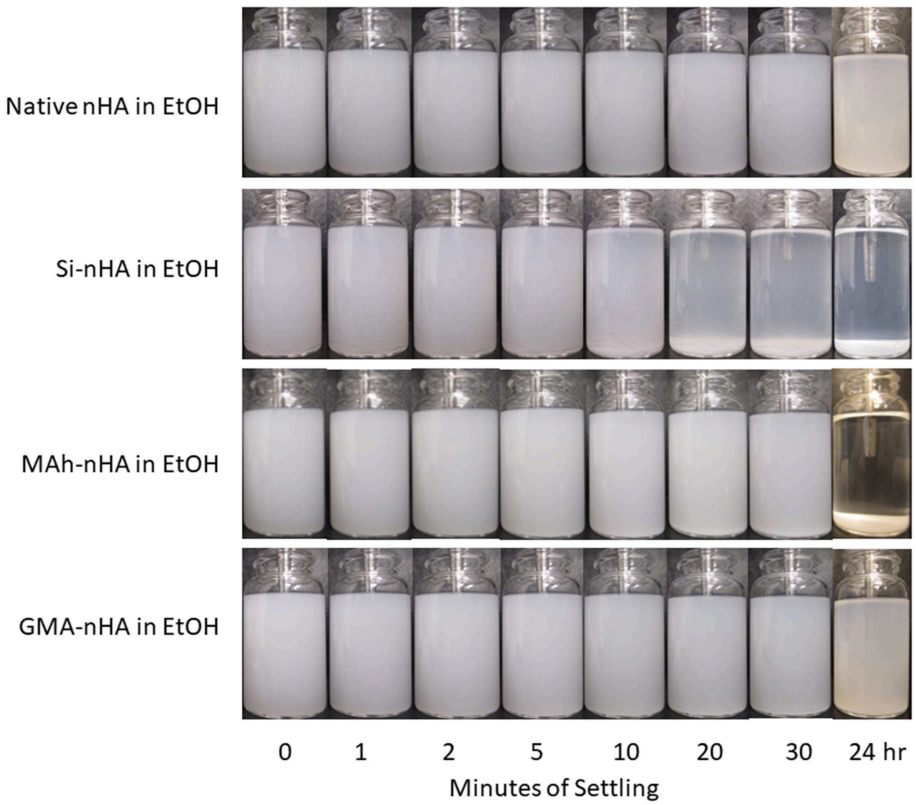


**FIGURE 7 |** Gravity settling of native, methacrylated, and silanated nHA in 100% ethanol (EtOH) at room temperature. In this study nHA is methacrylated using methacrylic anhydride (MAh) or glycidyl methacrylate (GMA); silanated nHA is represented by Si-nHA.

the other sample groups have a significant amount of powder suspended. This is again correlated with the zeta potential results as only native nHA and GMA nHA were found to have a charge >30 mV in magnitude (and some expected suspension stability) (Salopek et al., 1992; White et al., 2007). The lower the magnitude of zeta potential, the greater the ease of particle approach with other particles (i.e., less inter-particle repulsion). In considering the concentration of nHA in the suspension media, there is considerable room for the particles to move around in either media. The difference based on suspension media then is largely owing to how the particles interact with the media, the nature of the solvent layer, and how the various forces (e.g., attractive, repulsive) balance. A common law for understanding particle settling is Stoke's law. In accordance with this law, as ethanol has a lower density and greater dynamic viscosity than water, it is to be expected that particle settling will occur at a slightly slower rate. However, as Stoke's law minimizes the interactions between particles, these are not the only factors to consider. For example, ethanol ($C_2H_5OH$) has only one polar end which, upon interaction with the surface of nHA, manages to neutralize some of the attractive forces, minimize agglomeration, and improve the overall dispersion of nHA (compared to that observed in water). Of significance is that while native nHA and GMA-modified nHA have similar settling behavior in either media, the GMA-modified nHA also offer C=C groups which should benefit the mechanical and swelling performance of future nHA-added bone-inspired composites. Future study may consider additional quantification of the particle settling behavior qualified here (including additional settling time points), as well as that within the future composite of interest.

Under dry conditions, and using SEM to image the powder following 30 min of dispersion, the differences observed in zeta potential measurement were less strongly evident owing to a relatively small magnitude of surface charge in most conditions (**Figure 8**). Typically powder dispersion is qualified by a zeta potential magnitude >15 mV, and while native nHA and GMA-nHA do report such a high magnitude in EtOH, this is not strongly evident in the SEM images. Each sample groups shows some agglomeration, with both methacrylation and silanization protocols appearing to have slightly reduced this agglomeration tendency (compared to native nHA). In addition, while agglomeration is evident in all SEM images the proportion of small, fine particles appears to be greater in samples collected after 30 min in ethanol than in samples after 30 min in water. The minimal impact of sample group on short-term dispersion (i.e., up to 30 min) is likely indicative of the strong role dispersion media has on nanoparticle settling and the random motion of the nanoparticles themselves (i.e., gravity is not the biggest contributor to settling here).

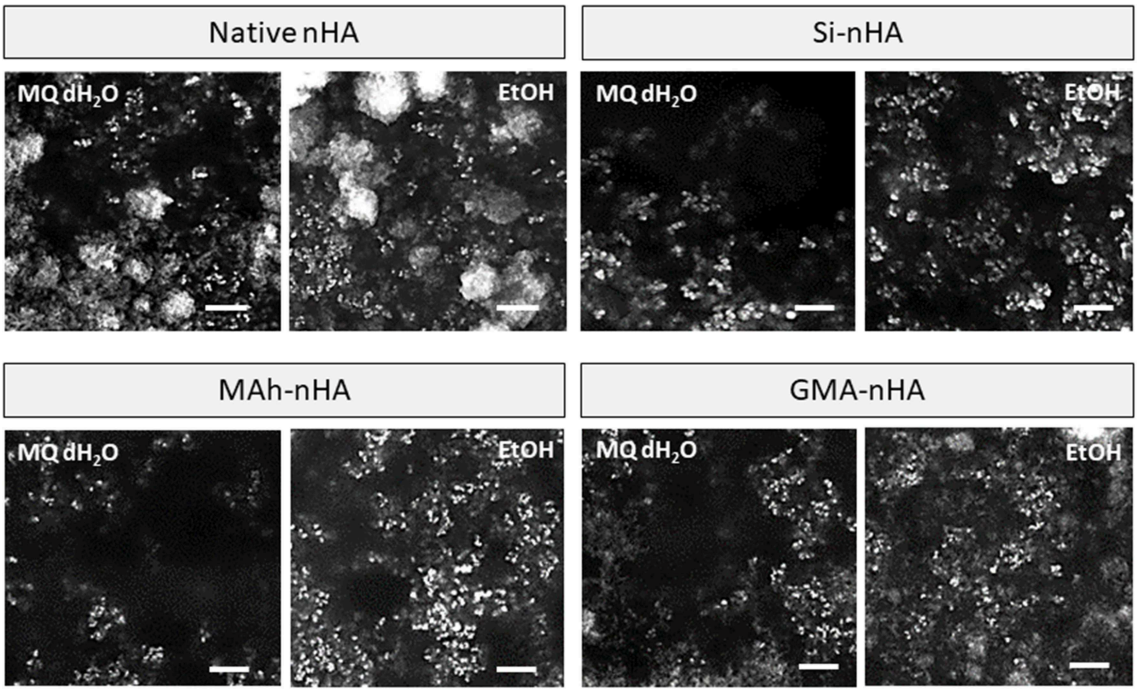


**FIGURE 8 |** SEM images of native, methacrylated, and silanated nHA particles with left-side showing particles collected from $dH_2O$ suspension, and right-side images showing particles collected from EtOH suspension. In this study nHA is methacrylated using methacrylic anhydride (MAh) or glycidyl methacrylate (GMA); silanated nHA is represented by Si-nHA. White scale bar represents 1 μm.

## nHA-Added GelMA Composite

Following characterization of the modified nHA particles alone, the next objective of this study was to investigate the impact of nHA surface methacrylation on the dynamic stiffness and swelling of nHA-added GelMA composite; both of which are integral to the potential application of this material. In this proof-of-concept investigation 8 % /vol nHA was dispersed into an aqueous GelMA solution (62 % w/v). Following initial ink processing, it was observed that both MAh-nHA and Si-nHA particles settled out of the GelMA phase relatively quickly, while native nHA remained well-dispersed for at least 30 min and GMA-nHA experienced only a small amount of settling in this same time period. While all inks were re-mixed immediately prior to preparing the UV-cured samples, this settling behavior is of great significance and correlates well with prior zeta potential observations in an aqueous environment. Meanwhile, a univariate general linear model revealed that the type of surface functionalizing agent impacted dynamic stiffness ($E^*$), storage modulus ($E_{storage}$), loss modulus ($E_{loss}$), and change in mass during swelling ($p = 0.005$, 0.004, 0.014, and $p < 0.001$, respectively; **Figure 9**).

In fact, of the three nHA-modified GelMA composites, only the GMA nHA-GelMA composite had a detectably greater dynamic stiffness than the native nHA-GelMA composite ($p = 0.043$). In addition, GMA nHA-GelMA composite swelling after 3 d in water was comparable to that of native nHA-GelMA composite. Furthermore, the MAh nHA-GelMA composite had the only detectably increased change in mass during swelling compared to either native nHA-GelMA or Si nHA-GelMA composites ($p = 0.001$ and $p < 0.001$, respectively). Future studies will need to investigate the dispersion of the surface methacrylated nHA within the GelMA matrix and assess how such dispersion may have impacted the composite properties. In addition, the role that the introduced vinyl groups on the nHA surface have on composite properties, as a result of UV curing (and radical photopolymerization), requires further investigation.

Overall, the processing of nanocomposites suitable for various industries, such as biomedical materials, may be improved with the use of ethanol to improve dispersion of non-stoichiometric nHA, and the inclusion of directly methacrylated non-stoichiometric nHA particles within the composite. In turn, the resulting composite will be better suited to meet requisite properties (e.g., mechanical and swelling) for the given tissue engineering application.

# CONCLUSIONS

In this study, we investigated a new approach to the methacrylation of non-stoichiometric hydroxyapatite nanoparticles (nHA) using two different methacrylates. Methacrylation using methacrylic anhydride (MAh) was found to add more vinyl (i.e., C=C) groups than glycidyl methacrylate (GMA) upon characterization with ATR-FTIR and liquid-state $^{13}$C-NMR. However, the MAh interaction at the nHA surface was more electrostatic in nature, while for GMA-nHA there was additional evidence of epoxide ring opening and covalent bonding (in the form of P-O-C linkages). Meanwhile,

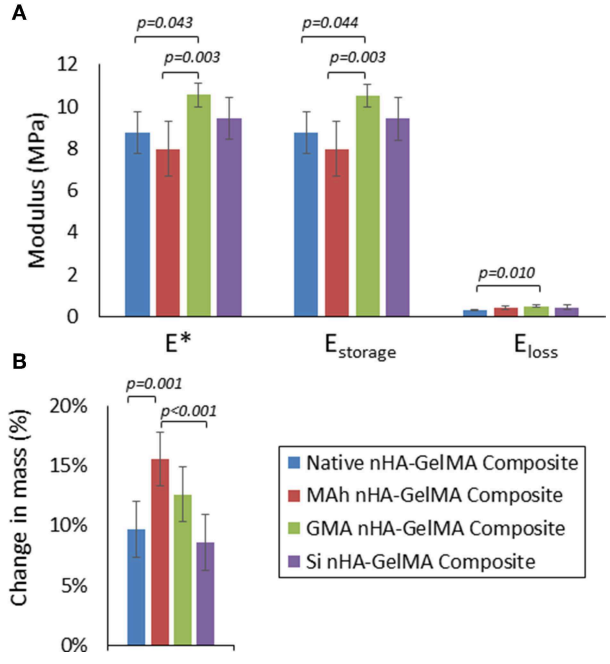


**FIGURE 9 | (A)** Dynamic stiffness (E*), storage modulus ($E_{storage}$), and loss modulus ($E_{loss}$), and **(B)** change in mass after 3d in 37°C water for the nHA-GelMA composites. In this study nHA was methacrylated using methacrylic anhydride (MAh) or glycidyl methacrylate (GMA); silanated nHA is represented by Si-nHA. Horizontal bars indicate statistically detectable difference (*p*-values indicated) ($n = 6$).

gravity settling experiments revealed a small dependence on methacrylate type after 24 h in ethanol; both native and GMA-modified nHA particles dispersed better in ethanol than the MAh- or Si-modified nHA particles. This latter result corroborated well with the detectably greater magnitude of zeta potential reported for native and GMA-nHA in ethanol (compared to the other sample groups). Finally, a proof-of-concept investigation revealed that a GMA-nHA-GelMA composite had a greater dynamic stiffness than the native nHA-GelMA composite, and comparable swelling after 3 d in water.

By analyzing the dependence of nHA surface methacrylation on the type of methacrylate agent, this study has improved current understanding of non-stoichiometric nHA surface affinity for methacrylates. This study also presents a gentler approach to methacrylation of the HA surface and introduction of vinyl groups. Lastly, this work highlights the significance of methacrylate reagent on non-stoichiometric nHA dispersion, with GMA-modified nHA particles showing a notable improvement in ethanol dispersion compared to MAh-modified nHA. As a result, the GMA-modified nHA particles are a viable alternative to silanated nHA in the fabrication of future biomimetic composites, owing to improved dispersion in ethanol and similar covalent nature of the nHA surface modification.

## DATA AVAILABILITY STATEMENT

The datasets generated and analyzed during the current study are available from the corresponding author upon reasonable request.

## AUTHOR CONTRIBUTIONS

PC conceived and conducted the experiments, analyzed and interpreted the results, and was the primary author of the manuscript. TW acquired the research operating funding, advised on the conception and conduction of the experiments and data analysis, and assisted in the editing and revisions of the manuscript as the senior author.

## FUNDING

The authors would like to thank the Natural Sciences and Engineering Research Council of Canada for their support in the form of a postdoctoral fellowship (PC) and a Discovery Grant (No. 3942, TW). This study was also partially supported by a grant from the Canadian Institutes of Health Research (No. 389569, TW).

## ACKNOWLEDGMENTS

We are grateful for the assistance of Jan Venne in the collection of the NMR data reported in this study, and Danielle Erb for her assistance in collecting dynamic stiffness data. The authors also thank Professor Leonardo Simon (University of Waterloo) for helpful discussions.

## REFERENCES

Amdjadi, P., Ghasemi, A., Najafi, F., and Nojehdehian, H. (2017). Pivotal role of filler matrix interface in dental composites: review. *Biomed. Res.* 28, 1054–1065.

Arcís, R. W., López-Macipe, A., Toledano, M., Osorio, E., Rodríguez-Clemente, R., Murtra, J., et al. (2002). Mechanical properties of visible light-cured resins reinforced with hydroxyapatite for dental restoration. *Dental Mater.* 18, 49–57. doi: 10.1016/S0109-5641(01)00019-7

Avci, D., and Mathias, L. J. (2005). Synthesis and photopolymerizations of phosphate-containing acrylate/(di)methacrylate monomers from 3-(acryloyloxy)-2-hydroxypropyl methacrylate. *Polymer Bull.* 54, 11–19. doi: 10.1007/s00289-005-0357-6

Cheng, K., Hirose, M., Wang, X., Sogo, Y., Yamazaki, A., and Ito, A. (2013). Correlation between cell attachment areas after 2h of culture and osteogenic differentiation activity of rat mesenchymal stem cells on hydroxyapatite substrates with various surface properties. *Biochem. Biophys. Res. Commun.* 430, 156–160. doi: 10.1016/j.bbrc.2012.11.054

Chesnut, D. B., Wright, D. W., and Krizek, B. A. (1988). NMR chemical shifts and intramolecular van Der Waals interactions: carbonyl and ether systems. *J. Mol. Struct.* 190, 99–111. doi: 10.1016/0022-2860(88)80275-8

Cisneros-Pineda, O. G., Herrera Kao, W., Loría-Bastarrachea, M. I., Veranes-Pantoja, Y., Cauich-Rodríguez, J. V., and Cervantes-Uc, J. M. (2014). Towards optimization of the silanization process of hydroxyapatite for its use in bone cement formulations. *Mater. Sci. Eng. C* 40, 157–163. doi: 10.1016/j.msec.2014.03.064

Comeau, P., and Willett, T. (2018). Impact of side chain polarity on non-stoichiometric nano-hydroxyapatite surface functionalization with amino acids. *Sci. Rep.* 8:12700. doi: 10.1038/s41598-018-31058-5

El Shafei, G. M., and Moussa, N. A. (2001). Adsorption of some essential amino acids on hydroxyapatite. *J. Colloid Interface Sci.* 238, 160–166. doi: 10.1006/jcis.2001.7474

El-Ghannam, A. (2005). Bone reconstruction: from bioceramics to tissue engineering. *Expert Rev. Med. Devices* 2, 87–101. doi: 10.1586/17434440.2.1.87

Figueiredo, M., Gamelas, J., and Martins, A. (2012). "Characterization of bone and bone-based graft materials using FTIR spectroscopy," in *Infrared Spectroscopy—Life and Biomedical Sciences*, eds T. Theophile (Rijeka: InTech), 315–38. doi: 10.5772/intechopen.68547

Frame, J. W., Browne, R. M., and Brady, C. L. (1981). Hydroxyapatite as a bone substitute in the jaws. *Biomaterials* 2, 19–22. doi: 10.1016/0142-9612(81)90082-X

Gamelas, J. A. F., and Martins, A. G. (2015). Surface properties of carbonated and non-carbonated hydroxyapatites obtained after bone calcination at different temperatures. *Colloids Surfaces A Physicochem. Eng. Aspects* 478, 62–70. doi: 10.1016/j.colsurfa.2015.03.044

Gonzalez-McQuire, R., Chane-Ching, J. Y., Vignaud, E., Lebugle, A., and Mann, S. (2004). Synthesis and characterization of amino acid-functionalized hydroxyapatite nanorods. *J. Mater. Chem.* 14, 2277–2281. doi: 10.1039/b400317a

Halvorson, R. H., Erickson, R. L., and Davidson, C. L. (2003). The effect of filler and silane content on conversion of resin-based composite. *Dental Mater.* 19, 327–333. doi: 10.1016/S0109-5641(02)00062-3

Jahromi, M. T., Yao, G., and Cerruti, M. (2013). The importance of amino acid interactions in the crystallization of hydroxyapatite. *J. R. Soc. Interface R. Soc.* 10:20120906. doi: 10.1098/rsif.2012.0906

Ji, X., Hampsey, J. E., Hu, Q., He, J., Yang, Z., and Lu, Y. (2003). Mesoporous silica-reinforced polymer nanocomposites. *Chem. Mater.* 15, 3656–3662. doi: 10.1021/cm0300866

Lee, H. J., Choi, H. W., Kim, K. J., and Lee, S. C. (2006). Modification of hydroxyapatite nanosurfaces for enhanced colloidal stability and improved interfacial adhesion in nanocomposites. *Chem. Mater.* 18, 5111–5118. doi: 10.1021/cm061139x

Leite Ferreira, B. J. M., Barroca, N. B., Lopes, P. R., Daniel-da-Silva, A. L., Helena, M., and Correla, R. N. (2014). Properties of novel PMMA-Co-EHA bone cements filled with hydroxyapatite. *Polymers Polymer Composites* 35, 759–767. doi: 10.1002/pc

Li, S., and Chesnut, D. B. (1986). Intramolecular van Der Waals interactions and $^{13}C$ chemical shifts: substituent effects in some cyclic and bicyclic systems. *Magn. Resonance Chem.* 24, 93–100. doi: 10.1002/mrc.1260240202

Liu, F., Wang, R., Cheng, Y., Jiang, X., Zhang, Q., and Zhu, M. (2013). Polymer grafted hydroxyapatite whisker as a filler for dental composite resin with enhanced physical and mechanical properties. *Mater. Sci. Eng. C* 33, 4994–5000. doi: 10.1016/j.msec.2013.08.029

Liu, H., Jiang, W., and Malshe, A. (2009). Novel Nanostructured Hydroxyapatite Coating for Dental and Orthopedix Implants. *JOM* 61, 67–69. doi: 10.1007/s11837-009-0137-0

Liu, Q., Ding, J., Chambers, D. E., Debnath, S., Wunder, S. L., and Baran, G. R. (2001). Filler-coupling agent-matrix interactions *in silica*/polymethylmethacrylate composites. *J. Biomed. Mater. Res.* 57, 384–393. doi: 10.1002/1097-4636(20011205)57:3<384::AID-JBM1181>3.0.CO;2-F

Liyanage, D. D., Thamali, R. J. K. A., Kumbalatara, A. A. K., Weliwita, J. A., and Witharana, S. (2016). An analysis of nanoparticle settling times in liquids. *J. Nanomater.* 2016:7061838. doi: 10.1155/2016/7061838

Logtenberg, E. H. P., and Stein, H. N. (1986). Zeta potential and coagulation of ZnO in alcohols. *Colloids Surfaces* 17, 305–312. doi: 10.1016/0166-6622(86)80254-2

Lung, C. Y., Sarfraz, Z., Habib, A., Khan, A. S., and Matinlinna, J. P. (2016). Effect of silanization of hydroxyapatite fillers on physical and mechanical properties of a Bis-GMA based resin composite. *J. Mech. Behav. Biomed. Mater.* 54, 283–294. doi: 10.1016/j.jmbbm.2015.09.033

Mertz, G., Fouquet, T., Becker, C., Ziarelli, F., and Ruch, D. (2014). A methacrylic anhydride difunctional precursor to produce a hydrolysis-sensitive coating by aerosol-assisted atmospheric plasma process. *Plasma Processes Polymers* 11, 728–733. doi: 10.1002/ppap.201400050

Murugan, R., and Panduranga Rao, K. (2003). Grafting of glycidyl methacrylate upon coralline hydroxyapatite in conjugation with demineralized bone matrix using redox initiating system. *Macromol. Res.* 11, 14–18. doi: 10.1007/BF03218272

Murugan, R., and Ramakrishna, S. (2004). Coupling of therapeutic molecules onto surface modified coralline hydroxyapatite. *Biomaterials* 25, 3073–3080. doi: 10.1016/j.biomaterials.2003.09.089

Pieters, I. Y., Van den Vreken, N. M., Declercq, H. A., Cornelissen, M. J., and Verbeeck, R. M. (2010). Carbonated apatites obtained by the hydrolysis of monetite: influence of carbonate content on adhesion and proliferation of MC3T3-E1 osteoblastic cells. *Acta Biomater.* 6, 1561–1568. doi: 10.1016/j.actbio.2009.11.002

Poralan, G. M., Gambe, J. E., Alcantara, E. M., and Vequizo, R. M. (2015). X-ray diffraction and infrared spectroscopy analyses on the crystallinity of engineered biological hydroxyapatite for medical application. *IOP Conf. Ser. Mater. Sci. Eng.* 79:012028. doi: 10.1088/1757-899X/79/1/012028

Redey, S. A., Razzouk, S., Rey, C., Bernache-Assollant, D., Leroy, G., Nardin, M., et al. (1999). Osteoclast adhesion and activity on synthetic hydroxyapatite, carbonated hydroxyapatite, and natural calcium carbonate: relationship to surface energies. *J. Biomed. Mater. Res.* 45, 140–147. doi: 10.1002/(SICI)1097-4636(199905)45:2<140::AID-JBM9>3.0.CO;2-I

Reis, A. V., Reis, A. V., Rubira, A. F., and Muniz, E. C. (2009). Reaction of glycidyl methacrylate at the hydroxyl and carboxylic groups of poly(vinyl alcohol) and poly(acrylic acid): is this reaction mechanism still unclear? *J. Org. Chem.* 74, 3750–3757. doi: 10.1021/jo900033c

Roether, J. A., and Deb, S. (2004). The effect of surface treatment of hydroxyapatite on the properties of a bioactive bone cement. *J. Mater. Sci. Mater. Med.* 15, 413–418. doi: 10.1023/B:JMSM.0000021112.51065.40

Salopek, B., Krasic, D., and Filipovic, S. (1992). Measurement and application of zeta-potential. *Rudarsko-Geolosko-Naftni Zbornik* 4, 147–151.

Sarig, S. (2004). Aspartic acid nucleates the apatite crystallites of bone: a hypothesis. *Bone* 35, 108–113. doi: 10.1016/j.bone.2004.02.020

Temenoff, J. S., Shin, H., Conway, D. E., Engel, P. S., and Mikos, A. G. (2003). In vitro cytotoxicity of redox radical initiators for cross-linking of oligo(poly(ethylene glycol) fumarate) macromers. *Biomacromolecules* 4, 1605–1613. doi: 10.1021/bm030056w

Tkalčec, E., Popović, J., Orlić, S., Milardović, S., and Ivanković, H. (2014). Hydrothermal synthesis and thermal evolution of carbonate-fluorhydroxyapatite scaffold from cuttlefish bones. *Mater. Sci. Eng. C* 42, 578–586. doi: 10.1016/j.msec.2014.05.079

Valle, L. J., Bertran, O., Chaves, G., Revilla-López, G., Rivas, M., Casas, M. T., et al. (2014). DNA adsorbed on hydroxyapatite surfaces. *J. Mater. Chem. B* 2, 6953–6966. doi: 10.1039/c4tb01184h

Vaz, C. M., Reis, R. L., and Cunha, A. M. (2002). Use of coupling agents to enhance the interfacial interactions in starch-EVOH/hydroxylapatite composites. *Biomaterials* 23, 629–635. doi: 10.1016/S0142-9612(01)00150-8

White, B., Banerjee, S., O'Brien, S., Turro, N. J., and Herman, I. P. (2007). Zeta-potential measurements of surfactant-wrapped individual single-walled carbon nanotubes. *J. Phys. Chem. C* 111, 13684–13690. doi: 10.1021/jp070853e

Witharana, S., Hodges, C., Xu, D., Lai, X., and Ding, Y. (2012). Aggregation and settling in aqueous polydisperse alumina nanoparticle suspensions. *J. Nanoparticle Res.* 14, 1–19. doi: 10.1007/s11051-012-0851-3

Xie, X. L., Tang, C. Y., Zhou, X. P., Li, R. K. Y., Yu, Z. Z., Zhang, Q. X., et al. (2004). Enhanced interfacial adhesion between PPO and glass beads in composites by surface modification of glass beads via *in situ* polymerization and copolymerization. *Chem. Mater.* 16, 133–138. doi: 10.1021/cm034512z

Zou, Z., Liu, X., Chen, L., Lin, K., and Chang, J. (2012). Dental enamel-like hydroxyapatite transformed directly from monetite. *J. Mater. Chem.* 22:22637. doi: 10.1039/c2jm35430f

**Conflict of Interest:** The authors declare that the research was conducted in the absence of any commercial or financial relationships that could be construed as a potential conflict of interest.

frontiers in Bioengineering and Biotechnology

ORIGINAL RESEARCH
published: 08 November 2019
doi: 10.3389/fbioe.2019.00296

# Non-invasive Production of Multi-Compartmental Biodegradable Polymer Microneedles for Controlled Intradermal Drug Release of Labile Molecules

*Mario Battisti[1†], Raffaele Vecchione[1*†], Costantino Casale[2], Fabrizio A. Pennacchio[1], Vincenzo Lettera[3], Rezvan Jamaledin[1], Martina Profeta[1], Concetta Di Natale[1], Giorgia Imparato[1], Francesco Urciuolo[2,4] and Paolo Antonio Netti[1,2,4]*

[1] Center for Advanced Biomaterials for Health Care (CABHC), Istituto Italiano di Tecnologia, Naples, Italy, [2] Interdisciplinary Research Centre on Biomaterials (CRIB), University of Naples Federico II, Naples, Italy, [3] Biopox Srl, Naples, Italy, [4] Department of Chemical Materials and Industrial Production (DICMAPI), University of Naples Federico II, Naples, Italy

OPEN ACCESS

**Edited by:**
*Laura Maria Vergani, Politecnico di Milano, Italy*

**Reviewed by:**
*Jianxun Ding, Changchun Institute of Applied Chemistry (CAS), China*
*Piergiorgio Gentile, Newcastle University, United Kingdom*

***Correspondence:**
*Raffaele Vecchione*
*raffaele.vecchione@iit.it*

*[†]These authors have contributed equally to this work*

**Specialty section:**
*This article was submitted to Biomaterials, a section of the journal Frontiers in Bioengineering and Biotechnology*

**Received:** *02 July 2019*
**Accepted:** *14 October 2019*
**Published:** *08 November 2019*

**Citation:**
*Battisti M, Vecchione R, Casale C, Pennacchio FA, Lettera V, Jamaledin R, Profeta M, Di Natale C, Imparato G, Urciuolo F and Netti PA (2019) Non-invasive Production of Multi-Compartmental Biodegradable Polymer Microneedles for Controlled Intradermal Drug Release of Labile Molecules. Front. Bioeng. Biotechnol. 7:296. doi: 10.3389/fbioe.2019.00296*

Transdermal drug delivery represents an appealing alternative to conventional drug administration systems. In fact, due to their high patient compliance, the development of dissolvable and biodegradable polymer microneedles has recently attracted great attention. Although stamp-based procedures guarantee high tip resolution and reproducibility, they have long processing times, low levels of system engineering, are a source of possible contaminants, and thermo-sensitive drugs cannot be used in conjunction with them. In this work, a novel stamp-based microneedle fabrication method is proposed. It provides a rapid room-temperature production of multi-compartmental biodegradable polymeric microneedles for controlled intradermal drug release. Solvent casting was carried out for only a few minutes and produced a short dissolvable tip made of polyvinylpyrrolidone (PVP). The rest of the stamp was then filled with degradable poly(lactide-co-glycolide) (PLGA) microparticles (μPs) quickly compacted with a vapor-assisted plasticization. The outcome was an array of microneedles with tunable release. The ability of the resulting microneedles to indent was assessed using pig cadaver skin. Controlled intradermal delivery was demonstrated by loading both the tip and the body of the microneedles with model therapeutics; POXA1b laccase from *Pleurotus ostreatus* is a commercial enzyme used for the whitening of skin spots. The action and indentation of the enzyme-loaded microneedle action were assessed in an *in vitro* skin model and this highlighted their ability to control the kinetic release of the encapsulated compound.

**Keywords: polymer microneedles, multi-compartmental, enzyme, controlled release, skin model**

## INTRODUCTION

Transdermal drug delivery is an attractive alternative to parenteral administration. It bypasses the hepatic first-pass metabolism, preventing intestinal degradation and reducing systemic drug exposure (Kumar and Philip, 2007; Chu et al., 2010; Nguyen et al., 2018). However, classic transdermal delivery systems are severely limited by the inability of the vast majority of drugs

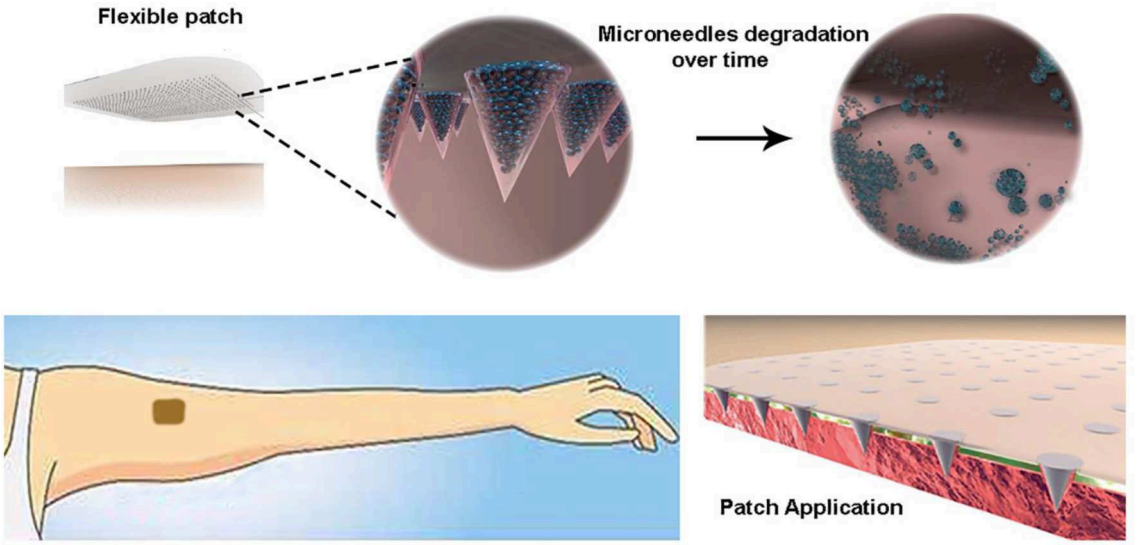


**GRAPHICAL ABSTRACT |** Highly controlled intradermal delivery can be performed with multi-compartmental polymer microneedles that are able to indent the skin and be implanted in it with a fast dissolving tip and a slow degradable body made of porous PLGA μPs.

to cross the skin barrier imposed by the stratum corneum, the outermost lipophilic layer of the skin (thickness of 10–30 μm), which only allows the transport of molecules of fewer than 400 Da (Schaefer et al., 1997, 2011; Naik et al., 2000; Bouwstra and Ponec, 2006).

Several techniques, such as microdermabrasion, laser ablation, radiofrequency, and thermal abrasion, are used to enhance skin permeability (Kumar and Philip, 2007). However, such techniques can seriously damage the skin, are painful for patients, and require both skin treatment and agent application.

These limitations can be overcome using needles of micrometer dimensions, namely microneedles, which penetrate the skin and then release their cargo (Bronaugh and Maibach, 1999; Joshi and Raje, 2002; Prausnitz et al., 2004). In fact, when inserted into the skin, they create microchannels that enable a broad range of therapeutic agents to be delivered, such as drugs, vaccines, enzymes, proteins, and peptides (Park et al., 2006; Jiang et al., 2007; Sullivan et al., 2010; Kim et al., 2012; Matsuo et al., 2012; Tsioris et al., 2012; Hiraishi et al., 2013; Edens et al., 2015a,b; Lee et al., 2015; Arya et al., 2016; Qiu et al., 2016; Ruggiero et al., 2018), without inducing serious skin damage, irritation, or infection (Nguyen and Banga, 2017). They are also painless because they do not stimulate the dermal nerves (Donnelly et al., 2010). Microneedle-based technology has also attracted the attention of the cosmetic industry for skin aging, acne, photodamage, and hyperpigmentation treatment (Preetha and Karthika, 2009).

One of the commonest and most reliable fabrication methods for polymeric microneedle preparation is the stamp-based technique (Raja et al., 2013; Yang et al., 2015). However, microneedles are commonly made of water-soluble materials, such as polymers and sugars, that will dissolve into the skin a few minutes after insertion (Park et al., 2005; Kim et al., 2012) or of biodegradable polymers that need to remain embedded in the skin for several days to promote a prolonged release (Park et al., 2006).

To overcome the long application times of the biodegradable polymers, Li et al. proposed a microneedle patch with rapidly separable biodegradable PLGA needles for the continuous release of a contraceptive hormone. The fabrication method consists of the casting step and the formation of a bubble at the base of the cone that rapidly separates the needles from the patch. Despite the interesting results obtained in terms of microneedle penetration in the skin, microneedle detachment from the patch, and therapeutic agent delivery, this method does not allow for a tunable drug release of the compounds over time (Li et al., 2019).

A spray-based method has recently been introduced to obtain controlled biphasic release (Park et al., 2019). Microneedles are detached from the stamp after overnight dehydration. A slow release from the biodegradable compartment is not easily tunable. Previously, to overcome the limitations related to controlling the delivery rate, a new approach had been proposed by Irvine (DeMuth et al., 2013) that combined poly(acrylic acid) (PAA), as a fast dissolvable polymer matrix, and PLGA μPs for sustained release. However, despite the clear improvements obtained, this method remains time consuming (at least 48 h). Apart from being expensive, long fabrication processes can promote the unloading of hydrophilic cargos from the μPs to the PAA matrix as well as the loss of moisture-sensitive drugs during the long drying step.

In order to overcome these drawbacks, we have developed a novel and fast stamp-based method for fabricating multi-compartmental polymeric microneedles with tunable drug delivery properties.

The first step in the production of microneedles was the fabrication of a master using a 2 photon polymerization (2PP)

technique that ensures a tip curvature radius smaller than 20 μm (Pennacchio et al., 2017, 2018). Then, after replicating PDMS stamps, multi-compartmental microneedles were fabricated. First, the cavities of the stamp were spin-coated with a hydrophilic polymer, the PVP, to obtain the fast-dissolvable tips, according to a recently proposed method (Vecchione et al., 2016). PVP is mechanically strong because of its chemical backbone, which contains rigid rings, and it has been widely used in the production of polymer microneedles (Lopérgolo et al., 2003). PVP is also water soluble, facilitating the rapid dissolution of the microneedles when inserted into the skin. Once dissolved in the body, PVP can be safely cleared within a few days (Kodaira et al., 2004). The cavities were then filled with porous PLGA μPs and assembled by a mild-softening method, creating the body of the microneedle, which is devoted to the prolonged release of the cargo. PLGA is one of the most successfully used biodegradable polymers approved by the Food and Drug Administration (FDA) and the European Medicine Agency (EMA) due to its biodegradability and biocompatibility (Bobo et al., 2016).

It is thus possible to fabricate multi-compartmental microneedles with tunable drug release properties that combine the fast release of the tip with the prolonged release of the cargo from the μPs as well as the possible co-delivery of two molecules.

Interestingly, the whole process is carried out at RT, thus allowing the encapsulation of thermo-sensitive molecules. We assessed the compliance of the method by monitoring the activity of an enzyme, namely POXA1b laccase from *Pleorutus ostreatus*, which was encapsulated both in the tip and the microparticles.

The performance of the microneedles was highlighted *in vitro* by assessing their indentation capacity in a pig cadaver skin model together with the enzyme diffusion and activity in an advanced *in vitro* human skin equivalent model.

# MATERIALS AND METHODS

## Materials

Poly (lactic-co-glycolic acid) 50:50 (PLGA RESOMER® RG 504H, 38,000–54,000 Dalton), was purchased from Boeringer Ingelheim. Polyvinylpyrrolidone (PVP 856568 Mw 55 KDa), Pluronic® F-68, dimethyl carbonate (DMC, D152927), dichloromethane (DCM) sodium acetate anhydrous, sulphorhodamine B (Rhod) (SulphoRh6G, S470899), fluorescein isothiocyanate isomer I (FITC), and 2,2′-azino-bis(3-ethylbenzothiazoline-6-sulfonic acid) diammonium salt (ABTS) were purchased from Sigma Aldrich. NOA 61 glue was purchased from Norland Optical Adhesive. Poly (dimethyl-siloxane) (PDMS) was provided by Sylgard® (184 Silicone Elastomer Kit, Dow Corning). Poly(methyl methacrylate) (PMMA) was purchased from GoodFellow. The medical tape came from 3 M. Pure recombinant POXA1b (rPOXA1b) laccase enzyme was provided by Biopox srl. IP-DIP negative tone photoresist was purchased from Nanoscribe GmbH. Bidistilled water was pretreated with a Milli-Q R Plus System (Millipore Corporation, Bedford, USA). The MPatch™ Mini Applicator was purchased from Micropoint Technologies Pte Ltd.

## Laccase-Atto 647 Conjugation

Laccase (Biopox, Naples, Italy) was covalently conjugated to Atto-647 NHs by ATTO-TEC GmbHprocedure (https://www.atto-tec.com/fileadmin/user_upload/Katalog_Flyer_Support/Procedures.pdf). To summarize, a solution of 2 mg/mL of the enzyme (Carbonate buffer, pH 8.5) was mixed with a 10-fold molar excess of reactive dye for 1 h at 25°C under magnetic stirring. Unbound dye was removed using a 5 kDa molecular weight cutoff Amicon Ultra-4 centrifuge filter. The correct enzyme-dye conjugation was validated by the UV-vis technique.

## Preparation of PLGA Microparticles

PLGA μPs were prepared by double emulsion solvent evaporation (De Alteriis et al., 2015). Briefly, the aqueous phase, composed of 100 μl of a 0.55 mg $ml^{-1}$ sulforhodamine B aqueous solution or 70 U of pure recombinant POXA1b water solution, was homogenized (Ultra-turrax, IKA T-25 ULTRA-TURRAX Digital High-Speed Homogenizer Systems) for 30 s at 15,000 rpm with 1 ml of a DCM solution composed of 83 mg $ml^{-1}$ of PLGA and 17 mg $ml^{-1}$ of Pluronic F68. The first emulsion was immediately poured into 10 ml of 2% (w/v) aqueous PVA solution and further homogenized for 1 min at 20,000 rpm. The second emulsion was immediately poured into 40 ml of water under mechanical stirring for 3 h at 450 rpm with a paddle stirrer for complete solvent diffusion and evaporation.

The same procedure was also used for Laccase-Atto647-loaded μPs. Briefly, a concentration of 8.4 μg/mL of protein was encapsulated, and, after washing, the microparticles were characterized by fluorescent microscopy (Olympus IX73P1F fluorescence microscope Tokyo, Japan) in order to evaluate the signal of the enzyme inside porous structures. Fluorescence images were acquired using an HCX IRAPO L 40×/0.95 water objective with a 633 nm laser as the excitation source. In order to maintain the enzyme activity, the laccase-loaded microparticles were entirely prepared under refrigeration on ice. The μPs suspension was then centrifuged three times for 10 min at 4°C and 10,000 rpm (AvantiTM J-25, Beckman, USA) for washing. Finally, μPs were lyophilized overnight (Heto PowerDry PL6000 Freeze Dryer, Thermo Electron Corp., USA; −50°C, 0.73 hPa).

## Morphological Characterization of the Microparticles

Microparticle morphology was investigated through a scanning electron microscope (SEM). SEM samples were prepared, depositing 50 μg of μPs on a cover slip mounted on a standard SEM pin stub. The samples were gold-sputtered (10 nm thickness) with a HR208 Cressington sputter coater and analyzed by FESEM ULTRA-PLUS (Zeiss) at 5 kV with the SE2 detector. μPs mean size was determined by static light scattering (Mastersizer 2000, Malvern Instruments, Malvern, UK) on a 0.4 mg $ml^{-1}$ μPs suspension in water.

## Laccase-Atto647 Entrapment Efficiency (%η) Within the μPs

The %η Laccase-Atto 647 μPs was measured by an extraction method as previously reported (Kirby et al., 2011). Briefly, 10 mg of Laccase-Atto647 μPs were incubated in a solution

of 50% dimethyl sulphoxide (DMSO)/0.5% Sodium dodecyl sulfate (SDS)/0.1 M Sodium hydroxide (NaOH) for 1 h, at 25°C. The final solution was then analyzed by fluorescence, using an EnSpire® Multimode Plate Reader and following the signal of Laccase-Atto647 at 663 nm. The content of the enzyme loaded was obtained using a titration curve of the free Laccase-Atto 647 conducted at the same time and under the same conditions (**Figure S1A**).

## Fabrication of Master and Flexible Support

The microcone master was fabricated by means of 2-photon polymerization (2PP) using the Nanoscribe Photonic Professional GT system (Nanoscribe GmbH). The Nanoscribe system uses a 780 nm Ti-Sapphire laser emitting ≈100 fs pulses at 80 MHz with a maximum power of 150 mW and equipped with a 63×, 1.4 NA oil immersion objective. The substrate was placed in a holder that fitted into a piezoelectric x/y/z stage. A galvo scanner determined the laser trajectories.

The master was fabricated by processing the IP-DIP negative tone photoresist (Nanoscribe GmbH). To speed up the process, a galvo stage was used, which is almost 100 times faster than the basic piezo mode setup. The basic master was fabricated with a conical shape and with a microneedle height of 600 μm and base diameter of 300 μm. To enhance the photoresist adhesion, an oxygen plasma treatment (1 min) was performed. A layer of IP-DIP was spin-coated onto the glass substrate (5,500 rpm for 30 s) and photo-polymerized by UV lamp exposure (16 mW/cm$^2$ for 4 h). A drop of photoresist was then dispensed onto the glass substrate and fabricated with the Nanoscribe to directly produce the microcone master.

The master produced by 2PP was put under a UV lamp (3 h) to induce microcone hardening before use. The master structure was then replicated by pouring a solution of liquid PDMS precursor and its curing agent (10:1 w/w) onto it. This was then put under vacuum to remove entrapped air bubbles and cured in an oven at 70°C for 1 h. After curing, the PDMS was peeled off and attached onto double-sided adhesive tape on a glass slide; then, NOA 60 was poured onto it and put under vacuum to remove the bubbles for about 1 h. NOA 60 is a clear, colorless, liquid photosensitive polymer that is cured when exposed to ultraviolet light in the wavelength range of 350–380 nm (www.norlandprod.com). The curing time depends on the thickness and on the energy of the ultraviolet light. In our case, the wavelength light was 365 nm and the optimized exposure time was 3 h. Finally, the PDMS negative stamp was removed and the NOA positive mold was obtained. The NOA positive mold was attached onto a petri dish or glass slide with double-sided adhesive tape. Finally, the PDMS precursor was poured onto the NOA positive mold, cured at 70°C for 1 h, and then peeled off from the NOA to obtain PDMS stamps. The master produced can thus be used many times without being damaged.

## Fabrication of the Microneedles

Microneedles tips were produced using the hydrophilic polymer PVP. Briefly, 200 μL of 25% (w/v) PVP aqueous solution was poured onto the PDMS stamp and then degassed and spin-coated (3,000 rpm, 1 min) (Laurell Technologies, WS-650-23NPP Spin Coater) to remove the excess. The PDMS stamp cavities were filled with the μPs with the aid of an optical stereomicroscope (Olympus, SZX16 double objective). For each stamp, several arrays of PMMA pillars were produced using a micromilling machine (CNC micromill, Minitech MiniMill 3/Pro, Minitech Machinery Corporation, Georgia, USA) to press the μPs into them. The μPs loaded in the stamps were then plasticized and induced with a solvent mixture made up of 4 ml of ethanol and 0.5 ml of DMC.

The temperature and the pressure were set at 25.3°C and 0.15 bar, respectively (Kodaira et al., 2004) while the time of exposure was 6 min. Microneedles were extracted from the stamps using a harvesting layer, produced as follows: the medical tape (3 M) was placed on a PMMA slice with the aid of double-sided adhesive tape and 200 μl of 25% (w/v) PVP aqueous solution was poured onto the adhesive medical tape (3 M) surface, dried out at 40°C for 2 h, and finally plasticized for 11 min under the previously reported conditions. The harvesting layer was then placed upon the stamp. After 3 h of drying at RT, the microneedles were extracted.

Depending on the type of analysis, FITC-loaded or enzyme-loaded microneedle tips were also produced by adding 0.1 mg ml$^{-1}$ of FITC or 70 U of enzyme into the 25% (w/v) PVP aqueous solution.

## Characterization of the Microneedles

### Optical Microscopy

After fabrication, the microneedles were analyzed by a stereomicroscope (Olympus, SZX16 double objective) to investigate the sharpness of the tips and the pattern distribution.

### Scanning Electron Microscopy

Microneedle morphology was investigated through a scanning electron microscope (SEM). SEM samples were prepared by attaching the microneedle patch onto a cover slip mounted on a standard SEM pin stub. The samples were gold-sputtered with a sputter coater (15 nm thickness) and analyzed by FESEM ULTRA-PLUS (Zeiss) at 10–20 kV with the SE2 detector.

### Fluorescent Microscopy

Fluorescent microscopy analyses were performed using FITC-loaded tips and Rhod-loaded μPs. Sample morphology was investigated using a confocal microscope (Leica Microsystems TCS SP5 II, Germany) with a 20× air objective. Images were acquired with a resolution of 1,024 × 1,024 pixels.

## Slicing of Microneedles and Microparticles

The internal morphological structure of both the microneedles and μPs was investigated according to a previously reported procedure (Kodaira et al., 2004). First, a 2 mm thickness PDMS base layer was produced and cured at 80°C for 30 min. After cooling, the microneedles or μPs were deposited on it and another 2 mm thickness PDMS layer was used to cover the microneedles and μPs. The PDMS was cured for 24 h, at RT, in order to preserve the state of the μPs and microneedles incorporated in it. Finally, the solid PDMS block was frozen in

liquid nitrogen (−196°C) and sectioned using a Leica CryoUltra Microtome EM-FC7-UC7. A total of five μm slices were deposited onto a 12 mm round glass cover slip for the confocal analysis and then mounted on a standard SEM pin stub for SEM imaging.

## Image Analysis of Microneedles and Microparticle Slices

To check the microstructure of the porous microneedles and μPs, sample slices were analyzed using a field emission SEM (FESEM ULTRA-PLUS, Zeiss). The samples were gold-sputtered with a sputter coater (15 nm thickness) and analyzed by SEM at 10 kV with the SE2 detector.

To investigate the distribution of the chromophores inside the microneedles, slices of fluorescent microneedles and μPs were then imaged by a confocal microscope (Leica Microsystems TCS SP5 II, Germany) with a 20× air objective. Images were acquired with a resolution of 1,024 × 1,024 pixels. A 3D reconstruction from the z-stack slices was made using LAS AF software.

## *In vitro* Release of Laccase-Atto647 From μPs Inside the Microneedles

Three patches of microneedles with Laccase-Atto647 μPs were suspended in 1.5 mL of phosphate buffered saline (PBS) pH 7.1 and incubated at 37°C under continuous stirring at 250 rpm. At different time periods (from 30 min to 24 h), 1 mL of PBS was removed and analyzed by fluorescence assay as previously reported. The patches were refreshed with the same amount of PBS. Calibration curves of free enzymes were prepared in PBS as previously described (**Figure S1B**).

## Microneedle Indentation Test in Cadaver Pig Skin

Microneedle arrays of 600 μm height were inserted into full thickness cadaver pig skin without the subcutaneous fat layer. The skin was shaved with depilatory cream and washed in a phosphate buffered saline (PBS) solution and placed on absorbent paper for a few minutes to eliminate excess water. Two different indentation tests were carried out with an MPatch™ applicator system. This applicator is engineered to apply microneedle patches effectively by ensuring a 100% penetration rate. The penetration speed and force are optimized to provide repeatable and reproducible results (www.micropoint-tech.com).

## Histological Analysis

The microneedle patch was removed after indentation and the skin was fixed in a solution of 10% neutral buffered formalin (Bio-Optica) for 24 h, dehydrated in an incremental series of ethanol (75, 85, 95, 100, and 100% again, each step performed for 30 min at RT), treated with two series of xylene (Sigma Aldrich) for 30 min, and then embedded in paraffin (Bio-Optica). Samples were then sectioned with a thickness of 3 μm and stained with hematoxylin and eosin (Bio-Optica), and finally the sections were mounted with Histomount Mounting Solution (INVITROGEN) on coverslips, and the morphological features of constructs were observed by optical microscope (BX53; Olympus).

## Enzyme Analysis

Laccase activity was determined by the ABTS oxidation method (Lettera et al., 2010). ABTS is oxidized by laccase to the most stable and preferred state of the cation radical. The concentration of the cation radical responsible for the intense blue-green color can be correlated to the enzyme activity and is read at 420 nm (Majcherczyk et al., 1998). The assay mixture contained 2 mM ABTS, 0.1 M sodium acetate (pH 3.0), and the enzymatic solution. In the case of enzymes encapsulated in μPs, 5 mg of μPs were dissolved in 200 μl of DMC for 1 min; then, 5 μl of DMC dissolved μPs solution were assayed in a final volume of 1 ml. Oxidation of ABTS was monitored by determining the increase in $A_{420}$ ($\varepsilon_{420}$, $3.6 \times 10^4\ M^{-1}{\cdot}cm^{-1}$). Absorbance was read at 420 nm in a spectrophotometer against a suitable blank. One unit was defined as the amount of laccase that oxidized 1 μmol of ABTS substrate per min.

## Comparison of Spatial Profile of the ABTS Oxidation Product Concentration at Different Time Points After Microneedle Array Indentation in the Full-Thickness Skin Model

Endogenous-Human Skin Equivalent (Endo-HSE) (Casale et al., 2016, 2018) was used as the assay platform to evaluate the diffusion profile of the oxidation product formed by the reaction of ABTS soaked in Endo-HSE with the Laccase encapsulated in the array of microneedles. Endo-HSE was soaked in the ABTS solution (11 mg/ml in sodium citrate) for 30 min at RT. In addition, Endo-HSE was kept on absorbent paper to remove excess solution and indented by microneedles in both configurations. Medical tape was used to maintain the microneedles and allow indentation. The medical tape was removed 1 min after the indention had been performed. The enzyme was loaded in the hydrophilic tip (configuration 1) or in the porous μPs (configuration 2), and its activity was assessed *in vitro*.

Observations of the epidermal side of Endo-HSE after indentation in both configurations were performed under a stereomicroscope. Images were recorded at different time points with the same magnification and in the same lightness conditions. The time sampling for each photo was 1, 30 min, 24, and 48 h after the indentation and medical tape removal. The images obtained were then analyzed using image analysis software (Image J®) to calculate the spatial profile of the ABTS oxidation product concentration at different time points. Briefly, each image was converted into 8-bit format and after the lookup table had been inverted. The diameter of the circular spatial profile of the ABTS oxidation product shown by the blue dark stain was subsequently measured three times. The intensity of the brightness pixel scale along the diffusion radius tracked for three time points were shown in the graphs. Three Endo-HSEs for each microneedle configuration were used for the diffusion tests. A total of five images for each sample (about eight microneedles per image) and for each time point were used for the analysis.

# RESULTS AND DISCUSSION

## Microparticles

PLGA μPs were chosen to produce the body of the multi-compartmental and biodegradable polymeric microneedles. The μPs were produced by means of double emulsion in order to obtain porous microstructures that ensure the encapsulation of hydrophilic molecules and show a kinetic degradation for extended release over time. Microparticle morphology was assessed using SEM microscopy. The images show that μPs have a homogeneous and spherical shape (**Figure 1A**) as well as a porous surface (**Figure 1B**). Particle size was analyzed with a Malvern mastersizer. The data show that microparticles have a narrow size distribution with a slightly higher mean diameter in the case of enzyme encapsulated μPs (from ∼8 to 10 μm) (**Figures 1C,D**).

## Master and Stamp

The microcones of the master were individually prepared in a serial production by 2PP onto a glass substrate. In order to improve the material-substrate adhesion of the microcones, the substrate was first treated with oxygen plasma and then a thin layer of photoresist was spin coated and cured on it. Finally, another layer of uncured photoresist was dispensed and processed by 2PP according to the defined 3D layout. In order to optimize the master fabrication time, only the external shell of the microcones was photopolymerized by 2PP, whereas their body was one-shot cured under a UV lamp.

A master of the microcones was produced with 300 μm base diameter and 600 μm height extended onto an area of 1 $cm^2$. A maximum density of 256 microneedles *per* $cm^2$ was chosen in order to avoid any "bend-of-nails" effect. In fact, if the tips bend when designing arrays of microneedles, this has a negative impact on the microneedles' ability to penetrate the skin as the insertion force would be distributed among too many microneedles so that none would be able to penetrate the skin (Yan et al., 2010).

Because of the fragility of the master material, the polydimethylsiloxane (PDMS) stamp was not used directly. In fact, in order to avoid master breakage, a less fragile master was fabricated using Norland Optical Adhesive (NOA) 60. Therefore, starting from the original positive master, a negative PDMS stamp was replicated on it first and then a positive replica was obtained using NOA. This stamp was then used as a final master, according to the procedure reported in the Materials and Methods section.

Optical images of the master produced by 2PP, the PDMS replica, the NOA master, and the final PDMS stamp are shown in **Figure 2**. The high quality of the PDMS stamps, achieved through replication from the starting master and from the NOA master, is highlighted in **Figures 2C,E**, which show sections of the tips belonging to the PDMS stamps.

## The Fabrication of Multi-Compartmental Polymeric Microneedles

The initial stage of the fabrication of the multi-compartmental microneedles consisted of pouring an aqueous PVP solution onto the PDMS stamp, which was then degassed and spin coated in order to spread out the excess solution from the stamp and allow a rapid evaporation of the residual solvent. The tips of the microneedles were thus produced (**Figure 3A**). Depending on the experimental needs, FITC- or enzyme-loaded tips were produced. PVP was chosen as the structural material for the fabrication of the microneedle tips because of its processability in an aqueous environment and at RT. These process conditions facilitate the encapsulation of several drugs, which are known to

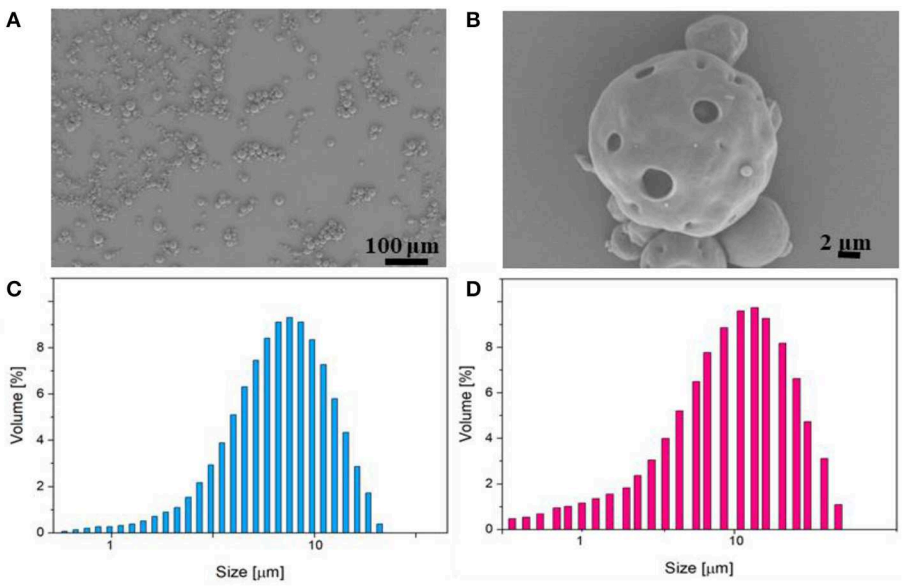


**FIGURE 1 | (A,B)** SEM images of enzyme-loaded μPs at different magnifications. Particle size distribution analysis of PLGA μPs performed by Mastersizer 3000. **(C)** Sulphorhodamine-loaded μPs. **(D)** Laccase-loaded μPs.

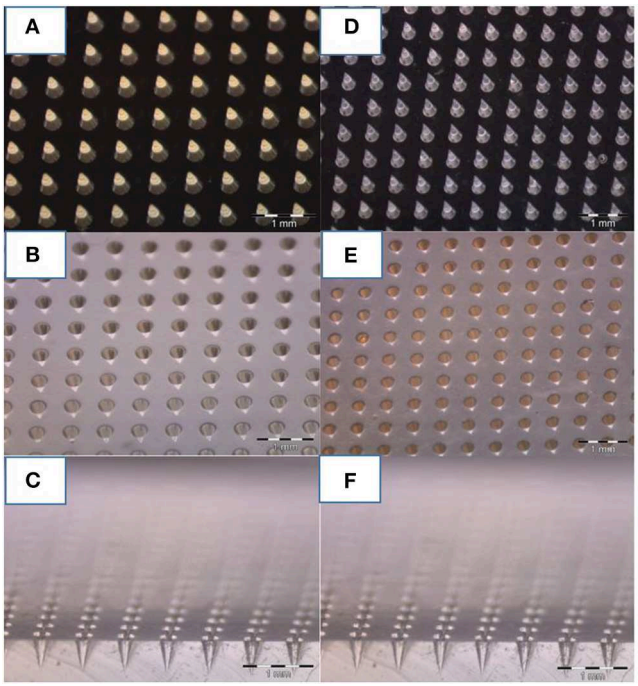


**FIGURE 2 |** Optical image of microneedles molded at various steps. **(A)** Master of 600 um of height and 300 um of bases of microneedles fabricated by 2PP, **(B)** PDMS stamp replicated on the master, and **(C)** cross-section of the PDMS mold. **(D)** NOA master replicated on the PDMS stamp, and **(E)** final PDMS stamp replicated on it **(F)** including a cross-section. A comparison of photos **(C,F)** reveal how, despite the various stages of replication, the needles keep tips with the same curvature radius.

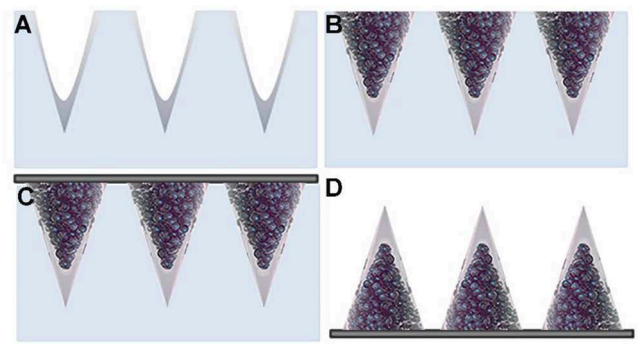


**FIGURE 3 |** Schematic view of the multi-compartmental microneedle array. PDMS stamp with **(A)** PVP deposited by spin coating and with **(B)** PLGA μPs compacted and sintered. **(C)** Application of the harvesting layer on the stamp. **(D)** Microneedle array extracted from the stamp.

be often denaturized by the interaction with an organic solvent and/or by the presence of high temperatures. Subsequently, stamp cavities were filled with PLGA μPs according to the procedure reported in the experimental section.

The stamp was then exposed to a solvent/non-solvent vapor mixture in order to carry out a mild plasticization for assembling; the μPs thus create the body of the microneedles while keeping the microstructure of the starting μPs (**Figure 3B**). This mild softening method (i.e., at room temperature using a solvent/non-solvent vapor mixture) was developed in one of our previous works for the mild deformation of single μPs located in the cavities of a PDMS stamp (Kodaira et al., 2004). Here, this patented method was applied for the first time to multiple μPs in order to promote their assembly by gentle sintering within the cavities of the stamp. Sharp microneedles were thus produced without needing to use the strong plasticization of single μPs (Kodaira et al., 2004). This approach preserves not only the internal microstructure of the μPs, but also the properties of the encapsulated drug, also allowing the use of thermo-labile cargo.

Finally, polymer microneedles were extracted from the stamp with the aid of a 3 M medical tape coated with PVP according to the procedure reported in the experimental section (**Figure 3C**). **Figure 3D** shows the double compartment microneedles peeled off from the PDMS stamp.

To the best of our knowledge, the most similar procedure reported for the fabrication of biodegradable microneedles is the one published by Irvine et al., who manufactured arrays of microneedles composed of drug-loaded PLGA μPs with a supporting and rapidly water-soluble PAA matrix (Park et al., 2019). The main limitation to this method is the assembly procedure. In fact, the dehydration of the matrix takes 48 h, which, apart from being a time-consuming and expensive step, can lead to the unloading of hydrophilic cargo from the μPs and its consequent diffusion into the external polymer matrix. Moreover, sensitive drugs may lose their activity because of the surrounding moisture.

On the other hand, a key advantage of our method is that it allows the polymer solution to dehydrate in just a few minutes. In addition, it is possible to work with particle sizes of up to 10 μm with a wider realm of possible porosities and therefore higher tunability of the kinetic release.

In the present work, the multi-compartmental feature of the proposed microneedles was obtained with a rapid protocol that provides a tip made of a hydrophilic polymer, namely PVP, and a body made of porous PLGA μPs, both embedding the enzyme. This facilitates the rapid release of the enzyme from the tips, followed by a prolonged release promoted by the μPs. The need for a combined release from multi-compartmental microneedles has also recently been addressed with a combination of PVP and PLGA deposited by spray coating (Park et al., 2019). In this case, the time to detach the microneedles from the stamp is <48 h but it still requires overnight dehydration. In addition, the biodegradable PLGA matrix is deposited by spray coating so the microstructure is not easy to tune, nor is the kinetic release from this compartment. Conversely, porous PLGA μPs can be provided with several microstructures that can promote a huge variety of kinetic releases.

## Morphological Microneedle Characterization

The morphological features of the microneedles were investigated by using optical, scanning electron, and confocal microscopy (**Figure 4**).

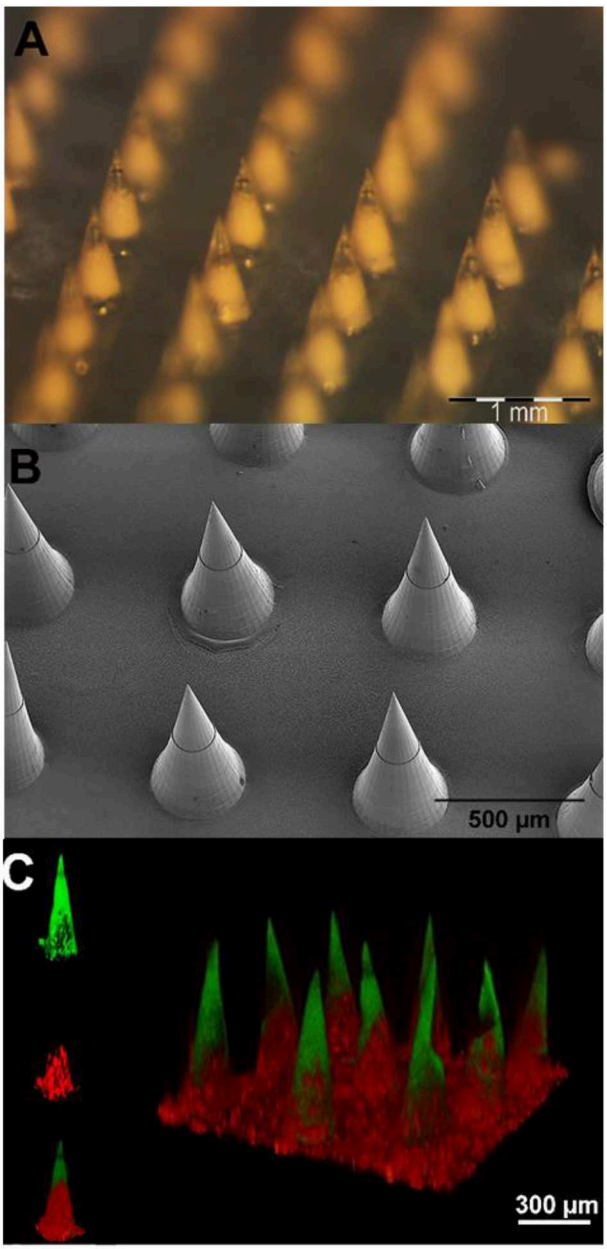


**FIGURE 4 | (A)** Stereomicroscope micrographs of microparticle-loaded microneedle patches. **(B)** Scanning electron microscopy images of microneedle arrays. **(C)** 3D confocal reconstruction of a microneedle array. The FITC loaded tips are shown in green, while the sulphorhodamine B loaded PLGA µPs are in red.

### Optical Microscopy

An optical stereomicroscope was employed to visualize the array and tips of the microneedles. The image shows (**Figure 4A**) a whole array of uniformly distributed 600 µm height microneedles with sharp tips.

### Scanning Electron Microscopy

SEM imaging was used to visualize the morphology of freshly fabricated 600 µm height microneedles. The image (**Figure 4B**) shows that the final multi-compartmental microneedles clearly reflect the stamp cavity architecture with fine and sharp tips. The base diameter and the height of the microcones are 300 and 600 µm, respectively, in agreement with the design parameters.

### Fluorescent Microscopy

Fluorescent imaging analyses were performed by means of confocal microscopy. The aim was to characterize the multi-compartmental structure of the microneedles using two different hydrophilic chromophores as reported in **Figure 4C**. The polymeric matrix was loaded with FITC, while the pores of the µPs were loaded with sulphorhodamine B. The 3D reconstructed image clearly shows that the PVP compartment (loaded with FITC) is located at the tip of the microneedles. On the other hand, as expected, the µPs (loaded with sulphorhodamine B) are located in the body of the microneedles.

## Image Analysis of Microneedles and Microparticle Slices

Morphological analyses were performed using a field emission SEM on porous microneedles and µPs slices. Images of both multi-compartmental microneedles and µPs were acquired. **Figure 5** shows that a similar porosity distribution can be observed on both samples, demonstrating that the microneedle production process does not significantly affect µPs morphology. This evidence suggests that in principle it is possible to import and exploit the extensive background of the PLGA µPs in terms of encapsulation and control of the kinetic release of the microneedles.

## *In vitro* Penetration Studies

It is fundamental that microneedles are able to pierce the stratum corneum of the skin. To assess this aspect, an MPatch™ applicator system (see Materials and Methods), which is recommended for performing reproducible indentations, was used. Pig cadaver skin was used as a model for the indentation test, and a patch of microneedles as previously described was applied to it for 5 min. The effectiveness of the indentation was confirmed by the cross section of indented skin stained with H/E (**Figure 6**, upper line). In addition, the optical image also shows the microneedles in the skin upon indentation and medical tape removal (**Figure 6**, bottom line).

The H/E images clearly show that the microneedles reached the dermis, thus confirming the potential use for drug delivery. In fact, they penetrated all the layers of the epithelium and part of the papillary dermis.

## Enzyme Encapsulation in Microneedles

The encapsulation of catalyzers in biodegradable polymeric microneedles is a simple and effective method to deliver enzymes into human skin for dermatology and cosmetic treatments (Haj-Ahmad et al., 2015; Pezzella et al., 2017). The cosmetic sector is interested in enzymes that enhance the beauty of the skin or help the skin to defend itself against the ravages of the environment. However, since creams are not effective in the delivery of compounds with high molecular weight, molecules, such as

proteins and invasive injection systems are typically used for enzyme dosage. Painless biodegradable polymeric microneedles therefore represent a promising tool.

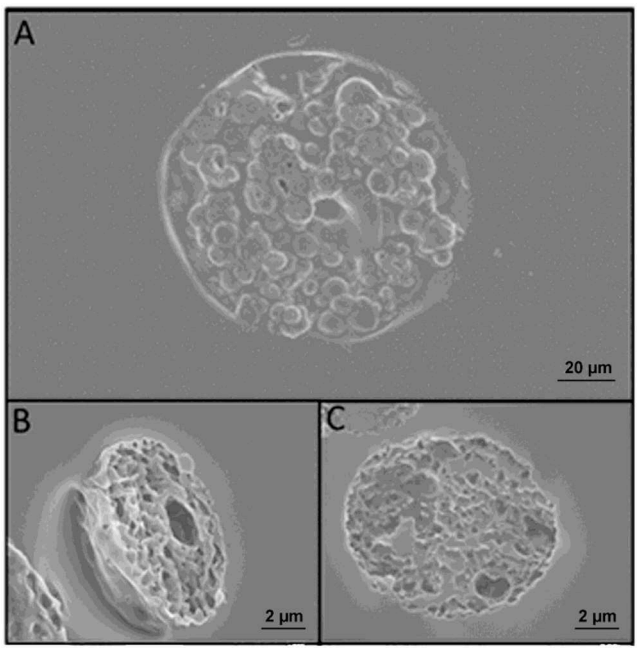


**FIGURE 5 | (A)** SEM images of microneedles slices obtained with cryosectioning. **(B)** Slice of a microparticle contained in the microneedle after sintering. **(C)** Slice of a microparticle just prepared. A comparison of **(B,C)** reveals that sintering does not change the morphology of the microparticles.

In the present work, we loaded polymeric and multi-compartmental microneedles with recombinant laccase POXA1b belonging to the edible fungus Pleurotus ostreatus as a model enzyme (Pezzella et al., 2013, 2017). Laccases are an interesting group of multi copper enzymes, which have received much attention in several biotechnological processes (Lettera et al., 2016; Patel et al., 2019).

In order to evaluate the content of the enzyme encapsulated in µPs and its release in physiological conditions, we conjugated a dye (Atto647) to the Lysine side chain in the protein, as reported in the Materials and Methods. The correct conjugation was evaluated by UV, monitoring the presence of two shoulders at 600 and 643 nm that are typical of the dye and the signal at 280 nm related to the protein (**Figure 7A**). We obtained a perfect degree of loading (DOL) equivalent to 2. Thereafter, we showed, using a fluorescence technique, that this formulation was able to encapsulate a high content of protein equal to 77.5% ± 3.5. This data was in ageemento with fluorescence imaging (**Figure 7B**) which highlighted a high fluorescent enzyme signal. Thanks to the fluorescence assays we were able to calculate that µPs from microneedles released 43.1% ± 6.2 of the laccase over 24 h. This result means the microparticles did not lose their morphological structure after plasticization and were thus still able to release the drug in a time frame of hours (**Figure 8**).

A laccase activity assay was used to monitor the presence and the preservation of laccase encapsulated in the PLGA µPs pores. A solution of ABTS and buffer was added onto the µPs slices in order to verify the enzyme activity. **Figures 9A,B** show the differences between the enzyme-loaded µPs slices in the presence and absence of ABTS, respectively. The ABTS solution highlights the enzyme activity, and the activity of the enzyme inside the

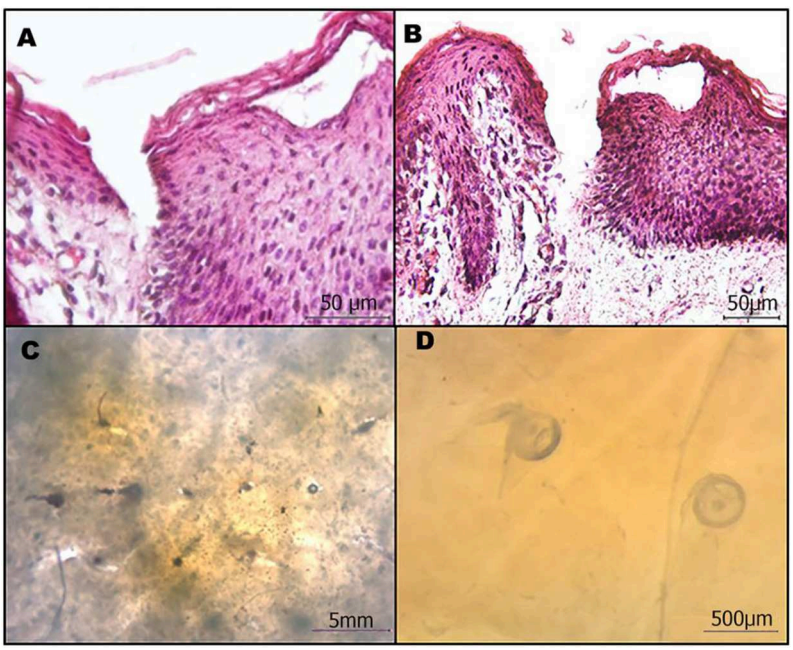


**FIGURE 6 |** Microneedle patches efficiently penetrate the skin. **(A,B)** Cross-sectional images of the H/E stained skin after microneedle removal. **(C,D)** Stereomicroscope image of microneedles in the skin.

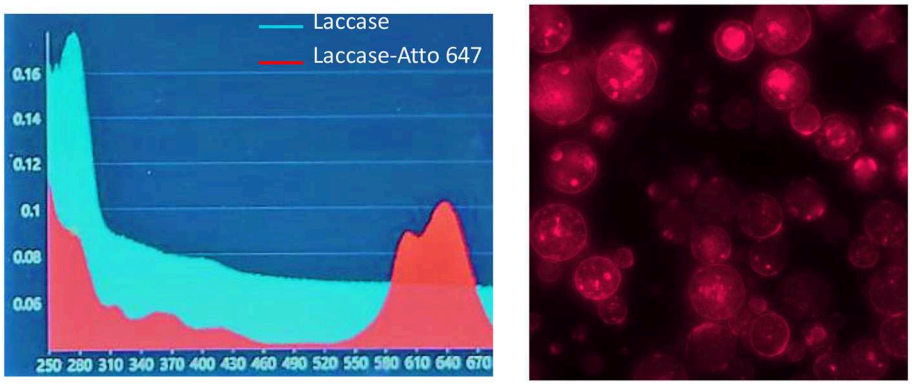


**FIGURE 7 |** Laccase-Atto 647 μPs. **(A)** UV spectrum of Laccase (light blue line) and Laccase Atto647 (red line). **(B)** Fluorescence image of Laccase-Atto647 μPs.

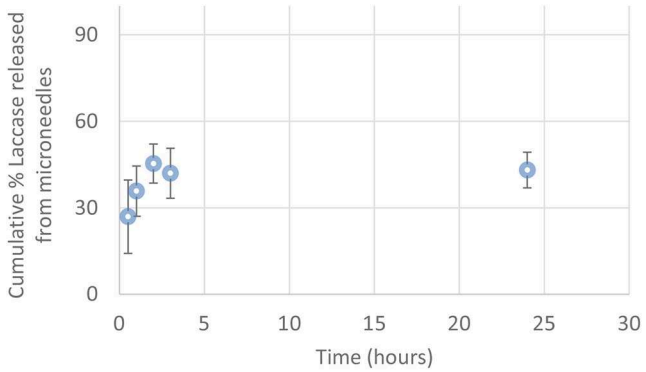


**FIGURE 8 |** Cumulative percentage of Laccase-Atto647 released from μPs in the microneedles (0.5–24 h) ($n = 3$).

μPs was confirmed by the presence of a green color located in the μPs pores due to the ABTS oxidation from the encapsulated enzyme itself. The activity of Laccase μPs was monitored for up to 14 days after production and after a slow reduction, registered in the first day, it was stable over time (**Figure 9C**).

## Enzyme Release and Activity in Skin Models

To check the enzyme activity, a preliminary test was performed on a 3 mm gelatin B substrate embedding the ABTS substrate. The results confirmed the activity of the encapsulated enzyme as reported in **Figure S2**.

Microneedles are designed to guarantee the reproducible transdermal indentation as well as the controlled and functional release of the encapsulated substance. To assess the microneedles' ability to satisfy such requirements, a human skin equivalent (Endo-HSE) was used as assay platform. Endo-HES is a functional and histological competent tissue that captures several fundamental features of the native human skin (Casale et al., 2016, 2018). In addition, in contrast to the use of pig skin, Endo-HSE is of human origin and can reproduce the sample's thickness

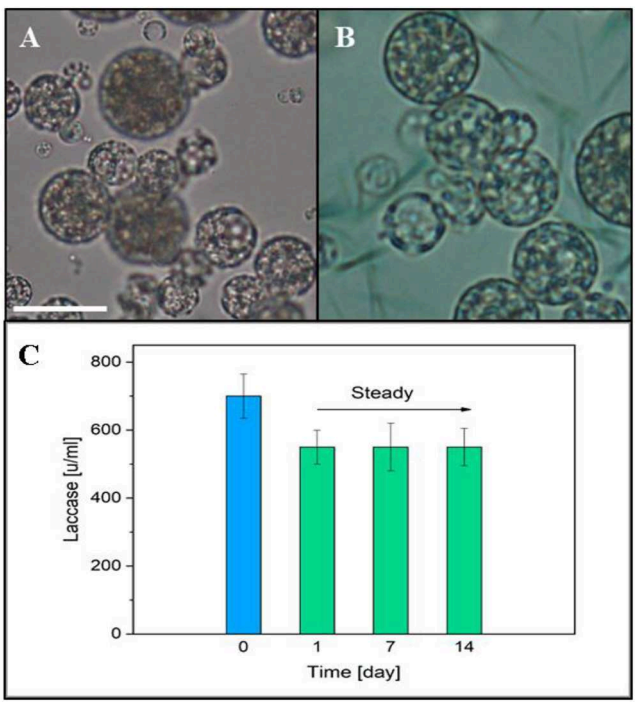


**FIGURE 9 | (A)** Optical image of μPs slice. **(B)** Optical μPs slice with a solution of ABTS and buffer. Scale bar 10 μm. **(C)** Laccase activity in μPs up to 14 days after the production. The blue column represents the initial enzyme activity used for μPs preparation.

as well as ECM compactness, thus avoiding the variability correlated to the age and region of the animal. Moreover, compared with other full thickness human skin models (Bellas et al., 2012; Carriel et al., 2012) that are formed with exogenous biopolymers, such as collagen and/or elastin, Endo-HSE is completely scaffold-free possessing a 1-mm thick dermis that is continuously assembled and remodeled by fibroblasts. The presence of such living and endogenous dermis may represent the best *in vitro* condition to perform transdermal transport

studies. Histological images of Endo-HSE cross sections after the indentation highlighted that the microneedles were able to penetrate Endo-HSE, going through the epidermis and reaching a depth of ∼250 μm for both microneedle configurations (**Figures 10A,D**).

The stereomicroscope images revealed the pattern of the microneedles' array and the ability of the enzyme loaded in each microneedle to react with the ABTS substrate. In fact, the ABTS oxidation product was blue and was detected easily. In the case of microneedle configuration 1, the ABTS oxidation occurred in a very short time since the enzyme loaded in the microneedle tip was rapidly available. In the case of microneedle configuration 2, the observation time was several hours because the laccase diffusion occurred upon μPs biodegradation.

**Figures 10C,F** plot the pixel intensity along the diffusion radius of the ABTS oxidation product for three time points. For configuration 1, diffusion began after 1 min and its radius was centered with the microneedle pattern for at least the first half hour, increasing for longer times as shown at 48 h. At 48 h, we observed an inversion of the bell apex indicating that no more enzymes were present in the microneedles, and, as a consequence, the ABTS oxidation product (dark pixels) was no longer present. The inversion of the bell apex was due to the accumulation of the ABTS oxidation product around the body of the microneedles (made of microparticles), which is located in the center of the pattern.

In configuration 2, the reaction product diffused more slowly than in configuration 1, and the concentration profile was flat at $t_0$. The PLGA μPs adsorbed the ABTS, which reacts inside the microneedles with the active enzyme, as reported at 24 h in **Figure 10F**. At 48 h, we still observed an intense staining in relation to the indented region very close to the walls of the microneedles (**Figure 10F**) due to the localization and preservation of the enzyme within μPs and its slow release from μPs.

We stopped observations at 48 h because the ABTS soaked in the Endo-HSE was by then oxidized by the air present in the atmosphere thereby making the sample completely dark.

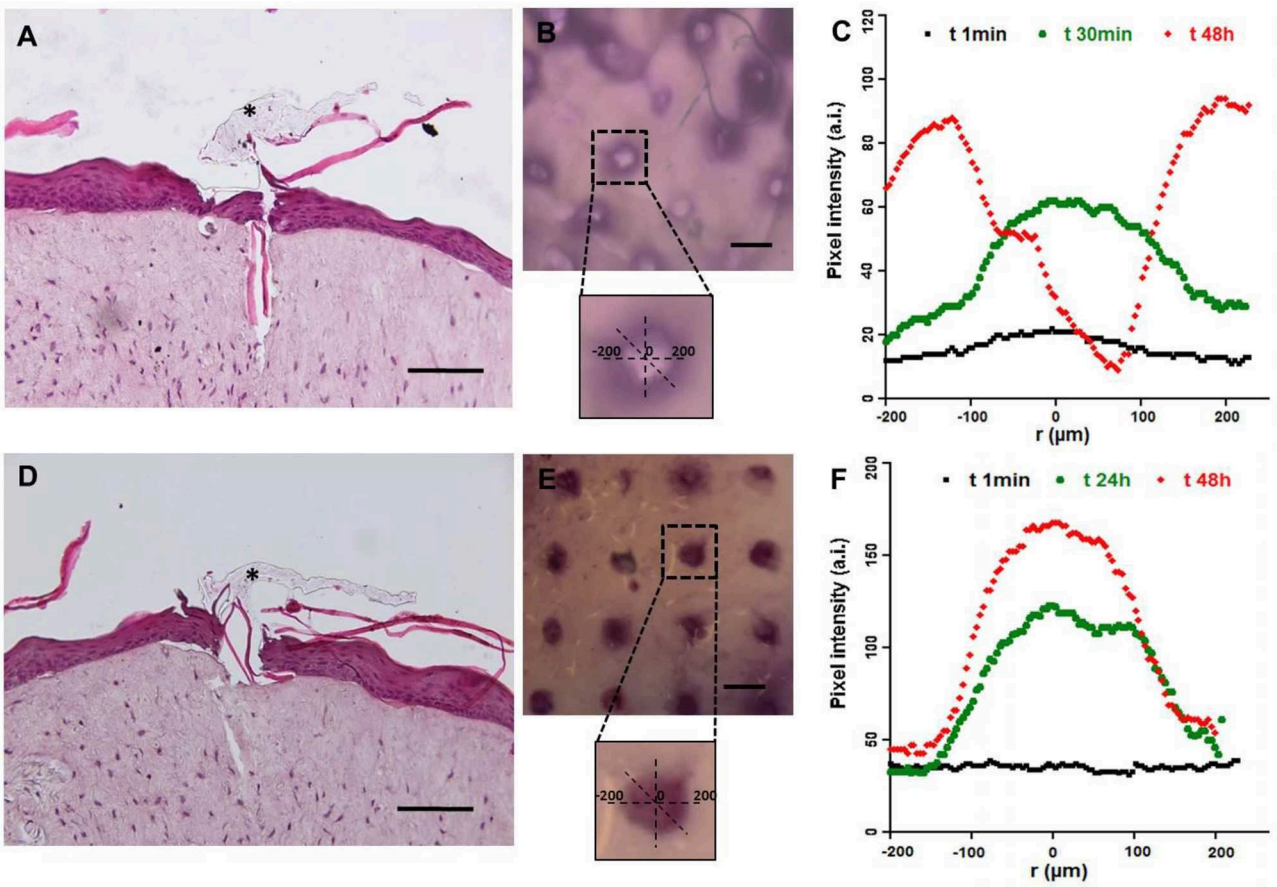


**FIGURE 10 |** Functional test of microneedles for transdermal delivery of high molecular weight substances in a full-thickness human skin model. The pictures in **(A–C)** refer to microneedle configuration 1, while **(D–F)** refer to configuration 2. **(A,D)** Histological images of Endo-HSE 48 h after microneedle indentation to highlight the transdermal penetration; black asterisks indicate the PVP polymer remaining after medical tape removal (scale bar = 100 μm). **(B,E)** Stereomicroscopic images of Endo-HSE 48 h after indentation (scale bar = 500 μm). The inserts of the stereomicroscopic images are the schematic representation of the methods used to calculate the diffusive radius. **(C,F)** The graphs plot the pixel intensity at three time points correlated to the concentration of the ABTS oxidation product diffusing into ECM vs. the radius of the diffusion pattern.

In conclusion, the experimental results showed that the activity of the enzyme was preserved after microneedle production in both encapsulation procedures. In addition, we demonstrated the more rapid diffusion of the encapsulated enzyme in configuration 1 compared to configuration 2 (**Figures 10B,C,E,F**). The release of the ABTS oxidation product through PLGA μPs occurred by means of a combined diffusion-degradation mechanism, which led to the prolonged release in the ECM. In fact, in configuration 2, the diffusion-controlled systems based on slow-biodegradable polymers were designed for the controlled release of the encapsulated substance. By encapsulating the enzyme in both compartments, therefore, we can combine a fast release with a prolonged release depending on the type of application required.

## CONCLUSIONS

In this work we have presented a novel, fast, and stamp-based procedure for the fabrication of microneedles.

First, the master production process was optimized by using a 2PP technique. In addition, the procedure to fabricate the microneedles was designed with an RT procedure that allows the use of thermo-sensitive biomolecules, such as laccase.

The tips of the microneedles are made of a biodegradable and biocompatible polymer, such as PVP, and the bodies of the microcones are made up of mild sintered PLGA microparticles. Both compartments can entrap therapeutic agents, leading to the production of a biodegradable, biocompatible and multi-compartmental system. The multi-compartmental feature enables the co-delivery of two molecules, along with a rapid and prolonged release of the cargo. This release was confirmed by the diffusion test. In fact, when the enzyme was incorporated into the hydrophilic matrix, there was an instantaneous release of the cargo, but when the enzyme was incorporated into the μPs, it was released over a prolonged period.

This method preserved the porous microstructure of the μPs, as testified by the morphological characterizations carried out, and the prolonged release of the cargo can be tuned by engineering the properties of the initial μPs.

In addition, due to the thin interconnecting layer between microneedles they can be integrated onto a flexible patch keeping the flexibility of the entire patch to improve the conformal contact with the skin and to facilitate the implantation of the microneedles upon indentation, as revealed during our *in vitro* tests.

The overall fabrication procedure is faster compared to other stamp-based techniques, this is fundamental for the possible future marketing of such a tool.

## DATA AVAILABILITY STATEMENT

All datasets generated for this study are included in the article/**Supplementary Material**.

## AUTHOR CONTRIBUTIONS

RV and MB conceived the experiments and the plasticizing setup, analyzed the main results. MB optimized the experimental protocol for the production of microneedles. RJ provided help in microneedles and microparticles preparation and bted to the layout of the images and TOC. MP contributed to the activity tests. CD carried out the Laccase-Atto 647 conjugation, enzyme encapsulation in PLGA microparticles together with morphological analysis and release tests. CC, GI, and FU contributed to the design and realization of the *in vitro* skin model. CC performed the characterization of the indentation tests. VL provided the enzyme and contributed to the activity tests. MB, RV, MP, and FP wrote the main manuscript text. PN provided the theoretical support and reviewed the manuscript.

## ACKNOWLEDGMENTS

The authors would like to thank Dr. Valentina Mollo for her support in the Cryo-sectioning and SEM imaging and Dr. Fabio Formiggini for his support in confocal imaging. We thank Antonelli Carmela of ASL Napoli 2 Nord for providing pig skin taken from the butchery implant ICS-Industria Carni Sud- of Caivano, Naples, IT.

## SUPPLEMENTARY MATERIAL

The Supplementary Material for this article can be found online at: https://www.frontiersin.org/articles/10.3389/fbioe.2019.00296/full#supplementary-material

## REFERENCES

Arya, J. M., Dewitt, K., Scott-Garrard, M., Chiang, Y.-W., and Prausnitz, M. R. (2016). Rabies vaccination in dogs using a dissolving microneedle patch. *J. Control. Release* 239, 19–26. doi: 10.1016/j.jconrel.2016.08.012

Bellas, E., Seiberg, M., Garlick, J., and Kaplan, D. L. (2012). *In vitro* 3D full-thickness skin-equivalent tissue model using silk and collagen biomaterials. *Macromol. Biosci.* 12, 1627–1636. doi: 10.1002/mabi.201200262

Bobo, D., Robinson, K. J., Islam, J., Thurecht, K. J., and Corrie, S. R. (2016). Nanoparticle-based medicines: a review of FDA-approved materials and clinical trials to date. *Pharm. Res.* 33, 2373–2387. doi: 10.1007/s11095-016-1958-5

Bouwstra, J. A., and Ponec, M. (2006). The skin barrier in healthy and diseased state. *Biochim. Biophys. Acta* 1758, 2080–2095. doi: 10.1016/j.bbamem.2006.06.021

Bronaugh, R., and Maibach, H. (1999). Percutaneous absorption drug-cosmetics-mechanism-methodology. *J. Appl. Cosmetol.* 17, 116–119.

Carriel, V., Garzón, I., Jiménez, J. M., Oliveira, A. C., Arias-Santiago, S., Campos, A., et al. (2012). Epithelial and stromal developmental patterns in a novel substitute of the human skin generated with fibrin-agarose biomaterials. *Cells Tissues Organs* 196, 1–12. doi: 10.1159/000330682

Casale, C., Imparato, G., Urciuolo, F., and Netti, P. A. (2016). Endogenous human skin equivalent promotes *in vitro* morphogenesis of follicle-like structures. *Biomaterials* 101, 86–95. doi: 10.1016/j.biomaterials.2016.05.047

Casale, C., Imparato, G., Urciuolo, F., Rescigno, F., Scamardella, S., Escolino, M., et al. (2018). Engineering a human skin equivalent to study dermis remodelling and epidermis senescence *in vitro* after UVA exposure. *J. Tissue Eng. Regen. Med.* 12, 1658–1669. doi: 10.1002/term.2693

Chu, L. Y., Choi, S.-O., and Prausnitz, M. R. (2010). Fabrication of dissolving polymer microneedles for controlled drug encapsulation and delivery: bubble and pedestal microneedle designs. *J. Pharm. Sci.* 99, 4228–4238. doi: 10.1002/jps.22140

De Alteriis, R., Vecchione, R., Attanasio, C., De Gregorio, M., Porzio, M., Battista, E., et al. (2015). A method to tune the shape of protein-encapsulated polymeric microspheres. *Sci. Rep.* 5:12634. doi: 10.1038/srep12634

DeMuth, P. C., Garcia-Beltran, W. F., Ai-Ling, M. L., Hammond, T., and Irvine, D. J. (2013). Composite dissolving microneedles for coordinated control of antigen and adjuvant delivery kinetics in transcutaneous vaccination. *Adv. Funct. Mater.* 23, 161–172. doi: 10.1002/adfm.201201512

Donnelly, R. F., Garland, M. J., Morrow, D. I., Migalska, K., Singh, T. R. R., Majithiya, R., et al. (2010). Optical coherence tomography is a valuable tool in the study of the effects of microneedle geometry on skin penetration characteristics and in-skin dissolution. *J. Control. Release* 147, 333–341. doi: 10.1016/j.jconrel.2010.08.008

Edens, C., Collins, M. L., Goodson, J. L., Rota, A., and Prausnitz, M. R. (2015a). A microneedle patch containing measles vaccine is immunogenic in non-human primates. *Vaccine* 33, 4712–4718. doi: 10.1016/j.vaccine.2015.02.074

Edens, C., Dybdahl-Sissoko, N. C., Weldon, W. C., Oberste, M. S., and Prausnitz, M. R. (2015b). Inactivated polio vaccination using a microneedle patch is immunogenic in the rhesus macaque. *Vaccine* 33, 4683–4690. doi: 10.1016/j.vaccine.2015.01.089

Haj-Ahmad, R., Khan, H., Arshad, M., Rasekh, M., Hussain, A., Walsh, S., et al. (2015). Microneedle coating techniques for transdermal drug delivery. *Pharmaceutics* 7, 486–502. doi: 10.3390/pharmaceutics7040486

Hiraishi, Y., Nakagawa, T., Quan, Y.-S., Kamiyama, F., Hirobe, S., Okada, N., et al. (2013). Performance and characteristics evaluation of a sodium hyaluronate-based microneedle patch for a transcutaneous drug delivery system. *Int. J. Pharm.* 441, 570–579. doi: 10.1016/j.ijpharm.2012.10.042

Jiang, J., Gill, H. S., Ghate, D., McCarey, B. E., Patel, S. R., Edelhauser, H. F., et al. (2007). Coated microneedles for drug delivery to the eye. *Invest. Ophthalmol. Vis. Sci.* 48, 4038–4043. doi: 10.1167/iovs.07-0066

Joshi, A., and Raje, J. (2002). Sonicated transdermal drug transport. *J. Control. Release* 83, 13–22. doi: 10.1016/S0168-3659(02)00200-6

Kim, Y.-C., Park, J.-H., and Prausnitz, M. R. (2012). Microneedles for drug and vaccine delivery. *Adv. Drug Deliv. Rev.* 64, 1547–1568. doi: 10.1016/j.addr.2012.04.005

Kirby, G., White, L. J., Rahman, C. V., Cox, H. C., Qutachi, O., Rose, F. R. A., et al. (2011). PLGA-based microparticles for the sustained release of BMP-2. *Polymers* 3, 571–586. doi: 10.3390/polym3010571

Kodaira, H., Tsutsumi, Y., Yoshioka, Y., Kamada, H., Kaneda, Y., Yamamoto, Y., et al. (2004). The targeting of anionized polyvinylpyrrolidone to the renal system. *Biomaterials* 25, 4309–4315. doi: 10.1016/j.biomaterials.2003.10.097

Kumar, R., and Philip, A. (2007). Modified transdermal technologies: breaking the barriers of drug permeation via the skin. *Trop. J. Pharm. Res.* 6, 633–644. doi: 10.4314/tjpr.v6i1.14641

Lee, I.-C., He, J.-S., Tsai, M.-T., and Lin, K.-C. (2015). Fabrication of a novel partially dissolving polymer microneedle patch for transdermal drug delivery. *J. Mater. Chem. B* 3, 276–285. doi: 10.1039/C4TB01555J

Lettera, V., Pezzella, C., Cicatiello, P., Piscitelli, A., Giacobelli, V. G., Galano, E., et al. (2016). Efficient immobilization of a fungal laccase and its exploitation in fruit juice clarification. *Food Chem.* 196, 1272–1278. doi: 10.1016/j.foodchem.2015.10.074

Lettera, V., Piscitelli, A., Leo, G., Birolo, L., Pezzella, C., and Sannia, G. (2010). Identification of a new member of Pleurotus ostreatus laccase family from mature fruiting body. *Fungal Biol.* 114, 724–730. doi: 10.1016/j.funbio.2010.06.004

Li, W., Terry, R. N., Tang, J., Feng, M. R., Schwendeman, S. P., and Prausnitz, M. R. (2019). Rapidly separable microneedle patch for the sustained release of a contraceptive. *Nat. Biomed. Eng.* 3, 220–229. doi: 10.1038/s41551-018-0337-4

Lopérgolo, L. C., Lugao, A. B., and Catalani, L. H. (2003). Direct UV photocrosslinking of poly (N-vinyl-2-pyrrolidone)(PVP) to produce hydrogels. *Polymer* 44, 6217–6222. doi: 10.1016/S0032-3861(03)00686-4

Majcherczyk, A., Johannes, C., and Hüttermann, A. (1998). Oxidation of polycyclic aromatic hydrocarbons (PAH) by laccase of Trametes versicolor. *Enzyme Microb. Technol.* 22, 335–341. doi: 10.1016/S0141-0229(97)00199-3

Matsuo, K., Yokota, Y., Zhai, Y., Quan, Y.-S., Kamiyama, F., Mukai, Y., et al. (2012). A low-invasive and effective transcutaneous immunization system using a novel dissolving microneedle array for soluble and particulate antigens. *J. Control. Release* 161, 10–17. doi: 10.1016/j.jconrel.2012.01.033

Naik, A., Kalia, Y. N., and Guy, R. H. (2000). Transdermal drug delivery: overcoming the skin's barrier function. *Pharm. Sci. Technol. Today* 3, 318–326. doi: 10.1016/S1461-5347(00)00295-9

Nguyen, H. X., and Banga, A. K. (2017). Fabrication, characterization and application of sugar microneedles for transdermal drug delivery. *Ther. Deliv.* 8, 249–264. doi: 10.4155/tde-2016-0096

Nguyen, H. X., Bozorg, B. D., Kim, Y., Wieber, A., Birk, G., Lubda, D., et al. (2018). Poly (vinyl alcohol) microneedles: fabrication, characterization, and application for transdermal drug delivery of doxorubicin. *Eur. J. Pharm. Biopharm.* 129, 88–103. doi: 10.1016/j.ejpb.2018.05.017

Park, J.-H., Allen, M. G., and Prausnitz, M. R. (2005). Biodegradable polymer microneedles: fabrication, mechanics and transdermal drug delivery. *J. Control. Release* 104, 51–66. doi: 10.1016/j.jconrel.2005.02.002

Park, J.-H., Allen, M. G., and Prausnitz, M. R. (2006). Polymer microneedles for controlled-release drug delivery. *Pharm. Res.* 23, 1008–1019. doi: 10.1007/s11095-006-0028-9

Park, S. C., Kim, M. J., Baek, S.-K., Park, J.-H., and Choi, S.-O. (2019). Spray-formed layered polymer microneedles for controlled biphasic drug delivery. *Polymers* 11:369. doi: 10.3390/polym11020369

Patel, N., Shahane, S., Majumdar, R., and Mishra, U. (2019). Mode of action, properties, production, and application of laccase: a review. *Recent Pat. Biotechnol.* 13, 19–32. doi: 10.2174/1872208312666180821161015

Pennacchio, F. A., Casale, C., Urciuolo, F., Imparato, G., Vecchione, R., and Netti, P. A. (2018). Controlling the orientation of a cell-synthesized extracellular matrix by using engineered gelatin-based building blocks. *Biomater. Sci.* 6, 2084–2091. doi: 10.1039/C7BM01093A

Pennacchio, F. A., Fedele, C., De Martino, S., Cavalli, S., Vecchione, R., and Netti, P. A. (2017). Three-dimensional microstructured azobenzene-containing gelatin as a photoactuable cell confining system. *ACS Appl. Mater. Interfaces* 10, 91–97. doi: 10.1021/acsami.7b13176

Pezzella, C., Giacobelli, V. G., Lettera, V., Olivieri, G., Cicatiello, P., Sannia, G., et al. (2017). A step forward in laccase exploitation: recombinant production and evaluation of techno-economic feasibility of the process. *J. Biotechnol.* 259, 175–181. doi: 10.1016/j.jbiotec.2017.07.022

Pezzella, C., Lettera, V., Piscitelli, A., Giardina, P., and Sannia, G. (2013). Transcriptional analysis of *Pleurotus ostreatus* laccase genes. *Appl. Microbiol. Biotechnol.* 97, 705–717. doi: 10.1007/s00253-012-3980-9

Prausnitz, M. R., Mitragotri, S., and Langer, R. (2004). Current status and future potential of transdermal drug delivery. *Nat. Rev. Drug Discov.* 3:115. doi: 10.1038/nrd1304

Preetha, J. P., and Karthika, K. (2009). Cosmeceuticals–an evolution. *Int. J. Chem. Tech. Res.* 1, 1217–1223.

Qiu, Y., Guo, L., Zhang, S., Xu, B., Gao, Y., Hu, Y., et al. (2016). DNA-based vaccination against hepatitis B virus using dissolving microneedle arrays adjuvanted by cationic liposomes and CpG ODN. *Drug Deliv.* 23, 2391–2398. doi: 10.3109/10717544.2014.992497

Raja, W. K., MacCorkle, S., Diwan, I. M., Abdurrob, A., Lu, J., Omenetto, F. G., et al. (2013). Transdermal delivery devices: fabrication, mechanics and drug release from silk. *Small* 9, 3704–3713. doi: 10.1002/smll.201202075

Ruggiero, F., Vecchione, R., Bhowmick, S., Coppola, G., Coppola, S., Esposito, E., et al. (2018). Electro-drawn polymer microneedle arrays with controlled shape and dimension. *Sens. Actuat. B Chem.* 255, 1553–1560. doi: 10.1016/j.snb.2017.08.165

Schaefer, H., Redelmeier, T. E., and Lademann, J. (2011). "Skin penetration," in *Contact Dermatitis*, eds J. D. Johansen, P. J. Frosch, and J. P. Lepoittevin (Berlin: Springer), 215–227. doi: 10.1007/978-3-642-03827-3_12

Schaefer, H., Redelmeier, T. E., and Potts, R. (1997). Skin barrier: principles of percutaneous absorption. *Arch. Dermatol.* 133:924. doi: 10.1001/archderm.1997.03890430146031

Sullivan, S. P., Koutsonanos, D. G., del Pilar Martin, M., Lee, J. W., Zarnitsyn, V., Choi, S.-O., et al. (2010). Dissolving polymer microneedle patches for influenza vaccination. *Nat. Med.* 16:915. doi: 10.1038/nm.2182

Tsioris, K., Raja, W. K., Pritchard, E. M., Panilaitis, B., Kaplan, D. L., and Omenetto, F. G. (2012). Fabrication of silk microneedles for controlled-release drug delivery. *Adv. Funct. Mater.* 22, 330–335. doi: 10.1002/adfm.201102012

Vecchione, R., Pitingolo, G., Guarnieri, D., Falanga, A. P., and Netti, P. A. (2016). From square to circular polymeric microchannels by spin coating technology: a low cost platform for endothelial cell culture. *Biofabrication* 8:025005. doi: 10.1088/1758-5090/8/2/025005

Yan, G., Warner, K. S., Zhang, J., Sharma, S., and Gale, B. K. (2010). Evaluation needle length and density of microneedle arrays in the pretreatment of skin for transdermal drug delivery. *Int. J. Pharm.* 391, 7–12. doi: 10.1016/j.ijpharm.2010.02.007

Yang, S., Wu, F., Liu, J., Fan, G., Welsh, W., Zhu, H., et al. (2015). Phase-transition microneedle patches for efficient and accurate transdermal delivery of insulin. *Adv. Funct. Mater.* 25, 4633–4641. doi: 10.1002/adfm.201500554

**Conflict of Interest:** VL was employed by company Biopox Srl, Naples.

The remaining authors declare that the research was conducted in the absence of any commercial or financial relationships that could be construed as a potential conflict of interest.

frontiers in Materials

ORIGINAL RESEARCH
published: 08 January 2020
doi: 10.3389/fmats.2019.00338

# Mechanical Characterization of Methanol Plasma Treated Fluorocarbon Ultrathin Films Through Atomic Force Microscopy

*Melania Reggente*[1†], *Livia Angeloni*[1,2†], *Daniele Passeri*[1,3*], *Pascale Chevallier*[2], *Stephane Turgeon*[2], *Diego Mantovani*[2] *and Marco Rossi*[1,3]

[1] Department of Basic and Applied Sciences for Engineering, University of Rome Sapienza, Rome, Italy, [2] Laboratory for Biomaterials and Bioengineering (CRC-I), Department of Min-Met-Materials Engineering, University Hospital Research Center, Laval University, Quebec City, QC, Canada, [3] Research Center for Nanotechnology Applied to Engineering of Sapienza University of Rome (CNIS), University of Rome Sapienza, Rome, Italy

Methanol plasma has been proposed as an effective way to improve the performances of fluorocarbon ($CF_x$) ultrathin films as stent coatings as it can successfully modulate fluorine content and wettability of the films. Nevertheless, plasma treatment may affect mechanical properties of the films, which therefore need comprehensively characterizing to verify the suitability of treated films for application as stent coating materials. In this work we investigate mechanical properties of methanol plasma treated $CF_x$ ultrathin films on stainless steel. In particular, cohesion of the films and their adhesion to the substrate is investigated using small punch test combined with atomic force microscopy (AFM) imaging. Also, elastic and viscoelastic properties are investigated at the nanometer scale using two different AFM based advanced technique for nanomechanical characterization, i.e., HarmoniX™ and contact resonance AFM (CR-AFM). Overall, methanol plasma treated $CF_x$ films have been demonstrated to be suitable for application as stent coating also on the basis of their nanomechanical properties.

**Keywords: fluorocarbon films, adhesion, elastic properties, viscoelastic properties, contact resonance atomic force microscopy, HarmoniX, methanol plasma, biomaterials**

OPEN ACCESS

***Edited by:***
*Admir Masic, Massachusetts Institute of Technology, United States*

***Reviewed by:***
*Dongyan Liu, Chinese Academy of Sciences, China*
*Antonio Greco, University of Salento, Italy*

***Correspondence:**
*Daniele Passeri*
*daniele.passeri@uniroma1.it*

*[†]These authors have contributed equally to this work*

***Specialty section:***
*This article was submitted to Polymeric and Composite Materials, a section of the journal Frontiers in Materials*

***Received:*** *28 August 2019*
***Accepted:*** *06 December 2019*
***Published:*** *08 January 2020*

***Citation:***
*Reggente M, Angeloni L, Passeri D, Chevallier P, Turgeon S, Mantovani D and Rossi M (2020) Mechanical Characterization of Methanol Plasma Treated Fluorocarbon Ultrathin Films Through Atomic Force Microscopy. Front. Mater. 6:338. doi: 10.3389/fmats.2019.00338*

## 1. INTRODUCTION

Mechanical characterization of thin coatings is increasingly emerging as a need in the development and optimization of biomaterials. Indeed, biomaterials for medical devices are often subjected to surface modification processes, such as functionalization and deposition of thin coatings, with the aim of improving their functionality and biocompatibility, without sacrificing the high structural properties given by the bulk materials. Besides the opportune chemical, physical and biocompatibility properties, a coating for medical devices must exhibit appropriate mechanical properties in order to maintain its integrity, cohesion and adhesion to the underlying substrate, even after significant elastic and plastic deformations to which the device can undergo. Together with cohesion and adhesion to the substrate, the stiffness of the coating, i.e., the part of the biomaterial in contact with the biological medium, is emerging as key factor, in addition to chemical composition, surface energy and roughness, in the regulation of the biological response. Indeed, the stiffness of biomaterials has been demonstrated to affect adhesion, proliferation, differentiation and migration of several kind of cells (Lo et al., 2000; Guo et al., 2006; Chowdhury et al., 2010).

For instance, neurons have been shown to proliferate better on soft substrates (Flanagan et al., 2002) while fibroblasts and chondrocytes exhibited maximum spread and proliferation on stiffer substrates (Subramanian and Lin, 2005; Hopp et al., 2013). Native mesenchymal stem cells undergo different differentiation behavior when interacting with surfaces with different elastic modulus (Engler et al., 2006). Endothelial cells have been observed to exhibit tube-like structures on soft substrates and high spread and proliferation on stiffer substrates (Califano and Reinhart-King, 2008, 2010); smooth muscle cells and myoblasts have been shown to have higher projected area on stiff substrates (Engler et al., 2004a,b). Moreover, substrate stiffness has been demonstrated to affect adhesion, spreading and activation of platelets, suggesting that the mechanical properties at the surface of cardiovascular devices could also have an effect on blood contact behavior and clot formation (Qiu et al., 2014). Therefore, the capability to characterize the mechanical properties of thin coatings for medical devices is fundamental, not only from the point of view of the integrity and mechanical behavior of the device, but also for the comprehension of the effect of surface stiffness on the biological events occurring at the interface of the device. Indeed, the capability of measuring and modulating the elastic modulus at the very surface of an implant might allow improved body response and implant performance. In previous studies, fluorocarbon ($CF_x$) thin films deposited by plasma enhanced chemical vapor deposition (PECVD) with thickness of about 35 nm have been demonstrated to be effective as coatings for cardiovascular stents, thanks to their chemical inertness, high uniformity, flexibility and adhesion to the substrate (Haïdopoulos et al., 2005). These characteristics make them resistant to corrosion (Touzin et al., 2010) and able to overcome the high deformation occurring during stent deployment (about 25%) (Lewis et al., 2008). The higher hemocompatibility of $CF_x$ coatings in respect of bare metallic surfaces has been shown (Montaño-Machado et al., 2017) and can be mainly attributed to the presence of fluorine content. Nevertheless, the hydrophobic nature of these coatings could limit protein adsorption, hemocompatibility and endothelialization (Arima and Iwata, 2007; Tang et al., 2008). Recently, a novel oxidative methanol plasma treatment has been developed and demonstrated to be effective in tuning the hydrophobicity of $CF_x$ coatings without affecting their integrity, uniformity and morphology (Montaño-Machado et al., 2019). By analyzing coatings with different wettability and oxygen and fluorine content, it has been shown that the blood contact behavior of $CF_x$ coatings can be improved by modulating surface energy and fluorine species content (Montaño-Machado et al., 2019). Nevertheless, the effect of the treatment on the mechanical properties of the modified films, which could affect the cohesion and adhesion to the substrate as well as the blood contact behavior, has not been evaluated yet. The mechanical characterization of these ultrathin coatings is challenging. The capability of the coating to maintain its integrity after a determined deformation can be tested by the method developed by Lewis et al. (2008), called small punch test, consisting in the application of a known deformation and the subsequent morphological analysis of the coating.

However, the quantitative evaluation of the elastic modulus cannot be obtained by conventional techniques, such as micro- and nanoindentation, due to the limited thickness which makes the results of the measurements strongly affected by the mechanical properties of the underlying substrate (Fischer-Cripps, 2006; Reggente et al., 2017). Moreover, micro- and nanoindentation do not allow one to visualize the distribution of these surface properties because of their poor spatial resolution. Alternatives methods, based on atomic force microscopy (AFM), can be used to obtain quantitative maps of mechanical properties, such as indentation modulus, damping, adhesion and energy dissipation (Passeri et al., 2013a) as well as viscoelastic moduli, i.e., storage and loss modulus, and loss tangent (Killgore and DelRio, 2018).

In this work, we perform an exhaustive mechanical characterization of methanol plasma treated $CF_x$ ultrathin films, with thickness in the range 30–65 nm, deposited on stainless steel in order to verify the effect of plasma treatment on the mechanical properties of the films. Cohesion of the films and their adhesion to the substrate after deformation was analyzed with small punch test method combined with AFM morphological characterization. The challenging analysis of elastic and viscoelastic response of ultrathin soft films on stiff substrates was performed with two different AFM based techniques for nanomechanical characterizations, i.e., HarmoniX$^{TM}$ and contact resonance AFM (CR-AFM), for the latter using two different data analysis procedures, in order to cross-validate these methods.

# 2. MATERIALS AND METHODS

## 2.1. Materials

### 2.1.1. Pre-treatment of 316L Stainless Steel Substrates

316 L stainless steel disks of 12.7 mm diameter and 0.5 mm thickness (Goodfellow, Devon, PA, USA) are used as substrates. First, they have been cleaned in an ultrasonic bath with acetone, deionized water, and methanol for 10 min for each solvent and then dried with particle-free compressed air. Then an electropolishing and an acid dipping treatment have been performed in order to reduce the surface roughness. Electropolishing has been carried out in 100 mL of solution containing glycerol, phosphoric acid and deionized water for 3 min at 90°C. Acid dipping was performed for 30 s at 50°C in a solution consisted in nitric acid, hydrofluoric acid, and deionized water (Montaño-Machado et al., 2019).

### 2.1.2. Plasma-Enhanced Chemical Vapor Deposition of Fluorocarbon Coating

$CF_x$ coatings with different wettability and oxygen and fluorine content have been obtained by PECVD, following the protocols previously developed (Montaño-Machado et al., 2019). Specimens were introduced into the previously described radio frequency (RF) plasma reactor (Lewis et al., 2008) at 6 cm below the electrode for a pulsed $H_2$ plasma etching at 100 W for 100 s ($t_{on}$ = 100 ms; $t_{off}$ = 300 ms). Etching was carried out to (i) remove the layer of organic contaminants and (ii) reduce

the oxide layer on the sample surface. After the plasma etching of the substrates, a fluorocarbon coating has been deposited by pulsed afterglow plasma polymerization using $C_2F_6$ and $H_2$ as precursors. The sample was placed at 11 cm below the electrode and the coating was realized using a peak power input of 150 W, a duty cycle of 20%, a pressure of 700 mTorr and a total gas flow rate of 20 sccm for a deposition time of 5 min. An oxidation treatment with methanol plasma was then carried out with the sample at 6 cm below the electrode, using a continuous power of 50 W and a flow of 10 sccm during 30 and 90 s. In this way, three different coatings with decreasing hydrophobicity (static contact angle of 117° for the unmodified $CF_x$ coating, 87° for the coating after 30 s methanol treatment and 68° for the coating after 90 s methanol treatment) and increasing O/F ratio (0.01 for the unmodified $CF_x$ coating, 0.44 for the coating after 30 s methanol treatment and 1.08 for the coating after 90 s methanol treatment) were obtained (Montaño-Machado et al., 2019). For the sake of clarity, from herein $CF_x$-A refers to the sample which has not been processed with methanol plasma treatment, while $CF_x$-B and $CF_x$-C indicate the samples modified by 30 and 90 s methanol plasma treatment, respectively.

## 2.2. Instrumentation and Equipment

### 2.2.1. X-Ray Photoelectron Spectroscopy Analysis

Chemical composition of the coating was analyzed by X-ray photoelectron spectroscopy (XPS), using an X-ray photoelectron spectrometer (XPS-PHI 5600-ci Spectrometer-Physical Electronics, Eden Prairie, MN, USA), with a base pressure below $5 \times 10^{-7}$ Pa. Survey and high resolution spectra were acquired using the K$\alpha$ line of a standard aluminum (K$\alpha$ = 1486.6 eV) and magnesium (K$\alpha$ = 1253.6 eV) X-ray sources, respectively, operated at 300 W, without charge compensation. Three spots on three samples were analyzed for each experiment.

### 2.2.2. Small Punch Test

A plastic deformation of 25%, i.e., the estimated maximum deformation to which a stent undergoes during deployment (Migliavacca et al., 2005), was applied to the coated samples using a custom-made small punch test device mounted on a SATEC T20000 testing machine (Instron, Norwood, MA, USA) as previously described (Lewis et al., 2007). All deformations were performed at room temperature at a displacement rate of 0.05 mm $s^{-1}$ and a maximal load of 2200 N. The state of the coating, i.e., the morphology and the eventual presence of delamination or cracks, after deformation was analyzed by AFM. A Dimension™ 3100 AFM (Veeco, Woodbury, NY, USA) was used in tapping mode with a silicon tip (OTESPA, Bruker). 20 × 20 $\mu$m images in correspondence of the topmost part of the samples, where the maximum deformation (25%) occurs, were acquired and analyzed. Three specimens for each condition ($CF_x$-A, $CF_x$-B and $CF_x$-C) were tested.

### 2.2.3. Nanomechanical Characterizations by Atomic Force Microscopy

Mechanical characterizations of the films have been performed through both CR-AFM and HarmoniX™.

HarmoniX™ has been carried out using a standard AFM apparatus (ICON, Bruker Inc.), equipped with a standard T-shape Si cantilever (HMX10, Bruker Inc.) having $k_c$ = 4 N/m (as reported by the manufacturer) and first flexural and torsional resonance frequencies in air equal to $f_{0,1}$ = 52.9 kHz and $t_{0,1}$ = 949 kHz, respectively. Cantilever force sensitivity has been measured from force-deflection curves performed on Si (100) single crystal. Calibration procedure has been performed using a blend of polystyrene (PS) and low-density polyethylene (LDPE) film deposited on a Si substrate (PS/LDPE, Bruker Inc.), being $M_{PS}$ = 1.6 GPa and $M_{LDPE}$ = 100 MPa the indentation modulus of PS and LDPE, respectively, as supplied by the producer.

CR-AFM has been carried out using a standard AFM apparatus (Solver, NT-MDT, Russia). The AFM setup was equipped with a Si cantilever (CSG10, NT-MDT, Russia) with spring constant $k_c$ = 0.116 N/m, determined through the method described by Sader et al. (1999). In order to evaluate the instrumental parameters required to analyze CR-AFM data, a well-established experimental procedure was followed (Reggente et al., 2015): standard force-deflection curves have been acquired on Si (100) single crystal to calibrate the cantilever force sensitivity; tip radius $R_t$ has been evaluated by reconstructing the tip shape through the analysis of the images collected on an array of inverted tips used as reference sample (TGZ1, NT-MDT, Russia); the exact position of the tip along the cantilever axis has been determined through scanning electron microscopy (SEM) analysis. Being the tip in contact with the sample surface, contact resonance frequencies (CRFs) were detected for each sample and CRFs values and the corresponding uncertainties have been evaluated from statistics performed on not <512 points of CR-AFM images. Calibration of CR-AFM has been performed using as the reference the PS regions of the above described PS/LDPE sample. Numerical simulation of the entire experimental session was performed using Matlab (version 7.1.0.246, 2005).

# 3. TECHNIQUES

## 3.1. HarmoniX™

HarmoniX™ is a tapping mode based AFM technique in which a T-shaped cantilever with an out-of-axis tip is used (Sahin et al., 2007; Sahin and Erina, 2008). The first flexural mode of the cantilever, characterized by the first flexural resonance frequency $f_{0,1}$, is used to reconstruct sample morphology, as in standard AFM tapping mode. During tapping performed at frequency $f_{0,1}$, the tip periodically (with period $T_0 = 1/f_{0,1}$) interacts with the sample surface. The actual tip-sample interaction force depends on the instantaneous value of tip-sample separation $d$, i.e., is given by the van der Waals force if $d > a_0$, and by the sum of van der Waals and repulsive (elastic) forces if $d < a_0$, where $a_0$ is an intermolecular distance. More explicitly, by modeling the repulsive force using the Derjaguin-Muller-Toporov (DMT) (Derjaguin et al., 1975) and assuming that the lateral extension of the sample is much bigger than the tip size (Santos et al., 2011), the tip-sample interaction force $F_{ts}$ is given by

$$F_{ts} = \begin{cases} -\dfrac{HR_t}{6d^2} & \text{if } d > a_0 \\ -\dfrac{HR_t}{6a_0^2} + \dfrac{4}{3}E^*\sqrt{R_t\left(a_0 - d\right)^3} & \text{if } d < a_0 \end{cases} \quad (1)$$

where $H$ is the Hamaker constant, $R_t$ is the tip radius, and $E^*$ is the reduced modulus given by $E^* = \left(M_s^{-1} + M_t^{-1}\right)^{-1}$ being $M_s$ and $M_t$ the indentation modulus of the sample and of the tip, respectively (Derjaguin et al., 1975; García and San Paulo, 1999). When $M_s \ll M_t$ as in the case of the materials investigated in this work, $E^* \approx M_s$. This force is measured by recording the cantilever deflection $\Delta z$ which is proportional to the tip-sample force through the (normal) spring constant $k_c$. Being periodic with period $T_0$, the force-separation curve could be, in principle, reconstructed through inverse Fourier transform after acquiring the harmonic components (multiple of $f_{0,1}$) of the deflection signal. Nevertheless, the presence of higher deflection modes of the cantilever distorts the harmonic components of the force-separation curve. A smart solution consists in using a T-shaped cantilever with an out-of-axis tip. Indeed, during tapping, the tip-sample interaction produces a torque $T_{ts} = F_{ts}l_t$ where $l_t$ is the distance between the tip location and the cantilever axis. This results in the torsion of the cantilever of an angle $\Delta\phi = T_{ts}/k_\phi$ where $k_\phi$ is the cantilever torsional spring constant (Green et al., 2004; Pettersson et al., 2007). Thus, the cantilever torsional signal is proportional to $F_{ts}$ and is periodic with period $T_0$. Therefore, the periodic $F_{ts}$ can be reconstructed by inverse Fourier transform of the components of the torsional signal at frequencies multiple of $f_{0,1}$. Being the value of the first free torsional resonance $t_{0,1}$ much higher than $f_{0,1}$, this allows the analysis of harmonic components of the torsional signal in an undistorted spectral region and leads signal-to-noise ratio higher than the one relative to the deflection signal. Therefore, the cantilever torsional signal can be analyzed using inverse Fourier transform analysis in order to extract a complete loading/unloading force-distance curve during each tapping cycle. Unloading force-distance curves are analyzed in real time to evaluate $M_s$ through the DMT model (Derjaguin et al., 1975) which is currently implemented in HarmoniX™ software, although the Johnson-Kendall-Roberts (JKR) model (Johnson et al., 1971) has been demonstrated to be more accurate in the range of materials analyzed in this work (Dokukin and Sokolov, 2012). To overcome the need for accurate calibration of the cantilever geometrical and elastic parameters, a phenomenological calibration is performed using a reference sample with well-known indentation modulus $M_{ref}$.

## 3.2. Contact Resonance Atomic Force Microscopy

In contact resonance AFM (CR-AFM) the tip is in contact with the sample surface and the system constituted by the cantilever, the tip, and a volume of the sample under the tip is set into oscillation using an ultrasonic transducer coupled to the sample (Rabe and Arnold, 1994) or to the cantilever (Yamanaka et al., 2008), or by the direct photothermal excitation of the cantilever (Wagner and Killgore, 2015). In these conditions, the resonance frequencies of the cantilever, namely the contact resonance frequencies (CRFs) $f_n$, can be detected. When the investigated material is considered elastic, the system can be described as sketched in **Figure 1A**. In this model: the cantilever is considered inclined by an angle $\alpha$ with respect to the sample surface; the tip is located at distance $L_1$ from the cantilever clamped end, so that the parameter $r = L_1/L$ can be defined being $L$ the cantilever length; the height of the tip is $h_t$; the tip interacts with the sample surface via both normal and lateral forces, and the contact is thus described by the normal and lateral contact stiffness, modeled through the linear springs $k^*$ and $k^*_{lat}$, respectively. The values of the CRFs are determined by $k^*$ and $k^*_{lat}$, which depends on the elastic parameters of the sample, i.e., on the indentation and shear moduli of the sample ($M_s$ and $G_s$, respectively). Therefore, the measured values of $f_n$ can be used to evaluate the elastic properties of the sample. Nevertheless, due the complexity of the model in **Figure 1A**, the analysis of CRFs data are generally carried out considering the simplified model depicted in **Figure 1B**, in which the cantilever inclination, the tip height, and the lateral tip-sample coupling are neglected. In the standard procedure, the values of two different CRFs (say $f_n$ and $f_m$ with $n \neq m$) are measured and used to determine $r$ and $k^*$ by numerically solving $k^*(f_n, r) = k^*(f_m, r)$ (Kester et al., 2000). The value of $k^*$ is related to that of $M_s$ through the relation

$$k^* = 2a_c M_s \quad (2)$$

where $a_c$ is the tip-sample contact radius and assuming $M_s \ll M_t$ and, thus, $E^* \approx M_s$. Using the Hertzian model to describe the tip-sample contact, Equation (2) can be rewritten as

$$k^* = \sqrt[3]{6M_s^2 R_t F_N} \quad (3)$$

where $F_N$ is the static normal load applied by the tip on the sample as a result of the selected deflection set point. To evaluate $M_s$ from $k^*$, the knowledge of the $R_t$ is required. As $R_t$ may change during a measurement session due to abrasion, especially when relatively stiff materials are investigated (Amelio et al., 2001), and thus the use of predetermined values of $R_t$ in Equation (3) may result in a not accurate estimation of $M_s$. The uncertainty in the value of $R_t$ is one of the major factors affecting the accuracy of CR-AFM measurements. Therefore the actual tip radius (and also the tip shape) should be determined during each experimental session by calibrating the tip radius using one sample with well-known indentation modulus as reference material (Yamanaka et al., 2000; Kopycinska-Müller et al., 2006; Marinello et al., 2010, 2011). Really, to avoid the explicit calculation of $R_t$, after the contact stiffness $k^*_{ref}$ is determined on the reference material with reduced modulus $E^*_{ref}$, the reduced modulus of the investigated sample $E^*_s$ is calculated from the measured contact stiffness $k^*_s$ as

$$E^*_s = E^*_{ref}\left(\frac{k^*_s}{k^*_{ref}}\right)^{3/2} \quad (4)$$

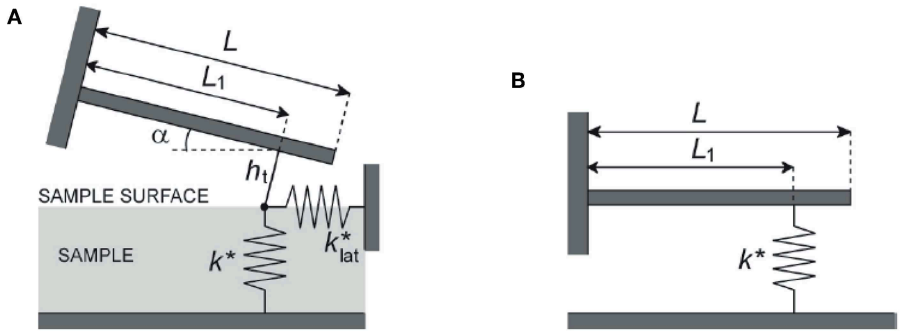


**FIGURE 1 | (A)** Beam model of the cantilever with length $L$, inclined of an angle $\alpha$ respect to the sample surface; the tip is located at distance $L_1$ from the cantilever clamped end, its height being $h_t$; the tip interacts with the sample surface via both normal and lateral forces, and the contact is thus described by the normal and lateral contact stiffness modeled through the linear springs $k^*$ and $k^*_{lat}$, respectively. **(B)** Simplified beam model of the cantilever, supposed parallel to the sample surface; the tip, the height of which is neglected, interacts with the sample only through normal forces modeled by the contact stiffness $k^*$. Reprinted and adapted from Passeri et al. (2013b).

if measurements on the investigated sample and on the reference material are performed at the same value of $F_N$ (Rabe et al., 1996; Hurley et al., 2005; Passeri et al., 2005). For the sake of clarity, this procedure—which is admittedly the most widespread one—will be referred to as "single reference" approach in the rest of the paper. In more accurate calibration procedures not only $R_t$ but also the indentation modulus of the tip $M_t$ can be calibrated using two (or more) reference materials (Stan and Price, 2006). In particular, using two reference materials, $M_s$ and $M_t$

$$M_s = \frac{\left(k^*_{ref1}/k^*_{ref2} - 1\right)^{3/2}}{\left(k^*_{ref1}/k^*_s\right)^{3/2}\left(1/M_{ref2} - 1/M_{ref1}\right) + \left(k^*_{ref1}/k^*_{ref2}\right)^{3/2} 1/M_{ref1} - 1/M_{ref2}} \tag{5}$$

and

$$M_t = \frac{M_{ref1}M_{ref2}\left(k^{*\,3/2}_{ref1} - k^{*\,3/2}_{ref2}\right)}{k^{*\,3/2}_{ref2}M_{ref1} - k^{*\,3/2}_{ref1}M_{ref2}} \tag{6}$$

where $k^*_{ref1}$ and $k^*_{ref2}$ are the contact stiffness measured on the first and second reference sample, respectively, and $M_{ref1}$ and $M_{ref2}$ are the indentation moduli of the two reference materials (Stan and Price, 2006). In particular, despite in a relatively limited range of elastic moduli, the use of multiple reference materials allows one to neglect lateral forces, thus using the model in **Figure 1B** instead of that in **Figure 1A** although apparent values of $R_t$ and $M_t$ (different from the real ones) are determined (Passeri et al., 2013b).

In this work, results of CR-AFM data analysis through the "single reference" approach were compared to those obtained using an original method, which we refer to as the "apparent stiffness" method. In the "apparent stiffness" method, the output of numerical simulations of CR-AFM experiments performed using the model in **Figure 1A** is analyzed using the simplified model reported in **Figure 1B** in order to obtain calibration curves in which the apparent value of $k^*$ is related to that of $M_s$. Therefore, these calibration curves are used to evaluate $M_s$ from the values of $k^*$ determined in the first steps of the "single reference" procedure.

Finally, not only can CR-AFM be used to study elastic but also viscoelastic materials (Killgore and DelRio, 2018). In order to account for the viscoelastic behavior of samples, a dashpot of dumping $\sigma$ is included in parallel to $k^*$ in the model in **Figure 1B** (Yuya et al., 2008). The tip-sample contact is described by the normalized tip-sample contact stiffness $\alpha$ and the normalized damping coefficient $\beta$. These parameters can be evaluated measuring the frequency $f_n$ of a given contact mode of the cantilever and the corresponding quality factor $Q_n$ (Yuya et al., 2011). Finally, the values of $\alpha$ and $\beta$ can be used to evaluate the storage and the loss modulus of the sample ($E'_s$ and $E''_s$, respectively) and the loss tangent defined as $\tan\delta = E''_s/E'_s$. In particular, a "single reference" approach can be followed, using a material with well-known storage and loss modulus ($E'_{ref}$ and $E''_{ref}$, respectively). In this case, considering the tip much stiffer than the sample, $E'_s$ and $E''_s$ can be calculated as $E'_s = E'_{ref}\left(\alpha/\alpha_{ref}\right)^{3/2}$ and $E''_s = E''_{ref}\left(f_n\beta/f_{n,ref}\beta_{ref}\right)^{3/2}$, where $f_{n,ref}$, $\alpha_{ref}$, and $\beta_{ref}$ are measured and calculated on the reference sample (Killgore et al., 2011). Conversely, $\tan\delta$ can be evaluated without the need for calibration using a reference material through the relation

$$\tan\delta = (k_nL)^2 r^2 \frac{\beta}{\alpha}\frac{f_n}{f_{0,n}} \tag{7}$$

where $k_nL = 7.855$ if the third mode of the cantilever is analyzed ($n = 3$) (Hurley et al., 2013), which we used in this work as it was demonstrated to be more sensitive than, e.g., the first one (Killgore and Hurley, 2012). In this work, we evaluated $E'_s$ using the "single reference" approach assuming the PS as the reference material, $\tan\delta$ was evaluated using Equation (7), and finally $E''_s$ was calculated as $E''_s = E'_s\tan\delta$.

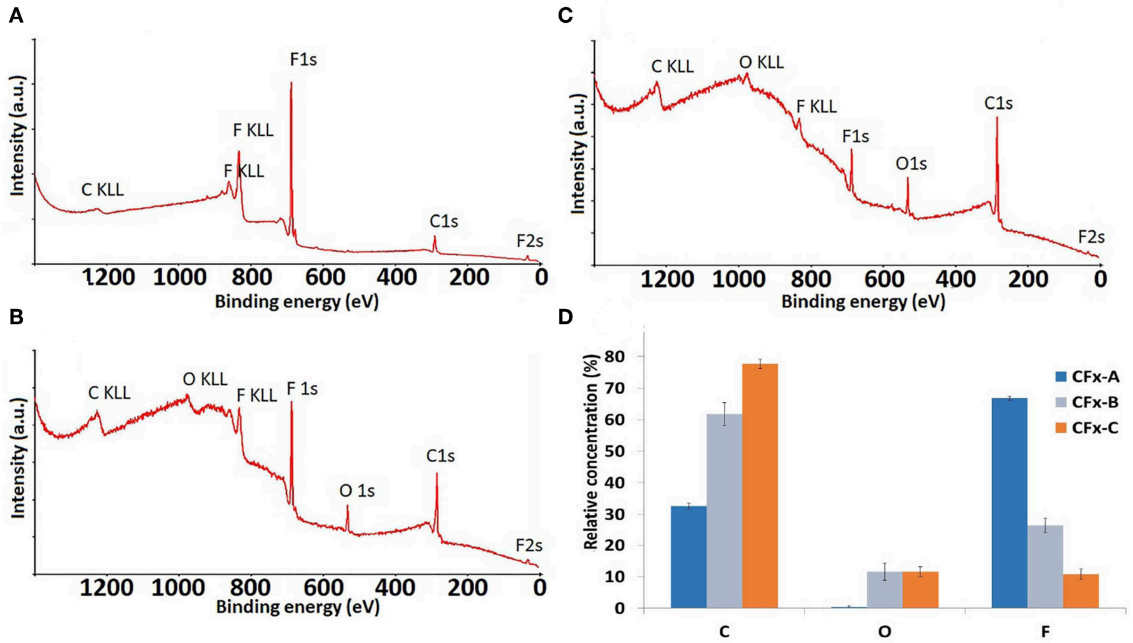


**FIGURE 2 |** XPS survey spectra of the untreated $CF_x$ film **(A)** and $CF_x$ films treated with 30 s **(B)** and 90 s **(C)** methanol plasma treatment and histogram of the relative concentration of C, O, and F **(D)**.

# 4. RESULTS

## 4.1. Chemical Analysis

Survey XPS spectra of $CF_x$ coatings before and after 30 and 90 s methanol plasma treatments are reported in **Figure 2** and show that methanol plasma treatment produced an increase of the oxygen amount of the coating (from 0% in $CF_x$-A to 12% in both $CF_x$-B and $CF_x$-C); the increase of the time of methanol plasma treatment produced the increase of carbon amount (from 32.75 in $CF_x$-A to 61.8% in $CF_x$-B and 77.75 in $CF_x$-C) and the corresponding decrease of fluorine content (from 66.9 in $CF_x$-A to 26.5% and 10.7% in $CF_x$-B and $CF_x$-C, respectively). No metal species were detected, demonstrating that the coating was not damaged by methanol plasma treatment.

**Figure 3** shows high resolution XPS spectra for C(1s) of the unmodified $CF_x$ coating (a) and $CF_x$ coatings after 30 and 90 s methanol plasma treatments. The C(1s) spectra of the $CF_x$ films are fitted with five spectral components, as assigned to C–H/C–C– (BE = 285 eV), C–CF/C–O (BE = 287), CF/C=O (BE = 289.5 eV), $-CF_2$ (BE = 292), and $CF_3$ (BE = 294 eV) groups, according to literature (Horie, 1995; Mackie et al., 1997; Bourgoin et al., 1999; Boehm, 2002). As a percentage of oxygen lower than 1% was detected at the surface of the untreated $CF_x$ coating, no attribution due to C–O (286.9) or C=O (288.1) is proposed, while for methanol treated samples, peaks at BE = 287 and 289.5 can be attributed to oxygen containing groups. **Figure 3A** shows the typical C(1s) spectrum of $CF_x$ coating without any methanol plasma treatment, which consists mainly of C–CF groups, $CF_2$ and $CF_3$ groups that are characteristic of fluorocarbon plasma-polymer films. High resolution spectra of $CF_x$ coating after 30 and 90 s methanol plasma treatments (**Figures 3B,C**) show the increasing hindrance of the $CF_2$ and $CF_3$ bands—characteristic of $CF_x$ coatings—with the increase of the time of oxidative treatment, from 55 to 15% and <2%, respectively, and the corresponding increase of C–C and C–O containing species. This demonstrates that methanol plasma treatments allows the deposition of oxygen species not containing fluoride on the surface of fluorocarbon coating, without damaging it. The increase of the time of methanol plasma treatment produces the increasing covering of the fluorocarbon coating by oxygen species, which is also consistent with the previously reported time-of-flight secondary ion mass spectrometry (ToF-SIMS) analysis and the previously observed increased thickness of the coating (from 30 nm for untreated $CF_x$ coating to 41 nm for 30 s and 64 nm for 90 s methanol treated samples) (Montaño-Machado et al., 2019).

## 4.2. Cohesion and Adhesion After Deformation (Small Punch Test)

In **Figure 4** typical AFM topographies of the areas corresponding to the topmost part of the deformed samples are reported. AFM analysis of all the deformed samples (unmodified $CF_x$ and $CF_x$ after methanol treatment of 30 and 90 s) shows the occurrence of slip bends due to the plastic deformation of the underlying stainless steel substrate, but does not show any cracks, delamination or failure. This demonstrates that the methanol treatment did not significantly affect cohesion and adhesion properties of the $CF_x$ films, which resulted in having sufficient interfacial adhesion and cohesion to be employed as stent coatings.

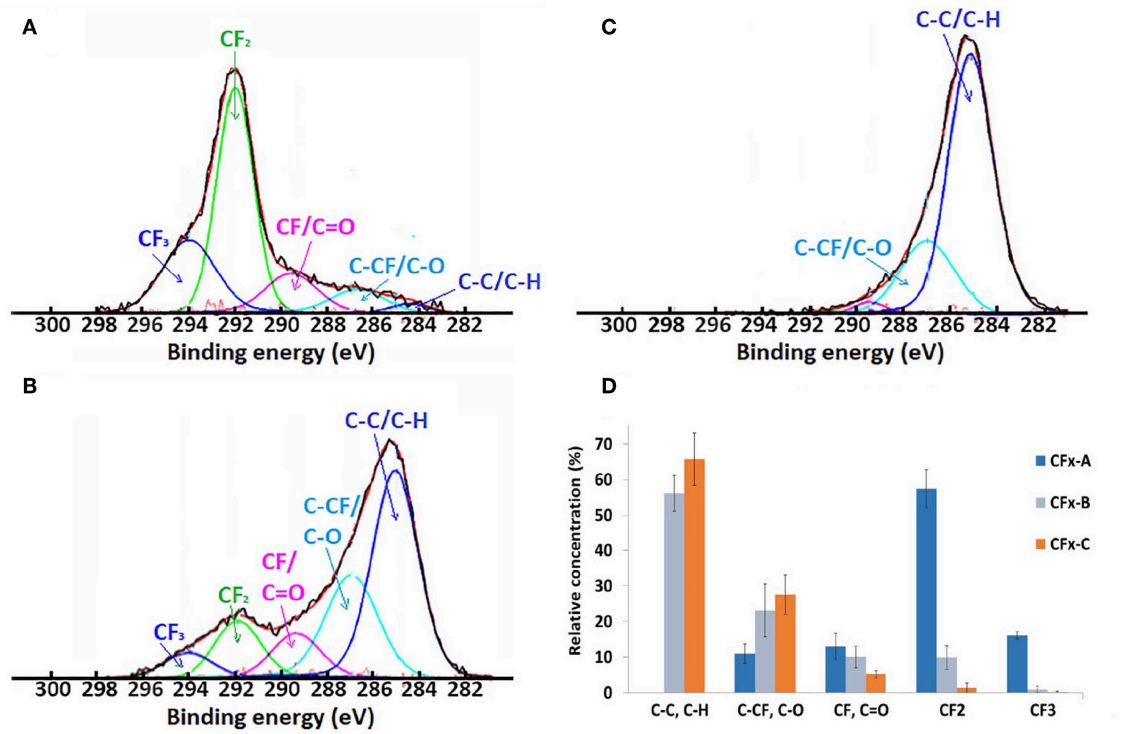


**FIGURE 3 |** XPS high resolution C (1s) spectra of CFx film **(A)** and CFx films treated with 30 s **(B)** and 90 s **(C)** methanol plasma treatment and histogram of the relative concentration of the characteristic bands **(D)**.

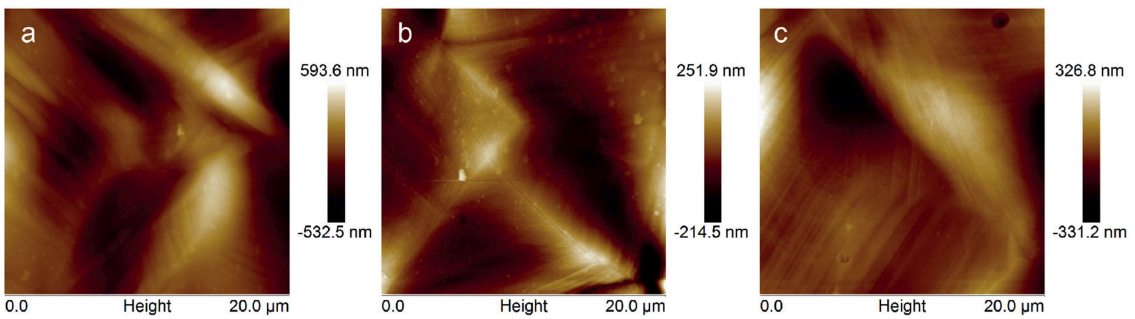


**FIGURE 4 |** AFM topography images of the topmost part of $CF_x$-A **(a)**, $CF_x$-B **(b)**, and $CF_x$-C **(c)** samples after application of 25% deformation.

## 4.3. Nanomechanical Characterizations

### 4.3.1. Elastic Modulus

A typical result of the characterization of $CF_x$ samples using HarmoniX$^{TM}$ is shown in **Figure 5**, where topography (**Figure 5A**), phase image (**Figure 5B**), map of the (not calibrated) indentation modulus (**Figure 5C**), and map of the (not calibrated) tip-sample adhesion force (**Figure 5D**) obtained on the sample $CF_x$−C are shown. Morphological reconstruction shows the presence of ripples on the surface, indicating that the film reproduces the features typical of the stainless-steel substrate. These features are observed also in phase, indentation modulus, and adhesion maps, and can be ascribed to the modulation of the local value of the tip-sample contact area (Stan and Cook, 2008) and to the variation of the local inclination of the surface with respect to the tip axis (Passeri et al., 2013b). Calibration of the indentation modulus maps was performed on the PS/LDPE reference sample (Passeri et al., 2013a). More specifically, the PS regions were used for calibration purposes, while LDPE regions were used to check the calibration range by comparing the obtained value to the one indicated by the vendor (100 MPa). In **Figure 6**, the histograms of the indentation modulus of the investigated $CF_x$ samples and those of the reference sample are reported. The obtained value of the indentation modulus of the LPDE is compatible with that

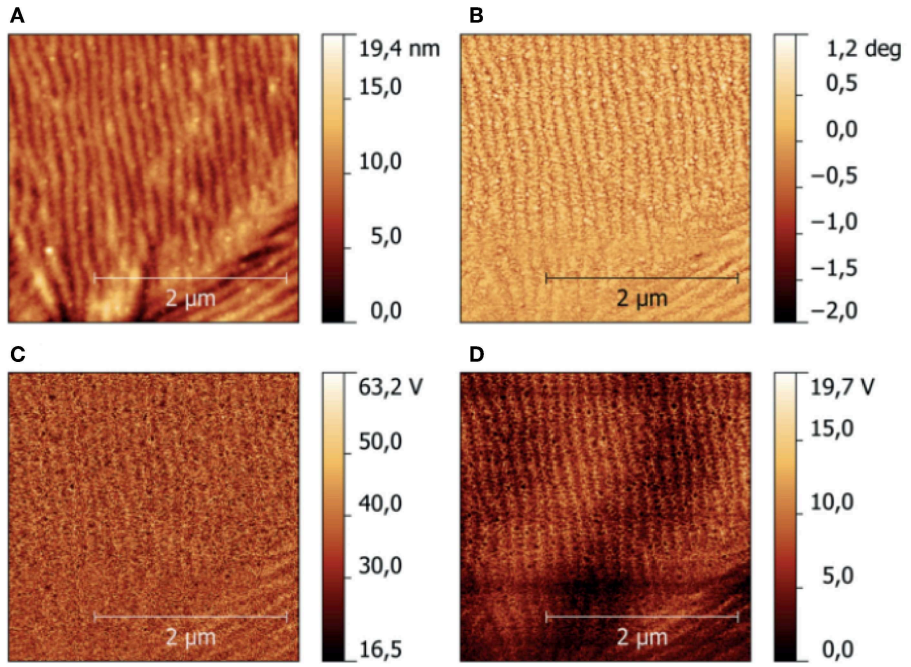


**FIGURE 5 |** Example of nanomechanical mapping of the $CF_x$−C sample using HarmoniX™: **(A)** height, **(B)** phase, **(C)** not calibrated indentation modulus, **(D)** not calibrated adhesion force.

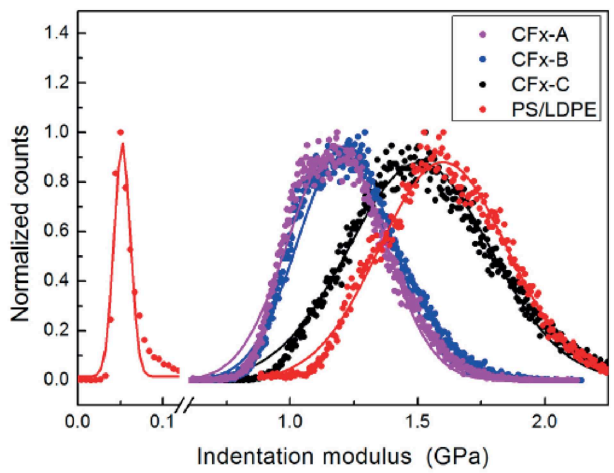


**FIGURE 6 |** Distribution of the values of indentation modulus of the three $CF_x$ samples and of the PS/LDPE reference, measured using HarmoniX™.

expected but lower (51 ± 1 MPa), indicating a not perfect calibration in low modulus range. Nevertheless, the moduli of $CF_x$ samples are comparable to those of PS, and thus the calibration can be considered accurate enough in the range of interest. Indentation modulus values with the corresponding uncertainty were obtained by Gaussian fitting of data in **Figure 6** and are reported in **Table 1**.

CR-AFM was first used to evaluate mechanical properties of the $CF_x$ thin films in elastic approximation. After characterization of the free cantilever resonance in air, the tip was brought in contact with the sample which was made oscillate by the piezoelectric transducer coupled with its back side. Values of $f_1$ and $f_3$ were obtained from statistics on the corresponding CRFs maps acquired simultaneously to the topographical images. For calibration purposes, CRFs maps on the reference sample were acquired before and after each measurement session. To limit the effect of tip wear, $CF_x$ samples were purposely analyzed following the decreasing order of their expected stiffness, i.e., starting from the sample expected to be the stiffer one. **Table 1** reports the values of $f_1$ and $f_3$ measured on the $CF_x$ samples and the corresponding value of $k^*$ calculated using the model in **Figure 1B**. The corresponding values of indentation modulus calculated through the "single reference" approach ($M_s^{s\text{-}r}$) are then reported. The measured values of CRFs confirm that the mechanical properties of the $CF_x$ samples are close to those of the reference PS film ($f_1 = 121-123$ kHz and $f_3 = 704-715$ kHz), encouraging the use of the "single reference" approach. Conversely, CRFs measured on LDPE seemed too low to use LDPE as a second reference sample ($f_1 = 111-112$ kHz and $f_3 = 660-685$ kHz). To verify the accuracy of the method, experimental data were analyzed through a numerical simulation (the "apparent stiffness" method). CR-AFM experiment was first simulated using the model in **Figure 1A** to obtain as output the pairs of CRFs $f_1$ and $f_3$ with a code which received as input the mechanical properties of the cantilever and the tip, their geometrical parameters, and the mechanical properties of the sample (Passeri et al., 2013b). The characteristic parameters of the system were optimized in order to simultaneously match $f_1$ and $f_3$ experimentally

**TABLE 1 |** Result of the nanomechanical characterizations using HarmoniX™ and CR-AFM: indentation modulus obtained with HarmoniX™ ($M_s$); first and third flexural CRFs ($f_1$ and $f_3$, respectively); calculated contact stiffness $k^*$; indentation modulus calculated using the "single reference" method and the "apparent stiffness" method ($M_s^{s-r}$ and $M_s^{a-s}$, respectively).

| | HarmoniX™ | CR-AFM | | | | |
|---|---|---|---|---|---|---|
| **Sample** | $M_s$ **(GPa)** | $f_1$ **(kHz)** | $f_3$ **(kHz)** | $k^*$ **(N/m)** | $M_s^{s-r}$ **(GPa)** | $M_s^{a-s}$ **(GPa)** |
| CFx-A | 1.18 ± 0.19 | 120.2 ± 0.4 | 711.5 ± 1.1 | 84 | 1.26 ± 0.13 | 1.27 ± 0.14 |
| CFx-B | 1.22 ± 0.20 | 121.2 ± 0.1 | 713.2 ± 1.5 | 91 | 1.43 ± 0.15 | 1.46 ± 0.16 |
| CFx-C | 1.51 ± 0.28 | 121.8 ± 0.3 | 715.2 ± 0.8 | 97 | 1.57 ± 0.16 | 1.59 ± 0.18 |

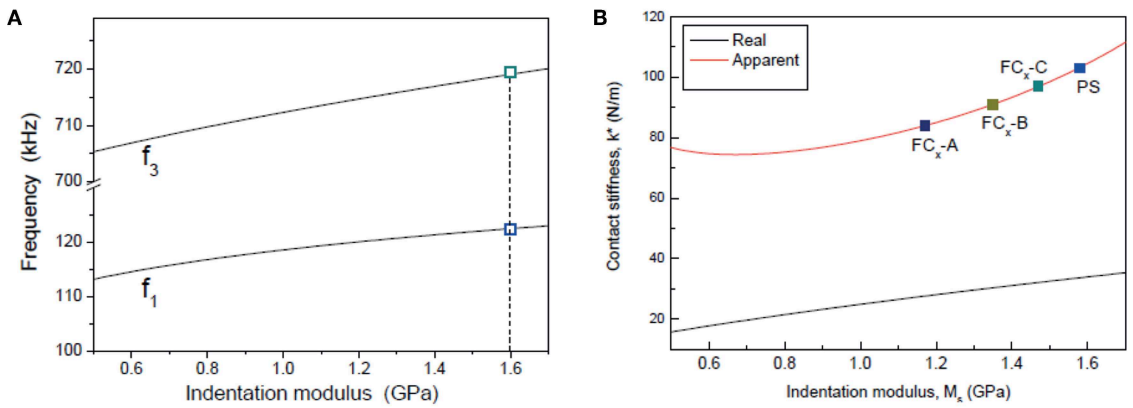


**FIGURE 7 | (A)** Values of the CRFs $f_1$ and $f_3$ calculated as a function of the sample indentation modulus $M_s$ using the model depicted in **Figure 1A** (solid lines) and values of $f_1$ and $f_3$ measured on the PS reference material (symbols). **(B)** Real and apparent contact stiffness (black and red solid line, respectively) as a function of the sample indentation modulus, and values corresponding to the $CF_x$ and PS samples (symbols).

**TABLE 2 |** Measured values of the contact resonance frequency and quality factor of the third mode of the cantilever ($f_3$ and $Q_3$, respectively), calculated values of the normalized contact stiffness ($\alpha$) and the normalized damping ($\beta$) and calculated values of the loss tangent $\tan\delta$, storage modulus ($E'$) and loss modulus ($E''$).

| **Sample** | $f_3$ **(kHz)** | $Q_3$ | $\alpha$ | $\beta$ | $\tan\delta$ | $E'$ **(GPa)** | $E''$ **(MPa)** |
|---|---|---|---|---|---|---|---|
| CFx-A | 711.5 ± 1.1 | 111 ± 7 | 724 | 0.057 | $7.37 \times 10^{-3}$ | 1.26 | 9.31 |
| CFx-B | 713.2 ± 1.5 | 137 ± 6 | 792 | 0.051 | $5.75 \times 10^{-3}$ | 1.45 | 8.31 |
| CFx-C | 715.2 ± 0.8 | 88 ± 5 | 833 | 0.011 | $1.21 \times 10^{-3}$ | 1.56 | 1.88 |

obtained in contact with the PS film. Pair of $f_1$ and $f_3$ were than calculated as a function of $M_s$ by varying $M_s$ in the range 0.5−1.7 GPa, obtaining the curves reported in **Figure 7A**, where the values of CRFs corresponding to the PS reference sample are indicated (symbols). Then, assuming the model in **Figure 1B**, for each $M_s$ the values of $f_1$ and $f_3$ were used to calculate $k^*$, which represents the "apparent" value of the tip-sample contact stiffness. Values of the apparent contact stiffness as a function of $M_s$ are shown in **Figure 7B** (red solid line). For comparison, the values of real contact stiffness calculated as $k^* \approx \sqrt[3]{6R_tF_NM_s^2}$ (black solid line), where $F_N$ is the static normal load applied by the cantilever during the contact and $M_s$ is used instead of the reduced modulus as $M_s \ll M_t$. As expected, the apparent value of $k^*$ is bigger than the real one as a result of neglecting lateral forces (Passeri et al., 2013b). Finally, the values of $k^*$ were calculated for the $CF_x$ samples using the model in **Figure 1B** and the curve of the apparent stiffness was used to determine the corresponding values of $M_s$ (symbols in **Figure 7B**). The procedure was repeated using the CRFs measured on the PS reference before and after the analysis of the $CF_x$ samples and the corresponding values of indentation modulus calculated using the "apparent stiffness" method ($M_s^{a-s}$) are reported in **Table 1**.

### 4.3.2. Viscoelastic Modulus

To characterize the viscoelastic response of the $CF_x$ films using CR-AFM, maps of the quality factor of the third mode ($Q_3$) have been acquired in addition to those of $f_3$ which are reported in **Table 2**. First, by approximating the samples as elastic, $f_1$ and $f_3$ were used as described in section 4.3.1 to determine the value of $r$, which was eventually used to calculate $\alpha$ and $\beta$ using a in-house written Matlab code (Passeri et al., 2013c) which are reported in **Table 2** together with the values of $\tan\delta$ calculated using Equation (7). The values of $\beta$ were used to calculate $E'$ through the "single reference" approach after determining $\beta$ on the PS reference sample and the values of $E''$ were determined as

$E' \times \tan\delta$. $E'$ and $E''$ calculated for the $CF_x$ samples are reported in **Table 2**.

## 5. DISCUSSION

$CF_x$ materials are attractive for the use as stent coatings, in particular after oxidative methanol plasma treatment which has been demonstrated to modulate the hydrophobicity of their surface in order to improve their performances, e.g., as far as blood contact behavior is regarded, without altering integrity, uniformity, and morphology (Montaño-Machado et al., 2019). Mechanical properties of $CF_x$ coatings can undergo significant changes when changes in the chemical composition and in the thickness occur. Indeed, it has been shown that fluorocarbon coatings thicker than 100 nm do not exhibit the required cohesion and adhesion properties to resist during stent expansion (Lewis et al., 2008). Furthermore, the elastic modulus of $CF_x$ coatings has been demonstrated to be strongly dependent on fluorine and crosslinking C–C units content (Tang et al., 2005). We showed that our methanol plasma treatment produces a significant increase of coating thickness and the decrease of fluorine content at the surface, which could significantly affect adhesion, cohesion and elastic modulus of the coatings. A comprehensive mechanical characterization was therefore necessary in order to evaluate the effect of methanol plasma treatment on the mechanical properties of the modified coatings.

Small punch tests have demonstrated that the innovative methanol plasma treatment does not undermine interfacial adhesion and cohesion to be employed as stent coatings as no delamination or cracks were observed even at plastic deformations as high as 25%, corresponding to the estimated maximum deformation which a stent may undergo during deployment (Migliavacca et al., 2005).

The effect of plasma treatment on mechanical properties of $CF_x$ films is another key issue that must be assessed to evaluate the suitability of $CF_x$ thin films as stent coatings. Indeed, depending on the polymerization and the post-deposition treatments, elastic modulus of $CF_x$ film is reported to vary from hundreds of megapascals like that of polytetrafluoroethylene (PTFE) (Ianev and Schwesinger, 2001), to a few gigapascals (Sirghi et al., 2009) and up to tens of gigapascals (Tang et al., 2005; Li et al., 2008; Koumoulos et al., 2012). Results reported in the present work show a good agreement between HarmoniX$^{TM}$ and CR-AFM. In particular, no discrepancies were observed between the two different methods for CR-AFM data analysis, i.e., the "single reference" approach and the simulation of the actual CRFs using the more comprehensive model depicted in **Figure 1A** and calculating the "apparent stiffness" using the simpler model in **Figure 1B**. The agreement between the two different approaches can be rationalized observing that all the investigated materials ($CF_x$ and PS) correspond to a region of the curve in **Figure 7B** in which $k^*$ is proportional to $M_s$, i.e., $k^* = cM_s$ being $c = 66$ nm. It must be observed that if softer materials were included among the investigated samples, the use of the single reference method using PS would imply an overestimation of their indentation modulus. Notably, considering the relatively large thickness of the coatings (i.e., in the range 30−60 nm), the similar nanometer tip-sample contact radius values typical of CR-AFM and HarmoniX$^{TM}$ make the results of both the techniques representative of the sole $CF_x$ thin films indentation modulus, without the effect of the stainless steel substrate (Reggente et al., 2017). This undoubtedly represents an advantage of these (and similar) techniques over AFM-based nanoindentation, which more extensively suffers from substrate effect in case of thin compliant films on stiff substrates (Kovalev et al., 2004; Shulha et al., 2004; Clifford and Seah, 2006; Passeri et al., 2011). Nevertheless, in case of thinner films are investigated and/or tip with larger $R_t$ are used, substrate effects may affect also CR-AFM and HarmoniX$^{TM}$ measurements and must be subtracted to obtain the elastic modulus of the sole film (Passeri et al., 2008, 2015). The obtained indentation modulus values, in the range 1.0−1.6 GPa, are compatible with those obtained on analogous materials using AFM based nanoindentation or conventional nanoindentation. Indeed, Sirghi et al. (2009) measured by AFM nanoindentation the elastic modulus of $CF_x$ films deposited by PECVD using $C_2F_8$ as precursor and found values between 1.75 GPa and 3.2 GPa depending on the deposition parameters (power of the RF discharge and dc bias potential). Tang et al. (2005) studied, by nanoindentation, the hardness and the elastic modulus of fluorocarbon coatings deposited by RF magnetron sputtering using a PTFE target using different process parameters (RF power, Ar and $H_2$ flux) and found a dependence of the studied properties with the fluorine and carbon content and, more specifically, on the content of $CF_x$ or C–C crosslinking units. The measured elastic modulus decreased with the increase of fluorine content (i.e., $CF_x$ units) and the decrease of carbon (i.e., crosslinking units) content from 18 GPa (for films having 33% fluorine and 67% carbon content) to 12 GPa (for films having 43% fluorine and 57% carbon content) (Tang et al., 2005). Considering the significantly higher fluorine content of our untreated $CF_x$ coating (66.9%), the value of the elastic modulus we measured by HarmoniX$^{TM}$ (1.18 GPa) and CR-AFM (1.26 GPa) appears to be coherent with the results of Tang et al. (2005). As shown in **Table 1**, indentation modulus of CFx films has been found dependent on the methanol plasma treatment. Indeed, a slight increase of the elastic modulus of the coating with the increase of the time of methanol plasma treatment was observed. An increase of about 30% is observed between the as prepared sample and that treated with methanol plasma for 90 s, which is coherent with the covering of the fluorocarbon coating by a thin layer of carbon and oxygen species not containing fluoride.

As expected, an analogous dependence with plasma exposure time is observed in the measured viscoelastic parameters, i.e., in $E'$, $E''$, and $\tan\delta$. In particular, although the comparison with PTFE properties is not always straightforward, we observe that the values of $E'$ obtained on both untreated and plasma treated $CF_x$ films are coherent with those reported for PTFE (Faughnan et al., 1998; Fu and Chung, 2001; Blumm et al., 2010). Conversely, the values of $\tan\delta$ ad thus of $E''$ are definitely lower than those observed on PTFE, indicating that the mechanical behavior of the films is characterized by a very low viscous component. However, it should be observed that viscoelastic parameters generally depend on the frequency at which the mechanical response of

the material is investigated, e.g., the viscous component may either increase or decrease with the frequency and depends on the specific polymer (Le Rouzic et al., 2009). Results by standard dynamical mechanical analysis (DMA) usually reported in literature are generally obtained for low frequency values, e.g., not exceeding 100 Hz, while CR-AFM investigates the sample at much higher frequencies, e.g., from tens to hundreds kilohertz or even a few megahertz (Hurley et al., 2013). In any case, plasma treatment is observed to be responsible for the reduction of the viscous component of the mechanical response of the films with respect to the untreated sample.

## 6. CONCLUSION

In conclusion, mechanical characterization of methanol plasma treated $CF_x$ ultrathin films on stainless steel demonstrated that methanol plasma treatment does not affect cohesion of the films and their adhesion to the substrate after deformation. Also, nanoscale analysis of elastic and viscoelastic response of films indicated that although these are slightly affected by methanol plasma, which is responsible for the stiffening and reduction of viscosity of the films. Nevertheless, such an effect is admittedly marginal and, especially from the point of view of the biological response, methanol plasma treatment does not significantly modify mechanical properties of the films. Thus, methanol plasma is a promising route to treat $CF_x$ ultrathin stent coating, which allows the modulation of the wettability (and fluorine content) of $CF_x$ coatings, without affecting their integrity, morphology, adhesion, and cohesion of the coatings, as well as their elastic and viscoelastic properties.

## DATA AVAILABILITY STATEMENT

The datasets generated for this study are available on request to the corresponding author.

## AUTHOR CONTRIBUTIONS

LA realized the $CF_x$ thin films and carried out chemical and ancillary characterizations, small punch test, and AFM morphological analysis under the supervision of PC, ST, and DM. MRe performed the AFM based mechanical nanocharacterizations with the supervision of DP. MRe and DP analyzed the results of mechanical tests, with the supervision of MRo. MRe, LA, and DP wrote the first draft of the manuscript which was then revised by all the authors.

## ACKNOWLEDGMENTS

Dr. Francesco Mura is cordially acknowledged for his help with the characterizations of AFM cantilevers using scanning electron microscopy (SEM) platform at Research Center for Nanotechnology Applied to Engineering of Sapienza University of Rome (CNIS).

## REFERENCES

Amelio, S., Goldade, A. V., Rabe, U., Scherer, V., Bhushan, B., and Arnold, W. (2001). Measurement of elastic properties of ultra-thin diamond-like carbon coatings using atomic force acoustic microscopy. *Thin Solid Films* 392, 75–84. doi: 10.1016/S0040-6090(01)00903-8

Arima, Y., and Iwata, H. (2007). Effect of wettability and surface functional groups on protein adsorption and cell adhesion using well-defined mixed self-assembled monolayers. *Biomaterials* 28, 3074–3082. doi: 10.1016/j.biomaterials.2007.03.013

Blumm, J., Lindemann, A., Meyer, M., and Strasser, C. (2010). Characterization of PTFE using advanced thermal analysis techniques. *Int. J. Thermophys.* 31, 1919–1927. doi: 10.1007/s10765-008-0512-z

Boehm, H. P. (2002). Surface oxides on carbon and their analysis: a critical assessment. *Carbon* 40, 145–149. doi: 10.1016/S0008-6223(01)00165-8

Bourgoin, D., Turgeon, S., and Ross, G. G. (1999). Characterization of hydrogenated amorphous carbon films produced by plasma-enhanced chemical vapour deposition with various chemical hybridizations. *Thin Solid Films* 357, 246–253. doi: 10.1016/S0040-6090(99)00536-2

Califano, J. P., and Reinhart-King, C. A. (2008). A balance of substrate mechanics and matrix chemistry regulates endothelial cell network assembly. *Cell. Mol. Bioeng.* 1:122. doi: 10.1007/s12195-008-0022-x

Califano, J. P., and Reinhart-King, C. A. (2010). Substrate stiffness and cell area predict cellular traction stresses in single cells and cells in contact. *Cell. Mol. Bioeng.* 3, 68–75. doi: 10.1007/s12195-010-0102-6

Chowdhury, F., Na, S., Li, D., Poh, Y. C., Tanaka, T. S., Wang, F., et al. (2010). Material properties of the cell dictate stress-induced spreading and differentiation in embryonic stem cells. *Nat. Mater.* 9, 82–88. doi: 10.1038/nmat2563

Clifford, C. A., and Seah, M. P. (2006). Modelling of nanomechanical nanoindentation measurements using an AFM or nanoindenter for compliant layers on stiffer substrates. *Nanotechnology* 17, 5283–5292. doi: 10.1088/0957-4484/23/16/165704

Derjaguin, B. V., Muller, V. M., and Toporov, Y. P. (1975). Effect of contact deformation on the adhesion of particles. *J. Colloid Interf. Sci.* 53, 314–326. doi: 10.1016/0021-9797(75)90018-1

Dokukin, M. E., and Sokolov, I. (2012). Quantitative mapping of the elastic modulus of soft materials with HarmoniX and PeakForce QNM AFM modes. *Langmuir* 28, 16060–16071. doi: 10.1021/la302706b

Engler, A., Bacakova, L., Newman, C., Hategan, A., Griffin, M., and Discher, D. (2004a). Substrate compliance versus ligand density in cell on gel responses. *Biophys. J.* 86, 617–628. doi: 10.1016/S0006-3495(04)74140-5

Engler, A. J., Griffin, M. A., Sen, S., Bönnemann, C. G., Sweeney, H. L., and Discher, D. E. (2004b). Myotubes differentiate optimally on substrates with tissue-like stiffness. *J. Cell Biol.* 166, 877–887. doi: 10.1083/jcb.200405004

Engler, A. J., Sen, S., Sweeney, H. L., and Discher, D. E. (2006). Matrix elasticity directs stem cell lineage specification. *Cell* 126, 677–689. doi: 10.1016/j.cell.2006.06.044

Faughnan, P., Bryan, C., Gan, Y., and Aglan, H. (1998). Correlation between the dynamic mechanical properties and the fatigue behavior of filled and unfilled PTFE materials. *J. Mater. Sci. Lett.* 17, 1743–1746. doi: 10.1023/A:1006695723138

Fischer-Cripps, A. C. (2006). Critical review of analysis and interpretation of nanoindentation test data. *Surf. Coat. Tech.* 200, 4153–4165. doi: 10.1016/j.surfcoat.2005.03.018

Flanagan, L. A., Ju, Y. E., Marg, B., Osterfield, M., and Janmey, P. A. (2002). Material properties of the cell dictate stress-induced spreading and differentiation in embryonic stem cells. *Neuroreport* 13, 2411–2415. doi: 10.1097/01.wnr.0000048003.96487.97

Fu, W., and Chung, D. D. L. (2001). Vibration reduction ability of polymers, particularly polymethylmethacrylate and polytetrafluoroethylene. *Polym. Polym. Compos.* 9, 423–426. doi: 10.1177/096739110100900607

García, R., and San Paulo, A. (1999). Attractive and repulsive tip-sample interaction regimes in tapping-mode atomic force microscopy. *Phys. Rev. B* 60, 4961–4967. doi: 10.1103/PhysRevB.60.4961

Green, C. P., Lioe, H., Cleveland, J. P., Proksch, R., Mulvaney, P., and Sader, J. E. (2004). Normal and torsional spring constants of atomic force microscope cantilevers. *Rev. Sci. Instrum.* 75, 1988–1996. doi: 10.1063/1.1753100

Guo, W. H., Frey, M. T., Burnham, N. A., and Wang, Y. L. (2006). Substrate rigidity regulates the formation and maintenance of tissues. *Biophys. J.* 90, 2213–2220. doi: 10.1529/biophysj.105.070144

Haïdopoulos, M., Turgeon, S., Laroche, G., and Mantovani, D. (2005). Chemical and morphological characterization of ultra-thin fluorocarbon plasma-polymer deposition on 316 stainless steel substrates: a first step toward the improvement of the long-term safety of coated-stents. *Plasma Process. Polym.* 2, 424–440. doi: 10.1002/ppap.200400066

Hopp, I., Michelmore, A., Smith, L. E., Robinson, D. E., Bachhuka, A., Mierczynska, A., et al. (2013). The influence of substrate stiffness gradients on primary human dermal fibroblasts. *Biomaterials* 34, 5070–5077. doi: 10.1016/j.biomaterials.2013.03.075

Horie M. (1995). Plasma-structure dependence of the growth mechanism of plasma-polymerized fluorocarbon films with residual radicals. *J. Vac. Sci. Technol. A* 13, 2490–2497. doi: 10.1116/1.579493

Hurley, D. C., Campbell, S. E., Killgore, J. P., Cox, L. M., and Ding, Y. (2013). Measurement of viscoelastic loss tangent with contact resonance modes of atomic force microscopy. *Macromolecules* 46, 9396–9402. doi: 10.1021/ma401988h

Hurley, D. C., Kopycinska-Müller, M., Kos, A. B., and Geiss, R. H. (2005). Nanoscale elastic-property measurements and mapping using atomic force acoustic microscopy methods. *Meas. Sci. Technol.* 16, 2167–2172. doi: 10.1088/0957-0233/16/11/006

Ianev, V., and Schwesinger, N. (2001). "Improving the adhesion of plasma polymerized thin fluorocarbon films on silicon using ($CHF_3$ + $SF_6$) radio-frequency discharge pretreatments," in *Adhesion Aspects of Thin Films*, Vol. 1, ed K. L. Mittal (Leiden: VSP International Science), 261–270.

Johnson, K. L., Kendall, K., and Roberts, A. D. (1971). Surface energy and the contact of elastic solids. *Proc. R. Soc. A* 324, 301–313. doi: 10.1098/rspa.1971.0141

Kester, E., Rabe, U., Presmanes, L., Tailhades, P., and Arnold, W. (2000). Measurement of Young's modulus of nanocrystalline ferrites with spinel structures by atomic force acoustic microscopy. *J. Phys. Chem. Solids* 61, 1275–1284. doi: 10.1016/S0022-3697(99)00412-6

Killgore, J. P., and DelRio, F. W. (2018). Contact resonance force microscopy for viscoelastic property measurements: from fundamentals to state-of-the-art applications. *Macromolecules* 51, 6977–6996. doi: 10.1021/acs.macromol.8b01178

Killgore, J. P., and Hurley, D. C. (2012). Low-force AFM nanomechanics with higher-eigenmode contact resonance spectroscopy. *Nanotechnology* 23:055702. doi: 10.1088/0957-4484/23/5/055702

Killgore, J. P., Yablon, D. G., Tsou, A. H., Gannepalli, A., Yuya, P. A., Turner, J. A., et al. (2011). Viscoelastic property mapping with contact resonance force microscopy. *Langmuir* 27, 13983–13987. doi: 10.1021/la203434w

Kopycinska-Müller, M., Geiss, R. H., and Hurley, D. C. (2006). Contact mechanics and tip shape in AFM-based nanomechanical measurements. *Ultramicroscopy* 106, 466–474. doi: 10.1016/j.ultramic.2005.12.006

Koumoulos, E. P., Charitidis, C. A., Papageorgiou, D. P., Papathanasiou, A. G., and Boudouvis, A. G. (2012). Nanomechanical and nanotribological properties of hydrophobic fluorocarbon dielectric coating on tetraethoxysilane for electrowetting applications. *Surf. Coat. Tech.* 206, 3823–3831. doi: 10.1016/j.surfcoat.2012.01.034

Kovalev, A., Shulha, H., Lemieux, M., Myshkin, N., and Tsukruk, V. V. (2004). Nanomechanical probing of layered nanoscale polymer films with atomic force microscopy. *J. Mater. Res.* 19, 716–728. doi: 10.1557/jmr.2004.19.3.716

Le Rouzic, J., Delobelle, P., Vairac, P., and Cretin, B. (2009). Comparison of three different scales techniques for the dynamic mechanical characterization of two polymers (PDMS and SU8). *Eur. Phys. J. Appl. Phys.* 48:11201. doi: 10.1051/epjap/2009124

Lewis, F., Horny, P., Hale, P., Turgeon, S., Tatoulian, M., and Mantovani, D. (2008). Study of the adhesion of thin plasma fluorocarbon coatings resisting plastic deformation for stent applications. *J. Phys. D Appl. Phys.* 41:045310. doi: 10.1088/0022-3727/41/4/045310

Lewis, F., Maheux-Lacroix, B., Turgeon, S., and Mantovani, D. (2007). "Adhesion assessment of ultra-thin plasma polymerized coatings on stainless steel stents using the small punch test," in *Adhesion Aspects of Thin Films*, Vol. 3, ed M. L. Mittal (Leiden: VSP International Science), 71–83.

Li, L., Zi, F., and Zheng, Y. (2008). The characterization of fluorocarbon films on NiTi alloy by magnetron sputtering. *Appl. Surf. Sci.* 255, 432–434. doi: 10.1016/j.apsusc.2008.06.174

Lo, C. M., Wang, H. B., Dembo, M., and Wang, Y. L. (2000). Cell movement is guided by the rigidity of the substrate. *Biophys. J.* 79, 144–152. doi: 10.1016/S0006-3495(00)76279-5

Mackie, N. M., Dalleska, N. F., Castner, D. G., and Fisher, E. R. (1997). Comparison of pulsed and continuous-wave deposition of thin films from saturated fluorocarbon/$H_2$ inductively coupled rf plasmas. *Chem. Mater.* 9, 349–362. doi: 10.1021/cm960388q

Marinello, F., Schiavuta, P., Carmignato, S., and Savio, E. (2010). Critical factors in quantitative atomic force acoustic microscopy. *CIRP J. Manuf. Sci. Technol.* 3, 49–54. doi: 10.1016/j.cirpj.2010.05.004

Marinello, F., Schiavuta, P., Vezzù, S., Patelli, A., Carmignato, S., and Savio, E. (2011). Atomic force acoustic microscopy for quantitative nanomechanical characterization. *Wear* 271, 534–538. doi: 10.1016/j.wear.2010.03.032

Migliavacca, F., Petrini, L., Montanari, V., Quagliana, I., Auricchio, F., and Dubini, G. (2005). A predictive study of the mechanical behaviour of coronary stents by computer modelling. *Med. Eng. Phys.* 27, 13–18. doi: 10.1016/j.medengphy.2004.08.012

Montaño-Machado, V., Angeloni, L., Chevallier, P., Klak, M. C., Turgeon, S., Rossi, M., et al. (2019). Oxidative plasma treatment of fluorocarbon surfaces for blood-contacting applications. *Mater. Sci. Forum* 941, 2528–2533. doi: 10.4028/www.scientific.net/MSF.941.2528

Montaño-Machado, V., Noël, C., Chevallier, P., Turgeon, S., Houssiau, L., Pauthe, E., et al. (2017). Interaction of phosphorylcholine with fibronectin coatings: surface characterization and biological performances. *Appl. Surf. Sci.* 396, 1613–1622. doi: 10.1016/j.apsusc.2016.11.224

Passeri, D., Alippi, A., Bettucci, A., Rossi, M., Alippi, A., Tamburri, E., et al. (2011). Indentation modulus and hardness of polyaniline thin films by atomic force microscopy. *Synth. Met.* 161, 7–12. doi: 10.1016/j.synthmet.2010.10.027

Passeri, D., Bettucci, A., Germano, M., Rossi, M., Alippi, A., Orlanducci, S., et al. (2005). Effect of tip geometry on local indentation modulus measurement via atomic force acoustic microscopy technique. *Rev. Sci. Instrum.* 76:093904. doi: 10.1063/1.2044607

Passeri, D., Biagioni, A., Rossi, M., Tamburri, E., and Terranova, M. L. (2013c). Characterization of polyaniline-detonation nanodiamond nanocomposite fibers by atomic force microscopy based techniques. *Eur. Polym. J.* 49, 991–998. doi: 10.1016/j.eurpolymj.2013.02.003

Passeri, D., Rossi, M., Alippi, A., Bettucci, A., Manno, D., Serra, A., et al. (2008). Atomic force acoustic microscopy characterization of nanostructured selenium-tin thin films. *Superlattices Microstruct.* 44, 641–649. doi: 10.1016/j.spmi.2007.10.004

Passeri, D., Rossi, M., Tamburri, E., and Terranova, M. L. (2013a). Mechanical characterization of polymeric thin films by atomic force microscopy based techniques. *Anal. Bioanal. Chem.* 405, 1463–1478. doi: 10.1007/s00216-012-6419-3

Passeri, D., Rossi, M., and Vlassak, J. J. (2013b). On the tip calibration for accurate modulus measurement by contact resonance atomic force microscopy. *Ultramicroscopy* 128, 32–41. doi: 10.1016/j.ultramic.2013.02.003

Passeri, D., Tamburri, E., Terranova, M. L., and Rossi, M. (2015). Polyaniline-nanodiamond fibers resulting from the self-assembly of nano-fibrils: a nanomechanical study. *Nanoscale* 7, 14358–14367. doi: 10.1039/c5nr02096d

Pettersson, T., Nordgren, N., Rutland, M. W., and Feiler, A. (2007). Comparison of different methods to calibrate torsional spring constant and photodetector for atomic force microscopy friction measurements in air and liquid. *Rev. Sci. Instrum.* 78:093702. doi: 10.1063/1.2779215

Qiu, Y., Brown, A. C., Myers, D. R., Sakurai, Y., Mannino, R. G., Tran, R., et al. (2014). Platelet mechanosensing of substrate stiffness during clot formation mediates adhesion, spreading, and activation. *Proc. Natl. Acad. Sci. U.S.A.* 111, 14430–14435. doi: 10.1073/pnas.1322917111

Rabe, U., and Arnold, W. (1994). Acoustic microscopy by atomic force microscopy. *Appl. Phys. Lett.* 64, 1493–1495. doi: 10.1063/1.111869

Rabe, U., Janser, J., and Arnold, W. (1996). Vibration of free and surface-coupled atomic force microscope cantilevers: theory and experiment. *Rev. Sci. Instrum.* 67, 3281–3293. doi: 10.1063/1.1147409

Reggente, M., Natali, M., Passeri, D., Lucci, M., Davoli, I., Pourroy, G., et al. (2017). Multiscale mechanical characterization of hybrid Ti/PMMA layered materials. *Colloid. Surface. A* 532, 244–251. doi: 10.1016/j.colsurfa.2017.05.011

Reggente, M., Rossi, M., Angeloni, L., Tamburri, E., Lucci, M., Davoli, I., et al. (2015). Atomic force microscopy techniques for nanomechanical characterization: a polymeric case study. *JOM* 67, 849–857. doi: 10.1007/s11837-015-1340-9

Sader, J. E., Chon, J. W. M., and Mulvaney, P. (1999). Calibration of rectangular atomic force microscope cantilevers. *Rev. Sci. Instrum.* 70, 3967–3969. doi: 10.1063/1.1150021

Sahin, O., and Erina, N. (2008). High-resolution and large dynamic range nanomechanical mapping in tapping-mode atomic force microscopy. *Nanotechnology* 19:445717. doi: 10.1088/0957-4484/19/44/445717

Sahin, O., Magonov, S., Su, C., Quate, C. F., and Solgaard, O. (2007). An atomic force microscope tip designed to measure time-varying nanomechanical forces. *Nat. Nanotechnol.* 2, 507–514. doi: 10.1038/nnano.2007.226

Santos, S., Barcons, V., Christenson, H. K., Font, J., and Thomson, N. H. (2011). The intrinsic resolution limit in the atomic force microscope: implications for heights of nano-scale features. *PLoS ONE* 6:e23821. doi: 10.1371/journal.pone.0023821

Shulha, H., Kovalev, A., Myshkin, N., and Tsukruk, V. V. (2004). Some aspects of afm nanomechanical probing of surface polymer films. *Eur. Polym. J.* 40, 949–956. doi: 10.1016/j.eurpolymj.2004.01.021

Sirghi, L., Ruiz, A., Colpo, P., and Rossi, F. (2009). Atomic force microscopy indentation of fluorocarbon thin films fabricated by plasma enhanced chemical deposition at low radio frequency power. *Thin Solid Films* 517, 3310–3314. doi: 10.1016/j.tsf.2009.01.055

Stan, G., and Cook, R. F. (2008). Mapping the elastic properties of granular Au films by contact resonance atomic force microscopy. *Nanotechnology* 19:235701. doi: 10.1088/0957-4484/19/23/235701

Stan, G., and Price, W. (2006). Quantitative measurements of indentation moduli by atomic force acoustic microscopy using a dual reference method. *Rev. Sci. Instrum.* 77:103707. doi: 10.1063/1.2360971

Subramanian, A., and Lin, H. Y. (2005). Crosslinked chitosan: its physical properties and the effects of matrix stiffness on chondrocyte cell morphology and proliferation. *J. Biomed. Mater. Res. A* 75A, 742–753. doi: 10.1002/jbm.a.30489

Tang, G., Ma, X., Sun, M., and Li, X. (2005). Mechanical characterization of ultra-thin fluorocarbon films deposited by R.F. magnetron sputtering. *Carbon* 43, 345–350. doi: 10.1016/j.carbon.2004.09.022

Thevenot, P., Hu, W., and Tang, L. (2008). Surface chemistry influences implant biocompatibility. *Curr. Top. Med. Chem.* 8, 270–280. doi: 10.2174/156802608783790901

Touzin, M., Chevallier, P., Turgeon, S., Horny, P., and Mantovani, D. (2010). Evaluation of the corrosion protection of ultra-thin plasma fluorocarbon film deposited on 316l stainless steel for long-term stable stents. *Mater. Sci. Forum* 638, 10–15. doi: 10.4028/www.scientific.net/MSF.638-642.10

Wagner, R., and Killgore, J. P. (2015). Photothermally excited force modulation microscopy for broadband nanomechanical property measurements. *Appl. Phys. Lett.* 107:203111. doi: 10.1063/1.4935982

Yamanaka, K., Kobari, K., and Tsuji, T. (2008). Evaluation of functional materials and devices using atomic force microscopy with ultrasonic measurements. *Jpn. J. Appl. Phys.* 47, 6070–6076. doi: 10.1143/jjap.47.6070

Yamanaka, K., Tsuji, T., Noguchi, A., Koike, T., and Mihara, T. (2000). Nanoscale elasticity measurement with *in situ* shape estimation in atomic force microscopy. *Rev. Sci. Instrum.* 71, 2403–2408. doi: 10.1063/1.1150627

Yuya, P. A., Hurley, D. C., Turner, J. A. (2008). Contact-resonance atomic force microscopy for viscoelasticity. *J. Appl. Phys.* 104:074916. doi: 10.1063/1.2996259

Yuya, P. A., Hurley, D. C., and Turner, J. A. (2011). Relationship between Q-factor and sample damping for contact resonance atomic force microscope measurement of viscoelastic properties. *J. Appl. Phys.* 109:113528. doi: 10.1063/1.3592966

**Conflict of Interest:** The authors declare that the research was conducted in the absence of any commercial or financial relationships that could be construed as a potential conflict of interest.

frontiers in Materials

ORIGINAL RESEARCH
published: 28 January 2020
doi: 10.3389/fmats.2019.00348

# Correlative Analysis of Specific Compatibilization in Composites by Coupling *in situ* X-Ray Scattering and Mechanical Tensile Testing

*Britta Seidt*[1,2], *Valeria Samsoninkova*[1,2,3], *Felix Hanßke*[3], *André Gjardy*[1], *Peter Fratzl*[1], *Hans G. Börner*[3] *and Wolfgang Wagermaier*[1]*

[1] Department of Biomaterials, Max Planck Institute of Colloids and Interfaces, Potsdam, Germany, [2] School of Analytical Sciences Adlershof, Humboldt-Universität zu Berlin, Berlin, Germany, [3] Laboratory for Organic Synthesis of Functional Systems, Department of Chemistry, Humboldt-Universität zu Berlin, Berlin, Germany

In this study, a bio-inspired hybrid material is investigated by *in situ* X-ray scattering experiments in combination with mechanical tensile testing. The material is composed of nanometer-sized spherical magnesium fluoride particles which are linked via material-specific peptide poly(ethylene glycol)-PEG conjugates to a semi-crystalline poly(ethylene oxide) PEO matrix. Mechanically relevant changes in crystal size and orientation in the PEO matrix are followed by wide angle X-ray scattering during the application of tensile stress. The amorphous phase of PEO is stabilized by the surface-engineered $MgF_2$ nanoparticles, leading to increased Young's modulus and tensile strength. Furthermore, small angle X-ray scattering experiments allowed the identification of a layer on the $MgF_2$ particle surfaces, which increases in thickness with the conjugate amount and leads to suppression of the agglomeration of $MgF_2$ nanoparticles. In conclusion, the use of selected peptide-PEG conjugates tailored to link $MgF_2$ particles to a PEO matrix successfully mimics the biological principle of interface polymers and suggests new directions for material fabrication for bio-applications.

**Keywords: wide and small angle X-ray scattering, peptide-polymer conjugate, structure-function relationships, interface stabilization, functional material**

OPEN ACCESS

***Edited by:***
*Mario Guagliano, Politecnico di Milano, Italy*

***Reviewed by:***
*Leif Erik Asp, Chalmers University of Technology, Sweden*
*Hortense Le Ferrand, Nanyang Technological University, Singapore*

***Correspondence:**
*Wolfgang Wagermaier*
*wagermaier@mpikg.mpg.de*

***Specialty section:***
*This article was submitted to Polymeric and Composite Materials, a section of the journal Frontiers in Materials*

***Received:*** *14 August 2019*
***Accepted:*** *31 December 2019*
***Published:*** *28 January 2020*

***Citation:***
*Seidt B, Samsoninkova V, Hanßke F, Gjardy A, Fratzl P, Börner HG and Wagermaier W (2020) Correlative Analysis of Specific Compatibilization in Composites by Coupling in situ X-Ray Scattering and Mechanical Tensile Testing. Front. Mater. 6:348. doi: 10.3389/fmats.2019.00348*

## INTRODUCTION

Inorganic fillers are widely used in synthetic polymers as well as in natural hybrid materials to enhance their mechanical performance. Especially biological hybrid materials, made of inorganic nanoparticles embedded in an organic matrix, are of great interest for material scientists in terms of their mechanical performance (Studart, 2012; Wegst et al., 2015). Bio-inspired hybrid materials with defined structuring of the material constituents across various length scales as well as precisely defined internal material interfaces exhibit advanced material properties (Bonderer et al., 2008; Munch et al., 2008; Studart, 2012; Wegst et al., 2015). Nature shows many examples of materials where the control over size, shape, and distribution of the composites' building blocks leads to hierarchically structured materials with outstanding mechanical properties. Bone is probably one of the most prominent examples of hierarchically structured hybrid materials with well-dispersed inorganic hydroxyapatite particles in a collagen matrix and tailored internal interfaces between these constituents (Fratzl et al., 2004b). The dominating influence of the nanostructure of hybrid

materials on their mechanical properties does not only depend on the properties of the individual components, but also on the interfaces between the components (Dujardin and Mann, 2002; Fratzl et al., 2004a; Meyers et al., 2008; Laaksonen et al., 2012). In Nature, the hydroxyapatite platelets in bone are bound to the collagen matrix by proteoglycans (Fratzl, 2003a; Fratzl et al., 2004a; Gupta et al., 2005) and the aragonite mineral crystals in nacre are linked by a series of proteins (Currey, 1977; Espinosa et al., 2009; Laaksonen et al., 2012). This concept of linking immiscible components by adding further polymer components to reduce the interfacial tension between phases is also used in hybrid materials science and usually termed as compatibilization (Kickelbick, 2003). The components are connected by thin layers of proteins that bind to the inorganic surfaces and compatibilize into the organic matrix to act as glue stabilizing the internal interfaces. The mineral phase in these materials provides strength, while the soft matrix allows ductility and toughness.

Research has been undertaken in recent years to develop new synthetic processing routes by applying design principles of Nature (Studart, 2012). One of the technical challenges during the embedding process of nanoparticles into the organic matrix is to avoid particle agglomeration to produce hybrid materials with homogeneously dispersed fillers. A large and diverse set of techniques is available in literature for the fabrication of bio-inspired hybrid materials, lasting from virus-based self-assembly to electrochemical deposition and sol-gel synthesis (Gregorczyk and Knez, 2016). Kemnitz et al. (2003) established a fluorolytic sol-gel synthesis for the preparation of nanoscopic metal fluorides with extraordinarily high specific surface areas. By using phosphonic acids to prevent agglomeration, Noack et al. (2011) utilized fluoride $MgF_2$ nanoparticles to prepare transparent organic-inorganic nanocomposites made of magnesium fluoride homogenously dispersed in organic polymers. $MgF_2$ has been shown to potentially being used in various biomedical applications, e.g., to coat the surface of biodegradable scaffolds for improved corrosion resistance and biological performance (Kang et al., 2016). Polymer composites consisting $MgF_2$ nanoparticles exhibit good biocompatibility and improved mechanical properties (Hansske et al., 2017).

In the last decades, few bio-inspired concepts were developed to tailor the interfaces between organic matrix and inorganic particles in synthetic hybrid materials (Palmer et al., 2008; Sommerdijk and de With, 2008; Hardy and Scheibel, 2010; Wang et al., 2011), e.g., by the use of material-affine peptide-PEG conjugates binding to the inorganic particles as well as anchoring the particles in the organic matrix (Hansske et al., 2015; Samsoninkova et al., 2017). By using a bio-combinatorial approach Hanßke et al. introduced specific stabilizers for sol-gel processes, which enable access to *de novo* modifying agents (Hansske et al., 2015). Twelve-mer peptides (comprised of 12 amino acids) have been selected from large peptide libraries covering a sequential space of $\sim 10^9$ different peptides. According to the adsorption behavior onto $MgF_2$ surfaces the most promising sequence was synthesized as a peptide-PEG conjugate (Hansske et al., 2015). The conjugates proved sequence-specific interactions with $MgF_2$ materials in a sol state, effectively stabilizing the sols in solution via surface modification and provided completely redispersible nanoparticles.

By using the peptide-PEG conjugates to stabilize and compatibilize $MgF_2$ nanoparticles in a PEO matrix Samsoninkova et al. prepared bio-inspired hybrid materials, which presented remarkable material properties in terms of stiffness and toughness (Samsoninkova et al., 2017). Increased Young's modulus ($E$) values and increased tensile toughness ($R_m$) values could be achieved. TEM showed an effective reduction of agglomeration and also influences on the form of the formed agglomerates by the presence of the peptide-PEG conjugates have been evident. SAXS measurements revealed sizes of primary particles to be in the range of 2–3 nm, while larger agglomerates of those were also present.

Within this study, structure-function relationship in model hybrid materials made of a PEO matrix and $MgF_2$ nanoparticles compatibilized by peptide-PEG conjugates were explored in view of material fabrication for bio-applications. The PEO matrix consists of (lamellar) crystalline and amorphous domains. The amounts of particles and conjugate were elucidated to optimize the mechanical performance of the hybrid materials. Multi-scale analysis tools were applied to perform simultaneous mechanical tensile testing and X-ray scattering experiments. By this approach, the role of unmodified nanoparticles, the use of the peptide-PEG conjugates alone and the combination of inorganic nanoparticles compatibilized by peptide-PEG conjugates in the PEO matrix in terms of the mechanical properties of the material were investigated. Changes in crystal orientation during applied tensile stress were followed to describe mechanically relevant reorientation effects of the crystalline domains. By examining the crystallite size and the deformation of the crystallites by recording the micro strain *in situ* on the crystallites, the crystalline as well as the amorphous phase were investigated.

# EXPERIMENTAL SECTION

## Sample Preparation

The hybrid materials were synthesized following a protocol described previously (Samsoninkova et al., 2017). In short, the surfaces of the spherical $MgF_2$ particles with a size of around 2–3 nm were non-covalently coated with a tailor-made peptide-PEG conjugate containing a monodisperse $MgF_2$-binding peptide sequence and a PEG block ($M_n = 3200\ g/mol$; GTQYYAYSTTQKS-*block*-$PEG_{73}$) to enhance the interactions with the PEO matrix material ($M_n = 900.000\ g/mol$) (Hansske et al., 2015). After solution blending in methanol, the hybrid materials were hot-pressed into thin hybrid films with a thickness of around 200 μm. Hot pressing of the hybrid materials was performed on a SPECAC device from Specac Limited (Orpington, UK) at a constant temperature of 70°C. First, the hybrid materials were heated without load for 3 min and then 1 ton of pressure was applied for 1 min, followed by 2 tons of pressure for 3 min. After cooling, samples were punched out with

**Abbreviations:** PEG, poly(ethylene glycol); PEO, poly(ethylene oxide); TEM, transmission electron microscopy; SAXS, small angle X-ray scattering; WAXS, wide angle X-ray scattering.

a bone-shaped stamp to match the tensile testing set-up. The sample compositions for the hybrid films were chosen with 15 wt.% $MgF_2$ and 0.5, 1.0, 2.0, 3.0, and 6.0 mol% conjugate, with non-filled PEO, PEO in combination with 3 mol% conjugate compatibilizer as well as PEO in combination with 15 wt.% $MgF_2$ fillers without the presence of compatibilizers as references.

## X-Ray Scattering Experiments and Mechanical Tensile Testing

X-ray scattering experiments were performed at the synchrotron source BESSY II [Helmholtz-Zentrum Berlin für Materialien und Energie (HZB), Adlershof, Germany] at the μSpot beamline. Using a synchrotron source has the advantage that SAXS and WAXS measurements are possible simultaneously and a suitable time resolution is facilitated which is required for combined X-ray scattering and *in situ* tensile testing. X-ray patterns were recorded using an X-ray beam (100 μm in diameter; wavelength $\lambda = 0.82656$ Å) with a 2D CCD detector (MarMosaic 225, Rayonix Inc., Evanston, U.S.A.) with a pixel size of 73.242 μm and an array of 3,072 × 3,072 pixels. The calibrations of the sample-to-detector distance and beam center were performed using a quartz standard and analyzed with the software Fit2d (by Andy Hammersley, ESRF, v. 12.077). All patterns were corrected for empty beam background. Using the software packages DPDAK (Benecke et al., 2014) and OriginPro data evaluation was performed.

The crystallite sizes $L$ of the polymer matrix were calculated by using the Scherrer equation:

$$L = \frac{k*\lambda}{C^* cos\,(\theta)}.$$

in which $\lambda$ represents the wavelength, $C$ the full width at half maximum of the (120) peak, $\theta$ the Bragg angle of the (120) peak and the Scherrer constant $k$ (Holzwarth and Gibson, 2011). To correct the peak widths for instrumental broadening the measurements were performed using a Si111 monochromator with known instrumental contributions to $C$.

The tensile testing device was developed to perform simultaneous X-ray scattering experiments and mechanical tensile testing at a synchrotron source. A 20 N load cell (11E-020N-1a, Althen, Kelkheim, Germany) was used with a DC-encoder motor (M-126 DG, Physik Instrumente, Karlsruhe, Germany) to fit the requirements of the samples. To track the strain of the samples during tensile stress over the whole sample area and to perform video extensometry a camera (piA2400-17gm, pilot serie, Basler AG, Ahrensburg, Germany) with corresponding objective (TC 23 024, 2/3-Mpx detector, OPTO Engineering, Munich Germany) was used. **Figure 1** shows the schematic design of the *in-situ* tensile testing set-up and two halves of typical x-ray scattering patterns for 0 and 50% strain.

To measure Young's modulus $E$ and nominal tensile strength $R_m$ stress-strain curves were recorded ($E = \frac{\sigma}{\varepsilon}$), where $\sigma$ represents the recorded stress and $\varepsilon$ the recorded strain, to the linear-elastic region between 1 and 3% strain of the recorded stress-strain curve Young's modulus values were achieved. The macro strain ε was obtained by video extensometry using a camera observing the elongation $\Delta l$ of the distance $l_0$ between black markers on the sample ($\varepsilon = \Delta l/l_0$). As reported earlier (Samsoninkova et al., 2017), samples exhibit different values for elongation at break, depending on the amount of conjugate, ranging from around 700 up to 900%. A limitation of our study is, that the used synchrotron *in-situ* tensile tester did not allow elongating up to such high deformations.

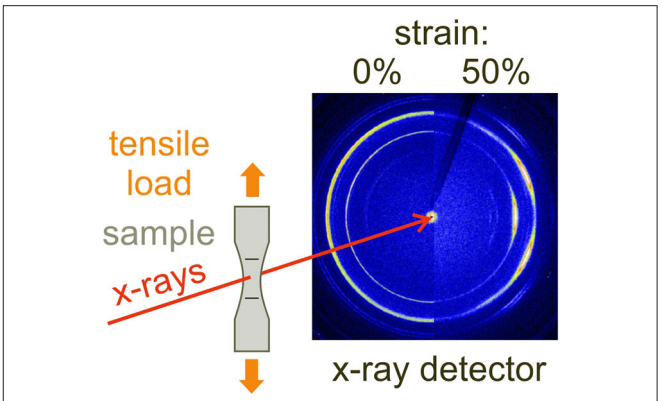


**FIGURE 1 |** Experimental *in-situ* X-ray scattering setup combined with mechanical tensile testing. Tensile load is applied to the sample, which is simultaneously scanned by an X-ray beam. Two-dimensional X-ray diffraction patterns are recorded by a two-dimensional detector (shown: two halves of diffraction patterns representing 0 and 50% strain).

Molecular deformations induced by applied tensile stress within polymers leads to a micro strain in crystallites and causes a peak shift of the crystalline X-ray diffraction peaks (Mallick et al., 2006). By applying the following equation to the X-ray scattering data the micro strain $\varepsilon_{micro}$ could be calculated:

$$\varepsilon_{micro} = \frac{q_0 - q_\varepsilon}{q_\varepsilon}$$

with $q_0$ as the $q$ value of the (120) signal position before applied tensile stress and $q_\varepsilon$ as the $q$ value after applied tensile stress.

# RESULTS

In this study, a combination of mechanical tensile testing in combination with SAXS and WAXS was used to provide insights into structure-function relationships. By performing SAXS experiments, the size and shape as well as the agglomeration behavior of the $MgF_2$ nanoparticles were investigated. *In situ* WAXS experiments combining X-ray scattering and mechanical tensile testing allowed a detailed analysis of the relationship between structure and mechanical properties of the hybrid material by examining the crystallite size and deformation of the crystallites during applied tensile stress of the matrix material PEO.

## Size and Arrangement of the Incorporated Nanoparticles

The radius of the $MgF_2$ particles $R$ (Samsoninkova et al., 2017), as well as the fractal dimension $D$ was determined by applying

the following equation described in Samsoninkova et al. (2017) on the SAXS data.

$$I(q) = I_0 B + I_0 \left[ V_0 S(q) P(q) \right]$$

For calculating the true layer thickness ($\delta$) of the conjugate layer coating the $MgF_2$ particles the following equation was used to relate the differences of the electron densities of $MgF_2$ with $\rho(r) = 0.91\ e^{-1}/Å^3$, $\rho(r) = 0.38\ e^{-1}/Å^3$ for PEO (Glatter et al., 1994) and $\rho(r) = 0.45\ e^{-1}/Å^3$ for the conjugate by using the biomolecular scattering length density calculator (http://psldc.isis.rl.ac.uk/Psldc/).

$$R^2 = \frac{(R_P + \delta)^5 C_K + R_P^5 (C_P - C_K)}{(R_P + \delta)^3 C_K + R_P^3 (C_P - C_K)}$$

The electron density difference between PEO and $MgF_2$ is defined as $C_P$, while $C_K$ is the electron density difference between PEO and conjugate. The radius of the primary particles is defined as $R$, while $R_P$ gives the particle radius in combination with peptide-PEG conjugates revealed by SAXS experiments (Samsoninkova et al., 2017). Therefore, the equation can be converted into the corrected layer thickness to calculate the increasing particle radius due to adhesion of the conjugate to the $MgF_2$ nanoparticle surface. **Table 1** shows the calculated values for the true layer thickness $\delta$ of different sample compositions. The dependency of $\delta$ on the conjugate amount is displayed in **Figure 2A**. Looking at the dependency of conjugate amount**,** up to 1.0 mol% conjugate a slight increase, followed by a strong increase starting at 2.0 mol% conjugate can be observed with a slow further increase.

Furthermore, by calculating the fractal dimension $D$ the morphology and the state of agglomeration can be investigated. It can be seen as a value for the degree of branching within the structure of a material (Logan and Kilps, 1995; Husing et al., 1998; Bushell et al., 2002; Fratzl, 2003b). Lower values for $D$ in aggregates refer to less branching, while higher values represent higher branching and therefore, more densely packed agglomerates (Emmerling et al., 1995; Logan and Kilps, 1995; Husing et al., 1998; Bushell et al., 2002). By plotting the fractal dimension $D$ *vs.* used mol% conjugate a dependency of the agglomeration behavior and amount of used conjugate could be observed. Up to 1.0 mol% conjugate, the values for the fractal dimension $D$ did not differ significantly and were maintained in a range between $D$ = 1.74-1.77. At 2.0 mol% conjugate a significant decrease to around $D$ = 1.47 can be observed with a slow further decrease. The dependency of the fractal dimension $D$ and the used conjugate ratio is shown in **Figure 2B**, which indicates an inverse behavior for the fractal dimension $D$ compared to the true layer thickness $\delta$. Both graphs exhibit strong changes between 1.0 and 2.0 mol% conjugate.

## *In situ* Tensile Testing

The samples were measured at the μSpot beamline at BESSY II to perform simultaneous tensile testing and X-ray scattering experiments. With the recorded stress-strain curves every sample could be investigated for Young's modulus $E$ and nominal tensile strength $R_m$ (based on the original cross section area). **Figure 3** shows an exemplary stress-strain curve of non-filled PEO as reference to demonstrate the origin of the determined values for Young's modulus $E$ and tensile strength $R_m$.

The measurements were interrupted to record WAXS patterns at 0, 1, 3, 5, 8, 10, 20, 30, 50% strain. These stops occurred as an area with decreasing stress in the stress-strain curves during constant strain. At every stop, 10 diffraction patterns were recorded to ensure measurements in the deformation area of the hybrid material. As the areas where necking occurred in the samples were hard to predict, 10 points with a distance of 300 μm were measured in longitudinal direction of the sample. **Table 2** shows the Young's moduli and the tensile strengths of the samples.

With the insertion of $MgF_2$ nanoparticles and conjugate the values for both determined material parameters increased. The values for Young's modulus increased by nearly factor 2 after $MgF_2$ incorporation and even more after addition of

**TABLE 1 |** Results for conjugate layer thickness $\delta$ and fractal dimension D.

| Sample | $\delta$ (nm) | D |
|---|---|---|
| PEO + 15 wt.% $MgF_2$ + 0.5 mol% conjugate | 2.9 | 1.77 ± 0.02 |
| PEO + 15 wt.% $MgF_2$ + 1.0 mol% conjugate | 3.7 | 1.74 ± 0.03 |
| PEO + 15 wt.% $MgF_2$ + 2.0 mol% conjugate | 6.4 | 1.47 ± 0.04 |
| PEO + 15 wt.% $MgF_2$ + 3.0 mol% conjugate | 6.6 | 1.47 ± 0.09 |
| PEO + 15 wt.% $MgF_2$ + 6.0 mol% conjugate | 7.4 | 1.44 ± 0.02 |

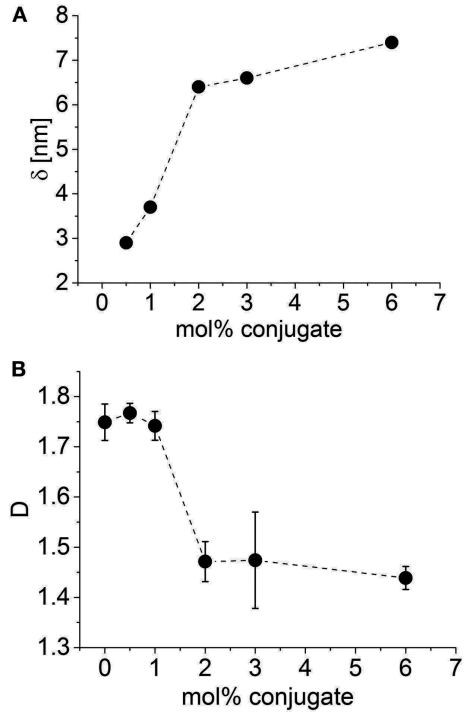


**FIGURE 2 |** Dependency of **(A)** true layer thickness δ and **(B)** fractal dimension D on amount of added conjugate in the composition. Both curves show strong changes between 1.0 and 2.0 mol% conjugate.

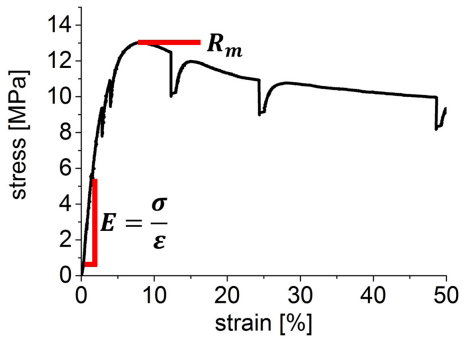


**FIGURE 3 |** Representative stress-strain curve of non-filled PEO with characteristic parameters marked on the graph showing the mechanical material properties by tensile strength $R_m$ and Young's modulus E. The drops in stress during constant tensile strain result from required stops during the measurements necessary to record X-ray diffraction patterns with larger accuracy.

**TABLE 2 |** Young's moduli and tensile strengths of *in situ* mechanical tensile testing experiments.

| Sample | $E$ (MPa) | $R_m$ (MPa) |
|---|---|---|
| Non-filled PEO | 330 ± 75 | 11.8 ± 0.9 |
| PEO +0 wt.% $MgF_2$ + 3.0 mol% conjugate | 374 ± 125 | 10.5 ± 1.1 |
| PEO + 15 wt.% $MgF_2$ + 0 mol% conjugate | 583 ± 30 | 12.9 ± 1.0 |
| PEO + 15 wt.% $MgF_2$ + 2.0 mol% conjugate | 592 ± 183 | 12.2± 0.7 |
| PEO + 15 wt.% $MgF_2$ + 3.0 mol% conjugate | 766 ± 202 | 12.0 ± 0.6 |
| PEO + 15 wt.% $MgF_2$ + 6.0 mol% conjugate | 890 ± 53 | 14.7 ± 1.2 |

conjugate. Also tensile strengths increased with $MgF_2$ and conjugate insertion. The sample composition with 6.0 mol% conjugate showed the highest values for Young's modulus and tensile strength.

## *In situ* Wide Angle X-Ray Diffraction Studies

The commonly observed WAXS patterns of semi-crystalline PEO samples describe a monoclinic lattice (Zhu et al., 2000). Based on this, several reflections in the reciprocal space could be seen, which were coexistent with the experimental WAXS data. Two prominent signals could be obtained in the WAXS signal with $q = 13.6\ nm^{-1}$ and $q = 16.4\ nm^{-1}$. The first signal corresponds to the reflection of the (120) plane lying perpendicular to the *c*-axis of the crystallites (crystalline domains). The second signal corresponds to the reflections of overlapping rings from the (032), ($\bar{1}$32), ($\bar{2}$12), (112), ($\bar{1}$24), ($\bar{2}$04), and (004) planes, which are hard to distinguish and therefore, not used for further analysis (Zhu et al., 2000; Lai et al., 2012).

At 50% strain, a clear texture of both signals was observed. **Figure 4** shows two-dimensional diffraction patterns of non-filled PEO (**Figure 4A**) before tensile testing and (**Figure 4B**) at 50% tensile strain during applied tensile stress. The (120) plane, which was used for further data evaluation showed a strong meridional texture after applied tensile stress. The (120) reflection has an angle of 90° to the *c*-axis in PEO crystals. Different integration angles were chosen for the two-dimensional data processing of the (120) signal to consider the differences of the crystallites according to the orientation of the *c*-axis during the applied tensile stress. This enables an interpretation of the progression of crystallite orientations during deformation. The angles were selected perpendicular to the tensile direction and directly in tensile direction with an angle of 30°. The defined integration areas are shown in **Figures 4A,B** with corresponding one-dimensional radial profiles where the *c*-axis crystallite orientation is aligned (**Figure 4C**) in tensile direction and (**Figure 4D**) perpendicular to the tensile direction.

Two effects on the radial profiles could be observed depending on the *c*-axis crystallite orientation. They show obvious differences in the peak broadening and the positions of the (120) signal. Perpendicular to the tensile direction, a peak broadening after applied tensile stress is visible, whereas in tensile direction broadening appeared with much less intensity. Additionally, the peak positions before tensile testing and at 50% strain with different integration areas differ greatly. Perpendicular to the tensile direction no peak shifting could be observed, whereas in tensile direction a peak shift to lower $q$ values appeared. These two effects on the (120) signal were evaluated to gain information about the crystalline and the amorphous phases. By quantifying the peak broadening of the signal it was possible to measure the average crystallite size (Holzwarth and Gibson, 2011) within the crystalline lamellae and hence, to make statements about the crystallite perfection of the crystalline phase. The crystallite size as well as the determined micro strain during applied tensile stress can be plotted against the applied macro strain to reveal information about structure-function relationships on both the micro and nanometer scale. In **Figure 5**, the crystallite size vs. the macro strain is drawn (**Figure 5A**) with the *c*-axis crystallite orientation in and (**Figure 5B**) perpendicular to the tensile direction, as well as the micro strain vs. the macro strain with (**Figure 5C**) the *c*-axis crystallite orientation in and (**Figure 5D**) perpendicular to the tensile direction. Evaluating the crystallite sizes with *c*-axis crystallite orientation in tensile direction, after the insertion of conjugate and $MgF_2$ nanoparticles a decrease of the crystallite sizes could be observed. With increasing macro strain the crystallite sizes strongly decreased for all investigated samples down to sizes of $L = 10 - 20\ nm$. The same applied for the crystallite sizes with the *c*-axis crystallite orientation perpendicular to the tensile direction but only down to sizes of $L = 30 - 40\ nm$, as the crystallites are getting aligned during applied tensile stress in tensile direction. For this reason, we focused on the crystallite sizes with *c*-axis crystallite orientation in tensile direction for further data evaluation.

By comparing the induced micro strain on the crystalline domains in PEO vs. macro strain a different behavior could be seen for the *c*-axis crystallite orientations. With a *c*-axis crystallite orientation (**Figure 5C**) in tensile direction negative values for micro strain appeared, whereas the crystallites oriented (**Figure 5D**) perpendicular to the tensile direction showed a strong increase of the micro strain, with increasing macro strain up to a plateau where the values reached a constant level.

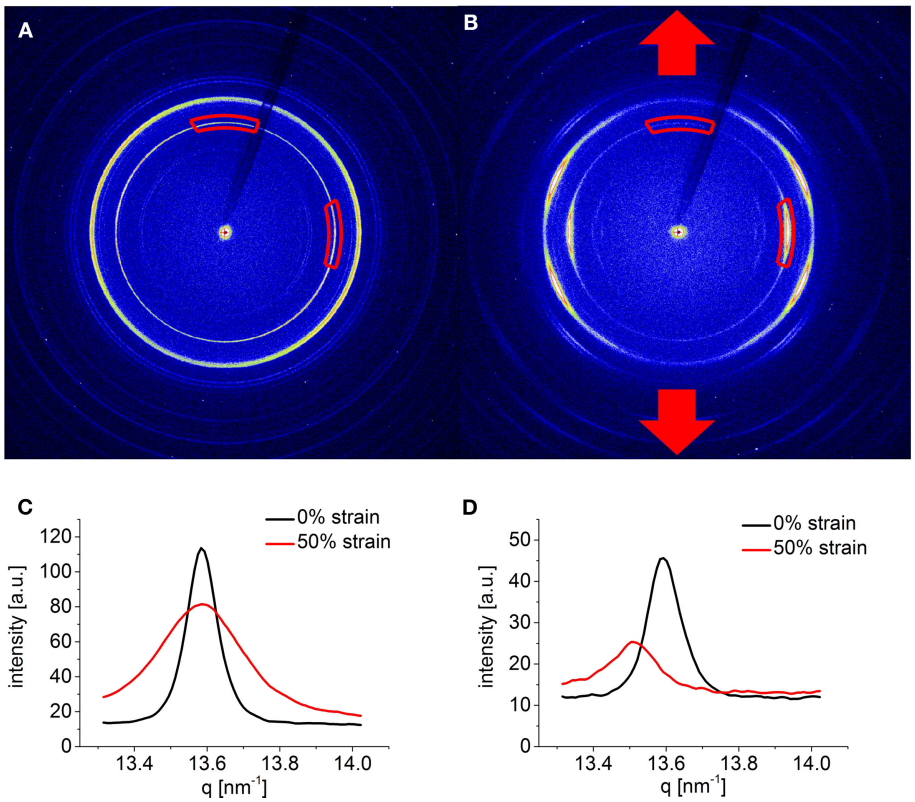


**FIGURE 4 |** Two-dimensional diffraction patterns of non-filled PEO **(A)** before and **(B)** at 50% tensile strain. Before applied tensile stress, only weak textures as a result of sample preparation were visible in the Debye Scherrer rings, whereas the rings at 50% strain show a distinct texture. **(C)** Radial profiles before and at 50% tensile strain of the (120) signal with a c-axis crystallite orientation in tensile direction. A broadening of the signal appeared at 50% tensile strain. **(D)** Radial profiles before and at 50% tensile strain of the (120) signal with a c-axis crystallite orientation perpendicular to the tensile direction. A peak shift to lower $q$ values appeared after applied tensile stress.

For further data interpretation and to compare the samples between themselves the percentage crystallite size change (CSC) was drawn *vs.* macro strain and the slope within the elastic range between 1 and 3% strain was determined (**Figure 6A**). The mean values and corresponding standard deviations were drawn as bar charts in **Figure 6B** for $n = 3$ samples. The insertion of the conjugate led to a strong decrease of the slope of the percentage CSC within the elastic range, whereas the insertion of $MgF_2$ in combination with conjugate led to an increase of the slope up to a factor 2. This means that only the insertion of $MgF_2$ nanoparticles compatibilized by the peptide-PEG conjugate caused faster decreasing crystallite sizes under load.

The slope of the micro strain *vs.* macro strain of the crystallites with the *c*-axis oriented perpendicular to the tensile direction was determined within the elastic regime (**Figure 6C**). Allowing statements on the force transmission from the amorphous to the crystalline phase of the organic semi crystalline matrix. This is a key point to explain materials mechanical properties. All values were drawn as bar charts for $n = 3$ samples in **Figure 6D** with corresponding standard deviations. By using compatibilized $MgF_2$ nanoparticles higher values of the slope up to a factor of 4 could be realized, whereas the plateau values (**Figure 6E**) stayed almost in the same range for all sample compositions of the stabilized composites. This means that the transmitted force from the amorphous to crystalline phase was the same for all sample compositions, but the force transmission from the amorphous to the crystalline phase occurred earlier after $MgF_2$ nanoparticle compatibilization.

## DISCUSSION

In this study, relations between nano-structure and deformation mechanisms at several length scales in a new hybrid material consisting of PEO as a semi-crystalline polymer matrix and $MgF_2$ nanoparticles was investigated. By using an $MgF_2$-affine peptide-PEG conjugate, the nanoparticles were compatibilized in the PEO matrix and the function of interface polymers as found in natural hybrid materials could be mimicked.

The samples were investigated for layer thickness of the conjugate $\delta$ and fractal dimension $D$ by performing small angle X-ray scattering experiments. Recently, a study with congeneric PEO/$MgF_2$ hybrid materials revealed decreasing agglomerate sizes on increased conjugate amounts (Samsoninkova et al., 2017). In the present system, this effect was explained by

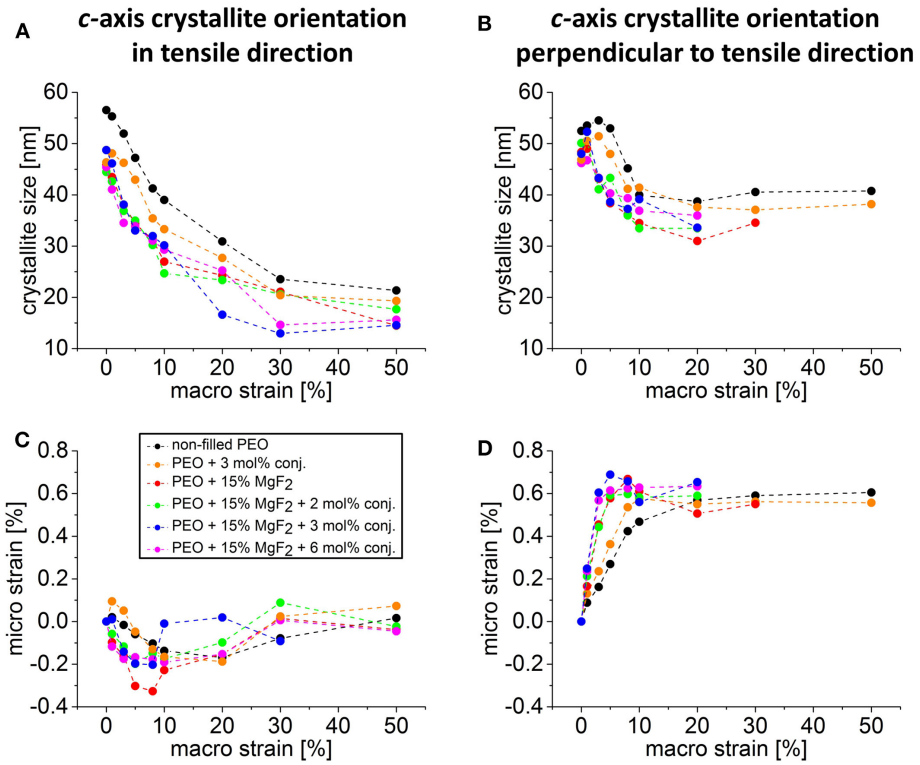


**FIGURE 5 |** Plots of crystallite sizes *vs.* macro strain with c-axis crystallite orientation **(A)** in and **(B)** perpendicular to the tensile direction of exemplary sample compositions. The crystallite size changes to lower sizes after $MgF_2$ and conjugate insertion and with increasing macro strain. Major changes of the crystallite sizes can be seen with increasing macro strain with the c-axis crystallite orientation in tensile direction. The applied micro vs. macro strain is drawn with the c-axis crystallite orientation **(C)** in tensile direction and **(D)** perpendicular to the tensile direction. With increasing macro strain the micro strain showed negative values for the c-axis crystallite orientation in tensile direction and increasing positive values up to a plateau perpendicular to the tensile direction. Dotted lines in the graph are shown to aid the eye.

the thickness of the conjugate layer on the $MgF_2$ surface, which was found to increase with the amount of conjugate. Based on the differences in electron density of the different components, the layer thickness was calculated. From these results, a saturation of the $MgF_2$ surface at 2 mol% conjugate with a layer thickness of $\delta = 6.4\ nm$ was concluded, because at this composition the system showed an abrupt change in δ. This conclusion was confirmed by calculating the fractal dimension $D$ as a value for the degree of branching within the system (Schmidt, 1991; Peterlik and Fratzl, 2006). The abrupt change between 1.0 and 2.0 mol% for the fractal dimension $D$ can be interpreted as the transition to more open fractal structures leading to a suppression of agglomeration. The effect of the addition of stabilizing agents to nanoparticles by binding to the particle surfaces was described in different studies as a prevention of uncontrolled growth and aggregation (Niemeyer, 2001), which can be also confirmed in this study. The interpretation of the SAXS results is schematically illustrated in **Figure 7A**. With increasing conjugate amount an increasing layer of conjugate around $MgF_2$ particles is found as well as reduced agglomeration of the particles. The investigated hybrid materials with higher conjugate amount showed less branched particle networks.

Improved mechanical properties were found with higher conjugate amounts, leading to increased Young's moduli and tensile strengths. The sample set with 15 wt.% $MgF_2$ stabilized by 6.0 mol% conjugate exhibited obviously the highest reinforcement effect. The Young's moduli of these compatibilized hybrid materials were increased almost by a factor of 2 compared to non-stabilized composites. This confirms prior observations that the amount of compatibilizers has to reach about 3.0–6.0 mol% to provide materials interface stabilization effectively (Samsoninkova et al., 2017). There, samples showed values for elongation at break from around 730% (15 wt.% $MgF_2$ and 0 mol% conjugate), a relative maximum of around 930% (15 wt.% $MgF_2$ and 1 mol% conjugate) to around 690% (15 wt.% $MgF_2$ and 3 mol% conjugate), while samples with 15 wt.% $MgF_2$ and 6 mol% conjugate showed a strong reduction in ductility and therefore only around 70% elongation at break. Therefore, an amount of around 1–3 mol% conjugate seems to give an optimal compromise to achieve relatively high stiffness and toughness in these hybrid materials with 15 wt.% $MgF_2$ nanoparticles.

By performing WAXS experiments two prominent peaks were identified as characteristic PEO signals corresponding to the (120) plane at $q = 13.6\ nm^{-1}$ and an overlay of different rings from the $(\bar{1}32)$, $(\bar{2}12)$, (032), (004), $(\bar{2}04)$, and $(\bar{1}24)$

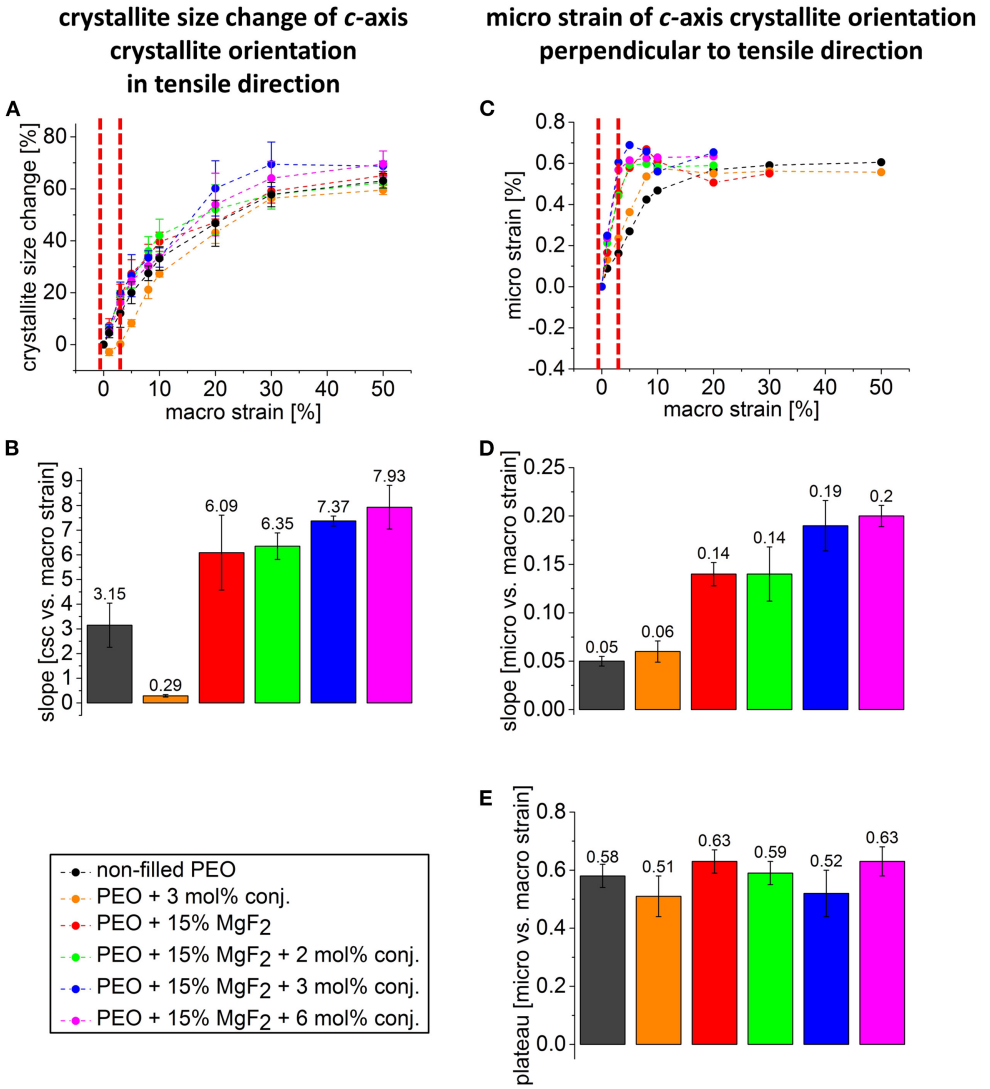


**FIGURE 6 |** Percentage crystallite size change **(A)** of the crystallites with the c-axis aligned in tensile direction. The slope was determined within the elastic range (red bars) and drawn as bar charts **(B)** with corresponding standard deviation for $n = 3$ samples. An increase of the values can be observed after the insertion of $MgF_2$ compatibilized by the peptide-PEG conjugate and therefore, a faster decrease of the crystallite sizes during applied tensile stress. Also the slope of micro *vs.* macro strain **(C)** within the elastic range (red bars) of the crystallites with the c-axis aligned perpendicular to the tensile direction was determined. The results were drawn as bar charts **(D)** as well as the plateau values **(E)** for $n = 3$ samples. Again an increase after insertion of compatibilized $MgF_2$ could be observed for the slope values, whereas the plateau values stayed in the same range for all sample compositions.

planes. During applied tensile stress a clear texture of both rings appeared in the two-dimensional WAXS pattern. The (120) signal showed two strong meridional arcs with increasing tensile strain. By comparing the WAXS patterns at 50% strain with simulated 2D WAXS patterns from literature, we could assume that during applied tensile stress the (120) plane, which lies perpendicular to the *c*-axis, is meridional aligned to the tensile direction. Therefore, the *c*-axis is becoming aligned in tensile direction (Adams et al., 1986; Petermann and Ebener, 1999; Zhu et al., 2000; Lai et al., 2012). Due to the crystalline structure of PEO with an angle of 90° between the (120) plane and the *c*-axis, this correlation can be used to make predictions about the crystalline structure by examining the peak broadening and position during applied tensile stress.

The crystallite size changes were evaluated by calculating the crystallite sizes of the (120) plane. By performing the two mentioned integration areas the crystallite size change during applied tensile stress of the crystalline phase aligned in tensile direction was described. The (120) plane lies perpendicular to the *c*-axis and is meridional aligned during applied tensile stress. This fact gives the possibility to make direct conclusions about the crystalline phase and correlate them with material properties. The determined slope of the percentage crystallite size change vs. macro strain, allows the making of statements

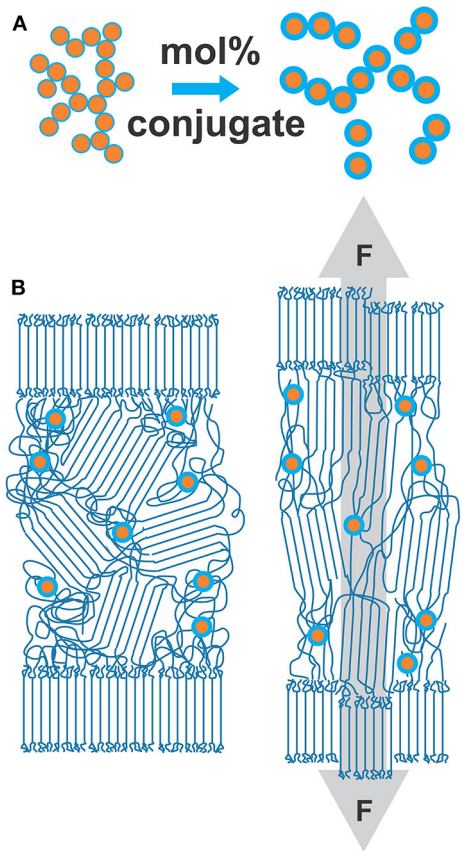


**FIGURE 7 |** Schematic representation of the hybrid material at the nanometer scale. **(A)** Increasing amount of conjugate leads to higher layer thickness and reduces agglomeration (less branched aggregates) as derived from the fractal dimension D. **(B)** Deformation mechanisms of PEO + 15 wt.% conjugated $MgF_2$ during applied tensile stress. The use of conjugate led to a stabilization of the amorphous phase. The stabilization of $MgF_2$ nanoparticles by the peptide-PEG conjugate blocked the movement of dislocations within the amorphous phase. The amorphous PEO chains cannot elongate as in non-filled PEO and the force transmission from the amorphous to the crystalline phase appears earlier resulting in a faster block-slip mechanisms and therefore, decreasing crystallite sizes.

concerning the deformation mechanism of the hybrid material. As reference, non-filled PEO was measured with a value of $m = 3.15$, whereas the reference sample of non-filled PEO in combination with compatibilized $MgF_2$ showed a clear decrease in the slope. This flatter slope can be explained by a softening of the amorphous phase. With a factor of 2, an increase of $m = 6.1$ could be seen after $MgF_2$ insertion with increasing values for increasing conjugate amounts. This increase can be rationalized probably by a positive effect of the compatibilized $MgF_2$ nanoparticles on the amorphous phase of the matrix. Comparable to the interface polymers in natural materials, the PEG-blocks adsorption on surfaces of compatibilized $MgF_2$ particles enhanced apparently the interactions with the PEO matrix, leading to a better mechanical performance of the interface-engineered hybrid materials. This effect is even improved by the use of higher equivalents of the peptide-PEG conjugate.

Additional information could be gained by calculating the micro strain within the crystalline domains. Firstly, the negative values of the strain aligned in tensile direction could be explained by reasonable Poisson ratio values of around $\mu = 0.3$. The Poisson ratio describes the relation between longitudinal to lateral deformation during tensile stress and the most common materials such as polymers or composites hold a Poisson ratio of $0.25 < \mu < 0.35$ (Askeland et al., 2010; Rawlings et al., 2013; Silberschmidt and Matveenko, 2015). These values fit well to the determined values and appoints to an increase of the volume during applied tensile stress, since materials with a Poisson ratio $\mu > 0.5$ show a decrease of the volume during applied tensile stress.

The process of deformation for bulk semi-crystalline polymers has been described by different studies (Adams et al., 1986; Petermann and Ebener, 1999; Zhu et al., 2000; Liu et al., 2006). The deformation in such materials during applied tensile load can be characterized by an initial elongation of the amorphous phase, followed by a shearing and tilting of the lamellar folded chains. Afterwards, block crystals are pulled out of the lamellae, which is referred to as "block slip" mechanism and those blocks become further aligned along the tensile axis (Adams et al., 1986; Petermann and Ebener, 1999; Lai et al., 2012).

Statements about the force transmission from the amorphous to the crystalline phase could be made by determining the slope of the micro vs. the macro strain of the crystallites aligned perpendicular to the tensile direction. Higher values indicate a faster force transmission from the amorphous to the crystalline phase, as it is known that deformation of semi-crystalline block polymers starts with an elongation of the amorphous phase. After insertion of $MgF_2$ compatibilized by the conjugate the energy transmission appeared faster with a factor of 4. This increase can be explained by the increased interactions between the filler particles and the polymer matrix, which resulted in a stabilization of the amorphous phase. As reported earlier (Samsoninkova et al., 2018), the $MgF_2$ particles are non-covalently coated with peptide-PEG conjugates and by means of NMR study we found mixtures of interactions but predominantly electrostatic ones. By applying uniaxial tensile stress on the hybrid material initially, the statistical coil conformation of the PEO chains in the amorphous phase were extended and aligned. This process is apparently modulated by the compatibilized $MgF_2$ filler that were anchored in the PEO matrix and thus leading as physically network points to a more efficient force transmission in the hybrid material. This accelerated pull out of the lamellae and decreasing crystallite sizes proved the block slip mechanism. The main findings of the *in situ* X-ray scattering experiments for the stabilized hybrid material are illustrated in **Figure 7B**. By stabilizing the $MgF_2$ particles with the conjugate the amorphous phase is becoming stabilized and therefore, the force transmission from the amorphous to the crystalline phase appeared earlier resulting in higher slopes for micro *vs.* macro strain and decreasing crystallite sizes. Samples with higher conjugate amount and less branched particle networks might also exhibit a reorientation of

these branches; most likely an alignment of single branches along the loading directions.

## CONCLUSIONS

A detailed study on the deformation mechanism in PEO/$MgF_2$ hybrid materials in the presence of specific compatibilizers was performed by the use of *in situ* X-ray scattering experiments and tensile testing. By evaluating the crystallite size change and the micro strain of the crystallites a stabilization of the amorphous phase followed by a more efficient force transmission from the amorphous to the crystalline phase could be proven by the combination of $MgF_2$ nanoparticles compatibilized by the $MgF_2$-binding peptide-PEG conjugate. The concept of tailor-made bio-inspired interfaces by the use of material-specific peptide-PEG conjugates was verified as a new route to prepare synthetic hybrid materials with enhanced mechanical properties. By mimicking aspects of interfacial proteins from biomaterials the peptide-PEG conjugates proved to act as interfacial "glue" and improved the tensile strength and Young's modulus in comparison to non-stabilized composite materials. This study provides new insights into possible approaches toward a new class of bio-inspired hybrid materials with tailored interface chemistry. By this approach, it might be possible to fabricate materials with similar structure-function relations as found in natural hybrid materials and making them therefore good candidates for bio-applications.

## DATA AVAILABILITY STATEMENT

All datasets generated for this study are included in the article/supplementary material.

## AUTHOR CONTRIBUTIONS

Samples have been prepared by VS and FH. Experiments have been performed by BS, AG, and WW. Data evaluation has been done by BS and AG. The manuscript has been written through contributions of all authors. All authors have given approval to the final version of the manuscript.

## FUNDING

We acknowledge financial support from the German Research Council in a frame of the excellence initiative at Graduate School of Analytical Sciences Adlershof (SALSA). HB acknowledges in addition the European Research Council under the European Union's 7th Framework Program (FP07-13)/ERC Starting grant Specifically Interacting Polymer–SIP (ERC 305064).

## ACKNOWLEDGMENTS

We would like to thank Dr. Chenghao Li (μSpot beamline), Dr. Stefan Siegel (μSpot beamline), Petra Leibner (MPI-KG), and Gunthard Benecke for technical support.

## REFERENCES

Adams, W. W., Yang, D., and Thomas, E. L. (1986). Direct visualization of microstructural deformation processes in polyethylene. *J. Mater. Sci.* 21, 2239–2253. doi: 10.1007/BF01114262

Askeland, D., Fulay, P., and Wright, W. (2010). *The Science and Engineering of Materials*. Cengage Learning.

Benecke, G., Wagermaier, W., Li, C. H., Schwartzkopf, M., Flucke, G., Hoerth, R., et al. (2014). A customizable software for fast reduction and analysis of large X-ray scattering data sets: applications of the new DPDAK package to small-angle X-ray scattering and grazing-incidence small-angle X-ray scattering. *J. Appl. Crystallogr.* 47, 1797–1803. doi: 10.1107/S1600576714019773

Bonderer, L. J., Studart, A. R., and Gauckler, L. J. (2008). Bioinspired design and assembly of platelet reinforced polymer films. *Science* 319, 1069–1073. doi: 10.1126/science.1148726

Bushell, G., Yan, Y., Woodfield, D., Raper, J., and Amal, R. (2002). On techniques for the measurement of the mass fractal dimension of aggregates. *Adv. Colloid Interface Sci.* 95, 1–50. doi: 10.1016/S0001-8686(00)00078-6

Currey, J. D. (1977). Mechanical properties of mother of pearl in tension. *Proc. R. Soc. Lond. B: Biol. Sci.* 196, 443–463. doi: 10.1098/rspb.1977.0050

Dujardin, E., and Mann, S. (2002). Bio-inspired materials chemistry. *Adv. Mater.* 14, 775–788. doi: 10.1002/1527-2648(20020717)4:73.0.CO;2-K

Emmerling, A., Petricevic, R., Beck, A., Wang, P., Scheller, H., and Fricke, J. (1995). Relationship between optical transparency and nanostructural features of silica aerogels. *J. Non-Cryst. Solids* 185, 240–248. doi: 10.1016/0022-3093(95)00021-6

Espinosa, H. D., Rim, J. E., Barthelat, F., and Buehler, M. J. (2009). Merger of structure and material in nacre and bone – perspectives on de novo biomimetic materials. *Prog. Mater. Sci.* 54, 1059–1100. doi: 10.1016/j.pmatsci.2009.05.001

Fratzl, P. (2003a). Cellulose and collagen: from fibres to tissues. *Curr. Opin. Colloid Interface Sci.* 8, 32–39. doi: 10.1016/S1359-0294(03)00011-6

Fratzl, P. (2003b). Small-angle scattering in materials science - a short review of applications in alloys, ceramics and composite materials. *J. Appl. Crystallogr.* 36, 397–404. doi: 10.1107/S0021889803000335

Fratzl, P., Burgert, I., and Gupta, H. S. (2004a). On the role of interface polymers for the mechanics of natural polymeric composites. *Phys. Chem. Chem. Phys.* 6, 5575–5579. doi: 10.1039/b411986j

Fratzl, P., Gupta, H. S., Paschalis, E. P., and Roschger, P. (2004b). Structure and mechanical quality of the collagen-mineral nano-composite in bone. *J. Mater. Chem.* 14, 2115–2123. doi: 10.1039/B402005G

Glatter, O., Scherf, G., Schillen, K., and Brown, W. (1994). Characterization of a poly (ethylene oxide)-poly (propylene oxide) triblock copolymer (EO27-PO39-EO27) in aqueous solution. *Macromolecules* 27, 6046–6054. doi: 10.1021/ma00099a017

Gregorczyk, K., and Knez, M. (2016). Hybrid nanomaterials through molecular and atomic layer deposition: top down, bottom up, and in-between approaches to new materials. *Prog. Mater. Sci.* 75, 1–37. doi: 10.1016/j.pmatsci.2015.06.004

Gupta, H. S., Wagermaier, W., Zickler, G. A., Raz-Ben Aroush, D., Funari, S. S., et al. (2005). Nanoscale deformation mechanisms in bone. *Nano Lett.* 5, 2108–2111. doi: 10.1021/nl051584b

Hanssske, F., Bas, O., Vaquette, C., Hochleitner, G., Groll, J., Kemnitz, E., et al. (2017). Via precise interface engineering towards bioinspired composites with improved 3D printing processability and mechanical properties. *J. Mater. Chem. B* 5, 5037–5047. doi: 10.1039/C7TB00165G

Hanssske, F., Kemnitz, E., and Borner, H. G. (2015). Generic biocombinatorial strategy to select tailor-made stabilizers for sol-gel nanoparticle synthesis. *Small* 11, 4303–4308. doi: 10.1002/smll.201500162

Hardy, J. G., and Scheibel, T. R. (2010). Composite materials based on silk proteins. *Prog. Polym. Sci.* 35, 1093–1115. doi: 10.1016/j.progpolymsci.2010.04.005

Holzwarth, U., and Gibson, N. (2011). The Scherrer equation versus the 'Debye-Scherrer equation'. *Nat Nano* 6, 534–534. doi: 10.1038/nnano.2011.145

Husing, N., Schubert, U., Misof, K., and Fratzl, P. (1998). Formation and structure of porous gel networks from Si(OMe)(4) in the presence of

A(CH2)(n)Si(OR)(3) (A = functional group). *Chem. Mater.* 10, 3024–3032. doi: 10.1021/cm980706g

Kang, M. H., Jang, T. S., Kim, S. W., Park, H. S., Song, J., Kim, H. E., et al. (2016). MgF2-coated porous magnesium/alumina scaffolds with improved strength, corrosion resistance, and biological performance for biomedical applications. *Mat. Sci. Eng. C Mater. Biol. Appl.* 62, 634–642. doi: 10.1016/j.msec.2016.01.085

Kemnitz, E., Gross, U., Rudiger, S., and Shekar, C. S. (2003). Amorphous metal fluorides with extraordinary high surface areas. *Angew. Chem. Int. Ed.* 42, 4251–4254. doi: 10.1002/anie.200351278

Kickelbick, G. (2003). Concepts for the incorporation of inorganic building blocks into organic polymers on a nanoscale. *Prog. Polym. Sci.* 28, 83–114. doi: 10.1016/S0079-6700(02)00019-9

Laaksonen, P., Szilvay, G. R., and Linder, M. B. (2012). Genetic engineering in biomimetic composites. *Trends Biotechnol.* 30, 191–197. doi: 10.1016/j.tibtech.2012.01.001

Lai, C. Y., Hiltner, A., Baer, E., and Korley, L. T. (2012). Deformation of confined poly(ethylene oxide) in multilayer films. *ACS Appl. Mater. Interfaces* 4, 2218–2227. doi: 10.1021/am300240r

Liu, L.-Z., Hsiao, B. S., Ran, S., Fu, B. X., Toki, S., Zuo, F., et al. (2006). *In situ* WAXD study of structure changes during uniaxial deformation of ethylene-based semicrystalline ethylene–propylene copolymer. *Polymer* 47, 2884–2893. doi: 10.1016/j.polymer.2006.01.090

Logan, B. E., and Kilps, J. R. (1995). Fractal dimensions of aggregates formed in different fluid mechanical environments. *Water Res.* 29, 443–453. doi: 10.1016/0043-1354(94)00186-B

Mallick, B., Patel, T., Behera, R. C., Sarangi, S. N., Sahu, S. N., and Choudhury, R. K. (2006). Microstrain analysis of proton irradiated PET microfiber. *Nucl. Instrum. Methods Phys. Res. Sect. B Beam Interact. Mater. Atoms* 248, 305–310. doi: 10.1016/j.nimb.2006.04.153

Meyers, M. A., Chen, P.-Y., Lin, A. Y. M., and Seki, Y. (2008). Biological materials: Structure and mechanical properties. *Prog. Mater. Sci.* 53, 1–206. doi: 10.1016/j.pmatsci.2007.05.002

Munch, E., Launey, M. E., Alsem, D. H., Saiz, E., Tomsia, A. P., and Ritchie, R. O. (2008). Tough, bio-inspired hybrid materials. *Science* 322, 1516–1520. doi: 10.1126/science.1164865

Niemeyer, C. M. (2001). Nanoparticles, proteins, and nucleic acids: biotechnology meets materials science. *Angew. Chem. Int. Ed.* 40, 4128–4158. doi: 10.1002/1521-3773(20011119)40:22<4128::AID-ANIE4128>3.0.CO;2-S

Noack, J., Schmidt, L., Glasel, H. J., Bauer, M., and Kemnitz, E. (2011). Inorganic-organic nanocomposites based on sol-gel derived magnesium fluoride. *Nanoscale* 3, 4774–4779. doi: 10.1039/c1nr10843c

Palmer, L. C., Newcomb, C. J., Kaltz, S. R., Spoerke, E. D., and Stupp, S. I. (2008). Biomimetic systems for hydroxyapatite mineralization inspired by bone and enamel. *Chem. Rev.* 108, 4754–4783. doi: 10.1021/cr8004422

Peterlik, H., and Fratzl, P. (2006). Small-angle X-ray scattering to characterize nanostructures in inorganic and hybrid materials chemistry. *Monatsh. Chem.* 137, 529–543. doi: 10.1007/s00706-006-0462-8

Petermann, J., and Ebener, H. (1999). On the micromechanisms of plastic deformation in semicrystalline polymers. *J. Macromol. Sci. Phys. B.* 38, 837–846. doi: 10.1080/00222349908248142

Rawlings, R. D., Alexander, J. M., Anderson, J. C., and Leaver, K. D. (2013). *Materials Science.* Springer.

Samsoninkova, V., Seidt, B., Hanßke, F., Wagermaier, W., and Börner, H. G. (2017). Peptide–polymer conjugates for bioinspired compatibilization of internal composite interfaces: via specific interactions toward stiffer and tougher materials. *Adv. Mater. Interfaces* 4. doi: 10.1002/admi.201600501

Samsoninkova, V., Venkatareddy, N. L., Wagermaier, W., Dallmann, A., and Borner, H. G. (2018). Precision compatibilizers for composites: in-between self-aggregation, surfaces recognition and interface stabilization. *Soft Matter* 14, 1992–1995. doi: 10.1039/C7SM02518A

Schmidt, P. (1991). Small-angle scattering studies of disordered, porous and fractal systems. *J. Appl. Crystallogr.* 24, 414–435. doi: 10.1107/S0021889891003400

Silberschmidt, V. V., and Matveenko, V. P. (2015). *Mechanics of Advanced Materials, Vol. 199*. Springer International Publishing.

Sommerdijk, N. A., and de With, G. (2008). Biomimetic CaCO3 mineralization using designer molecules and interfaces. *Chem. Rev.* 108, 4499–4550. doi: 10.1021/cr078259o

Studart, A. R. (2012). Towards high-performance bioinspired composites. *Adv. Mater.* 24, 5024–5044. doi: 10.1002/adma.201201471

Wang, E., Lee, S.-H., and Lee, S.-W. (2011). Elastin-like polypeptide based hydroxyapatite bionanocomposites. *Biomacromolecules* 12, 672–680. doi: 10.1021/bm101322m

Wegst, U. G. K., Bai, H., Saiz, E., Tomsia, A. P., and Ritchie, R. O. (2015). Bioinspired structural materials. *Nat Mater.* 14, 23–36. doi: 10.1038/nmat4089

Zhu, L., Cheng, S. Z. D., Calhoun, B. H., Ge, Q., Quirk, R. P., Thomas, E. L., et al. (2000). Crystallization temperature-dependent crystal orientations within nanoscale confined lamellae of a self-assembled crystalline-amorphous diblock copolymer. *J. Am. Chem. Soc.* 122, 5957–5967. doi: 10.1021/ja000275e

**Conflict of Interest:** The authors declare that the research was conducted in the absence of any commercial or financial relationships that could be construed as a potential conflict of interest.

frontiers in Materials

REVIEW
published: 19 February 2020
doi: 10.3389/fmats.2020.00036

# Mesoporous Silica Nanoparticles for Bio-Applications

*Violeta-Carolina Niculescu**

*National Research and Development Institute for Cryogenics and Isotopic Technologies - ICSI, Râmnicu Vâlcea, Romania*

Mesoporous materials with high specific surface, pores volume and unique pore size were recently intensively studied as bio-materials, such as carriers for controlled bio-active principles delivery. Mesoporous silica materials exhibit greater capacity for drugs loading and insure a controlled bio-active compound release if they are functionalized, in comparison with amorphous colloidal silica. Mesoporous silica nanomaterials have lately earned increasing interest also due to their substantial capability to be used in tumors treatment and imaging. Recently, functionalized mesoporous silica materials known a rapid development in imagistic and curative applications. This review summarizes the recent advancement in the obtaining and biological properties of mesoporous silica nanomaterials, emphasizing the synthesis methods and drug delivery application. Commonly used synthetic strategies are discussed, followed by a systematic review of applicability in optical and MRI imaging.

**Keywords: bio-application, drug delivery, functionalization, mesoporous silica, nanomaterial**

OPEN ACCESS

***Edited by:***
*Laura Maria Vergani,*
*Politecnico di Milano, Italy*

***Reviewed by:***
*Philippe Boisse,*
*Institut National des Sciences Appliquées de Lyon (INSA Lyon), France*
*Gabriella Epasto,*
*University of Messina, Italy*

***Correspondence:**
*Violeta-Carolina Niculescu*
*violeta.niculescu@icsi.ro*

***Specialty section:***
*This article was submitted to Polymeric and Composite Materials, a section of the journal Frontiers in Materials*

***Received:*** *23 July 2019*
***Accepted:*** *31 January 2020*
***Published:*** *19 February 2020*

***Citation:***
*Niculescu V-C (2020) Mesoporous Silica Nanoparticles for Bio-Applications. Front. Mater. 7:36. doi: 10.3389/fmats.2020.00036*

## INTRODUCTION

In 1906, Paul Ehrlich introduced the term "*magic bullet,*" referring to an antigen capability to specific select "side chains" on the cells surface (Strebhardt and Ullrich, 2008; Li et al., 2012). In the cytotoxic chemotherapy, the design of a targeted component is essential if an efficient dose of a drug must attack only the damaged region, without affecting healthy cells. Hypothetically, this "magic bullet" must contain a nanoscale delivery system able to specifically targeting tumor, avoiding premature degradation (Peer et al., 2007). This integrated concept could result in a controlled-release upon activation.

Various theranostic drugs have been developed over the past 30 years, the most clinically used being multifunctional liposomes and polymeric micelles. However, the aim of this investigation is to draw special attention to the use of silica-based mesoporous nanomaterials as drugs robust and tuneable delivery systems.

Nanotherapeutics have been intensively studied in the last years, as a consequence of the capability to be used as effective drug delivery frameworks with decreased unwanted secondary effects (Lin et al., 2012). Contrary to the classical therapies, nanomaterials can be designed properly to target affected sites (tumors) and selectively deliver their load. Until now, different nanomaterials (polymers, metal, metal oxide, etc.) have been obtained and used as systems for integrating active principles and diagnostic functions in a single nanomaterial, called multifunctional nano-theranostic (Sanvicens and Marco, 2008; Lammers et al., 2010; Xie et al., 2010).

The unstoppable nanotechnology development resulted in the design of various nanomaterials with important therapeutic potential. For example, there have been discovered many materials suitable for treating various pathologies (Anselmo and Mitragotri, 2015, 2016), such as: magnetic (Hao et al., 2010; Lin et al., 2012; Wu et al., 2016) or plasmonic compounds

(Lin et al., 2012; Liu et al., 2016), that can be isolated excited with a magnetic field and light, resulting a thermic reaction able to induce cell death (Lin et al., 2012).

Mesoporous silica gained a raised interest, due to its extensive multi-functionality, based on its high specific surface, uniform and tuneable pore size, high pore volume, and facile functionalization (Rosenholm et al., 2011; Lin et al., 2012).

The first surfactant-assisted synthesis of MCM-41 mesoporous silica (Mobil Composition of Matter No. 41) was achieved by Mobil Company in 1992 (Kresge et al., 1992), but MCM-41 begun to be studied for bio-applications since 2001 as a matrix for drugs release (Vallet-Regi et al., 2001; Lin et al., 2012). Also, other studies reported silica derivates with reduced dimensions for drugs release (Cai et al., 2001; Fowler et al., 2001; Lin et al., 2012). Since then, extensive research have been carried out in order to improve nanosilica synthesis, its functionalization and to study *in vitro*/*in vivo* activity. **Figure 1** reflects a scheme used for highlighting the development of mesoporous silica nanomaterials used in biomedical-applications (Lin et al., 2012).

First modified mesoporous silica nanomaterials for stimuli-reactive guided liberation of active compounds through chemically extractible nanoparticles as coatings were obtained in 2003 (Lai et al., 2003; Lin et al., 2012). Since then, research focused on the addition of different compounds to obtain various diagnostic or therapeutic effects, which include: controlled drug delivery (Lai et al., 2003; Schlossbauer et al., 2009; Shen et al., 2017) and targeting (Wang et al., 2010; Shen et al., 2017).

Multifunctional mesoporous silica with imaging capabilities were synthesized and reported in 2006 (Kim et al., 2006; Lin et al., 2006). Until now, various routes to incorporate imaging agents were designed, for example fluorophores (for fluorescence imaging, Lin et al., 2005; Wu et al., 2008), or superparamagnetic nanoparticles (Kim et al., 2006; Lin et al., 2006).

From 2008, *in vivo* investigations have been achieved for the identification of mesoporous silica biodistribution (Kim et al., 2008; Lin et al., 2012), toxicity (Huang et al., 2011; Meng et al., 2011), and therapeutic effect (Kim et al., 2008; Meng et al., 2011).

Although these nanomaterials have gain an increased interest and proved their compatibility for bio-applications in the last 10 years, various aspects must be taken into consideration prior to be clinically used (Lin et al., 2012). For instance, if they are intravenous injected, the biodistribution depends on the particles diameters and surface properties, therefore, the concern must be targeted in the size and stability control under the biological environment (37°C, highly salted or serum-containing media) before injection (He et al., 2010; Lin et al., 2012). Another aspect that must be taken into consideration is the toxicity of mesoporous silica nanomaterials, the adverse effects being carefully examined.

Various studies concentrated on *in vitro* drug delivery, controlled release, or toxicity of mesoporous silica materials (Rosenholm et al., 2010; He and Shi, 2011; Lin et al., 2011; Xu et al., 2012). This review will mainly emphasize advancement in the domain, underlining the emergent synthesis methods, strategies to improve mesoporous silica stability and biodegradability.

Nowadays, the chemotherapeutics delivery evolved, resulting nano-encapsulated drug formulations which can improve the pharmacological profile of the free drugs. However, mesoporous silica materials are gradually receiving interest due to their unique properties, such as well-established drug delivery properties (Vallet-Regi et al., 2007) and versatility for creating high-performing hybrid materials. Besides mesoporous silica, other multifunctional devices based on various nano-platforms were discovered (Soenen et al., 2011; Monnier et al., 2014; Chauhan et al., 2018; Hameed et al., 2018).

It is well-known that bulk silica is intensively used in food or cosmetic industry, indicating that it has low toxicity. FDA (US Food and Drug Administration) cataloged silica compound

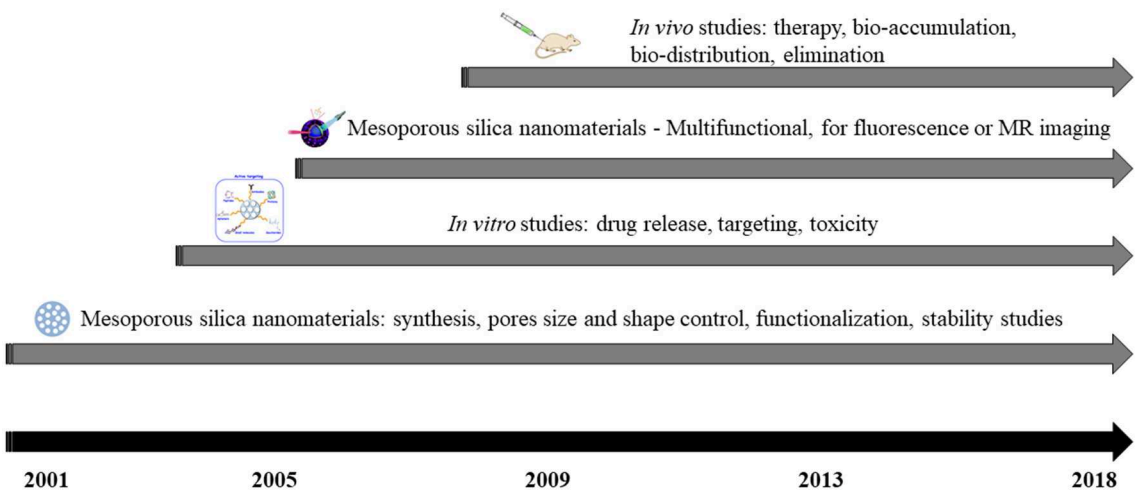


**FIGURE 1 |** Timeline scheme of mesoporous silica nanomaterials development for bio-applications.

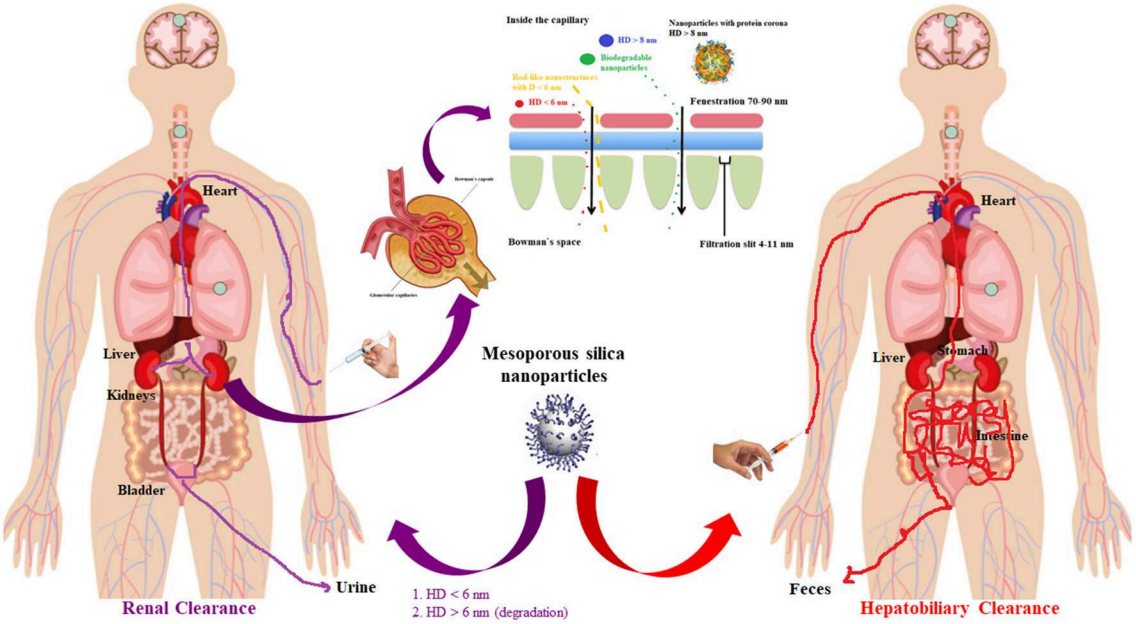


**FIGURE 2 |** Scheme of the main nanoparticles metabolic path and the glomerular filtration barrier.

as safe (ID Code: 14808-60-7)[1]. However, when a chemical compound is conceived like a nanomaterial, new limitations or safety risks arise, caused by their particles size (Lin et al., 2012). As an example, the interaction that appears between the nanoparticles and the cells, allowing their assimilation by the tumor cells, could result in unpredicted side effects in the healthy cells (Buzea et al., 2007).

For the mesoporous silica utilization in bio-approaches (Santos et al., 2015), the matrix degradation should be considered for the elucidation of the release kinetics, although for functionalized silica the parameter is harder to manage (Allen and Cullis, 2013; Sercombe et al., 2015).

The parameters and effects that must be monitored include, beside the degradability and the possibility to be eliminated (**Figure 2**), the size (Shang et al., 2014), shape (Huang et al., 2010; Li et al., 2015), pore volume (Li et al., 2018), and surface functionalization. Mesoporous silica with 100–200 nm nanoparticles dimensions are considered the optimal choice, preventing fast release (Li et al., 2012; Lin et al., 2012) and acute toxic effect (Napierska et al., 2009; Nishimori et al., 2009; Abbaraju, 2017), without aggregating on physiological fluids, blood capillaries and alveoli (McCarthy et al., 2012; Abbaraju, 2017).

Furthermore, the rod-like particles are considered more satisfactory than the spherical particles, as a consequence to easily achieve polyvalent interactions with the membranes (Huang et al., 2010; Meng et al., 2011; Lin et al., 2012).

The interest on mesoporous silica for drug delivery depends on various factors the most important being the scale of the silica nanoparticles interaction with living systems. Before reaching the market, all nanomedicines must be industrially transferred, obviously, after clinical translation. Regarding the first step, the industrial technology is related to the scaling up process, involving also the reproducibility and the total costs, resulting in the ordinary barriers for commercialization. For example, the mesoporous silica nanoparticles are obtained in the lab from milligrams to grams of product, but the large-scale batches production under Good Manufacturing Practices (GMP) conditions is a roadblock to their commercialization. Furthermore, reproducibility on their synthesis at small scale is relatively easy, but at the industrial scale is difficult. In this respect, the mesoporous silica clinical translation has been delayed, being blocked in the first milestone, whether or not the nanoparticles are reproducible and scalable, in terms of stability and high loading capacity. So far, researchers have not overlapped this milestone, although some advances were made. The next milestone to consider must be related to their potential toxicity and immunogenicity, which has been found to strongly depend on the surface functionalization. It has been demonstrated that mesoporous silica was perfectly biocompatible, in different animal models, in which toxicity has been discarded. However, until now, the mesoporous silica nanomaterials were not evaluated into any clinical trial, this being a delicate step, since many nanodrugs failed the clinical translation even before the clinical trials because of reiterative pitfalls.

Taking into account all the above-mentioned drawbacks and limitations, the integration of various features in a single entity could be considered a mirage. This review will highlight

[1]https://www.drugs.com/inactive/silicon-dioxide-colloidal-200.html (accessed July 28, 2019).

also the evolution of hybrid inorganic-silica nanomaterials with various bio-applications.

Taking into account all aspects, to currently categorize the mesoporous silica nanomaterials as appropriate tools for bio-applications, they must act in accordance with modification requirements with respect of morphology and surface, resulting in the minimization of the immune reply and enhance tissue/cell recognition—targeting.

## SYNTHESIS OF MESOPOROUS SILICA NANOMATERIALS

At the beginning, scientists focused on improving the synthesis of mesoporous silica nanomaterials, trying to control their pore structure, size, and stability. **Table 1** summarizes some typical synthesis methods for the mesoporous silica nanomaterials.

Typical scanning and transmission electron microscopy (SEM and TEM) images of mesoporous silica prepared by our group are presented in mesoporous **Figure 3** (Miricioiu et al., 2019).

Mesoporous silica nanoparticles can be used as host materials for transporting therapeutics medicaments or encapsulation of molecules due to their biocompatibility, high loading capacity, the capability to attach target ligands for specific cellular recognition, or the design of well-defined and tuneable porosity (Tang et al., 2012; Hao et al., 2016; Vazquez et al., 2017). In order to achieve these, the morphology of the silica must be considered as one of the most important factors. One common synthesis method for mesoporous silica is the use of structure directing agents (neutral or charged surfactants) (Yuan et al., 2011; Vazquez et al., 2017). Generally, mesoporous silica are obtained from a silica precursor (or sodium silicate tetraethylorthosilicate-TEOS) by incorporating a surfactant, in an alcoholic solution under basic conditions (Pang and Tang, 2005; Hodali et al., 2016). Some studies focused on the mechanism of silica nanospheres and nanorods formation, by modifying the surfactant concentration (Lelong et al., 2008; Wang et al., 2013) and sol-gel dilution (Chen and Wang, 2012). The interaction between the Si–O–Si/species and the surfactant was monitored, and the pore diameters, shape, order, and morphology were correlated with the surfactant properties (size, length, etc.) (Vazquez et al., 2017). Also, the mesoporous silica obtaining was studied in non-alcoholic medium (Lelong et al., 2008; Chen and Wang, 2012; Vazquez et al., 2017), but the spherical particles formation was restricted by the surfactant amount (under 1 wt.%). The specific surface area of the mesoporous silica materials was around 1,030–1,070 $m^2/g$, with a pore volume of 0.81–0.85 $cm^3/g$. The use of EtOH was considered, maintaining a fixed amount of CTAB (4.1 wt.%) and ordered spherical and rod-like particles was obtained (Wang et al., 2013). The mesoporous silica material presented a specific surface area of 1,500 $m^2/g$ and a pore volume of 0.86 $cm^2/g$. As it can be noticed, the dilution of the sol-gel results in the modification of the specific surface area and in the transformations of the particles morphology (from spherical to rod-like), highlighting that silica mesoporosity and morphology are related to the micelles formation and ordering.

A general synthetic route follows some typical steps: a silica source (tetraethyl orthosilicate-TEOS or sodium orthosilicate-$Na_2SiO_6$) is mixed with a surfactant, then, a hydroxide ($NH_4OH$ or NaOH) is added, allowing that the silicate is hydrolyzed, surrounding the spherical micelles; finally, in order to silicate micelles self-assemble into cylinders, the mixture must be subjected to hydrothermal treatment (Lin et al., 2012). Surfactant can be removed by calcination, solvent extraction, or dialysis. First mesoporous silica with nanoparticles adequate for bio-application were obtained in 2001 (Fowler et al., 2001; Lin et al., 2012). Afterwards, many investigations adopted the introduction of a co-solvent or another surfactant (Lin et al., 2012) for particles growth suppression, in order to get mesoporous silica nanomaterials with controlled size—**Table 1** (Cai et al., 2001; Fowler et al., 2001; Lin and Tsai, 2003; Han and Ying, 2005; Berggren and Palmqvist, 2008; Sutewong et al., 2011).

The addition of surfactant during the synthesis generates a structure with many small pores (mesoporous structure) between 2 and 50 nm, according to IUPAC notation (Assefa et al., 2016). Recently, templates as chitosan were used to inherent amino and hydroxyl functional groups, intermediating future functionalization of the mesoporous silica (Lalchhingpuii et al., 2017).

In order to produce silica nanomaterials with size suitable for bio-applications, a catalyzed sol–gel process has been employed. This process uses the organo-silane precursors which, by hydrolysis (1) and condensation (2), generating a new state (sol) (Brinker and Scherer, 1990; Mai and Meng, 2013):

$$Si\,(OR)_4 + OH^- \rightarrow Si(OR)_3OH + RO^- \quad (1)$$

$$SiO^- + Si\,(OR)_4 \rightarrow Si - O - Si + OH^- \quad (2)$$

For example, monodispersed nanosilica with particles size between 50 and 2,000 nm was obtained by Stober process, using the hydrolysis of tetraethylorthosilicate, catalyzed by ammonia, in an aqueous alcohol solution (Stober et al., 1968; Yanagisawa et al., 1990). The first *sanvicens* mesoporous silica nanomaterials were synthesized for catalytic applications (Yanagisawa et al., 1990; Kresge et al., 1992). Later, sub-micrometer-scaled MCM-41 particles were prepared by a modified Stober process (Grun et al., 1997) and MCM-41 with 100 nm was synthesized by means of a diluted surfactant solution (Cai et al., 2001). Nano-silica with particle diameter under 50 nm were synthesized by applying two surfactants or dialysis (Suzuki et al., 2004; Li et al., 2012).

MCM-41 silica was typically obtained via a surfactant (hexadecyltrimethylmonium bromide) dispersed in ultrapure water; the mixture is stirred for several hours in ambient conditions; then the silica source, for example sodium silicate is added, stirring continuously the mixture. After that, the mineralizer, tetramethyl ammonium hydroxide is added, stirring the mixture another 30 min (Oshima et al., 2006). Then, the pH is adjusted to 10.5, checking it after 15 min. The mixture is agitated for 24 h and then it is subjected to hydrothermal treatment, by introduction into an autoclave 3–5 days, at 100–120°C. The resulting mixture is filtered under vacuum, washed with water and dried (Miricioiu et al., 2019). After aging,

**TABLE 1 |** An overview of some synthesis methods for mesoporous silica nanomaterials.

| Surfactant | Silica source | Size control method | Particle size (nm) | Pore structure | Surfactant removal | References |
|---|---|---|---|---|---|---|
| Hexadecyltrimethyl monium bromide | Tetraethyl orthosilicate | Water dilution and neutralization | 60–100 | Ordered 2D hexagonal | Calcination | Fowler et al., 2001 |
| Hexadecyltrimethyl monium bromide | Tetraethyl orthosilicate | Dilution | 100–2,500 | Ordered 2D hexagonal | Calcination | Cai et al., 2001 |
| $C_n$TAMX alkyltrimethyl ammonium halide ($n$ = 14-18; X = Br or Cl) | Sodium silicate | Low concentration of surfactant-silica source | 30–70 | Disordered | Calcination | Lin and Tsai, 2003 |
| Pluronic P65, P123, F108, F127 | Tetraethyl orthosilicate | Surfactant suppresses particles growth | 100–300 | Ordered 3D cubic | Calcination | Han and Ying, 2005 |
| Pluronic P123 | Tetraethyl orthosilicate | Water and salt addition | 50–300 | Ordered 2D hexagonal | Calcination | Berggren and Palmqvist, 2008 |
| Hexadecyltrimethyl monium bromide | Tetraethyl orthosilicate and (3-aminopropyl) triethoxysilane | Dye incorporation and pore expander addition | 100–220 | Ordered 3D cubic | Ethanolic acid extraction | Sutewong et al., 2011 |

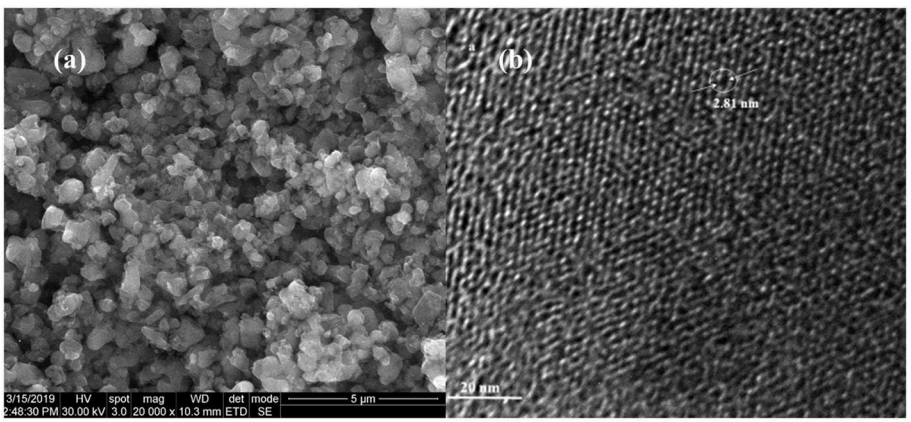


**FIGURE 3 |** Typical scanning electron **(a)** and transmission electron **(b)** microscopy for MCM-41 mesoporous nanosilica.

the resulting nanoparticles are calcined at 550–600°C in order to eliminate the excess of hexadecyltrimethylmonium bromide and to weaken the interactions between the surfactant and the formed silica (Li et al., 2012). Scanning and transmission electron microscopy certified the hexagonal arrangement after the hexadecyltrimethylmonium bromide removal (**Figure 3**; Miricioiu et al., 2019).

## FUNCTIONALIZATION OF THE MESOPOROUS SILICA NANOMATERIALS

For the silica nanomaterials extension in the bio-domain, physical and chemical surface modifications have been applied. In this manner, the biocompatibility can be enhanced, the non-specific adsorption can be prevented and functional groups for further biomolecule conjugation purposes can be provided. The most common surface modification includes layer by layer self-assembly (LSA) and chemical surface functionalization (Jafari et al., 2019).

The mesoporous silica nanomaterials can be functionalized by incorporation during the synthesis of metal or metal oxide nanocrystals (**Figures 4a,b**).

A heterogeneous mixture formed by the surfactant-coated metal nanocrystals in an organic solvent must be added to a solution of a surfactant (such as hexadecyltrimethylmonium bromide), in order to obtain a metal-functionalized silica (Li et al., 2012). Then, a silicate source is added to the mixture to promote the condensation reaction, thus, gold, silver and iron oxide being embedded into the mesoporous silica (Coti et al., 2009; Thomas et al., 2010). This functionalized systems can possess various bio-activities, for example antimicrobial, assured by the dissolved metallic ions, plasmonic, or magnetic characteristics (Li et al., 2012).

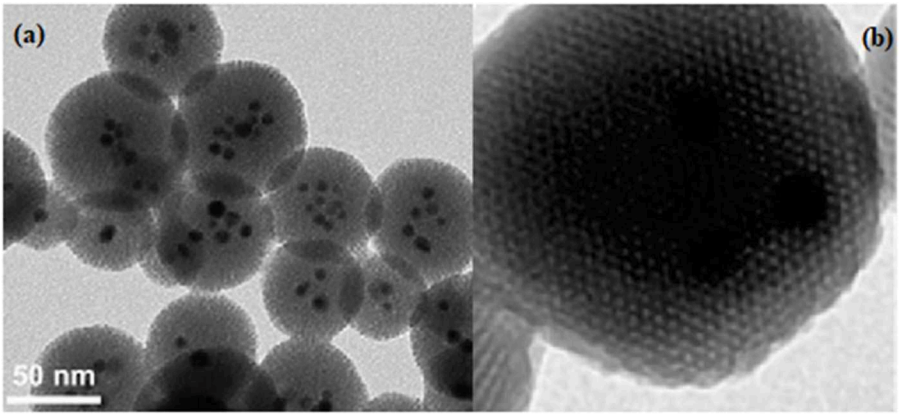


**FIGURE 4 |** Typical TEM image for **(a)** mixed iron-oxide and silver mesoporous silica and **(b)** Zn embedded in mesoporous silica.

To evaluate the substantial effect of different functionalization methods, research have been achieved to design colloidal core–shell mesoporous silica with various types of linear PEG (polyethylene glycol) modifications (Cauda et al., 2010). The silica functionalization can decrease the degradation rate comparing with the un-functionalized ones, the explication being the existence of the PEG matrix on the nanomaterial surface. PEG is hydrophilic, preventing in this manner the proteins adsorption and it reduces unwanted interactions of the physiological environment with the nanosilica (Yang et al., 2019).

Other research highlighted the silica surface functionalization with hydroxyl, carboxyl and PEG groups (noted OH–SiNPs, COOH–SiNPs, and PEG–SiNPs)and their bio-distribution and urinary excretion were studied (**Figures 5A,B**; He et al., 2008).

*In vivo* optical data from the urinary bladder showed that the nanomaterials were partially eliminated through renal route, highlighting that these modifications are independent on the renal elimination (**Figure 5C**; Yang et al., 2019). Nevertheless, PEG derivate manifested longer blood circulation and lower liver uptake compared to the hydroxyl and carboxyl derivates.

Various research investigated the SBA-15 silica functionalization. For studying the effect of surface functionalization upon deterioration behavior, Kim et al. explored the biodegradation of functionalized SBA-15, modified with hydroxyl, amine and carboxyl moieties on the surface (Choi et al., 2015; Yang et al., 2019). The carboxyl functionalized silica had the lowest degradation percentage. These studies indicated that the SBA-15 surface functionalization results in a reduction of the degradation rate then the neat silica, highlighting that the functionalization could affect the silica shell corrosion by connecting with the cations from the biological media for reducing the SBA-15 clearance rate (Choi et al., 2015; Yang et al., 2019).

A key factor that enables silica nanomaterials to be used in bio-applications is the capability to capture various loads in the pores channels, thus protecting the active compounds from enzymatic degradation (Li et al., 2012). The mesoporous silica nanoparticles are usually charged by immersion in the active compound solution, the therapeutic being assimilated through adsorption. When silica surface is functionalized, the cargo is able to be controllable released at the targeted damaged tissue, no premature release in the bloodstream being observed, reducing any secondary effect and increasing the therapeutic efficiency (Li et al., 2012). For example, Niculescu et al. reported SBA-15 mesoporous silica functionalized with amino groups from organic amines (aminopropyl triethoxysilane) for bio-active coordinative complex delivery (Niculescu et al., 2018). It was observed a linkage between the functional groups from the coordination compound and the amino groups from the silica surface, resulting an improvement of the hydrophobic interaction with the hydrophobic active principle (Niculescu et al., 2018). Once the degree of silylation is decreased by amination, the drug release rate will be improved.

## BIOCOMPATIBILITY

In the context of bio-applications, mesoporous silica nanomaterials are generally considered biocompatible, with minimal non-specific or adverse effects. However, there are several factors that affect the silica biocompatibility, such as individual size, shape, and surface chemistry, until this moment the mesoporous silica biocompatibility remaining inconclusive (Hudson et al., 2008; Tang et al., 2012). This review take into account the current advances on how particles shape, size and surface properties influence the interaction with living cells (Jafari et al., 2019).

The biocompatibility, bio-distribution and clearance are influenced by the mesoporous silica nanomaterials morphology. For example, short-rod mesoporous silica is distributed predominantly at the liver level, whereas long-rod silica is caught in the spleen and manifest a reduced elimination rate (Huang et al., 2011; Jafari et al., 2019). The particles shape also influences cellular uptake, *in vitro* research reporting that the shape is independent of the endocytosis rates and dependent on endocytotic rate (Trewyn et al., 2008; Jafari et al., 2019).

Particles dimensions can influence the biological parameters (distribution, duration of blood circulation, or elimination rate) (Jafari et al., 2019). When the nanoparticles are intravenously delivered, they are predominantly directed to the liver and

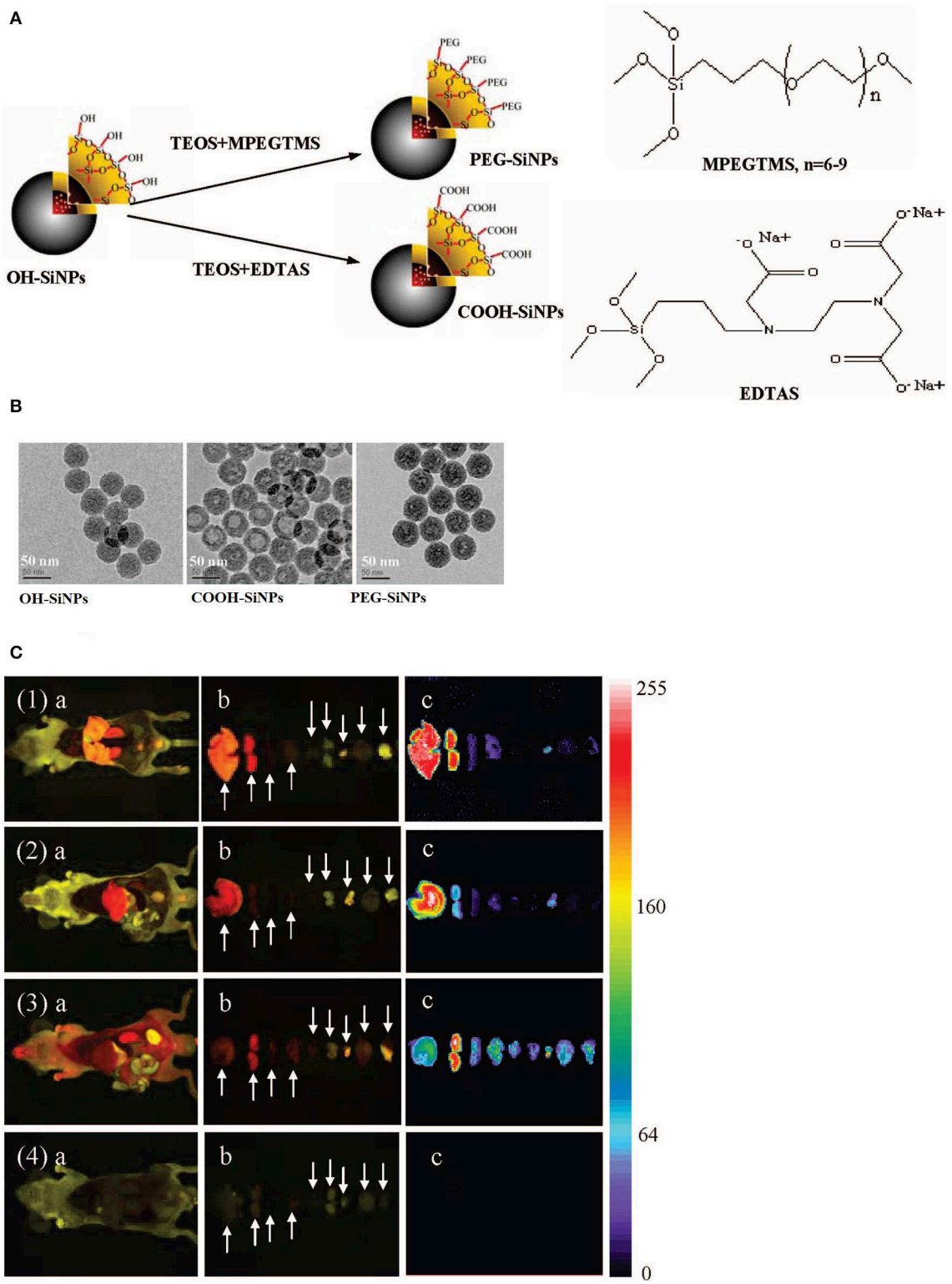


**FIGURE 5 |** Illustration **(A)** and TEM images **(B)** of three silica surface functionalized nanomaterials. **(C)** *Ex vivo* imaging of mice after intravenous injection, with various organs throughout necropsy after 4.5 h, for treated mice (1) OH–SiNPs, (2) COOH–SiNPs; (3) PEG–SiNPs and untreated mice (4). Arrows represent from left to right: liver, kidney, spleen, lung, heart, spermary, bladder, brain, and muscle. Reproduced with permission He et al. (2008) Copyright 2008, American Chemical Society.

spleen (Maleki and Hamidi, 2016). The silica nanoparticles with smaller size have a longer blood circulation lifetime (He et al., 2011). The mesoporous silica nanoparticles elimination by urine increases with the particles size, affecting the degradation rate and the biocompatibility. *In vitro* studies showed some toxicity for spherical 1,220 nm nanoparticles at concentration levels higher than 25 mg/mL (He et al., 2009).

Furthermore, the mesoporous silica nanomaterials biocompatibility may be influenced by the surface properties. Cationic charges on the surface may produce considerable immune reaction and cytotoxicity in contrast with the neutral and anion counterparts (Nel et al., 2009; Verma and Stellacci, 2010; Jafari et al., 2019), but they are favorable for trans-vascular transport in tumors. A negative zeta potential is considered related to the serum opsonin. The mesoporous silica biocompatibility is affected by the silanol groups at the outer layer, they negatively interacting with the biological molecules and destroying their structure (Slowing et al., 2009). Therefore, surface functionalization is essential for altering surface reactivity, in order to enhance the biocompatibility.

# BIO-APPLICATIONS

## Drug Delivery

Mesoporous silica nanomaterials present unique properties that qualify them as ideal nano-carriers for hosting, protecting and transporting drugs to the target site. The incorporation of targeting agents at the mesoporous silica surface is feasible for conducting them to the damaged tissue, growing the specificity and reducing unwanted secondary effects (Lin et al., 2012). Furthermore, multifunctional mesoporous silica nanomaterials can be design so that they possess synergistic therapeutic effects against diseased tissues. Most of the investigations on the mesoporous silica for drug delivery has been dedicated to cancer therapy.

The first study on silica type-MCM-41 for ibuprofen controlled release was achieved by the group of Vallet-Regi et al. (2001). The ibuprofen liberation profile highlighted a divergent behavior, which depends on the way that the active substance is loaded in the silica, but it is independent on the pore size. The *in vitro* experiments were achieved within constant state and the mixture was not stirred while the drug was released, limiting the diffusion at the particles surface (Wang, 2009). Later on, other study focused on the effect of pores size from the MCM-41 on the ibuprofen release rate, revealing that, in a simulating body fluid (SBF) solution, it is decreasing direct proportional with the pores size decreasing in the domain of 2.5–3.6 nm (Horcajada et al., 2004).

Another important mesoporous material for therapeutics delivery systems is MCM-48 silica, recently attracting interest due to its matrix containing unique penetrating bi-continuous channels, which can be used when easy molecule accessibility and rapid transport is required. MCM-48 was investigated as carrier for ibuprofen and erythromycin (Izquierdo-Barba et al., 2005), the therapeutics release rate decreasing with the pores diameters and the surface chemical modification (Izquierdo-Barba et al., 2005).

Several investigations have been reported for drug delivery based on organic modified mesoporous materials. It is generally accepted that the functionalization influences the adsorption and delivery. MCM-41-based materials were modified with organic aminopropyl groups for the control of the ibuprofen release, the functionalization being decisive for the active compound adsorption and release (Munoz et al., 2003; Zeng et al., 2005).

From the same class of mesoporous silica, SBA-15 with large and controlled pore size has a high ordered hexagonal matrix (Zhao et al., 1998). The SBA-15 has pores with an average diameter around 6 nm, larger than the MCM-41 pores diameter, which is around 3 nm (Niculescu et al., 2011). Due to this characteristic, it is generally assumed that SBA-15 will present less limitation for the release of bulk molecules. Calcined SBA-15 was tested for the antibiotic amoxicillin delivery (Vallet-Regi et al., 2004), proven that the drug quantity incorporated within the silica network depends on the solvent, pH, and amoxicillin concentration (Zhang et al., 2018). In the pure SBA-15, the Si-OH groups exist only at the surface, forming weak hydrogen bonds with the active compound; this is the reason why silica is not strong enough to retain the drug and allow it to be delivered in a sustained manner (Hashemikia et al., 2015; Zhang et al., 2018). In order to surpass this milestone, functional groups were introduced on the surface of SBA-15 (Doadrio et al., 2006).

SBA-15 nanomaterials were post- and one-pot reaction modified with amino groups for ibuprofen (IBU) and bovine serum albumin (BSA) delivery (Song et al., 2005). Results showed that the drugs assimilation and delivery were extremely influenced by the SBA-15 silica surface properties. The ibuprofen delivery from the post-synthesis functionalized SBA-15 was efficiently controlled, because of the ionic interaction established between the ibuprofen carboxylic groups and the amino groups from silica surface. Recently, SBA-16 mesoporous silica was used for immobilization and release of two antiseptic organic complexes with Zn was tested in deionized water, not in a simulated body fluid (Zelenak et al., 2005). The complexes were liberated after 10 h. Nevertheless, traces of the active compounds were found in the silica after 80 h, as a consequence of the vigorous immobilization in the silica matrix.

MSU-type mesoporous silica has also been studied for drug delivery, such as penta-peptide drug, which is instantaneously delivered after the solid was washed with dimethylformamide (DMF) (Tourne-Peteilh et al., 2003; Wang, 2009). Ibuprofen and antipyrine can be delivered by carbonized mesoporous silicon microparticles, but no release profile was reported (Lehto et al., 2005).

## Cell Imaging and Photosensitizer Carrier

The silica nanoparticles can be used in imaging, dye-doped materials being synthesized by Stöber or reverse micro-emulsion method. Monodispersed solid nanosilica with particle diameter between 50 nm and 2 μm was obtained by Stöber method, which is a simple and efficient approach. The first well-dispersed colloidal silica spheres including fluorophores or dyes were

synthesized by Vanblaaderen and Vrij (1992) and Abbaraju (2017). This study was extended for obtaining fluorescent core-shell nanosilica particles (C dots), which are water-soluble and non-toxic and having particle diameters between 20 and 30 nm (Ow et al., 2005; Abbaraju, 2017). These dots constitute biological exploration devices with increased bio-stability, dye quantum effectiveness and diminished energy transfer reaction, caused by the limited rotational motility of the dye captured in the C dots nucleus, assuring the preservation against a dissolution medium effect or molecular quenchers (Burns et al., 2009; Abbaraju, 2017). FDA approved the use of the C dots in human clinical trial in 2011, the study showing that the nanoparticles were harmless in human use, without any traces after renal elimination (Abbaraju, 2017).

The reverse micro-emulsion method for obtaining dye-doped nanosilica particles involves the use of water, surfactant and oil (Jin et al., 2011). The silica precursor's hydrolysis, condensation, and the formation of dye trapped nanoparticles occur at the surfactant-oil interface, to form fluorescent nanoparticles. By using this method, monodispersed silica nanoparticles with the diameters of 30–60 nm were obtained (Santra et al., 2001a,b; Bagwe et al., 2004; Sanvicens and Marco, 2008; Yoo and Pak, 2013). In 2004, a modified micro-emulsion method was reported for the incorporation of organic dye into silica nanoparticles (Zhao et al., 2004). The same approach was applied for obtaining hybrid silica nanoparticles doped with Pb-Se quantum dots for cell imaging, their toxicity being lowered by individual or multiple covering of the silica (Tan et al., 2007; Abbaraju, 2017).

Moreover, hollow nanosilica containing vast cavity and mesopores were used for optical magnetic resonance imagistic, positron emission tomography (PET) (Suschek et al., 2002; Abbaraju, 2017) and ultrasound imaging (Shi et al., 2013).

Photodynamic therapy is a photosensitizer-based tumor ablative treatment, followed by the tumor local radiation at a specific wavelength in order to activate the photosensitizer (Suschek et al., 2002; Abbaraju, 2017). After activation, it shifts the energy to molecular oxygen, producing reactive oxygen entities with cytotoxic effect, which are able to oxidize the target cellular macromolecule, resulting in the tumor cell removal (**Figure 6**; Lucky et al., 2015).

Mesoporous silica nanomaterials have also been employed as vehicles for fluorescent agents, being optically transparent due to their nanoscale particle size, not disturbing the emission of fluorescent agents. Taking into account that quantum dots can be easily oxidized, exhibiting fluorescence, PEGylated liposome-coated quantum dots-mesoporous silica were developed the oxidation prevention and the dispersion stability improvement (Pan et al., 2011; Wang et al., 2015). For example, the *in vitro* study of cadmium ions as quantum dots highlighted that the liposome-modified mesoporous silica prevented the quantum dots degradation (Pan et al., 2011).

An effective biomedical tool is considered the magnetic resonance imaging (MRI), providing the capacity to non-invasively get anatomic and functional data with high resolution (Wang et al., 2015). Mesoporous silica nanomaterials-based magnetic resonance contrast agents exhibit an increased sensitivity due to their high specific surface, providing increased payloads of the active magnetic centers (Wartenberg et al., 2013; Cha and Kim, 2019). Moreover, silica mesoporous structure provides easy access into the magnetic center. Mesoporous silica nanomaterials functionalized with targeted ligands may be efficiently conducted to damaged tissue for diagnostic goals, the accumulation of these nanomaterials-based magnetic resonance contrast agents at the selected site conferring an augmented imaging susceptivity (Wang et al., 2015).

Mesoporous silica nanoparticles are also used for application in photodynamic therapy, being vectors due to their flexible synthesis, porosity and the matrix capacity to absorb the light (Abbaraju, 2017). For example, there were prepared organically modified nanosilica particles for the retention of 2-devinyl-2-(1-hexyloxyethyl)-pyropheophorbide (HPPH), which is a photosensitizer used in phase I/II of clinical trials for treating esophageal cancer (Roy et al., 2003; Abbaraju, 2017). The entrapment of the photosensitizer into mesoporous silica nanoparticles can conduct to the discharge from the nanocarrier, inducing reduced efficiency. Some mesoporous silica nanomaterials were obtained for combined photodynamic and photothermal therapy, by using the release of carboxy aluminum phthalocyanine with small Pb nanosheets (Zhao et al., 2014; Abbaraju, 2017). The mesoporous silica nanomaterials covalently bond the photosensitizer, while the Pb electrostatically covered

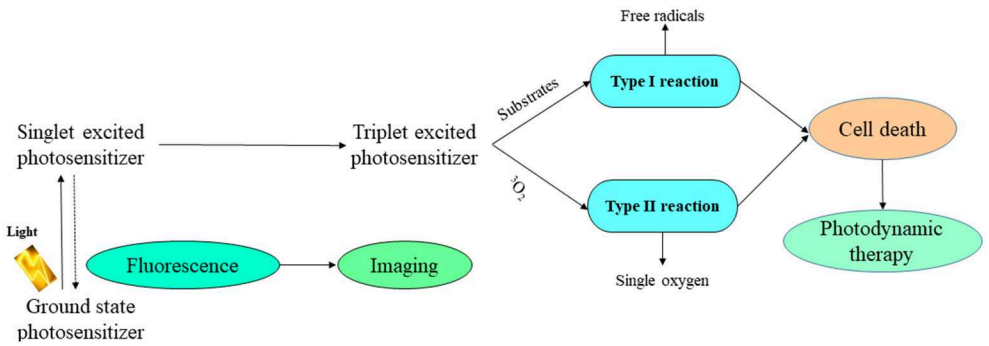


**FIGURE 6 |** Schematic photodynamic reaction. Adapted with permission Lucky et al. (2015) Copyright 2015, American Chemical Society.

the silica surface. The HeLa-type cervical cancer cells viability decreased with 65% after the administration of functional nanocomposites, the effect being significant than the individual treatment (Abbaraju, 2017).

## Mesoporous Silica Nanomaterials in Vaccines

The actual challenge in vaccines includes the induction of strong and safely immune-protective response in the host at low cost. Mesoporous silica nanomaterials can be used as an antigen carrier due to antigen preservation and its delivery to presenting cells (Kapczynski et al., 2012; Abbaraju, 2017).

For example, SBA-15-type nanomaterial possesses enhanced immunogenicity and immune reaction than $Al(OH)_3$, *in vitro* macrophages studies showing that silica manifested increased phagocyte intake and minimal interaction with the cells (Carvalho et al., 2010; Abbaraju, 2017). Furthermore, the highest concentration of SBA-15 also conducted to a significant increase of the cells number, creating interleukin(IL)-4 and interleukin(IL)-13 and, generating a heterogeneous reaction of both Th1-type and Th2-type cytokines (Abbaraju, 2017).

Mesoporous silica rods were tested in adjusting the immune cells and potential application as a vaccine matrix to induce adaptive immune reaction (Kim et al., 2015; Abbaraju, 2017). *In vivo* tests showed that mice immunized with full mesoporous silica rods vaccine manifested important growth of Thy $1.2^{+}$ leukemic cells, inducing increased expression of the Peripheral blood $CD^{4+}$ $CXCR^{5+}$ T helper cell clonal and T follicular helper cells differentiation (Kim et al., 2015). The silica surface modification effect upon immune cell activation was studied (Abbaraju, 2017). The mesoporous silica nanomaterials were modified with poly(ethylene glycol) (PEG) and poly(ethylene glycol) (PEG)/arginine-glycine-aspartic (RGD) and they were investigated in the immune cell adhesion and infiltration, the PEG derivate inducing higher CD86 expression than the RGD derivate (Abbaraju, 2017). Also, the PEG-RGD derivate exhibited lower inflammatory effect than the PEG-one.

However, the impact of all the crucial factors in adjusting the immune reaction was not completely elucidated. The effect of nanomaterials pores and particles size on immunological properties was studied by orally administration to mice, using Bovine serum albumin as model adjuvant (Wang et al., 2012). Three types of nanosilica particles with various particles diameters {S1, [S2 and 1-2(SBA-15)]} were applied, the Immunoglobulin G antibody from the plasma after oral administration of bovine serum albumin-loaded S1, S2, SBA-15 being in the sequence SBA-15<S2<S1 (Abbaraju, 2017).

Also, the influence of particle size on targeting dendritic cells was studied, demonstrating that the particles smaller than 20–30 nm in diameter can straight get to dendritic cell. **Figure 7** presents the silica nanoparticles delivery into lymph nodes. Nevertheless, particles with diameters higher than 20 nm can be phagocyted and the dendritic cells uptake is also presented (Navarro-Tovar et al., 2016).

On the other hand, silica nanomaterials were also used for DNA vaccines delivery, relying on the transitory manner of the intended antigen in the host cells (Navarro-Tovar et al., 2016). Silica nanomaterials-DNA exhibited a clear enhancement in the immunogenicity, in contrast with DNA at a reduced magnitude as against the conventional vaccine. Silica-based vaccine also manifested increased proliferative responses, suggesting that silica nanomaterials can be considered as good delivery systems for the DNA vaccines, stimulating cellular and humoral reactions. This perspective for the distribution by mucosal routes constitutes an important target, due to the advantages of mucosal immunization such as easy administration and immune profiles.

## CONCLUSIONS

Various types of nanosystems for cancer-targeted imaging and therapy were developed in the last decade. Among them, silica-based nanomaterials have been extensively synthesized, due to their non-toxic nature and facile chemistry for surface functionalization. The state-of-the-art reflected that

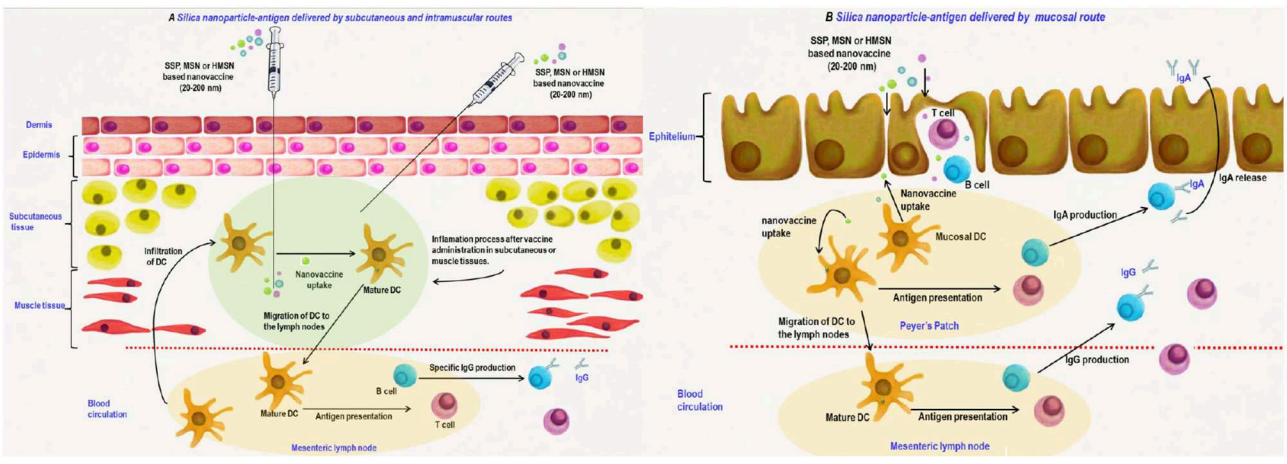


**FIGURE 7 |** Silica nanomaterials-based vaccines delivery by parenteral **(A)** and mucosal **(B)** routes. Adapted with permission Navarro-Tovar et al. (2016) Copyright 2016, Taylor & Francis.

materials based on nanosilica constitute fascinating media for new vaccines design, insuring the antigen conjugation (Cassano et al., 2017) and cellular adaptive immune responses. Mesoporous silica nanoparticles have been used in clinical trials for diagnostic purposes and drug delivery. The toxicity of these nanomaterials should be further investigated and evaluated at the clinical and pre-clinical levels. Concluding, the utilization of silica nanoparticles is significantly influencing the medicine domain, by obtaining new compounds to fight epidemiologic diseases.

This review drew special attention the main progress in drug delivery and bio-applications (Wang et al., 2015) of mesoporous silica nanomaterials. Mesoporous silica nanomaterials have attractive characteristics, such as a large specific surface, uniform and tuneable pores, increased pore volume, and decreased mass density (Kumar et al., 2018). They were intensively studied for drug delivery since 2000, to provide the improvement of the drug loading capacity and *in vivo* targeting efficiency, decreasing the unwanted effects on healthy organs. Due to their versatile mesoporous structure and porosity, they possess important advantages, for example, as drug delivery system, the release of the cargo is well controlled. Also, magnetic and luminescent mesoporous silica nanomaterials provide the simultaneous bioimaging and drug delivery.

However, significant milestones must be addressed, for example, obtaining novel multifunctional mesoporous silica nanomaterials with controllable drug release, which can also be supervised via on line bioimaging in the target tissue (Wang et al., 2015). Also, more comprehensive and detailed toxicity tests are required before the mesoporous silica nanomaterials may be used in human patients. In order to design mesoporous silica nanomaterials appropriate in biomedical applications with no side effects, intensive *in vivo* tests are still required.

## AUTHOR CONTRIBUTIONS

V-CN conceived and designed the study, contributed to the collection of data, performed the data interpretation, and the manuscript writing.

## FUNDING

This research have been financed by the Romanian Ministry of Scientific Research and Innovation, under Contract no. 9N/2019 NUCLEU Program, Project PN 19 11 03 01—Studies on the obtaining and improvement of the acido-basic properties of the nanoporous catalytic materials for application in wastes valorization.

## REFERENCES

Abbaraju, P. L. (2017). *Mesoporous Silica Nanoparticles for Biomedical Application*. Aust Institute for Bioengineering & Nanotechnology Institution; The University of Queensland. Available online at: https://espace.library.uq.edu.au/view/UQ:681687 (accessed July 20, 2019).

Allen, T. M., and Cullis, P. R. (2013). Liposomal drug delivery systems: from concept to clinical applications. *Adv. Drug Deliv. Rev.* 65, 36–48. doi: 10.1016/j.addr.2012.09.037

Anselmo, A. C., and Mitragotri, S. (2015). A review of clinical translation of inorganic nanoparticles. *AAPS J.* 17, 1041–1054. doi: 10.1208/s12248-015-9780-2

Anselmo, A. C., and Mitragotri, S. (2016). Nanoparticles in the clinic. *Bioeng. Transl. Med.* 1, 10–29. doi: 10.1002/btm2.10003

Assefa, D., Zera, E., Campostrini, R., Soraru, G. D., and Vakifahmetoglu, C. (2016). Polymer-derived SiOC aerogel with hierarchical porosity through HF etching. *Ceram. Int.* 42, 11805–11809. doi: 10.1016/j.ceramint.2016.04.101

Bagwe, R. P., Yang, C., Hilliard, L. R., and Tan, W. (2004). Optimization of dye-doped silica nanoparticles prepared using a reverse microemulsion method. *Langmuir* 20, 8336–8342. doi: 10.1021/la049137j

Berggren, A., and Palmqvist, A. E. C. (2008). Particle control of colloidal suspensions of mesostructured silica. *J. Phys. Chem. C* 112, 732–737. doi: 10.1021/jp0766858

Brinker, C. J., and Scherer, G. W. (1990). *Sol Gel Science: The Physics and Chemistry of Sol Gel Processing*. San Diego, CA: Academic Press, Inc.

Burns, A. A., Vider, J., Ow, H., Herz, E., Penate-Medina, O., Baumgart, M., et al. (2009). Fluorescent silica nanoparticles with efficient urinary excretion for nanomedicine. *Nano Lett.* 9. 442–448. doi: 10.1021/nl803405h

Buzea, C., Pacheco, I. I., and Robbie, K. (2007). Nanomaterials and nanoparticles: sources and toxicity. *Biointerphases* 2, MR17–MR71. doi: 10.1116/1.2815690

Cai, Q., Luo, Z.-S., Pang, W.-Q., Fan, Y.-W., Chen, X.-H., and Cui, F.-Z. (2001). Dilute solution routes to various controllable morphologies of MCM-41 Silica with a basic medium. *Chem. Mater.* 13, 258–263. doi: 10.1021/cm990661z

Carvalho, L. V., Ruiz, R., de, C., Scaramuzzi, K., Marengo, E. B., Matos, J. R., et al. (2010). Immunological parameters related to the adjuvant effect of the ordered mesoporous silica SBA-15. *Vaccine* 28, 7829–7836. doi: 10.1016/j.vaccine.2010.09.087

Cassano, D., Pocoví-Martinez, S., and Voliani, V. (2017). Ultrasmall-in-nano approach: enabling the translation of metal nanomaterials to clinics. *Bioconjug. Chem.* 17, 4–16. doi: 10.1021/acs.bioconjchem.7b00664

Cauda, V., Argyo, C., and Bein, T. (2010). Impact of different PEGylation patterns on the long-term bio-stability of colloidal mesoporous silica nanoparticles. *J. Mater. Chem.* 20, 8693–8699. doi: 10.1039/c0jm01390k

Cha, B. G., and Kim, J. (2019). Functional mesoporous silica nanoparticles for bio-imaging applications. *Wiley Interdiscip Rev. Nanomed. Nanobiotechnol.* 11:e1515. doi: 10.1002/wnan.1515

Chauhan, D. S., Prasad, R., Devrukhkar, J., Selvaraj, K., and Srivastava, R. (2018). Disintegrable NIR light triggered gold nanorods supported liposomal nanohybrids for cancer theranostics. *Bioconjug. Chem.* 29, 1510–1518. doi: 10.1021/acs.bioconjchem.7b00801

Chen, B., and Wang, Z. (2012). *In vitro* and *in vivo* evaluation of ordered mesoporous silica as a novel adsorbent in liquisolid formulation. *Int. J. Nanomed.* 7, 199–209. doi: 10.2147/IJN.S26763

Choi, Y., Lee, J. E., Lee, J. H., Jeong, J. H., and Kim, J. (2015). A biodegradation study of SBA-15 microparticles in simulated body fluid and *in vivo*. *Langmuir*. 31:6457. doi: 10.1021/acs.langmuir.5b01316

Coti, K. K., Belowich, M. E., Liong, M., Ambrogio, M. W., Lau, Y. A., Khatib, H. A., et al. (2009). Mechanized nanoparticles for drug delivery. *Nanoscale* 1, 16–39. doi: 10.1039/b9nr00162j

Doadrio, J. C., Sousa, E. M. B., Izquierdo-Barba, I., Doadrio, A. L., Perez-Pariente, J., and Vallet-Regi, M. (2006). Functionalization of mesoporous materials with long alkyl chains as a strategy for controlling drug delivery pattern. *J. Mater. Chem.* 16, 462–466. doi: 10.1039/B510101H

Fowler, C. E., Khushalani, D., Lebeau, B., and Mann, S. (2001). Nanoscale materials with mesostructured interiors. *Adv. Mater.* 13, 649–652. doi: 10.1002/1521-4095(200105)13:9<649::AID-ADMA649>3.0.CO;2-G

Grun, M., Lauer, I., and Unger, K. K. (1997). The synthesis of micrometer- and submicrometer-size spheres of ordered mesoporous oxide MCM-41. *Adv. Mater.* 9, 254–257. doi: 10.1002/adma.19970090317

Hameed, S., Bhattarai, P., and Dai, Z. (2018). Cerasomes and Bicelles: hybrid bilayered nanostructures with silica-like surface in cancer theranostics. *Front. Chem*. 6:127. doi: 10.3389/fchem.2018.00127

Han, Y., and Ying, J. Y. (2005). Generalized fluorocarbon-surfactant-mediated synthesis of nanoparticles with various mesoporous structure. *Angew. Chem. Int. Ed*. 44, 288–292. doi: 10.1002/anie.200460892

Hao, N., Li, L., and Tang, F. (2016). Shape matters when engineering mesoporous silica-based nanomedicines. *Biomater. Sci*. 4, 575–591. doi: 10.1039/c5bm00589b

Hao, R., Xing, R., Xu, Z., Hou, Y., Gao, S., and Sun, S. (2010). Synthesis, functionalization, and biomedical applications of multifunctional magnetic nanoparticles. *Adv. Mater*. 22, 2729–2742. doi: 10.1002/adma.201000260

Hashemikia, S., Hemmatinejad, N., Ahmadi, E., and Montazer, M. (2015). Optimization of tetracycline hydrochloride adsorption on amino modified SBA-15 using response surface methodology. *J. Colloid. Interface. Sci*. 443, 105–114. doi: 10.1016/j.jcis.2014.11.020

He, Q., and Shi, J. (2011). Mesoporous silica nanoparticle based nano drug delivery systems: synthesis, controlled drug release and delivery, pharmacokinetics and biocompatibility. *J. Mater. Chem*. 21, 5845–5855. doi: 10.1039/c0jm03851b

He, Q., Zhang, J., Shi, J., Zhu, Z., Zhang, L., Bu, W., et al. (2010). The effect of PEGylation of mesoporous silica nanoparticles on nonspecific binding of serum protein and cellular responses. *Biomaterials* 31, 1085–1092. doi: 10.1016/j.biomaterials.2009.10.046

He, Q., Zhang, Z., Gao, F., Li, Y., and Shi, J. (2011). *In vivo* biodistribution and urinary excretion of mesoporous silica nanoparticles: effects of particle size and PEGylation. *Small* 7, 271–280. doi: 10.1002/smll.201001459

He, Q., Zhang, Z., Gao, Y., Shi, J., and Li, Y. (2009). Intracellular localization and cytotoxicity of spherical mesoporous silica nano- and microparticles. *Small* 5, 2722–2729. doi: 10.1002/smll.200900923

He, X., Nie, H., Wang, K., Tan, W., Wu, X., and Zhang, P. (2008). *In vivo* study of biodistribution and urinary excretion of surface-modified silica nanoparticles. *Anal. Chem*. 80:9597–9603. doi: 10.1021/ac801882g

Hodali, H. A., Marzouqa, D. M., and Tekfa, F. Z. (2016). Evaluation of mesoporous silicate nanoparticles for the sustained release of the anticancer drugs 5-fluorouracil and 7-hydroxycoumarin. *J. Sol–Gel Sci. Technol*. 80, 417–425. doi: 10.1007/s10971-016-4127-8

Horcajada, P., Ramila, A., Perez-Pariente, J., and Vallet-Regi, M. (2004). Influence of pore size of MCM-41 matrices on drug delivery rate. *Micropor. Mesopor. Mat*. 68, 105–109. doi: 10.1016/j.micromeso.2003.12.012

Huang, X., Li, L., Liu, T., Hao, N., Liu, H., Chen, D., et al. (2011). The shape effect of mesoporous silica nanoparticles on biodistribution, clearance, and biocompatibility *in vivo*. *ACS Nano* 5, 5390–5399. doi: 10.1021/nn200365a

Huang, X., Teng, X., Chen, D., Tang, F., and He, J. (2010). The effect of the shape of mesoporous silica nanoparticles on cellular uptake and cell function. *Biomaterials* 31, 438–448. doi: 10.1016/j.biomaterials.2009.09.060

Hudson, S. P., Padera, R. F., Langer, R., and Kohane, D. S. (2008). The biocompatibility of mesoporous silicates. *Biomaterials* 29, 4045–4055. doi: 10.1016/j.biomaterials.2008.07.007

Izquierdo-Barba, I., Martinez, A., Doadrio, A. L., Perez-Pariente, J., and Vallet-Regi, M. (2005). Release evaluation of drugs from ordered three-dimensional silica structures. *Eur. J. Pharm. Sci*. 26, 365–373. doi: 10.1016/j.ejps.2005.06.009

Jafari, S., Derakhshankhah, H., Alaei, L., Fattahi, A., Varnamkhasti, B. S., and Saboury, A. A. (2019). Mesoporous silica nanoparticles for therapeutic/diagnostic applications. *Biomed. Pharmacother*. 109, 1100–1111. doi: 10.1016/j.biopha.2018.10.167

Jin, D.-Y., and Yuan, J., Piper, J. (2011). "Long-lifetime luminescent nanobioprobes for advanced cytometry biosensing," in *Nanotechnology in Australia: Showcase of Early Career Research* (Singapore: Pan Stanford Publishing Pte. Ltd.), 317–345. doi: 10.1201/b11034-11

Kapczynski, A., Park, C., and Sampat, B. (2012). Polymorphs and prodrugs and salts (Oh My!): an empirical analysis of "secondary" pharmaceutical patents. *PLoS ONE* 7:e49470. doi: 10.1371/journal.pone.0049470

Kim, J., Kim, H. S., Lee, N., Kim, T., Kim, H., Yu, T., et al. (2008). Multifunctional uniform nanoparticles composed of a magnetic nanocrystal core and a mesoporous silica shell for magnetic resonance and fluorescence imaging and for drug delivery. *Angew. Chem. Int. Ed*. 47, 8438–8441. doi: 10.1002/anie.200802469

Kim, J., Lee, J. E., Lee, J., Yu, J. H., Kim, B. C., An, K., et al. (2006). Magnetic fluorescent delivery vehicle using uniform mesoporous silica spheres embedded with monodisperse magnetic and semiconductor nanocrystals. *J. Am. Chem. Soc*. 128, 688–689. doi: 10.1021/ja0565875

Kim, J., Li, W. A., Choi, Y., Lewin, S. A., Verbeke, C. S., Dranoff, G., et al. (2015). Injectable, spontaneously assembling, inorganic scaffolds modulate immune cells *in vivo* and increase vaccine efficacy. *Nat. Biotechnol*. 33, 64–72. doi: 10.1038/nbt.3071

Kresge, C. T., Leonowicz, M. E., Roth, W. J., Vartuli, J. C., and Beck, J. S. (1992). Ordered mesoporous molecular-sieves synthesized by a liquid–crystal template mechanism. *Nature* 359, 710–712. doi: 10.1038/359710a0

Kumar, P., Tambe, P., Paknikar, K. M., and Gajbhiye, V. (2018). Mesoporous silica nanoparticles as cutting-edge theranostics: advancement from merely a carrier to tailor-made smart delivery platform. *J. Control. Release* 10, 35–57. doi: 10.1016/j.jconrel.2018.08.024

Lai, C.-Y., Trewyn, B. G., Jeftinija, D. M., Jeftinija, K., Xu, S., Jeftinija, S., et al. (2003). A mesoporous silica nanosphere-based carrier system with chemically removable CdS caps for stimuli-responsive controlled release of neurotransmitters and drug molecules. *J. Am. Chem. Soc*. 125, 4451–4459. doi: 10.1021/ja028650l

Lalchhingpuii, Tiwari, D., Lalhmunsiama, and Lee, S. M. (2017). Chitosan templated synthesis of mesoporous silica and its application in the treatment of aqueous solutions contaminated with cadmium (II) and lead (II). *Chem. Eng. J*. 328, 434–444. doi: 10.1016/j.cej.2017.07.053

Lammers, T., Kiessling, F., Hennink, W. E., and Storm, G. (2010). Nanotheranostics and image-guided drug delivery: current concepts and future directions. *Mol. Pharm*. 7, 1899–1912. doi: 10.1021/mp100228v

Lehto, V. P., Vaha-Heikkila, V., Paski, J., and Salonen, J. (2005). Use of thermoanalytical methods in quantification of drug load in mesoporous silicon microparticles. *J. Therm. Anal. Calori*. 80, 393–397. doi: 10.1007/s10973-005-0666-x

Lelong, G., Bhattacharyya, S., Kline, S., Cacciaguerra, T., Gonzalez, M. A., and Saboungi, M. L. (2008). Effect of surfactant concentration on the morphology and texture of MCM-41 materials. *J. Phys. Chem. C* 112, 10674–10680. doi: 10.1021/jp800898n

Li, J., Shen, S., Kong, F., Jiang, T., Tang, C., and Yin, C. (2018). Effects of pore size on *in vitro* and *in vivo* anticancer efficacies of mesoporous silica nanoparticles. *RSC Adv*. 8, 24633–24640. doi: 10.1039/C8RA03914C

Li, L., Liu, T., Fu, C., Tan, L., Meng, X., and Liu, H. (2015). Biodistribution, excretion, and toxicity of mesoporous silica nanoparticles after oral administration depend on their shape. *Nanomed. Nanotechnol. Biol. Med*. 11, 1915–1924. doi: 10.1016/j.nano.2015.07.004

Li, Z., Barnes, J. C., Bosoy, A., Stoddart, J. F., and Zink, J. I. (2012). Mesoporous silica nanoparticles in biomedical applications. *Chem. Soc. Rev*. 41, 2590–2605. doi: 10.1039/c1cs15246g

Lin, H.-P., and Tsai, C.-P. (2003). Synthesis of mesoporous silica nanoparticles from a low-concentration CnTMAX-sodium silicate components. *Chem. Lett*. 32, 1092–1093. doi: 10.1246/cl.2003.1092

Lin, Y.-S., Abadeer, N., and Haynes, C. L. (2011). Stability of small mesoporous silica nanoparticles in biological media. *Chem. Commun*. 47, 532–534. doi: 10.1039/c0cc02923h

Lin, Y.-S., and Hurley, K. R., Haynes C, L. (2012). Critical considerations in the biomedical use of mesoporous silica nanoparticles. *Phys. Chem. Lett*. 3, 364–374. doi: 10.1021/jz2013837

Lin, Y.-S., Tsai, C.-P., Huang, H.-Y., Kuo, C.-T., Hung, Y., Huang, D.-M., et al. (2005). Well-ordered mesoporous silica nanoparticles as cell markers. *Chem. Mater*. 17, 4570–4573. doi: 10.1021/cm051014c

Lin, Y.-S., Wu, S.-H., Hung, Y., Chou, Y.-H., Chang, C., Lin, M.-L., et al. (2006). Multifunctional composite nanoparticles: magnetic, luminescent, and mesoporous. *Chem. Mater*. 18, 5170–5172. doi: 10.1021/cm061976z

Liu, B., Li, C., Cheng, Z., Hou, Z., Huang, S., and Lin, J. (2016). Functional nanomaterials for near-infrared-triggered cancer therapy. *Biomater. Sci*. 4, 890–909. doi: 10.1039/c6bm00076b

Lucky, S. S., Soo, K. C., and Zhang, Y. (2015). Nanoparticles in photodynamic therapy. *Chem. Rev*. 115, 1990–2042. doi: 10.1021/cr5004198

Mai, W. X., and Meng, H. (2013). Mesoporous silica nanoparticles: a multifunctional nano therapeutic system. *Integr. Biol*. 5, 19–28. doi: 10.1039/c2ib20137b

Maleki, A., and Hamidi, M. (2016). "Nanoarchitectured mesoporous silica-based drug-delivery systems: toward perfect nanomedicine," in *Nanoarchitectonics for Smart Delivery and Drug Targeting* (Cambridge, MA: Elsevier), 345–377. doi: 10.1016/B978-0-323-47347-7.00013-6

McCarthy, J., Inkielewicz-Stepniak, I., Corbalan, J. J., and Radomski, M. W. (2012). Mechanisms of toxicity of amorphous silica nanoparticles on human lung submucosal cells *in vitro*: protective effects of fisetin. *Chem. Res. Toxicol.* 25, 2227–2235. doi: 10.1021/tx3002884

Meng, H., Xue, M., Xia, T., Ji, Z., Tarn, D. Y., Zink, J. I., et al. (2011). Use of size and a copolymer design feature to improve the biodistribution and the enhanced permeability and retention effect of doxorubicin-loaded mesoporous silica nanoparticles in a murine xenograft tumour model. *ACS Nano*. 5, 4131–4144. doi: 10.1021/nn200809t

Miricioiu, M. G., Iacob, C., Nechifor, G., and Niculescu, V. C. (2019). High selective mixed membranes based on mesoporous MCM-41 and MCM-41-$NH_2$ particles in a polysulfone matrix. *Front. Chem.* 7:332. doi: 10.3389/fchem.2019.00332

Monnier, C. A., Burnand, D., Rothen-Rutishauser, B., Lattuada, M., and Petri-Fink, A. (2014). Magnetoliposomes: opportunities and challenges. *Eur. J. Nanomed.* 6, 201–215. doi: 10.1515/ejnm-2014-0042

Munoz, B., Ramila, A., Perez-Pariente, J., Diaz, I., and Vallet-Regi, M. (2003). MCM-41 organic modification as drug delivery rate regulator. *Chem. Mater.* 15, 500–503. doi: 10.1021/cm021217q

Napierska, D., Thomassen, L. C. J., Rabolli, V., Lison, D., Gonzalez, L., Kirsch-Volders, M., et al. (2009). Size-dependent cytotoxicity of monodisperse silica nanoparticles in human endothelial cells. *Small* 5, 846–853. doi: 10.1002/smll.200800461

Navarro-Tovar, G., Palestino, G., and Rosales-Mendoza, S. (2016). An overview on the role of silica-based materials in vaccine development. *Expert Rev. Vaccines.* 15, 1449–1462. doi: 10.1080/14760584.2016.1188009

Nel, A. E., Madler, L., Velegol, D., Xia, T., Hoek, E. M. V., Somasundaran, P., et al. (2009). Understanding biophysicochemical interactions at the nano–bio interface. *Nat. Mater.* 8, 543–557. doi: 10.1038/nmat2442

Niculescu, V. C., Ene, R., and Parvulescu, V. (2011). An overview of the synthesis, characterization techniques and applications of silica mesoporous materials. *Progress Cryogenics Isotopes Separa.* 14, 111–120.

Niculescu, V. C., Paun, G., and Parvulescu, V. (2018). New organometallic complex supported on mesoporous silica and its enzymes activity inhibition properties. *Appl. Organomet. Chem.* 32:e4590. doi: 10.1002/aoc.4590

Nishimori, H., Kondoh, M., Isoda, K., Tsunoda, S., Tsutsumi, Y., and Yagi, K. (2009). Silica nanoparticles as hepatotoxicants. *Eur. J. Pharm. Biopharm.* 72, 496–501. doi: 10.1016/j.ejpb.2009.02.005

Oshima, S., Perera, J. M., Northcott, K. A., Kokusen, H., Stevens, G. W., and Komatsu, Y. (2006). Adsorption behaviour of Cadmium(II) and Lead(II) on mesoporous silicate MCM-41. *Sep. Sci. Technol.* 41, 1635–1643. doi: 10.1080/01496390600674786

Ow, H., Larson, D. R., Srivastava, M., Baird, B. A., Webb, W. W., and Wiesner, U. (2005). Bright and stable core-shell fluorescent silica nanoparticles. *Nano Lett.* 5, 113–117. doi: 10.1021/nl0482478

Pan, J., Wan, D., and Gong, J. (2011). PEGylated liposome coated QDs/mesoporous silica core-shell nanoparticles for molecular imaging. *Chem Commun.* 47, 3442–3444. doi: 10.1039/c0cc05520d

Pang, X. L., and Tang, F. Q. (2005). Morphological control of mesoporous materials using inexpensive silica sources. *Micropor Mesopor Mater.* 85, 1–6. doi: 10.1016/j.micromeso.2005.06.012

Peer, D., Karp, J. M., Hong, S., Farokhzad, O. C., Margalit, R., and Langer, R. (2007). Nanocarriers as an emerging platform for cancer therapy. *Nat. Nanotechnol.* 2, 751–760. doi: 10.1038/nnano.2007.387

Rosenholm, J. M., Sahlgren, C., and Linden, M. (2010). Towards mutifunctional, targeted drug delivery systems using mesoporous silica nanoparticles-opportunities & challenges. *Nanoscale* 2, 1870–1883. doi: 10.1039/c0nr00156b

Rosenholm, J. M., Sahlgren, C., and Lindén, M. (2011). Multifunctional mesoporous silica nanoparticles for combined therapeutic, diagnostic and targeted action in cancer treatment. *Curr. Drug Targets.* 12, 1166–1186. doi: 10.2174/138945011795906624

Roy, I., Ohulchanskyy, T. Y., Pudavar, H. E., Bergey, E. J., Oseroff, A. R., Morgan, J., et al. (2003). Ceramic-based nanoparticles entrapping water-insoluble photosensitizing anticancer drugs: a novel drug-carrier system for photodynamic therapy. *J. Am. Chem. Soc.* 125, 7860–7865. doi: 10.1021/ja0343095

Santos, H. A., Salonen, J., Bimbo, L. M., Lehto, V.-P., Peltonen, L., and Hirvonen, J. (2015). Mesoporous materials as controlled drug delivery formulations. *J. Drug. Deliv. Sci. Technol.* 21, 139–155. doi: 10.1016/S1773-2247(11)50016-4

Santra, S., Wang, K., Tapec, R., and Tan, W. (2001b). Development of novel dye-doped silica nanoparticles for biomarker application. *J. Biomed. Optic.* 6, 160–166. doi: 10.1117/1.1353590

Santra, S., Zhang, P., Wang, K., Tapec, R., and Tan, W. (2001a). Conjugation of biomolecules with luminophore-doped silica nanoparticles for photostable biomarkers. *Anal. Chem.* 73, 4988–4993. doi: 10.1021/ac010406+

Sanvicens, N., and Marco, M. P. (2008). Multifunctional nanoparticles properties and prospects for their use in human medicine. *Trends Biotechnol.* 26, 425–433. doi: 10.1016/j.tibtech.2008.04.005

Schlossbauer, A., Kecht, J., and Bein, T. (2009). Biotin-avidin as a protease-responsive cap system for controlled guest release from colloidal mesoporous silica. *Angew. Chem. Int. Ed.* 48, 3092–3095. doi: 10.1002/anie.200805818

Sercombe, L., Veerati, T., Moheimani, F., Wu, S. Y., Sood, A. K., and Hua, S. (2015). Advances and challenges of liposome assisted drug delivery. *Front. Pharmacol.* 6:286. doi: 10.3389/fphar.2015.00286

Shang, L., Nienhaus, K., and Nienhaus, G. (2014). Engineered nanoparticles interacting with cells: size matters. *J. Nanobiotechnol.* 12:5. doi: 10.1186/1477-3155-12-5

Shen, S.-C., Dong, Y., Letchmanan, K., and Ng, W. K. (2017). "Mesoporous materials and technologies for development of oral medicine" in *The Micro and Nano Technologies, Nanostructures for Oral Medicine*, eds E. Andronescu, and A. M. Grumezescu (Cambridge, MA: Elsevier Inc.), 699–749. doi: 10.1016/B978-0-323-47720-8.00024-9

Shi, S. X., Chen, F., and Cai, W. B. (2013). Biomedical applications of functionalized hollow mesoporous silica nanoparticles: focusing on molecular imaging. *Nanomedicine.* 8, 2027–2039. doi: 10.2217/nnm.13.177

Slowing, I. I., Wu, C. W., Vivero-Escoto, J. L., and Lin, V. S. (2009). Mesoporous silica nanoparticles for reducing hemolytic activity towards mammalian red blood cells. *Small* 5, 57–62. doi: 10.1002/smll.200800926

Soenen, S. J., Velde, G. V., Ketkar-Atre, A., Himmelreich, U., and De Cuyper, M. (2011). Magnetoliposomes as magnetic resonance imaging contrast agents. *Wiley Interdiscip. Rev. Nanomed. Nanobiotechnol.* 3, 197–211. doi: 10.1002/wnan.122

Song, S. W., Hidajat, K., and Kawi, S. (2005). Functionalized SBA-15 materials as carriers for controlled drug delivery: influence of surface properties on matrix-drug interactions. *Langmuir* 21, 9568–9575. doi: 10.1021/la051167e

Stober, W., Fink, A., and Bohn, E. (1968). Controlled growth of monodisperse silica spheres in the micron size range. *J. Colloid Interface Sci.* 26, 62–69. doi: 10.1016/0021-9797(68)90272-5

Strebhardt, K., and Ullrich, A. (2008). Paul Ehrlich's magic bullet concept: 100 years of progress. *Nat. Rev. Cancer* 8, 473–480. doi: 10.1038/nrc2394

Suschek, C. V., Bonmann, E., Kapsokefalou, A., Hemmrich, K., Kleinert, H., Forstermann, U., et al. (2002). Revisiting an old antimicrobial drug: amphotericin B induces interleukin-1-converting enzyme as the main factor for inducible nitric-oxide synthase expression in activated endothelia. *Mol. Pharmacol.* 62, 936–946. doi: 10.1124/mol.62.4.936

Sutewong, T., Sai, H., Cohen, R., Wang, S., Bradbury, M., Baird, B., et al. (2011). Highly aminated mesoporous silica nanoparticles with cubic pore structure. *J. Am. Chem. Soc.* 133, 172–175. doi: 10.1021/ja1061664

Suzuki, K., Ikari, K., and Imai, H. (2004). Synthesis of silica nanoparticles having a well-ordered mesostructure using a double surfactant system. *J. Am. Chem. Soc.* 126, 462–463. doi: 10.1021/ja038250d

Tan, T. T., Selvan, S. T., Zhao, L., Gao, S., and Ying, J. Y. (2007). Size control, shape evolution, and silica coating of near-infrared-emitting PbSe quantum dots. *Chem. Mater.* 19, 3112–3117. doi: 10.1021/cm061974e

Tang, F., Li, L., and Chen, D. (2012). Mesoporous silica nanoparticles: synthesis, biocompatibility and drug delivery. *Adv. Mater.* 24, 1504–1534. doi: 10.1002/adma.201104763

Thomas, C. R., Ferris, D. P., Lee, J. H., Choi, E., Cho, M. H., Kim, E. S., et al. (2010). Noninvasive remote-controlled release of drug molecules *in vitro* using magnetic actuation of mechanized nanoparticles. *J. Am. Chem. Soc.* 132, 10623–10625. doi: 10.1021/ja1022267

Tourne-Peteilh, C., Lerner, D. A., Charnay, C., Nicole, L., Begu, S., and Devoisselle, J. M. (2003). The potential of ordered mesoporous silica for the storage of drugs: the example of a pentapeptide encapsulated in a MSU-tween 80. *Chemphyschem* 4, 281–286. doi: 10.1002/cphc.200390045

Trewyn, B. G., Nieweg, J. A., Zhao, Y., and Lin, V. S. Y. (2008). Biocompatible mesoporous silica nanoparticles with different morphologies for animal cell membrane penetration. *Chem. Eng. J.* 137, 23–29. doi: 10.1016/j.cej.2007.09.045

Vallet-Regi, M., Balas, F., and Arcos, D. (2007). Mesoporous materials for drug delivery. *Angew. Chem. Int. Ed.* 46, 7548–7558. doi: 10.1002/anie.200604488

Vallet-Regi, M., Doadrio, J. C., Doadrio, A. L., Izquierdo-Barba, I., and Perez-Pariente, J. (2004). Hexagonal ordered mesoporous material as a matrix for the controlled release of amoxicillin. *Solid State Ionics*. 172, 435–439. doi: 10.1016/j.ssi.2004.04.036

Vallet-Regi, M., Ramila, A., del Real, R. P., and Perez-Pariente, J. (2001). A new property of MCM-41: drug delivery system. *Chem. Mater.* 13, 308–311. doi: 10.1021/cm0011559

Vanblaaderen, A., and Vrij, A. (1992). Synthesis and characterization of colloidal dispersions of fluorescent, monodisperse silica spheres. *Langmuir* 8, 2921–2931. doi: 10.1021/la00048a013

Vazquez, N. I., Gonzalez, Z., Ferrari, B., and Castro, Y. (2017). Synthesis of mesoporous silica nanoparticles by sol–gel as nanocontainer for future drug delivery applications. *Bol. Soc. Esp. Ceram. V* 56, 139–145. doi: 10.1016/j.bsecv.2017.03.002

Verma, A., and Stellacci, F. (2010). Effect of surface properties on nanoparticle–cell interactions. *Small* 6, 12–21. doi: 10.1002/smll.200901158

Wang, H., Van Der Voort, P., Qu, H., and Liu, S. (2013). A simple room-temperature synthesis of mesoporous silica rods with tuneable size and porosity. *J. Nanoparticle Res.* 15:1501. doi: 10.1007/s11051-013-1501-0

Wang, L.-S., Wu, L.-C., Lu, S.-Y., Chang, L.-L., Teng, I.-T., Yang, C.-M., et al. (2010). A. biofunctionalized phospholipid-capped mesoporous silica nanoshuttles for targeted drug delivery: improved water suspensibility and decreased nonspecific protein binding. *ACS Nano*. 4, 4371–4379. doi: 10.1021/nn901376h

Wang, S. (2009). Ordered mesoporous materials for drug delivery. *Micropor. Mesopor. Mat.* 117, 1–9. doi: 10.1016/j.micromeso.2008.07.002

Wang, T. Y., Jiang, H., Zhao, Q., Wang, S., Zou, M., and Cheng, G. (2012). Enhanced mucosal and systemic immune responses obtained by porous silica nanoparticles used as an oral vaccine adjuvant: effect of silica architecture on immunological properties. *Int. J. Pharm.* 436, 351–358. doi: 10.1016/j.ijpharm.2012.06.028

Wang, Y., Zhao, Q., Han, N., Bai, L., Li, J., Liu, J., et al. (2015). Mesoporous silica nanoparticles in drug delivery and biomedical applications. *Nanomedicine* 11, 313–327. doi: 10.1016/j.nano.2014.09.014

Wartenberg, N., Fries, P., Raccurt, O., Guillermo, A., Imbert, D., and Mazzanti, M. (2013). A gadolinium complex confined in silica nanoparticles as a highly efficient T1/T2 MRI contrast agent. *Chem. A Eur. J.* 19, 6980–6983. doi: 10.1002/chem.201300635

Wu, L., Mendoza-Garcia, A., Li, Q., and Sun, S. (2016). Organic phase syntheses of magnetic nanoparticles and their applications. *Chem. Rev.* 116, 10473–10512. doi: 10.1021/acs.chemrev.5b00687

Wu, S.-H., Lin, Y.-S., Hung, Y., Chou, Y.-H., Hsu, Y.-H., Chang, C., et al. (2008). Multifunctional mesoporous silica nanoparticles for intracellular labeling and animal magnetic resonance imaging studies. *ChemBioChem* 9, 53–57. doi: 10.1002/cbic.200700509

Xie, J., Lee, S., and Chen, X. (2010). Nanoparticle-based theranostic agents. *Adv. Drug Delivery Rev.* 62, 1064–1079. doi: 10.1016/j.addr.2010.07.009

Xu, W., Riikonen, J., and Lehto, V. P. (2012). Mesoporous systems for poorly soluble drugs. *Int. J. Pharm.* 30, 181–197. doi: 10.1016/j.ijpharm.2012.09.008

Yanagisawa, T., Shimizu, T., Kuroda, K., and Kato, C. (1990). The preparation of alkyltrimethylammonium-kanemite complexes and their conversion to microporous materials. *Bull. Chem. Soc. Jpn.* 63, 988–992. doi: 10.1246/bcsj.63.988

Yang, G., Phua, S. Z. F., Bindra, A. K., and Zhao, Y. (2019). Degradability and clearance of inorganic nanoparticles for biomedical applications. *Adv. Mater.* 31:1805730. doi: 10.1002/adma.201805730

Yoo, H., and Pak, J. (2013). Synthesis of highly fluorescent silica nanoparticles in a reverse microemulsion through double-layered doping of organic fluorophores. *J. Nanopart. Res.* 15:1609. doi: 10.1007/s11051-013-1609-2

Yuan, L., Tang, Q., Yang, D., Zhang, J. Z., Zhang, F., and Hu, J. (2011). Preparation of pH-responsive mesoporous silica nanoparticles and their application in controlled drug delivery. *J. Phys. Chem. C* 115, 9926–9932. doi: 10.1021/jp201053d

Zelenak, V., Hornebecq, V., and Llewellyn, P. (2005). Zinc(II)-benzoato complexes immobilised in mesoporous silica host. *Micropor. Mesopor. Mat.* 83, 125–135. doi: 10.1016/j.micromeso.2005.03.022

Zeng, W., Qian, X. F., Zhang, Y. B., Yin, J., and Zhu, Z. K. (2005). Organic modified mesoporous MCM-41 through solvothermal process as drug delivery system. *Mater. Res. Bull.* 40, 766–772. doi: 10.1016/j.materresbull.2005.02.011

Zhang, J., Chen, M., Zhao, X., Zhang, M., Mao, J., Cao, X., et al. (2018). Controlled and localized delivery of c-myc AS-ODN to cells by 3-aminopropyl-trimethoxylsilane modified SBA-15 mesoporous silica. *AIP Adv.* 8:015220. doi: 10.1063/1.5012535

Zhao, D. Y., Feng, J. L., Huo, Q. S., Melosh, N., Fredrickson, G. H., Chmelka, B. F., et al. (1998). Triblock copolymer syntheses of mesoporous silica with periodic 50 to 300 angstrom pores. *Science* 279, 548–552. doi: 10.1126/science.279.5350.548

Zhao, X. J., Bagwe, R. P., and Tan, W. H. (2004). Development of organic-dye-doped silica nanoparticles in a reverse microemulsion. *Adv. Mater.* 16, 173–176. doi: 10.1002/adma.200305622

Zhao, Z. X., Huang, Y. Z., Shi, S. G., Tang, S. H., Li, D. H., and Chen, X. L. (2014). Cancer therapy improvement with mesoporous silica nanoparticles combining photodynamic and photothermal therapy. *Nanotechnology* 25:285701. doi: 10.1088/0957-4484/25/28/285701

**Conflict of Interest:** The author declares that the research was conducted in the absence of any commercial or financial relationships that could be construed as a potential conflict of interest.

frontiers in Materials

REVIEW
published: 20 March 2020
doi: 10.3389/fmats.2020.00062

# Bioinspired Cementitious Materials: Main Strategies, Progress, and Applications

*Rouzbeh Shahsavari*[1,2,3]* *and Sung Hoon Hwang*[1]

[1] Materials Science and Nanoengineering, Rice University, Houston, TX, United States, [2] Civil and Environmental Engineering, Rice University, Houston, TX, United States, [3] C-Crete Technologies LLC, Stafford, TX, United States

Nature-inspired ensemble of organic and inorganic constituents, such as that found in the microstructure of nacre and dactyl clubs of Mantis shrimp, has evolved into the model system for the structural design of industrial composites. This novel design concept, which helps attaining the balance between strength, toughness and ductility, has not only induced a paradigm shift in the synthesis of advanced materials such as graphene-based composites but also, in the development of more abundant, low-cost materials such as cement and concretes. The advance in synthetic techniques and the advent of new manufacturing technologies such as 3D printing has enabled effective integration of cementitious materials with soft materials across various length scales. Furthermore, novel functional properties such as self-healing have also been materialized based on a variety of strategies. This review will provide the comprehensive overview on the ongoing research efforts, encompassing 3D printing, self-healing strategies and integration of C-S-H with organic components, all of which are actively exploited in synthesizing bioinspired, multifunctional cementitious materials.

**Keywords: cement-based materials, bio-inspired materials, organic-inorganic composites, mechanical properties, cement, biomaterial, toughness, hybrid materials**

OPEN ACCESS

***Edited by:***
*Laura Maria Vergani,*
*Politecnico di Milano, Italy*

***Reviewed by:***
*Chuying Ma,*
*Pennsylvania State University (PSU), United States*
*Jae-Young Jung,*
*University of California, San Francisco, United States*

***Correspondence:**
*Rouzbeh Shahsavari*
*Rouzbeh@ccretetech.com*

***Specialty section:***
*This article was submitted to Biomaterials, a section of the journal Frontiers in Materials*

***Received:*** *02 September 2019*
***Accepted:*** *28 February 2020*
***Published:*** *20 March 2020*

***Citation:***
*Shahsavari R and Hwang SH (2020) Bioinspired Cementitious Materials: Main Strategies, Progress, and Applications. Front. Mater. 7:62. doi: 10.3389/fmats.2020.00062*

## INTRODUCTION

Nature provides a large pool of living examples, where materials with distinct types of properties are orchestrated with each other synergistically at various length scales. The unique structural arrangement coupled with bioinspired compositional properties often induces exceptional mechanical properties at macroscale. Notable examples encompass a nacre, where strong, platelet-shaped calcium carbonate minerals are periodically stacked upon each other and organic materials, totaling only 5% of the material's entire composition, exist between the platelets. As illustrated in **Figure 1**, this tiny fraction of the organic components serves as a major driving force behind the exceptional mechanical properties, which are marked by high strength and high toughness (Sakhavand and Shahsavari, 2015; Wegst et al., 2015).

Human bones are also marked by the close interplay between two constituent nanophases, hydroxyapatite nanocrystals and collagen fibrils, thereby introducing multiple toughening mechanisms across different length scales (Wegst et al., 2015). Intrinsic toughening, characterized by plasticity, which is primarily caused by fibrillar sliding governs the toughening process at nano and sub-micron scale. Extrinsic toughening mechanisms, largely induced by crack bridging and crack deflections dominate at a larger, micro and macro scale. Human teeth are also perfect examples, where organic and inorganic components are arranged synergistically to overcome

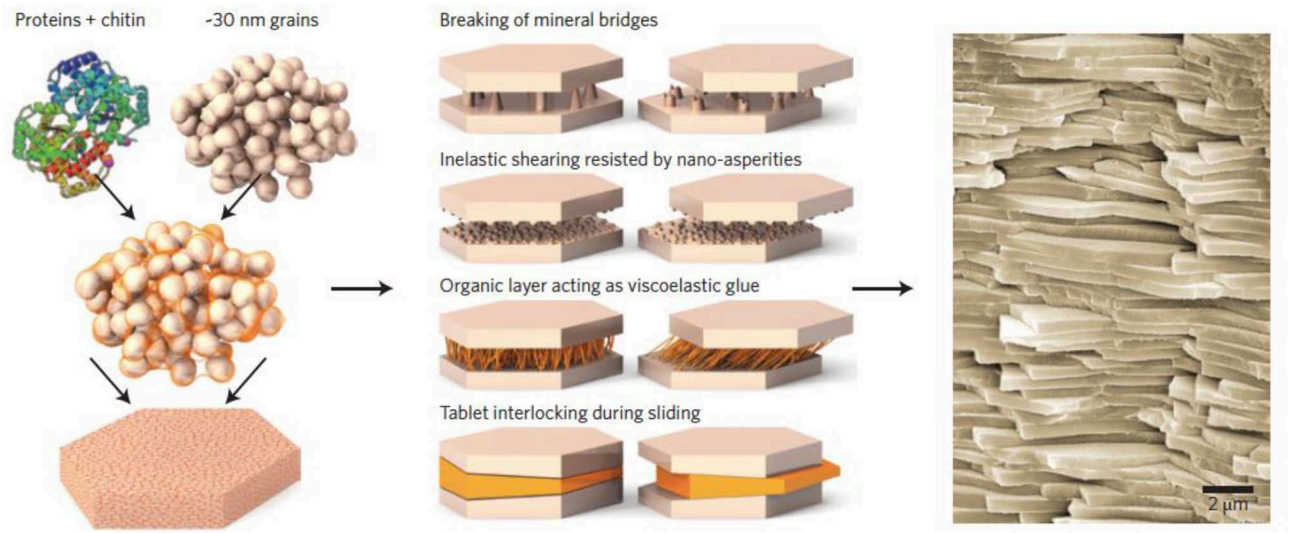


**FIGURE 1 |** Structural features of a nacre leading to enhanced fracture resistance at different length scales. Figure adapted from Wegst et al. (2015), with permission from Springer Nature.

inherent mechanical shortcomings of the latter. Cracks initiated in enamel, the highly mineralized, brittle component of teeth are arrested at a junction between enamel and dentin. Dentin the inner component of teeth exhibit distinct types of structural arrangement at different length scales While it shows bone-like arrangement marked by a matrix of mineralized fibrils at nanoscale, it consists of dentinal tubules surrounded by mineral, which introduces extrinsic toughening mechanism via creation of microcracks upon loading. Spider silk also shows structural arrangement of distinct types of materials, characterized by beta-sheet nanocrystals confined within semi-amorphous protein matrix. The elastic matrix phase plays critical roles during small mechanical deformation while the crystalline phases play major roles during larger deformation (Nova et al., 2010).

Overall, the strength-enhancing bioinspired features, coupled with novel functional properties found in nature such as self-healing are now being actively employed as a design guideline for material scientists. Those bioinspired strategies can now be implemented using a variety of synthetic techniques and also, newly rising manufacturing technologies including 3D printing.

Cementitious materials, including concretes, which are the most widely employed synthetic material on the planet, are strong, cost-effective but highly brittle and thus, greater diversity in industrial applications is being impeded. The high brittleness in turn induces high susceptibility toward the formation of small-scale cracks, which if left unhealed, can induce rapid propagation and ultimately, results in a complete failure of entire structures. Since cementitious materials are ubiquitous in today's modern infrastructures, implementation of bioinspired structural features to overcome their inherent mechanical shortcomings has been the ultimate goal for numerous research efforts. For example, advanced synthetic techniques have enabled fine-tuning of structural and compositional features of their most fundamental building units and also, the advent of novel manufacturing technologies such as 3D printing has enabled automatized, facile production of bioinspired reinforcement materials for concretes.

This review provides an overview on the ongoing research efforts, which are currently devoted to implementing bioinspired structural concepts using cementitious materials. The review discusses the current status of research in each major strategy and also, states the major obstacles in applying the aforesaid concepts at large-scale construction sites. The research efforts can be broadly divided into three major areas, self-healing, 3D printing, and the synthesis of bioinspired calcium-silicate-hydrate (**Table 1**), the most basic building blocks of cementitious materials.

## Self-Healing Cementitious Materials

One of the most exciting phenomena observed in many of living organisms is self-healing capability. For example, bones in vertebrates undergo a series of healing steps upon the occurrence of damage, with bone cells known as osteoclasts and osteoblasts working in tandem with each other to eventually secrete extracellular matrix at the wound site, which undergoes mineralization to wrap up the healing process (Cremaldi and Bhushan, 2018). Furthermore, when skin and blood vessels underneath the skin are damaged, blood platelets reach the damaged site, initially forming a plug and subsequently, they become activated by collagen to undergo coagulation with fibrin, eventually forming a clot to prevent further blood loss[1]. Although the real skin repair process involves a greater number of different chemicals and much more complex sequence of chemical reactions, similar concept has also been applied for inanimate materials. Artifical "stores" in the form of microcapsules, tubes or network of microchannels can be embedded inside matrix,

[1]Boundless.com: Hemostasis. CC BY-SA: Attribution-ShareAlike.

**TABLE 1 |** Summary of three major implementation routes for biomimetic, cementitious composites.

| Major areas for biomimetic cementitious materials | Strategy for implementation | Relevant examples in nature |
|---|---|---|
| Self-healing concretes | Capsule-based approach | Skin repair induced by the network of blood vessels[1] (Cremaldi and Bhushan, 2018) |
| | Bacteria-based approach | |
| | Shape-changing polymer | Self-shaping tree branches, wheat awn (Fratzl et al., 2008; Fratzl and Barth, 2009; Studart and Erb, 2014) |
| 3D printing | Complex geometries and orientations of constituents | Dactyl clubs of Mantis shrimp (Weaver et al., 2012) |
| | Reinforcement materials with auxetic behavior | Skin of salamander, cat's skin, cancellous bone (Prawoto, 2012; Santulli and Langella, 2016) |
| | Reinforcement materials with hierarchical structures | Nacres within hard shells of mollusks (Sun and Bhushan, 2012) |
| Biomimetic C-S-H | C-S-H particles with identical morphology | |
| | Integration of C-S-H with polymer at various length scales | Human bones and teeth (Wegst et al., 2015) |

thereby carrying multiple types of healing agents, which become released upon damage and undergo further reactions to heal the damaged region.

Concretes, unlike majority of inanimate materials, possess the ability to recover from small-scale cracks via autogenous healing (Van Tittelboom and De Belie, 2013). This is possible due to the coexistence of multiple phases, which, even when the hardening process of concretes is complete, can undergo further reactions to yield strength-giving or space-filling phases. For example, unhydrated clinker phases, such as tricalcium silicate ($C_3S$) and dicalcium silicate ($C_2S$) can react with water entering through micro- or millimeter-sized cracks to produce more of calcium-silicate-hydrate, C-S-H, which is the primary, strength-giving binder phase of concretes (Van Tittelboom and De Belie, 2013). Portlandite $Ca(OH)_2$, another product from the hydration of Portland cement, can also react with carbon dioxide dissolved in water to produce space-filling minerals of calcium carbonate (Possan et al., 2017). Despite this inherent ability to self-heal without autonomous agents, the size and the total number of cracks, which could be healed by this autogenous healing are restricted. Consequently, researchers proposed autonomous and simultaneously, novel and tailored strategies for self-healing cement-based materials. Over the past decade, remarkable progress has been attained, eventually reaching the point where the combination of those strategies has been evaluated at full-construction sites, thereby exhibiting promising potentials (Teall et al., 2016).

## Glass Tube-Based Approach

The early efforts in implementing self-healing concretes were primarily focused on manually embedding thin hollow glass tubes filled with external healing agents inside concretes. Cracking would naturally fracture the tubes thereby prompting the release of inner contents to the damaged areas (Dry, 1994; Van Tittelboom and De Belie, 2013). This basic concept somewhat resembles the network of blood vessels existing underneath human skin, where external cut would trigger the release of blood and clotting at damaged areas. This "network-inside-matrix" concept has also been successfully employed for polymeric materials (Toohey et al., 2007).

However, incorporating cargo-loaded glass tubes inside concretes has numerous shortcomings. For example, polymeric agents filled inside tubes are often too viscous at ambient conditions and consequently, they would not possess sufficient flowability to penetrate into microcracks and induce sufficient self-healing effects. This is verified by the recent work, where Van Belleghem et al. found that polyurethane with lower viscosity induces higher surface coverage and also, higher self-healing efficiency in cementitious mortar samples (Van Belleghem et al., 2018). Furthermore, glass tubes, which are often employed as carriers are brittle and thus, they could possibly undergo premature fracture during vigorous mixing procedures rather than fracturing exclusively upon the formation of cracks. In the light of those shortcomings, new types of microscopic carriers coupled with wide variations in types of healing agents, have been developed.

Hu et al. incorporated miniaturized glass tubes (30 mm length and 8 mm diameter) filled with a mixture of polyurethane, which is one-component healing agent with high viscosity and acetone, which serves as a viscosity-decreasing agent (Hu et al., 2018). The authors confirmed that acetone decreased the overall viscosity to a sufficient level, which eventually led to filling of the crack with the size of 300 um.

## Capsule-Based Approach

Microscopic carriers or capsules from more elastic types of materials have also been developed using various processing techniques such as polymer extrusion. Dong et al. synthesized polymer-based, core-shell type microcapsules with the size ranging between 400∼1,200 um using extrusion-spheronization technique and endowed the capsules with pH-responsive behavior, which triggers release and chemical dissociation of the inner self-healing contents (Dong et al., 2015). When the authors placed the microcapsules in calcium hydroxide solutions, which were employed to simulate concrete pore solutions, high pH values served as external stimulus. They triggered release of the core content, sodium monofluorophophate, which subsequently dissociates into its constituent ions, $Na^+$ and $PO_3F^{2-}$.

Since the survival of those external capsules during the vigorous mixing process and also, during casting procedures is critical for this capsule-based methodology, researchers also developed new evaluation techniques for self-healing efficiency. Araujo et al. extruded microscale poly(methyl methacrylate) capsules with the width less than a millimeter using a single screw extruder (Araujo et al., 2018). The authors encapsulated an

accelerating agent inside those PMMA capsules and backtracked the number of capsules broken during the mixing process by quantifying the accelerating effect observed during the setting process.

In order to increase the survival ratio of the external capsules, Hilloulin et al. extruded three different types of polymeric capsules, poly(lactic acid), polystyrene and Poly(methyl methacrylate/n-butyl methacrylate), all of which possess low glass transition temperatures below 100°C, using a twin screw extruder (Hilloulin et al., 2015). The authors applied heat to raise the temperature beyond their glass transition temperatures, in order to induce a switch in mechanical behavior from brittle to elastomeric states. This heat-induced "brittle-to-rubbery" transition ultimately increased the survival ratio of the capsules even in a high temperature concrete mixing. Certain fractions of heat-treated P(MMA/n-BMA) based capsules were found to possess a well-balanced and optimized mechanical properties, enabling them to survive vigorous mixing procedure and simultaneously, become successfully fractured upon the formation of cracks during 3-point bending loading.

In addition to the aforementioned extrusion-based synthesis of polymeric capsules, solution-based polymerization has also been used to synthesize polymeric capsules with even smaller ranges of sizes below one millimeter. Pelletier encapsulated sodium silicate solution in polyurethane microcapsules, with the size of 40∼800 μm using *in situ* interfacial polymerization (Pelletier et al., 2011). The authors artificially introduced microcracks in cement mortar samples and measured the flexural strengths, which were found to be at least 10% higher for the cement mortar samples containing the microcapsules compared to control samples without external agents.

Advanced and innovative technique has also been employed to synthesize core-shell type microcapsules for self-healing concretes. Yang et al. prepared sulfonated polystyrene (PS) particles and dispersed them in a oil/water solution, where the oil is comprised of methyl methacrylate (MMA), triethylborane and tetraethylorthosilicate (TEOS) (Yang et al., 2011). The PS particles become attracted to the oil droplets and sulfonated groups on surfaces of the particles serve as catalysts for the hydrolysis and condensation of TEOS, thereby synthesizing silica microcapsules, which encapsulate MMA monomer. Uniaxial fatigue testing revealed that the microcapsules served to enhance crack resistance in cementitious mortar samples reinforced with carbon microfiber.

## Bacteria-Based Approach

Although the abovementioned capsule-based approach has been widely employed for various types of materials, certain self-healing strategies have been designed exclusively for cementitious materials. One example is bacteria based self-healing. Bacterial species, like many other microorganisms, can perform a wide range of chemical conversions if they are provided with the appropriate chemical substrate and the appropriate conditions.

Jonkers and Schlangen confirmed the potential of applying bacterial species for self-healing concretes by directly adding bacterial spores along with calcium lactate during the concrete mixing process (Jonkers and Schlangen, 2008). The authors saw that naturally-formed calcite ($CaCO_3$) minerals were much more pronounced in size than those formed from intact concretes. Jonkers and Schlangen subsequently confirmed that the strategy based on the addition of bacterial spores along with the mineral substrate, calcium lactate, exhibits high $CaCO_3$-forming capacity on cracked surfaces of young-aged concrete samples (Jonkers and Schlangen, 2008). On the other hand, the authors also confirmed the inability of the bacterial spores to survive the long curing age (∼28 days), thereby confirming both promising potentials and limitations of bacterial-based self-healing strategy.

Since the aforementioned early attempts in applying bacterial-based self-healing, a large number of subsequent research efforts have been directed toward overcoming the key restrictions, which impede widespread materialization at practical scales. Luo et al. found numerous factors, which influence the efficiency of bacteria-based self-healing, including the crack width, curing condition and the age of concrete at the time of crack formation (Luo et al., 2015). Herein, the authors confirmed via the electron microscopy that at the initial and 20 day period, bacterial self-healing system exhibited different self-healing capacity for different crack widths, 0.3 and 0.8 mm, inducing only partial degree of healing for the latter. Also, the authors found that curing in water was more effective in inducing healing phenomenon than wet curing.

Tziviloglou et al. encapsulated bacterial spores, calcium lactate and yeast extract inside lightweight aggregates via a vacuum-induced incorporation and used them as replacement for normal sand in preparing cementitious mortar (Tziviloglou et al., 2016). Self-healing capability was evaluated by introducing a crack with the width of 350 um using three-point bending test and measuring water permeability test. The test proved that the self-healing system induced less water flow compared to the intact mortar samples. Although the bacteria-loaded aggregates decreased compressive strengths compared normal sand aggregates, they verified their potential to serve as carriers for bacterial-based healing agents.

Novel monitoring techniques were also introduced to further enhance the efficiency of bacterial-based self-healing system. Liu et al. employed coda wave interferometry to evaluate and quantify the degree of self-healing induced by the formation of $CaCO_3$ in a non-destructive way (Liu et al., 2016).

## Shape-Memory Polymer-Based Approach

Certain natural materials can alter their shapes in response to external stimuli. This is often observed for plant-based materials such as branches of trees and pine cones, which can control orientations of their constituent fibers to adopt different structural states (Studart and Erb, 2014). Albeit being based on a different type of mechanism, certain petroleum-based polymers, including polyethylene terephthalate (PET) tendons also exhibit shape changes upon external stimuli. While PET polymer undergoes certain processing techniques, its constituent molecules are aligned and subsequently frozen, thereby developing shrinkage potential. Consequently, the external application of heat induces shrinkage of the tendons. The aforesaid heat-responsive shape memory polymer can be incorporated in concrete structures as reinforcement materials

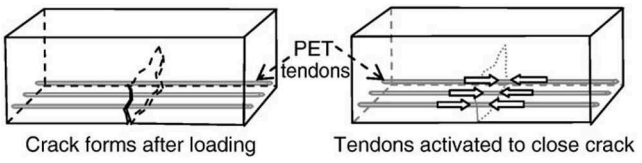


**FIGURE 2 |** Self-healing of a concrete induced by shrinkage of PET tendons with shape-memory capability. Figure reproduced from Jefferson et al. (2010), with permission from Elsevier.

and induce self-healing when cracks are formed. The strategy is based on the mechanism that once cracks are formed, external heat stimulus can be applied to induce a shape change that facilitates closing the cracks and strength recovery. Jefferson employed PET tendons as prestressing tendons and evaluated their ability to close cracks upon heating and induce strength recovery (Jefferson et al., 2010). As illustrated in **Figure 2**, the shrinkage potential developed during heating and cooling procedure induces shrinkage upon heating, thereby exerting a compressive force on cracked faces.

After the validity and potential of the strategy using shape memory polymer were first verified, the subsequent efforts were devoted to improving the method further by implementing new additional ideas. Teall et al. encapsulated the assembly of PET filaments inside heat distribution layer, equipped with nichrome wire coiling around on the outer surface and placed the assemblies inside concrete beams to confirm if electrical currents can serve as external stimulus for a shape change (Teall et al., 2018). The authors found that the tendons not only induced around 85% crack closure in unreinforced concretes but they also enhanced the overall stiffness of the concrete samples.

Overall, the large depth and breadth of the proposed self-healing strategies and a large number of research efforts devoted to each strategy eventually led to full-scale trials. Various self-healing concepts described above have been implemented at real construction sites via EPSRS funded research project, named as "Materials for Life (M4L)" (Davies et al., 2018). The project built several concrete panels, each of which was designed to evaluate one of the three representative self-healing concepts for concretes discussed above, capsule-based approach, shape-memory polymer and bacteria-based concretes. Implementation of this project, evaluating formerly lab-based self-healing strategies at a large-scale itself can be seen as a huge step forward. Despite this remarkable progress, there still exists major obstacles in attaining widespread commercialization. Although the effectiveness of the self-healing strategies has been notably improved when viewed from technical perspective at lab- and a pilot-scale, attaining economic feasibility for continuous, and widespread use at real world-scale still remains a challenge.

# 3D PRINTING

## General Introduction to 3D Printing

As stated in the Introduction, natural materials often exhibit exceptional mechanical properties stemming from the interplay between different types of materials. Furthermore, their constituent materials often adopt specific geometries and orientations with respect to each other in order to maximize beneficial effects on macroscale mechanical properties. The advent of advanced manufacturing technologies, such as 3D printing, has now enabled the implementation of those bioinspired features for cement-based structures. 3D printing is a modern, generic term for an automated layer-by-layer assembly, where various types of industrial materials including polymer, metal and ceramic are directly employed as constituents of printing "ink" and thin layers are deposited in sequential steps. Overall, the global market for 3D printing is expanding rapidly owing to an increase in the range of types of print materials and also, to the advent of different techniques ranging from stereolithography, fused deposition modeling and selective laser sintering (Du et al., 2018; Snikhovska, 2019). For example, bioactive, ceramic based scaffolds have been 3D printed for utilization in bone repair and the ongoing research efforts are devoted to ultimately attaining widespread practical applications (Du et al., 2018).

The idea of applying 3D printing for cementitious materials was materialized as early as 1997, when Pegna performed a sequential layer-by-layer deposition of Portland cement and sand and applied post-steam curing to prompt hardening process (Pegna, 1997; Shahsavari and Hwang, 2017). Since then, 3D printing in construction industry has branched into different types of techniques emcompassing controur crafting, D-shape technology and concrete printing, with the ongoing research efforts to enhance practical applicability at real construction sites (Bos et al., 2016). Once the latter is attained, shelters can be provided at underdeveloped, homeless regions in a short amount of time and tall buildings could be finally printed, saving cost, and time required for manual construction.

One of the most renowned 3D printing techniques in construction industry is contour crafting, which is computer-controlled and originally developed by Hager et al. (2016). Herein, cementitious paste with the optimized composition, which in turn leads to the appropriate rheology for 3D printing is extruded through a nozzle and two trowels, which constitute important parts of the nozzle system constrain the flow of the extruded ink *in situ* to ensure a smooth surface (Khoshnevis and Bekey, 2002; Hwang and Khoshnevis, 2004). The proper application of this cement-based, 3D printing technique started with the creation of small-scale sections having the size of around 10 inches and the technique was later developed further to create a two-feet tall, five-feet long concrete wall as illustrated in **Figure 3** (Hwang and Khoshnevis, 2004).

The active, ongoing research efforts encompass coupling software-based technologies with contour crafting in order to take the efficiency to a next level. Davatalab et al. recently introduced a software platform called "A Planning and Operations Control Software for Automated Construction" (PROSAC), which can be employed to link information from building information modeling (BIM) with contour crafting (Davtalab et al., 2018). Zhang et al. introduced a new 3D printing system where multiple robots work together on a single structure.

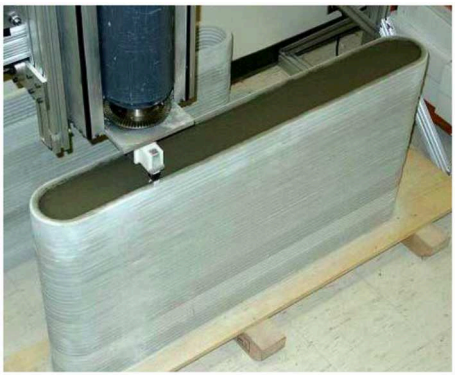

**FIGURE 3 |** Concrete wall synthesized via contour crafting technique. Figure adapted from Hwang and Khoshnevis (2004), with permission from Int. J. Industrial and Systems Engineering.

This indicates a potential for utilizing 3D printing for full scale construction (Zhang X. et al., 2018).

## 3D Printable Cementitious Mix

The major research efforts in cement-based 3D printing were focused on obtaining appropriate rheological properties of the print ink, which would ensure sufficient flowability closely linked to successful extrusion without compromising buildability and mechanical properties of the final object. Two of the critical factors for successful extrusion of cement-based ink are pumpability, which represents how readily the paste material can be pumped from storage to the point of extrusion and buildability, which implies the degree of stability for the sequential deposition of extruded layers (Weng et al., 2018; Zhang Y. et al., 2018). Fresh properties of a novel 3D printing concrete ink. Both factors are highly correlated with rheological behavior of the cement-based and thus, a large number of research efforts has been devoted to optimizing its rheological properties by altering its composition.

Weng et al. employed a gradation technique based on Fuller-Thompson theory for sand aggregates and also, packing fraction based on Mercy-Percy model in preparing the cementitious mix for 3D printing (Weng et al., 2018). The authors compared the "Fuller-Thompson"-based gradation with other known gradation techniques, which are uniform gradations and gap gradations. They investigated and compared the gradation-induced rheological behavior between the samples, revealing that the Fuller-Thompson-based gradation was evidently more effective in enhancing buildability of the cementitious mix for 3D printing.

Among the research efforts to optimize composition of the mix for 3D printing, a large proportion has also been directed toward utilizing industrial waste as a part of the ink composition. This would ultimately enhance eco-friendliness of the slurry material due to the decreased utilization of Portland cement and increased recycling of the waste. Furthermore, it would facilitate reducing the cost issues associated with 3D printing in construction industry. In general, industrial waste such as fly ash, rice husk and ground blast furnace slag, has been subjected to active research as potential candidates for replacement of Portland cement, whose production is carbon dioxide intensive (Barnett et al., 2006; Habeeb and Mahmud, 2010; Hwang and Shahsavari, 2018).

Ma et al. partially replaced sand in cement mortar with copper tailing, the industrial waste from mining industry and evaluated 3D printing-related properties of the resultant mortar (Ma et al., 2018). The authors varied the replacement ratio from 0 to 50% and investigated the resultant effect on 3D printing-related properties, encompassing flowability, extrudability, and buildability. They found that owing to the fine particulate size of copper tailing, increasing the ratio of replacement favored flowability while it degraded the buildability. In general, the overall printability of the cementitous mix is dependent on a series of factors, which at large, can be divided into material properties including strength, flowability, and stiffness and processing conditions such as print path and extrusion rate. The aforementioned material properties and processing conditions are often interrelated with each other. Consequently, the authors evaluated the printability of this environmentally-friendly mortar by obtaining two critical coefficients, buildability and extrudability, based on various types of parameters mentioned above, thereby proposing a new design scheme for 3D printable cementitious mix.

Panda et al., also prepared geopolymer-based mix for 3D printing using fly ash F and ground granulated blast-furnace slag and utilized the paste to perform a computer-controlled, layer-by-layer deposition (Panda et al., 2017). The printed object exhibited a direction-dependent enhancement in compressive strengths, thereby verifying the potential of using geopolymer-based ink as environmentally-friendly mortar for 3D printing.

Prompted by the large availability of 3D printing instruments for research purposes and also, the notable progress in enhancing printability using various types of cement-based mixes as depicted above, research efforts have also been devoted to attaining bioinspired, cementitious composites based on 3D printing.

## Bio-Inspired, 3D-Printed Cementitious Composites

One way of applying 3D printing for bioinspired cementitious composites is utilizing cement-based mortar directly as print ink and creating structures with biomimetic complex geometries. The exceptional mechanical properties of natural materials or body parts of living organisms arise not only from the mere coexistence of organic and inorganic materials but in many cases, also from unique geometrical complexities at various length scales. Dactyl clubs of Mantis shrimp are the perfect, representative example, where the helicoidal arrangement of soft organic components serves as the foundation for exceptional toughness (Weaver et al., 2012). In the "impact" region of the dactyl clubs, which constitute the outermost parts, are primarily composed of hard, hydroxyapatite crystallites arranged in specific orientations, which favor the overall rigidity. Furthermore, the "periodic" region located underneath the impact region is

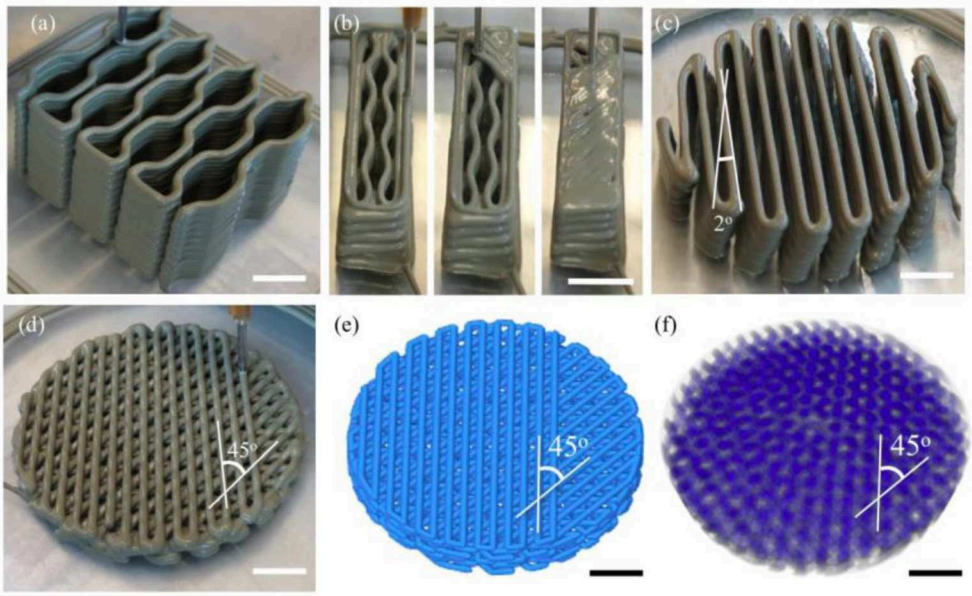


**FIGURE 4 |** 3D printed cementitious structures with complex geometries. (Scale bar−10 mm) Figure adapted from Moini et al. (2018), with permission from John Wiley and Sons. **(a–f)** Different printed morphologies along with respective schematics.

marked by the helicoidal arrangement of chitin fibrils, which introduces helicoidal and thus, more tortuous pathways for crack propagation.

Cement-based paste can be directly utilized as an ink for 3D printing and bioinspired structures with complex geometrical features such as honeycomb or Bouligand architecture with varying pitch angles can be created as shown in **Figure 4** (Moini et al., 2018). Martin et al. also applied 3D magnetic printing to synthesize a polymer/ceramic composite where the ceramic fillers are arranged in specific orientations inside polymer matrix, thereby inducing a direction-dependent mechanics in composites (Martin et al., 2015). The individual cases above have verified the potential of utilizing 3D printing technique to endow cementitious materials with bioinspired, geometric complexities as those seen in living organisms. Nevertheless, the aforesaid cases have been implemented at a laboratory-scale and various challenges regarding cement-based 3D printing need to be overcome in order to accomplish bioinspired, structural complexities at a larger scale.

## 3D-Printed Reinforcement Materials With Biomimetic Features

3D printing can also be used to print "reinforcement" materials with biomimetic features, which can be incorporated inside concretes to enhance mechanical properties. They often perform their strength-enhancing functions by introducing additional failure mechanisms during mechanical loading. Certain types of materials, including polymer are widely established as a material source for 3D printing and thus, polymeric fibers with a greater variety of bioinspired structural features, such as auxetic or hierarchical properties can be synthesized.

Rosewitz et al. 3D-printed acrylonitrile butadiene (ABS)-based mesh, with the geometry of individual unit cells ranging from reentrant, "bow-tie" to tubular structures, thereby exhibiting auxetic behavior i.e., Negative Poisson's ratio upon mechanical loading (Rosewitz et al., 2019). Auxetic behavior is observed by several living organisms in nature, for example in skin of salamander and also, in cat's skin, which exhibits out-of-plane auxetic behavior (Veronda and Westmann, 1970; Santulli and Langella, 2016). Mechanical evaluation after 7 days of curing revealed that the auxetic reinforcement, also with the "brick-and-mortar" geometry increased the flexural strength, toughness and compressive strength via newly introduced failure mechanisms. The reinforcement triggered lateral shear failure as verified by the sliding of layers during fracture, while the intact cementitious samples exhibited shear failure in diagonal directions.

Similarly, Xu et al., also 3D printed polymeric meshes composed of repeating triangular cells using renowned fused-deposition modeling (FDM) technique and incorporated the meshes inside cementitious mortar beam (Xu et al., 2019). The authors varied the size of individual, triangular unit cells and performed tensile, as well as four-point bending test to reveal the effects of those polymeric meshes on the overall mechanical properties. It was found that the polymeric meshes can induce strain hardening and also enhance ductility via crack-bridging effect, which accompanies the formation of multiple cracks near the failure point.

Structural hierarchy is one of the key biomimetic features observed in natural materials including the red abalone, where mineral bridges connecting individual aragonite tablets exist in addition to the organic layers comprising chitin proteins in the interlayer spaces (Sun and Bhushan, 2012). 3D printing

has opened up the door toward introducing such hierarchical structures within cementitious composites. Farina et al., 3D printed both polymeric and metallic fibers with structural hierarchies, with the first level of hierarchy induced by small lattices attached on the surface and the second level attained by fractal geometries formed by those lattices along the fiber (Farina et al., 2016). The authors found that the fibers with higher degree of surface roughness induce shear failure mechanism while the smooth fibers undergo flexural failures during three-point bending test.

The advance in manufacturing technologies such as 3D printing has enabled the implementation of such naturally-observed geometrical complexities using industrial building blocks. Martin et al. applied 3D magnetic printing to synthesize a polymer/ceramic composite where the ceramic fillers are arranged in specific orientations inside polymer matrix and this verifies that 3D printing can induce a direction-dependent mechanics in composites (Martin et al., 2015).

In this section, two distinct ways of exploiting 3D printing techniques for bio-inspired, cementitious structures have been discussed. The first way is creating a biomimetic structure using cementitious slurry directly as print ink and the second way is printing reinforcement materials with unique bioinspired features and incorporating them inside concretes afterwards. In addition to those two general routes, polymer-reinforced concretes have also been directly extruded using cementitious mix composed of high-density polyethylene fibers. Ogura et al. applied an extrusion-based 3D printing to create a seven-layered, cement-based composite wall containing high density polyethylene microfibers and the mechanical evaluation on tensile and compressive strength was performed after 28 days of curing (Ogura et al., 2018). The evaluation confirmed that larger strain capacity was attained for the cementitious-HDPE composite under tensile loading with the formation of multiple cracks.

Overall, several challenges need to be overcome to render the automated 3D printing process to construction industry more widespread. Despite several successes in creating full-construction scale components via 3D Printing and the upward trend in the number of relevant projects worldwide, current extrusion-based 3D printing requires expert control on the usage of equipment and preparation of the printing materials (Buswell et al., 2018). Furthermore, ensuring reliability in materializing the pre-designed geometry of the component during the printing process remains a challenging task, since material properties, such as rheology and setting time of the printing ink as well as processing parameters can affect final shape of the structure.

## Synthesis and Biomimetic Modification of C-S-H

Another bioinspired strategy for cementitious materials is the bottom-up approach, where the most fundamental building blocks, called calcium-silicate-hydrate abbreviated as C-S-H are synthesized and their structural, physicochemical, and size properties are engineered at a microscopic scale. This enables controlled integration of the most fundamental building units of cementitious materials with organic components even from the length scale as microscopic as nano- and submicron scale. This integration of different types of materials from a microscopic scale is the common feature observed in natural materials. Structural, compositional and morphological properties of C-S-H can now be engineered and optimized for the subsequent assembling process, which would ultimately lead to enhanced mechanical properties at macroscale. Synthetic C-S-H can be produced via several routes including slurry-phase reaction between calcium oxide and silica, mechanochemical synthesis using a vibration mill and solution-based synthesis between calcium nitrate and sodium silicate (Sasaki et al., 2005; Foley et al., 2012; Mogghaddam et al., 2017).

The synthesis of hybrid, organic-inorganic composites composed of C-S-H particles as inorganic components can be attained via two major experimental routes. It can either occur in one step, whereby organic components are incorporated during the actual synthesis of C-S-H. The second route can occur in two separate stages, where the integration of organic components with C-S-H is attained following the synthesis of C-S-H. In the second route, synthesized C-S-H particles can be integrated with organic components via various assembly techniques including self-assembly and pressure-induced assembly.

## Synthesis of C-S-H/Polymer Composites

Matsuyama and Young incorporated cationic and anionic polymer with high molecular weights within the structure of quasicrystalline C-S-H at varying Ca/Si ratios and studied the nature of interactions using a variety of characterization techniques encompassing (Jefferson et al., 2010) Si nuclear magnetic resonance magic angle spinning and Fourier Transform Infrared Spectroscopy (Matsuyama and Young, 1999a,b). Expansion of basal spacing within the structure of a C-S-H crystallite, which in turn indicates the interlayer intercalations within the structure of C-S-H was observed for both cationic and anionic polymers, including poly (diallyldimethylammonium chloride) (PDC), poly(4-vinylbenzyltrimethylammonium chloride) (PVC), and poly(methacrylic) acid.

Similar to the work above performed by Matsuyama and Young, Pelliser et al. also added poly(diallyldimethylammonium chloride) during the synthesis of C-S-H using direct precipitation method and found the sign of its intercalation between the C-S-H lamellae based on XRD analysis (Pelisser et al., 2010). The authors also verified via nanoindentation testing that the polymer-induced structural change led to a decrease in packing density of C-S-H at mesoscale, thereby leading to a decrease in indentation hardness and elastic modulus.

In contrast to the previous reports on C-S-H/polymer composites implying the intercalation of polymeric molecules within the layered structure of C-S-H, Merlin et al. did not find an as-evident sign of nanoscale and intercalative interactions for cationic and anionic polymers (Merlin et al., 2002). Instead, the authors found the sign of mesocale interactions between polymer and C-S-H crystallites instead of nanoscale intercalation within the structure of each C-S-H crystallite.

Alizadeh et al. also incorporated aniline during the synthesis of C-S-H based on the reaction between calcium oxide and

silica in water and the resultant C-S-H/aniline composite was further subjected to the reaction with ammonium persulfate, thereby prompting homopolymerization of aniline (Alizadeh et al., 2010). This two-step process, where compositing C-S-H with organic monomer was followed by polymerization, resulted in the formation of C-S-H/polyaniline composite.

Aside from simply adding polymeric materials during the solution-based synthesis of C-S-H as described above, creative techniques for the synthesis of C-S-H/polymer nanocomposites have also been introduced at a laboratory scale. Kamali and Ghahremaninezhad applied the layer-by-layer assembly technique using two types of solutions, one containing cationic polymer such as poly(ethyleneimine) along with calcium nitrates and another type, containing negatively charged polymer such as poly(sodium 4-styrenesulfonate) (PSS) along with sodium silicates (Kamali and Ghahremaninezhad, 2018). The authors found via atomic force microscope (AFM)-based nanoindentation that the C-S-H/polymer composite synthesized using this layer-by-layer assembly exhibits similar indentation properties to the previously reported values of C-S-H polymer composites.

Picker et al. created a mesocrystalline, organic-inorganic superstructure from a colloidal solution of C-S-H, stabilized by polymeric materials (Picker et al., 2017). Two types of copolymer, PVP-co-PAA and PAAm-co-PAA were employed as organic dispersants, preventing the random aggregation of colloidal C-S-H particles. Controlled self-assembly was induced via a pH increase or via regulating the C-S-H/polymer ratio, ultimately leading to the formation of a hybrid, crystalline superstructure. A long-range order extending over the scale of millimeters was observed. The layered structure composed of inorganic C-S-H and polymeric materials resembles the microstructure of a nacre, which contains calcium carbonate platelets stacked upon each other with organic components existing at interfaces. Mechanical evaluation of the crystals using nanoindentation and bending test based on a focused ion beam microscope revealed that the hybrid C-S-H/polymer crystals exhibit much more elastic behavior and also, higher flexural strength compared to cement paste. The results verify the potential of synthesizing hybrid, biomimetic superstructures, which can directly enhance mechanical properties.

The advance in synthetic techniques has now enabled the synthesis of C-S-H particles with specific, well-designed properties such as morphology, meso- or nanoporosity, and varying Ca/Si molar ratios, which are closely related to structural and mechanical properties. Specific, well-defined morphology can facilitate inducing a nacre-like microstructure, marked by repeating, stacked patterns of similarly-shaped minerals. Furthermore, meso- or nano-porosity can facilitate inducing submicron or micro-scale integration of inorganic C-S-H with organic materials using, for example, infiltration techniques.

## Synthesis of CS-Based Particles With Specific Morphologies

Mogghadam et al. employed a seed-mediated, surfactant-assisted approach to attain specific, well-defined morphology for C-S-H (Mogghaddam et al., 2017). The authors employed naturally formed calcite particles in aqueous solution as basic seeds, thereby prompting heterogenous nucleation and growth of C-S-H on top of them. Mechanical evaluation from the state of single, individual particles to assembled, compacted state revealed that that the well-defined, rectangular morphology exerts positive effects on mechanical properties across different length scales. If the technique is developed further and a larger yield of C-S-H with well-defined cubic morphology can be produced at a large scale with acceptable economic feasibility in future, the particles could be assembled with organic components to produce a nacre-mimetic cementitious composite for applications in real construction sites.

Hwang et al. employed porous calcium silicate-based (CS) particles with well-defined, spherical morphology and employed them as the most basic building blocks for a heat-responsive, self-healing composite. The particles had similar composition to C-S-H, narrow distribution in size between 200 and 300 nm and also, narrow distribution in pore size around 3 nm. The authors integrated the particles with epoxy-based, heat responsive self-healing system, thereby synthesizing organic-inorganic hybrid particles (Hwang et al., 2017). The composite produced by compacting those hybrid particles showed superior micromechanical properties compared to the composite comprised of only CS particles with organic components and also, the composite exhibited heat-responsive, self-healing behavior.

## Computational Approach on Studying C-S-H/Polymer Composites

In designing bioinspired, C-S-H/polymer composites, computational techniques encompassing molecular dynamics and atomistic simulation play enormous roles in revealing the nature of interactions at various length scales (Zhou et al., 2017). Particularly, molecular dynamics has been a powerful tool for studying varying degrees of affinities between C-S-H, which lacks long-range structural order and organic polymer. The technique has often been employed for finding the dominant mechanism of interactions.

Zhou et al. employed molecular dynamics to study the nature of interactions between C-S-H and three different types of polymer, poly(acrylic acid) (PAA), poly (vinyl alcohol) and poly (ethylene glycol), all of which have been investigated experimentally as an organic component for C-S-H/polymer composites (Zhou et al., 2018). The authors found that PAA exhibits the strongest interaction among the three types of polymer, primarily via bonding between calcium from C-S-H and double bonded oxygen of carboxylic acid.

Sakhavand et al. also studied the interaction between poly(vinyl alcohol), which had been composited with C-S-H numerous times in previous experimental studies and tobermorite, the crystalline analog of C-S-H. Tobermorite is often adopted as a model system for C-S-H (Tao and Shahsavari, 2017; Zhang et al., 2017). The authors employed the combination of various computational techniques including molecular dynamics and the first-principles study, thereby

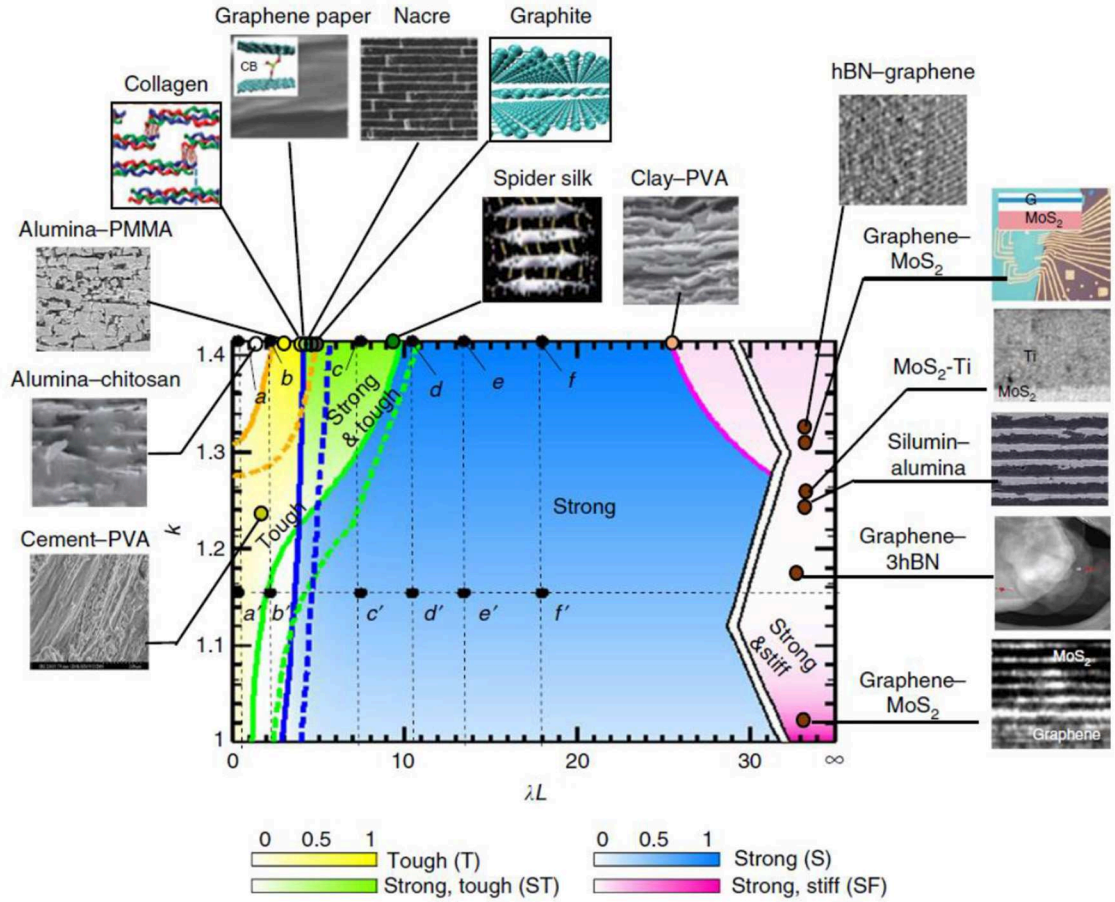


**FIGURE 5 |** Universal map for mechanical properties of nacre-mimetic hybrid structures obtained based on dimensionless parameters. Figure reproduced from Sakhavand and Shahsavari (2015), with permission from Springer Nature.

finding that the maximum toughness, instead of shear strength, dominates the breaking process of interfacial hydrogen bonds, which form the primary route for interaction between the two types of constituent materials (Sakhavand et al., 2013).

The same authors also devised the universal composition-structure-property map for hybrid, "brick-and-mortar"-type composites based on only four dimensionless parameters, encompassing those, which define platelet dissimilarity and symmetry of elastic stress distributions (Sakhavand and Shahsavari, 2015). The map, as shown in **Figure 5**, was proposed as a possible "design tool" for the synthesis of nacre-mimetic composites since it enables quantifying strength and toughness of any type of nacre-mimetic structures, thereby verifying the potential of producing synthetic, biomimetic cementitious composites with mechanical properties tailored for specific industrial applications.

## CONCLUSIONS

The review has provided an extensive insight into three major areas of research efforts, self-healing, 3D printing and nano/mesoscale integration of organic materials with C-S-H, all of which have been actively exploited in attaining novel, biomimetic cementitious materials. Bioinspired materials often characterized by the unique microstructural arrangement of soft and hard materials as observed in nacre and human bones. Furthermore, bioinspired features in nature also encompass self-healing capability, auxetic behavior, and geometrical complexities at various length scale. The advance in synthetic techniques such as the controlled self-assembly of C-S-H with organic materials and seed-mediated synthesis of C-S-H has led to the production of C-S-H or calcium silicate-based materials with well-defined morphological properties and also, successful integration of C-S-H with organic materials. Furthermore, the decade-long research efforts to optimize material and process parameters of cement-based 3D printing have introduced novel routes for biomimetic implementation, for example, creating polymeric reinforcement materials with hierarchical and auxetic features. The three major areas introduced in this review, self-healing, 3D printing, and the integration of C-S-H with organic materials have all led to notable progress based on a variety of implementation strategies.

In order to accomplish further widespread commercialization of aforesaid strategies, self-healing concepts in particular, further efforts need to be devoted to enhancing their cost-effectiveness. For example, despite the aforesaid success in generating a large number of self-healing agent-loaded microcapsules and incorporating them inside concrete panels during field trials, the production cost for these hybrid cementitious composites could become incredibly high if the scale become even larger. Consequently, the development of cost-effective, mass production technique for healant-loaded microcapsules could be one of the bottlenecks in materializing widespread application of capsule-based self-healing strategy for concretes at large scale. Furthermore, if the trial scale become larger, evaluating the effectiveness of the embedded self-healing systems could also become challenging. This is because conventional techniques for strength testing and crack introduction would become more difficult to implement if the test scale becomes larger than the field trials recently performed via the "Materials for Life" project. Therefore, appropriate evaluation techniques should also be devised for large-scale self-healing.

## AUTHOR CONTRIBUTIONS

RS designed the review subjects and logistics. SH and RS wrote the manuscript.

## REFERENCES


Alizadeh, A. R., Beaudoin, J. J., Raki, L., and Terskikh, V. (2010). C–S–H/polyaniline nanocomposites prepared by *in situ* polymerization. *J. Mater. Sci.* 46, 460–467. doi: 10.1007/s10853-010-4918-1

Araujo, M., Chatrabhuti, S., Gurdebeke, S., Alderete, N., Van Tittelboom, K., Raquez, J. M., et al. (2018). Poly(methyl methacrylate) capsules as an alternative to the "proof-of-concept" glass capsules used in self-healing concrete. *Cement Concrete Composites* 89, 260–271. doi: 10.1016/j.cemconcomp.2018.02.015

Barnett, S. J., Soutsos, M. N., Millard, S. G., and Bungey, J. H. (2006). Strength development of mortars containing ground granulated blast-furnace slag: Effect of curing temperature and determination of apparent activation energies. *Cement Concrete Res.* 36, 434–440. doi: 10.1016/j.cemconres.2005.11.002

Bos, F., Wolfs, R., Ahmed, Z., and Salet, T. (2016). Additive manufacturing of concrete in construction: potentials and challenges of 3D concrete printing. *Virtual Phys. Prototyp.* 11, 209–225. doi: 10.1080/17452759.2016.1209867

Buswell, R. A., Leal de Silva, W. R., Jones, S. Z., Dirrenberger, J., (2018). 3D printing using concrete extrusion: a roadmap for research. *Cement Concrete Res.* 112, 37–49. doi: 10.1016/j.cemconres.2018.05.006

Cremaldi, J. C., and Bhushan, B. (2018). Bioinspired self-healing materials: lessons from nature. *Beilstein J. Nanotechnol.* 9, 907–935. doi: 10.3762/bjnano.9.85

Davies, R., Teall, O., Pilegis, M., Kanellopoulos, A., Sharma, T., Jefferson, A., et al. (2018). Large scale application of self-healing concrete: design, construction, and testing. *Front. Mater.* 5:51. doi: 10.3389/fmats.2018.00051

Davtalab, O., Kazemian, A., and Khoshnevis, B. (2018). Perspectives on a BIM-integrated software platform for robotic construction through Contour Crafting. *Automat. Construct.* 89, 13–23. doi: 10.1016/j.autcon.2018.01.006

Dong, B., Wang, Y., Fang, G., Han, N., Xing, F., and Lu, Y. (2015). Smart releasing behavior of a chemical self-healing microcapsule in the stimulated concrete pore solution. *Cement Concrete Composites* 56, 46–50. doi: 10.1016/j.cemconcomp.2014.10.006

Dry, C. (1994). Matrix cracking repair and filling using active and passive modes for smart timed release of chemicals from fibers into cement matrices. *Smart Mater. Struct.* 3:118. doi: 10.1088/0964-1726/3/2/006

Du, X., Fu, S., Zhu, Y., and (2018). 3D printing of ceramic-based scaffolds for bone tissue engineering: an overview. *J. Mater. Chem. B.* 6, 4397–4412. doi: 10.1039/C8TB00677F

Farina, I., Fabbrocino, F., Carpentieri, G., Modano, M., Amendola, A., Goodall, R., et al. (2016). On the reinforcement of cement mortars through 3D printed polymeric and metallic fibers. *Composites Part B Eng.* 90, 76–85. doi: 10.1016/j.compositesb.2015.12.006

Foley, E. M., Kim, J. J., and Reda Taha, M. M. (2012). Synthesis and nano-mechanical characterization of calcium-silicate-hydrate (C-S-H) made with 1.5 $CaO/SiO_2$ mixture. *Cement Concrete Res.* 42, 1225–1232. doi: 10.1016/j.cemconres.2012.05.014

Fratzl, P., and Barth, F. G. (2009). Biomaterial systems for mechanosensing and actuation. *Nature* 462, 442–448. doi: 10.1038/nature08603

Fratzl, P., Elbaum, R., and Burgert, I. (2008). Cellulose fibrils direct plant organ movements. *Faraday Discuss.* 139,275–282; discussion: 309–325, 419–420. doi: 10.1039/b716663j

Habeeb, G. A., and Mahmud, H. B. (2010). Study on properties of rice husk ash and its use as cement replacement material. *Mater. Res.* 13, 185–190. doi: 10.1590/S1516-14392010000200011

Hager, I., Golonka, A., Putanowicz, R. (2016). 3D printing of buildings and building components as the future of sustainable construction? *Proc. Eng.* 151, 292–299. doi: 10.1016/j.proeng.2016.07.357

Hilloulin, B., Van Tittelboom, K., Gruyaert, E., De Belie, N., and Loukili, A. (2015). Design of polymeric capsules for self-healing concrete. *Cement Concrete Composites* 55, 298–307. doi: 10.1016/j.cemconcomp.2014.09.022

Hu, Z.-X., Hu, X.-M., Cheng, W.-M., Zhao, Y.-Y., and Wu, M.-Y. (2018). Performance optimization of one-component polyurethane healing agent for self-healing concrete. *Construct. Building Materials* 179, 151–159. doi: 10.1016/j.conbuildmat.2018.05.199

Hwang, D., and Khoshnevis, B. (2004). "Concrete wall fabrication by contour crafting," in *The 21st ISARC* (Jeju). doi: 10.22260/ISARC2004/0057

Hwang, S., and Shahsavari, R. (2018). High calcium cementless fly ash binder with low environmental footprint: optimum Taguchi design. *J. Am. Ceramic Soc.* 102, 2203–2217. doi: 10.1111/jace.15873

Hwang, S. H., Miller, J. B., and Shahsavari, R. (2017). Biomimetic, strong, tough, and self-healing composites using universal sealant-loaded, porous building blocks. *ACS Appl. Mater. Interfaces* 9, 37055–37063. doi: 10.1021/acsami.7b12532

Jefferson, A., Joseph, C., Lark, R., Isaacs, B., Dunn, S., and Weager, B. (2010). A new system for crack closure of cementitious materials using shrinkable polymers. *Cement Concrete Res.* 40, 795–801. doi: 10.1016/j.cemconres.2010.01.004

Jonkers, H. M., and Schlangen, E. (2008). "Development of a bacteria-based self healing concrete," in *Tailor Made Concrete Structures,* eds J. C. Walraven and D. Stoelhorst (London: Taylor and Francis Group). doi: 10.1201/9781439828410.ch72

Kamali, M., and Ghahremaninezhad, A. (2018). A study of calcium-silicate-hydrate/polymer nanocomposites fabricated using the layer-by-layer method. *Materials* 11:527. doi: 10.3390/ma11040527

Khoshnevis, B., and Bekey, G. (2002). "Automated construction using contour crafting – applications on earth and beyond," in *The 19th ISARC* (Washington, DC), 489–495. doi: 10.22260/ISARC2002/0076

Liu, S., Bundur, Z. B., Zhu, J., and Ferron, R. D. (2016). Evaluation of self-healing of internal cracks in biomimetic mortar using coda wave interferometry. *Cement Concrete Res.* 83, 70–78. doi: 10.1016/j.cemconres.2016.01.006

Luo, M., Qian, C., and Li, R. (2015). Factors affecting crack repairing capacity of bacteria-based self-healing concrete. *Construct. Build. Mater.* 87, 1–7. doi: 10.1016/j.conbuildmat.2015.03.117

Ma, G., Li, Z., and Wang, L. (2018). Printable properties of cementitious material containing copper tailings for extrusion based 3D printing. *Construct. Build. Mater.* 162, 613–627. doi: 10.1016/j.conbuildmat.2017.12.051

Martin, J. J., Fiore, B. E., and Erb, R. M. (2015). Designing bioinspired composite reinforcement architectures via 3D magnetic printing. *Nat. Commun.* 6:8641. doi: 10.1038/ncomms9641

Matsuyama, H., and Young, J. F. (1999a). Synthesis of calcium silicate hydrate/polymer complexes: Part 1. Anionic and nonionic polymers. *J. Mater. Res.* 14, 3379–3388. doi: 10.1557/JMR.1999.0458

Matsuyama, H., and Young, J. F. (1999b). Synthesis of calcium silicate hydrate/polymer complexes: Part II. Cationic polymers and complex formation with different polymers. *J. Mater. Res.* 14, 3389–3396. doi: 10.1557/JMR.1999.0459

Merlin, F., Lombois, H., Joly, S., Lequeux, N., Halary, J.-L., and Van Damme, H. (2002). Cement-polymer and clay-polymer nano- and meso-composites: spotting the difference. *J. Mater. Chem.* 12, 3308–3315. doi: 10.1039/B205279M

Mogghaddam, S. E., Hejazi, V., Hwang, S., Sreenivasan, S., Miller, J., Shi, B., et al. (2017). Morphogenesis of cement hydrate. *J. Mater. Chem. A* 5, 3798–3811. doi: 10.1039/C6TA09389B

Moini, M., Olek, J., Youngblood, J. P., Magee, B., and Zavattieri, P. D. (2018). Additive manufacturing and performance of architectured cement-based materials. *Adv. Mater.* 30:e1802123. doi: 10.1002/adma.201802123

Nova, A., Keten, S., Pugno, N. M., Redaelli, A., and Buehler, M. J. (2010). Molecular and nanostructural mechanisms of deformation, strength and toughness of spider silk fibrils. *Nano Lett.* 10, 2626–2634. doi: 10.1021/nl101341w

Ogura, H., Nerella, V. N., and Mechtcherine, V. (2018). Developing and testing of Strain-Hardening Cement-Based Composites (SHCC) in the context of 3d-printing. *Materials.* 11, 1375–1385. doi: 10.3390/ma11081375

Panda, B., Paul, S. C., Hui, L. J., Tay, Y. W. D., and Tan, M. J. (2017). Additive manufacturing of geopolymer for sustainable built environment. *J. Clean. Prod.* 167, 281–288. doi: 10.1016/j.jclepro.2017.08.165

Pegna, J. (1997). Exploratory investigation of solid freeform construction. *Automat. Construct.* 5, 427–437. doi: 10.1016/S0926-5805(96)00166-5

Pelisser, F., Gleize, P. J. P., and Mikowski, A. (2010). Effect of poly(diallyldimethylammonium chloride) on nanostructure and mechanical properties of calcium silicate hydrate. *Mater. Sci. Eng. A* 527, 7045–7049. doi: 10.1016/j.msea.2010.07.057

Pelletier, M. M., Brown, R., Shukla, A., and Bose, A. (2011). *Self-Healing Concrete with a Microencapsulated Healing Agent*. https://pdfs.semanticscholar.org/e48b/937bde7c53ce059d464822ebc837a31647dc.pdf (accessed September 3, 2020).

Picker, A., Nicoleau, L., Burghard, Z., Bill, J., Zlotnikov, I., Labbez, C., et al. (2017). Mesocrystalline calcium silicate hydrate: a bioinspired route toward elastic concrete materials. *Sci. Adv.* 3:e1701216. doi: 10.1126/sciadv.1701216

Possan, E., Thomaz, W., Aleandri, G. A., Felix, E. F., and dos Santos, A. C. P. (2017). $CO_2$ uptake potential due to concrete carbonation: a case study. *Case Stud. Construct. Mater.* 6, 147–161. doi: 10.1016/j.cscm.2017.01.007

Prawoto, Y. (2012). Seeing auxetic materials from the mechanics point of view: a structural review on the negative Poisson's ratio. *Comput. Mater. Sci.* 58, 140–153. doi: 10.1016/j.commatsci.2012.02.012

Rosewitz, J. A., Choshali, H. A., and Rahbar, N. (2019). Bioinspired design of architected cement-polymer composites. *Cement Concrete Composites* 96, 252–265. doi: 10.1016/j.cemconcomp.2018.12.010

Sakhavand, N., Muthuramalingam, P., and Shahsavari, R. (2013). Toughness governs the rupture of the interfacial H-bond assemblies at a critical length scale in hybrid materials. *Langmuir* 29, 8154–8163. doi: 10.1021/la4014015

Sakhavand, N., and Shahsavari, R. (2015). Universal composition-structure-property maps for natural and biomimetic platelet-matrix composites and stacked heterostructures. *Nat. Commun.* 6:6523. doi: 10.1038/ncomms7523

Santulli, C., and Langella, C. (2016). Study and development of concepts of auxetic structures in bio-inspired design. *Int. J. Sust. Design* 3, 1443–1453. doi: 10.1504/IJSDES.2016.078947

Sasaki, K., Masuda, T., Ishida, H., and Mitsuda, T. (2005). Synthesis of calcium silicate hydrate with Ca/Si = 2 by mechanochemical treatment. *J. Am. Ceramic Soc.* 80, 472–476. doi: 10.1111/j.1151-2916.1997.tb02853.x

Shahsavari, R., and Hwang, S. (2017). Innovative concretes provide the ultimate solution for rising construction costs and environmental footprint. *Am. Ceramic Soc. Bull.* 97, 2–8. Available online at: https://pdfs.semanticscholar.org/91b0/06945446e9fbaef01d60c9c391ed454db506.pdf

Snikhovska, K. (2019). *The Different Types of 3D Printing Technology*. Available online at: penandplastic.com (accessed September 3, 2020).

Studart, A. R., and Erb, R. M. (2014). Bioinspired materials that self-shape through programmed microstructures. *Soft Matter* 10, 1284–1294. doi: 10.1039/C3SM51883C

Sun, J., and Bhushan, B. (2012). Hierarchical structure and mechanical properties of nacre: a review. *RSC Adv.* 2, 7617–7632. doi: 10.1002/chin.201250224

Tao, L., and Shahsavari, R. (2017). Diffusive, displacive deformations and local phase transformation govern the mechanics of layered crystals: the case study of tobermorite. *Sci. Rep.* 7:5907. doi: 10.1038/s41598-017-05115-4

Teall, O., Davies, R., Pilegis, M., Kanellopoulos, A., Sharma, T., Paine, K., et al. (2016). Self-healing concrete full-scale site trials," in *11th fib International PhD Symposium in Civil Engineering* (Tokyo: The University of Tokyo), 639–646.

Teall, O., Pilegis, M., Davies, R., Sweeney, J., Jefferson, T., Lark, R., et al. (2018). A shape memory polymer concrete crack closure system activated by electrical current. *Smart Mater. Struct.* 27, 1–12. doi: 10.1088/1361-665X/aac28a

Toohey, K. S., Sottos, N. R., Lewis, J. A., Moore, J. S., and White, S. R. (2007). Self-healing materials with microvascular networks. *Nat. Mater.* 6, 581–585. doi: 10.1038/nmat1934

Tziviloglou, E., Wiktor, V., Jonkers, H. M., and Schlangen, E. (2016). Bacteria-based self-healing concrete to increase liquid tightness of cracks. *Construct. Build. Mater.* 122, 118–125. doi: 10.1016/j.conbuildmat.2016.06.080

Van Belleghem, B., Gruyaert, E., Van Tittelboom, K., Moerman, W., Dekeyser, B., Van Stappen, J., et al. (2018). Effect of polyurethane viscosity on self-healing efficiency of cementitious materials exposed to high temperatures from sun radiation. *J. Mater. Civil Eng.* 30, 1–12. doi: 10.1061/(ASCE)MT.1943-5533.0002360

Van Tittelboom, K., and De Belie, N. (2013). Self-healing in cementitious materials-a review. *Materials* 6, 2182–2217. doi: 10.3390/ma6062182

Veronda, D. R., and Westmann, R. A. (1970). Mechanical characterization of skin-finite deformations. *J. Biomech.* 3, 111–124. doi: 10.1016/0021-9290(70)90055-2

Weaver, J. C., Milliron, G. W., Miserez, A., Evans-Lutterodt, K., Herrera, S., Gallana, I., et al. (2012). The stomatopod dactyl club: a formidable damage-tolerant biological hammer. *Science* 336, 1275–1280. doi: 10.1126/science.1218764

Wegst, U. G., Bai, H., Saiz, E., Tomsia, A. P., and Ritchie, R. O. (2015). Bioinspired structural materials. *Nat. Mater.* 14, 23–36. doi: 10.1038/nmat4089

Weng, Y., Li, M., Tan, M. J., and Qian, S. (2018). Design 3D printing cementitious materials via Fuller Thompson theory and Marson-Percy model. *Construct. Build. Mater.* 163, 600–610. doi: 10.1016/j.conbuildmat.2017.12.112

Xu, Y., Schlangen, E., and Savija, B. (2019). "Creating Strain Hardening Cementitious Composites (SHCCS) through use of additively manufactured polymeric meshes as reinforcement," in *10th International Conference on Fracture Mechanics of Concrete and Concrete Structures*, eds G. Pijaudier-Cabot, P. Grassl, and C. La Borderie (Bayonne). doi: 10.21012/FC10.235158

Yang, Z., Hollar, J., He, X., and Shi, X. (2011). A self-healing cementitious composite using oil core/silica gel shell microcapsules. *Cement Concrete Composites* 33, 506–512. doi: 10.1016/j.cemconcomp.2011.01.010

Zhang, N., Carrez, P., and Shahsavari, R. (2017). Screw-dislocation-induced strengthening-toughening mechanisms in complex layered materials: the case study of tobermorite. *ACS Appl. Mater. Interfaces* 9, 1496–1506. doi: 10.1021/acsami.6b13107

Zhang, X., Li, M., Lim, J. H., Weng, Y., Tay, Y. W. D., Pham, H., et al. (2018). Large-scale 3D printing by a team of mobile robots. *Automat. Construct.* 95, 98–106. doi: 10.1016/j.autcon.2018.08.004

Zhang, Y., Zhang, Y., Liu, G., Yang, Y., Wu, M., and Pang, B. (2018). Fresh properties of a novel 3D printing concrete ink. *Construct. Build. Mater.* 174, 263–271. doi: 10.1016/j.conbuildmat.2018.04.115

Zhou, Y., Hou, D., Geng, G., Feng, P., Yu, J., and Jiang, J. (2018). Insights into the interfacial strengthening mechanisms of calcium-silicate-hydrate/polymer nanocomposites. *Phys. Chem. Chem. Phys.* 20, 8247–8266. doi: 10.1039/C8CP00328A

Zhou, Y., Hou, D., Manzano, H., Orozco, C. A., Geng, G., Monteiro, P. J. M., et al. (2017). Interfacial connection mechanisms in calcium-silicate-hydrates/polymer nanocomposites: a molecular dynamics study. *ACS Appl. Mater. Interfaces* 9, 41014–41025. doi: 10.1021/acsami.7b12795

**Conflict of Interest:** The authors declare that the research was conducted in the absence of any commercial or financial relationships that could be construed as a potential conflict of interest.

frontiers in Materials

ORIGINAL RESEARCH
published: 08 April 2020
doi: 10.3389/fmats.2020.00075

# On Simulating the Formation of Structured, Crystalline Systems via Non-classical Pathways

*John C. Mergo III*[1] *and Jong Seto*[2,3]*

[1] BitWrex, LLC, Morton, IL, United States, [2] Department of Bioengineering and Therapeutic Sciences, UCSF, San Francisco, CA, United States, [3] Lawrence Berkeley National Laboratory, Molecular Foundry, Berkeley, CA, United States

Observations in crystal growth and assembly from recent *in situ* methods suggest alternative, non-classical crystallization pathways play an important role in the determination of the micro- and meso- structures in crystalline systems. These processes display parallels that cross-cut multiple disciplines investigating crystallization across four orders of magnitude in size scales and widely differing environments, hinting that alternative crystal growth pathways may be a fundamental scheme in natural crystal formation. Using a system of short-range attractive microbeads, we demonstrate that the addition of a small concentration of sub-species incommensurate with the lattice spacing of the dominant species results in a stark change in crystal size and morphology. These changes are attributed to the presence of fleeting, amorphous-like configurations of beads that ultimately change the melting and growth dynamics in preferred directions. From these *real-time* observations, we hypothesize the amorphous mineral precursors present in biological mineralized tissues undergo similar non-classical crystallization processes resulting in the complex structures found in biomineralization.

**Keywords: non-classical crystallization pathways, biological mineralization, multiscale interactions, bead-bead interactions, amorphous precursors, colloidal crystallization**

OPEN ACCESS

***Edited by:***
*Admir Masic,*
*Massachusetts Institute of Technology, United States*

***Reviewed by:***
*Lucas Kuhrts,*
*Max Planck Institute of Colloids and Interfaces, Germany*
*Thierry Azaïs,*
*Sorbonne Universités, France*

***Correspondence:**
*Jong Seto*
*JMSeto@lbl.gov*

***Specialty section:***
*This article was submitted to Biomaterials, a section of the journal Frontiers in Materials*

***Received:*** *07 October 2019*
***Accepted:*** *12 March 2020*
***Published:*** *08 April 2020*

***Citation:***
*Mergo JC III and Seto J (2020) On Simulating the Formation of Structured, Crystalline Systems via Non-classical Pathways. Front. Mater. 7:75. doi: 10.3389/fmats.2020.00075*

## INTRODUCTION

Functional biological materials possess a myriad of intricate architectures and material properties, brought about by similarly diverse and complex formation processes (Coelfen and Antonietti, 2008; Noorduin et al., 2013). Biology has adapted mechanisms to sequester and organize local environments to provide the conditions necessary for growth of these materials while the organism exists in a global environment unsuited for growth or development of these materials. Local environments have shown to be controlled in numerous ways, such as regulation of pH, material concentration, protein concentration, and cellular density (Fritz et al., 1994; Aizenberg, 2004; Seto et al., 2004; Dunlop and Fratzl, 2010; Schenk et al., 2012; Seto, 2012; Rao et al., 2017). For example, organic scaffolds can template inorganic mineral components to create hierarchical composites such as teeth, sea shells, and bones (Lowenstam, 1981; Ashby et al., 1995; Weiner and Wagner, 1998; Fratzl and Weinkamer, 2007; Huang et al., 2019). Crystallization plays an essential role in the development of these materials, though the exact physical processes governing this process are not well understood. However, there is intense interest in these fundamental mechanisms (Gasser, 2009; Dalmaschio et al., 2010; Vekilov, 2010; Weiner and Addadi, 2011; Vekilov and Vorontsova, 2014), and the results of recent studies have produced valuable insights that may enable better

understanding of these processes. Important among these insights is that classical nucleation and crystal growth paradigms cannot sufficiently explain the existence of certain phases, structures, or properties of various materials developed in solution, many of which are found in biological materials. Thus, alternative pathways for the structure and growth of these crystalline materials must be considered (Auer and Frenkel, 2001; Filion et al., 2010).

Many of these crystallization processes relevant to formation and structuring in biological materials can now be studied at the single-particle level even at the nanoscale *in situ* due to advances in computational and experimental methods. Thus, a growing body of evidence showing the importance of non-classical nucleation and growth mechanisms utilizing intermediate, metastable or kinetically-determined states can arise that considerably alter the resulting crystal growth (DeYoreo and Vekilov, 2003; Ivanov et al., 2014; Deyoreo et al., 2015). For example, crystal growth assisted by structured pre-crystalline states (Gebauer et al., 2008; Dey et al., 2010; Demichelis et al., 2011), nucleation from metastable phases (Chung et al., 2009; Washington et al., 2012; Baumgartner et al., 2013; Maes et al., 2015), oriented attachment of crystallites (Banfield et al., 2000; Li et al., 2012; Nielsen et al., 2014), and growth emerging out of amorphous phases (Weiss et al., 2002; Politi et al., 2004; Killian et al., 2009; Savage and Dinsmore, 2009; Mahamid et al., 2010; Lechner et al., 2011; Salvalaglio et al., 2014; Ma et al., 2017; Pendola et al., 2018) have all been shown to alter growth in non-trivial ways, often resulting in complex structure formation that appear to defy the evolution of the system toward its ultimate lowest energy configuration. Moreover, these types of alternative growth mechanisms have been suggested in systems with widely different environmental conditions, from biological context such as protein crystal nucleation (Vekilov and Vorontsova, 2014), calcite growth (Weiss et al., 2002; Politi et al., 2004; Killian et al., 2009; Seto et al., 2012), tissue mineralization (Wang et al., 2012; Weaver et al., 2012; Tao et al., 2019), magnetite nucleation and growth (Kuhrts et al., 2019; Mirabello et al., 2019; Rawlings et al., 2019), as well as inorganic contexts like cadmium selenide quantum dot growth (Washington et al., 2012), iron oxide growth (Banfield et al., 2000; Baumgartner et al., 2013; Dideriksen et al., 2015), and colloidal microparticle crystallization (Savage et al., 2006; Savage and Dinsmore, 2009), just to name a few examples. The vast range of systems exhibiting these behaviors is paralleled by the span of the size scales of the crystallizing components, from the micro to the atomic scale.

Looking at tissue mineralization in particular, intermediate mineral phases in mineralization have been shown to exist and form metastable assemblies that eventually undergo a transition to high crystallinity over time (Mahamid et al., 2010; Seto et al., 2013, 2014). Several groups have shown that interactions with these intermediate phases drive mineralization along diverse paths (Teng et al., 1998; De Yoreo et al., 2015; Mass et al., 2017; Zhou et al., 2019). The presence of these mineralization precursors across such a diverse range of systems implies that there are underlying universal mechanisms at play (**Figure 1**). From previous work, specific macromolecules are known in nature to interact with minerals and form metastable phases as well as select specific crystalline polymorphs and form unique bulk crystalline arrangements (Zou et al., 2017) as measured by select *in situ* techniques such as Raman, electron microscopy and X-ray scattering methods (**Figure 1**). In perturbing such organic-inorganic interactions through physiochemical and microfluidic methods, it can be shown that local ion supersaturation can be altered to drive mineralization along specific mineral-organic assemblies (Wang et al., 2012; Seto et al., 2014). The characteristics of these assemblies are crucial in changing the local chemical environments as they stabilize/destabilize neighboring assemblies (Noorduin et al., 2009). Thus, neighboring non-crystalline assemblies have an indirect effect on nucleation, crystal growth mechanisms, and subsequently, final structure. By delineating the basic components and parameters (both thermodynamic and kinetic) that drive some of these crystallization processes, an improved understanding of nucleation and crystal growth events can be updated in the context of recent observations with advanced methods.

In the case of biomineralization, specialized cells lay the groundwork for the mineralized tissue by secreting an organic scaffold that serves as a template for crystal growth, regardless of mineral type (Politi et al., 2004; Seto et al., 2004; Jee et al., 2010; Gong et al., 2012; Cho et al., 2016; de Melo Pereira and Habibovic, 2018). Using the developing sea urchin larval spine as an example organism, we extracted the proteinaceous extracellular matrix and performed remineralization to determine the roles of constituent proteins in the mineralization of the highly crystalline larval spicule. Of specific interest is understanding the organization and the specific components involved in stabilization of an amorphous mineral precursor phase in the growing spicule. As shown in **Figure 2**, physio-chemical selective domains of these scaffolds initially bind directly to nascent intermediate phases and amorphous precursors to create localized layer-by-layer arrangements of mineral on/within an organic layer. The mineral precursors in this case are promoted and cover an organic layer in order to start an initial epitaxial growth process (**Figures 2B,C,E,F**). Eventually, this isotropic epitaxy of stabilized mineral precursors and their organic counterparts fill voids and spaces not already occupied (**Figures 2A,D**). Through this biological control of mineral precursors, subsequent assemblies are arranged such that crystallinity and organization of the organic and mineral constituents in the forming mineralized material are highly regulated.

To simplify these interactions and crystalline states found in biological crystallization, we utilize a model system of attractive polystyrene microbeads to focus on the interactions of the mineral phases involved in the early formation processes in mineralized tissues. With the ability to fine-tune the strength of the interaction between microspheres, we can investigate crystal nucleation, growth, and melting with single-particle precision. This technique is well-suited for investigating the effects of phenomena that occur on short timescales or within rare assemblies, because the individual particles can be imaged in real-time (Crocker and Grier, 1996; Larsen and Grier, 1996;

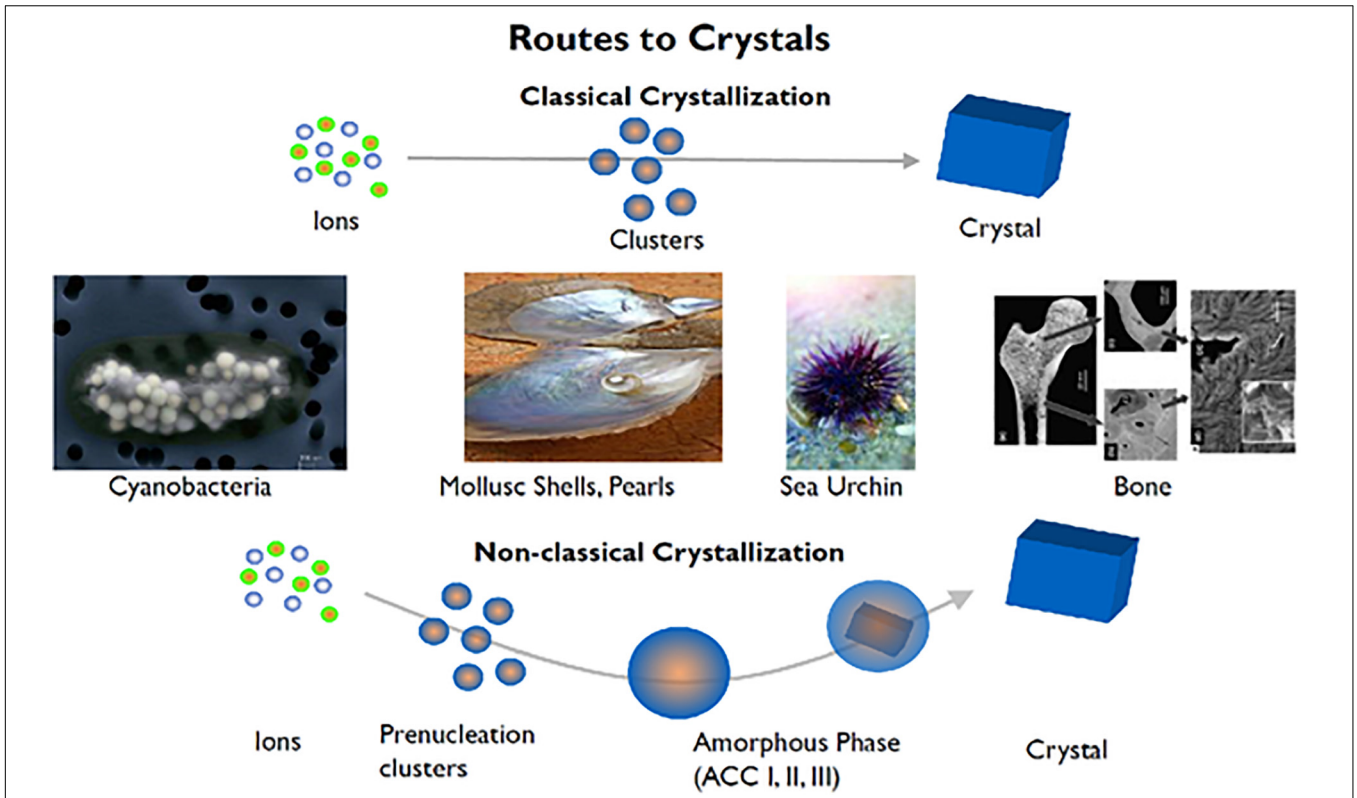


**FIGURE 1 |** Biological crystallization of diverse mineralized tissues ranging from sea urchin spines to bones and teeth demonstrate a non-classical crystallization pathway. From calcium carbonate ($CaCO_3$) to hydroxyapatite ($Ca_{10}(PO_4)_6(OH)$), these divergent mineralization systems have been found to contain intermediates mineral phases not explained by classical crystallization theories. Adapted from Coelfen and Antonietti (2008) with permission from John Wiley and Sons.

Ganapathy et al., 2010; Zeravcic et al., 2014; Mergo, 2017). Through use of this system, assembly and dissociation kinetics can be observed without the added complexity of material properties or solution chemistry, allowing us to relate the effects of kinetics to the final crystal state on the single-particle scale. These direct observations enable for the investigation of events immediately before and after nucleation as well as during crystal growth in order to observe intermediate and "exotic" states altering particle dynamics that are difficult to observe on smaller scales and only now becoming noticed as important for driving growth along specific pathways (Gebauer et al., 2008; Dey et al., 2010; Picker et al., 2017). Of specific interest are questions related to amorphous precursors, neighboring crystal domains, and their effects on the resulting material structure as observed by previous work in biological materials and systems (Aizenberg, 2004; Politi et al., 2004; Munch et al., 2008; Meyers et al., 2013; Fischer et al., 2017; Tao et al., 2019). Similar model systems of attractive microbeads have revealed that island formation, step-edge barriers (Ganapathy et al., 2010), and even multi-layer growth on heavily strained substrates (Lechner et al., 2011; Savage et al., 2013) arise even when the length scale of the interparticle interaction is far shorter than a particle radius. In all these cases, the particles' dynamics are slowed via interactions with their neighbors, creating a dynamic analog to structures often attributed to the influence of a particle's next-nearest-neighbors. The ability to identify individual particles allows us the ability to measure changes to crystal morphology via controlled variation of the microbead population itself (i.e., slight variations in bead population like: 100% small beads, 0% large beads or 90% small beads, 10% large beads, lead to drastic changes in morphology)—perturbations that are prevalent in the formation of biological tissues.

In this microbead system, we observe the evolution of a bidisperse quasi-2D colloidal system during crystal nucleation, growth, and coarsening. In a monodisperse system, crystallization and growth occur in a manner consistent with prior observations representative of that which is expected of particles with short-range attractive interactions (Dinsmore et al., 1997; Dullens et al., 2006; Palberg, 2014). In our bidisperse system consisting of microbeads of two different diameters, crystal growth results in a fundamentally different final morphology. During growth, crystals of the more numerous particle species slows and reverses while a second layer nucleates and grows on most islands. The intermixing of this secondary species with the primary species in the regions between crystal islands, before eventual separation into crystals of similar species, determines the time scales over which they can act as either promoters of crystallization or intermediate phase stabilizers—corresponding to natural interactions

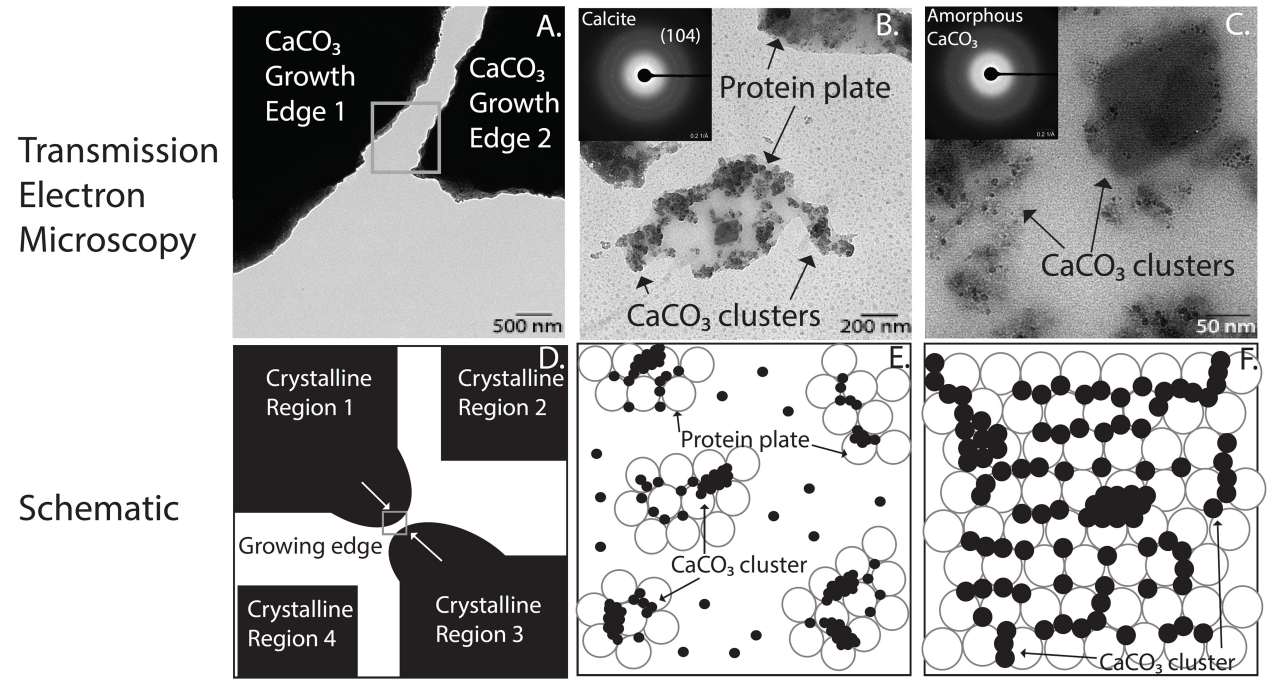


**FIGURE 2 |** High spatial and temporal arrangement of organic and mineral islands of $CaCO_3$ intermediate phases of crystallization found in the developing sea urchin larval spine. **(A–C)** Transmission electron micrographs (TEM) of $CaCO_3$ remineralized proteinaceous scaffolds from sea urchin spine at increasing magnification insets in panels **(B,C)** show diffraction patterns of crystalline and amorphous regions, respectively. **(D–F)** A schematic diagram demonstrates a biphasic behavior found in protein mediated biological $CaCO_3$ mineralization systems among the organic and mineral components. Subsequent panels are corresponding higher magnification zoom-ins of the previous panel.

of proteins and metals found in the mineralization of sea urchin larval spicule.

We can not only observe sequences of events as a function time, but also can quantify the energetic states found in certain configurations of bead assemblies. This uniquely enables an opportunity to fill in gaps left behind by Ostwald's theory on classical nucleation as these diverse states form (Ostwald, 1897). These states include the immediate events after nucleation processes when a nucleate reaches a specific size, classical nucleation theory states that the nucleate continues to grow larger from the nucleated state, however, it does not reconcile observations from *in situ* cryo-Transmission Electron Microscopy (TEM) and X-ray studies that demonstrate that neighboring nucleates can also predominantly shrink, divide, and merge at the sake of growing nucleates (Noorduin et al., 2009; Nielsen et al., 2014; Smeets et al., 2015; Zhou et al., 2019). Recent experiments using *in situ* TEM of iron-palladium composite nanoparticles composed of only 10s of atoms to seed nucleation and observe crystallization processes (Zhou et al., 2019) while in dissolution experiments with glucose isomerase crystallization, the density of mesoscopic clusters are found to control the rate of nucleation (Sleutel and Van Driessche, 2014). Like the microbeads, these nanoparticles and protein crystals show intermediate states that are not explainable in the framework of classical nucleation theory. We show a system that can concisely describe inter-bead interactions on a time scale that is manipulatable as well as containing enough accuracy to attribute kinetic and thermodynamic parameters in order to expand on recent findings of non-classical nucleation behaviors occurring in nucleation and crystallization processes on a non-infinite time-scale.

With these observations, we can begin to characterize the configuration states of rare physical states along the crystallization pathway (i.e., prenucleation and intermediate phases) recently observed with *in situ* techniques at the molecular level (Gebauer et al., 2008; Mahamid et al., 2010; Demichelis et al., 2011; Habraken et al., 2013; Hedges and Whitelam, 2013; Zou et al., 2017). It is also noteworthy that these observations can detail how nascent states develop and translate into the final microstructural configurations in the mineralized tissue over time despite possessing the same assumed final configurations on an infinite timescale. Although these mixed states are not stable, their presence creates a long-lasting effect on the final structures of these biomineralized materials as found in nature. This improved understanding about nucleation and crystallization processes involved in the growth and development of mineralized tissues over multiple scales not only provides a window how biological regulation and control can take root at tissue formation, but encourages inspiration to search for novel approaches that utilize these biological strategies in creating synthetic, bulk functional crystalline materials with tunable materials properties and structures.

# MATERIALS AND METHODS

## Remineralization of Sea Urchin Larval Spine

Organic extracellular matrices (ECM) were precipitated from demineralized sea urchin larval spines collected after 48 h of fertilization. The ECM were resuspended in $ddH_2O$ and aliquoted onto copper TEM grids (Quantifoil, Ted Pella, Inc.). Supersaturated solutions of 10 mM $CaCl_2$ and 10 mM $Na_2CO_3$ and 10 mM $NaHCO_3$ were added to initiate remineralization as described elsewhere (Seto et al., 2013). A TEM (Libra 120, Zeiss SMT) examined the remineralized structures after subsequent $ddH_2O$ washes and air-drying.

## Bead-Bead Interactions

The solvent used in these experiments consisted of 2 mM NaCl in $H_2O$ (Millipore). The non-ionic surfactant hexaethylene glycol monododecyl ether ($C_{12}E_6$), 2.5 mM, was added to induce an attraction between microparticles via depletion and was gently shaken until the surfactant was dissolved. Colloidal microspheres were introduced by adding an additional 2% of sample volume of polystyrene microbeads suspended in water. Bidisperse samples were prepared using a mixture of polystyrene microbeads with radii of $r_l$ = 0.6 and $r_s$ = 0.5 μm and less than 4% size polydispersity, mixed 1:10 by volume, both drawn from stock solutions of 8% solids by volume from Sigma Aldrich. Monodisperse samples used as a control were prepared using the 0.5 μm spheres.

Samples were pipetted into glass chambers that had been cleaned with a strong base and rinsed with methanol and deionized (DI) water. The chambers were sealed and loaded onto an inverted optical microscope. Because of the temperature sensitivity of the depletant, the microscope was thermally isolated from its surroundings using an extruded polystyrene box 5 cm in thickness (Owens Corning). The target temperature of the sample was controlled using two PID heating elements placed above and below the sample. Colloids sedimented for about 12 h at 22°C before undergoing a temperature ramp of+0.1°C every 30 min until failed nucleation events were observed. The temperature ramp was halted, and images of the sample were captured at one frame per minute for 78 h.

Particle locations were extracted from the video data using custom software based on previously developed particle tracking methods (Seto et al., 2014). Significant effort went into implementing additional segmentation and featuring algorithms, as well as manual checks to account for optical artifacts that arise from setting the focal plane at the second layer (Mahamid et al., 2010).

## Free Energy Computation

A heatmap of the bond energy states of the microbeads shows the energy landscape presented to small particles due to the presence of particles on the glass substrate. This is computed by generating two sparse binary matrices, one for each particle size, marking the pixels containing a particle center-of-mass. The images are convolved with a thin annulus representing the extent of the depletion interaction at the height of the crystals' second layer and scaled by the relative bond strength of the small-small and large-small bonds. The images are then superimposed and summed, resulting in a heatmap depicting the bond energy for a small test particle placed at the corresponding location.

# RESULTS

We observe that monodisperse solutions form single layer islands that display previously observed growth behaviors (Dinsmore et al., 1997; Savage and Dinsmore, 2009). Remarkably, bidisperse samples form crystals consisting of two full layers of small particles in the same time span. A characteristic image of the crystals formed at the end of the experiments on the monodisperse and bidisperse samples are shown in **Figures 3A,B**, respectively. Microbeads that reside on the glass substrate of the sample chamber appear as black circles, while microbeads at the height of the top layer appear white. To illustrate the evolution of the bilayer crystal morphology, we display a time lapse image of the bidisperse sample in the four panels that make up **Figure 3C**. Within the first 400 min, the sample transitions from a quasi-2D gas composed of mixed large and small particles to a gas crystal coexistence of small particles and a gas of large particles. The large particles are excluded from the solid phase of small particles and can be seen near the crystal edges. Rather than continuing to grow and coarsen, the crystal islands melt from their periphery while a second layer nucleates and grows on a subset of the islands. This simultaneous melting of the bottom layer and growth of the top layer continues until all crystal islands have either evaporated or have grown two full layers of small particles.

For clarity, we will refer to the top layer as the second layer, and the bottom as the first layer. To quantify the growth behavior of the two crystalline layers, we measure the total number of particles in the first and second layers of the crystals and plot these in **Figure 4**. A particle is considered part of a layer if it has at least two neighbors and a bond orientational order parameter $\psi_6$ value greater than 0.8, where $\psi_6$ is defined as $|\ 1/N_j \sum_k \exp(6i\theta_{jk})|$, $N_j$ is the particle's total number of nearest neighbors, and $\theta_{jk}$ is the angle between the particle and its $k^{\text{th}}$ neighbor relative to a reference axis (Mergo, 2017).

We observe that the number of particles incorporated into the first crystal layer, $N_1$ (black squares), rises rapidly during the first 200 min, during which nucleation and subsequent growth of monolayers occur. The number of particles in the first layer peaks at 300 min and then declines by roughly one-third at later times. Meanwhile the number of particles in the second crystal layer, $N_2$ (black diamonds), increases monotonically. The growth rate of the second layer (red open circles) peaks at roughly 550 min and decays to zero when all second layer positions are filled. In addition, we observe that particles are never promoted to the top layer from the interior of an island during the span of the experiment (**Figure 3**). We also observe that any adatoms atop a monolayer that nucleate or join a second layer edge remain bound to the second layer.

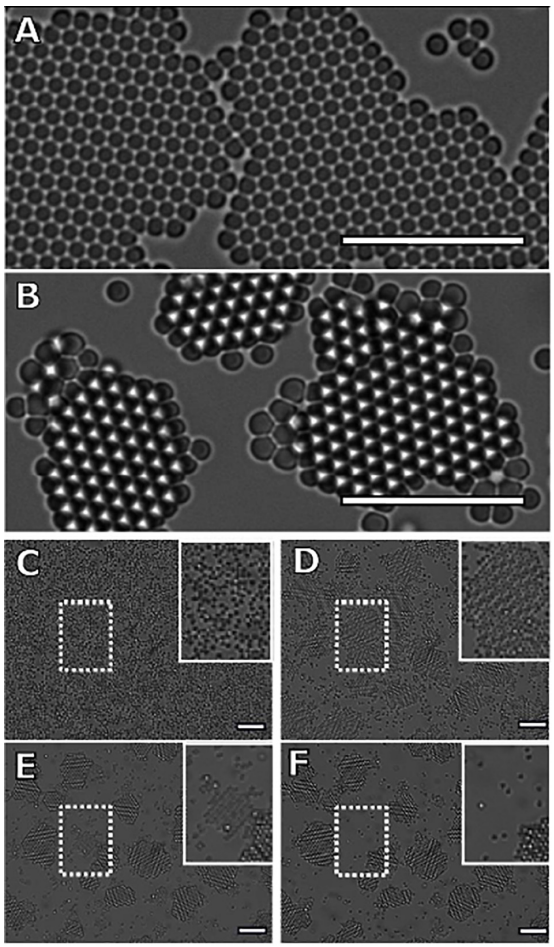


**FIGURE 3 |** Characteristic images of crystallizing mixtures of attractive colloidal hard spheres. Dark particles reside on the glass sample chamber. White particles are in focus, about 1 μm above the black particles. Crystals formed from panel **(A)** monodisperse and **(B–F)** bidisperse mixtures show distinctly different "final" morphologies, 20 h after initial nucleation. The monodisperse sample forms monolayer crystals, while the bidisperse sample forms bilayer crystals of small particles. To illustrate the formation of bilayer crystals in the bidisperse sample, we show one image every 400 min (scale bar = 10 μm). **(C)** At 0 min, the system is a gas of bidisperse particles (scale bar = 10 μm). **(D)** After 400 min, the nucleation and growth of the monolayer crystals of small particles has completed, with the larger particles displaced to the periphery of the islands. In addition, we observe the nucleation and growth of a second crystal layer as indicated by the white particles (scale bar = 10 μm). **(E)** The top layers continue to grow through 800 min, while the exposed monolayer regions shrink. The large particles have formed monolayers of their own species at the crystal edges (scale bar = 10 μm). **(F)** The final panel shows the final configuration of the system after 1200 min. We see that all islands throughout the sample chamber consist of two full layers (scale bar = 10 μm). Furthermore, we find that the largest crystal island in the field of view completely melts during the transition to a two-layer system, while the smallest two-layer islands persist.

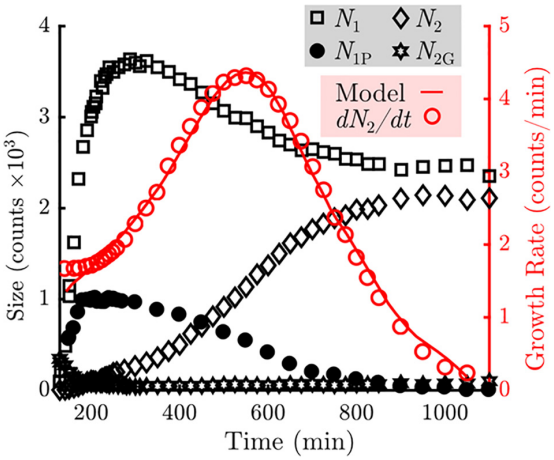


**FIGURE 4 |** Measurement of the counts of particles in various states in the sample (Left axis, black). The number of particles in the bottom ($N_1$) layers are indicated by the squares. The number of particles in the top ($N_2$) layers are indicated by the diamonds. The number of unblocked perimeter particles ($N_{1P}$) are indicated by the closed circles. The number of gaseous particles promoted off of the sample floor ($N_{2G}$) are indicated by the stars. Measurement of the growth rate of the top layer as a function of time is indicated by the open circles (Right axis, red). A fit using the model described in Eq. 1 is overlaid as a solid red line.

Collectively, these observations indicate that to model the top layer growth, incorporation into the top layer crystal can be treated as a permanent adsorbing state. Thus, the top-layer growth rate should only depend on the number of particles elevated off of the substrate that may resediment onto a crystal island, $N_{2G}$, and the number of particles at the perimeter of the first layer that are able to take a neighboring position above the first layer. This restriction is critical: in addition to gaining another bond to the crystal, particles on the first layer's perimeter become geometrically blocked from vertical motion by neighboring second layer particles. It is this "mobile perimeter," $N_{1P}$, that is free to participate directly in growth of the second layer. $N_{1P}$ is plotted in **Figure 4** and follows a similar trend to $N_1$, while $N_{2G}$ contains about 300 particles at the onset of monolayer nucleation but nearly vanishes by 200 min. This level is held for the majority of the experiment, and slowly increases to about 100 particles at the end of the experiment.

We fit the growth rate data for the top layer with a simple model of the form

$$\frac{dN_2}{dt} = k_1 N_{2G} + k_2 N_{1P} \frac{N_2}{N_1}, \quad (1)$$

where $k_1$ and $k_2$ are fit constants and each term represents the contribution from one of the two pathways described in the previous paragraph. While we assume the simplest relationship for $N_{2G}$ particles to contribute to second-layer growth, the same cannot be true for particles along the mobile perimeter. Once promoted to the top layer, the rate of capture into second layer must depend on the fraction of sites adjacent to the growing layer. $N_2/N_1$ represents a rough but useful approximate to this fraction (personal communication with Peter Harrowell). We find a good qualitative fit for the second layer growth rate with $k_1 = 2 \times 10^{-2}$ min$^{-1}$ and $k_1/k_2 = 3.1$. The results are plotted in **Figure 4**.

## DISCUSSION

We have identified two major contributions to the growth of the bilayer of beads in this system. The initial top-layer growth is heavily influenced by the resedimenting gas (N2G), above the plane of the bottom layer particles. During this time, there are no attachment sites for particles promoted onto the top layer, and the number of perimeter particles is small due to the relatively small number of crystals and crystal sizes. The elevated gas particles contribute to the top layer growth by increasing the particle density, encouraging nucleation of a new layer. After the onset of new layer growth, these particles are captured faster than they are created, causing a decrease in N2G. Promotion from the island edges becomes the dominant contribution to total top-layer growth once N2G is depleted. This does not hold true for every individual island. An island that does not nucleate a second layer after N2G is depleted has a vastly reduced chance to capture an adatom on its surface, as multiple adatoms must converge to nucleate a new layer. As a result, first-layer melting is observed, decreasing the footprint of islands over time. To illustrate this effect, the position of a large monolayer crystal – the largest crystal in the field of view – is highlighted in **Figures 3D–F**. Adatoms are promoted to the surface of this crystal, where they diffuse and detach without participating in a nucleation event. The island eventually evaporates, along with noticeably fast melting of large monolayer regions, as seen in **Supplementary Video S1**.

Assuming an island has nucleated a bilayer before $N_{2G}$ has depleted, second-layer growth accelerates as the top layer becomes larger until the top layer begins to stabilize the perimeter. Top layer growth slows as the sizes of the top and bottom layers begin to converge.

It would be reasonable to conclude that the growth model is applicable for both monodisperse and bidisperse samples, as the model has no explicit dependence on particle size. In either system, the lowest energy position that a particle can assume is inside the interior of a multilayer crystal. Thus, the energetically preferred structures are large, 3D, close-packed crystals of microparticles. Nevertheless, only samples containing bidisperse particles exhibit 3D growth during the course of the experiment. The nucleation and growth of these crystals spanned 15 h, while the monodisperse samples showed no second-layer growth after 78 h. This indicates that large particles are enabling an accelerated pathway to the promotion of small particles onto the crystal islands. We hypothesize that this is due to a combination of effects: the observed inability of the large particles to incorporate into crystals of small particles, and the energetic preference of a bond between a large and small particle over the bond between two small particles.

The preference for small particles to bond with larger particles arises from the linear dependence of the depletion interaction's strength on the diameter of the particles experiencing the depletion force (Asakura and Oosawa, 1954; Lekkerkerker and Tuinier, 2011). Combined with relegation of large particles to the crystal exterior, this leads to intermixing of large and small particles and the formation of short-lived amorphous clusters in the regions unoccupied by crystals. Examples of such arrangements are shown from our experiment in **Figure 5A**. The energetic differences associated with 2D clusters consisting of small particles versus similar clusters with one large particle replacing the central small particle are shown to scale in **Figure 5B**. Keeping the number of particles constant, a cluster containing a large particle is energetically favored until the central particle is close-packed and has six nearest neighbors. Interstitial sites involving a large particle also present a stronger bond site as shown schematically in **Figure 5C**.

In the absence of a second crystal layer, these interstitials are the energetically preferred top-layer sites. In addition to being present in amorphous configurations, these interstitials are always formed by large particles at a crystal's edge, effectively halting monolayer growth while simultaneously presenting advantageous bonding sites for small particles in- and out-of-plane. A particle at a preferred site may take up residence on the monolayer surface but will eventually leave the crystal if it does not participate in a nucleation event. Thus, the second layer growth depends on the prior nucleation of the layer. Once a second layer has formed on the island, the lowest energy sites are always interstitial sites that border a second layer.

Given these energetic arguments, we hypothesize that the mechanism by which large particles accelerate promotion of particles onto crystal islands is intricately related to their role in the formation of amorphous clusters of particles. In a true 2D system, particles in these mixed regions of neighbors and crystal interfaces have no means to reduce their free energy by rearrangement. In our quasi-2D system, small particles have access to a unique option: promotion off of the substrate. Promoted particles retain contact with the strongly interacting large particles as well as any surrounding small particles. In this model, the promotion is driven by the exchange of a strained or frustrated interfacial environment on the lower layer with a less constrained environment on the upper layer. Once promoted, the presence of a surface particle atop this interface constrains any further local promotion until the particle eventually moves away, allowing the interface to participate in another promotion. Once promoted, these particles are elevated gas particles, which were the drivers of initial top-layer nucleation in our experiment. The overall effect of the large particles is to catalyze second-layer growth by enabling the formation of temporary low-energy sites that cannot form in a monodisperse system, while also geometrically inhibiting crystal growth of the smaller particle species, forcing the system to evolve along a different pathway.

When these interactions between bidisperse particles are allowed an infinite amount of time to react, we will observe complete phase separation between the large and small particles as homogenous bonding (between large-on-large and small-on-small particles) begins to occur more frequently. While heterogeneous bonding is common, the presence of incommensurate particles at crystal boundaries inhibits growth at nearby lattice positions while also restricting the ability of compatible particles to diffuse away from the growing crystal. In biological systems, the amorphous and intermediate phase assemblies are often stabilized by an accompanying organic component at the interface and energetically stabilized, with the ultimate effect of "jamming" the pathway to initiate and complete

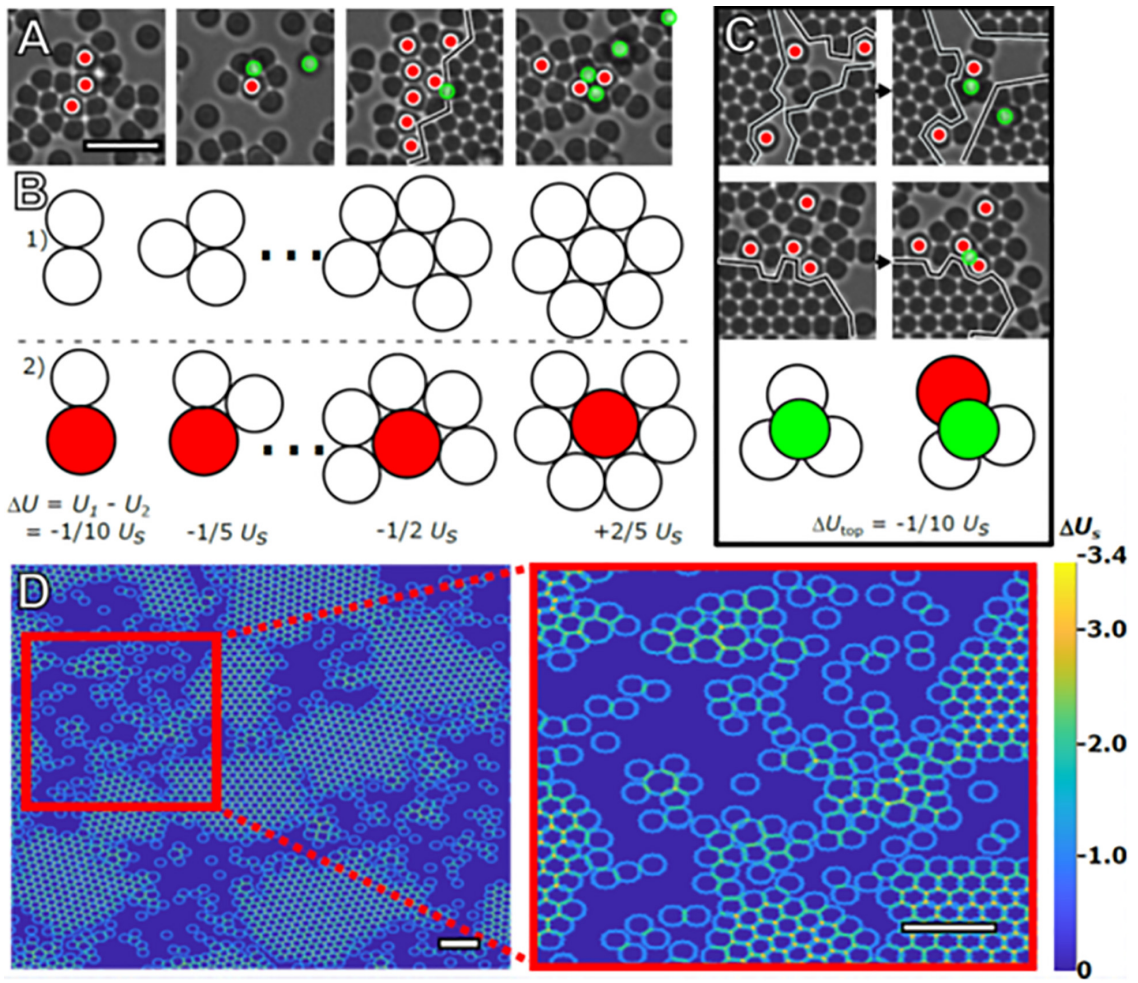


**FIGURE 5 |** Stabilization of amorphous clusters. Four representative images of the intermixing of large and small particles taken from the same time frame **(A)**. Red circles mark large particles. The black line marks the boundary of crystal islands (scale bar = 4 μm). Using $U_S$ as the bond energy between two small particles in contact due to depletion, the effect of the increased bond strength on total cluster bond energy is illustrated in **(B)**. 2D clusters of small particles (Row 1) have a higher total bond energy, $U$, compared to clusters containing a large particle (Row 2), and until close-packed clusters of seven particles are formed. Particles are drawn to scale. Images of promotion and/or capture events occurring between subsequent frames are displayed in **(C)**. The illustration demonstrates the energetic preference, $\Delta U_{top}$, for adatoms (green) occupying interstitials formed with large particles vs. those formed with only small particles. These configurations are commonly observed in the experiment, with examples also visible in **(A)**. **(D)** Heat map demonstrating the different energetic configurations presented to a hypothetical small particle that takes up residence on the second layer due to the presence of particles present on the substrate. Although there are relatively strong bonding locations located at the interstitial sites (orange) and troughs (teal), there are stronger bonding locations in the amorphous areas near large particles (scale bar = 4 μm, inset scale bar = 4 μm).

phase separation. In the case of bacterial S layer formation, the nucleation and growth of carbonate minerals on organic template surfaces is widespread, such that at the subsurface organic constituents directly promote carbonate mineralization through an amorphous transition (Chung et al., 2010). All of these organic mediated interactions are short ranged and provide local stability to maximize the energy input and material output ratio. We observe these interactions with an organic component in the formation of mollusk shells where compartmentalization of these assemblies is partitioned away from the larger milieu of mineral particles. In sea urchin larval spicules, a similar sequestration route occurs within a syncytial membrane that enables for local regulation for tissue growth (Seto et al., 2004; Killian et al., 2009). A similar parallel with hydroxyapatite mineral is found with the periosteum in bone in the formation and growth of bone tissue (Weiner and Wagner, 1998; Fratzl and Weinkamer, 2007). It is interesting to note, all the organic interacting components in all these biomineralization cases have similar structural effects and chemical characteristics, but are very different in amino acid sequence and kinetic behaviors when compared independently. Unlike the bead experiments, none of the mineralized tissues formed from intermediate phases occur in a "clean, non-interacting" chamber but within biological environments that skew the pathways of mineralized tissue formation and growth. This makes it exceedingly difficult to ascertain underlying causes for growth pathway selection,

especially when structure formation may depend on rare but important events.

Further experiments altering the size ratios and concentration of these secondary particles should determine the parameter space where such mechanisms most strongly alter the crystallization pathways. Additionally, tailoring future experiments to focus on the various growth regimes we have identified in this work would enable identification and better characterization of the various mechanisms at play. During the onset of accelerated second-layer growth, high frame-rate imaging of the interface between amorphous clusters and the crystal edge would elucidate mechanisms for particle detachment and promotion to the second layer via the types of intermediary structures seen in **Figure 5**, providing direct measurement of interfacial fluctuations and rearrangements occurring in these regions. Similar imaging techniques could be used to measure the evolution of the free energy of amorphous clusters in these bidisperse, attractive colloidal systems based on analysis methods outlined in Dullens et al. (2006). In addition, using total internal reflection microscopy or scanning probe methods it should be possible to identify the direct effects of the large particles on the detachment of small particles from the substrate (Ganapathy et al., 2010; Chen et al., 2019). We anticipate that the lessons learned by extensive study of these colloidal systems will ultimately shed light on molecular processes where crystallization occurs in the presence of unwanted impurities in solution.

## CONCLUSION

Biological mineralization has provided examples of materials with a diversity of morphologies and functions found in the biological world. Contrary to studies on crystal nucleation and growth from the last century, biology utilizes mechanisms where regulation of crystallite size and distribution takes on intermediate phases and metastable clusters as precursors to crystalline assemblies. From recent *in situ* investigations on a diversity of biomineralization model systems, we find common themes in the construction of strong, tough biological materials from their nano-scale constituents. Specifically, many of these model systems involve the utility of a proteinaceous scaffold to interact with nascent mineral precursors and the formation of intermediate mineral states like amorphous phases, and subsequently, the assembly and growth of crystallization states. As shown here in this work, we describe mechanistic behaviors from a simple colloidal system that parallel biological mineralization showing insights into biological materials utilizing 2D pathways to form 3D materials at molecular length-scales. This biphasic model concisely shows the energetic and kinetic advantages of intermediate states and non-classical crystallization paths to crystallization states. These intermediate states, like their biological equivalents, are templated by an organic component and their utility is to aid in the pre-programed construction of larger, complex assemblies required to build the hierarchical architectures observed in biological materials. By manipulating the unit assemblies and local parameters, the same mechanistic behaviors can be utilized and lead to drastic divergence in morphology (Etinger-Geller et al., 2017; Zhao et al., 2018; Kartha et al., 2019) and subsequently materials properties. Biological control of substrate chemistry is vital and determines the energetic barriers of the following layers of assemblages. With these constraints, the designing of bio-inspired hierarchically architecture materials with high toughness and strength can be realized from the presence of specific constituents at the molecular scale and the control of their interactions at interfaces for bottom-up, bioinspired materials engineering.

## DATA AVAILABILITY STATEMENT

The datasets generated for this study are available on request to the corresponding author.

## AUTHOR CONTRIBUTIONS

Both authors contributed to the experimentation, analyses of data, discussion of data, and writing of the resulting manuscript.

## FUNDING

Funding for this work was supported by NSF DMR-CMP Award No. 1507607 and NSF DGE Award No. 0654193. We also acknowledge Aperion Information Technologies for student funding, computational resources for simulations and data analysis. Data was acquired at the Cohen laboratory (Cornell University). JS was currently on sabbatical at Berkeley Labs and supported by the user programs at the Advanced Light Source (ALS) and Molecular Foundry (MF) (ALS-10280, MF-0088, and MF-0090). This work is supported by the Office of Science, Office of Basic Energy Sciences, of the United States Department of Energy under Contract No. De-AC02-05CH11231.

## ACKNOWLEDGMENTS

The authors thank Drs. Megan Comins, Brian Leahy, James Sethna, and Matthew Warkentin for helpful conversations and guidance. Professor Peter Harrowell (University of Sydney) was thanked for their technical expertise and theoretical contributions to this work.

## SUPPLEMENTARY MATERIAL

The Supplementary Material for this article can be found online at: https://www.frontiersin.org/articles/10.3389/fmats.2020.00075/full#supplementary-material

**VIDEO S1 |** A compressed video of the microparticle system outlined in the experimental methods which demonstrates the initial monolayer growth, melting, and simultaneous second-layer growth of crystal islands. The video is accelerated in time by 1500x, such that 1 s of video playback spans 25 min in real time.

## REFERENCES


Aizenberg, J. (2004). Crystallization in patterns: a bio-inspired approach. *Adv. Mater.* 16, 1295–1302. doi: 10.1002/adma.200400759

Asakura, S., and Oosawa, F. (1954). On interaction between two bodies immersed in a solution of macromolecules. *J. Chem. Phys.* 22, 1255–1256. doi: 10.1063/1.1740347

Ashby, M., Gibson, L., Wegst, U., and Olive, R. (1995). The mechanical properties of natural materials I. *Material property charts. Proc. R. Soc. A* 450, 123–140. doi: 10.1098/rspa.1995.0075

Auer, S., and Frenkel, D. (2001). Prediction of absolute crystal-nucleation rate in hard-sphere colloids. *Nature* 409, 1020–1023. doi: 10.1038/35059035

Banfield, J., Welch, S., Zhang, H., Ebert, T., and Penn, R. (2000). Aggregation-based crystal growth and microstructure development in natural iron oxyhydroxide biomineralization products. *Science* 289, 751–754. doi: 10.1126/science.289.5480.751

Baumgartner, J., Dey, A., Bomans, P., Le Coadou, C., Fratzl, P., Sommerdijk, N., et al. (2013). Nucleation and growth of magnetite from solution. *Nat. Mater.* 12, 310–314. doi: 10.1038/nmat3558

Chen, J., Zhu, E., Liu, J., Zhang, S., Lin, Z., Duan, X., et al. (2019). Building two-dimensional materials one row at a time: avoiding the nucleation barrier. *Science* 362, 1135–1139. doi: 10.1126/science.aau4146

Cho, K., Kim, Y., Yang, P., Cai, W., Kulak, P. H. A., Lau, J., et al. (2016). Direct observation of mineral-organic composite formation reveals occlusion mechanism. *Nat. Commun.* 7, 1–7. doi: 10.1038/ncomms10187

Chung, S., Kim, Y., Kim, J., and Kim, Y. (2009). Multiphase transformation and Ostwald's rule of stages during crystallization of a metal phosphate. *Nat. Phys.* 5, 68–73. doi: 10.1038/nphys1148

Chung, S., Shin, S., Bertozzi, C., and De Yoreo, J. (2010). Self-catalyzed growth of S layers via an amorphous-to-crystalline transition limited by folding kinetics. *PNAS* 107, 16536–16541. doi: 10.1073/pnas.1008280107

Coelfen, H., and Antonietti, M. (2008). *Mesocrystals and Nonclassical Crystallization. Ltd*. Berlin: John Wiley and Sons.

Crocker, J., and Grier, D. (1996). Methods of digital video microscopy for colloidal studies. *J. Coll Interf Sci.* 179, 298–310. doi: 10.1006/jcis.1996.0217

Dalmaschio, C., Ribeiro, C., and Leite, E. (2010). Impact of the colloidal state on the oriented attachment growth mechanism. *Nanoscale* 2, 2336–2345. doi: 10.1039/c0nr00338g

de Melo Pereira, D., and Habibovic, P. (2018). Biomineralization-inspired material design for bone regeneration. *Adv. Health Mater* 7, 1–18. doi: 10.1002/adhm.201800700

De Yoreo, J., Gilbert, P., Sommerdijk, N., Penn, R., Whitelam, S., Joester, D., et al. (2015). Crystallization by particle attachment in synthetic, biogenic, and geological environments. *Science* 349, 6760–6769. doi: 10.1126/science.aaa6760

Demichelis, R., Raiteri, P., Gale, J., Quigley, D., and Gebauer, D. (2011). Stable prenucleation mineral clusters are liquid-like ionic polymers. *Nat. Commun.* 2, 1–8. doi: 10.1038/ncomms1604

Dey, A., Bomans, P., Mueller, F., Will, J., Frederik, P., de With, G., et al. (2010). The role of prenucleation clusters in surface-induced calcium phosphate crystallization. *Nat.Mater* 9, 1010–1014. doi: 10.1038/nmat2900

Deyoreo, J., Gilbert, P., Sommerdijk, N., Penn, R., Whitelam, S., Joester, D., et al. (2015). Crystallization by particle attachment in synthetic, biogenic, and geologic environments. *Science* 349:aaa6760. doi: 10.1126/science.aaa6760

DeYoreo, J., and Vekilov, P. (2003). Principles of crystal nucleation and growth. *Rev. Mineral. Geochem.* 54, 57–93.

Dideriksen, K., Frandsen, C., Bovet, N., Wallace, A., Sel, O., Arbour, T., et al. (2015). Formation and transformation of a short range ordered iron carbonate precursor. *Geochim. Cosmochm. Acta* 164, 94–109. doi: 10.1016/j.gca.2015.05.005

Dinsmore, A., Warren, P., Poon, W., and Yodh, A. (1997). Fluid-solid transitions on walls in binary hard-sphere mixtures. *Europhys. Lett.* 40, 337–342. doi: 10.1209/epl/i1997-00468-4

Dullens, R., Aarts, D., and Kegel, W. (2006). Direct measurement of the free energy by optical microscopy. *PNAS* 103, 529–531. doi: 10.1073/pnas.0507052103

Dunlop, J., and Fratzl, P. (2010). Biological composites. *Ann. Rev. Mater Sci.* 40, 1–24.

Etinger-Geller, Y., Katsman, A., and Pokroy, B. (2017). Density of nanometrically thin amorphous films varies by thickness. *Chem. Mater* 29, 4912–4919. doi: 10.1021/acs.chemmater.7b01139

Filion, L., Hermes, M., Ni, R., and Dijkstra, M. (2010). Crystal nucleation of hard spheres using molecular dynamics, umbrella sampling, and forward flux sampling: a comparison of simulation techniques. *J. Chem. Phys.* 133, 1–15. doi: 10.1063/1.3506838

Fischer, F., Kolednik, O., Predan, J., Razi, H., and Fratzl, P. (2017). Crack driving force in twisted plywood structures. *Acta Biomaterialia* 55, 349–359. doi: 10.1016/j.actbio.2017.04.007

Fratzl, P., and Weinkamer, R. (2007). Nature's hierarchical materials. *Prog. Mater Sci.* 52, 1263–1334.

Fritz, M., Belcher, A., Radmacher, M., Walters, D., Hansma, P., Stucky, G., et al. (1994). Flat pearls from biofabrication of organized composites on inorganic substrates. *Nature* 371, 49–51. doi: 10.1038/371049a0

Ganapathy, R., Buckley, M., Gerbode, S., and Cohen, I. (2010). ). Direct measurements of island growth and step-edge barriers in colloidal epitaxy. *Science* 327, 445–448. doi: 10.1126/science.1179947

Gasser, U. (2009). Crystallization in three- and two- dimensional colloidal suspensions. *J. Phys: Condensed Matter* 21, 1–24.

Gebauer, D., Voelkel, A., and Coelfen, H. (2008). Stable prenucleation calcium carbonate clusters. *Science* 322, 1819–1822. doi: 10.1126/science.1164271

Gong, Y., Killian, C., Olson, I., Appathurai, N., Amasino, A., Martin, M., et al. (2012). Phase transitions in biogenic amorphous calcium carbonate. *PNAS* 109, 6088–6093. doi: 10.1073/pnas.1118085109

Habraken, W., Tao, J., Brylka, L., Friedrich, H., Bertinetti, L., Schenk, A., et al. (2013). Ion-association complexes unite classical and non-classical theories for the biomeimetic nucleation of calcium phosphate. *Nat. Commun.* 4, 1–12. doi: 10.1038/ncomms2490

Hedges, L., and Whitelam, S. (2013). Selective nucleation in porous media. *Soft. Matter* 8, 9763–9766.

Huang, W., Restrepo, D., Jung, J., Su, F., Liu, Z., Ritchie, R., et al. (2019). Multiscale toughening mechanisms in biological materials and bioinspired designs. *Adv. Mater* 1901561, 1–37. doi: 10.1002/adma.201901561

Ivanov, V., Fedorov, P., Baranchikov, A., and Osiko, V. (2014). Oriented aggregation of particles: 100 years of investigations of non-classical crystal growth. *Russian Chem. Rev.* 83, 1204–1222. doi: 10.1070/rcr4453

Jee, S., Culver, L., Li, Y., Douglas, E., and Gower, L. (2010). Biomimetic mineralization of collagen via an enzyme-aided PILP process. *J. Crystal. Growth* 312, 1249–1256. doi: 10.1016/j.jcrysgro.2009.11.010

Kartha, K., Allampally, N., Politi, A., Prabhu, D., Ouchi, H., Albuquerque, R., et al. (2019). Influence of metal coordination and light irradiation on hierarchical self-assembly processes. *Chem. Sci.* 10, 752–760. doi: 10.1039/c8sc03875a

Killian, C., Metzler, R., Gong, Y., Olson, I., Aizenberg, J., and Politi, Y. (2009). Mechanism of Calcite Co-orientation in the sea urchin tooth. *J. Am. Chem. Soc.* 131, 18404–18409. doi: 10.1021/ja907063z

Kuhrts, L., Macias-Sanchez, E., Tarakina, N., and Hirt, A. (2019). Shaping magnetite with Poly-L-arginine and pH: from small single crystals to large mesocrystals. *J. Phys. Chem. Lett.* 10, 5514–5518. doi: 10.1021/acs.jpclett.9b01771

Larsen, A., and Grier, D. (1996). Melting of metastable crystallites in charge-stabilized colloidal suspensions. *PRL* 76, 3862–3865. doi: 10.1103/physrevlett.76.3862

Lechner, W., Dellago, C., and Bolhuis, P. (2011). Role of the prestructured surface cloud in crystal nucleation. *PRL* 106, 1–4.

Lekkerkerker, H., and Tuinier, R. (2011). *Colloids and the Depletion Interaction*. Heidelberg: Springer.

Li, D., Nielsen, M., Lee, J., Frandsen, C., Banfield, J., and De Yoreo, J. (2012). Direction-specific interactions control crystal growth by oriented attachment. *Science* 336, 1014–1018. doi: 10.1126/science.1219643

Lowenstam, H. (1981). Minerals formed by organisms. *Science* 211, 1126–1131. doi: 10.1126/science.7008198

Ma, X., Zhang, S., Jiao, F., Newcomb, C., Zhang, Y., and Prakash, A. (2017). Tuning crystallization pathways through sequence engineering of biomimetic polymers. *Nat. Mater* 16, 767–774. doi: 10.1038/nmat4891

Maes, D., Vorontsova, M., Potenza, M., Sanvito, T., Sleutel, M., Giglio, M., et al. (2015). Do protein crystals nucleate within dense liquid clusters? *Acta Crystallo F Struct. Biol. Commun.* 71(Pt 7), 815–822. doi: 10.1107/S2053230X15008997

Mahamid, J., Aichmayer, B., Shimoni, E., Ziblat, R., Li, C., Siegel, S., et al. (2010). Mapping amorphous calcium phosphate transformation into crystalline

mineral from the cell to the bone in zebrafish fin rays. *PNAS* 107, 6316–6321. doi: 10.1073/pnas.0914218107

Mass, T., Giuffre, A., Sun, C., Stifler, C., Frazier, M., Neder, M., et al. (2017). Amorphous calcium carbonate particles form coral skeletons. *PNAS* 114, E7670–E7678. doi: 10.1073/pnas.1707890114

Mergo, J. (2017). *Statistical Dynamics of Multicomponent Quasi-Two-Dimensional Colloidal Systems. Applied Physics*. Ithaca, NY.: Cornell University, 100.

Meyers, M., Mckittrick, J., and Chen, P. (2013). Structural biological materials: critical mechanics-materials connections. *Science* 339, 773–779. doi: 10.1126/science.1220854

Mirabello, G., Keizer, A., Bomans, P., Kovacs, A., Dunin-Borkowski, R., Sommerdijk, N., et al. (2019). Understanding the formation mechanism of magnetic mesocrystals with (Cryo-)electron microscopy. *Chem. Mater* 31, 7320–7328. doi: 10.1021/acs.chemmater.9b01836

Munch, E., Launey, M., Alsem, D., Saiz, E., Tomsia, A., and Ritchie, R. (2008). Tough, bio-inspired hybrid materials. *Science* 322, 1516–1520. doi: 10.1126/science.1164865

Nielsen, M., Aloni, S., and DeYoreo, J. (2014). In situ TEM imaging of CaCO3 nucleation reveals coexistence of direct and indirect pathways. *Science* 345, 158–162. doi: 10.1126/science.1254051

Noorduin, W., Grinthal, A., Mahadevan, L., and Aizenberg, J. (2013). Rationally designed complex, hierarchical microarchitectures. *Science* 340, 832–837. doi: 10.1126/science.1234621

Noorduin, W., Vlieg, E., Kellogg, R., and Kaptein, B. (2009). From ostwald ripening to single chirality. *Angew Chem.Int. Ed.* 48, 9600–9606. doi: 10.1002/anie.200905215

Ostwald, W. (1897). Studies on the formation and transformation of solid bodies. *Z.Phys. Chem.*22, 289–330.

Palberg, T. (2014). Crystallization kinetics of colloidal model suspensions: recent achievements and new perspectives. *J. Phys. Condensed Matter* 26, 1–23. doi: 10.1088/0953-8984/26/33/333101

Pendola, M., Jain, G., Huang, Y., Gebauer, D., and Evans, J. (2018). Secrets of the sea urchin spicule revealed: protein cooperativity is responsible for ACC transformation, intracrystalline incorporation, and guided mineral particle assembly in biocomposite material formation. *ACS Omega* 3, 11823–11830. doi: 10.1021/acsomega.8b01697

Picker, A., Nicoleau, L., Burghard, Z., Bill, J., Zlotnikov, I., Labbez, C., et al. (2017). Mesocrystalline calcium silicate hydrate: a bioinspired route toward elastic concrete materials. *Sci. Adv.* 3, 1–6. doi: 10.1126/sciadv.1701216

Politi, Y., Arad, T., Klein, E., Weiner, S., and Addadi, L. (2004). Sea urchin spine calcite forms via a transient amorphous calcium carbonate phase. *Science* 306, 1161–1164. doi: 10.1126/science.1102289

Rao, A., Arias, J., and Coelfen, H. (2017). On mineral retrosynthesis of a complex biogenic scaffold. *Inorganics* 5, 1–16.

Rawlings, A., Somner, L., Fitzpatrick-Milton, M., Roebuck, T., Gwyn, C., Liravi, P., et al. (2019). Artificial coiled coil biomineralisation protein for the synthesis of magnetic nanoparticles. *Nat. Commun.* 10, 1–9. doi: 10.1038/s41467-019-10578-2

Salvalaglio, M., Perego, C., Giberti, F., Mazzotti, M., and Parrinello, M. (2014). Molecular-dynamics simulations of urea nucleation from aqueous solution. *PNAS* 112, 1–14.

Savage, J., Blair, D., Levine, A., Guyer, R., and Dinsmore, A. (2006). Imaging the sublimation dynamics of colloidal crystallites. *Science* 314, 795–798. doi: 10.1126/science.1128649

Savage, J., and Dinsmore, A. (2009). Experimental evidence for two-step nucleation in colloidal crystallization. *PRL* 102, 1–4.

Savage, J., Hopp, S., Ganapathy, R., Gerbode, S., Heuer, A., and Cohen, I. (2013). Entropy-driven crystal formation on highly strained substrates. *PNAS* 110, 9301–9304. doi: 10.1073/pnas.1221529110

Schenk, A., Zlotnikov, I., Pokroy, B., Gierlinger, N., Masic, A., Zaslansky, P., et al. (2012). Hierarchical calcite crystals with occlusions of a simple polyeletrolyte mimic complex biomineral structures. *Adv Func Mater* 22, 4668–4676. doi: 10.1002/adfm.201201158

Seto, J. (2012). *Advanced Topics in Biomineralization*. Rijeka: InTech, 176.

Seto, J., Azais, T., and Coelfen, H. (2013). Formation of aragonitic layered structures from kaolinite and amorphous calcium carbonate precursors. *Langmuir* 29, 7521–7528. doi: 10.1021/la400442j

Seto, J., Ma, Y., Davis, S., Meldrum, F., Gourrier, A., Kim, Y., et al. (2012). Structure-property relationships of a biological mesocrystal in the adult sea urchin spine. *PNAS* 109, 3699–3704. doi: 10.1073/pnas.1109243109

Seto, J., Picker, A., Chen, Y., Rao, A., Evans, J., and Coelfen, H. (2014). nacre protein sequence compartmentalizes mineral polymorphs in solution. *Crystal. Growth and Des.* 14, 1501–1505. doi: 10.1021/cg401421h

Seto, J., Zhang, Y., Hamilton, P., and Wilt, F. (2004). The localization of occluded matrix proteins in calcareous spicules of sea urchin larvae. *J. Struc. Biol.* 148, 123–130. doi: 10.1016/j.jsb.2004.04.001

Sleutel, M., and Van Driessche, A. (2014). Role of clusters in nonclassical nucleation and growth of protein crystals. *PNAS* 111, E546–E553. doi: 10.1073/pnas.1309320111

Smeets, P., Cho, K., Kempen, R., Sommerdijk, N., and DeYoreo, J. (2015). Calcium carbonate nucleation driven by ion binding in a biomimetic matrix revealed by in situ electron microscopy. *Nat. Mater* 14, 394–399. doi: 10.1038/nmat4193

Tao, J., Shin, Y., Jayasinha, R., Buchko, G., Burton, S., Dohnalkova, A., et al. (2019). The energetic basis for hydroxyapatite mineralization by amelogenin variants provides insights into the origin of amelogenesis imperfect. *PNAS* 116, 13867–13872. doi: 10.1073/pnas.1815654116

Teng, H., Dove, P., Orme, C., and DeYoreo, J. (1998). Thermodynamics of calcite growth: baseline for understanding biomineral formation. *Science* 282, 724–727. doi: 10.1126/science.282.5389.724

Vekilov, P. (2010). The two-step mechanism of nucleation of crystals in solution. *Nanoscale* 2, 2346–2357. doi: 10.1039/c0nr00628a

Vekilov, P., and Vorontsova, M. (2014). Nucleation precursors in protein crystallization. *Acta Crystallo F Struct. Biol. Commun.* 70, 271–282.

Wang, Y., Azais, T., Robin, M., Vallee, A., Catania, C., Legriel, P., et al. (2012). The predominant role of collagen in the nucleation, growth, structure and orientation of bone apatite. *Nat.Mater* 11, 724–733. doi: 10.1038/nmat3362

Washington, A. II, Foley, M., Cheong, S., Quffa, L., Breshike, C., Watt, J., et al. (2012). Ostwald's Rule of Stages and its role in CdSe quantum dot crystallization. *J. Am. Chem. Soc.* 134, 17046–17052. doi: 10.1021/ja302964e

Weaver, J., Milliron, G., Miserez, A., vans-Lutterodt, K. E., Herrera, I. Gallana, and Mershon, W. (2012). The stomatopod dactyl club: a formidable damage-tolerant biological hammer. *Science* 336, 1275–1280. doi: 10.1126/science.1218764

Weiner, S., and Addadi, L. (2011). Crystallization Pathways in Biomineralization. *Ann. Rev. Mater Res.* 41, 21–40. doi: 10.1146/annurev-matsci-062910-095803

Weiner, S., and Wagner, H. (1998). The material bone: structure-mechanical function relations. *Ann. Rev. Mater Sci.* 28, 271–298. doi: 10.1016/j.bone.2013.10.023

Weiss, I., Tuross, N., Addadi, L., and Weiner, S. (2002). Mollusc larval shell formation: amorphous calcium carbonate is a precursor phase for aragonite. *J. Exp. Zool.* 293, 478–491. doi: 10.1002/jez.90004

Zeravcic, Z., Manoharan, V., and Brenner, M. (2014). Size limits of self-assembled colloidal structures made using specific interactions. *PNAS* 111, 15918–15923. doi: 10.1073/pnas.1411765111

Zhao, R., Li, M., Ren, Z., Zhu, Y., and Han, G. (2018). Three-dimensional oriented attachment growth of single-crystal pre-perovskite PbTiO3 hollowed fibers. *Cryst. Eng. Commun.* 20, 448–453. doi: 10.1039/c7ce01780d

Zhou, J., Yang, Y., Yang, Y., Kim, D., Yuan, A., Tian, X., et al. (2019). Observing crystal nucleation in four dimensions using atomic electron tomography. *Nature* 570, 500–503. doi: 10.1038/s41586-019-1317-x

Zou, Z., Bertinetti, L., Politi, Y., Fratzl, P., and Habraken, W. (2017). Control of polymorph selection in amorphous calcium carbonate crystallization by poly(Aspartic Acid): two different mechanisms. *Small* 13, 1–11. doi: 10.1002/smll.201603100

**Conflict of Interest:** JM was currently affiliated with BitWrex.

The remaining author declares that the research was conducted in the absence of any commercial or financial relationships that could be construed as a potential conflict of interest.

frontiers in Materials

ORIGINAL RESEARCH
published: 07 May 2020
doi: 10.3389/fmats.2020.00099

# Modulating the Surface Properties of Metallic Implants and the Response of Breast Cancer Cells by Surface Relief Induced via Bulk Plastic Deformation

*Benay Uzer**

*Department of Mechanical Engineering, Abdullah Gül University, Kayseri, Turkey*

Micro/nanoscale textured surfaces have presented promising tissue–implant integration via increasing surface roughness, energy, and wettability. Recent studies indicate that surface texture imparted on the metallic implants via surface relief induced with simple bulk plastic deformation methods (e.g., tension or compression tests) does result in enhanced cell response. Considering these recent findings, this study presents a thorough investigation of the effects of surface relief on surface properties of implants and cell adhesion. Experiments are conducted on the samples subjected to interrupted tensile tests up to the plastic strains of 5, 15, 25, and 35%. Main findings from these experiments suggest that, as the plastic deformation level increases up to 35% from the undeformed (control) level, (1) average surface roughness ($R_a$) increases from 17.58 to 595.29 nm; (2) water contact angle decreases from 84.28 to 58.07°; (3) surface free energy (SFE) increases from 36.06 to 48.89 mJ/m$^2$; and (4) breast cancer cells show 2.4-fold increased number of attachment. Increased surface roughness indicates the distorted topography via surface relief and leads to increased wettability, consistent with Wenzel's theory. The higher levels of SFE observed were related to high-energy regions provided via activation of strengthening mechanisms, which increased in volume fraction concomitant with plastic deformation. Eventually, the displayed improvements in surface properties have increased the number of breast cancer cell attachments. These findings indicate that surface relief induced upon plastic deformation processes could be utilized in the design of implants for therapeutic or diagnostic purposes through capturing breast cancer cells on the material surface.

**Keywords: plastic deformation, surface relief, metallic implants, breast cancer cells, adhesion, wettability, surface free energy, roughness**

OPEN ACCESS

***Edited by:***
*Laura Maria Vergani,*
*Politecnico di Milano, Italy*

***Reviewed by:***
*Agata Przekora,*
*Medical University of Lublin, Poland*
*Jindan Wu,*
*Zhejiang Sci-Tech University, China*

***Correspondence:**
*Benay Uzer*
*benay.uzer@agu.edu.tr*

***Specialty section:***
*This article was submitted to Biomaterials, a section of the journal Frontiers in Materials*

***Received:*** *06 January 2020*
***Accepted:*** *31 March 2020*
***Published:*** *07 May 2020*

***Citation:***
*Uzer B (2020) Modulating the Surface Properties of Metallic Implants and the Response of Breast Cancer Cells by Surface Relief Induced via Bulk Plastic Deformation. Front. Mater. 7:99. doi: 10.3389/fmats.2020.00099*

## INTRODUCTION

Metallic materials constitute approximately 70% of the total production volume in biomedical applications (Peron et al., 2017), which stems from a set of excellent properties, such as mechanical strength, ductility, biocompatibility, and corrosion resistance (Chen and Thouas, 2015; Uzer et al., 2016; Peron et al., 2017; Nune et al., 2018). Austenitic stainless steels, titanium alloys, and cobalt–chromium alloys can be listed among the most commonly used metallic biomaterials, which could

find application in a wide variety of biomedical fields including cardiovascular surgery, orthopedics, dentistry, or cranioplasty (Misra et al., 2009; Chen and Thouas, 2015; Uzer et al., 2016; Nune et al., 2018).

Clinical success of the implantation strongly relies on early tissue–implant integration along with the elimination of fibrous connective tissue formation on the interface (Le Guéhennec et al., 2007; Hanawa, 2019). This integration can be influenced strongly by the implant surface wettability, which is indeed governed by surface free energy (SFE) and roughness of the material (Liu and Jiang, 2011; Latifi et al., 2013). Modification of these aforementioned surface properties can be utilized to trigger specific molecular reactions controlling the adhesion, proliferation, or differentiation behavior of the cells (Ventre et al., 2012; Barthes et al., 2014; Huo et al., 2017; Raines et al., 2019). For instance, microscale textured surfaces can regulate the expression of integrin, which is a transmembrane receptor protein enabling cell adhesion on the metal surface (Raines et al., 2019), or hydrophilic surfaces (contact angle $<90$ °) can promote enhanced cell response via promoting the deposition of focal adhesion proteins (Ponsonnet et al., 2003; Ranella et al., 2010; Bauer et al., 2013; Rupp et al., 2014; Cicek et al., 2019). Surface properties obviously play a crucial role in cell adhesion, and in order to reveal their cumulative effects, more thorough analyses are required.

Research carried out on the relationship between the surface properties and tissue–implant interaction has shown that mimicking the tissue microenvironment on the material surface via micro/nanoscale patterns can stimulate cell adhesion significantly (Le Guéhennec et al., 2007; Gentile et al., 2010; Barthes et al., 2014; Gui et al., 2018; Raines et al., 2019). These textured materials can provide increased mechanical stability and rigid tissue formation on the implant, which can lead to an earlier recovery after implantation (Kunrath and Hübler, 2019). Various surface treatment techniques have been utilized to create micro/nanoscale topography on the surface, such as acid etching, electrochemical polishing, passivation, or anodization (Le Guéhennec et al., 2007; Gentile et al., 2010; Latifi et al., 2013). These physical or chemical treatments have created textured structures, which have stimulated cell growth via providing greater surface area for the formation of focal adhesion points (Uzer et al., 2016). Moreover, increased roughness through these treatments has led to enhanced surface wettability, catalyzing the deposition of extracellular matrix (ECM) proteins on the surface (Miyajima et al., 2019).

Similar results were also obtained via surface mechanical treatments such as shot peening, sliding friction, or surface mechanical attrition treatment (SMAT) (Multigner et al., 2010; Arifvianto et al., 2011; Bagherifard et al., 2016; Valiev et al., 2016; Huo et al., 2017). Activation of these deformation mechanisms subdividing coarse grains into smaller sizes provided grain refinement in the near surface layer of the material (Arifvianto et al., 2011). Furthermore, these methods improved the fatigue resistance of the materials via inducing compressive residual stress on the surface (Arifvianto et al., 2011; Bagherifard et al., 2016). However, all of the aforementioned physical, chemical, or mechanical treatment methods were confined to the surface layer of the material.

Research has shown that micro/nanoscale topography mimicking morphology of ECM could also be utilized to control the response of cancer cells (Beri et al., 2018). For instance, Beri et al. (2018) found that circulating tumor cells' (CTCs') adhesion can be promoted on biomaterials with nanoscale roughness. It should be noted that metastasis accounts for approximately 90% of cancer-related diseases (Conde et al., 2016), and CTCs are believed to play crucial role in metastatic processes (Chen et al., 2016). Thus, use of surface roughness to enhance cancer cell–substrate interactions would enable the capturing of CTCs and therefore decrease disease dissemination (Beri et al., 2018; Chen et al., 2016). Moreover, directional adhesion of breast cancer cells, which is necessitated for cancer invasion and metastasis, has been achieved by micro/nanoscale-patterned topography (Ray et al., 2017; Tabdanov et al., 2018). Overall, these studies can indicate that biomaterials with modulated topography could be promising tools for detection and treatment of cancer cells via controlling their adhesion response.

Recently, simple bulk plastic deformation methods (e.g., tension or compression tests) have been utilized to impart micro/nanoscale topography on the metal surface (Matsugaki et al., 2012; Matsugaki and Nakano, 2016; Uzer et al., 2016, 2018; Nune et al., 2018). These studies showed that texture reflecting the activated strengthening mechanisms, namely, surface relief, can alter surface topography significantly (Matsugaki et al., 2012; Matsugaki and Nakano, 2016; Uzer et al., 2016; Cicek et al., 2019). Specifically, markings produced by twinning or slip are shown to form groove- or step-like surface topographical features that can increase surface roughness and provide ideal sites for the deposition of focal adhesion proteins (Matsugaki et al., 2012; Uzer et al., 2016, 2018; Uzer and Canadinc, 2018).

Surface relief can be induced on the implant surface via manufacturing processes or during the deployment of the implants (Weiss and Mitevski, 2015). Furthermore, it can enable the oriented elongation of the osteoblast cells, which promotes the formation of anisotropic bone tissue necessary for its mechanical function (Matsugaki et al., 2012; Matsugaki and Nakano, 2016). Consequently, these microstructural features can increase cell viability and adhesion, which enhances tissue formation on the implant surface (Uzer et al., 2018). Moreover, they could be used to increase the adhesion of cancer cells (Uzer et al., 2016). It is noteworthy that the level of plastic strain constitutes importance, because excessive plastic deformation is accommodated through the activation of strengthening mechanisms in greater volume fractions within the bulk material. As a result, each deformation level results with a different surface state, causing healthy or cancer cell response to vary along each plastic strain level (Matsugaki et al., 2012; Uzer et al., 2016, 2018).

The aforementioned studies regarding plastic deformation of bulk materials have established a firm relationship between surface relief, roughness, and cell response. However, current state of knowledge in this area falls short of elucidating the relative change in surface wettability and energy, which are also strongly modulated via surface topography (Rupp et al., 2014). Given the established influence of these properties on cell

response, this study aims to investigate the role of surface relief on surface wettability, energy, roughness, and cell attachment behavior. The findings propose the idea that surface relief could be an effective means to control surface properties and cell response. This knowledge could enable the design of metallic biomaterials that could be used for therapeutic purposes in dealing with cancer cells.

## MATERIALS AND METHODS

The specimens investigated in the current study were 304L grade stainless steels with the elemental composition of Fe balance-0.029C-18.414Cr-8.314Ni-1.044Mn-0.091Mo-0.369Si-0.022P-0.023S-0.416Cu (in weight%). Dog bone–shaped tensile test specimens with the technical drawing explained elsewhere (Cicek et al., 2019) were obtained by laser cutting. These samples were subjected to interrupted tensile tests (AGS-X 10kN; Shimadzu, Kyoto, Japan) up to the engineering strains of 5, 15, 25, and 35% with the strain rate of $10^{-4}$ $s^{-1}$. These varying strain values enabled the activation of strengthening mechanisms in different volume fractions throughout the bulk material, which also helped to have materials with different microstructural and surface properties. Moreover, one set of the samples was kept as undeformed in order to use as a control group.

After plastic deformation the gauge sections of the samples were cut with a precision saw. Microstructure of the undeformed and deformed specimens was captured via differential interference contrast (DIC) technique in optical microscope (Axiocam 506 color; Zeiss, Jena, Germany). For that purpose, the undeformed sample was ground with 800, 1,000, 1,200, and 2,500 grit *SiC* papers and then polished with 3- and 1-μm sized diamond abrasives, respectively. In order to reveal its microstructure, this polished specimen was then etched by immersing in a mixture of 10 mL nitric acid, 30 mL hydrochloric acid, and 30 mL distilled water for 3 min long at room temperature. The deformed sample's microstructure has been captured via extended depth of field imaging technique. The microstructures of the samples were also analyzed in detail via field emission scanning electron microscope (GeminiSEM 300; Zeiss, Jena, Germany) utilizing secondary electron (SE) detector, which operated at accelerating voltage of 10 kV.

In order to elucidate the effect of surface relief on the topography of the deformed and undeformed samples, atomic force microscopy was utilized (Multimode 8, Bruker). The analyses were carried out with tapping mode in air utilizing a phosphorus-doped silicon cantilever with a rotated tip (radius of 8 nm), and linear scanning rate was of 1 Hz (1 line/s). Average surface roughness ($R_a$) of the samples was calculated by taking the average of the roughness values of at least three different regions with the scanning area of 50 × 50 μ m.

Wettability and SFE of the undeformed and deformed samples were analyzed with sessile drop technique (Attension Theta Optical Tensiometer; Biolin Scientific, Gothenburg, Sweden). Prior to the analyses, the samples were ultrasonically cleaned with acetone and 70% vol/vol ethanol for 15 min and then dried in air. For the wettability analysis, deionized (DI) water droplet with the volume of 2 μL was dispensed on the surface, and its shape was recorded with a high-speed camera. The final contact angle was reported as the average of the right and left angle, which is between the tangent of the drop at liquid–gas interface and horizontal baseline at solid–liquid interface. The analyses were run on three different samples for each strain level, and measurements were repeated five times on each one. For the SFE analyses, diiodomethane was used as the dispersive component; formamide and DI water were utilized as the polar components. Similar to the wettability measurements, the samples were cleaned with the same procedure before conducting measurements with different liquids. The measurements were repeated three times on each sample (three samples for each strain level). Recorded contact angle values of the three liquids were implemented in the Owens–Wendt (OW) theoretical method as (Miyajima et al., 2019):

$$\gamma_l\ (1 + cos\theta) = 2\sqrt{\gamma_s^d\ \gamma_l^d} + 2\sqrt{\gamma_s^p\ \gamma_l^p}$$

where $\gamma_l$ and $\gamma_s$ represent liquid and solid free energy; superscripts $d$ and $p$ represents the dispersive and polar components, respectively (Rupp et al., 2014).

In order to evaluate the effect of surface relief on cell response, breast cancer cells were seeded on the undeformed control sample and the 35% deformed sample (highest degree of plastic deformation). Initially, SKBR3 breast cancer cells obtained from the American Type Culture Collection were grown in McCoy's 5A medium with 10% fetal bovine serum and 1% penicillin/streptomycin. Then, three samples from each set were sterilized in an autoclave for 1 h and placed in 12-well cell culture plate. Cancer cells were seeded in each well ($1 \times 10^5$ cells per well) containing 2 mL of growth medium and then incubated for 24 h. Afterward, the medium was removed, and the samples were rinsed with phosphate-buffered saline (PBS). The cells were fixed with 2.5% glutaraldehyde for 2 h at 37°C, followed by rinsing with PBS. After this, the nuclei of these fixed cells were labeled with DAPI and incubated for 5 min at ambient temperature. Then the samples were rinsed again with PBS, and the cell adhesion was observed with confocal microscope through capturing three different images from each sample surface (LSM 900; Zeiss). The number of attached cells was quantified manually, and their average value was reported.

The morphology and adhesion behavior of cells were further analyzed via SEM under an accelerating voltage of 2 kV with the SE detector. In order to enhance the quality of the SEM images, the metallic samples were cleaned with DI water to remove the residues of the PBS and sputtered with a 2-nm thickness of gold to eliminate the charging problem. To the best of the author's knowledge, the adhesion response of the breast tumor cells has not been analyzed on a metallic biomaterial surface earlier. Hence, this study can pave the way for future research regarding the relationship between breast cancer cells and metallic biomaterials.

All of the reported results are presented as mean ± standard deviation. Statistical significance of the differences between the means was determined with one-way analysis of variance (ANOVA) followed by least-squares difference (LSD) *post hoc*

comparison tests or *t* tests. The findings were also supported by non-parametric equivalents of the aforementioned tests. A $p$ value smaller than 0.05 was required for the rejection of null hypotheses (highest type I error level deemed acceptable was set at 0.05).

## RESULTS

The optical microscope image of the undeformed sample in **Figure 1A** presents smooth surface with annealing twins, where a detailed image of one of these twins can be observed in **Figure 2A** captured via SEM. As the sample is plastically strained, deformation markings become prevalent, and surface gets distorted significantly (**Figure 1B**). These activated deformation traces have been presented more clearly in **Figure 2B**. The interaction of these mechanisms (i.e., mechanical twinning, slip, or martensite) with each other can be also observed. Microstructures of the samples have been further analyzed via AFM (**Figure 3**). The effect of plastic deformation can be visible specifically on the 35% deformed sample, where significant grain elongation concomitant with plastic straining was captured (**Figure 4**).

The detailed AFM images present the topographies of the samples in **Figure 3**, where they get distorted gradually in parallel with plastic straining. Furthermore, increasing height between the peaks and valleys can be observed as the plastic deformation increases. Moreover, grain boundaries protruding out of the surface becomes prevalent on the 15, 25, and 35% samples (**Figure 3**). In order to quantitatively analyze the influence of plastic deformation on the surface topography, average surface roughness ($R_a$) of the samples is evaluated. The results present that $R_a$ values of the samples vary from 17.58 ± 1.12 nm in the undeformed sample to 595.29 ± 32.74 nm in the 35% deformed sample (**Table 1**). One-way ANOVA results of the roughness data indicate that all group means are not equal [$F_{(4,18)} = 459.16$, $p < 0.001$]. Additional *post hoc* multiple comparisons (LSD) indicate that all group means are significantly different from each other at $p < 0.05$ level or better. These results are also confirmed by non-parametric Kruskal–Wallis tests [$\chi^2_{(4)} = 20.91$; $p < 0.001$].

The wettability measurements carried out by the DI water droplets on the samples subjected to the varying degrees of plastic deformation are presented in **Table 1**. The angle on the undeformed sample is captured as 84.28° ± 3.02°, whereas it decreases down to 58.07° ± 1.67° on the sample deformed up to 35% of plastic strain. **Figure 4** presents this gradual decline clearly, where water droplets spread more on the surface in parallel with plastic deformation. These results are plotted against

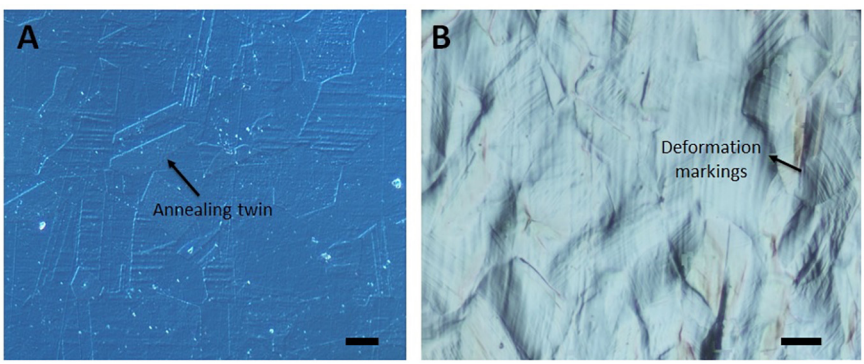


**FIGURE 1 |** Optical microscope DIC images of the **(A)** undeformed and **(B)** 25% deformed sample. Scale bars are 10 μm. (Figure is more readable and visible on the screen rather than in print).

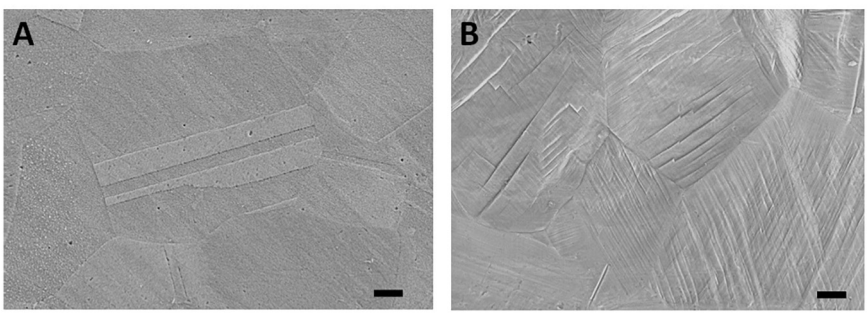


**FIGURE 2 |** Scanning electron microscopy images of the **(A)** undeformed and **(B)** 25% deformed samples. Scale bars are 3 μm. (Figure is more readable and visible on the screen rather than in print).

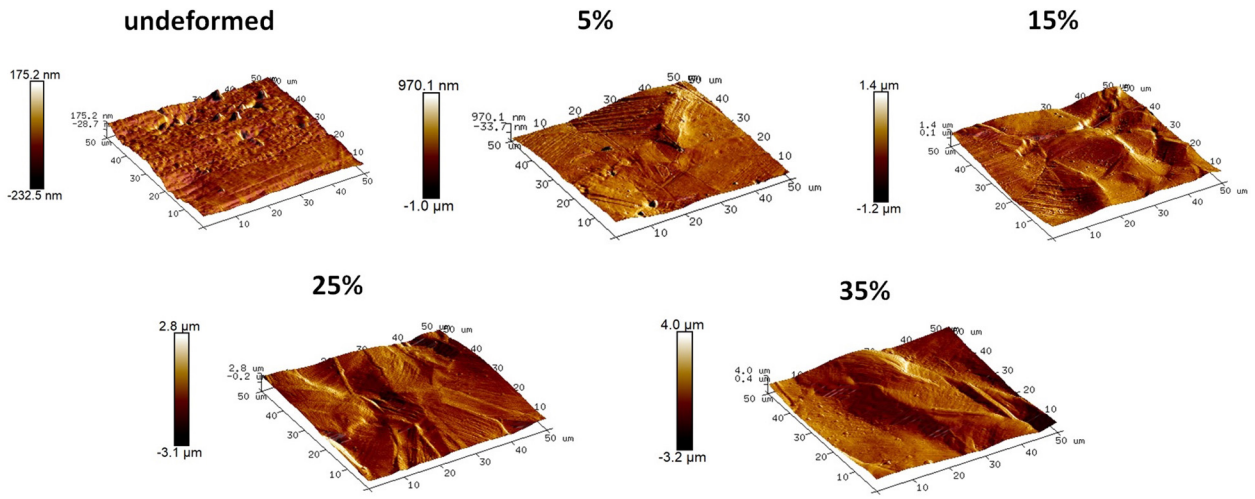


**FIGURE 3 |** Topographical images of the undeformed and deformed samples obtained via AFM. (Figure is more readable and visible on the screen rather than in print).

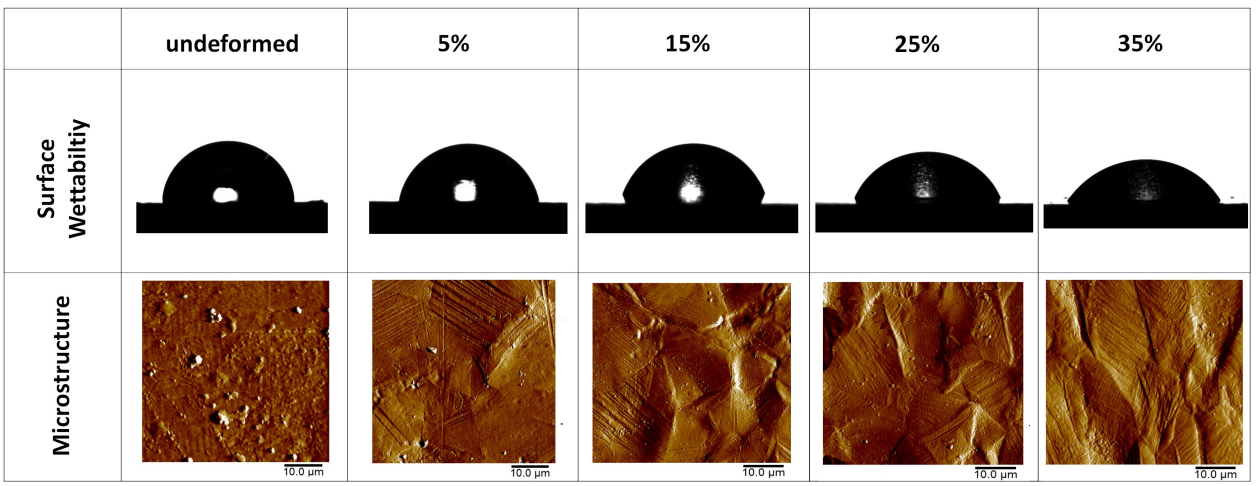


**FIGURE 4 |** Photographs of the water droplets on the undeformed and deformed samples represent the wettability of the samples. AFM amplitude images of the undeformed and deformed samples show the influence of plastic deformation on the microstructure. (Figure is more readable and visible on the screen rather than in print).

**TABLE 1 |** Water contact angle, surface free energy, average surface roughness, and number of attached cells values of the undeformed and deformed samples.

| | Undeformed | 5% | 15% | 25% | 35% |
|---|---|---|---|---|---|
| Contact angle (°) | 84.28 ± 3.02 | 76.8 ± 0.91 | 70.13 ± 1.86 | 65.97 ± 1.03 | 58.07 ± 1.67 |
| Surface free energy (mJ/m$^2$) | 36.06 ± 0.82 | 38.14 ± 0.19 | 42.45 ± 0.18 | 45.37 ± 0.23 | 48.89 ± 0.75 |
| Average surface roughness (nm) | 17.58 ± 1.12 | 141.75 ± 9.57 | 286.4 ± 20.03 | 392.3 ± 31.00 | 595.29 ± 32.74 |
| No. of attached cells | 232.78 ± 3.78 | – | – | – | 557 ± 90.67 |

plastic strain in order to clearly present the relative changes measured in surface roughness and water contact angle values (**Figure 5**). One-way ANOVA results of the surface wettability data indicate that all group means are not equal [$F_{(4,10)} = 58.49$, $p < 0.001$]. Additional *post hoc* multiple comparisons (LSD) indicate that all group means are significantly different from each other at $p < 0.05$ level or better. These results are also confirmed by non-parametric Kruskal–Wallis tests [$\chi^2_{(4)} = 13.5$; $p < 0.01$].

Next, presented in **Table 1** are the results of the SFE analyses. As can be observed in this table, surface energy increases from 36.06 ± 0.82 to 48.89 ± 0.75 mJ/m$^2$ as the applied plastic strain reaches up to 35% from the non-deformed state, and the

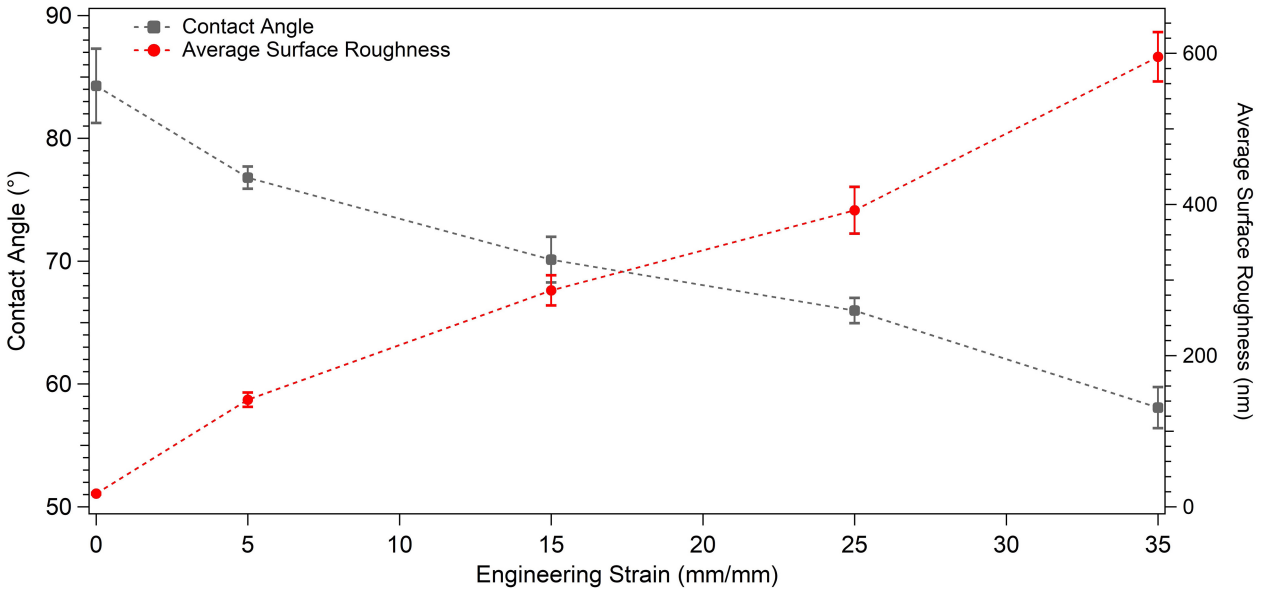


**FIGURE 5 |** Graph presenting the water contact angle and average surface roughness values of the undeformed and plastically deformed samples.

observed difference is statistically significant ($p < 0.001$). More specifically, the null hypothesis stating that all five group means are equal is rejected [$F_{(4,10)} = 199.8$, $p < 0.001$], and *post hoc* multiple comparisons (LSD) indicate that each group mean is significantly different from others at $p < 0.05$ level or better. These results are also confirmed by non-parametric Kruskal–Wallis tests [$\chi^2_{(4)} = 13.5$; $p < 0.01$].

The adhesion and spreading behavior of the cells were closely monitored with SEM. **Figures 6**, **7** present similar cell morphology and attachment behaviors on the undeformed and 35% deformed samples. Cytoplasmic protrusions, such as filopodia or lamellipodia, can be observed on both of these samples.

Breast cancer cells with DAPI-labeled nuclei on the undeformed and 35% deformed samples were also monitored via confocal microscope (**Figure 8**). The quantified data of the attached cells are presented in **Table 1**. These results show that the cell attachment increases on average 2.4-fold on the 35% deformed sample compared to the control sample. Furthermore, a non-parametric Mann-Whitney *U* test indicates that the difference in number of cell attachments on these two samples is statistically significant ($p < 0.001$).

## DISCUSSION

The significant microstructural differences observed between the undeformed and deformed samples via optical microscopy and SEM techniques stem from the introduction of surface relief via activated plastic deformation mechanisms in different volume fractions. Slip, mechanical twinning, or martensite can get activated on 304L stainless-steel samples, contributing to hardening and ductility of the material (Hamdi and Asgari, 2008; Shen et al., 2012). The hierarchical structures of these mechanisms can be observed in **Figure 2B**, where they interact with each other and further contribute to strengthening of the material (Uzer et al., 2016). Moreover, elongated grains observed on the 35% deformed sample can show tensile plasticity of the steel sample (Qu et al., 2008), which constitutes importance in defining the plastic deformation capability of the bulk material.

Increasing volume fraction of the strengthening mechanisms within the bulk material is represented with a more distorted surface, as indicated in the literature (Sinha et al., 2015). The reflection of these mechanisms on the material surface, namely, surface relief, can be observed in the SEM and AFM observations. Specifically, it is clearly seen in **Figures 3**, **4** that the deformation markings protruding out of the material surface modify surface topography significantly and increase surface roughness (Matsugaki et al., 2012; Matsugaki and Nakano, 2016; Uzer et al., 2016). Misorientation angle between the neighboring grains might increase with plastic straining further contributing to the roughness of the samples (Sinha et al., 2015; Srinivasan et al., 2016). $R_a$ of the 35% deformed sample showed approximately 34-fold increase compared to the undeformed sample (**Table 1**). It is important to note that this increase on the polycrystalline stainless steels was related earlier specifically with the activation of deformation twinning, which causes abrupt changes on the texture (Uzer et al., 2016). Hence, designing the material microstructure, which would preferably activate twinning upon deformation, could be advantageous to achieve microscale surface topography and advanced tissue–implant integration.

The water contact angle results show that the 35% deformed sample presents the highest hydrophilicity. This increase in the wettability behavior can be stemming from the increased surface roughness due to surface relief and high-energy regions provided

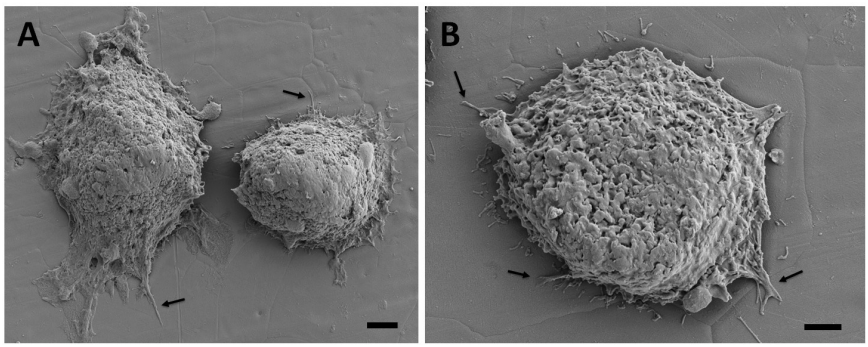


**FIGURE 6 |** Scanning electron microscopy images of the breast cancer cells attached on the undeformed stainless-steel samples. Figure in **(A)** shows two neighboring cells and **(B)** shows a single cell with higher magnification. Arrows point out the cytoplasmic protrusions. Scale bars are 3 and 2 μm, respectively.

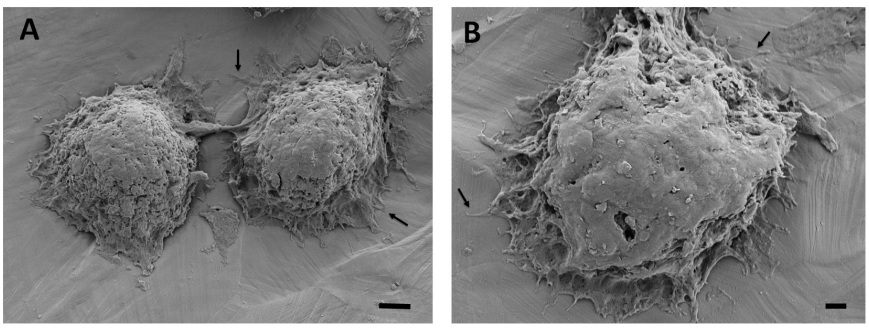


**FIGURE 7 |** Scanning electron microscopy images of the breast cancer cells attached on the 35% deformed stainless-steel samples. Figure in **(A)** shows two neighboring cells and **(B)** shows a single cell with higher magnification. Arrows point out the cytoplasmic protrusions. Scale bars are 3 and 1 μm, respectively.

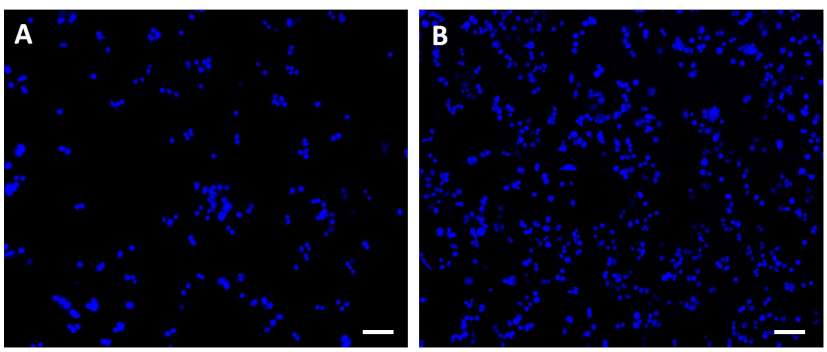


**FIGURE 8 |** Confocal microscope images of the breast cancer cells with DAPI-labeled nuclei attached on the **(A)** undeformed and **(B)** 35% deformed sample. Scale bars are 100 μm.

by the activated strengthening mechanisms. It is noteworthy that surface wettability along with surface roughness may play pivotal role in the early tissue–implant integration (Rupp et al., 2014). That is, surfaces with enhanced wettability and roughness promote the deposition and spreading of cellular adhesion proteins on the implant surface via increasing surface exposure of biological molecules (Venkatsurya et al., 2012). This eventually could lead to improved tissue–implant integration within a shorter period of time (Venkatsurya et al., 2012; Uzer et al., 2016). Hence, increased surface hydrophilicity as a result of bulk plastic deformation and surface relief can be effective for achieving a successful implantation.

The observed increase of surface wettability in parallel with surface roughness can be explained further with Wenzel's equation ($\cos\theta_w = r \cdot \cos\theta_{young}$; where $r$, $\theta_w$, and $\theta_{young}$ are roughness factor, apparent Wenzel contact angle, and Young contact angle, respectively) (Rupp et al., 2014; Cicek et al., 2019). Considering the $\theta_w$ of 58.07°, and $\theta_{young}$ of 84.28°,

$r$ can be predicted as 5.3, which is the ratio between the actual and projected surface area. On the hydrophilic surfaces ($\theta_{young} < 90°$), Wenzel equation suggests that surface wettability increases with higher levels of surface roughness. The greater hydrophilicity observed on the 35% deformed sample thus conforms well with Wenzel's theory.

Moreover, wetting is favored on the high-energy solid surfaces (Rupp et al., 2014), and therefore SFE of the material can also play significant role in tissue–implant integration (Rupp et al., 2014; Uzer et al., 2016). For instance, enhanced protein absorption, attachment, and differentiation of osteoblasts have been related with higher SFE of metallic implants (Miyajima et al., 2019). The SFE values calculated based on OW method in the current study increased gradually with plastic straining (**Table 1**). This result could be attributed to the activated strengthening mechanisms, which have created high-energy regions (Toker et al., 2014; Uzer et al., 2016; Nune et al., 2018). The interaction of slip, twinning, and martensite mechanisms can further increase these energetic regions, which can facilitate the adhesion of biological molecules on the surface (Toker et al., 2014). The role of metallic biomaterial's microstructure on cell response has been analyzed earlier, and enhanced cell adhesion was reported on the smaller grain sized sample, possibly due to increased grain boundary area and SFE (Choubey et al., 2009; Misra et al., 2013). In the current study, the energy-rich twin boundaries, which increase in total area parallel with plastic straining, can also contribute to increased levels of SFE concomitant with the preexisting grain boundaries.

Scanning electron microscopy analyses of the breast cancer cells attached on the undeformed and 35% deformed samples show similar morphologies. Specifically, cytoplasmic protrusions (i.e., lamellipodia or filopodia), which play a crucial role in cancer cell invasion and metastasis (Caswell and Zech, 2018), were formed on both of these samples (**Figures 6**, **7**). These integrin-rich protrusions can regulate cell adhesion, because they are involved in the formation of focal contact points (Caswell and Zech, 2018). Next, the observed 2.4-fold increase in the number of breast cancer cell attachment on the 35% deformed sample compared to the undeformed sample (**Figure 8**) indicates that the aforementioned improved surface properties have provided an advantageous environment for cancer cells. Specifically, increased SFE and wettability on the 35% deformed sample (the highest level of surface relief) would have promoted the deposition of the adhesion proteins, enhancing the attachment of a greater number of cells. Overall, these results indicate that enhanced surface properties via surface relief may increase the number of cell attachments on the implant surface, but may not be influential in the morphology or spreading behavior of the breast cancer cells. Further investigations would be needed to understand mechanisms governing the greater number of cell attachment on the deformed surfaces.

It is well known that the initial interaction of healthy cells (e.g., osteoblasts or fibroblasts) with implant surfaces constitutes significance for establishing successful tissue–implant integration (Nune et al., 2018; Uzer et al., 2018; Raines et al., 2019). When it comes to cancer cells, however, enhanced attachment on the biomaterial surface could be utilized for therapeutic purposes, where cells could be captured on the material before metastasizing to other tissues (Azarin et al., 2015). Azarin et al. (2015) have shown a decrease in tumor burden by developing a polymer implant, which has been used to capture and detect metastasizing breast cancer cells before reaching another organ. In that way, the metastatic disease has been identified at an early stage, and the progression of the disease has been halted. Findings from the current study could also pave the way for a new stream of research revealing potential applications of metallic biomaterials for a similar purpose, whereby cancer cells' attachment would be regulated via modulated surface properties and the progression of the disease could be slowed.

Improvement of the surface properties and cell response was also achieved by surface plastic deformation methods, such as sandblasting, shot peening, or sliding friction earlier (Frutos et al., 2010; Bagherifard et al., 2016; Huo et al., 2017). Arifvianto et al. (2011) have investigated the wettability of the SMAT applied 316L stainless steels, which showed decrease in the contact angle from 88.6 to 74.4°, while surface roughness of the deformed sample increased up to a range of 681 to 909 nm, which is greater than the $R_a$ attained in the current study. Greater hydrophilicity obtained in the current study could be stemming from the activation of deformation mechanisms throughout the bulk material (in comparison to activation in Arifvianto et al. (2011) study predominantly on the material surface). Specifically, surface plastic deformation methods can cause early saturation of the activation of slip, twinning, or martensite, because plastic deformation takes place within the limited deformation zone (Arifvianto et al., 2011). However, bulk plastic deformation can lead to the activation of the strengthening mechanisms in greater densities throughout the bulk material, which can increase high-energy regions more significantly.

This finding is consistent with those in prior studies, where the materials have been subjected to bulk plastic deformation methods, for example, rolling or equal angular channel pressing (ECAP) processes (Misra et al., 2013; Günay-Bulutsuz et al., 2018). Specifically, as the grains of the pure titanium samples were refined through the ECAP process, contact angle decrease from 82.56° down to 41.28° was captured on the postmortem polished surface (Günay-Bulutsuz et al., 2018). This can imply that bulk plastic deformation methods can effectively increase hydrophilicity of materials. Hence, bulk plasticity could play a crucial role in determining surface characteristics of the material. However, it is important to note that surface wettability and energy can also be influenced strongly by surface chemistry (Latifi et al., 2013). Therefore, in order to thoroughly elucidate the role of plastic deformation on surface properties and cell response, further systematic analyses need to be carried out.

## CONCLUSION

In this study, surface properties regulating cell–implant interactions have been investigated on the plastically deformed 304L stainless-steel samples. The tensile loading of the samples up to 5, 15, 25% and 35% of plastic strains has resulted with surface relief in different volume fractions. The greatest surface

wettability ($\theta_w$ = 58.07° ± 1.67°), SFE (48.89 ± 0.75 mJ/m$^2$), and roughness ($R_a$ = 595.29 ± 32.74 nm) were attained on the 35% deformed sample. Furthermore breast cancer cells presented an approximately 2.4-fold increased number of cell attachment on the 35% deformed sample compared to the undeformed control one. Whereas cell morphology and spreading showed similarity on these two samples. The following markings have been concluded:

1. Increasing volume fraction of the twinning, slip, and martensite activated on the samples via bulk plastic deformation technique can be an effective way to impart micro/nanoscale texture and modulate surface properties.
2. Increased SFE could be stemming from the high-energy regions created with strengthening mechanisms and increased surface area of the energy-rich boundaries (twin and grain).
3. Relatively higher number of cells attached on the 35% deformed sample can indicate that implants with surfaces modulated by plastic deformation processes can be utilized for therapeutic purposes via capturing metastatic cancers and slowing the progression of disease.
4. Bulk and surface plastic deformation techniques can each result with different surface properties, which could influence cell response accordingly.

Overall, the aforementioned listed findings provide insight on how surface relief can influence surface properties of the implants and attachment behavior of the breast cancer cells. These results could be utilized in the design of implants for therapeutic or diagnostic purposes. Further investigations would be needed to understand mechanisms governing the cancer cell adhesion on the metallic implants.

## DATA AVAILABILITY STATEMENT

All datasets generated for this study are included in the article/supplementary material.

## AUTHOR CONTRIBUTIONS

The author confirms being the sole contributor of this work and has approved it for publication.

## ACKNOWLEDGMENTS

The author would like to thank Şeyma Dadı for contact angle measurements, Nazende Nur Akşit for cell culture experiments and İhsan Aksit for AFM analyses. The author also acknowledges Dr. M. Serdar Onses for his valuable comments.

## REFERENCES

Arifvianto, B., Suyitno, M., Mahardika, M., Dewo, P., Iswanto, P. T., and Salim, U. A. (2011). Effect of surface mechanical attrition treatment (SMAT) on microhardness, surface roughness and wettability of AISI 316L. *Mater. Chem. Phys.* 125, 418–426. doi: 10.1016/j.matchemphys.2010.10.038

Azarin, S. M., Yi, J., Gower, R. M., Aguado, B. A., Sullivan, M. E., Goodman, A. G., et al. (2015). In vivo capture and label-free detection of early metastatic cells. *Nat. Commun.* 6, 1–9. doi: 10.1038/ncomms9094

Bagherifard, S., Slawik, S., Fernández-pariente, I., Pauly, C., Mücklich, F., and Guagliano, M. (2016). Nanoscale surface modification of AISI 316L stainless steel by severe shot peening. *Mater. Design* 102, 68–77. doi: 10.1016/j.matdes.2016.03.162

Barthes, J., Özçelik, H., Hindie, M., Ndreu-Halili, A., Anwarul, H., and Vrana, N. E. (2014). Cell Microenvironment engineering and monitoring for tissue engineering and regenerative medicine: the citation accessed citable link cell microenvironment engineering and monitoring for tissue engineering and regenerative medicine: the recent advances. *Biomed. Res. Intern.* 2014, 1–18. doi: 10.1155/2014/921905

Bauer, S., Schmuki, P., von der Mark, K., and Park, J. (2013). Engineering biocompatible implant surfaces. *Prog. Mater. Sci.* 58, 261–326. doi: 10.1016/j.pmatsci.2012.09.001

Beri, P., Matte, B. F., Fattet, L., Kim, D., Yang, J., and Engler, A. J. (2018). Biomaterials to model and measure epithelial cancers. *Nat. Rev. Mater.* 3, 418–430. doi: 10.1038/s41578-018-0051-6

Caswell, P. T. and Zech, T. (2018). Actin-based cell protrusion in a 3D matrix. *Trends Cell Biol.* 28, 823–834. doi: 10.1016/j.tcb.2018.06.003

Chen, Q., and Thouas, G. (2015). Metallic implant biomaterials. *Mater. Sci. Eng. R Rep.* 87, 1–57. doi: 10.1016/j.mser.2014.10.001

Chen, W., Allen, S. G., Reka, A. K., Qian, W., Han, S., Zhao, J., et al. (2016). Nanoroughened adhesion-based capture of circulating tumor cells with heterogeneous expression and metastatic characteristics. *BMC Cancer* 16:614. doi: 10.1186/s12885-016-2638-x

Choubey, A., Marton, D., and Sprague, E. A. (2009). Human aortic endothelial cell response to 316L stainless steel material microstructure. *J. Mater. Sci. Mater. Med.* 20, 2105–2116. doi: 10.1007/s10856-009-3780-7

Cicek, S., Karaca, A., Torun, I., Onses, M. S., and Uzer, B. (2019). The relationship of surface roughness and wettability of 316L stainless steel implants with plastic deformation mechanisms. *Mater. Today Proc.* 7, 389–393. doi: 10.1016/j.matpr.2018.11.100

Conde, J., Shomron, N., and Artzi, N. (2016). Biomaterials for metastasis: bridging the gap between basic and translational research. *Adv. Healthc. Mater.* 5, 2312–2319. doi: 10.1002/adhm.201600414

Frutos, E., Multigner, M., and González-Carrasco, J. L. (2010). Novel approaches to determining residual stresses by ultramicroindentation techniques: application to sandblasted austenitic stainless steel. *Acta Mater.* 58, 4191–4198.

Gentile, F., Tirinato, L., Battista, E., Causa, F., Liberale, C., di Fabrizio, E. M., et al. (2010). Biomaterials cells preferentially grow on rough substrates. *Biomaterials* 31, 7205–7212. doi: 10.1016/j.biomaterials.2010.06.016

Gui, N., Xu, W., Tian, J., Rosengarten, G., Brandt, M., and Qian, M. (2018). Fabrication and anisotropic wettability of titanium-coated microgrooves. *J. Appl. Phys.* 123:95306. doi: 10.1063/1.5020517

Günay-Bulutsuz, A., Berrak, O., Aygül Yeprem, H., and Arisan, E. D. (2018). Materials science & engineering C biological responses of ultra Fi Ne grained pure titanium and their sand blasted surfaces. *Mater. Sci. Eng. C* 91, 382–388. doi: 10.1016/j.msec.2018.05.056

Hamdi, F., and Asgari, S. (2008). Evaluation of the role of deformation twinning in work hardening behavior of face-centered-cubic polycrystals. *Metallurg. Mater. Trans. A* 39, 294–303. doi: 10.1007/s11661-007-9356-6

Hanawa, T. (2019). Titanium – tissue interface reaction and its control with surface treatment. *Front. Bioeng. Biotechnol.* 7:170. doi: 10.3389/fbioe.2019.00170

Huo, W. T., Zhao, L. Z., Yu, S., Yu, Z. T., Zhang, P. X., and Zhang, Y. S. (2017). Significantly enhanced osteoblast response to nano-grained pure tantalum. *Sci. Rep.* 7, 1–13. doi: 10.1038/srep40868

Kunrath, M. F., and Hübler, R. (2019). A Bone preservation protocol that enables evaluation of osseointegration of implants with micro- and nanotextured surfaces. *Biotech. Histochem.* 94, 261–270. doi: 10.1080/10520295.2018.1552017

Latifi, A., Imani, M., Khorasani, M. T., and Joupari, M. D. (2013). Electrochemical and chemical methods for improving surface characteristics of 316L stainless steel for biomedical applications. *Surf. Coat. Technol.* 221, 1–12. doi: 10.1016/j.surfcoat.2013.01.020

Le Guéhennec, L., Soueidan, A., Layrolle, P., and Amouriq, Y. (2007). Surface treatments of titanium dental implants for rapid osseointegration. *Dent. Mater.* 23, 844–854. doi: 10.1016/j.dental.2006.06.025

Liu, K., and Jiang, L. (2011). Metallic surfaces with special wettability. *Nanoscale* 3, 825–838.

Matsugaki, A., Aramoto, G., and Nakano, T. (2012). The alignment of MC3T3-E1 osteoblasts on steps of slip traces introduced by dislocation motion. *Biomaterials* 33, 7327–7335. doi: 10.1016/j.biomaterials.2012.06.022

Matsugaki, A., and Nakano, T. (2016). Control of cellular arrangement by surface topography induced by plastic deformation. *Crystals* 6:73. doi: 10.3390/cryst6060073

Misra, R. D. K., Nune, K. C., Pesacreta, T. C., Somani, M. C., and Karjalainen, L. P. (2013). Understanding the impact of grain structure in austenitic stainless steel from a nanograined regime to a coarse-grained regime on osteoblast functions using a novel metal deformation-annealing sequence. *Acta Biomater.* 9, 6245–6258. doi: 10.1016/j.actbio.2012.12.003

Misra, R. D. K., Thein-Han, W. W., Pesacreta, T. C., Hasenstein, K. H., Somani, M. C., and Karjalainen, L. P. (2009). Cellular response of preosteoblasts to nanograined/ultrafine-grained structures. *Acta Biomater.* 5, 1455–1467. doi: 10.1016/j.actbio.2008.12.017

Miyajima, H., Awadzi, G., Ozer, F., and Mante, F. K. (2019). Effect of surface physico-chemico-biological modification of titanium on critical and theoretical surface free energy. *Appl. Surf. Sci.* 470, 386–394. doi: 10.1016/j.apsusc.2018.11.133

Multigner, M., Ferreira-Barragáns, S., Frutos, E., Jaafar, M., Ibáñez, J., Marín, P., et al. (2010). Surface & coatings technology superficial severe plastic deformation of 316 LVM stainless steel through grit blasting: effects on its microstructure and subsurface mechanical properties. *Surf. Coat. Technol.* 205, 1830–1837. doi: 10.1016/j.surfcoat.2010.07.126

Nune, K. C., Montes, I., Injeti, V. S. Y., Somani, M. C., and Misra, R. D. K. (2018). The determining role of nanoscale mechanical twinning on cellular functions of nanostructured materials. *J. Mech. Behav. Biomed. Mater.* 88, 185–195. doi: 10.1016/j.jmbbm.2018.08.033

Peron, M., Torgersen, J., and Berto, F. (2017). Mg and its alloys for biomedical applications: exploring corrosion and its interplay with mechanical failure. *Metals* 252, 1–41. doi: 10.3390/met7070252

Ponsonnet, L., Reybier, K., Jaffrezic, N., Comte, V., Lagneau, C., Lissac, M., et al. (2003). Relationship between surface properties (roughness, wettability) of titanium and titanium alloys and cell behaviour. *Mater. Sci. Eng. C* 23, 551–560. doi: 10.1016/S0928-4931(03)00033-X

Qu, S., Huang, C. X., Gao, Y. L., Yang, G., Wu, S. D., Zang, Q. S., et al. (2008). Tensile and compressive properties of AISI 304L stainless steel subjected to equal channel angular pressing. *Mater. Sci. Eng. A* 475, 207–216. doi: 10.1016/j.msea.2007.04.111

Raines, A. L., Berger, M. B., Schwartz, Z., and Boyan, B. D. (2019). Osteoblasts grown on microroughened titanium surfaces regulate angiogenic growth factor production through specific integrin receptors. *Acta Biomater.* 97, 578–586. doi: 10.1016/j.actbio.2019.07.036

Ranella, A., Barberoglou, M., Bakogianni, S., Fotakis, C., and Stratakis, E. (2010). Tuning cell adhesion by controlling the roughness and wettability of 3D Micro/Nano Silicon structures. *Acta Biomater.* 6, 2711–2720. doi: 10.1016/j.actbio.2010.01.016

Ray, A., Slama, Z. M., Morford, R. K., Madden, S. A., and Provenzano, P. P. (2017). Enhanced directional migration of cancer stem cells in 3D aligned collagen matrices. *Biophys. J.* 112, 1023–1036. doi: 10.1016/j.bpj.2017.01.007

Rupp, F., Gittens, R. A., Scheideler, L., Marmur, A., Boyan, B. D., Schwartz, Z., et al. (2014). A review on the wettability of dental implant surfaces i: theoretical and experimental aspects. *Acta Biomater.* 10, 2894–2906. doi: 10.1016/j.actbio.2014.02.040

Shen, Y. F., Li, X. X., Sun, X., Wang, Y. D., and Zuo, L. (2012). Twinning and martensite in a 304 austenitic stainless steel. *Mater. Sci. Eng. A* 552, 514–522. doi: 10.1016/j.msea.2012.05.080

Sinha, S., Szpunar, J. A., Kiran Kumar, N. A. P., and Gurao, N. P. (2015). Tensile deformation of 316L austenitic stainless steel using in-situ electron backscatter diffraction and crystal plasticity simulations. *Mater. Sci. Eng. A* 637, 48–55. doi: 10.1016/j.msea.2015.04.005

Srinivasan, N., Kain, V., Birbilis, N., Sunil Kumar, B., Gandhi, M. N., Sivaprasad, P. V., et al. (2016). Plastic deformation and corrosion in austenitic stainless steel: a novel approach through microtexture and infrared spectroscopy. *Eval. Program Plan.* 111, 404–413. doi: 10.1016/j.corsci.2016.05.027

Tabdanov, E. D., Puram, V. V., Win, Z., Alamgir, A., Alford, P. W., and Provenzano, P. P. (2018). Bimodal sensing of guidance cues in mechanically distinct microenvironments. *Nat. Commun.* 9, 1–18. doi: 10.1038/s41467-018-07290-y

Toker, S. M., Canadinc, D., Maier, H. J., and Birer, O. (2014). Evaluation of passive oxide layer formation–biocompatibility relationship in NiTi shape memory alloys: geometry and body location dependency. *Mater. Sci. Eng. C* 36, 118–129. doi: 10.1016/j.msec.2013.11.040

Uzer, B., and Canadinc, D. (2018). The effect of plastic deformation on the cell viability and adhesion behavior in metallic implant materials. *Process. Prop. Design Adv. Ceram. Composi. II Ceram. Trans.* 261, 187–196. doi: 10.1002/9781119423829.ch16

Uzer, B., Monte, F., Kamal, R. A., Aswath, P. B., Varanasi, V. G., and Canadinc, D. (2018). The influence of plastic deformation mechanisms on the adhesion behavior and collagen formation in osteoblast cells. *Miner. Metals Mater. Ser. Part F* 12, 295–301. doi: 10.1007/978-3-319-72526-0_27

Uzer, B., Toker, S. M., Cingoz, A., Bagci-Onder, T., Gerstein, G., Maier, H. J., et al. (2016). An exploration of plastic deformation dependence of cell viability and adhesion in metallic implant materials. *J. Mech. Behav. Biomed. Mater.* 60, 177–186. doi: 10.1016/j.jmbbm.2016.01.001

Valiev, R. Z., Estrin, Y., Horita, Z., Langdon, T. G., Zehetbauer, M. J., and Zhu, Y. (2016). Producing bulk ultrafine-grained materials by severe plastic deformation: ten years later. *JOM* 68, 1216–1226.

Venkatsurya, P. K. C., Girase, B., Misra, R. D. K., Pesacreta, T. C., Somani, M. C., and Karjalainen, L. P. (2012). The interplay between osteoblast functions and the degree of nanoscale roughness induced by grain boundary grooving of nanograined materials. *Mater. Sci. Eng. C* 32, 330–340. doi: 10.1016/j.msec.2011.10.036

Ventre, M., Causa, F., and Netti, P. A. (2012). Determinants of cell – material crosstalk at the interface: towards engineering of cell instructive materials. *J. R. Soc. Interf.* 9, 2017–2032. doi: 10.1098/rsif.2012.0308

Weiss, S., and Mitevski, B. (2015). Microstructure and deformation of coronary stents from CoCr-Alloys with different designs. *Materials* 8, 2467–2479. doi: 10.3390/ma8052467

**Conflict of Interest:** The author declares that the research was conducted in the absence of any commercial or financial relationships that could be construed as a potential conflict of interest.

frontiers in Materials

ORIGINAL RESEARCH
published: 08 May 2020
doi: 10.3389/fmats.2020.00104

# Mechanical Behavior of PET-G Tooth Aligners Under Cyclic Loading

*Claudia Cianci[1]*, Giovanni Pappalettera[1], Gilda Renna[1], Caterina Casavola[1], Michele Laurenziello[2], Giovanni Battista[2], Carmine Pappalettere[1] and Domenico Ciavarella[2]*

*[1] Dipartimento di Meccanica, Matematica e Management, Politecnico di Bari, Bari, Italy, [2] Dipartimento di Medicina Sperimentale e Clinica, Università di Foggia, Foggia, Italy*

Invisible aligners are medical devices, which allow repositioning of teeth through a treatment designed by the orthodontists. During this orthodontic treatment, patients use several aligners each for a couple of weeks. The aligner will apply a system of forces on the teeth to shift them to desired position. Since aligners exert forces thanks to their particular shape, it is important that during lifetime's service they do not undergo significant deformations. This research aims to study the mechanical behavior of invisible aligners made by polyethylene terephthalate-glycol (PET-G), which is one of most used the plastic materials to produce such devices. In this study, cyclic compression tests in atmospheric environment (∼25°C) as well as in the presence of saliva (to simulate intraoral environment) were performed. The mechanical behavior of aligners with two different thicknesses (0.75 and 0.88 mm) was studied. In particular, each aligner was subjected to 22500 load cycles from 0 to 50 N. The chosen number of load cycles simulates the average load history to which an aligner is subjected during its lifetime. The tests were performed on a testing machine, using a hard resin dental cast properly fixed to the machine. Analysis of the results shows that the stiffness of the aligners increases during the cyclic test. In particular, a gradual reduction of the crosshead displacement was observed during the test, highlighting the occurrence of cyclic hardening phenomena. It was also found that the aligners show a residual strain recovery after removing the applied load. Moreover, in the analyzed range of load rate, the aligners show a low tendency to accumulate residual strains as loading cycles progress.

**Keywords: compression cyclic loading, mechanical characterization, PET-G, invisible aligners, residual stress**

OPEN ACCESS

***Edited by:***
*Admir Masic, Massachusetts Institute of Technology, United States*

***Reviewed by:***
*Joanna Mystkowska, Bialystok University of Technology, Poland*
*Hon Fai Chan, The Chinese University of Hong Kong, China*

****Correspondence:***
*Claudia Cianci*
*claudia.cianci@poliba.it*

***Specialty section:***
*This article was submitted to Biomaterials, a section of the journal Frontiers in Materials*

***Received:*** *05 December 2019*
***Accepted:*** *06 April 2020*
***Published:*** *08 May 2020*

***Citation:***
*Cianci C, Pappalettera G, Renna G, Casavola C, Laurenziello M, Battista G, Pappalettere C and Ciavarella D (2020) Mechanical Behavior of PET-G Tooth Aligners Under Cyclic Loading. Front. Mater. 7:104. doi: 10.3389/fmats.2020.00104*

## INTRODUCTION

Polyethylene terephthalate-glycol (PET-G) is one of the most famous and used thermoplastic materials in the world. In particular, it is widely used in many applications such as displays, vending machine windows, food packaging, cosmetics and electronics. This material is an amorphous copolymer of PET but, unlike this one, it is not able to undergo strain-induced crystallization independently of the stretching rates and temperatures used during processing (Dupaixa and Boyce, 2005; Elkholy et al., 2019). Due to the favorable combination of excellent

esthetic characteristics, formability, high mechanical strength, excellent flexibility and high impact resistance (Sheridan et al., 1994; Sheridan and Armbruster, 1999; Oh and Wang, 2007; Lloyd et al., 2001), this material has gained great interest in the last decade in the medical device industry. In fact, it is adopted for manufacturing orthodontic retainers, temporomandibular joint splints, periodontal splints, and mouth guards (Ryokawa et al., 2006; Fang et al., 2013; Ma et al., 2016). At the same time, its excellent transparency makes PET-G copolymer promising in manufacturing removable tooth aligners for orthodontics (Ponitz, 1971; McNamara et al., 1985; Lindauer and Shoff, 1998). Orthodontic aligners allow repositioning of teeth through a treatment designed by the orthodontists. During this orthodontic treatment, the patients wear several aligners, each of them for about 2 weeks. Aligners are typically removed only during eating and teeth brushing (Jeremiah et al., 2010). The aligner will apply a system of forces on the teeth to shift them to the desired position. As the teeth move, the forces applied by the aligner decrease as a consequence of the shifting of the teeth. Since aligners exert forces thanks to their particular shape, it is important therefore that during lifetime's service they do not undergo significant deformations (Kesling, 1945; Nahoum, 1964; Ponitz, 1971; Pohl and Yoshii, 1994; Boyd et al., 2006). Generally, a number of factors may contribute to affect the deformation of the thermoplastic materials under loading. These may include environmental conditions (i.e., temperature and humidity), thickness of the aligner, time after elastic deformation and forming procedures features (Landel and Nielsen, 1993; Ryokawa et al., 2006).

Several studies have looked at the effect of different environmental conditions on the mechanical behavior of thermoplastic materials used for invisible aligners. These studies have shown that the mechanical properties differ depending on the environmental factors and that they are influenced by molecular structure and orientation (Ryokawa et al., 2006). In particular, under wet conditions, the water molecules are able to penetrate into the polymer chain or to form hydrogen bonding with the hydrogen end group thereby altering the free volume and mobility of neighboring polymer chains. In addition, water in the polymer matrix may attack the hard and soft-segment domains (Scaffaro et al., 2008; Rajeesh et al., 2010; Xu and Muldowney, 2015; Kim et al., 2016). Moreover, since PET-G is a thermoplastic material with highly viscoelastic properties, the stress induced by initial deformation affects severely the co-polymer's mechanical properties (Tricca and Li, 2006). This phenomenon is known as stress relaxation. In (Fang et al., 2013) the dynamic stress relaxation of a variety of commercial orthodontic thermoplastic materials was studied including PET-G and PET. It was observed that hygrothermal environment can significantly accelerate the stress relaxation of these materials. Moreover, the residual stress within all materials decreases with time. In (Lombardo et al., 2017) the relaxation behavior during a 24-h loading time was evaluated during a three-point-bending test. It was observed that PET-G specimens show stress relaxation value of 44% after the first 8 h, reaching a value of 62% after a 24-h loading period.

Other experimental studies report results from tensile tests or uniaxial and plane strain compression tests conducted over a wide range of temperatures and strain rates (Eliades and Bourauel, 2005; Kwon et al., 2008; Pascual et al., 2010; Zhang et al., 2011; Elkholy et al., 2019).

Nowadays the literature is very poor of experimental data on the cyclic deformation behavior of thermoplastic materials, despite of this it is well known that the cyclic stress-strain behavior of polymers is not the same as that of static loading. The investigation of the cyclic deformation behavior is a very important topic for a correct design of aligners made by these materials. The cyclic deformation behavior was investigated experimentally in Kizypow and Rimnac (2000) and in Ariyama (1993, 1996), respectively, for the ultra-high-molecular-weight polyethylene (UHMWPE) and for PET. In particular, regarding PET polymer, also the effects of strain rate, number of cycles, mean strain, and strain amplitude on the constitutive curves were investigated.

Unfortunately, to date, the response of PET-G co-polymer under cyclic loading has not been investigated.

Therefore, this study presents the experimental results of compression cyclic tests performed on PET-G invisible aligners. Each aligner was subjected to 22500 loading cycles ranging from 0 to 50 N. The number of load cycles was chosen to simulate the average load history to which an aligner is subjected normally during its lifetime. In particular, aligners with two different thicknesses (0.75 and 0.88 mm) were produced and analyzed. The tests have been conducted in atmospheric environment (∼25°C) and in presence of artificial saliva to simulate intraoral environment. The effects of thicknesses and environmental conditions on the mechanical behavior of the co-polymer have been analyzed. A better comprehension of the mechanical behavior of the aligners at room temperature and under simulated intraoral conditions will be helpful for a better product design.

# MATERIALS AND METHODS

## Specimen Preparation

An intraoral scan (TRIOS-3Shape) was performed on a patient with a moderate crowding of upper and lower incisors. This scan has been used to generate a STL file, using the 3Shape OrthoAnalyzer® software (TRIOS-3Shape). Subsequently the STL file was used to 3D print a resin cast (Daylight Hard Resin, Photocentric Ltd.) by means of a Liquid Crystal HR2 3D printer (Photocentric Ltd.).

The aligners specimens were produced from PET-G discs with two different nominal thicknesses: 0.75 and 0.88 mm. In particular the PET-G was a Ace® Plastic produced by GAC International. Its composition was as it follows: 95% copolyester and 5% trade secret. Starting from these transparent disks the aligners were thermoformed using the Essix® SelectVac vacuum machine. The Essix® SelectVac vacuum machine used to fabricate the invisible aligners of different thicknesses is shown in **Figure 1**. Before testing, the aligners were stored at room temperature (approximately 25°C) and indoor humidity (ambient conditions) for 24 h while saliva was added just a few minutes before starting the test.

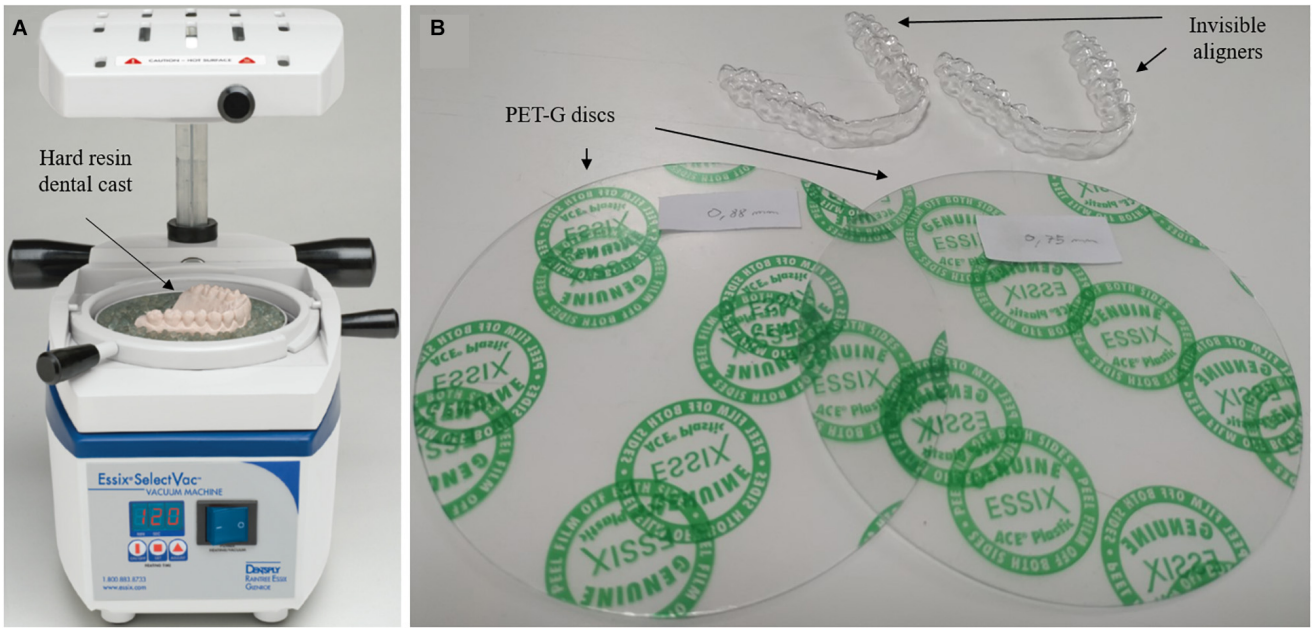


**FIGURE 1 | (A)** Essix® SelectVac vacuum machine used for fabricated the invisible aligners and **(B)** PET-G discs used and specimen produced.

## Compression Cyclic Testing

The compression cyclic tests were performed by using a model 3344 single column universal testing machine produced by Instron (Norwood, MA, United States) equipped with a 1 kN loading cell. The loading machine is directly controlled by a PC through the Instron Bluehill software which was programmed in order to define the desired test procedure (e.g., features of the cycle and number of the cycles). The hard resin dental casts were gripped by flat face hydraulic jaws at a pressure of 10 MPa. During assembling of the dental casts, particular attention was paid to ensure that they were perfectly lined up one above the other and perpendicular to the direction of application of the load. The invisible aligner was placed on the upper dental cast and then casts were put in occlusion obtaining the contact between the upper and lower dental cast. For the case of tests in saliva they were performed by impregnating a thin sponge with artificial saliva. Sponge was preliminary cut in order to follow the shape of the dental cast. In such a way it was possible to insert the cast and the over imposed aligners inside the sponge. A thin transparent film of cellulose hydrate was used to envelope the entire system in order to preserve humidity of the system and avoid fast evaporation.

**Figure 2** illustrates the PET-G specimen undergoing to the cyclic compression test. The tests were performed under load control mode at constant cyclic load frequency $f$ = 0.25 cycles/s. The applied load history is schematized in **Figure 3**. **Figure 3** shows that each loading cycle is constituted by four stages each one lasting 1 s. In the first stage the load increases from 0 to 50 N. That maximum load is maintained for 1 s (stage 2) and then the descending ramp starts down to 0 N (stage 3). Finally, the sample is kept at 0 N for 1 s (stage four) and then a new cycle starts. Compression cycles were repeated 22500 times, distributed over 4 days in order to simulate also the non-loading time corresponding to the phases when the aligner is not used. The chosen number of load cycles simulates the average load history to which an aligner is subjected normally during its lifetime. The number of cycles and ramp duration was calculated on the basis of the average number of daily dental contacts during the swallowing act (1500 swallowing act) and the time of swallowing act (1 s).

Samples with two different thicknesses (0.75 and 0.88 mm) were tested in atmospheric environment (∼25°C). Furthermore, tests in presence of artificial saliva and at room temperature were performed to understand better the mechanical behavior of PET-G aligner within the oral environment. To this scope, commercially available artificial saliva was used whose composition is reported in **Table 1**.

Three samples for each test condition and for each thickness were tested. Average values and standard deviations were calculated for each analyzed point. The total energy and stiffness were calculated to compare their behaviors. In particular, total energy was determined by integrating the load-displacement hysteresis loops while the stiffness was determined as the slope of a linear regression fitting the loops.

# RESULTS AND DISCUSSION

The evolution of the load–displacement hysteresis loops (ratcheting displacement) for each specimen tested at both atmospheric environment (∼25°C) and at presence of artificial saliva is shown in **Figure 4**. The data reported in the figure are

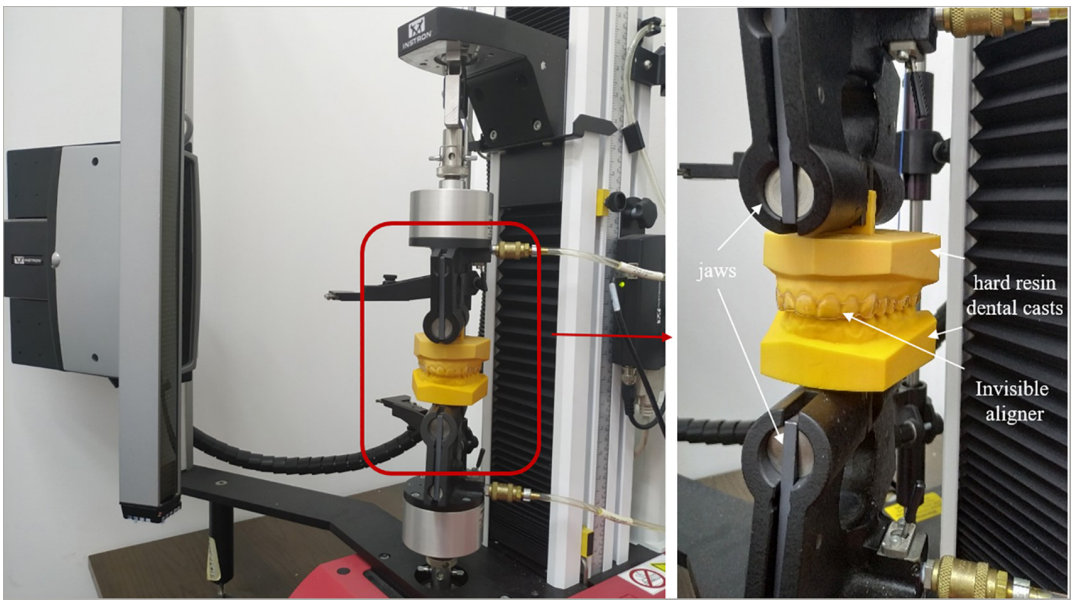


**FIGURE 2 |** Setup for the cyclic compression testing.

referred to the first day of cyclic loading. Similar ratchetting behavior can be found on other days.

In **Figures 4A–D** it is possible to observe that the two samples tested at both atmospheric environment and with artificial saliva follow analog trends. As it can be observed, the hysteresis loops of two samples are shifted to the left (lower displacements) during the cyclic compression testing. Furthermore, it is noted that, for the sample of 0.75 mm thick ($s_{0.75}$) tested at atmospheric environment (**Figure 4A**), the hysteresis loops are almost non-linear in shape during the entire cycling process. This behavior is similar that observed in Shen et al. (2004) for the case of the hardened epoxy resin Epon 826/Epi-Cure Curing Agent 9551. While, for the $s_{0.75}$ sample tested in presence of artificial saliva the hysteresis loops exhibit, initially, some non-linear response, but with the increase number of cycles ($N$) the hysteresis loops become slimmer and more linear (**Figure 4B**). The 0.88 mm thick samples ($s_{0.88}$) tested with and without saliva display similar behavior (**Figures 4C,D**). In fact, it can be observed that the hysteresis loops in the high cycle region become slightly stiffer while the corresponding irreversible work decreases.

Moreover, it was observed that the ratcheting displacement reduction was greater in the first cycles than in the final ones. In general, above the 1000 cycles the displacement reduction tends to stabilize (**Figure 4**). The $s_{0.75}$ sample both at atmospheric environment and with artificial saliva displays in the low cycle region (between 2 and 1000 cycles), a decrease in the ratcheting displacement of about 20%. The same level of displacement reduction was also observed for the $s_{0.88}$ sample both with or without artificial saliva.

In order to assess the viscoelastic nature and explain the mechanical behavior of aligners tested at environmental ambient and with artificial saliva, the stiffness and the viscoelastic energy loss per cycle were determined. **Figures 5** and **6** show, respectively, the relative stiffness defined as the stiffness per unit length multiplied by the resistant area, and the energy as a function of the number of cycles ($N$). In particular, in

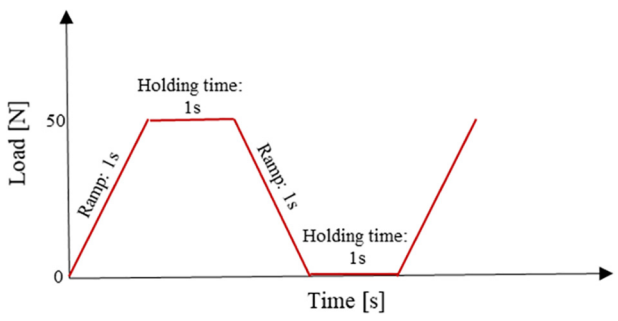


**FIGURE 3 |** Load vs time history for the time specimen; cycles were repeated 22500 times.

**TABLE 1 |** Chemical composition of artificial saliva.

| Composition | Content (%) |
|---|---|
| KCl | 0.12 |
| NaCl | 0.085 |
| $MgCl_2$ | 0.005 |
| $CaCl_2 \times 2H_2O$ | 0.013 |
| $K_2HP0_4$ | 0.013 |
| Sorbitol (70%) | 4.3 |
| E218 | 0.05 |
| Xantnan Gum | 0.1 |
| Water | Remaining |

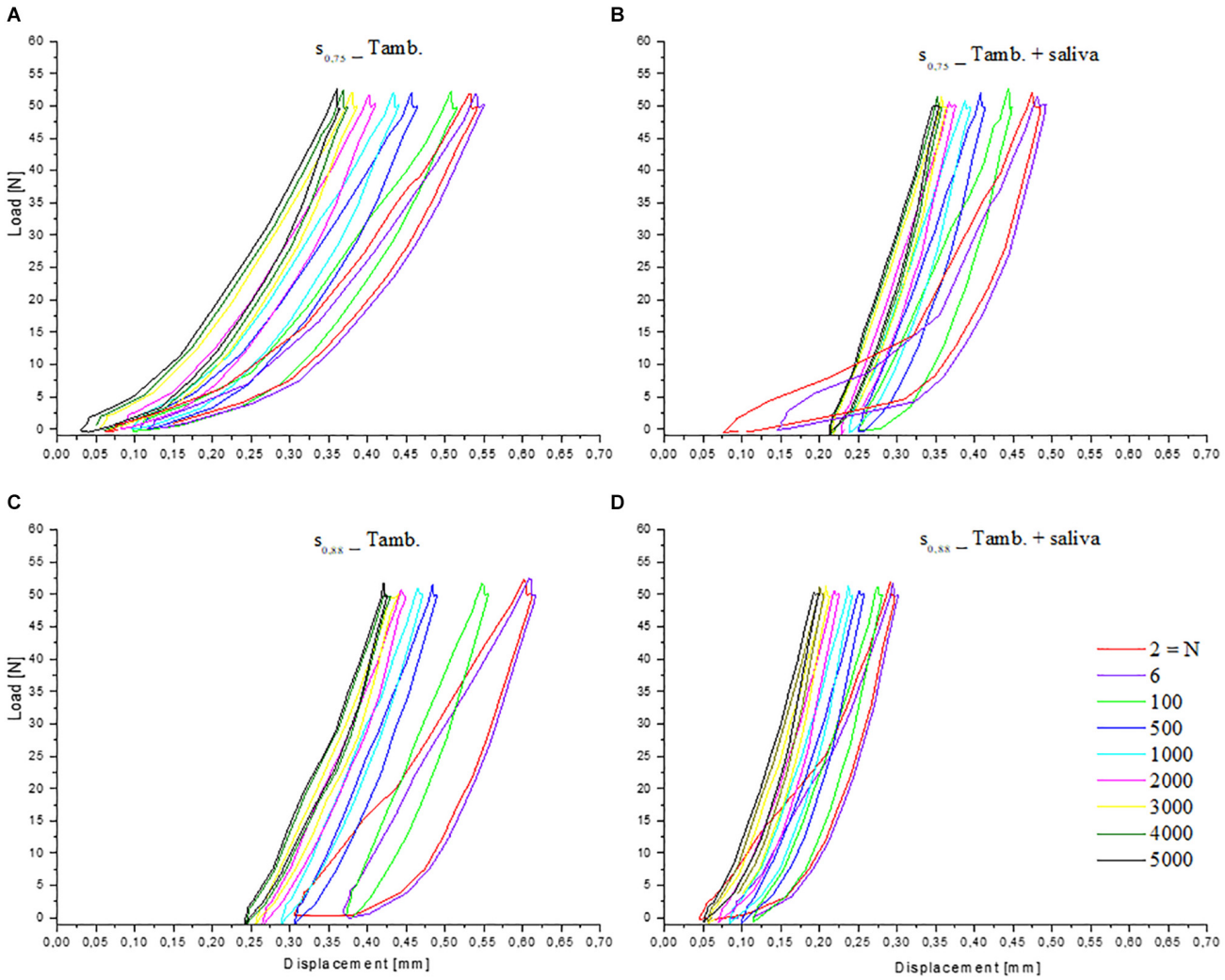


**FIGURE 4 |** Evolution of the load–displacement loops for each sample tested under different environmental conditions. 0.75 mm sample tested **(A)** in atmospheric environment (~25°C) and **(B)** in presence of artificial saliva. 0.88 mm sample tested **(C)** in atmospheric environment (~25°C) and **(D)** in presence of artificial saliva. The serial number of the compression cycle (*N*) increases from right to left.

**Figure 5** it can be noted an abrupt increase in stiffness in the aligners in the low cycle region (during the first 1000 cycles), after that the stiffness values remained almost constant. The maximum stiffness value obtained was 400 N/mm. This trend was observed for both the thicknesses, for both the testing conditions and for all days of cyclic loading (**Figure 5**). A possible interpretation of this stiffening effect could be connected with molecular orientation and/or polymeric chain entanglement (network) which takes place as the compression test progresses (Schrauwen, 2003; Dupaixa and Boyce, 2005). In addition, another effect that contributes to increase the stiffness of the aligners can be connected with the stress generated during cyclic mechanical compression. In fact, stresses in aligners tend to accumulate during fatigue. As a consequence, stress level rises throughout the test, making the aligners at the same time stiffer and less viscoelastic. Finally, also the absorption of water molecules through humidity in the air or immersion in water may alter the behavior of the aligner during compression loading (Ryokawa et al., 2006).

By comparing the behavior of $s_{0.75}$ and $s_{0.88}$ samples tested in presence of artificial saliva with those tested at atmospheric environment, two observations are possible. The first is that during the compression loading the increase of stiffening of samples tested in presence of saliva was higher with respect to the same samples tested at atmospheric environment. The increase of stiffness observed is, in fact, also due to the absorption of the saliva (compare **Figures 5A,B** and **Figures 5C,D**). Such water absorption can produce not only an expansion of the aligner but it can contributes to a change in the molecular orientation (Ryokawa et al., 2006). At the same time, the authors believed that subsequent water molecules absorption or binding into material makes the overall structure more rigid due to modification (reduction) of the free volume. This phenomenon is particularly evident at the beginning of the test in the first day of loading,

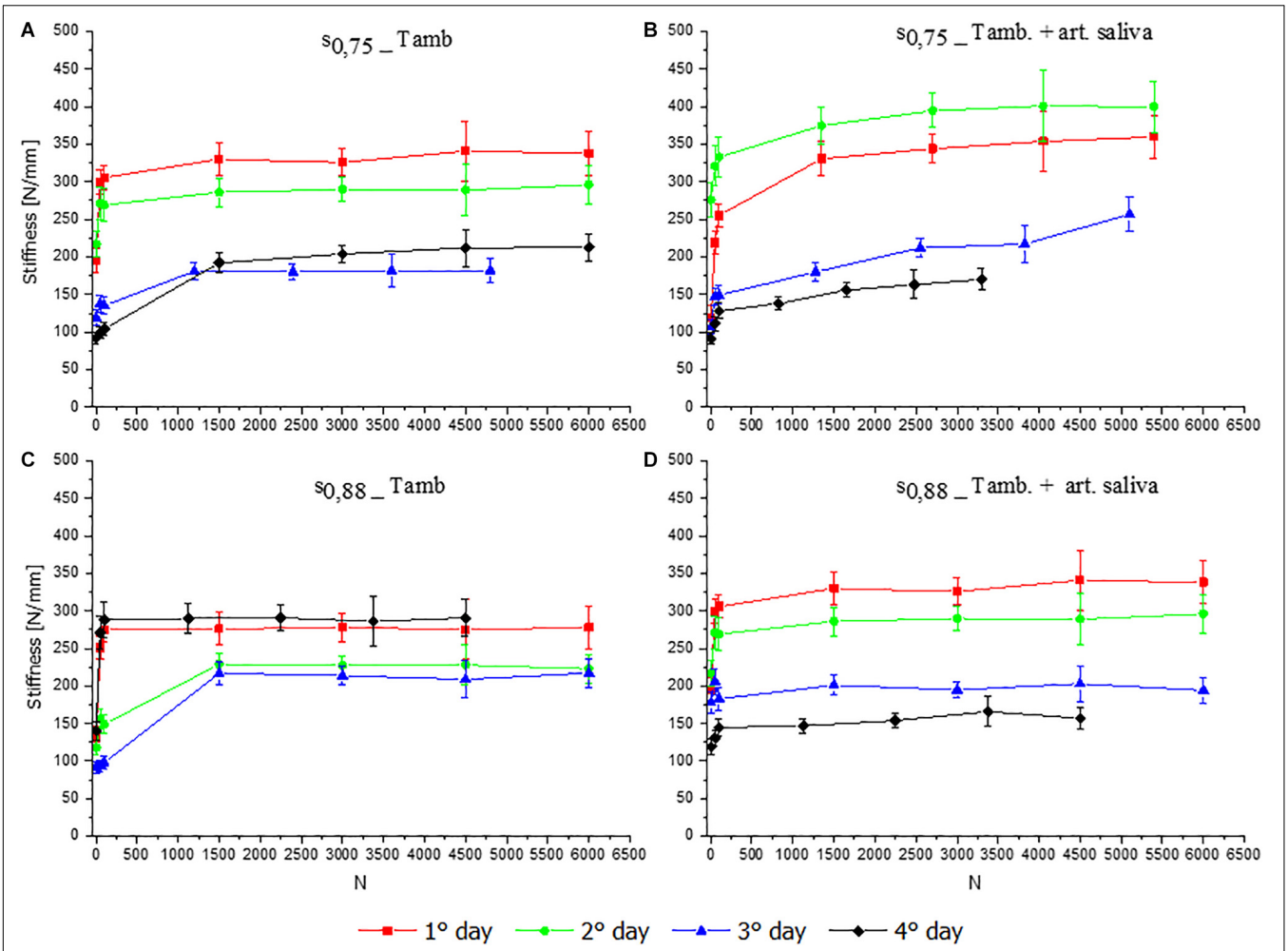


**FIGURE 5 |** Relative stiffness vs. number of cycles for the two copolymer thicknesses: **(A)** 0.75 mm sample tested in atmospheric environment (∼25°C), **(B)** 0.75 mm sample tested in presence of artificial saliva and at room temperature, **(C)** 0.88 mm sample tested in atmospheric environment (∼25°C), and **(D)** 0.88 mm sample tested in presence of artificial saliva and at room temperature.

when the level of saliva absorbed is poor, and tends to increase along the test contributing to increase the stiffness.

A second observation can be done for the case of samples tested in presence of saliva. In this case, in fact, a more marked difference, in average, between the stiffening experienced at the end of the previous test and that shown at the beginning of the next one (**Figures 5B,D**) can be deduced if these data are compared with those obtained in absence of saliva. This is due to a stress relaxation effect during unloading time (time between two subsequent days of testing). This indicates that a hygrothermal environment, such as that connected with the presence of saliva, can accelerate stress relaxation of aligners (Fang et al., 2013). In other words, the aligners tested in presence of saliva display higher capability to recover the local stress, after load removal, with respect to samples tested at environmental ambient.

Moreover, as already evidenced by the hysteresis response (**Figure 4**) of the aligners, the energy (irreversible work) decreases as the cycles increase (**Figure 6**). This trend was observed for the two thicknesses both in presence and without saliva even if, for the case of $s_{0.88}$ in presence of saliva higher data deviation is observed that would require more consistent statistic to be confirmed. The initial higher value of energy can be attributed to the progressive accumulation of stress inside the material as observed before. This effect is high in the initial parts of the test and tends to stabilize while the loading cycles increase. As a consequence, the accumulated energy tends to reduce. In the non-exercise time between two subsequent days of testing, stress recovery was observed and, as consequence, the amount of energy dissipation is observed to increase again in the first cycles of a new session of cyclic compression test.

To understand better the relative ratcheting displacement of the aligners when the tests are conducted both at atmospheric environment (∼25°C) and with artificial saliva the maximum displacement was calculated. **Figure 7** shows the relationship between the maximum displacement and the number of cycles ($N$) for the two thicknesses tested under the same conditions, throughout the 4 days. In close accordance with the above presented results (**Figure 5**), the maximum displacement

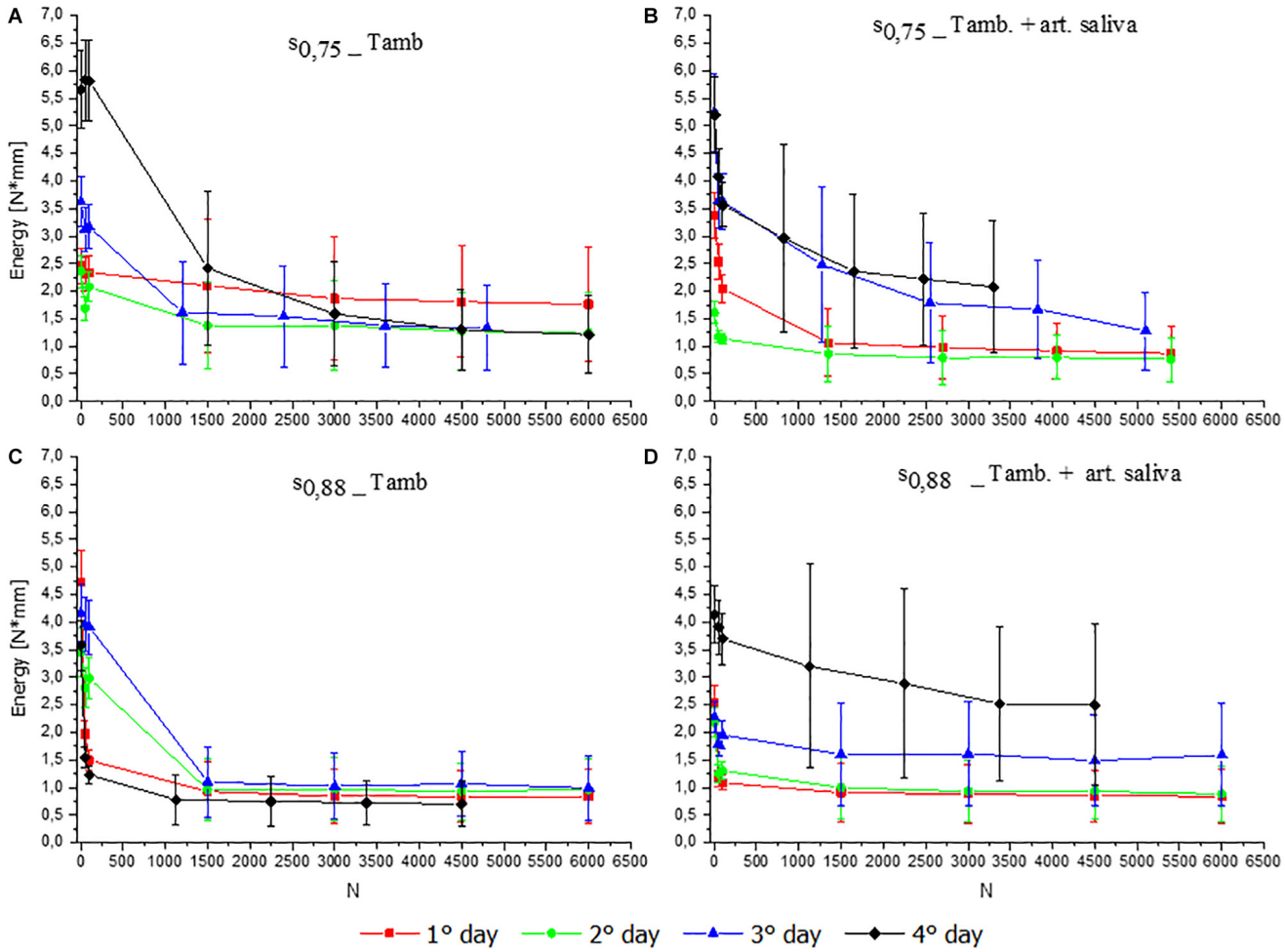


**FIGURE 6 |** Variation of hysteresis loop energy vs. number of cycles for the two copolymers thicknesses. 0.75 mm sample tested **(A)** in atmospheric environment (∼25°C) and **(B)** in presence of artificial saliva and at room temperature. 0.88 sample mm tested **(C)** in atmospheric environment (∼25°C) and **(D)** 0.88 mm sample tested in presence of artificial saliva and at room temperature.

decreases with increasing *N* (**Figure 7**). This trend was observed for both the thicknesses, for both the testing conditions, and throughout the 4 days. The displacement reduction is directly related to the stiffening of aligners. In addition, it can be observed that the displacement at the first cycle of a new test session is always greater than that at the last cycle of the previous day (**Figures 7A–D**) moreover, the displacement values (for the same *N*) recorded during a test day are always lower than those of the previous day (**Figures 7A,B**) if tests in absence of saliva are considered. Hence, the data indicate that after load removal (unloading time: time between 1 day and the next day) the aligners recover a part of the displacement because of their viscoelasticity. So, when the aligner is completely unloaded it can recover from the loading cycle.

During cyclic compression loading in presence of artificial saliva, aligners exhibit extensive recovery (**Figures 7B,D**). Indeed, it may be observed that increased the displacement recovery occurs, between 1 day and the next one, due to the stress relaxation of aligners. At the same time, the hygrothermal environment contributes to stress relaxation even during the loading cycles within of the same day. As a result, only a small amount of displacement reduction was observed with increase of *N* for each day. Our results, therefore, indicate that samples tested in presence of saliva undergo major deformations in the last days of loading unlike of same tested at environmental ambient. Of course, the residual stress win aligners tested with saliva decrease with time (**Figure 7B**) and this confirms higher displacement during the last days (Ryokawa et al., 2006).

**Figure 8** depicts the displacement variation as a function of fraction of compression test life ($N/N_{final}$) for the two copolymer thicknesses tested under the same conditions. In particular, the displacement variation along the different days was calculated as the difference between the displacement value of the first cycle of a new test session and that recorded at the end of the previous test session. An increase of displacement variation indicates an increase of deformation recovery. Therefore, it was found that displacement recovery of $s_{0.75}$ sample tested in ambient environmental was greater in halfway of compression test life,

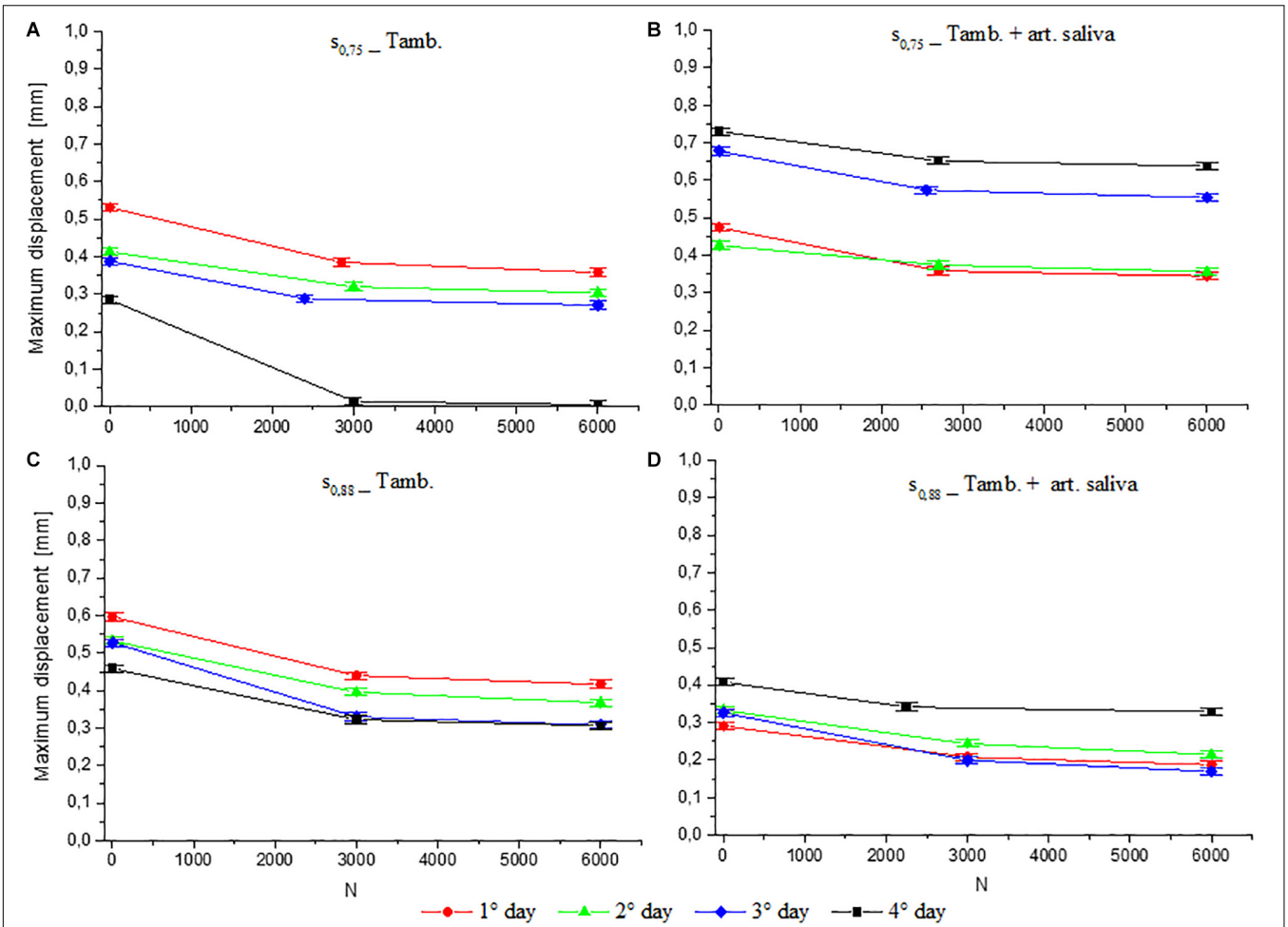


**FIGURE 7 |** Relationship between maximum displacement and number of cycles of two sample: **(A)** 0.75 mm sample tested in atmospheric environment (~25°C), **(B)** 0.75 sample tested in presence of artificial saliva and at room temperature, **(C)** 0.88 mm sample tested in atmospheric environment (~25°C), and **(D)** 0.88 mm sample tested in presence of artificial saliva and at room temperature.

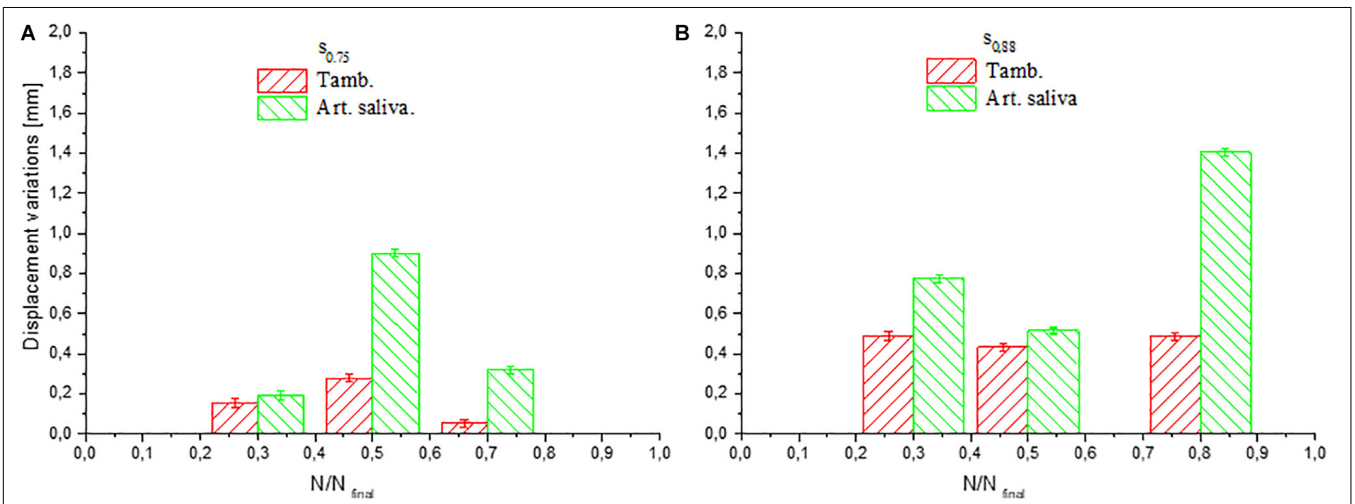


**FIGURE 8 |** Displacement variation among the different days for the two PET_G copolymer thickness: **(A)** sample of 0.75 mm thick tested in both atmospheric environment (~25°C) and in presence of artificial saliva and **(B)** sample of 0.88 mm thick tested in both atmospheric environment (~25°C) and in presence of artificial saliva. ($N/N_{final}$ = fraction of compression test life).

after which the polymer is not able to recover the displacement due to the high level of accumulated stress (**Figure 8A**). While, for $s_{0.88}$ tested under the same conditions (**Figure 8B**), a constant deformation recovery for each interval in which the load is removed was observed, indicating that a greater thickness allows a more uniform stress distribution, and consequently a slower loss of viscoelastic nature. Finally as it was previously observed the presence of saliva increases displacement recovery, expressing a stress relaxation effect (**Figures 8A,B**) which is not reduced during the test.

## CONCLUSION

The compression behavior under cyclic loading of PET_G invisible aligners was studied for two different thickness and two different testing conditions: atmospheric environment (∼25°C) and in presence of artificial saliva. It was observed for the first day of testing of the aligners in the four different configurations that stiffening effects occur while cyclic loading progresses. It was also observed that stiffening decreases during the non-loading time between two successive sessions of test while stiffening effects are observed again when a new set of cycles is applied to the aligners. Moreover, a work dissipative effect is also observed during cycling loading, this is more pronounced at the beginning of the test while it tends to reduce and stabilize while the test progresses. Also in this case, the time elapsed during two subsequent sessions is observed to contribute to increase again the work dissipative effect in the first cycles of the new session of loadings. With reference to the comparison between the test performed at atmospheric environment and those performed in presence of saliva, it was observed that, in this last case, an higher stress recovery is observed between two subsequent loading sessions; moreover, the hygrothermal environment showed a contribution to reduce the stress accumulation effect during the test. In addition, with reference to the comparison between the two thicknesses, it was observed a reduction in the capability to recover accumulated stresses with the increasing of the total number of applied cycles for the case of 0.75 mm. This effect was not observed for the thicker aligner (0.88 mm) this being an indication that larger thickness allows more even distribution of accumulated stress and minor degradation of viscoelastic properties. Tests have shown that aligners with 0.75 mm thickness have a greater deformation than those with 0.88 mm thickness, in presence of artificial saliva. This result is important from a clinical point of view by taking into account that, in the management of orthodontic treatment, the replacement of the aligner occurs every 15 days. This research suggests that the 0.75 mm thickness aligners should therefore be replaced more quickly due to the modification of their initial rigidity and therefore of the fitting on dental elements, while the 0.88 mm thickness aligners can be used for a longer time.

## DATA AVAILABILITY STATEMENT

The datasets generated for this study are available on request to the corresponding author.

## ETHICS STATEMENT

Ethical review and approval was not required for the study on human participants in accordance with the local legislation and institutional requirements. The patient/participant provided their written informed consent to participate in this study.

## AUTHOR CONTRIBUTIONS

CCi contributed to design the experiment, to perform the mechanical tests, to elaborate and analyze data, to prepare and review the manuscript, and to elaborate state of the art. GP and GR contributed to elaborate and analyze the data, to prepare and review the manuscript, and to elaborate state of the art. CCa contributed to design the experiment. ML and GB specialized medical doctor and contributed to the experimental campaign. CP and DC contributed to ideate the research, to design the experiment, and to analyze the data.

## FUNDING

The specimens were designed and manufactured in the laboratory of the Department of Clinical and Experimental Medicine, University of Foggia. The tests were done in the laboratory of Experimental Mechanics of the Dept. of Mechanical, Mathematics and Management of Politecnico di Bari.

## ACKNOWLEDGMENTS

The authors acknowledge Fabio Salcuni for his contribution to the manufacturing of casts and aligners used in this work.

## REFERENCES

Ariyama, T. (1993). Stress relaxation behavior after cyclic preloading in polypropylene. *Polym. Eng. Sci.* 33, 1494–1501. doi: 10.1002/pen.760332209

Ariyama, T. (1996). Viscoelastic-plastic behaviour with mean strain changes in polypropylene. *J. Mater. Sci.* 31, 4127–4131. doi: 10.1007/bf00352678

Boyd, R. L., Oh, H., Fallah, M., and Vlaskalic, V. (2006). An update on present and future considerations of aligners. *J. Calif. Dent. Assoc.* 34, 793–805.

Dupaixa, R. B., and Boyce, M. C. (2005). Finite strain behavior of poly (ethylene terephthalate) (PET) and poly (ethylene terephthalate)-glycol (PETG). *Polymer* 46, 4827–4838. doi: 10.1016/j.polymer.2005.03.083

Eliades, T., and Bourauel, C. (2005). Intraoral aging of orthodontic materials: the picture we miss and its clinical relevance. *Am. J. Orthod. Dentofac.* 127, 403–412. doi: 10.1016/j.ajodo.2004.09.015

Elkholy, F., Schmidt, S., Amirkhani, M., Schmidt, F., and Lapatki, B. G. (2019). Mechanical characterization of thermoplastic aligner materials:

recommendations for test parameter standardization. *J. Healtc. Eng.* 2019:8074827. doi: 10.1155/2019/8074827

Fang, D., Zhang, N., Chen, H., and Bai, Y. (2013). Dynamic stress relaxation of orthodontic thermoplastic materials in a simulated oral environment. *Dent. Mater.* 32, 946–951. doi: 10.4012/dmj.2013-131

Jeremiah, H. G., Bister, D., and Newton, J. T. (2010). Social perceptions of adults wearing orthodontic appliances: a cross-sectional study. *Eur. J. Orthod.* 33, 476–482. doi: 10.1093/ejo/cjq069

Kesling, H. D. (1945). The philosophy of the tooth positioning appliance. *Am. J. Orthod. Oral Surg.* 31, 297–304. doi: 10.1016/0096-6347(45)90101-3

Kim, D. H., Yoo, S. S., Kim, H. J., and Kim, D. E. (2016). Surface damage behavior of polyurethane O-rings in automated material handling system for glass panels. *Int. J. Precis. Eng. Man.* 17, 43–50. doi: 10.1007/s12541-016-0006-z

Kizypow, D. J., and Rimnac, C. M. (2000). Cyclic steady state stress-strain behavior of UHMW polyethylene. *Biomaterials* 21, 2081–2087. doi: 10.1016/s0142-9612(00)00138-1

Kwon, J. S., Lee, Y. K., Lim, B. S., and Lim, Y. K. (2008). Force delivery properties of thermoplastic orthodontic materials. *Am. J. Orthod. Dentofac.* 133, 228–234. doi: 10.1016/j.ajodo.2006.03.034

Landel, R. F., and Nielsen, L. E. (1993). *Mechanical Properties of Polymers and Composites*. Boca Raton, FL: CRC Press.

Lindauer, S. J., and Shoff, R. C. (1998). Comparison of Essix and Hawley retainers. *J. Clin. Orthod.* 32, 95–97.

Lloyd, T., Nightingale, C., and Edler, R. (2001). The use of vacuum formed splints for temporary intermaxillary fixation in the management of unilateral condylar fractures. *Br. J. Oral Maxillofac. Surg.* 39, 301–303. doi: 10.1054/bjom.2001.0649

Lombardo, L., Martines, E., Mazzanti, V., Arreghini, A., Mollica, F., and Siciliani, G. (2017). Stress relaxation properties of four orthodontic aligner materials: a 24-hour in vitro study. *Angle Orthodontist.* 87, 11–18. doi: 10.2319/113015-813.1

Ma, Y. S., Yu Fang, D. N., Zhang, X. J., Ding, K., Zhang, Y., and Bai, Y. X. (2016). Mechanical properties of orthodontic thermoplastic PETG/PC2858 after blending. *Chinese J. Dent. Res.* 19, 43–48. doi: 10.3290/j.cjdr.a35696

McNamara, J. A., Kramer, L., and Juenker, J. P. (1985). Invisible retainers. *J. Clin. Orthod.* 19, 570–578.

Nahoum, H. I. (1964). The vacuum formed dental contour appliance. *NY State Dent. J.* 9, 385–390.

Oh, W. S., and Wang, C. (2007). Use of thermoplastic vacuum-formed matrix for emergency management of crown-root fracture. *J. Prosthet. Dent.* 98, 335–336. doi: 10.1016/s0022-3913(07)60109-7

Pascual, A. L., Beeman, C. S., Hicks, E. P., Bush, H. M., and Mitchell, R. J. (2010). The essential work of fracture of thermoplastic orthodontic retainer materials. *Angle Orthodontist.* 80, 554–561. doi: 10.2319/042809-232.1

Pohl, M., and Yoshii, O. (1994). Der Osamu-Retainer und sein Indikationsbereich. Kieferorthop, Prakt. *Kieferothop* 8:89.

Ponitz, R. J. (1971). Invisible retainers. *Am. J. Orthod.* 59, 266–272. doi: 10.1016/0002-9416(71)90099-6

Rajeesh, K. R., Gnanamoorthy, R., and Velmurugan, R. (2010). Effect of humidity on the indentation hardness and flexural fatigue behavior of polyamide 6 nanocomposite. *Mater. Sci. Eng. A* 527, 2826–2830.

Ryokawa, H., Miyazaki, Y., Fujishima, A., Miyazaki, T., and Maki, K. (2006). The mechanical properties of dental thermoplastic materials in a simulated intraoral environment. *Orthod. Waves* 65, 64–72. doi: 10.1016/j.odw.2006.03.003

Scaffaro, R., Dintcheva, N. T., and La Mantia, F. P. (2008). A new equipment to measure the combined effects of humidity, temperature, mechanical stress and UV exposure on the creep behaviour of polymers. *Polym. Test.* 27, 49–54. doi: 10.1016/j.polymertesting.2007.08.005

Schrauwen, B. A. G. (2003). *Deformation and Failure of Semicrystallie Polymer Systems: Influence of Micro and Molecular Structure*. Eindhoven: Technische Universiteit Eindhoven.

Shen, X., Xia, Z., and Ellyin, F. (2004). Cyclic deformation behavior of an epoxy polymer. part I: experimental investigation. *Polym. Eng. Sci.* 44, 2240–2246. doi: 10.1002/pen.20251

Sheridan, J. J., and Armbruster, P. (1999). Bleaching teeth during supervised retention. *J. Clin. Orthod.* 33, 339–344.

Sheridan, J. J., Ledoux, W., McMinn, R., and Essix, R. (1994). Technology for the fabrication of temporary anterior bridges. *J. Clin. Orthod.* 28, 482–486.

Tricca, R., and Li, C. (2006). "Properties of aligner materia Ex30," in *The Invisalign System*, ed. O. C. Tuncay, (Philadelphia: Quintessence Publishing), 177–186.

Xu, W., and Muldowney, G. (2015). Quantification of water diffusion in CMP pad polymers and impact on mechanical properties. *ECS J. Solid State Sci.* 4, 5078–5087.

Zhang, N., Bai, Y., Ding, X., and Zhang, Y. (2011). Preparation and characterization of thermoplastic materials for invisible orthodontics. *Dent. Mater. J.* 30, 954–959. doi: 10.4012/dmj.2011-120

**Conflict of Interest:** The authors declare that the research was conducted in the absence of any commercial or financial relationships that could be construed as a potential conflict of interest.

frontiers in Materials

ORIGINAL RESEARCH
published: 27 May 2020
doi: 10.3389/fmats.2020.00156

# Humidity-Sensing Material Cottonid – Microstructural Tuning for Improved Actuation and Fatigue Performance

*Ronja Scholz[1]*, Matthias Langhansl[2], Cordt Zollfrank[2] and Frank Walther[1]*

*[1] Department of Materials Test Engineering (WPT), TU Dortmund University, Dortmund, Germany, [2] Biogenic Polymers, TUM Campus Straubing (TUMCS), Technical University of Munich, Munich, Germany*

Adaptive actuators are stimuli-responsive materials able to make a direct use of primary energy to produce motion, as it is well known from motile plant structures. Changes in environmental conditions, such as temperature and humidity, trigger passive movements without the need of metabolism or the use of electrical energy. This bioinspired adaptive mechanism is an alternative and sustainable approach in terms of energy conservation in technical applications. The cellulose-based functional material Cottonid is a promising candidate in this context. It is hygroscopic and possesses a process-related structural anisotropy, which results in direction-dependent actuation and fatigue performance. Since Cottonid is a modified natural material, its microstructure is tunable through chemical modification of the cellulose during the manufacturing process. To assess the influence of varying manufacturing parameters on the microstructure, the actuation behavior as well as the mechanical properties, a parameter study was carried out to identify the most promising modifications for stimuli-responsive element production while maintaining mechanical robustness. This was accomplished with respect to variations of the cellulose source, the chemical catalyst for cellulose modification, temperature of the catalyst bath $T_{cat}$ as well as reaction time $t_{react}$. Specimens' microstructures were investigated with scanning electron microscopy, infrared spectroscopy as well as X-ray diffraction. The actuation behavior was characterized over instrumented experiments in a climate chamber in varying environmental conditions, whereas the environmental fatigue behavior was evaluated in tests with superimposed medial and mechanical loading. Obtained results identified $T_{cat}$ as most influential process parameter onto resulting material actuation properties, which enables a limitation of the possible process window. The findings are used to develop tailored functional materials, where anisotropy and hygroscopicity can be adjusted through the manufacturing process.

**Keywords: Cottonid, bioinspired materials, microstructural tuning, cellulose modification, humidity-driven actuators, environmental fatigue, stimuli-responsive element production**

OPEN ACCESS

***Edited by:***
*Laura Maria Vergani, Politecnico di Milano, Italy*

***Reviewed by:***
*Raffaella Sesana, Politecnico di Torino, Italy*
*Francesca Maria Curà, Politecnico di Torino, Italy*

****Correspondence:***
*Ronja Scholz*
*ronja.scholz@tu-dortmund.de*

***Specialty section:***
*This article was submitted to Polymeric and Composite Materials, a section of the journal Frontiers in Materials*

***Received:*** *01 July 2019*
***Accepted:*** *01 May 2020*
***Published:*** *27 May 2020*

***Citation:***
*Scholz R, Langhansl M, Zollfrank C and Walther F (2020) Humidity-Sensing Material Cottonid – Microstructural Tuning for Improved Actuation and Fatigue Performance. Front. Mater. 7:156. doi: 10.3389/fmats.2020.00156*

## INTRODUCTION

Active adaptation to changing environmental conditions as an intrinsic material function is a biological mechanism that is increasingly used as an energy-efficient approach in the development of technical systems. A large proportion of plants react to external stimuli, such as varying temperature and relative humidity of the environment or solar radiation, with adaptive behavior

expressed by passive or active movements (Markin et al., 2008; Forterre, 2013). Depending on the weather conditions, these movements serve, e.g., for seed dispersal or protection, to catch prey (in carnivorous plants) or for defense. The direction of the resulting movements is determined either by the microstructural structure of the cell walls (passive) or by the position of the acting stimulus (active). A vivid example of moisture-driven passive movements is the pinecone, which opens its scales for reproduction in a dry environment and closes them at high humidity to protect the seed. The reason for the bending movement of the scales lies in their bilayered structure, whereas the layers have a divergent orientation of the cellulose fibrils, which results in differently pronounced swelling and shrinking behavior (Fratzl and Barth, 2009; Reyssat and Mahadevan, 2009; van Opdenbosch et al., 2016).

In current research, this efficient relationship between structure and function of a material is implemented in many ways in bio-based or artificial material systems. The transfer and targeted use of the structural properties of biological systems is fundamental, whereby the pine cone is a frequently used model as a bilayered actuator. Stimulus-adaptive material systems can offer advantages in a wide variety of technical applications. Based on thermo-, hygro-, or light-sensitive materials, such sensor/actuator systems can directly convert primary energy, such as solar radiation or hydropower, into a technically usable kinetic energy, which is energetically advantageous (Dai et al., 2013; Guiducci et al., 2016; Shin et al., 2018).

In addition to saving energy, the use of renewable resources in material development is also an important aspect. Cellulose-based material systems are hygroscopic and an efficient raw material basis for humditiy-responsive actuators. With wood as a traditional construction material, the moisture-controlled swelling and shrinkage behavior is exploited, for example, in the manufacture of curved architectural elements. Through the intelligent combination of layers with varying microstructural composition, complex geometries are developed by treatment with moisture, which are used, among other things, in the form of facade elements. As smart building skins, they adapt their position and orientation to the ambient conditions as required and provide shade in the event of high solar energy irradiation without permanently obstructing the view (Menges, 2012; Grönquist et al., 2018).

In this context, Cottonid is a functional material based on chemically modified cellulose, which shows a pronounced and directed swelling and shrinking behavior in reaction to varying relative humidity. It is manufactured over the parchmentizing process, which is a chemical process used to modify organic polymers, like native cellulose, changing its molecular structure. The chemical catalyst partly dissolves the polymer chains, whereas the degree of dissolution is highly dependent on the source of the cellulose as well as the process conditions (Vieweg and Becker, 1965; Jedvert and Heinze, 2017). As cellulosic raw material, unsized filter paper is used, based on cotton linters, wood pulp or a mixture of the two. The paper is fed into a tempered catalyst bath, comprising a zinc chloride ($ZnCl_2$) solution or a sulfuric acid ($H_2SO_4$) solution, where the surfaces of the cellulose fibrils are etched superficially and new intra- and intermolecular hydrogen bonds can form in one and between several paper layers. This results in a chemical modification of the native cellulose (cellulose 1) in the raw paper. The amount of paper layers fed into the process defines the thickness of the end product. This provides a simple and energy-efficient procedure to manufacture thin and flexible Cottonid for actuators or thicker, dimensionally stable material for construction purposes. After the catalyst bath, Cottonid is washed out until no chemical residuals are left and subsequently dried and planned. Due to the directed paper making process, the cellulose short fibers have a preferred direction, which can be seen in the anisotropic material behavior of Cottonid. The highest mechanical strength can be detected in manufacturing direction and is comparable to common technical plastics, like PA or PVC. Perpendicular to manufacturing direction, a pronounced swelling and shrinking behavior in reaction to humidity is present (Mittendorf, 2016; Scholz et al., 2016, 2019b; Esch, 2018).

Cottonid was already patented in the late 19th century but was replaced later by synthetic plastics in most technical applications. Today, with regard to sustainability and eco-friendliness, Cottonid is a resource-efficient alternative again (Taylor, 1871; Scholz et al., 2019a). Further, the motivation for investigations on this material lies in the fact, that in contrast to wood it is possible to influence and tune the microstructure of Cottonid by specifically adjusting the manufacturing parameters. Delignified cellulose bulk materials e.g., are also wood-derived and structure and properties are highly dependent on the heterogeneity of the wood substrate (Rüggeberg and Burgert, 2015; Frey et al., 2018; Scholz et al., 2019b). Since structural directionality is a beneficial attribute in terms of mechanical as well as – besides hygroscopicity – swelling properties, Cottonid is an efficient candidate for adaptive humidity-driven actuators. A targeted combination of different Cottonid variants would provide an efficient way of producing architectural components with complex adaptive deformation behavior. To determine the influence of individual process parameters, four different Cottonid variants were investigated in this study with regard to their microstructure and actuation performance. Further, to assess the influence of the process-related predefined orientation of the cellulose fibrils, specimens for fatigue experiments were prepared with different locations in respect to manufacturing direction of the Cottonid sheet.

In this study, the influence of a variation of $T_{cat}$ and $t_{react}$ on the actuation and fatigue properties of Cottonid is focused taking into account the process-related anisotropic behavior as well as the hygroscopicity of Cottonid.

# EXPERIMENTAL PROCEDURE

## Sample Preparation

The raw paper for the produced Cottonid variants was obtained from Hahnemühle FineArt GmbH (Dassel, Germany) and has a weight of 320 g/m$^2$ with a material thickness $t_{mat}$ = 0.9 mm. It consists of 100% cotton linters, this raw material basis

is subsequently marked as "M." A 70 wt-% $ZnCl_2$ solution, hereinafter referred to as "Z," is used as the chemical catalyst for parchmentizing.

In order to determine the influence of the temperature of the catalyst bath $T_{cat}$ as well as the reaction time $t_{react}$ on the resulting material properties, one paper layer was parchmentized at $T_{cat,I} = 20°C$ and one at $T_{cat,II} = 50°C$ with respective reaction times of $t_{react,I} = 10$ s and $t_{react,II} = 60$ s. The term catalyst bath is defined as a 70 wt-% $ZnCl_2$ solution in which the chemical modification of the native cellulose in the paper layers takes place. The investigation of interdependencies between a variation of the temperature of this bath ($T_{cat}$) and the time a paper layer is placed in it ($t_{react}$) was focused in this study. The sample designation of the resulting Cottonid variants consists out of the chosen manufacturing parameters (see **Table 1**). After the chemical reaction, the catalyst residues are washed out again. This is first accomplished in washing baths with decreasing $ZnCl_2$ concentration, starting at 30% by weight and ending at 5% by weight. Finally, it is washed out with pure water until a chloride detection with silver nitrate no longer shows any precipitation. The samples are then smoothed and dried in a calander (Sumet, Denklingen, Germany) under pressure and temperature. In order to prevent a dimensional change of the material due to water absorption from the environment, the samples are stored under-weight in a dry atmosphere until further analysis.

For actuation tests, bilayered Cottonid/paper actuators were prepared, whereas the Cottonid variants represent the hygroscopically active layer and the untreated office paper (area weight 80 $g/m^2$) the passive one. The layers were adhesively bonded with water resistant wood glue D4 (Leimwerk, Nuremberg, Germany). Specimens' dimensions were $15.0 \times 30.0 \times 0.5$ $mm^3$. To get a first impression on the influence of the manufacturing parameters on the humidity-driven actuation behavior of Cottonid, one specimen was tested for each variant.

For mechanical testing, specimen geometry was chosen according to DIN EN ISO 527. The investigations were carried out on industrial material ("Hornex," Ernst Krüger GmbH & Co., KG, Geldern, Germany) with a material thickness of $t_{mat} = 4.5$ mm. Hornex is also parchmentized using a $ZnCl_2$ solution. Specimens were manufactured in 0°, 45°, and 90° according to manufacturing direction of the Cottonid sheet (Scholz et al., 2016, 2019b). **Figure 1C** displayes Cottonid specimens for mechanical tests and in **Figure 1D** test setup for fatigue experiments with integrated climate chamber is shown. During fatigue investigations, 16 specimens were tested in sum, i.e., three samples for each varied parameter.

**TABLE 1** | Sample designation of the produced Cottonid variants.

| Cottonid variant | Raw material | Reaction time $t_{react}$ [sec] | Catalyst | Process temp. $T_{cat}$ [°C] |
|---|---|---|---|---|
| I | M | 10 | Z | 20 |
| II | M | 60 | Z | 20 |
| III | M | 10 | Z | 50 |
| IV | M | 60 | Z | 50 |

## Microstructural Investigations and Analytics

Scanning electron microscopy (SEM) and infrared (IR) spectroscopy are applied to the raw paper "M" and to the manufactured variants M10Z20, M60Z20, M10Z50, and M60Z50 to visualize structural changes in the raw paper caused by the action of the $ZnCl_2$ solution and a variation of $T_{cat}$ during manufacturing of Cottonid.

The microstructure images were obtained with an FE-REM (MIRA3, Tescan GmbH, Dortmund, Germany) and provide optical information on the reaction degree of the cellulose fibrils as a function of $T_{cat}$ and $t_{react}$. Surfaces of the raw paper and Cottonid variants were sputtered with a conductive medium. The absorption of IR radiation is an energy absorption of the material, which, depending on its chemical composition, results in a material-specific spectrum with peaks at characteristic frequencies f or wavelengths $\tilde{\nu}$. A Nicolet 380 spectrometer (Thermo Scientific Inc., Waltham, MA, United States) with an ATR module in attenuated total reflection was used for the measurements. In contrast to transmission, this method enables a surface analysis of opaque substances and thus allows a correlation of the information about microstructural changes on the surface obtained by SEM images with the associated chemical processes. The focus lies on the evaluation of the influences of the process parameters $T_{cat}$ and $t_{react}$. For the wave number interval from 3,600 to 400 $cm^{-1}$, 32 scans per sample with a resolution of 4 $cm^{-1}$ were performed and averaged using the corresponding software (Omnic 7.4.127 Thermo Electron Corp.). A background scan was performed prior to each measurement to avoid overlay of sample material and ambient air. The ratio of crystallinity was determined by the following equitation:

$$Cr.R.I = \frac{A_{1430}}{A_{893}}$$

With $A_{1430}$ is the absorbance ratio at 1,430 $cm^{-1}$ and $A_{893}$ is the absorbance ration at 893 $cm^{-1}$ (Ciolacu et al., 2011).

X-ray diffractograms were collected on a Rigaku Miniflex 600. The diffracted intensity of CuKα radiation ($\lambda = 0.154$ nm, 40 kV and 15 mA) was measured in a 2θ range between 5° and 40°, with scan steps 0.02° at 10°/60 s. The crystallinity of the samples was analyzed by using the method of Segal et al. (1951). This method estimates a crystallinity index, which is defined as:

$$Cr.R.II = \frac{I_{002} - I_{am}}{I_{002}}$$

Where $I_{002}$ is the maximum intensity (in a.u.) of the 002 plane diffraction for cellulose $I_\alpha$ at ∼22°. $I_{am}$ is the intensity of the amorphous background at $2\theta = 18°$. Since this is an empirical method for the determination of crystallinity, the values are not absolute, but they indicate the crystallinity change for the Cottonid samples (Bertran and Dale, 1986).

## Investigations on Humidity-Driven Actuation Behavior

Investigations on the actuation performance of the different Cottonid variants M10Z20, M60Z20, M10Z50, and M60Z50

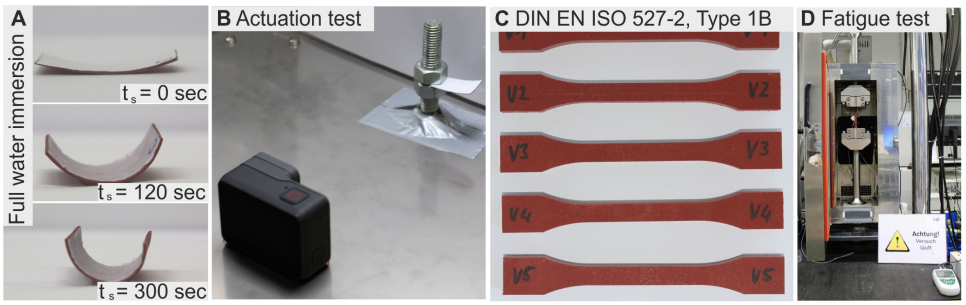


**FIGURE 1 | (A)** Full water immersion of Cottonid/paper bilayer actuator, **(B)** Optical monitoring of actuation performance, **(C)** Cottonid specimens for fatigue testing, **(D)** Test set up for fatigue testing.

were carried out in an alternating climate chamber (MKF 115, Binder, Tuttlingen, Germany). The bilayered Cottonid/paper actuators were clamped at one side and deflection angle $\Delta\alpha$ was measured on the free end by optical monitoring of a tracking point. Within the test duration, i.e., swelling time of $t_s$ = 6 h, several hygroscopic loading cycles between $\varphi_{max}$ = 95% r.H. and $\varphi_{min}$ = 40% r.H. were performed, where adsorption and desorption phases were ∼30 min. Ambient temperature was held constant at $T_{amb}$ = 23°C. In **Figure 1A** a Cottonid/paper actuator in different swelling states when fully immersed in water and in **Figure 1B** an extract of the test setup is presented.

## Investigations on Fatigue Performance

For the investigation of microstructural and environmental influences on the fatigue behavior of Cottonid, multiple step tests (MST) where performed, which represent a time- and energy-efficient methodology to evaluate and compare the fatigue performance of various materials (Colombo et al., 2012, 2018; Schmiedt-Kalenborn et al., 2019). The detection of physical measured variables during a cyclic mechanical loading provides the basis for characterization of initiation and development of microstructural damage within the specimen before final failure. The test methodology is a resource-efficient alternative for the conventional creation of a SN experimental curve (Walther, 2014).

In this study, MST were performed to evaluate the influence of different specimen locations according to manufacturing direction, meaning investigation of anisotropic deformation behavior, and ambient atmospheres on the fatigue behavior of Cottonid. Tests were performed on a servo hydraulic testing machine ($F_{max}$ = 30 kN, Shimadzu, Duisburg, Germany) equipped with an integrable climate chamber (THC, Shimadzu, Duisburg, Germany) to control the surrounding atmosphere. The cyclic loading was applied with a frequency of $f$ = 5 Hz and a sinusoidal load-time function. Stress ratio was $R$ = 0.1, so tension-tension loading was present. Maximum stress at start was $\sigma_{max,start}$ = 15 MPa and was increased stepwise with $\Delta\sigma_{max}$ = 2.5 MPa every $\Delta N = 10^4$ cycles until failure of the specimen. To detect material's reactions during loading, specimens were instrumented with thermocouples and deformations were detected contact free via digital image correlation (DIC, Limess Messtechnik & Software GmbH, Krefeld, Germany). For that, a speckle pattern is applied on specimens' surfaces, which can be monitored by a camera system. MST were performed at two different humidity levels ($\varphi_{low}$ = 20% r.H., $\varphi_{high}$ = 95% r.H.), whereas ambient temperature was held constant at $T_{amb}$ = 23°C.

# RESULTS

## Microstructure

**Figure 2** displays scanning electron microscopy (SEM) micrographs of the Cottonid variants (**Figure 2A**) M10Z20, (**Figure 2B**) M60Z20, (**Figure 2C**) M10Z50, and (**Figure 2D**) M60Z50. From left to right, microstructural changes on Cottonid's surface caused by an increase of the reaction time about $\Delta t_{react}$ = 50 s and from top to bottom, changes caused by an increase of the process temperature about $\Delta T_{cat}$ = 30 K can be seen. In **Figure 2A** can be discovered for M10Z20, that due to the short reaction time of $t_{react,I}$ = 10 s and the low process temperature of $T_{cat,I}$ = 20°C the reaction of the cellulose fibrils has already begun at some locations, but in wide areas there are still unconnected fibrils and defects visible. Increased reaction time of $t_{react,II}$ = 60 s in **Figure 2B** seems to result in less defects on the surface, but in general the surfaces of M10Z20 and M60Z20 are very similar with regard to the modification stadium of the cellulose. In comparison to that, an increased process temperature of $T_{cat,II}$ = 50°C results in a stronger reaction of the cellulose fibrils. In **Figure 2C** only a few very small defects are visible and the fibrils seem to be interconnected over the whole area. The combination of $t_{react,II}$ = 60 s and $T_{cat,II}$ = 50°C results in the strongest reaction. The fibrils are thicker and shorter in comparison to the other Cottonid variants, are interconnected over the whole area and almost no defects are visible. In general, during the process the fibrils are just superficially etched, so that the original fibrous structure of the paper is still visible. This is reflected in the direction-dependent deformation behavior of Cottonid (Scholz et al., 2016, 2019b). The small white crystals on and in between the fibers are remaining zinc chloride.

**Figure 3** shows infrared spectra of the raw paper M in relation to the Cottonid variants (**Figure 3A**) M10Z20, (**Figure 3B**) M60Z20, (**Figure 3C**) M10Z50, and (**Figure 3D**) M60Z50. The

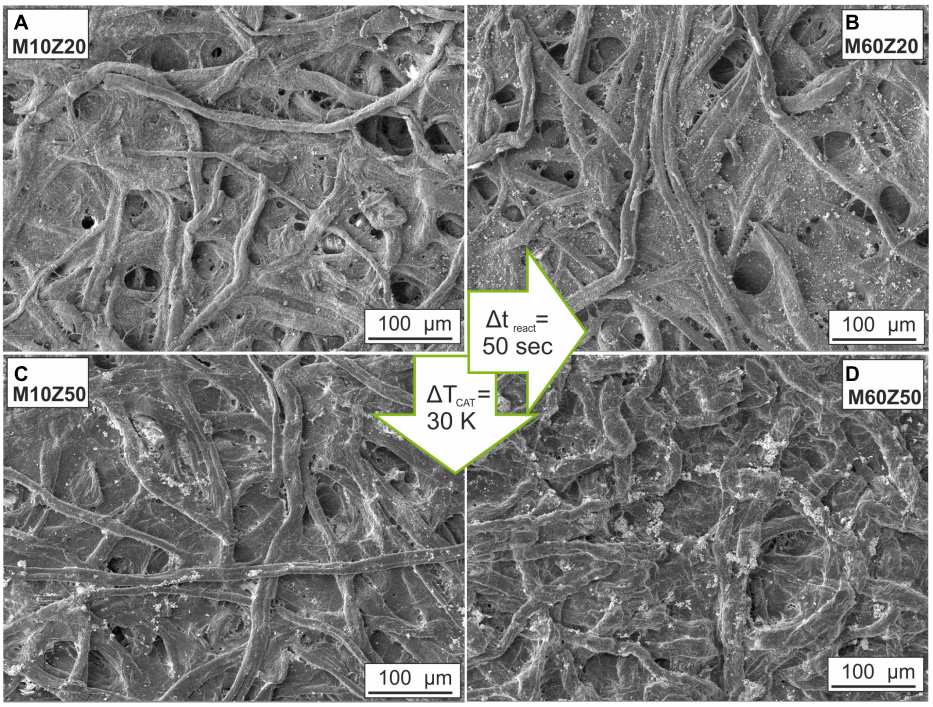


**FIGURE 2 |** SEM micrographs of different Cottonid variants: **(A)** M10Z20, **(B)** M60Z20, **(C)** M10Z50 and **(D)** M60Z50.

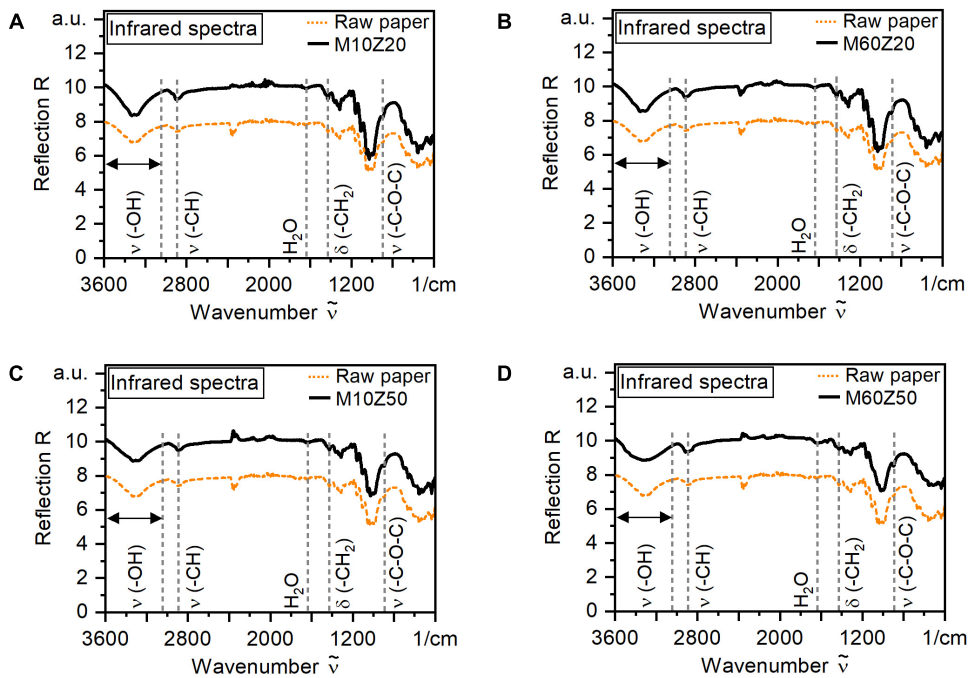


**FIGURE 3 |** Infrared spectra with peak definition of raw paper M (Basis: cotton linters, Hahnemühle FineArt GmbH) and Cottonid variants **(A)** M10Z20, **(B)** M60Z20, **(C)** M10Z50, and **(D)** M60Z50.

spectra were collected in a wavelength interval between 3,600 and 400 $cm^{-1}$ and all of them show the characteristic peaks for cellulose. In the interval between 3,600 and 3,100 $cm^{-1}$ the stretching vibrations of the hydroxyl group [$\nu$(–OH)] of the cellulose chains can be seen. The height and area of the peak therefore provides information about the inter- and

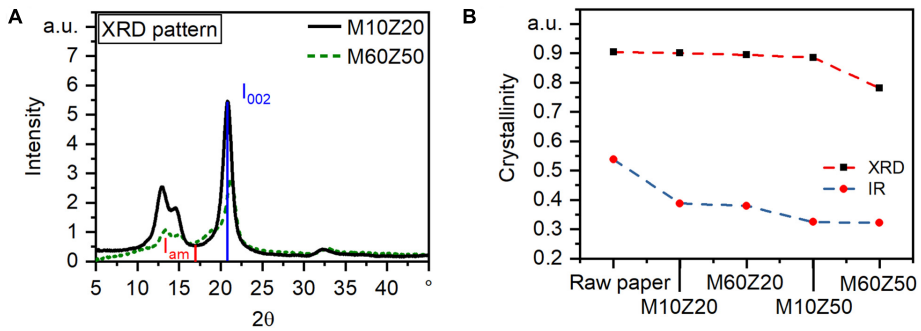


**FIGURE 4 | (A)** Determination of crystallinity exemplary on XRD pattern of Cottonid variant M10Z20, **(B)** Cristallinity determined on the base of IR spectra and XRD patterns for all Cottonid variants.

intra-molecular hydrogen bonds present in the material. The much lower peak at 2,900 $cm^{-1}$ stands for the stretching vibrations of the alkyle [ν(–CH)] groups. Absorbed water is the reason for the peak at 1,640 $cm^{-1}$. In the interval between 1,300 and 900 $cm^{-1}$ peaks of the alcohols derived from to the cellulose chains can be observed. The peak of the glycosidic linkage, which is also known as amorphous peak, can be found at 898 $cm^{-1}$ (Ciolacu et al., 2011).

By comparative evaluation of the spectra it becomes clear, that the basic structure of cellulose sustains the chemical treatment during parchmentizing as a step of the manufacturing process. Choosing a process temperature of $T_{cat,I}$ = 20°C results in no distinct change in microstructure. Even when increasing the reaction time in the $ZnCl_2$ solution to $t_{react,II}$ = 60 s, the spectra of M10Z20 in **Figure 3A** and M60Z20 in **Figure 3B** are nearly identical to the one of the raw paper M. With an increase of the process temperature to $T_{cat,II}$ = 50°C changes can be seen concerning the peak in the interval from 3,600 to 3,100 $cm^{-1}$ for M10Z50 in **Figure 3C**. The peak becomes more flat and wider. The change in this interval marks the modification of cellulose taking place during parchmentizing and indicates the formation of new inter- and intramolecular hydrogen bonds. This effect is even more significant for variant M60Z50 in **Figure 3D** with longer reaction time $t_{react,II}$.

**Figure 4A** displayes obtained XRD patterns exemplary for M10Z20 and M60Z50. Whereas the pattern of M10Z20 is still characteristic for cellulose I, for M60Z20 and M10Z50 the intensity and sharpness of the marked peaks at 2θ = 18° and 2θ = 22° decrease with increasing reaction time $t_{react}$ and process temperature $T_{cat}$. The first significant changes could be obtained for M60Z50 (dotted green line). Here two new peaks occur at 2θ = 10.5° and in the range of 2θ = 18–20°. In **Figure 4B** the results of crystallinity determination based on IR spectra and XRD patterns for all Cottonid variants characterized in this study. Even if both methods show values that are very far apart, a relative decrease in crystallinity becomes clear with increasing process temperature $T_{cat}$ and reaction time $t_{react}$. With both measurements, a loss of crystallinity of about 25% from M10Z20 to M60Z50 in relation to raw paper M can be seen. It also underlines, that the influence of $T_{cat}$ is more significant than the effect of $t_{react}$.

## Humidity-Driven Actuation

In **Figure 5** the results of cyclic actuation experiments on the Cottonid variants (**Figure 5A**) M10Z20, (**Figure 5B**) M60Z20, (**Figure 5C**) M10Z50, and (**Figure 5D**) M60Z50 are shown. Deflection angle Δα as material reaction is plotted over the swelling time $t_s$. Also shown are relative humidity φ as cyclic control parameter and temperature T as constant variable. The bilayered Cottonid/paper actuators are clamped at one side, whereas the hygro-sensitive Cottonid layer was on the bottom and more hygro-passive office paper on top. A positive Δα during the adsorption phase from $\varphi_{min}$ = 40% r.H. to $\varphi_{max}$ = 95% r.H. therefore represents a swelling of the Cottonid layer.

When comparing the actuation curves it can be observed, that the M10Z20 and he M60Z20 bilayer actuators show an acyclic actuation behavior. When increasing φ, both specimens react with a negative Δα, which means, that the untreated office paper shows a stronger swelling and shrinking behavior than Cottonid. The relative deflection angle balances over the whole test duration are $\Delta\alpha_{10}/_{20}$ = −19.8° and $\Delta\alpha_{60}/_{20}$ = −12.3°. When looking at the variants with higher process temperature $T_{cat,II}$, as expected, when increasing relative humidity to $\varphi_{max}$ the M10Z50 and M60Z50 bilayer actuators show a positive Δα, so the Cottonid layer shows a stronger hygroscopic reaction than the untreated office paper layer. This effect is even more significant for variant M60Z50 in **Figure 5D** with longer reaction time $t_{react,II}$. The relative deflection angle balances over the whole test duration are $\Delta\alpha_{10}/_{50}$ = +24.9° and $\Delta\alpha_{60}/_{50}$ = +96.1°.

## Fatigue

**Figure 6** displays the results of the fatigue investigations. In **Figure 6A** microstructural influences are focused and Cottonid specimens are tested in 0°, 45°, and 90° with regard to the manufacturing direction of the Cottonid sheet. Maximum stress $\sigma_{max}$ as control value is plotted over number of cycles N. As material reaction, maximum total strain $\varepsilon_{max,t}$ is shown. It can be seen, that different specimen orientations result in different maximum stresses $\sigma_{max,f}$ and maximum strains $\varepsilon_{max,t,f}$ at failure. As it was already shown by the authors in quasi-static investigations on industrial

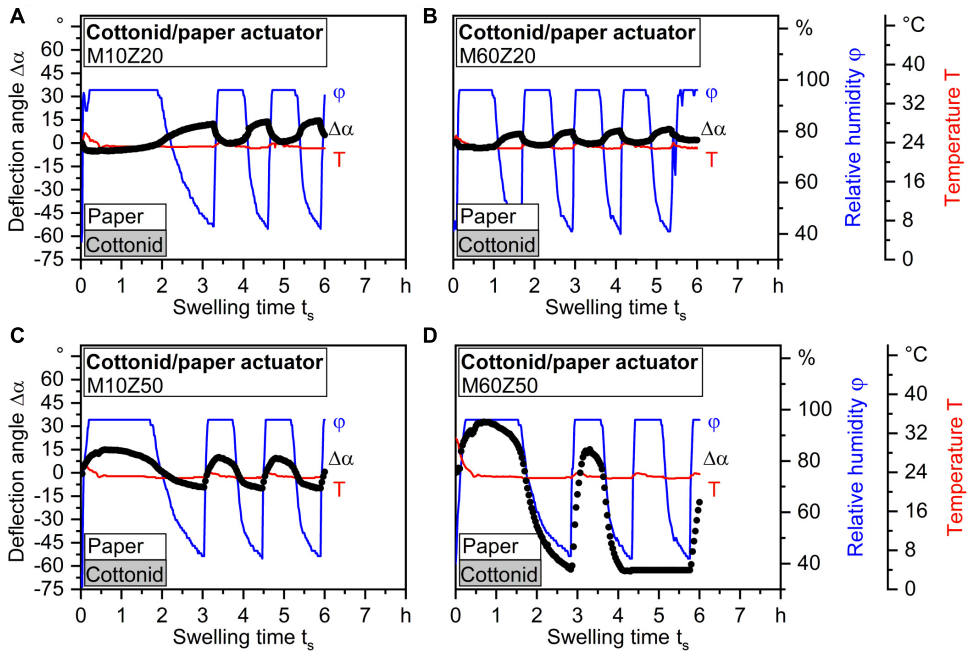


**FIGURE 5 |** Cyclic actuation test (Deflection angle $\Delta\alpha$ vs. swelling time $t_s$): **(A)** M10Z20, **(B)** M60Z20, **(C)** M10Z50, and **(D)** M60Z50.

Cottonid material (Scholz et al., 2016), the specimen, which was prepared in manufacturing direction of the Cottonid sheet, shows highest values for $\sigma_{max,f}$, whereas the specimen perpendicular to it shows the lowest one. The 45°-specimen lies between them. **Table 2** sums up the obtained values. In **Figure 6B** environmental influences on the fatigue behavior of Cottonid are shown exemplary on 45°-specimens. It is clearly visible, that a high relative humidity of $\varphi_{high}$ = 95% r.H. has a negative influence on the fatigue behavior, i.e., mechanical robustness during service loading. $\sigma_{max,f,45,95}$ reaches ∼23.5% lower values than $\sigma_{max,f,45,20}$. **Figure 6C** gives an insight in the integrated climate chamber with mounted fatigue specimen, where the speckle pattern for contact free strain measurement via DIC can be seen within the gauge length.

## DISCUSSION

The analysis of the structural investigations via SEM and IR spectroscopy leads to the conclusion, that the basic structure of cellulose is not affected by the chemical modification during parchmentizing. However, slight differences between the SEM micrographs and the IR spectra of the different Cottonid variants are present. When cellulose is exposed to a tempered catalyst both, the amorphous and crystalline regions are affected. The reduce of crystallinity becomes obvious through the visible microstructural linking of the cellulose micro fibrils, which correlates with changes in the IR spectra in the interval between 3,600 and 3,100 $cm^{-1}$. The changes indicate the modification of cellulose taking place during the manufacturing process, which is characterized by formation of additional inter- and intramolecular hydrogen bonds. This also becomes clearer when evaluating the crystallinity determination using XRD and IR. The formation of new hydrogen bonds leads to an increase of the amorphous regions and therefore to a loss of crystallinity caused by the treatment with a tempered chemical catalyst. Since amorphous regions are essential for water uptake, the cellulose is now able to absorb more moisture from its environment, hence its hygroscopicity gets improved.

Accordingly, increasing the temperature of the catalyst bath by $\Delta T_{cat}$ = 30 K, which leads to a stronger chemical reaction during manufacturing, has a positive effect on the actuation behavior of Cottonid. Bertran and Dale (1986) verified this phenomenon in their studies with differential scanning calorimetry on cellulose with different crystallinities. They came to the result, that hygroscopicity and crystallinity have a linear relation. So, the semi-crystalline cellulose I transforms within the parchmentizing process into another cellulose modification. The formation of two new peaks in the XRD pattern of M60Z50 in comparison to the other Cottonid variants investigated in this study underlines this statement. If the M60Z50 pattern is compared to simulated diffractographs according to French (2014) it can be assumed, that some parts of the cellulose I are transformed into cellulose

**TABLE 2 |** Direction-dependent fatigue properties of Cottonid.

| Value | 0° | 45° | 90° |
|---|---|---|---|
| $\sigma_{max,f}$ [MPa] | 52.5 ± 2.4 | 42.5 ± 0.0 | 37.5 ± 0.0 |
| $\varepsilon_{max,t,start}$ [%] | 0.2 ± 0.0 | 0.2 ± 0.0 | 0.3 ± 0.1 |
| $\varepsilon_{max,t,f}$ [%] | 0.9 ± 0.1 | 0.7 ± 0.1 | 0.8 ± 0.1 |

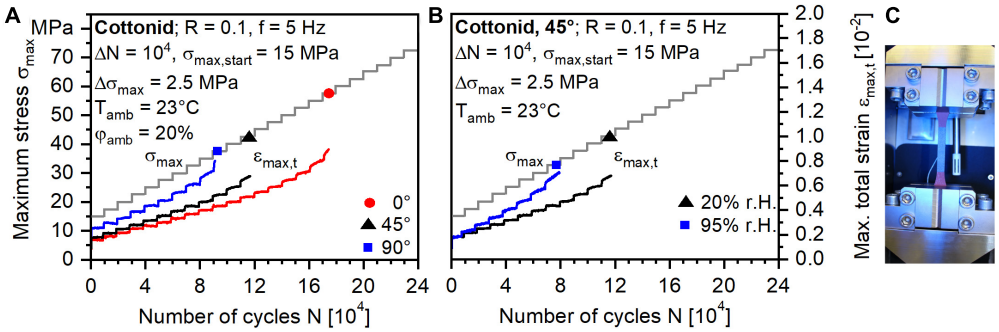


**FIGURE 6 |** Results of multiple step test (MST): **(A)** Direction-dependent and **(B)** Humidity-dependent fatigue properties of Cottonid, **(C)** Mounted and instrumented fatigue specimen.

II. The angular displacement of ∼1.5° is due to the sample height. That would mean, that Cottonid is a mixture of cellulose I and II. In this context (Schestakow et al., 2016) reported, that the mechanical properties of cellulose aerogels from aqueous zinc chloride solution have more in common with cellulose II aerogels from ionic liquids compared to aerogels made of other salt hydrate melts. Esch (2018) came to the same conclusion in her doctoral thesis, that cellulose II is formed, when treating cellulose I with a zinc chloride solution some cellulose II is formed.

The obtained fatigue properties of Cottonid are strongly dependent on the specimen location according to manufacturing direction of the Cottonid sheet, which is expressed by varying strength and deformation values at failure. Accompanying to the quasi-static investigations on industrial Cottonid material (Scholz et al., 2016), these observations verify the direction-dependent deformation behavior of Cottonid. This strong influence of the cellulose short fibers, which just have a predefined orientation due to the directed paper making process, can be exploited for a microstructural tuning of Cottonid to produce architectural components with complex adaptive deformation behavior. Further, the surrounding environmental conditions show a large influence on the mechanical strength. A high relative humidity, which ensures a pronounced actuation performance in case of humidity-adaptive elements, reduces the maximum stress at failure in the fatigue tests about 25%. Since mechanical robustness would also be an important factor when considering the material for architectural applications, these property-function relations have to be further investigated to identify ideal service conditions.

## SUMMARY AND OUTLOOK

In this study, the influence of manufacturing parameters, microstructural orientation as well as environmental factors on the actuation and fatigue performance of Cottonid was investigated. For that, different Cottonid variants were manufactured by varying process temperature $T_{cat}$ as well as reaction time $t_{react}$ in the catalyst bath. Further, fatigue specimens were prepared in 0°, 45°, and 90° according to manufacturing direction of the Cottonid sheet and tested in varying environmental surroundings to assess the impact of microstructure and humidity on the mechanical robustness.

The variation of $T_{cat}$ and $t_{react}$ resulted in Cottonid variants with significant differences in material properties. They differ concerning their microstructure, which is visible in the SEM micrographs as well as in the infrared spectra and XRD patterns. Further, it has an impact on the humidity-driven swelling and shrinking behavior. Generally it could be obtained, that $T_{cat}$ is the decisive parameter. An increase about $\Delta T_{cat}$ = 30 K has a positive effect on the actuation performance, whereas a too low process temperature seems to impair these properties. If $T_{cat}$ is high enough, an increase of the reaction time $t_{react}$ is also beneficial for improving actuation performance. When $T_{cat}$ is too low, an increase of $t_{react}$ shows no positive effect. With the results of XRD measurements in addition to SEM and IR spectroscopy and correlation with the actuation performance it could be proved, that a decrease of crystallinity through the formation of additional intra- and intermolecular hydrogen bonds, standing for an increase of amorphous areas, causes these findings. The next step is the investigation of fundamental mechanisms concerning transformation from cellulose I into cellulose II in aqueous zinc chloride solutions.

In fatigue experiments, specimens with varying microstructural orientation according to manufacturing direction show different cyclic strength and deformation values. This underlines the anisotropic behavior of Cottonid comparable to fiber-reinforced plastics, although the cellulose short fibers exhibit just a process-related predefined orientation. In addition, a high relative humidity has a negative influence on the mechanical robustness. This behavior can be exploited in the design of adaptive elements with programmed actuation performance via microstructural tuning. Since up to now mechanical tests were just performed on industrial material, the investigations will be repeated on the Cottonid variants I to IV (see **Table 1**).

In ongoing studies, the influence of further manufacturing parameters, like raw material for cellulose derivation, e.g., wood pulp instead of cotton linters, or chemical basis

of the catalyst, e.g., sulfuric acid instead of zinc chloride solution, on the actuation and fatigue performance of Cottonid will be investigated. The obtained mechanical values serve further as a scientific basis for material-adapted modeling and prediction of deformations as a function of changing environmental parameters.

## DATA AVAILABILITY STATEMENT

The datasets generated for this study are available on request to the corresponding author.

## AUTHOR CONTRIBUTIONS

ML manufactured and provided the Cottonid variants and performed IR and XRD measurements. RS obtained SEM micrographs and performed actuation and fatigue experiments. RS and ML developed the testing procedure, prepared figures, and wrote the manuscript. CZ and FW supervised the project.

## FUNDING

The authors thank the German Research Foundation (Deutsche Forschungsgemeinschaft, DFG) for funding the research project Biomechanical qualification of the structure-optimized functional material Cottonid as an adaptive element (WA 1672/23-1; ZO 113/22-1).

## ACKNOWLEDGMENTS

We thank the Hahnmühle FineArt GmbH (Dassel, Germany) and the Ernst Krüger GmbH & Co., KG (Geldern, Germany) for providing raw material for Cottonid manufacturing and industrial reference material "Hornex."

## REFERENCES

Bertran, M. S., and Dale, B. E. (1986). Determination of cellulose accessibility by differential scanning calorimetry. *J. Appl. Poly. Sci.* 32, 4241–4253. doi: 10.1002/app.1986.070320335

Ciolacu, D., Ciolacu, F., and Popa, V. I. (2011). Amorphous cellulose - structure and characterization. *Cell. Chem. Technol.* 45, 13–21.

Colombo, C., Harhash, M., Palkowski, H., and Vergani, L. (2018). Thermographic stepwise assessment of impact damage in sandwich panels. *Composite Struct.* 184, 279–287. doi: 10.1016/j.compstruct.2017.10.001

Colombo, C., Vergani, L., and Burman, M. (2012). Static and fatigue characterisation of new basalt fibre reinforced composites. *Composite Struct.* 94, 1165–1174. doi: 10.1016/j.compstruct.2011.10.007

Dai, M., Picot, O. T., Verjans, J. M. N., Haan, L., Schenning, A. P. H., Peijs, T., et al. (2013). Humidity-responsive bilayer actuators based on a liquid-crystalline polymer network. *ACS Appl. Mater. Interf.* 5, 4945–4950. doi: 10.1021/am400681z

Esch, K. (2018). *Röntgendiffraktion An Papier und Vulkanfiber*. Ph. D thesis, Technische Universität Dortmund, Dortmund.

Forterre, Y. (2013). Slow, fast and furious: understanding the physics of plant movements. *J. Exp. Bot.* 64, 4745–4760. doi: 10.1093/jxb/ert230

Fratzl, P., and Barth, F. G. (2009). Biomaterial systems for mechanosensing and actuation. *Nature* 462, 442–448. doi: 10.1038/nature08603

French, A. D. (2014). Idealized powder diffraction patterns for cellulose polymorphs. *Cellulose* 21, 885–896. doi: 10.1007/s10570-013-0030-4

Frey, M., Widner, D., Segmehl, J. S., Casdorff, K., Keplinger, T., and Burgert, I. (2018). Delignified and densified cellulose bulk materials with excellent tensile properties for sustainable engineering. *ACS Appl. Mater. Interf.* 10, 5030–5037. doi: 10.1021/acsami.7b18646

Grönquist, P., Wittel, F. K., and Rüggeberg, M. (2018). Modeling and design of thin bending wooden bilayers. *PLoS One* 13:e0205607. doi: 10.1371/journal.pone.0205607

Guiducci, L., Razghandi, K., Bertinetti, L., Turcaud, S., Rüggeberg, M., Weaver, J. C., et al. (2016). Honeycomb actuators inspired by the unfolding of ice plant seed capsules. *PLoS One* 11:e0163506. doi: 10.1371/journal.pone.0163506

Jedvert, K., and Heinze, T. (2017). Cellulose modification and shaping – a review. *J. Poly. Eng.* 37, 845–860. doi: 10.1515/polyeng-2016-0272

Markin, V. S., Volkov, A. G., and Jovanov, E. (2008). Active movements in plants: mechanism of trap closure by *Dionaea muscipula* ellis. *Plant Signal. Behav.* 3, 778–783. doi: 10.4161/psb.3.10.6041

Menges, A. (2012). Biomimetic design processes in architecture: morphogenetic and evolutionary computational design. *Bioinspirat. Biomimet.* 7:15003. doi: 10.1088/1748-3182/7/1/015003

Mittendorf, R.-M. (2016). *Entwicklung einer Richtlinie Für Die Auslegung Von Direktschraubverbindungen In Vulkanfiber*. Ph. D thesis, Technische Universität Dortmund, Dortmund.

Reyssat, E., and Mahadevan, L. (2009). Hygromorphs: from pine cones to biomimetic bilayers. *J. R. Soc. Interf.* 6, 951–957. doi: 10.1098/rsif.2009.0184

Rüggeberg, M., and Burgert, I. (2015). Bio-inspired wooden actuators for large scale applications. *PLoS One* 10:e0120718. doi: 10.1371/journal.pone.0120718

Schestakow, M., Karadagli, I., and Ratke, L. (2016). Cellulose aerogels prepared from an aqueous zinc chloride salt hydrate melt. *Carbohyd. Poly.* 137, 642–649. doi: 10.1016/j.carbpol.2015.10.097

Schmiedt-Kalenborn, A., Lingnau, L. A., Manka, M., Tillmann, W., and Walther, F. (2019). Fatigue and corrosion fatigue behaviour of brazed stainless steel joints AISI 304L/BAu-4 in synthetic exhaust gas condensate. *Materials* 12:1040. doi: 10.3390/ma12071040

Scholz, R., Langhansl, M., Zollfrank, C., and Walther, F. (2019a). "Cottonid – ein effizienter funktionswerkstoff für feuchtegetriebene aktuatoren," in *Proceedings of the Smarte Strukturen und Systeme – Tagungsband des 4Smarts-Symposiums*, Munich.

Scholz, R., Langhansl, M., Zollfrank, C., and Walther, F. (2019b). Experimental study on the actuation and fatigue behavior of the biopolymeric material cottonid. *Mater. Today Proc.* 7, 476–483. doi: 10.1016/j.matpr.2018.11.112

Scholz, R., Mittendorf, R.-M., Engels, J. K., Hartmaier, A., Kuenne, B., and Walther, F. (2016). Direction-dependent mechanical characterization of cellulose-based composite vulcanized fiber. *Mater. Test.* 58, 813–817. doi: 10.3139/120.110929

Segal, L., Nelson, M. L., and Conrad, C. M. (1951). Experiments on the reduction of the crystallinity of cotton cellulose. *J. Phys. Chem.* 55, 325–336. doi: 10.1021/j150486a001

Shin, B., Ha, J., Lee, M., Park, K., Park, G. H., Choi, T. H., et al. (2018). Hygrobot. A self-locomotive ratcheted actuator powered by environmental humidity. *Sci. Rob.* 3:eaar2629. doi: 10.1126/scirobotics.aar2629

Taylor, T. (1871). Improvement in the Treatment Of Paper And Paper-Pulp. U.S. Patent No 114,880. Pittsburgh, PA: Unites States Patent Office. doi: 10.1126/scirobotics.aar2629

van Opdenbosch, D., Fritz-Popovski, G., Wagermaier, W., Paris, O., and Zollfrank, C. (2016). Moisture-driven ceramic bilayer actuators from a biotemplating approach. *Adv. Mater.* 28, 5235–5240. doi: 10.1002/adma.201600117

Vieweg, R., and Becker, E. (1965). *Kunststoff-Handbuch Band III: Abgewandelte Naturstoffe:. Herstellung, Eigenschaften, Verarbeitung und Anwendung.* München: Carl Hanser.

Walther, F. (2014). Microstructure-oriented fatigue assessment of construction materials and joints using short-time load increase procedure. *Mater. Test.* 56, 519–527. doi: 10.3139/120.110592

**Conflict of Interest:** The authors declare that the research was conducted in the absence of any commercial or financial relationships that could be construed as a potential conflict of interest.

frontiers in Materials

ORIGINAL RESEARCH
published: 24 September 2020
doi: 10.3389/fmats.2020.00233

# Gentamicin-Loaded $TiO_2$ Nanotubes as Improved Antimicrobial Surfaces for Orthopedic Implants

*Lorenza Draghi[1,2], Valeria Preda[1], Monica Moscatelli[1,2], Matteo Santin[3] and Roberto Chiesa[1,2]**

[1] Department of Chemistry, Materials and Chemical Engineering "G. Natta," Politecnico di Milano, Milan, Italy, [2] INSTM – National Interuniversity Consortium of Materials Science and Technology, Firenze, Italy, [3] School of Pharmacy and Biomolecular Sciences, University of Brighton, Brighton, United Kingdom

Titanium oxide nanotube arrays are extremely promising materials for localized drug delivery in orthopedic implants due to their excellent properties and facile preparation. $TiO_2$ nanotubes can act as an effective drug reservoir to prevent bacterial colonization and implant infection and, at the same time, could promote tissue regeneration and effective osseointegration. Here, highly ordered $TiO_2$ nanotubes (NTs) were synthesized by electrochemical anodization of titanium foils and the process parameters were varied in order to obtain a large range of NT diameters to evaluate its influence. The effect of NTs' diameter on gentamicin loading/release and on osteosarcoma cell and bacterial adhesion was assessed. Anodization was confirmed as an easy and effective method to prepare highly ordered, open top nanotubes with predictable diameter as a function of imposed voltage. A lower amount of bacteria *Staphylococcus Aureus* adhesion was found on unloaded NTs surfaces at 24 h. When gentamicin was loaded, protracted release and antibacterial action was observed and bacteria adhesion was prevented on all NTs dimension. However, higher cell proliferation and a more favorable cell morphology was observed on smaller nanotubes, to support the indication toward a reduction in NTs diameter for the preparation of effective implant surfaces.

**Keywords: nanotubes, titanium oxide, drug delivery, anodization, antibacterial**

OPEN ACCESS

***Edited by:***
*Hasan Uludag,*
*University of Alberta, Canada*

***Reviewed by:***
*Shun Duan,*
*Beijing University of Chemical Technology, China*
*Gabriella Epasto,*
*University of Messina, Italy*

***Correspondence:**
*Roberto Chiesa*
*roberto.chiesa@polimi.it*

***Specialty section:***
*This article was submitted to Biomaterials, a section of the journal Frontiers in Materials*

***Received:*** *05 October 2019*
***Accepted:*** *25 June 2020*
***Published:*** *24 September 2020*

***Citation:***
*Draghi L, Preda V, Moscatelli M, Santin M and Chiesa R (2020) Gentamicin-Loaded $TiO_2$ Nanotubes as Improved Antimicrobial Surfaces for Orthopedic Implants. Front. Mater. 7:233. doi: 10.3389/fmats.2020.00233*

## INTRODUCTION

One of the main challenges in the orthopedic field is the development of implant surfaces that combine a fast and durable fixation with an effective limitation of bacterial adhesion, to prevent implant failure and the incidence of implant-associated osteomyelitis.

Among the large variety of methods aimed at improving the interfacial properties of titanium implants (Giavaresi et al., 2008; De Nardo et al., 2012; LeGeros et al., 2016; Jäger et al., 2017; Zhao et al., 2018; Stewart et al., 2019), the generation of $TiO_2$ nanotubes (NTs) by anodization has recently attracted considerable attention with the objective to evolve from osteoconductive to osteoinductive implant performance (Farid, 2019).

$TiO_2$ nanotubes were first described in the nineties as having a "columnar honeycomb-like lattice," observed upon addition of fluoride ionic species to the electrolyte in the anodization of Ti and Ti6Al4V (Zwilling and Darque-Ceretti, 1997). More recently, titania nanotubes have gained interest as bone contact surfaces mainly for two characteristic properties: a unique topography, to support early osteoblast adhesion and proliferation (Iwata et al., 2017) and the possibility to

incorporate different classes of biologically-active molecules (either with osteogenic or antimicrobic activity) (Liu et al., 2016; Tao et al., 2019; Ion et al., 2020).

*In vitro* experiments on nanotube surfaces have shown improved cell adhesion, proliferation, and differentiation, as well as enhanced bone-forming abilities (Xia et al., 2012). *In vivo* experiments with screw- and disk-shaped implants have shown that nanotubes' surfaces increase direct bone/cell contact and improve osseointegration strength compared to their blasted counterpart (Bjursten et al., 2010; Sul, 2010; Li et al., 2019).

The effectiveness of different bioactive agents differently loaded into nanotubes, which includes the simple adsorption of growth factors (e.g., bone morphogenetic protein-2; Li et al., 2019) or antibiotic compounds, as well as coatings with biopolymers (Huang et al., 2014; Saha et al., 2019), was investigated. Gentamicin-loaded nanotubes, in particular, were used to deliver high doses of antibiotics locally and inhibit bacterial adhesion without systemic toxicity and with no significant effect on osteogenic differentiation (Lin et al., 2014).

Together with the potential benefits in terms of clinical response, the processes for the preparation of nanotubes is simple, scalable, reproducible (Maher et al., 2018), and applicable to relatively complex 3D geometries. $TiO_2$ nanotubes can be effectively grown on any pure titanium surface, and, in principle, to different titanium alloys' surfaces of implantable orthopedic devices. Sandblasted surfaces, as well as machined surfaces, are eligible substrates for their preparation by anodization. Furthermore, according to specific clinical needs, drug loading can be performed either during the implant production, or, technically, even during surgery.

The array of nanotubes obtained on titania through electrochemical anodization is highly controllable in dimensions by acting on applied voltage and processing time. To date, however, there appears to be no consensus on the optimal nanotube diameter to promote cellular adhesion and proliferation and effective drug delivery. Although nanotubes with an 100–150 nm diameter were shown to promote cell viability (Brammer et al., 2009; Zhang et al., 2015), apoptosis was also reported for diameters larger than 50 nm (Park et al., 2007, 2009; von Wilmowsky et al., 2009; Kulkarni et al., 2016). Similarly, different works (Popat et al., 2007; Lin et al., 2014) have studied the interaction between gentamicin-loaded nanotubes with bacteria, but little attention has been dedicated to the optimization of drug release in time.

Here, highly ordered and open top nanotubes with different diameters were prepared and loaded with gentamicin to evaluate the effect of dimensions on their "reservoir effect," loading capacity, and release profiles together with the effectiveness in inhibiting bacterial adhesion and growth and on cellular interaction.

# MATERIALS AND METHODS

If not otherwise specified, all reagents were purchased from Sigma-Aldrich and used without further purification.

## $TiO_2$ Nanotubes Synthesis

Titanium disks (12 mm Φ, 0.07 mm thick) were punched from cold-rolled grade 2 titanium foils (Titalia S.p.A.) with $R_a = 0.22 \pm 0.05$ μm and $R_{max} = 1.98 \pm 0.7$ μm. $TiO_2$ nanotubes (Roy et al., 2011; Regonini et al., 2013; Apolinario et al., 2014) were generated on the surface of titanium disks in a conventional two-electrode cell at room temperature. A platinum electrode was used as the cathode. Before anodization, Ti samples were sonicated for 5 min in acetone and then in Milli-Q water. After a preliminary evaluation on different ethylene glycol- (EG) based solutions and anodization times, a solution of $NH_4F$ 0.5% and 5.5 M Milli-Q water in EG and 3 h were, respectively chosen to generate nanotubes with different diameters by changing the anodization voltage.

After anodization, the samples were washed in ethanol for 1 h on a shaking platform to remove organic residuals, sonicated for 20 s in Milli-Q water to remove the nanograss structures generated during the process, and finally oven-dried at 37°C.

The morphology of $TiO_2$ nanotubes was observed using a scanning electron microscope (SEM Stereoscan 360, Cambridge Instruments). ImageJ image processing software (Schneider et al., 2012) was used to calculate the external and internal diameter of nanotubes on the acquired images.

## Antibiotic Loading

To load samples with antibiotic (Kulkarni et al., 2016; Stewart et al., 2019), 100 μl of gentamicin solution 5 mg/mL in PBS were pipetted on the surface of titanium disks to cover their entire surface and samples were allowed to dry in an orbital shaker at 50 rpm and 40°C. Deposition and evaporation steps were repeated four times in order to load each disk with a total of 2 mg of gentamicin. After the final drying, sample surfaces were rinsed by pipetting 1 mL of PBS to remove weakly bounded antibiotics.

## Drug Loading and Release

Gentamicin loading efficiency was calculated as:

$$\eta = \frac{(m_o - m_r)}{m_o}$$

Where η is the loading efficiency, $m_o$ is the amount of gentamicin in the loading solution, and $m_r$ is the antibiotic found in the rinsing solution.

Release kinetics of gentamicin was investigated at 37°C with loaded samples individually soaked in 500 μl of PBS solution, collected, and replaced at selected time-points up to 48 h.

The presence of gentamicin in the eluates was analyzed using a colorimetric assay (Schneider Frutos et al., 2000). Briefly, 2.5 g of o-phthaldialdehyde, 62.5 mL of methanol, and 3 mL of 2-mercaptoethanol were mixed in 560 mL 0.04 M sodium borate solution in deionized water and refrigerated for at least 24 h. Eluates from gentamicin loaded samples were mixed 1:1 with phthaldialdehyde solution and incubated for 30 min at room temperature, protected from light, to allow the formation of gentamicin o-phthaldialdehyde complexes that were spectrophotometrically read at 332 nm.

A calibration curve using six known gentamicin concentrations was used to calculate the actual amount of gentamicin released by nanotubes.

## Agar Diffusion Test

An agar diffusion test (Hudzicki, 2009) was performed to test the ability of nanotubular surfaces to inhibit bacterial growth using *Staphylococcus aureus* (NCTC 10788). Antibiotic-loaded samples were placed on the agar plate seeded with bacteria and incubated overnight at 37°C; the growth inhibition zone was then measured.

## Microbial Adhesion and Proliferation

A quantitative measure of antibacterial activity of gentamicin-loaded nanotubes samples were obtained by Colonies Forming Units (CFU) counting (Mathur et al., 2006) of *Staphylococcus aureus*. Ti samples were soaked in a suspension of $10^7$ bacteria in 1 mL of trypticase soy broth (TSB) and incubated at 37°C, then both planktonic and adhered cells were evaluated. Bacterial suspension incubated with no material was used as control.

To count planktonic bacteria, 50 µl of supernatant was collected after 7 and 24 h, plated on agar, and incubated at 37°C for 24 h. To count adherent bacteria, titanium disks were washed in PBS to eliminate non-adherent bacteria, inserted in a centrifuge tube with 2 mL of fresh PBS and 3 small glass spheres (∼ 3 mm diameter), and vortexed for 30 sec to ensure complete detachment of cells.

## Osteosarcoma Cells Adhesion and Proliferation

Cells' adhesion and proliferation on both loaded and unloaded NTs was evaluated using a human osteosarcoma cell model (Saos 2) and by evaluating cell adhesion and proliferation on samples after 24 and 72 h (von der Mark et al., 2009; Demetrescu et al., 2010; Pérez-Jorge et al., 2012).

To determine the number of viable and non−viable cells, 50 µl of Hoechst dye and 50 µl propidium iodide were diluted in 900 µl of medium and 60 µl of the resulting solution was added to each culture well. Images of stained samples were acquired under a fluorescence microscope to count live (blue), apoptotic (brighter blue), and dead (red) cells.

Phalloidin staining was used to evaluate cell morphology. Briefly, 80 µl of 3.7% paraformaldehyde solution in PBS was added in each well to fix the samples. After soaking for 5 min in 1% Triton X solution in PBS to permeabilize the cell membrane, 100 µl phalloidin solution (1:100 in PBS) was added and incubated for 1 h at room temperature.

## Statistical Analysis

All statistical analyses were performed using GraphPad Prism 7. Groups were compared using one-way ANOVA and *post-hoc* tests after verification of data normality. $P < 0.05$ were considered statistically significant.

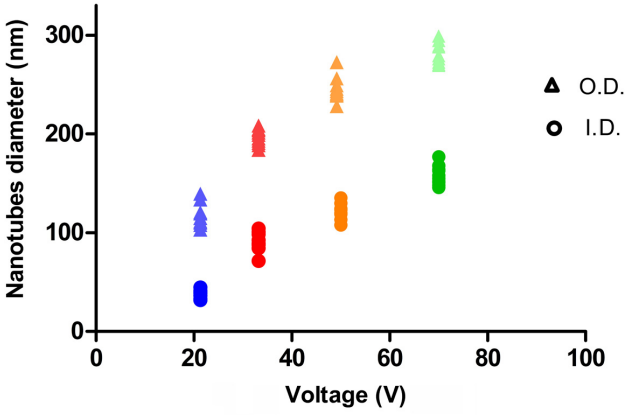


**FIGURE 1 |** Diameter vs. voltage relationship in NTs' anodization.

# RESULTS

## Production and Characterization of $TiO_2$ Nanotubes

The relation between anodization voltage and nanotube outer (O.D) and inner diameter (I.D.) are illustrated in **Figure 1** and were consistent with previous findings (Lin et al., 2014). However, in the chosen conditions, a voltage threshold of 10 V was found, as no formation of nanotubes could be observed below this value.

As can be seen in **Figure 2**, an array of highly ordered nanotubes with a well-defined and open top morphology is found on the titanium surface.

To build an experimental group on a representatively extended range of diameters, the voltage values in **Table 1** were chosen for experimental samples of NTs' preparation. For each voltage, the corresponding NTs' diameters, lengths, and the designations used hereafter are indicated. If the length of nanotubes is considered, a reduction in nanotube depth is observed at lower voltages.

## Drug Loading and Release

The loading efficiency of gentamicin calculated based on the quantity of antibiotic in the rinsing solution is reported in **Table 2**. As can be observed, similar values were generally found, but bigger nanotubes (NT160) appeared to have a slightly higher loading efficiency compared to smaller ones.

When the *in vitro* release was considered (**Figure 3**), a significant fraction of loaded gentamicin was found to be released from NTs after 1 h (about 30%). After this initial burst, the antibiotic release decreased slowly to become undetectable after 48 h.

A comparatively higher amount of gentamicin was released from larger nanotubes, but this is only partially attributable to the higher loading efficiency. Release from larger nanotubes was, in fact, notably faster between 1 and 2 h.

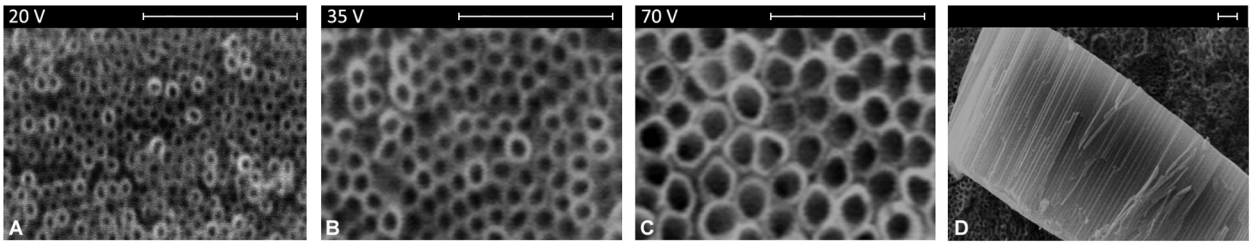


**FIGURE 2 |** Surface morphology of nanotubes' array obtained at different voltages **(A–C)** and section view **(D)**. Scale bar = 1 μm.

**TABLE 1 |** $TiO_2$ nanotubes' diameter, length, and sample designation.

| Voltage (V) | I.D (nm) | O.D (nm) | Length (μm) | Designation |
|---|---|---|---|---|
| 20 | 31.4 ± 1.2 | 101.9 ± 3.3 | 7.67 ± 0.02 | NT30 |
| 35 | 78.7 ± 2.6 | 168.2 ± 2.1 | 8.56 ± 0.03 | NT80 |
| 70 | 158.2 ± 3.1 | 257.1 ± 3.0 | 10.26 ± 0.04 | NT160 |

**TABLE 2 |** Estimated loading efficiency of gentamicin in $TiO_2$ nanotubes.

| Samples | Loading efficiency (%) |
|---|---|
| NT30/G | 60.6 |
| NT80/G | 61.9 |
| NT160/G | 65.1 |

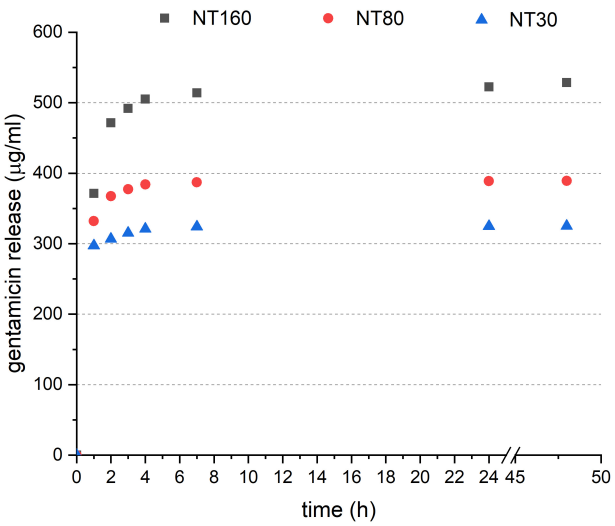


**FIGURE 3 |** Cumulative gentamicin release from loaded NTs.

## Agar Diffusion Test

After incubation at 37°C, an inhibition area was observed for all loaded NT samples on agar plates (**Figure 4**). All gentamicin-loaded disks were characterized by an inhibition zone with a diameter of about 30 mm, surrounding samples, with no statistically significant difference between the three different NTs' dimensions. As reasonably expected, untreated Ti samples did not show any detectable inhibition zone.

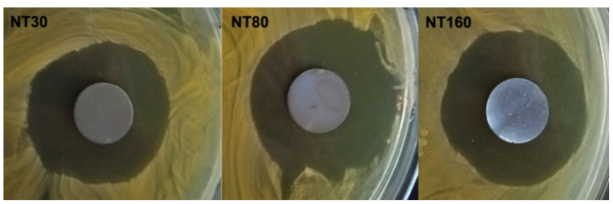


**FIGURE 4 |** Representative images of inhibition zones in Agar diffusion test for gentamicin-loaded samples.

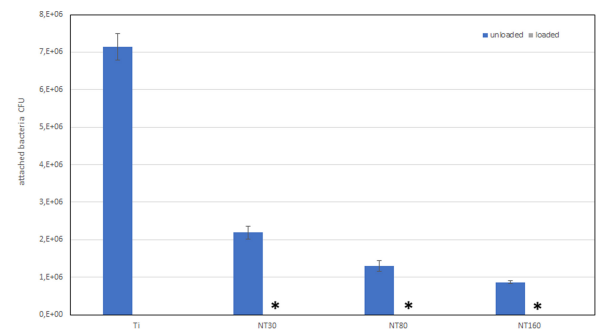


**FIGURE 5 |** Number of adhered bacteria on Ti surface after 24 h incubation. * indicates that no bacteria were detected.

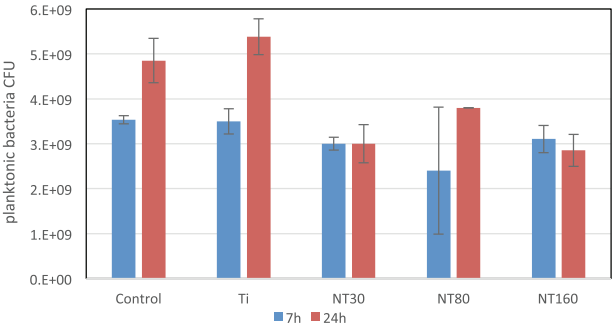


**FIGURE 6 |** Bacteria number in planktonic form at 7 and 24 h.

## Bacterial Adhesion and Proliferation

The number of adhered bacteria for gentamicin loaded and unloaded Ti samples after 24 h incubation is shown in **Figure 5**.

Compared to untreated Ti disks, nanotube samples show a considerable reduction in bacterial adhesion even without gentamicin. When gentamicin was loaded, bacteria could not be detected.

Interestingly, a significant difference in the number of adhered bacteria was found among nanotube diameters size. Specifically, nanotubes with larger diameters were found to allow a lower bacterial adhesion compared to smaller NTs.

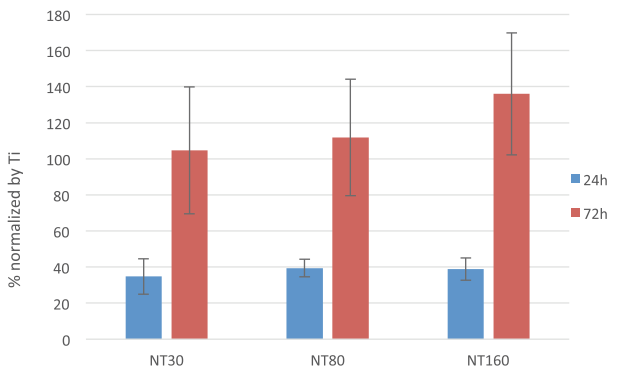


**FIGURE 7 |** Cell density after 24 and 72 h.

When planktonic bacteria were considered (**Figure 6**), a comparable CFU count was observed for all samples after 7 h. Conversely, after 24 h a statistically significant difference in bacteria number among untreated Ti and all nanotubes samples was observed, with an average 40% reduction. For planktonic bacteria, however, no significant differences were noticed among the different nanotube diameters size.

## Cells Adhesion and Proliferation

The normalized number of live cells on the surface of NTs samples after 24 and 72 h are reported for unloaded samples in **Figure 7**. When gentamicin – loaded samples were considered, superimposable results were found (data not shown). In both cases, statistical analysis did not evidence any significant differences in cell number among NTs with different diameter sizes.

Interestingly, initial cell density is notably lower on NTs samples compared to the control (40% less in average), but the number of cells increases comparatively faster on NTs and the number of cells reaches and overcomes the values on control after 72 h.

Differences in cell morphology were instead observed as a result of change in diameter (**Figure 8**) and phalloidin staining revealed more spindle-shaped cells on nanotubes with a smaller diameter, whereas more rounded cells were observed for larger NTs.

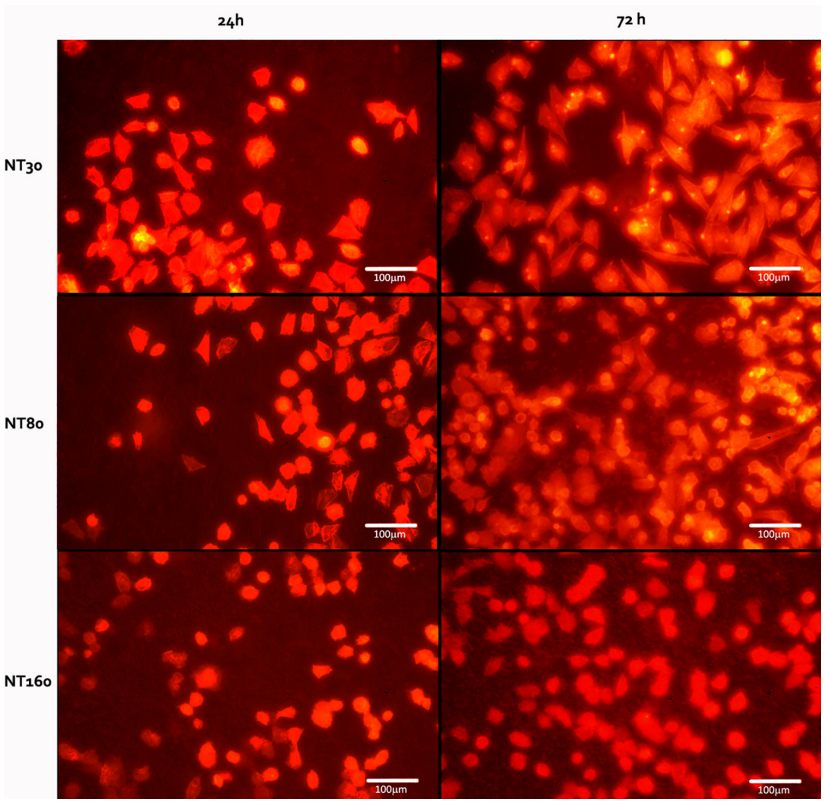


**FIGURE 8 |** Representative images of the Saos 2 cells on the nanotube samples (NT30, NT80, and NT160) after 24 and 72 h.

## DISCUSSION AND CONCLUSION

To act as an effective drug reservoir and to offer a high number of anchoring sites for cells, $TiO_2$ nanotube arrays should possess an open top morphology. In this regard, the protocol for NTs preparation optimized in this work appeared extremely effective. In our experience, the balance of water content and fluoride concentration was critical for obtaining nanotubes with an almost 100% open top while containing the process duration. A higher water content, in fact, results in a more open top structure, but generally requires longer treatment times, while time reduction can be obtained by increasing fluoride content in the solution (the morphologies of NTs' optimization can be found in **Supplementary Material**).

By changing the anodization voltage, NTs' diameter can be easily controlled, as a consistent dependence with applied voltage exists and the size of resulting structures is highly predictable.

The reservoir capability of NTs was confirmed by the observed release of loaded gentamicin for up to 48 h. After this time interval, the release quantity was too small to be detected by our assay. However, based on the cumulative release, about half the drug loaded is still present in the nanotubes and is potentially effective for a longer time.

In this work we specifically focused on the effect of nanotubes' diameters and we tried to analyze the largest range possible to evaluate its effect on drug release and cell adhesion. The diameter of nanotubes was confirmed to be a very relevant variable for both drug release and cell/bacteria interaction. Bigger nanotubes (NT160) were capable of accommodating a comparatively higher quantity of antibiotics than smaller ones, but faster release was observed. On the other hand, smaller nanotubes have a higher available surface, are more likely to withhold the antibiotic molecules more effectively, and showed a slightly slower release.

When Ti samples were incubated with bacteria, no adherent cells were found for all gentamicin samples, to indicate that the quantity of loaded antibiotics is sufficient for an effective antibacterial action. Interestingly, a significant reduction of bacterial adhesion was also observed for unloaded samples, but this phenomenon can possibly be explained by the presence of residual fluoride ions (Ercan et al., 2011; Anitha et al., 2015). The number of adhered bacteria was significantly lower for larger nanotubes (160 nm), and this can also be related to the fact that smaller NTs stimulate bacterial cells to produce pili and attach to the surface (Ercan et al., 2011).

When osteosarcoma cells were seeded on the sample surface, although no statistical difference was observed among NTs with different nanotubes, samples with larger nanotubes appeared to induce cellular apoptosis more than smaller ones. A higher cell compatibility of these latter NTs was also confirmed by the spindle-like morphology observed on their surfaces. This more favorable behavior can be explained with the higher number of anchoring site provided (Roy et al., 2011), as small-sized NTs can promote cell growth and differentiation by supporting a higher density of integrin focal contacts (Zhang et al., 2015).

When using gentamicin, many authors report the use of very high doses (up to 20-fold the recommended concentrations) without appreciable side effect on cells *in vitro* (Schafer et al., 1972; Sigma-Aldrich, 2002; Kovacikanton et al., 2017). To confirm these results, here no difference in the cell viability between loaded and unloaded samples was observed. However, the chosen gentamicin quantity appears adequate to eliminate the bacteria.

Overall, our results confirm that anodization of titanium substrates to prepare $TiO_2$ nanotubes is an extremely favorable surface treatment and has the potential to both improve osseointegration of orthopedic prosthesis and prevent infection-related failures. Within the tested range, smaller NTs appear as the more promising option for further investigation, as they offer effective antibacterial action together with a more favorable cell interaction.

## DATA AVAILABILITY STATEMENT

All datasets generated for this study are included in the article/**Supplementary Material**.

## AUTHOR CONTRIBUTIONS

RC contributed to the conception and design of the study. LD, VP, and MM performed the experiments and wrote the first draft of the manuscript. MS performed the *in vitro* tests. All authors contributed to manuscript revision, read and approved the submitted version.

## SUPPLEMENTARY MATERIAL

The Supplementary Material for this article can be found online at: https://www.frontiersin.org/articles/10.3389/fmats.2020.00233/full#supplementary-material

## REFERENCES

Anitha, V. C., Lee, J. H., Lee, J., Narayan Banerjee, A., Woo Joo, S., and Ki Min, B. (2015). Biofilm formation on a TiO2 nanotube with controlled pore diameter and surface wettability. *Nanotechnology* 26:65102.

Apolinario, A., Sousa, C. T., Ventura, J., Costa, J. D., Leitao, D. C., Moreira, J. M., et al. (2014). The role of the Ti surface roughness in the self-ordering of TiO 2 nanotubes: a detailed study of the growth mechanism. *J. Mater. Chem.* 2, 9067–9078. doi: 10.1039/c4ta00871e

Bjursten, L. M., Rasmusson, L., Oh, S., Smith, G. C., Brammer, K. S., and Jin, S. (2010). Titanium dioxide nanotubes enhance bone bonding in vivo. *J. Biomed. Mater. Res. Part A.* 92, 1218–1224.

Brammer, K. S., Oh, S., Cobb, C. J., Bjursten, L. M., van der Heyde, H., and Jin, S. (2009). Improved bone-forming functionality on diameter-controlled TiO2 nanotube surface. *Acta Biomat.* 5, 3215–3223. doi: 10.1016/j.actbio.2009.05.008

De Nardo, L., Altomare, L., Del Curto, B., Cigada, A., and Draghi, L. (2012). Electrochemical surface modifications of titanium and titanium alloys for

biomedical applications. *Coat. Biomed. Appl.* 2012, 106–142. doi: 10.1533/9780857093677.1.106

Demetrescu, I., Pirvu, C., and Mitran, V. (2010). Effect of nano-topographical features of Ti/TiO2 electrode surface on cell response and electrochemical stability in artificial saliva. *Bioelectrochemistry* 79, 122–129. doi: 10.1016/j.bioelechem.2010.02.001

Ercan, B., Taylor, E., Alpaslan, E., and Webster, T. J. (2011). Diameter of titanium nanotubes influences anti- bacterial efficacy. *Nanotechnology* 22:295102. doi: 10.1088/0957-4484/22/29/295102

Farid, S. B. H. (2019). Osteoinduction, osteoconduction, and osseointegration. *Bioceramics Mater. Sci. Engin.* 10, S96–S101.

Giavaresi, G., Chiesa, R., Fini, M., and Sandrini, E. (2008). Effect of a multiphasic anodic spark deposition coating on the improvement of implant osseointegration in the osteopenic trabecular bone of sheep. *Internat. J. Oral Maxillofacial Impl.* 23:659-68.

Huang, P., Wang, J., Lai, S., Liu, F., Ni, N., Cao, Q., et al. (2014). Surface modified titania nanotubes containing anti-bacterial drugs for controlled delivery nanosystems with high bioactivity. *J. Mater. Chem. B* 2, 8616–8625. doi: 10.1039/c4tb01281j

Hudzicki, J. (2009). *Kirby-Bauer disk diffusion susceptibility test protocol*. Washington, DC : American Society for Microbiology, 1–14.

Ion, R., Necula, M. G., Mazare, A., Mitran, V., Neacsu, P., Schmuki, P., et al. (2020). Drug Delivery Systems Based on Titania Nanotubes and Active Agents for Enhanced Osseointegration of Bone Implants. *Curr. Med. Chem.* 27, 854–902. doi: 10.2174/0929867326666190726123229

Iwata, N., Nozaki, K., Horiuchi, N., Yamashita, K., Tsutsumi, Y., Miura, H., et al. (2017). Effects of controlled micro-/nanosurfaces on osteoblast proliferation. *J. Biomed. Mater. Res. Part A* 105, 2589–2596. doi: 10.1002/jbm.a.36118

Jäger, M., Jennissen, H., Dittrich, F., Fischer, A., and Köhling, H. (2017). Antimicrobial and osseointegration properties of nanostructured titanium orthopaedic implants. *Materials* 10:1302. doi: 10.3390/ma10111302

Kovacikanton, A., Eva, T., Diana, F., Peter, C., Eva, K., Katarina, Z., et al. (2017). In Vitro Assessment of Gentamicin Cytotoxicity on the Selected Mammalian Cell Line (Vero cells). *Adv. Res. Life Sci* 1, 111–116. doi: 10.1515/arls-2017-0018

Kulkarni, M., Mazare, A., Schmuki, P., and Iglic, A. (2016). Influence of anodization parameters on morphology of TiO2 nanostructured surfaces. *Adv. Mater. Lett.* 7, 23–28. doi: 10.5185/amlett.2016.6156

LeGeros, R. Z., Coelho, P. G., Holmes, D., Dimaano, F., and LeGeros, J. P. (2016). "Orthopedic and dental implant surfaces and coatings," in *Biological and Biomedical Coatings Handbook*. S. Zhang Florida: CRC Press.

Li, Y., Song, Y., Ma, A., and Li, C. (2019). Surface Immobilization of TiO2 Nanotubes with Bone Morphogenetic Protein-2 Synergistically Enhances Initial Preosteoblast Adhesion and Osseointegration. *BioMed. Res. Internat.* 2019:5697250.

Lin, W.-T., Tan, H.-L., Duan, Z.-L., Yue, B., Ma, R., He, G., et al. (2014). Inhibited bacterial biofilm formation and improved osteogenic activity on gentamicin-loaded titania nanotubes with various diameters. *Int. J. Nanomed.* 9, 1215–1230. doi: 10.2147/ijn.s57875

Liu, X., Zhang, Y., Li, S., Wang, Y., Sun, T., Li, Z., et al. (2016). Study of a new bone-targeting titanium implant–bone interface. *Internat. J. Nanomed.* 11, 6307–6324. doi: 10.2147/ijn.s119520

Maher, A. S., Mazinani, A., Barati, M. R., and Losic, D. (2018). Engineered titanium implants for localized drug delivery: recent advances and perspectives of Titania nanotubes arrays. *Exp.Ert Opin. Drug Del.* 15, 1021–1037. doi: 10.1080/17425247.2018.1517743

Mathur, A. R. T., Singhal, S., Khan, S., Upadhyay, D. J., and Fatma, T. (2006). Detection of biofilm formation among the clinical isolates of staphylococci: An evaluation of three different screening methods. *Indian J. Med. Microbiol.* 24, 25–29. doi: 10.4103/0255-0857.19890

Park, J., Bauer, S., Schlegel, K. A., Neukam, F. W., Der Von, Mark, K., et al. (2009). TiO2 nanotube surfaces: 15 nm - an optimal length scale of surface topography for cell adhesion and differentiation. *Small* 5, 666–671. doi: 10.1002/smll.200801476

Park, J., Bauer, S., Von Der, Mark, K., and Schmuki, P. (2007). Nanosize and vitality: TiO2 nanotube diameter directs cell fate. *Nano. Lett.* 7, 1686-91.

Pérez-Jorge, C., Conde, A., Arenas, M. A., Pérez-Tanoira, R., Matykina, E., de Damborenea, J. J., et al. (2012). In vitro assessment of Staphylococcus epidermidis and Staphylococcus aureus adhesion on TiO 2 nanotubes on Ti-6Al-4V alloy. *J. Biomed. Mater. Res. Part A* 100, 1696–1705. doi: 10.1002/jbm.a.34118

Popat, K. C., Eltgroth, M., LaTempa, T. J., Grimes, C. A., and Desai, T. A. (2007). Decreased Staphylococcus epidermis adhesion and increased osteoblast functionality on antibiotic-loaded titania nanotubes. *Biomaterials* 28, 4880–4888. doi: 10.1016/j.biomaterials.2007.07.037

Regonini, D., Bowen, C. R., Jaroenworaluck, A., and Stevens, R. (2013). A review of growth mechanism, structure and crystallinity of anodized TiO 2 nanotubes. *Mater. Sci. Eng. R* 74, 377–406. doi: 10.1016/j.mser.2013.10.001

Roy, P., Berger, S., and Schmuki, P. (2011). TiO2 nanotubes: Synthesis and applications. *Angew. Chem. Int* 50, 2904–2939. doi: 10.1002/anie.201001374

Saha, S., Pramanik, K., and Biswas, A. (2019). Silk fibroin coated TiO2 nanotubes for improved osteogenic property of Ti6Al4V bone implants. *Mater. Sci. Engin. C* 105:109982. doi: 10.1016/j.msec.2019.109982

Schafer, T., Pascale, A., Shimonaski, G., and Came, P. E. (1972). Evaluation of gentamicin for use in virology and tissue culture. *Appl. Microbiol* 23, 565–570. doi: 10.1128/aem.23.3.565-570.1972

Schneider, C. A., Rasband, W. S., and Eliceiri, K. W. (2012). NIH Image to ImageJ: 25 years of image analysis. *Nat. Methods* 9, 671–675. doi: 10.1038/nmeth.2089

Schneider Frutos, P. C., Díez Peña, E., Barrales-Rienda, J. M., and Frutos, G. (2000). Validation and in vitro characterization of antibiotic-loaded bone cement release. *Int. J. Pharm.* 209, 15–26. doi: 10.1016/s0378-5173(00)00520-2

Sigma-Aldrich (2002). *Gentamicin solution Cell Cultured Tested*. St. Louis: Sigma-Aldrich.

Stewart, C., Akhavan, B., Wise, S. G., and Bilek, M. M. (2019). A review of biomimetic surface functionalization for bone-integrating orthopedic implants: Mechanisms, current approaches, and future directions. *Progr. Mater. Sci.* 106:100588. doi: 10.1016/j.pmatsci.2019.100588

Sul, Y. T. (2010). Electrochemical growth behavior, surface properties, and enhanced in vivo bone response of TiO2 nanotubes on microstructured surfaces of blasted, screw-shaped titanium implants. *Internat. J. Nanomed.* 5, 87–100. doi: 10.2147/ijn.s8012

Tao, B., Deng, Y., Song, L., Ma, W., Qian, Y., Lin, C., et al. (2019). BMP2-loaded titania nanotubes coating with pH-responsive multilayers for bacterial infections inhibition and osteogenic activity improvement. *Colloids Surfaces B Biointer.* 177, 242–252. doi: 10.1016/j.colsurfb.2019.02.014

von, der Mark, K., Bauer, S., Park, J., and Schmuki, P. (2009). Another look at 'Stem cell fate dictated solely by altered nanotube dimension. *Proc. Natl. Acad. Sci* 106, E60.

von Wilmowsky, C., Bauer, S., Lutz, R., Meisel, M., Neukam, F. W., Toyoshima, T., et al. (2009). In Vivo Evaluation of Anodic TiO2 Nanotubes; An Experimental Study in the Pig. *J. Biomed. Mater. Res. Part B Appl. Biomater* 89, 165–171.

Xia, L., Feng, B., Wang, P., Ding, S., Liu, Z., Zhou, J., et al. (2012). In vitro and in vivo studies of surface-structured implants for bone formation. *Internat. J. Nanomed.* 7, 4873–4881. doi: 10.2147/ijn.s29496

Zhang, R., Wu, H., Ni, J., Zhao, C., Chen, Y., Zheng, C., et al. (2015). Guided proliferation and bone- forming functionality on highly ordered large diameter TiO2 nanotube arrays, Mater. *Sci. Eng.* 53, 272–279. doi: 10.1016/j.msec.2015.04.046

Zhao, H., Huang, Y., Zhang, W., Guo, Q., Cui, W., Sun, Z., et al. (2018). Mussel-inspired peptide coatings on titanium implant to improve osseointegration in osteoporotic condition. *ACS Biomater. Sci. Engin.* 4, 2505–2515. doi: 10.1021/acsbiomaterials.8b00261

Zwilling, V., and Darque-Ceretti, E. (1997). Characterization of porous and compact oxide films on titanium and Ti-6A1-4V Annales de Chimie: Science des Materiaux. *J. Global.* 22, 481–493.

**Conflict of Interest:** The authors declare that the research was conducted in the absence of any commercial or financial relationships that could be construed as a potential conflict of interest.

# Advantages of publishing in Frontiers

**OPEN ACCESS**
Articles are free to read for greatest visibility and readership


**FAST PUBLICATION**
Around 90 days from submission to decision

**HIGH QUALITY PEER-REVIEW**
Rigorous, collaborative, and constructive peer-review

**TRANSPARENT PEER-REVIEW**
Editors and reviewers acknowledged by name on published articles

**Frontiers**
Avenue du Tribunal-Fédéral 34
1005 Lausanne | Switzerland

**Visit us:** www.frontiersin.org
**Contact us:** info@frontiersin.org | +41 21 510 17 00

**REPRODUCIBILITY OF RESEARCH**
Support open data and methods to enhance research reproducibility

**DIGITAL PUBLISHING**
Articles designed for optimal readership across devices


**FOLLOW US**
@frontiersin

**IMPACT METRICS**
Advanced article metrics track visibility across digital media

**EXTENSIVE PROMOTION**
Marketing and promotion of impactful research

**LOOP RESEARCH NETWORK**
Our network increases your article's readership